

Lecture Notes in Mechanical Engineering

Pawan Kumar Rakesh
Apurbba Kumar Sharma
Inderdeep Singh *Editors*

Advances in Engineering Design

Select Proceedings of ICOIED 2020

 Springer

Lecture Notes in Mechanical Engineering

Series Editors

Francisco Cavas-Martínez, Departamento de Estructuras, Universidad Politécnica de Cartagena, Cartagena, Murcia, Spain

Fakher Chaari, National School of Engineers, University of Sfax, Sfax, Tunisia

Francesco Gherardini, Dipartimento di Ingegneria, Università di Modena e Reggio Emilia, Modena, Italy

Mohamed Haddar, National School of Engineers of Sfax (ENIS), Sfax, Tunisia

Vitalii Ivanov, Department of Manufacturing Engineering Machine and Tools, Sumy State University, Sumy, Ukraine

Young W. Kwon, Department of Manufacturing Engineering and Aerospace Engineering, Graduate School of Engineering and Applied Science, Monterey, CA, USA

Justyna Trojanowska, Poznan University of Technology, Poznan, Poland

Lecture Notes in Mechanical Engineering (LNME) publishes the latest developments in Mechanical Engineering—quickly, informally and with high quality. Original research reported in proceedings and post-proceedings represents the core of LNME. Volumes published in LNME embrace all aspects, subfields and new challenges of mechanical engineering. Topics in the series include:

- Engineering Design
- Machinery and Machine Elements
- Mechanical Structures and Stress Analysis
- Automotive Engineering
- Engine Technology
- Aerospace Technology and Astronautics
- Nanotechnology and Microengineering
- Control, Robotics, Mechatronics
- MEMS
- Theoretical and Applied Mechanics
- Dynamical Systems, Control
- Fluid Mechanics
- Engineering Thermodynamics, Heat and Mass Transfer
- Manufacturing
- Precision Engineering, Instrumentation, Measurement
- Materials Engineering
- Tribology and Surface Technology

To submit a proposal or request further information, please contact the Springer Editor of your location:

China: Dr. Mengchu Huang at mengchu.huang@springer.com

India: Priya Vyas at priya.vyas@springer.com

Rest of Asia, Australia, New Zealand: Swati Meherishi
at swati.meherishi@springer.com

All other countries: Dr. Leontina Di Cecco at Leontina.dicecco@springer.com

To submit a proposal for a monograph, please check our Springer Tracts in Mechanical Engineering at <http://www.springer.com/series/11693> or contact Leontina.dicecco@springer.com

Indexed by SCOPUS.

All books published in the series are submitted for consideration in Web of Science.

More information about this series at <http://www.springer.com/series/11236>

Pawan Kumar Rakesh · Apurbba Kumar Sharma ·
Inderdeep Singh
Editors

Advances in Engineering Design

Select Proceedings of ICOIED 2020

Editors

Pawan Kumar Rakesh
Department of Mechanical Engineering
National Institute of Technology
Uttarakhand
Srinagar, Uttarakhand, India

Apurbba Kumar Sharma
Indian Institute of Technology Roorkee
Roorkee, Uttarakhand, India

Inderdeep Singh
Indian Institute of Technology Roorkee
Roorkee, Uttarakhand, India

ISSN 2195-4356 ISSN 2195-4364 (electronic)
Lecture Notes in Mechanical Engineering
ISBN 978-981-33-4017-6 ISBN 978-981-33-4018-3 (eBook)
<https://doi.org/10.1007/978-981-33-4018-3>

© The Editor(s) (if applicable) and The Author(s), under exclusive license to Springer Nature Singapore Pte Ltd. 2021

This work is subject to copyright. All rights are solely and exclusively licensed by the Publisher, whether the whole or part of the material is concerned, specifically the rights of translation, reprinting, reuse of illustrations, recitation, broadcasting, reproduction on microfilms or in any other physical way, and transmission or information storage and retrieval, electronic adaptation, computer software, or by similar or dissimilar methodology now known or hereafter developed.

The use of general descriptive names, registered names, trademarks, service marks, etc. in this publication does not imply, even in the absence of a specific statement, that such names are exempt from the relevant protective laws and regulations and therefore free for general use.

The publisher, the authors and the editors are safe to assume that the advice and information in this book are believed to be true and accurate at the date of publication. Neither the publisher nor the authors or the editors give a warranty, expressed or implied, with respect to the material contained herein or for any errors or omissions that may have been made. The publisher remains neutral with regard to jurisdictional claims in published maps and institutional affiliations.

This Springer imprint is published by the registered company Springer Nature Singapore Pte Ltd. The registered company address is: 152 Beach Road, #21-01/04 Gateway East, Singapore 189721, Singapore

Committees

Organizing Committee

Prof. Ajit Kumar Chaturvedi, Director, IIT Roorkee
Prof. Shyam Lal Soni, Director, NIT Uttarakhand
Er. Narendra Singh, President, The Institution of Engineers, India

Patrons

Prof. Apurbba Kumar Sharma, IIT Roorkee
Prof. Rajat Agarawal, IIT Roorkee
Prof. Inderdeep Singh, IIT Roorkee
Er. Jagroop Singh, FIE, Chairman, MCDB, IEI
Er. M. P. Jain, FIE Member, IEI, UKSC

Chairmans

Dr. Hariharan Muthusamy, NIT Uttarakhand
Dr. Dharmendra Tripathi, NIT Uttarakhand
Dr. Pawan Kumar Rakesh, NIT Uttarakhand
Dr. Rakesh Kumar Mishra, NIT Uttarakhand
Dr. Vinod Singh Yadav, NIT Uttarakhand

Conveners

Er. A. K. Dinkar, Chairman, IEI, UKSC
 Er. S. C. Goyal, FIE, E C Member IEI, UKSC
 Er. Ambrish Kumar, FIE, E C Member IEI, UKSC
 Er. A. C. Goel, FIE, E C Member IEI, UKSC
 Er. A. B. Garg, FIE, E C Member IEI, UKSC
 Er. D. C. Gupta, FIE, E C Member IEI, UKSC
 Er. Dharm Chandra, Hony. Secy., IEI, UKSC
 Er. S. C. Chauhan, FIE, E C Member, MCDB, IEI, UKSC
 Er. Amit Agarwal, FIE, E C Member, CPDB IEI, UKSC

Organizing Secretaries

Dr. Aditya Kumar Anupam, NIT Uttarakhand
 Dr. Anshul Sharma, NIT Uttarakhand
 Dr. Nitin Kumar, NIT Uttarakhand
 Dr. Mahiraj Singh Rawat, NIT Uttarakhand
 Dr. Yogesh Kumar Prajapati, NIT Uttarakhand
 Dr. Vikas Kukshal, NIT Uttarakhand
 Dr. Dungali Sreehari, NIT Uttarakhand
 Dr. Apurba Mandal, NIT Uttarakhand

Technical Advisory Committee

Er. Narendra Singh, Council Member, IEI
 Er. A. S. Bakshi, Vice President, IEI
 Dr. S. Bhaumik, Vice President, IEI
 Er. R. V. S. Chauhan, Immediate Past Chairman, IEI, UKSC
 Er. Ram Shankar, FIE, E C Member, MCDB, IEI, UKSC
 Er. V. K. Saxena, Past Honorary Secretary, IEI, UKSC
 Er. Sanjay Mathur, FIE, Chairman, IEI, Pantnagar
 Er. Achal Kumar Mittal, FIE, Chairman, IEI, Roorkee
 Er. S. M. Saxena, FIE, E C Member IEI, UKSC
 Er. J. P. Tomar, FIE, E C Member IEI, UKSC
 Er. J. C. Belwal, FIE, E C Member IEI, UKSC
 Er. K. L. Goyal, FIE, E C Member IEI, UKSC
 Er. M. K. Tayal, FIE, E C Member IEI, UKSC
 Er. Neeta Mittal, MIE, E C Member IEI, UKSC
 Er. R. P. Jamloki, FIE, E C Member IEI, UKSC

Er. C. P. Sharma, FIE, E C Member IEI, UKSC
Er. H. P. Thapliyal, FIE, E C Member IEI, UKSC
Er. V. C. Purohit, FIE, E C Member IEI, UKSC
Er. Krishna Kumar, FIE, E C Member IEI, UKSC
Er. Ram Shankar, FIE, E C Member, MCDB, IEI, UKSC
Er. H. K. Upreti, FIE, E C Member IEI, UKSC
Er. Bhajan Singh, FIE, E C Member IEI, UKSC
Er. Devendra Singh, FIE, E C Member IEI, UKSC
Er. P. K. Goel, FIE, E C Member IEI, UKSC
Er. Prithipal Singh, AMIE, E C Member IEI, UKSC
Er. S. C. Bhasin, FIE, E C Member IEI, UKSC
Er. S. P. Singh, FIE, E C Member IEI, UKSC
Dr. Gurinder Singh Brar, NIT Uttarakhand
Er. Rakesh Kumar, FIE, E C Member IEI, UKSC
Er. Hemashwari Sharma, FIE, E C Member IEI, UKSC
Dr. Lalta Prasad, NIT Uttarakhand
Dr. Renu Bhadola Dangwal, NIT Uttarakhand
Dr. Tajinder Singh Arora, NIT Uttarakhand
Dr. Kranti Jain, NIT Uttarakhand
Dr. Hardeep Kumar, NIT Uttarakhand
Dr. Pankaj Kandwal, NIT Uttarakhand
Dr. Nitin Sharma, NIT Uttarakhand
Dr. Krishan Kumar, NIT Uttarakhand
Dr. Sourav Bose, NIT Uttarakhand

International Advisory Committee

Prof. Chris Berndt, Director SEM Australia
Prof. Negel Garrow, Sheffield, SIWB UK
Prof. Manoj Gupta, Engineering Drive, NUS Singapore
Prof. Kemal Polat, BAIB University, Turkey
Prof. Lee Yoot Khuan, UiTM Shah Alam, Malaysia
Prof. U. Rajendra Acharya, Ngee Ann Polytechnic, Singapore
Prof. Om Prakash Yadav, NDS University, North Dakota
Prof. Ernst Wintner, Vienna University of Technology, Austria
Prof. J. Paulo Davim, University of Aveiro, Aveiro
Prof. Xun Chen, Liverpool John Moores University, UK

National Advisory Committee

Dr. Ram Bilas Pachori, Indian Institute of Technology Indore, Simrol
Dr. M. L. Meena, Malaviya National Institute of Technology Jaipur
Dr. Dheeraj K. Khatod, Indian Institute of Technology Roorkee
Dr. Sheela Tiwari, National Institute of Technology Jalandhar
Prof. Indra Vir Singh, Indian Institute of Technology Roorkee
Prof. Satinder Paul Singh, Indian Institute of Technology Delhi
Prof. Dilip Sharma, Malaviya National Institute of Technology Jaipur
Prof. Arun B. Samaddar, JIS Group
Prof. Puneet Mahajan, Indian Institute of Technology Delhi
Dr. Abhishek Singh, National Institute of Technology Patna
Prof. Manabendra Pathak, Indian Institute of Technology Patna
Prof. Amar Patnaik, Malaviya National Institute of Technology Jaipur
Dr. Shelly Vadhera, National Institute of Technology Kurukshetra
Prof. R. K. Garg, National Institute of Technology Jalandhar
Dr. Kishore Debnath, National Institute of Technology Meghalaya
Prof. Ashok Pandey, CSIR-Indian Institute of Toxicology Research, Lucknow
Prof. Sriman Kumar Bhattacharyya, Indian Institute of Technology Kharagpur
Prof. J. Jerald, National Institute of Technology Trichy
Dr. Kalyan Kumar Singh, Indian Institute of Technology (ISM) Dhanbad
Dr. Devesh Punera, Indian Institute of Technology Bhubaneswar
Prof. Avinash Kumar Agarwal, Indian Institute of Technology Kanpur
Dr. Anil Birru, National Institute of Technology Manipur
Dr. Pavan Kumar Kankar, Indian Institute of Technology Indore

Keynote Speakers

Prof. Anantharajan Senthil Kumar, NUS Singapore
Dr. Tej Singh, Eotvos Lorand University, Hungary
Dr. Deepak Joshi, Indian Institute of Technology Delhi (IITD), India
Dr. Amar Patnaik, Malaviya National Institute of Technology Jaipur, Rajasthan, India
Prof. Gaurav Raheja, Indian Institute of Technology Roorkee, Uttarakhand, India
Prof. S. P. Singh, Indian Institute of Technology Delhi
Prof. Subir Das, National Institute of Design, Ahmedabad, India
Dr. Sarbjit Singh, Punjab Engineering College, Chandigarh, India
Prof. Amar Jain, CSIR IIP Dehradun

Preface

The book titled *Advances in Engineering Design* comprises papers presented at *International Conference on Innovative Engineering Design 2020 (ICOIED 2020)*, which was organized at The Institution of Engineers, Dehradun, during 18–20 January 2020. This book aims to provide an innovative approach in the field of product design which is very useful for the upliftment of society and contribution to the global economy. The Ministry of Human Resource Development (MHRD), New Delhi, under the scheme National Initiative for Design Innovation has established 20 **Design Innovation Centers (DIC)** in the country, and Indian Institute of Technology Roorkee (IIT Roorkee) is one of them. IIT Roorkee is a hub, and National Institute of Technology Uttarakhand (NIT Uttarakhand) is one of the spoke partners. Both the centres have taken keen interest to organize this international conference to promote the innovation culture among the undergraduate and postgraduate students, entrepreneurs, industry professionals, and engineers and scientists in the country.

This book is comprised of 53 chapters and is divided into two parts, namely **Part One**: Design Process and **Part Two**: Product Development. Part One deals with the design of knee prosthesis, hybrid bearings, joint design for composite laminates, and finite element analysis and modelling of pivoted slipper and functionally graded piezoelectric materials. Part Two deals with the development and characterization of pellet machine, microwave joining of similar and dissimilar materials, and enhancement of mechanical properties of H-BN nanosheets, functionally graded materials, alloys and nanocomposites. The authors have given full dedication and support to interestingly write every chapter in a phased manner.

We hope this book becomes a handy reference for the engineers, scientists, entrepreneurs, and industry professionals who are working in the fields of innovative product design and development.

Srinagar, India
Roorkee, India
Roorkee, India

Dr. Pawan Kumar Rakesh
Prof. Apurbba Kumar Sharma
Prof. Inderdeep Singh

Acknowledgements

We would like to thank Prof. Shyam Lal Soni, Director, NIT Uttarakhand; Prof. Ajit Kumar Chaturvedi, Director, IIT Roorkee; and Er. Narender Singh, President, IEL, Kolkata, for their organizational support and motivation.

We also would like to thank all the reviewers, namely Dr. Monia Ajmeri, NIT Patna; Dr. Manisha Sharma, NIT Hamirpur; Dr. Aditya Anupum, NIT Uttarakhand; Dr. Suryanarayan Gogulu, NIT Uttarakhand; Dr. Krishan Kumar, NIT Uttarakhand; Dr. Sheela Tiwari, Dr. B R Ambedkar National Institute of Technology, Jalandhar; Dr. Shelly Vadhera, National Institute of Technology Kurukshetra; Dr. Vinay Kumar Patel, Govind Ballabh Pant Institute of Engineering and Technology, Pauri; Dr. Brijesh Gangil, HNB Garhwal University; Dr. Ravi Pratap Singh, NIT Jalandhar; Dr. Arvind Kumar Rajput, IIT Jammu; Dr. Suman Kant, PEC Chandigarh; Dr. Venkatesh Gudipadu, NIT Warangal; Dr. Abhishek Singh, National Institute of Technology Patna; Dr. Sarbjit Singh, PEC Chandigarh; Dr. Kishore Debnath, National Institute of Technology Meghalaya; Prof. J. Jerald, National Institute of Technology Trichy; Dr. Kalyan Kumar Singh, Indian Institute of Technology (ISM) Dhanbad; Dr. Parmendra Kumar Bajpai, NSIT Delhi; Dr. Anil Birru, National Institute of Technology Manipur; Prof. Srinath M. S., Visvesvaraya Technological University, Belgavi, Karnataka, India; Dr. Radha Raman Mishra, IIT Roorkee; Dr. Manoj Kumar Gupta, HNB Garhwal University; Dr. Somnath Bhattacharya, NIT Raipur; Dr. Pawan Kumar Kankar, IIT Indore; Dr. Anand Mishra, Cornell University, USA; and Dr. Yogesh Kumar Prajapati, NIT Uttarakhand, for timely checking and their valuable suggestions to improve the quality of the chapters. We would like to extend our heartfelt thanks to all the contributors for their valuable chapters in this book. We would also like to thank the sponsors of the conference, namely TEQIP-III, NIT Uttarakhand; Science and Engineering Research Board, New Delhi; Uttarakhand State Council for Science and Technology, Dehradun; and Uttarakhand Handloom and Handicraft

Development Council, Dehradun. We also would like to thank **Springer Nature** publishers, namely Dr. Akash Chakraborty and Mr. Daniel Joseph Glarance, for their continuous guidance and support during editing and publishing of this book.

Srinagar, India
Roorkee, India
Roorkee, India

Dr. Pawan Kumar Rakesh
Prof. Apurbba Kumar Sharma
Prof. Inderdeep Singh

Contents

Design Process

Design Analysis and Fatigue Life Prediction of an Indigenously Developed Affordable Knee Prosthesis	3
Shaurya Bhatt, Anoop Godiyal, Deepak Joshi, and Pawan Kumar Rakesh	
Parametric Optimization of FDM Process for Fabricating High-Strength PLA Parts	15
Tejas Pramod Naik, Ram Singh Rana, Radha Raman Mishra, Inderdeep Singh, and Apurbba Kumar Sharma	
Characterization of SiC-Reinforced AZ91 Magnesium Alloy Composites Produced Using In situ Microwave Casting	23
Radha Raman Mishra, Parvej Alam, Jitendra Yadav, Gaurav Kumar, and Apurbba Kumar Sharma	
Design of a Customized Fixture for Joining Jute Fiber-Based Composites Using Microwave Energy	31
Ravi Saukta, Ram Singh Rana, Tejas Pramod Naik, Kassahun Gashu Melese, and Radha Raman Mishra	
Design of Hybrid Bearings and Its Development: A Review	41
Nisha Singh and Praveen Kumar Agarwal	
Shape and Vibration Control of Spherical Shell Using Functionally Graded Piezoelectric Materials	61
Chanderkant Susheel	
Development of Aluminum Matrix Composite Through Microwave Stir Casting	75
Ganesh R. Panchal and M. S. Srinath	

Process Optimization of WEDM for Machining of Aluminum (6063)/Graphite Metal Matrix Composites	85
Tejas Pramod Naik, Promod Kumar Patowari, Kassahun Gashu Melese, Ram Singh Rana, Inderdeep Singh, and Apurbba Kumar Sharma	
Enhanced Mechanical Properties of h-BN Nanosheets via Edge Passivation Using Various Radicals	97
Bharat Bhushan Sharma and Avinash Parashar	
Evaluation of Interfacial Shear Strength of h-BN/PE Nanocomposites Using Molecular Dynamics	105
Ankur Chaurasia, Avinash Parashar, and Rahul S. Mulik	
Effect of the Material Hardness and Operating Conditions on the Friction and Wear During Lubricated Sliding	115
Amar Kumar Jain, Manoj Kumar, and Gananath Doulat Thakre	
Investigation on Microwave Joining of Mild Steel Plates at 2.45 GHz and Joint Characterization	127
Gaurav Kumar, Dungali Sreehari, Radha Raman Mishra, Vivekshel Yadav, and Apurbba Kumar Sharma	
Effects of Tool Pin Profiles on Mechanical Properties of Al/TiB₂ Surface Composite Fabricated by Friction Stir Process	137
Manoj Kumar Gupta, Brijesh Gangil, Lalit Ranakoti, Pawan Kumar Rakesh, and Vinay Kumar Patel	
Designing of an Electromagnet Producing Gradient MF and Its Effect on Water Properties	149
Ashish Kumar, Apurba Mandal, and T. Sudhakar	
Thermal and Thermo-Mechanical Analysis of Vinyl-Ester-Carbon/CBPD Particulate-Filled FGMS and Their Homogenous Composites	159
Brijesh Gangil, Manoj Kumar Gupta, Lalit Ranakoti, and Tej Singh	
Experimental Investigation for Quality of Micro-holes Machined Using Electrochemical Discharge Machining Process	169
Mohinder Pal Garg, Manpreet Singh, and Sarbjit Singh	
Influence of Parameters on Powder Mixed Electric Discharge Machining of EN-31 Tool Steel	177
Sharanjit Singh and Pawan Kumar Rakesh	
Joint Design for Adhesive Joining of Sisal/Epoxy Composite Laminates	189
Kassahun Gashu Melese, Tejas Pramod Naik, Ram Singh Rana, and Inderdeep Singh	

Product Development

Influence of Different Tool Profiles and Process Parameters on Mechanical Properties of Dissimilar AA6061 and AA7075 Aluminium Alloys by Friction Stir Welding 201
 Rajeev Rana, D. B. Karunakar, and Anish Karmakar

Numerical Analysis of Savonius Vertical Axis Wind Turbine with Dimpled Blades 209
 Paarth Tantia, Pratyush Singh, Punit Prakash, and Nishant Mishra

An Effect of Current on Mechanical Properties and SEM Characterization of Butt Joint of Aluminium AA6082 Using GTAW 225
 Sunil Kumar, Prabhkiran Kaur, and Amrik Singh

Review: Composite Materials for Armour Application 239
 Timo Nieberle, Shiv Ranjan Kumar, Amar Patnaik, and Chandramani Goswami

Identification of Effective Potassium Permanganate Fiber Surface Treatments on Mechanical Properties of Epoxy/*Ricinus communis* L Fiber Composites 249
 Rajesh Egala and Srinivasu Gangi Setti

Effect of Fiber Hybridization on the Mechanical Behaviors of Basalt/Borassus Fruit Fiber (BFF)-Reinforced Epoxy Composites 259
 Nitish Kumar and Abhishek Singh

Influence of Cryorolling on Spray-Formed Al-Si Alloy 269
 S. K. Chourasiya and G. Gautam

Optimization of Hybrid Aluminium Metal Matrix Composite Using Red Mud and Wheat Husk Ash 277
 Rishi Dewangan, Pankaj Kumar Pandey, Nitesh Singh Rajput, and Rajeev Dohare

Investigation of Efficiency of Flat Plate Collector Using CuO-H₂O Nanofluid 285
 Nitesh Singh Rajput, Sudhanshu Singh, and Shweta Kulshreshtha

Numerical Study of Copper Oxide/Therminol VP-1 Nanofluid in Solar Parabolic Trough Collector 297
 Gopal Nandan and Nafees Alam Wani

Physical Modelling of Terrain Using Different File Formats: A Review 311
 Jagdish Rana and Sanat Agrawal

Finite Element Modeling and Analysis of Natural Fiber-Reinforced Composite	321
Subham Prasad, Vaibhav Mishra, Vikas Khoj, and Vikas Kukshal	
Numerical Simulation of Spinning Kinetic Energy Projectile Against Reinforced Concrete Target Using ANSYS AUTODYN	329
Ghanshyam Singh Kushwah, B. V. S. Nagendra Reddy, Mukesh Kumar, and Pravendra Kumar	
Fracture Mechanism Characteristics Study of Explosive Bolt Through Explicit Analysis Tool	343
Prashant Kumar, P. C. Tewari, and Subhash Chander	
Numerical Simulation and Parametric Study of Penetration Effect for an Ogive-Nose-Shaped Projectiles Against Concrete Target	353
Patel Yash Bipinbhai, P. C. Tewari, Mukesh Kumar, and Pravendra Kumar	
Process Parameters Optimization of Wire EDM on AISI 304 Using the Taguchi Method	363
Vidyanand Kumar, Manjeet Kharub, Rajesh Kumar, and Pawan Kumar Rakesh	
Modelling and Analysis of Pivoted Slipper and Its Component at 40 Ton Load	373
Amit Yadav, Ajai Jain, and Subhash Chander	
Moisture and Flammability Behaviour of flax Fibre and Natural Fillers-Based Hybrid Epoxy Composites	385
Sudhir Kumar Chaudhary, Hitesh Sharma, and Gaurav Kumar	
TiO₂/PVDF-Based Polymer Nanocomposites and Their Various Characterizations	393
Sudhanshu Singh, Deepshikha Rathore, Nitesh Singh Rajput, and Umesh Kumar Dwivedi	
Fault Detection in Bevel Gear Using Condition Indicators	403
Mahendra Singh Raghav, Rahul Tiwari, and Ram Bihari Sharma	
A Review on Forward and Inverse Kinematics of Classical Serial Manipulators	417
Randheer Singh, Vikas Kukshal, and Vinod Singh Yadav	
Whale Optimization Algorithm for Static and Dynamic Load Dispatch	429
Himanshu Raj and Manisha Sharma	
A Comparison Between Passive Islanding Detection Methods in Grid Integrated Photovoltaic System	441
Isha Chandra and Mahiraj Singh Rawat	

Optimization of a Single-Channel Optical Communication System and an 8-Channel WDM System Using EDFA 453
 Prem Babu, Maneesh Kumar Singh, and Sarika Pal

Adaptive Unknown Input Observer for Actuator Fault Detection and Isolation of PEM Fuel Cell Systems 465
 Vikash Sinha and Sharifuddin Mondal

Solving the Multi-server Queuing Model by Big-M Method 475
 S. Vijay Prasad and Anil Kumar Birru

Ultra-Lightweight Cenospheres Cement for Lost Circulation Control with Improved Curing and Reduced Shrinkage 481
 Gaurav Richhariya, T. K. Dora, Naveen Singhal, Mayur Rai, Yash Goyal, Preeti Rathi, Yash Gupta, Praman Singh, P. P. Kundu, Kishori Lal, and Pawan Kumar Rakesh

Augmentation of Thermal Performances in a Tubular Heat Exchanger Using Internal Flow Baffle: Recent Study 489
 Gopal Nandan, Nafees Alam Wani, and Satish Kumar

Analysis of Mechanical Behavior of Sandwich Panels 499
 Swati Devi, Yogesh K. Prajapati, and Vinod Singh Yadav

Development of Pellet Machine for Utilization of Biogas Slurry 509
 Madhuri More, Chitranjan Agrawal, Deepak Sharma, Neelam Rathore, and Kapil Samar

Analysis of the Effect of Shock Waves on Fretting Behavior of Graphene Hydroxyl Reinforced Aluminum 6061 Composites 521
 M. R. Srinivasa, Y. S. Rammohan, and M. Sadashiva

A Review on Friction Stir Spot Welding of Similar and Dissimilar Materials 531
 Neeru, Sarbjit Singh, and P. S. Satsangi

Mechanism-Driven Piezoelectric Energy Harvester 543
 Rajat Nayal and Anshul Sharma

Stabilizing x - y Inverted Pendulum via Variable Structure Control 553
 Satyendra Kumar and Moina Ajmeri

Selection of Process Parameters and Their Machine Levels for Electro-discharge Face Grinding of D2 Steel 563
 Akshat Srivastava Kulshrestha, Ashok Kumar Dargar, and Deepak Rajendra Unune

About the Editors

Dr. Pawan Kumar Rakesh is serving as an Assistant Professor, Department of Mechanical Engineering, National Institute of Technology Uttarakhand, (NIT Uttarakhand) Srinagar Garhwal. Currently, he is discharging the duties of the Associate Dean (Faculty Welfare) from 2016 to till date. He has also served as Head of Department, Mechanical Engineering (2013-2016). Working in a growing organization, he has got substantial exposure of several lab developments, academic structure and student welfare. He is also the Coordinator of Design Innovation Center, NIT Uttarakhand. He has authored 36 articles published in reputed International/National journals and conferences. He has edited one book title “Processing of Green Composites” Springer. He has contributed four book chapters in different book published by Woodhead Publishing, UK; Wiley-VCH, Verlag GmbH, Germany; and Springer Nature Singapore Pte. Ltd.

Dr. Apurbba Kumar Sharma is currently a Full Professor in the Department of Mechanical and Industrial Engineering at IIT Roorkee, India. He is also the Coordinator of Design Innovation Center, IIT Roorkee. Earlier, he was holding the positions of Associate Dean, Academic Studies and Chairman, Institute Academic Performance Evaluation Committee in this Institute during July 2013 to April, 2017. He has obtained his Bachelor degree from Dibrugarh University, Assam. He has subsequently obtained his Masters and PhD degrees from IIT Madras. Dr. Sharma has filed 9 Indian Patents; 3 of them have already been granted. He has published more than 100 research papers in International Journals. He has also presented/published more than 120 research papers in various International and National Conferences. Dr. Sharma is also a reviewer of several reputed international journals. He has also edited one International Conference Proceedings and was guest Co-Editor of the International Journal of Advanced Manufacturing Technology.

Dr. Inderdeep Singh completed his Bachelor’s degree in Mechanical Engineering from NIT Hamirpur, (Himachal Pradesh) in 1998. He got first position in the class of Mechanical Engineering. He completed his Masters of Technology and Ph.D.

from I.I.T. Delhi in 2000 and 2004, respectively. His doctoral research work was awarded by the Foundation for Innovation and Technology Transfer (FITT) as the “Best Industry Relevant Ph.D. Project” during the session of 2004-2005. He started his career as Lecturer at Indian Institute of Technology, BHU in 2004. He joined the Indian Institute of Technology Roorkee as Lecturer in 2005 and is currently working as Professor. He has served as the Associate Dean of Students Welfare from July, 2013 to February, 2017. He has published over 180 research papers in journals and conferences. He has contributed 15 chapters in different books published by internationally renowned publishers. His current research focus is in the direction of developing fully bio-degradable green composites.

Design Process

Design Analysis and Fatigue Life Prediction of an Indigenously Developed Affordable Knee Prosthesis



Shaurya Bhatt, Anoop Godiyal, Deepak Joshi, and Pawan Kumar Rakesh

1 Introduction

A large number of people in this world are estimated to need prosthetic and orthotic devices [1]. A significant part of this population do not receive proper healthcare services and are not able to get proper access to health and education services and hence lag in receiving employment opportunities [2]. In India alone, 2.21% of the total population is disabled, i.e. nearly 26.8 million people. Out of the total disabled population, 20% has a disability-related to the movement in which 62% are male, and 38% are female [3]. It was reported that a large percentage of the amputee population switched their occupation after the incident of amputation as they were involved in work that requires physical movement and force application [4]. In India, an estimated 2,30,000 are lower limb amputee with above-knee amputation [5]. In recent times, the lower limb prosthesis has made tremendous advances from using wooden sticks as a prosthesis to the smart and intelligent prosthesis, but still, very few prosthetics are being designed that are focused on low-income countries such as India, Nepal, and Bangladesh. The prosthetics that are highly capable of giving a good life to an amputee are still out of reach of most of the population, and the ones that are available at low cost do not provide functionality anywhere close to high-end prosthetics. With the recent advancement in the fields of smart devices and the use of more computerized methods, new methods for the design of knee mechanisms and prosthetic sockets are being used. This not only increases the functionality of the prosthetic leg, but it also brings the prosthesis closer to the expectation of its user [6]. An amputee wearing prosthesis forms a biomechanical system whose behaviour is

S. Bhatt (✉) · P. K. Rakesh
Mechanical Engineering Department, National Institute of Technology Uttarakhand, Srinagar,
Uttarakhand 246174, India
e-mail: shauryain@yahoo.co.in

A. Godiyal · D. Joshi
Centre for Biomedical Engineering, Indian Institute of Technology Delhi, Delhi 110016, India

governed by several factors such as its mechanical and physical properties, how the prosthesis fits the amputee and its alignment, weight of components of the prosthesis [7–9]. Thus, it is essential to study the behaviour of prosthesis for better design and performance of the parts/components.

Several experimental methods such as a static proof test, ultimate static loading, and cyclic loading test have been used to study to load behaviour and stress distribution of the prosthesis [6, 10]. With the use of numerical and computational methods such as finite element analysis (FEA), one can figure out the load capacity of the prosthesis, the effect of material properties on the behaviour of prosthesis, and the effect of alignment parameter without actually fabricating the actual prosthesis, so that design process can be expedited without needing much efforts and resources. For all these reasons, FEA is becoming a very prominent technique for carrying out behavioural analysis of prosthesis [6, 11].

Optimization of the prosthesis by varying design parameters for studying its effect on the strength of the prosthesis structure has not been explored much. It has mostly been used to evaluate the stress distribution without actually manufacturing the knee [12–14]. Some work has focused on the topology optimization of the knee using FEA that helps to reduce the weight of the structure while retaining its physical strength [15]. FEA is a proven and reliable method for non-destructive testing of the prosthesis and assessment of the life of medical equipment [11, 16].

The need for an intelligent transfemoral prosthesis for low-resource settings was addressed in previous work. The details on design and development are available elsewhere [17]. However, the work did not report about the strength and load distribution in the structure of the prosthesis. Therefore, the present work aims to analyse the design strength and fatigue life of the structure without doing any destructive testing, thus saving the resources. Here, FEA is used to compare the design features of the second and third generations of the prosthesis with the first-generation prosthesis. The changes in the mechanical properties of the structure with the modifications in the design are addressed. It is hypothesized that the changes implemented in second- and third-generation prosthesis will bring about improvement in mechanical properties of the prosthesis structure and provide it with a new feature of height adjustment.

2 Analytical Method

The present work explores a transfemoral prosthesis fitted with a SACH foot, as shown in Fig. 1. In this analysis, the foot is a standard part of the prosthesis and was excluded from the test. The work discussed in the present paper considers a previously designed prosthesis and its modified version, with new features and materials added to enhance its usability by the amputee over the previous model.

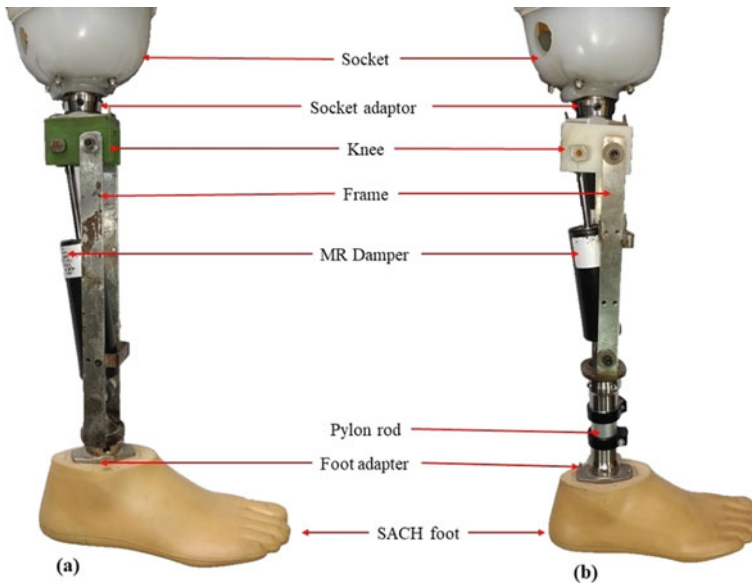


Fig. 1 Prosthetic leg developed at IITD, **a** first-generation leg **b** second-generation leg

2.1 Computer-Aided Design

The first step of analysis is to model the parts of the prosthesis and then combined together to form an assembly. Other than some standard components and MR damper, most components were custom-designed according to the requirement of the prosthesis design. After the FEA testing of the first generation, parts of the second generation were modelled according to the requirement, and necessary changes were implemented to achieve the desired results. The mechanical structure of the first-generation and second-generation prosthesis is shown in Fig. 2.

The components for the first generation were custom-designed to the height of the individual user. The component measurements were adjusted so that the distance from the knee axis to the ground of the user and the prosthesis remains the same. But for the second-generation prosthesis, an introduction of a feature of height adjustment in the prosthesis so that the structure was designed for its minimum length and later on, it could be adjusted according to users' need. This height adjustment feature was incorporated in the prosthesis using a naive approach. A pylon rod was introduced between the lower adaptor of the prosthesis and the adaptor of the foot. This pylon rod is made of lightweight aluminium alloy, which is easy to machine. With the change in the length of the pylon rod, a variable height adjustment was performed. Since the frame was the component that showed the major change from the first-generation to second-generation, its design drawing can be seen in Fig. 3.

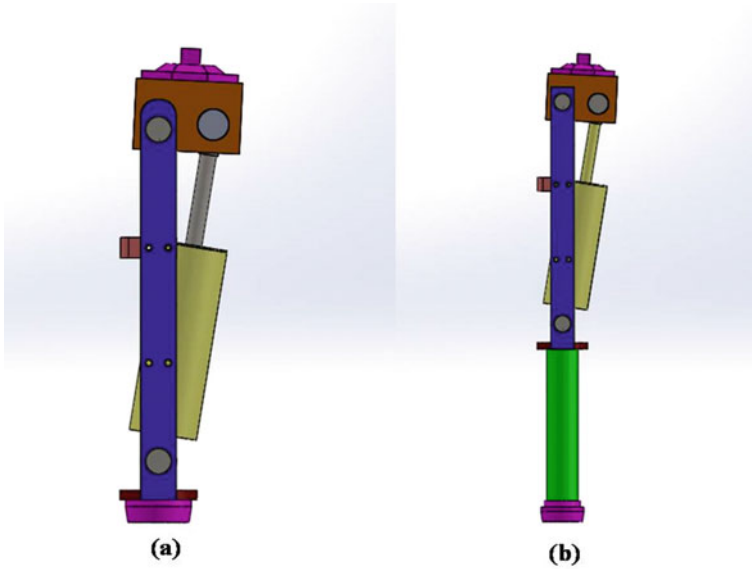


Fig. 2 Mechanical structure of prosthesis, a first generation b second generation

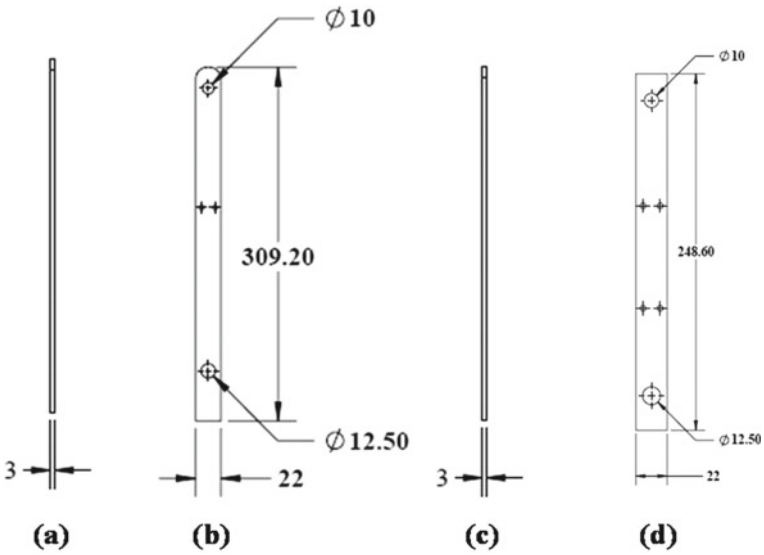


Fig. 3 Design dimensions of frame side pillars, a and b first generation and c and d second generation (all units in mm)

Table 1 Material properties of components used in the prosthesis

Component	Material	Young's modulus(GPa)	Poisson's ratio
Knee	Nylon-66	2.93	0.35
Frame	Mild Steel	200	0.3
Screws	Mild Steel	200	0.3
Foot (female) adapter	Aluminium alloy	71	0.33
Socket (male) adapter	Aluminium alloy	71	0.33
Pylon rod	Aluminium alloy	71	0.33

All the parts included in the prosthesis were designed on SolidWorks®2014, and an assembly was designed for the complete prosthetic structure. This assembly was then imported to FEA software (ANSYS 18.0) for the analysis work.

The standard components were included in the fabrication of prosthesis assembly were: (1) female pyramid adapter fitted at the lower end that aids in attachment of SACH foot to the prosthesis, (2) male pyramid adapter fitted at the top of the knee structure, (3) MR damper (Make: LORD Corporation, RD-8041-1 for the first generation, and RD-8040-1 for the second generation), (4) Pylon Rod (second generation).

2.2 Selection of Material

The prime factor in choosing the material was to meet the weight criterion of the prosthesis. According to a recent study, decreasing prosthesis mass to 25% of physiological leg mass can reduce absolute hip work by 22% [18]. The aforementioned study also indicated that varying the mass of the lower leg has more effect on the absolute hip work in comparison with upper leg mass. Thus, the material has to be selected in such a way so as to keep the mass of prosthesis at a minimum without affecting the strength of the prosthesis. The material selected for different components, along with material properties, is mentioned in Table 1. The material properties for nylon were taken from [19–21].

2.3 Finite Element Analysis

Custom-designed and load-bearing components were chosen for FE analysis. These components were: (1) knee (2) frame (3) screws (4) foot adaptor (5) socket adapter. The damper in the prosthesis structure assembly was replaced by a solid rod to transfer the load to the lower joints and screws so that all the components could be evaluated for the strength. This was done keeping in mind that only the parts that can be altered on our choice should be tested for failure so that they can be modified

later according to our requirements of weight and strength of the structure. The rod was assigned the same material properties as that of the frame structure.

FE analysis was carried out on ANSYS Workbench. The entire assembly meshed with tet-10 type of elements. The assembly was given fixed support at the bottom, and load was applied at the top in such a way that it gave the prosthesis one leg support condition, i.e. the entire body weight is on the prosthetic structure. A cyclic load of 1050 N was applied to the structure. The properties that are to be evaluated using FEA in this work are stress, deformation, fatigue life, and safety factor. For the calculation of fatigue life, Soderberg criteria were used. The factor of safety was also included in the analysis, keeping in mind the safety of the user.

A preliminary test was done, and on the basis of preliminary test results, critical components were identified, and the mesh was refined on the critical component, and the simulation was run again to get the final results.

3 Results and Discussion

On running the simulation for both the structures, the results showed a substantial improvement for the strength in the structure of the second generation. The peak stress in the first generation reached a peak value of 1.47×10^8 Pa, while for the second generation, the value of peak stress was limited to 1.11×10^8 Pa (Table 2).

For a prosthetic to be in safe limits, the deformation in its structure on loading should not exceed a value of 2.5 mm [11]. On comparing the deformation values for both the structures, the maximum deformation in the first generation had a peak value of 0.816 mm and that for the second generation had a peak value of 0.273 mm which is below the recommended limit. The contour plot obtained from FEA for stress distribution and displacement is shown in Fig. 4.

On comparing the results of FEA for the first-generation and second-generation prosthesis, it was observed that the second-generation prosthesis has reduced level of peak stress in its components. A reduction of 24.5% was seen in peak stress value, while the peak deformation was reduced by 66.5%. This reduced peak stress is due to a reduction in the effective length of the assembly. On comparing the

Table 2 Comparison of mechanical properties of two generations of a prosthetic leg

	First generation	Second generation
Maximum stress	1.4719×10^8 Pa	1.1161×10^8 Pa
Maximum deformation	0.00081628 m	0.00027349 m
Minimum fatigue life	78,932 cycles	$202,597 \times 10^5$ cycles
Minimum safety factor	0.58563	0.77234

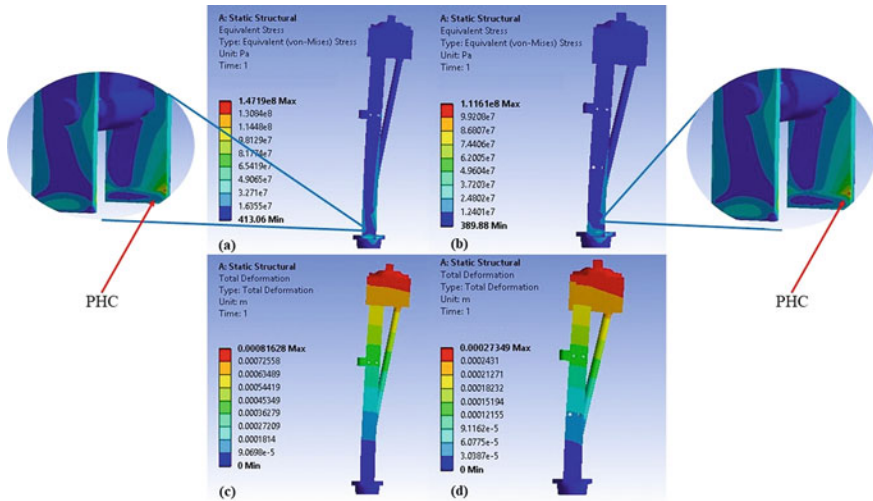


Fig. 4 Contour plot obtained by FEA **a** stress distribution in the first generation **b** stress distribution in the second generation **c** deformation level in the first generation **d** deformation level in the second generation, where PHC denotes the point of the highest concentration of stress

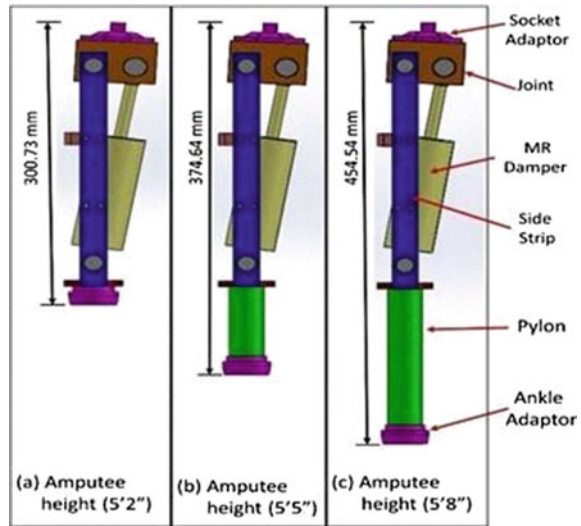
fatigue life for the two, it was found that the life of the second-generation prosthesis became 2.8 times of the previous version. Also, on comparing the safety factor for the second-generation prosthesis, it became 1.3 times of the first-generation prosthetic structure.

Maximum stress levels were observed in the frame of the prosthesis. The frame was also noted to be maximally deformed with the least factor of safety and the lowest life. After analysing the first-generation prosthesis, further modifications were made to the design of the frame to provide more strength. The reduction in length of the assembly provided a sturdier frame and gave it enough strength to support the load being transferred to it. By reducing the effective length of the assembly, the buckling load, that is inversely proportional to the square of the effective length, was increased for the structure, so the structure can now even tolerate higher loads. This resulted in lower deformation along with the higher factor of safety and enhanced the overall life of the prosthesis without adding much to the weight component as the extra material was added only to the region of stress concentration.

The results obtained for the second-generation prosthesis were following our hypothesis. The modifications made in the design of the frame gave an enhanced structural rigidity to the frame. Deformations were reduced, and the life of the prosthesis went up by a considerable amount. The factor of safety also plays an important role in design reliability, and the modifications made in the design gave a positive boost to the reliability factor and enhanced the life of the structure.

The new design not only improved the mechanical properties of the structure, but also enhanced its practical applicability. The new design of the second-generation prosthesis made it feasible to adjust the length of the prosthesis for any height of

Fig. 5 Variable height arrangement that can be achieved with the second-generation prosthesis



user that is greater than 5 feet 2 inches just by using a pylon of variable size as can be seen in Fig. 5.

This can help in mass manufacturing the frame of the prosthesis, and by using pylons of variable lengths, the prosthesis can be easily made to fit users of different heights. With the implementation of the new design, the weight of the prosthesis structure was also reduced by 235gms. This may not be a significant change, but even a small reduction in prosthesis mass can help in saving a lot of work and energy of the prosthesis user [18].

A few limitations that are still to be worked are (1) mass of the damper and (2) minimum achievable height. Mass of the damper used in the prosthesis shares a large portion of the overall weight of the prosthesis. With an indigenously developed MR damper, the weight of the prosthesis can be reduced to a great amount, and the length of the prosthesis can be made further short so that it can be made to fit users of almost all height range.

The second-generation prosthesis developed above fulfils all the requirements in terms of usage and mechanical aspects, but to further strengthen the structure, it is developed an advanced model to enhance its mechanical properties further. It was observed that the maximum stress and lowest life were observed on the lower end of the frame; so to reduce the stress level further and to enhance life, the lower end of the frame was made stronger by making the frame pillars thicker at the bottom. The structure of the frame mentioned above is given in Fig. 6.

On comparing the third frame structures for different aspects, it can see that the third modification gave extra strength to the structure over the previous modifications. Figure 7 shows a comparison of the mechanical properties of the three different phases of the prosthesis. It was observed that providing extra thickness enhanced the load-carrying capacity of the assembly, and this was reflected by a decreased level of

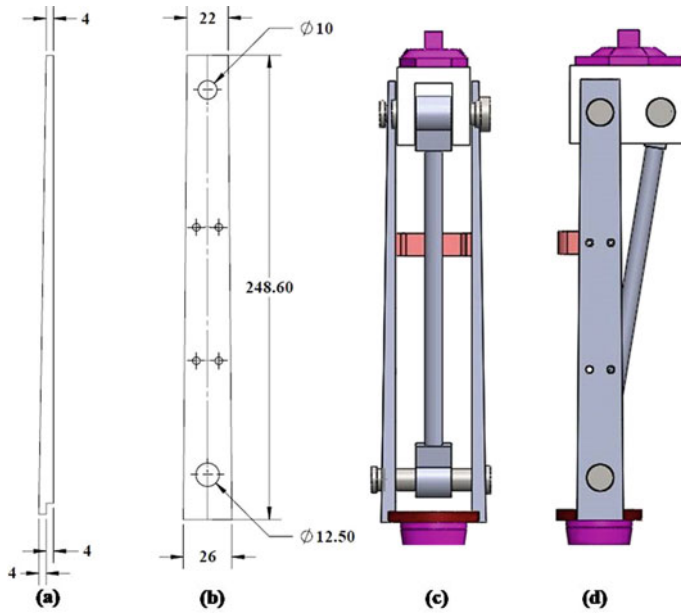


Fig. 6 Frame pillar designed for extra strength of the structure **a** side view of frame pillar **b** front view of frame pillars **c** front view of the prosthesis after phase 3 **d** side view of the new prosthesis design (all units in mm)

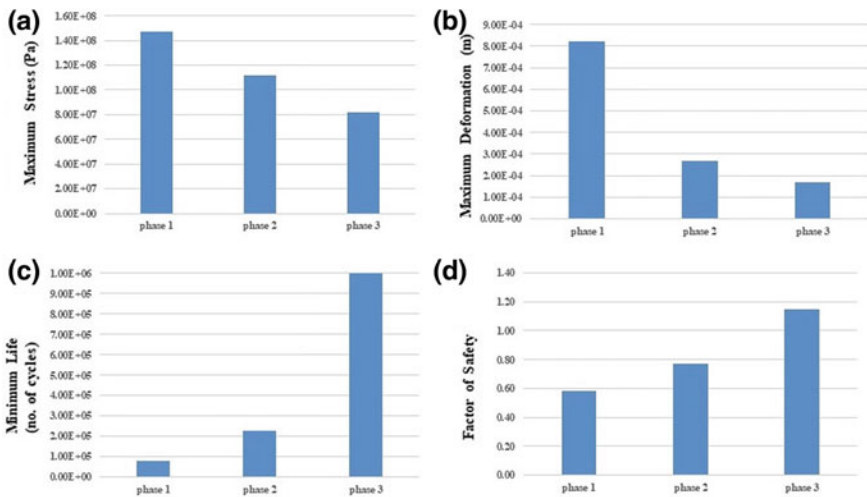


Fig. 7 Comparison of mechanical aspects for three phases of the prosthesis. **a** Comparison of maximum stress generated in the prosthesis, **b** maximum deformation observed **c** minimum life of prosthesis in number of cycles performed, **d** minimum factor of safety (FoS)

peak stresses in the assembly. Though the maximum deformation reduced slightly, it was due to the fact that deformation in the previous structure was already a minimal value. The best result was seen in the enhancement of life of the structure.

The structure achieved standard infinite mechanical life which means the weakest component as depicted in the analysis will last at least 10^6 cycles of fatigue loading. The factor of safety was also noted to increase by 46% of its value for the second-generation prosthesis, which means the structure can now sustain even higher loads.

4 Conclusions

The above analysis shows that the changes made in the structure of the prosthesis not only gave the newer version a weight reduction of 235 grams, but it also made the second-generation prosthetic more compact and user-friendly. These modifications also improved the mechanical strength and reliability of the structure and enhanced the fatigue life of the structure. Also, as it was observed that adding extra material can increase the life and reduce the level of stresses in the prosthesis. It is suggested to be a good idea to provide reinforcement to the structure at critical points to make the prosthesis structure more durable and enhance their strength without affecting the weight of the prosthesis.

5 Future Work

Collection of user data for loading of the prosthesis in various phases of the gait cycle and then testing the prosthesis according to actual loading conditions and comparing gait features of prosthesis user to that of a healthy subject to get a measure of gait rehabilitation achieved with the prosthesis.

Acknowledgements The authors are grateful to the Design Innovation Center, National Institute of Technology, Uttarakhand, for providing support to complete this work.

Funding We thank the Indian Council of Medical Research (ICMR) New Delhi, Govt. of India for funding this research via research grant No.5/20/13/Bio/2011-NCD-I.

References

1. World Health Organization (2005) Guidelines for training personnel in developing countries for prosthetics and orthotics services. <https://apps.who.int/iris/handle/10665/43127>
2. Seelman KD (2011) The world health organization/world bank's first world report on disability. *Int J Telerehabilitation* 3(2):11

3. Kraus L (2017) 2016 Disability statistics annual report. University of New Hampshire, Durham, NH
4. Narang IC, Mathur BP, Singh P, Jape VS (1984) Functional capabilities of lower limb amputees. *Prosthet Orthot Int* 8(1):43–51
5. Narang YS (2013) Identification of design requirements for a high-performance, low-cost, passive prosthetic knee through user analysis and dynamic simulation (Doctoral dissertation, Massachusetts Institute of Technology)
6. Omasta M, Paloušek D, Návrát T, Rosický J (2012) Finite element analysis for the evaluation of the structural behaviour, of a prosthesis for trans-tibial amputees. *Med Eng Phys* 34(1):38–45
7. Geil MD, Lay A (2004) Plantar foot pressure responses to changes during dynamic trans-tibial prosthetic alignment in a clinical setting. *Prosthet Orthot Int* 28(2):105–114
8. Seelen HAM, Anemaat S, Janssen HMM, Deckers JHM (2003) Effects of prosthesis alignment on pressure distribution at the stump/socket interface in transtibial amputees during unsupported stance and gait. *Clinical Rehab* 17(7):787–796
9. Bateni H, Olney SJ (2004) Effect of the weight of prosthetic components on the gait of transtibial amputees. *JPO: J Prosthet Orthot* 16(4):113–120
10. Jensen JS, Treichl HB (2007) Mechanical testing of prosthetic feet utilized in low-income countries according to ISO-10328 standard. *Prosthet Orthot Int* 31(2):177–206
11. Phanphet S, Dechjarern S, Jomjanyong S (2017) Above-knee prosthesis design based on fatigue life using finite element method and design of experiment. *Med Eng Phys* 43:86–91
12. Completo A, Talaia P, Fonseca F, Simões JA (2009) Relationship of design features of stemmed tibial knee prosthesis with stress shielding and end-of-stem pain. *Mater Des* 30(4):1391–1397
13. Baldwin MA, Clary CW, Fitzpatrick CK, Deacy JS, Maletsky LP, Rullkoetter PJ (2012) Dynamic finite element knee simulation for evaluation of knee replacement mechanics. *J Biomech* 45(3):474–483
14. Chen NZ, Lee WC, Zhang M (2006) A numerical approach to evaluate the fatigue life of monolimb. *Med Eng Phys* 28(3):290–296
15. Reist TA, Andrysek J, Cleghorn WL (2010) Topology optimization of an injection moldable prosthetic knee joint. *Comput-Aided Des Appl* 7(2):247–256
16. Driscoll M (2018) The impact of the finite element method on medical device design. *J Med Biol Eng* 39(2):1–2
17. Pandit S, Godiyal AK, Vimal AK, Singh U, Joshi D, Kalyanasundaram D (2018) An affordable insole-sensor-based trans-femoral prosthesis for normal gait. *Sensors* 18(3):706
18. Narang YS, Arelekatti VM, Winter AG (2015) The effects of prosthesis inertial properties on prosthetic knee moment and hip energetics required to achieve able-bodied kinematics. *IEEE Trans Neural Syst Rehabil Eng* 24(7):754–763
19. Starkweather HW Jr, Brooks RE (1959) Effect of spherulites on the mechanical properties of nylon 66. *J Appl Polym Sci* 1(2):236–239
20. Van Hooreweder B, De Coninck F, Moens D, Boonen R, Sas P (2010) Microstructural characterization of SLS-PA12 specimens under dynamic tension/compression excitation. *Polym Testing* 29(3):319–326
21. Van Hooreweder B, Moens D, Boonen R, Kruth JP, Sas P (2013) On the difference in material structure and fatigue properties of nylon specimens produced by injection molding and selective laser sintering. *Polym Test* 32(5):972–981

Parametric Optimization of FDM Process for Fabricating High-Strength PLA Parts



Tejas Pramod Naik, Ram Singh Rana, Radha Raman Mishra, Inderdeep Singh, and Apurbba Kumar Sharma

1 Introduction

Rapid prototyping (RP) is a recently developed layer-by-layer manufacturing technology for producing products in various applications, including medical, educational, and manufacturing industries [1–3]. Solid, liquid, and powder materials can be used as an input material in different RP processes [4]. Polymer-based fused deposition modeling (FDM) process is widely used in different applications as the process is rapid and capable of producing complex products with net shape, almost zero waste and economy. In this technique, the solid wire of polymer (input) is fed to a liquefier head which is placed above the nozzle. The material gets soften inside the liquefier; subsequently, it is extruded through the nozzle to build part on the platform [4]. The material having a higher melting temperature is less preferred in the FDM process [5]. Various thermoplastic materials, including acrylonitrile butadiene styrene (ABS), polylactic acid (PLA), polycarbonate, polyvinyl alcohol, and polyetherimide, are used for prototyping [5]. However, the use of polymers (mostly

T. P. Naik · R. R. Mishra · I. Singh · A. K. Sharma
Design Innovation Center, Indian Institute of Technology Roorkee, Roorkee, Uttarakhand 247667, India
e-mail: rmishra@me.iitr.ac.in

I. Singh
e-mail: inderdeep.singh@me.iitr.ac.in

A. K. Sharma
e-mail: aks@me.iitr.ac.in

T. P. Naik (✉) · R. S. Rana · I. Singh · A. K. Sharma
Mechanical and Industrial Engineering Department, Indian Institute of Technology Roorkee, Roorkee, Uttarakhand 247667, India
e-mail: tejasnit@gmail.com

R. S. Rana
e-mail: ramsingh.mech17@gmail.com

ABS and PLA) in the FDM process limits the load-bearing capacity of developed products [6]. Therefore, achieving higher mechanical properties in the FDM fabricated products has always been a challenge [7]. Some studies have been reported to address the issue. Ahn et al. [8] investigated the effect of raster orientation, bead width, temperature and color on tensile, and compressive properties of FDM fabricated ABS specimen. It was found that the air gap and raster orientation affect the tensile strength greatly. Bead width, model temperature, and color have little effect. The compressive strength of the FDM specimen was higher than the tensile strength and was not affected much by build direction. In another study, the author reported that the mechanical properties of the ABS parts fabricated using FDM technology depend on the path and orientation of the build specimens [9]. It was reported that the horizontally build specimen gives more strength compared to vertically build specimen. In another study, the effect of part orientation and raster angle on surface roughness, mechanical behavior, and production time, as well as cost, was investigated [10]. It was reported that part orientation plays a more significant role than the raster angle on the surface roughness, mechanical behavior, and cost. The parts fabricated in the perpendicular direction result in weak bonding between the deposited materials so it is not preferred. The mechanical properties of ABS based composites have also been reported in the past. In one such study, ABS + hydrous magnesium silicate composite was fabricated using FDM technology, and the effects' layer height and print speed were studied [11]. It was reported that the low print speed and low layer height is preferred for getting better mechanical properties because a better bonding with the previous layer occurs. In the present research trend, researchers have started working on the fabrication of the scaffolds which is used in medical application to grow cells. In the recent study, ABS-based scaffolds were fabricated using FDM technology [12]. The effect of process parameters, namely air gap, build orientation, raster width, build layer, and build profile, on the porosity and mechanical properties of the ABS material-based scaffold was investigated. It was reported that air gap and raster width are the most significant parameters affecting the porosity and mechanical properties. The best mechanical properties were observed in low porosity scaffolds. Effect of process parameters like layer thickness, infill density, and post heat treatment was carried out on PLA-based FDM parts [13]. It was reported that the heat treatment increases the strength, but the ductility decreases. So, it was suggested to use low level of heat treatment to improve strength while preserving ductility and reliability. It has been observed in the literature that limited study has been conducted to optimize the parameters for achieving better tensile properties in PLA parts fabricated using FDM process. Therefore, in the present study, the effect of FDM parameters like layer height, nozzle speed, and infill pattern has been analyzed using Taguchi approach for PLA parts.

2 Experimental

The polylactic acid (PLA) polymer in the form of solid wire (supplier: Spakas Information Systems Limited, Delhi, India) was used as the input material to fabricate the specimens. The experiments were carried out on a 3D printing machine (Ultimaker² Extended + , make: Ultimaker, Netherland) which is shown in Fig. 1a. The 3D printer consists of a build platform, nozzle, PLA material in wire form, heaters, and controller. The solid wire of polymer (input) is fed to a liquefier head which is placed above the nozzle. The material gets soften inside the liquefier; subsequently, it is extruded through the nozzle to build part on the platform.

It has been observed during the initial trials that layer height, nozzle speed, infill pattern affect the tensile properties of 3D-printed PLA specimens. Subsequently, different levels of the selected parameters were fixed for the present study, as shown in Table 1. Each factor is investigated at three levels to determine the maximum strength of the fabricated PLA specimen. The Design of Experiment (DOE) with Taguchi’s L9 orthogonal array based on three input parameters having three different levels was used, as shown in Table 2.

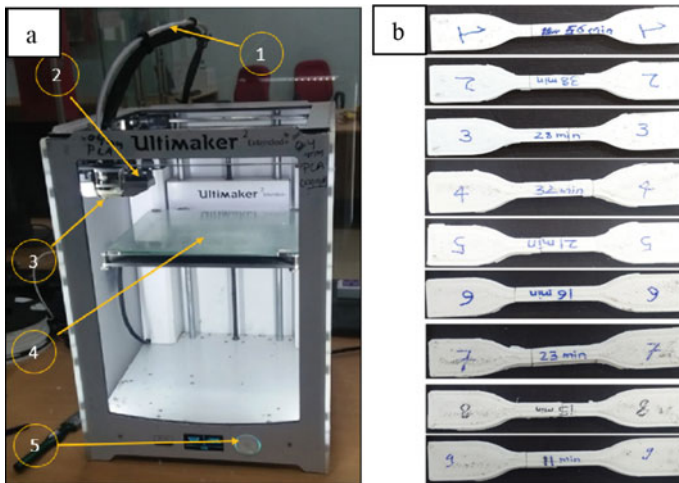


Fig. 1 a Ultimaker² 3D printer used in study 1: PLA wire; 2: heater; 3: nozzle; 4: build platform; 5: control panel, and b fabricated specimens

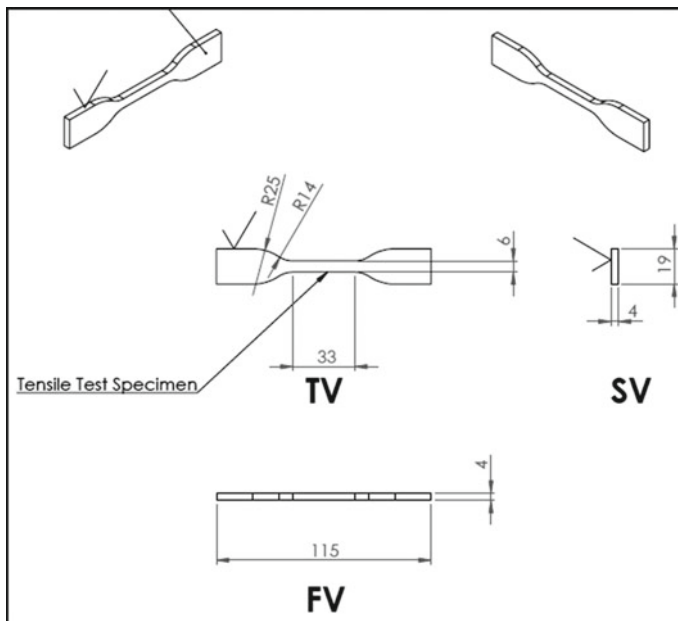
Table 1 Control parameters and their levels

Control factors	Unit	Level 1	Level 2	Level 3
Layer height	mm	0.2	0.4	0.6
Nozzle speed	mm/s	5	10	15
Infill pattern	-	line	zig-zag	concentric

Table 2 Taguchi L₉ design of experiment

Exp. No	Layer height	Nozzle speed	Infill pattern
1	0.2	5	Line
2	0.2	10	Zig-zag
3	0.2	15	Concentric
4	0.4	5	Zig-zag
5	0.4	10	Concentric
6	0.4	15	Line
7	0.6	5	Concentric
8	0.6	10	Line
9	0.6	15	Zig-zag

The specimens were fabricated at 100% infill density using a nozzle of 0.4 mm diameter. The 3D printing of the tensile specimen was accomplished using the digital model drafted through SOLIDWORKS 2018. The dimensions of the fabricated tensile specimen are shown in Fig. 2. The digital model was converted to the 'dot stl' file to import it into the CURA software for 3D printing. The printed tensile specimens are shown in Fig. 1b. The tensile testing was accomplished using the test standard ASTM D-638 Type IV on the UTM machine (make: Instron-1342). The

**Fig. 2** Dimensions of fabricated specimens (ASTM D-638 TYPE IV)

fractographic study of the fractured tensile specimens was done by analyzing the micrographs obtained from FE-SEM (make: Carl Zeiss).

3 Results and Discussion

3.1 Tensile Test

The tensile test of the fabricated specimens has been evaluated using the UTM machine at a strain rate of 1 mm/min, as shown in Fig. 3. Figure 4 indicates stress–strain characteristics of the fabricated specimens under the tensile loading. It is clear from the stress–strain curves that the tensile strength of specimen 7 having input parameters as layer height–0.6 mm, nozzle speed–5 mm s⁻¹, and infill pattern–concentric is the highest (54.437 MPa). It is observed that improvement in the strength is due to the higher layer height, which reduces the number of layers required to build the specimens. Consequently, it results in fewer air gaps/voids formation and tensile strength gets improved. However, an increase in nozzle speed decreases tensile strength due to reduced time for the better bond formation between the two adjacent layers. The % elongation of the specimen 6 with layer height–0.4 mm, nozzle speed–15 mm s⁻¹, and infill pattern—the line was found maximum (13.19% elongation). It is due to the raster pattern, i.e., line which aligns with the direction of the applied tensile load and ultimately results in the maximum % elongation.



Fig. 3 Tensile testing of 3D-printed samples

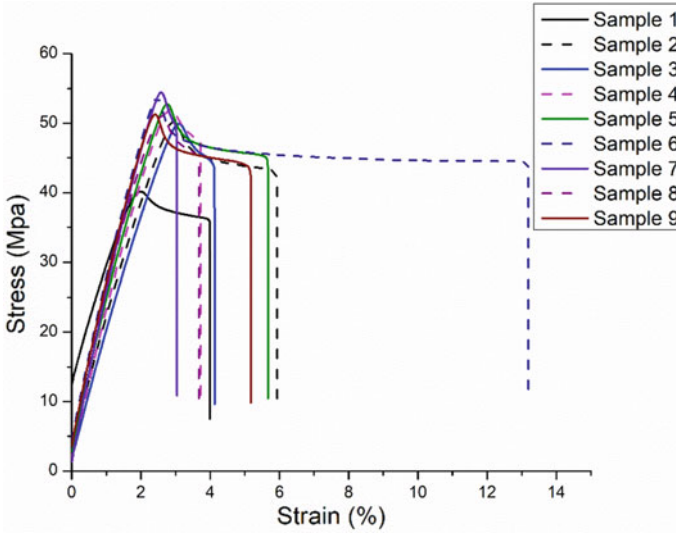


Fig. 4 Stress v/s strain curve of all the fabricated samples

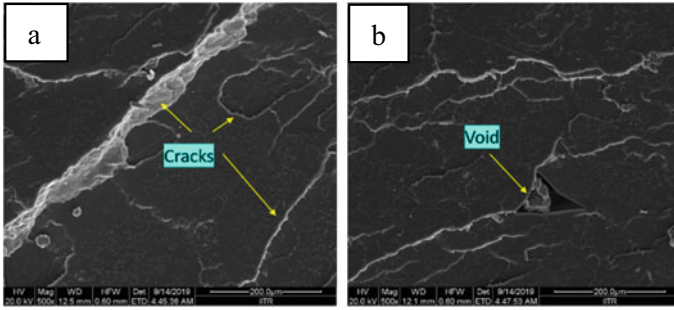
3.2 Fractography Study

Figure 5 shows the SEM micrographs of the fractured surfaces of the tensile specimens. It is evident from the figures that fractures in PLA specimens are brittle in nature and the presence of many cracks indicates that propagation of cracks resulted in the reduction in tensile strength. Moreover, the voids and air gaps present inside the specimens are also responsible for reducing the tensile strength. It can be observed in the specimen 7 that lesser number of voids/air gaps is present as compared to specimen 1, which enhances tensile strength by 35.53%. It is due to the higher layer height in specimen 7 (0.6 mm) that the layer height in sample 1 (0.2 mm).

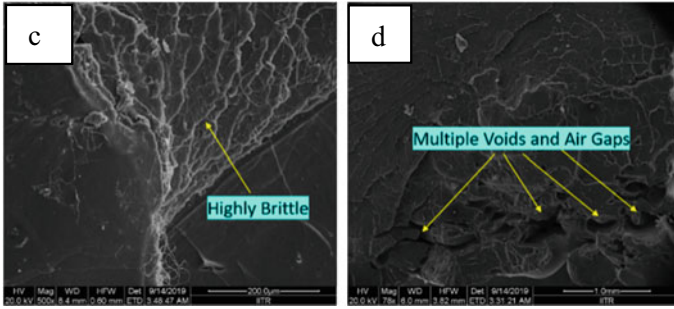
4 Conclusions

The following can be concluded from the study:

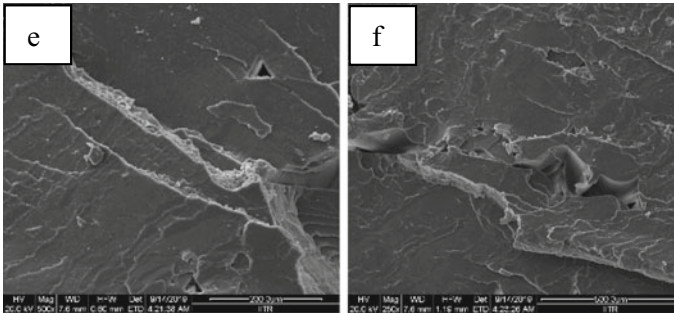
- The tensile strength of specimen 7 (layer height—0.6 mm, nozzle speed— 5 mm s^{-1} , and infill pattern—concentric) was found the highest (54.437 MPa) among the fabricated specimens due to the higher layer height. There are less number of air gaps/voids and less nozzle speed which provides time for better bonding to take place between the adjacent layers.
- The % elongation of the specimen 6 (layer height—0.4 mm, nozzle speed – 15 mm s^{-1} , and infill pattern—line) was 13.19% which is the highest among the



FE- SEM image of fracture in sample no. 7



FE- SEM image of fracture in sample no. 1



FE- SEM image of fracture in sample no. 6

Fig. 5 FE-SEM micrographs of the tested samples

3D-printed specimens. It is due to the fact that the infill raster pattern, i.e., line is along the direction of the applied tensile load.

- The fractography analysis revealed that failure of PLA specimens under tensile loading was due to brittle fracture. The presence of voids/air gaps between the layers significantly decreases the tensile strength.

Acknowledgement The authors would like to acknowledge the financial support provided by the Ministry of Human Resource and Development (MHRD), Government of India, under the scheme National Initiative for Design and Innovation for the present research.

References

1. Kai CC, Fai LK, Chu-Sing L (2003) In: Rapid prototyping: principles and applications in manufacturing. World Scientific Publishing Co., Inc
2. Gibson I, Rosen D, Stucker B (2015) In: Additive manufacturing technologies: 3D printing, rapid prototyping, and direct digital manufacturing, 2nd edn, pp 1–498 <https://doi.org/10.1007/978-1-4939-2113-3>
3. Negi S, Dhiman S, Sharma RK (2014) Basics and applications of rapid prototyping medical models. *Rapid Prototyp J* 20:256–267. <https://doi.org/10.1108/RPJ-07-2012-0065>
4. Pham D, Dimov SS (2012) Rapid manufacturing: the technologies and applications of rapid prototyping and rapid tooling. Springer Science and Business Media
5. Torrado Perez AR, Roberson DA, Wicker RB (2014) Fracture surface analysis of 3D-printed tensile specimens of novel ABS-based materials. *J Fail Anal Prev* 14:343–353. <https://doi.org/10.1007/s11668-014-9803-9>
6. Dudek P (2013) FDM 3D printing technology in manufacturing composite elements. *Arch Metall Mater* 58:1415–1418. <https://doi.org/10.2478/amm-2013-0186>
7. Torrado AR, Roberson DA (2016) Failure analysis and anisotropy evaluation of 3D-printed tensile test specimens of different geometries and print raster patterns. *J Fail Anal Prev* 16:154–164. <https://doi.org/10.1007/s11668-016-0067-4>
8. Ahn SH, Montero M, Odell D et al (2002) Anisotropic material properties of fused deposition modeling ABS. *Rapid Prototype J* 8:248–257. <https://doi.org/10.1108/13552540210441166>
9. Bellini A, Güçeri S (2003) Mechanical characterization of parts fabricated using fused deposition modeling. *Rapid Prototype J* 9:252–264. <https://doi.org/10.1108/13552540310489631>
10. Christiyan KGJ, Chandrasekhar U, Venkateswarlu K (2016) A study on the influence of process parameters on the mechanical properties of 3D printed ABS composite. *IOP Conf Ser Mater Sci Eng* 114. <https://doi.org/10.1088/1757-899X/114/1/012109>
11. Durgun I, Ertan R (2014) Experimental investigation of FDM process for improvement of mechanical properties and production cost. *Rapid Prototype J* 20:228–235. <https://doi.org/10.1108/RPJ-10-2012-0091>
12. Ang KC, Leong KF, Chua CK, Chandrasekaran M (2006) Investigation of the mechanical properties and porosity relationships in fused deposition modelling-fabricated porous structures. *Rapid Prototype J* 12:100–105. <https://doi.org/10.1108/13552540610652447>
13. Torres J, Coteló J, Karl J, Gordon AP (2015) Mechanical property optimization of FDM PLA in shear with multiple objectives. *Jom* 67:1183–1193. <https://doi.org/10.1007/s11837-015-1367-y>

Characterization of SiC-Reinforced AZ91 Magnesium Alloy Composites Produced Using In situ Microwave Casting



Radha Raman Mishra, Parvej Alam, Jitendra Yadav, Gaurav Kumar, and Apurbba Kumar Sharma

1 Introduction

In recent years, time compression and energy-saving attributes of microwave energy over conventional heating processes while processing metallic materials have been explored in various researches [1, 2]. It has been reported that microwaves induce two-directional heating during microwave hybrid heating (MHH) of metallic materials that results in more uniform heating [3]. Various processes such as sintering [4–10], joining [11], cladding [12], and casting [13, 14] have been developed to process metallic materials using MHH technique. Microwaves couple with metallic powder particles rapidly at room temperature due to availability of higher surface area and comparable particles size and microwave penetration depth [1].

On the other hand, bulk metallic materials reflect almost all microwaves from their surfaces, owing to very small skin depth and negligible heating of bulk material occurs at room temperature [15]. However, the increase in temperature of bulk metals allows microwaves to penetrate deeper in the target metal and enables the

R. R. Mishra (✉) · A. K. Sharma

Design Innovation Center, Indian Institute of Technology Roorkee, Roorkee, Uttarakhand 247667, India

e-mail: rmishra@me.iitr.ac.in

A. K. Sharma

e-mail: aks@me.iitr.ac.in

P. Alam · J. Yadav · G. Kumar · A. K. Sharma

Department of Mechanical and Industrial Engineering, Indian Institute of Technology Roorkee, Roorkee, Uttarakhand 247667, India

e-mail: parvejalam33@gmail.com

J. Yadav

e-mail: jkyadav1@hotmail.com

G. Kumar

e-mail: grv.kmr2015@gmail.com

material to attain microwave absorbing characteristics beyond its critical temperature [11–13]. Microwave casting of metallic materials is one of the novel applications of microwave energy. Prior to casting, melting of bulk metallic materials using microwave energy was demonstrated [16–20]. For better utilization of microwave energy during the melting of metals, understanding of microwave-metallic material interaction phenomena is required. Experimental and theoretical studies were reported to explore physics of microwave melting of metallic materials [17, 19, 21]. Microwave melting of metals in the inert atmosphere was reported, and a comparison was also carried out with conventional furnaces melting [17]. Microwave melting was found faster and significant energy-saving process than conventional melting processes. The thermal profile of aluminum alloy 7039 while exposed to microwaves in the ambient environment was studied [19, 21]. It was reported that the electromagnetic properties of the oxide layer, which forms on the surface of alloy influences the microwave heating significantly at elevated temperatures. Various metals/alloys such as aluminum, copper, steel, titanium, lead, and tin were melted using microwave energy; however, melting of magnesium was hardly reported. The lower ignition temperature of the magnesium might result in limited research in the casting of magnesium. In spite of the fact, magnesium and its alloys offer ease of recycling, superior specific mechanical properties, high damping capability, and significant electromagnetic shielding capability. These properties place them in highly demanded industries, including aerospace and automotive. In the present work, microwave energy at 2.45 GHz was used to cast AZ91 magnesium alloy-based silicon carbide metal matrix composite (AZ91 Mg alloy/SiC MMC) inside a multi-mode microwave applicator. The produced composites cast were characterized. Microstructural properties of the composites vis-à-vis micro-indentation hardness were discussed.

2 Materials and Method

Magnesium alloy AZ91D was used as charge material for the experimental trials. The optical image of the alloy indicating the microstructure is shown in Fig. 1a. The elemental composition of as-received alloy is presented in Table 1.

The silicon carbide (SiC) powder particle of 800 grit size (average diameter of 6.5 μm) was used as a reinforced constituent in the process. The SEM image of SiC powder particles is shown in Fig. 1b. A microwave applicator (Mode: multi-mode, Model: MH-1514–101-V6, Make: Enerzi Microwave Systems Pvt. Ltd.) and a casting setup including a base, split mold, pouring basin, susceptor, and sprue were used for experimental trials. A schematic diagram of the in situ microwave casting setup is shown in Fig. 2. The ceramic crucible acts as a pouring basin and absorbs microwave energy rapidly during microwave irradiation. The charge was hybrid heated using the pouring basin. The alumina sprue was used to facilitate self-pouring of the melt into a mold cavity. The split mold made of graphite was used for solidification of the melt. A ceramic plate of low dielectric loss was used for the base

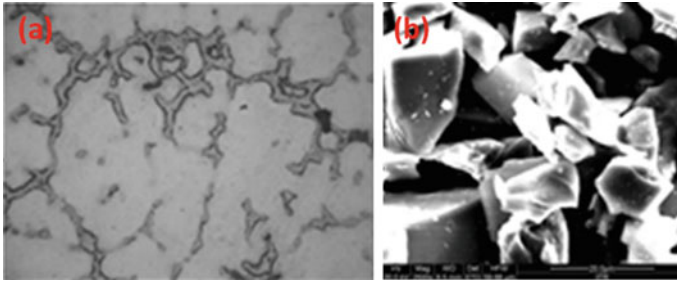


Fig. 1 **a** Optical image of as-received AZ91 alloy (500 ×) and **b** SEM image of the SiC powder particles

Table 1 Elemental composition of the as-received alloy

Elements	Al	Fe	Zn	Cu	Mn	Mg
% Wt	6.81	0.01	0.35	0.03	0.01	Bal

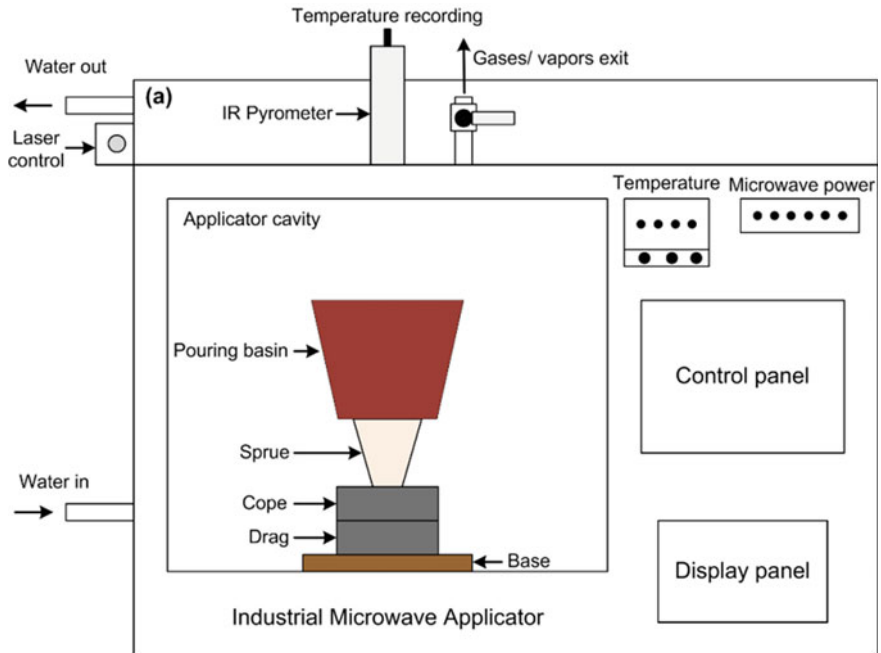


Fig. 2 Schematic diagram of the microwave casting setup

to avoid any possibility of thermal damage in the cavity. The setup was insulated using a microwave transparent material to reduce heat losses from mold assembly to the cavity environment. The mold assembly was placed inside the cavity. The position of the charge (50 g) and mold assembly was fixed using a laser control. The SiC powder works as a susceptor and also accelerates the microwave heating process. Monitoring of temperature at the top surface of charge was carried out using a built-in infrared (IR) pyrometer (range: 350–1800 °C, least count: 1 °C). The charge and SiC mixture was exposed to microwaves at 2.45 GHz and 1400 W in the ambient cavity environment. The temperature of the top surface of the charge was monitored up to its melting. A sharp decrease in charge temperature indicated self-pouring of the melt inside the cavity. The experiments were repeated at least thrice to ensure that the data were reproducible.

The produced casts were sectioned and polished using standard metallographic techniques. The polished samples were cleaned with acetone and dried. The microstructural analysis was carried out using an optical microscope (Make: Dewinter, Model: LT-23B) and a software tool (Dewinter Material plus, version 4.2). Moreover, a field emission scanning electron microscope (FE-SEM, Make: Carl Zeiss, Model: Ultra Plus) equipped with energy-dispersive X-ray spectroscopy (EDS, Make: Oxford X-max) was also used to see the various phases present in the cast and their chemical compositions. The phase analysis was carried out at room temperature using X-ray diffraction (XRD) in a Bruker AXS diffractometer with Cu-K α X-ray with a scan rate at 1° min⁻¹ within the scan range of 5–100°. A Vickers microhardness tester (Make: Chennai Metco, Model: Economet VH 1MD) was used to measure the hardness of the developed casts using the load of 100 g with dwell time 30 s.

3 Results and Discussion

3.1 Microstructural Analysis

Figure 3a shows the optical image of a selected area of the cast cross section. It is evident from Fig. 1a that the grain size of the cast is lesser as compared to as-received materials. The presence of SiC particles in the cast cross section is also visible. The high-resolution image (Fig. 3b) of the cast cross section indicates the presence of various phases at grain boundaries and distribution of SiC particles inside the grains and along the grain boundaries. The dark areas in the SEM micrograph correspond to α -Mg phase, whereas the lighter areas indicate the precipitated intermetallic phases. The shiny particles are traces of the η -phase which predominantly contains aluminum.

Distribution of various elements which are present in the developed cast along a selected line (Fig. 4a) on the cast cross section is shown in Fig. 4b. The EDS analysis along the line clearly shows the presence of elements Mg, Al, Si, Ni, Zn and C in the

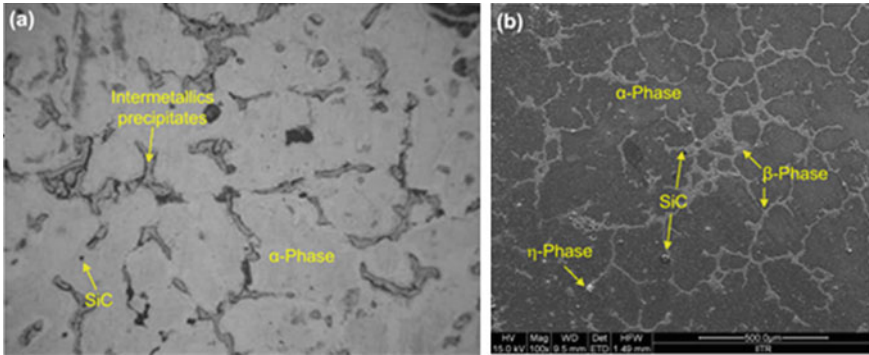


Fig. 3 a Optical image b Fe-SEM micrograph of the cast AZ91 alloy

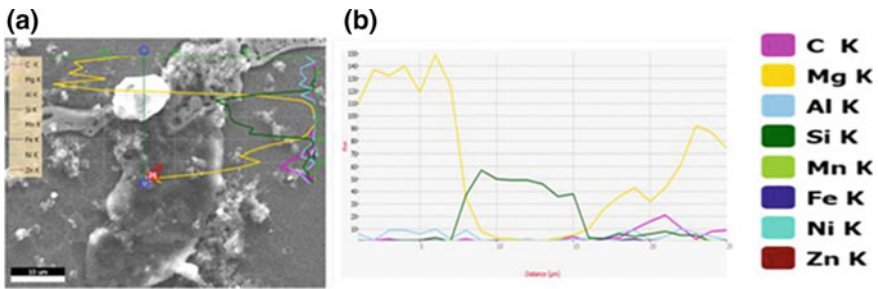


Fig. 4 a SEM image of a selected area of the cast and b distribution of various elements present along a specified length in a

cast. It indicates the possible presence of SiC particles, α -Mg phase, Mg_2C , Mg_2C_3 , $Mg_{17}(Al, Zn)_{12}$, and the phase β - $Mg_{17}Al_{12}$.

3.2 X-Ray Diffraction Analysis

The X-ray diffraction pattern of the various produced composite cast samples is shown in Fig. 5. It indicates that α -Mg phase is mainly present in the composite cast. Also, the presence of SiC, phase Mg_2Si , and phase β - $Mg_{17}Al_{12}$ was observed. However, no trace of metallic carbides was observed.

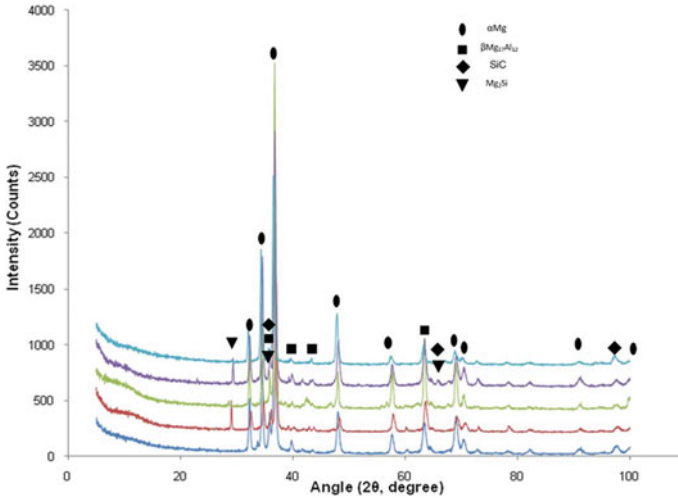


Fig. 5 Image indicating the X-ray diffraction pattern of different composite casts of alloy AZ91/SiC

3.3 Microhardness Analysis

Microhardness analysis was carried out on the developed composite casts and as-received alloy. The average value of microhardness for the base alloy was found to be 115 ± 10 HV, whereas microhardness of the composite cast was observed 206 ± 28 HV. The increase in hardness of the composite cast is due to the presence of harder SiC and Mg_2Si intermetallic phase. Moreover, the decrease in grain size as evident from Figs. 1a and 3a also affects the hardness. According to the Hall–Petch relationship, the decrease in grain size enhances the hardness of a material. Therefore, in the present study, the increase in hardness of the cast composite as compared to the base alloy is attributed to (a) presence of SiC particles and intermetallic phases and (b) finer grains of the composite cast.

4 Conclusions

In the present work, a new approach called in situ microwave casting is used for casting the magnesium alloy (AZ91)-based SiC-reinforced metal matrix composites. The following may be concluded from the study -

- (a) Microwave hybrid heating approach can be utilized for the casting of metal matrix composites.
- (b) The microstructural analysis-indicated finer grains are formed in the composite cast as compared to the base alloy.

- (c) The presence of SiC particles in the composite cast was observed; however, more iteration is required to achieve uniform distribution of SiC particles.
- (d) Presence of various phases— α -Mg, β -Mg₁₇Al₁₂, Mg₂C, Mg₂C₃, Mg₁₇(Al, Zn)₁₂, and Mg₂Si and SiC were confirmed by the EDS and XRD results.
- (e) Presence of SiC, Mg₂Si phase, and finer grains in the cast composite results in higher microhardness.

References

1. Oghbaei M, Mirzaee O (2010) Microwave versus conventional sintering: a review of fundamentals, advantages and applications. *J Alloy Compd* 494(1–2):175–189. <https://doi.org/10.1016/j.jallcom.2010.01.068>
2. El Khaled D, Novas N, Gazquez JA, Manzano-Agugliaro F (2018) Microwave dielectric heating: applications on metals processing. *Renew Sustain Energy Rev* 82:2880–2892. <https://doi.org/10.1016/j.rser.2017.10.043>
3. Gupta M, Wong WLE (2005) Enhancing overall mechanical performance of metallic materials using two-directional microwave assisted rapid sintering. *Scripta Mater* 52(6):479–483. <https://doi.org/10.1016/j.scriptamat.2004.11.006>
4. Roy R, Agrawal D, Cheng J, Gedevisanishvili S (1999) Full sintering of powdered-metal bodies in a microwave field. *Nature* 399(6737):668–670
5. Mahmoud MM, Link G, Thumm M (2015) The role of the native oxide shell on the microwave sintering of copper metal powder compacts. *J Alloy Compd* 627:231–237. <https://doi.org/10.1016/j.jallcom.2014.11.180>
6. Muthuchamy A, Kumar R, Annamalai AR, Agrawal DK, Upadhyaya A (2016) An investigation on effect of heating mode and temperature on sintering of Fe-P alloys. *Mater Charact* 114:122–135. <https://doi.org/10.1016/j.matchar.2016.02.015>
7. Mondal A, Upadhyaya A, Agrawal D (2010) Microwave and conventional sintering of 90W–7Ni–3Cu alloys with premixed and prealloyed binder phase. *Mater Sci Eng: A* 527(26):6870–6878. <https://doi.org/10.1016/j.msea.2010.07.074>
8. Sueyoshi H, Hashiguchi T, Nakatsuru N, Kakiuchi S (2011) Effect of surface oxide film and atmosphere on microwave heating of compacted copper powder. *Mater Chem Phys* 125(3):723–728. <https://doi.org/10.1016/j.matchemphys.2010.09.066>
9. Rajkumar K, Aravindan S (2009) Microwave sintering of copper–graphite composites. *J Mater Process Technol* 209(15–16):5601–5605. <https://doi.org/10.1016/j.jmatprotec.2009.05.017>
10. Xu L, Srinivasakannan C, Peng J, Guo S, Xia H (2017) Study on characteristics of microwave melting of copper powder. *J Alloy Compd* 701:236–243. <https://doi.org/10.1016/j.jallcom.2017.01.097>
11. Bansal A, Sharma AK, Kumar P, Das S (2014) Characterization of bulk stainless steel joints developed through microwave hybrid heating. *Mater Charact* 91:34–41. <https://doi.org/10.1016/j.matchar.2014.02.005>
12. Zafar S, Sharma AK (2014) Development and characterizations of WC–12Co microwave clad. *Mater Charact* 96:241–248. <https://doi.org/10.1016/j.matchar.2014.08.015>
13. Mishra RR, Sharma AK (2017a) Structure-property correlation in Al–Zn–Mg alloy cast developed through in-situ microwave casting. *Mater Sci Eng, a* 688:532–544. <https://doi.org/10.1016/j.msea.2017.02.021>
14. Singh S, Gupta D, Jain V (2016) Novel microwave composite casting process: theory, feasibility and characterization. *Mater Des* 111:51–59. <https://doi.org/10.1016/j.matdes.2016.08.071>
15. Mishra RR, Sharma AK (2016a) Microwave–material interaction phenomena: heating mechanisms, challenges and opportunities in material processing. *Compos a Appl Sci Manuf* 81:78–97. <https://doi.org/10.1016/j.compositesa.2015.10.035>

16. Agrawal D (2006) Microwave sintering, brazing and melting of metallic materials. In: Sohn international symposium on advanced processing of metals and materials. New improved and existing technologies, Non-Ferrous materials extraction and processing, vol 4. pp 183–192
17. Chandrasekaran S, Basak T, Ramanathan S (2011) Experimental and theoretical investigation on microwave melting of metals. *J Mater Process Technol* 211(3):482–487. <https://doi.org/10.1016/j.jmatprotec.2010.11.001>
18. Moore AF, Schechter DE, Morrow MS (2006) Method and apparatus for melting metals. United States Patent No. US 7,011,136 B2
19. Mishra RR, Sharma AK (2016b) On mechanism of in-situ microwave casting of aluminium alloy 7039 and cast microstructure. *Mater Des* 112:97–106. <https://doi.org/10.1016/j.matdes.2016.09.041>
20. Lingappa MS, Srinath MS, Amarendra HJ (2017) Microstructural and mechanical investigation of aluminium alloy (Al 1050) melted by microwave hybrid heating. *Mater Res Expr* 4(7):076504
21. Mishra RR, Sharma AK (2017b) On melting characteristics of bulk Al-7039 alloy during in-situ microwave casting. *Appl Therm Eng* 111:660–675. <https://doi.org/10.1016/j.applthermaleng.2016.09.122>

Design of a Customized Fixture for Joining Jute Fiber-Based Composites Using Microwave Energy



Ravi Saukta, Ram Singh Rana, Tejas Pramod Naik,
Kassahun Gashu Melese, and Radha Raman Mishra

1 Introduction

Nowadays, natural fiber-reinforced composites are preferred over the synthetic fiber-reinforced composites in many engineering applications such as marine, automotive and aerospace industry due to its various benefits of using natural fibers as reinforcement in composite like their biodegradability in the environment owing to its conversion in the form of H₂O and CO₂, once decomposed by the action of the microorganism in the environment [1]. The context of using natural fiber-based composites in automobile industries is to reduce the overall weight of components, which further leads to an improvement in fuel efficiency and finally helps in vehicle weight reduction. As a result of this, researchers nowadays have turned toward the use of natural fiber (jute, sisal, kenaf, bagasse, etc.) based polymer matrix composites. Though it is practically not possible to replace all of the synthetic-based PMCs by natural fiber-based PMCs, because of the high strength provided by synthetic fibers,

R. Saukta
THDC India Limited, Rishikesh 249201, India
e-mail: ravisaukta99999@gmail.com

T. P. Naik (✉) · R. R. Mishra
Design Innovation Center, Indian Institute of Technology Roorkee, Roorkee, Uttarakhand 247667, India
e-mail: tejasnit@gmail.com

R. R. Mishra
e-mail: rmishra@me.iitr.ac.in

R. S. Rana · T. P. Naik · K. G. Melese
Mechanical and Industrial Engineering Department, Indian Institute of Technology Roorkee, Roorkee, Uttarakhand 247667, India
e-mail: ramsingh.mech17@gmail.com

K. G. Melese
e-mail: kassahun28@yahoo.com

still the natural fiber-based PMCs can be used in areas where load-bearing is not the main concern [2]. To make the product commercially viable, joining operation is required to assemble the individual parts manufactured independently into the intricate final product. The joining of component is generally accomplished by the adhesive joining, mechanical joining and fusion joining processes. The adhesive joining provides uniform distribution of stress at the joining area. However, the interfaces of adhesive and adherents are more prone to failure in the adhesive joint. The adhesive joining also depends upon the curing time, which is around 24 h to cure the adhesive properly in between the adherents. The applications of adhesive joining are limited as it only holds good in case of natural fiber-reinforced thermoset composites [3]. However, the mechanical joining (non-permanent nature) provides adequate strength as compared to adhesive joining, and it is also a commercially available technique to join the various components by using mechanical fasteners like rivets, screws, etc [4]. However, the drilling of adherents is required before their mechanical joining, which further depends upon the various parameters like tool geometry, the force required to drill, etc. The optimization of all the drilling parameters required otherwise, it leads to various types of defects during the mechanical joining of natural fiber-based composites like rapid tool wear, delamination, fiber pullout, matrix burning, etc. [5, 6]. Therefore, various researchers have been using different types of fusion-based techniques like friction, ultrasonic and microwave-based techniques for joining purposes, and out of all the available fusion-based techniques, the microwave energy-based technique preferred over the others due to its less processing time, volumetric heating, less thermal gradient as compared to conventional types of processing routes [7].

The electromagnetic waves in the frequency domain of 300 MHz–300 GHz are representing the microwave energy domain. Electric and magnetic fields in EM waves are 90° to each other, having a wavelength range from 1 to 1000 mm [8, 9]. The microwave processing of PMCs depends upon the dielectric constant values of both fibers and matrix, and its value for natural fibers lies in the range of 3–6. In contrast, for thermoplastic matrix material, it varies from 2.26 to 2.4. So, the constituent with higher dielectric constant gets heated first through microwave energy as compared to a lower dielectric constant constituent. The fiber gets heated through microwave energy and via conduction heat transferred to the surrounding constituent [10]. The microwave heating predominantly occurs by the electric field through dipolar and conduction losses in the case of non-magnetic materials like water, aluminum, polymers, etc. Mainly, dipolar losses are predominant in dielectric insulators. In dielectric insulators like polymers, dipoles are produced in the material due to oscillating electric field during reorienting themselves, generate heat and increase the temperature due to friction generated between them [11–14].

Nowadays, a lot of works have been reported by various researchers across the world on the joining of natural-based fiber composites. The authors prepared green sisal fiber-reinforced polylactic acid composites with variable fiber content using compression molding, joined them using microwave energy process with charcoal as an accelerator and reported that the time taken for bond formation was more for samples with lower fiber content [15]. In another study, biodegradable natural fiber

(*Grewia optiva*)-reinforced PLA composite has been developed and joining in the lap configuration done using adhesive bonding and microwave joining using charcoal as a susceptor and the outcome of the results were validated through simulation work. The tensile strength of neat PLA resin increased by 75% by the addition of *Grewia optiva* and better joint strength obtained using microwave than adhesive joining, as reported by the author [16]. The author fabricated the four different types of *Grewia optiva* (GO) and nettle fiber (NF) based PLA and PP composites by varying the percentage of fiber content and did the comparative analysis in between adhesive and microwave joining by comparing their joint strength. PLA-based composite showed higher failure load because the failure strength of neat PLA resin was higher than PP. Joint strength was observed more in the case of microwave joining as compared to adhesive joining. Power input, microwave exposure time, susceptor and location of the specimen in the microwave cavity were found to be playing an important role in the fabricating of effective joint [17].

In this current investigation, the jute fiber-reinforced polypropylene composite was developed by compression molding to join them using microwave energy. To accomplish the joining of composite specimens, a special type of Aluminum -based fixture was designed and developed to improve the joint strength. The purpose of a special fixture is also to concentrate the microwave energy at the joint area. The SiC being a good absorber of the microwave due to its high loss insulator was used to provide heat to the joining area. The SiC brick was kept on both sides of the fixture for effective transfer of heat to the fixture.

2 Materials and Methods

2.1 Fiber and Matrix

Polypropylene used for fabrication of composite was supplied by Reliance Industries Limited, Mumbai, India, in the form of homopolymer pellets having a density of 0.905 g/cm^3 at room temperature. The melting point temperature of PP is $170 \text{ }^\circ\text{C}$, and its glass transition temperature is $100 \text{ }^\circ\text{C}$ with a melt flow index of 10.5 g/10 min . Woven jute fiber used as reinforcement in composite was supplied by Uttarakhand Bamboo and Fiber Development Board (UBFDB), Dehradun, Uttarakhand, India.

2.2 Methodology

Polypropylene sheets of dimensions $150 \text{ mm} \times 80 \text{ mm} \times 1 \text{ mm}$ were prepared by compressing 200 g of PP pellets in the compression molding machine at 120 kg/cm^2 , which has been heated up to $180 \text{ }^\circ\text{C}$, and it was then allowed to cool for 20 min in the die itself. Alternate layers of woven jute fiber and PP polymer matrix were kept over

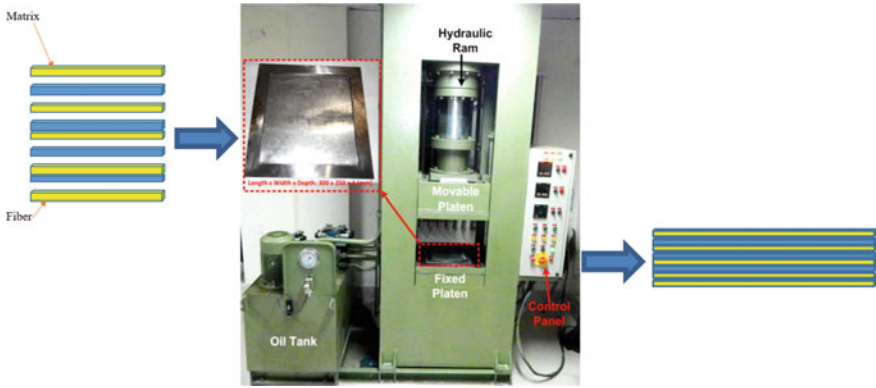


Fig. 1 Pictorial view of sample preparation via a compression molding process

each other so that polymer can bind the fiber firmly with it. Sticking of the composite to the mold of the compression molding machine is avoided using a polyester sheet. The pictorial overview of the compression molding process is shown in Fig. 1.

2.3 Microwave Specification

The microwave used is a domestic microwave with a fixed frequency of 2.45 GHz (make:LG). The power output was kept at 900 W while doing the experimentation on the composite made. The dimensions of the microwave cavity was $527 \times 392 \times 480$ mm. The microwave joining setup along with aluminum fixture assembly is shown in Fig. 2.

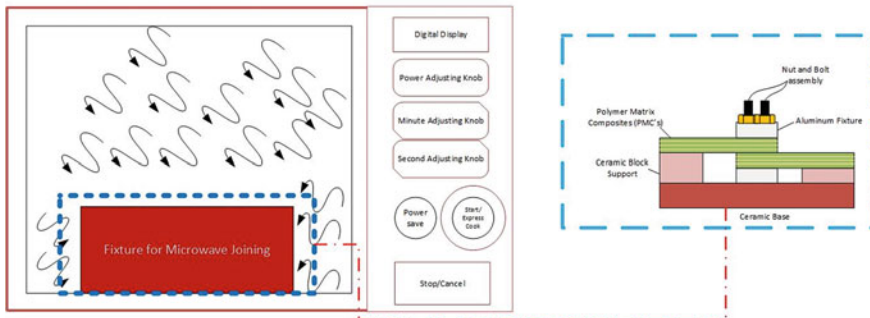


Fig. 2 Pictorial view of microwave joining assembly setup




2.4 Specimen Preparation

The parent composite fabricated by compression molding was cut as per ASTM D3039 to perform the tensile test. The composite specimen for joint lap configuration was prepared for tensile as per ASTM D 5868. The tensile strength of the parent composite specimens was compared with the tensile strength of the lap joint of the composite specimen. Both kinds of specimens were tested using a universal testing machine capacity of one tonne. An extension rate of 3 mm/min was used during the tensile test of both the parent specimens and the lap joint specimens. For parent composite, seven specimens were tested, and for the lap joint specimen, three specimens of three different kinds of configuration were tested. Scanning electron microscope was used to study the microstructures obtained to predict the kind of failure taking place during the testing of the specimen.

Three different types of lap joint configurations of the joint have been investigated in this research endeavor, as shown in Table 1. In the first type of lap joint, it was fabricated between specimens without using any filler material. The joint fabricated using a combination of heat and pressure is generated through the microwave curing and tightening of screws.

In type 2 kind of configuration, the lap joint was fabricated using a thin PP layer of 1-mm thickness at the interface of adherents. The polymer layer presence at the interface was expected to provide further strengthening to the joint obtained. In the third kind of configuration, two thin polymer layers of 1-mm thickness, along with a layer of fiber, were used at the interface of adherents. The fiber layer was expected to provide more additional heat at the interface due to its higher dielectric constant compared to the matrix material, which would further improve the fiber and polymer bonding to achieve the desired strength.

Table 1 Lap joint samples via microwave joining process

S. No	Type of composite configurations	Lap joint samples
1	Type 1	
2	Type 2	
3	Type 3	

3 Results and Discussion

All the experiments were conducted within a specific time ranged from 60 s to 90 s based on previous trial experiments. In all the experiments, the actual specimen strength was compared with different types of configuration samples. The average tensile strength came out nearly 26.42 MPa for pure specimen after taking the average of seven samples, and it was done to avoid any ambiguity occurred during the sample preparation via compression molding machine.

3.1 Lap Joint Efficiency

In the first type of configuration, the joint failed from the area nearer to joint rather than from the interface of the bonded area, which depicted good joint strength as supported by tensile test results. Consequently, it provided maximum joint efficiency of 81.05%. However in the second type of lap joint configurations, the presence of PP sheet instead of providing the strength to the joint by proper bonding with the fiber, it becomes the site of susceptible failure during the tensile loading. The failure can be attributed to the insufficient heat generated at the interface of the joint for proper melting owing to the lower dielectric constant value of PP material. All the samples represent a similar type of failure region during the tensile test. The mean and standard deviation graphs of both average maximum strength and lap joint efficiency are shown in Figs. 3 and 4.

In most of the cases, the strength obtained was nearly 25% of parent composite strength, which was significantly lesser than the strength as compared to joints of

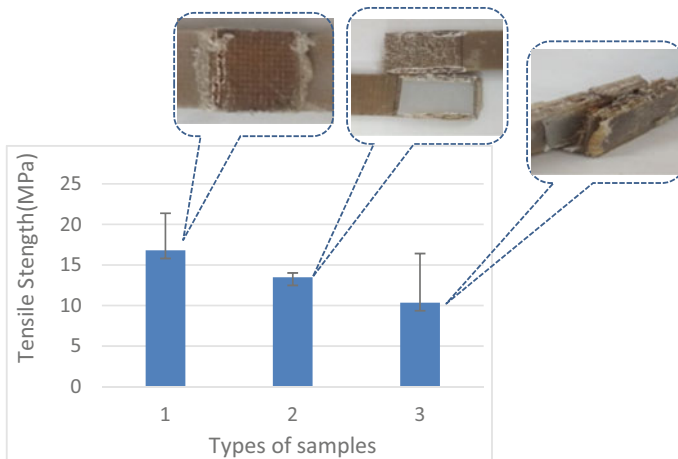
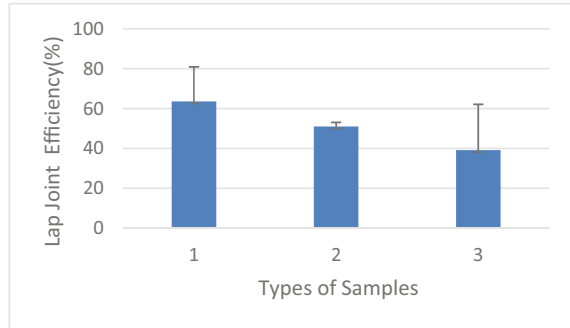


Fig. 3 Average tensile strength of different types of configurations

Fig. 4 Average lap joint efficiency of different types of configurations



Type 1 and Type 2. In that case, fiber got more heat at the interface as compared to the PP matrix sheet due to its higher dielectric constant, resulting in more microwave absorbing capacity as compared to PP material. However, the improper heating of the PP layers could be attributed by lesser heat transferred via conduction to the adjacent PP material sheets placed in between the adherents. Consequently, improper bonding occurred in between fiber and matrix.

3.2 FE-SEM

The microstructures of the fractured samples of highest and lowest lap joint efficiency were analyzed through field emission scanning electron microscope. The improper wetting and weak interfacial bonding between the fiber and polymer matrix due to less polymer impregnation in between the woven jute fiber were responsible for the failure of the specimen during the tensile test (Fig. 5), whereas in the case of a specimen of highest lap joint efficiency agglomeration and fiber pullout were seen as a responsible factor for failure of joint. These responsible factors can be minimized during the sample preparation via a compression molding.

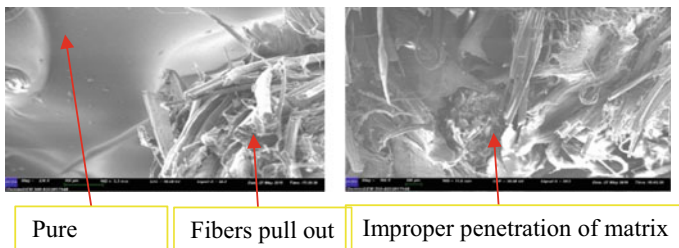


Fig. 5 FE-SEM of a fractured joint

4 Conclusions

In the present study, three different kinds of lap joints of natural fiber-based polymer matrix composite were fabricated. Microwave heating was used as a heating source for joining to take place by melting the interface in between the adherents.

Based on experiments, the following conclusions could be drawn:

1. As no susceptor material was used, no external impurity defects are observed, which has led to a tremendous increase in joint strength as compared to earlier obtained joint strength by various researchers.
2. Type 1 lap joint shows the most reliable and repeatable results as compared to Type 2 and Type 3 joints. So to have a good lap joint, no filler material should be used as it is giving results as high as 81.05% joint efficiency.
3. For Type 1 lap joint, the optimum time for microwave heating is 1 min 15 s, which gives 81% joint efficiency. For Type 2 lap joint, the optimum time for microwave heating is 1 min 19 s, which gives 52.93% efficiency. For Type 3 lap joint, the optimum time for microwave heating is 1 min 20 s, which gives 65.65% joint efficiency. So, microwave joining using designed fixture can be proved to be a feasible solution for joining of natural fiber-based partially biodegradable composites, because of the better strength compared to joint prepared without using fixture.

Acknowledgement The authors would like to acknowledge the financial support provided by the Ministry of Human Resource and Development (MHRD), Government of India to carry out this research work.

References

1. Mohammed L, Ansari MNM, Pua G, Jawaid M, Saiful Islam M (2015) A review on natural fiber reinforced polymer composite and its applications. *Int J Polymer Sci* Article ID 243947 <https://doi.org/10.1155/2015/243947>
2. Singh AP, Sharma M, Singh I (2013) A review of modeling and control during drilling of fibre-reinforced plastic composites. *Compos Part B: Eng* 47:118–125
3. Parashar A, Mertiny P (2012) Adhesively bonded composite tubular joints. *Rev Int J Adhes Adhes* 38:58–68
4. Pramendra Kumar Bajpai (2017) Kishore Debnath, Inderdeep Singh, Hole making in natural fiber-reinforced polylactic acid laminates: an experimental investigation. *J Thermoplast Compos Mater* 30(1):30–46
5. Singh I, Bhatnagar N, Viswanath P (2008) Drilling of uni-directional glass fiber reinforced plastics: experimental and finite element study. *Mater Des* 29(2):546–553
6. Bhatnagar DN, Nayak D, Singh I, Chouhan H, Mahajan P (2004) Determination of machining-induced damage characteristics of fiber reinforced plastic composite laminates. *Mater Manuf Process* 19(6):1009–1023
7. Bajpai PK, Singh I, Madaan J (2011) Joining of Natural Fiber Reinforced Composites using Microwave Energy. *Exp Finite Elem Study Mater Des* 35:596–602

8. Mishra RR, Sharma AK (2016) Microwave–material interaction phenomena: heating mechanisms, challenges and opportunities in material processing. *Compos a Appl Sci Manuf* 81:78–97
9. Clark DE, Sutton WH (1996) Microwave processing of materials. *Annu Rev Mater Sci* 26:299–331
10. Cabral H, Cisneros M, Kenny JM et al (2005) Structure–properties relationship of short jute fiber-reinforced polypropylene composites. *J Compos Mater* 39:51–65
11. Zhang H, Datta AK (2003) Microwave power absorption in single-and multiple item foods. *Food Bioprod Process* 81(3):257–265
12. Saltiel C, Datta AK (1999) Heat and mass transfer in microwave processing. *Adv Heat Transfer* 33(1):1–94
13. Clark DE, Folz DC, West JK (2000) Processing materials with microwave energy. *Mater Sci Eng a* 287:153–158
14. Pozar DM (2001) *Microwave engineering*, 2nd edn. John Wiley, Toronto, pp 1–49
15. Singh I, Bajpai PK, Malik D, Sharma AK, Kumar P (2011) Feasibility study on microwave joining of green composites. *J Akademia* 1
16. Singh I, Bajpai PK, Malik D, Madaan J, Bhatnagar N (2012) Microwave joining of natural fiber reinforced green composites. *Adv Mater Res* 410:102–105
17. Bajpai PK, Singh I, Madaan J (2013) Tribological behavior of natural fiber reinforced PLA composites. *Wear-An Int J Sci Technol Friction Lubr Wear* 297:829–840

Design of Hybrid Bearings and Its Development: A Review



Nisha Singh  and Praveen Kumar Agarwal 

1 Introduction

The term ‘hybrid’ is commonly described as a combination of two or more things together. Hybrid technology is a combination of two or more techniques to achieve efficient systems or better products. In the case of hybrid bearings, it combines two or more bearing technologies in one type of bearing to get the most of the advantages and reduce the limitations. Bearings are generally found in different types of applications in various kinds of machinery to adopt the desirable features, such as high load-carrying capacity, maximum pressure (P_{\max}), minimum fluid-film thickness (h_{\min}), high stiffness and damping, long life and temperature resistance. Hybrid bearings have various benefits over conventional bearings such as low friction and wear, high-precision positioning of the rotor, better load-carrying capacity (LCC), increased minimum film thickness, film stiffness and damping for different directions of loading, high-temperature applications [1].

Hybrid bearings are based on a combination of physical mechanisms such as hydrodynamic, hydrostatic, magnetic, grooves, recesses and pockets, holes and slots, foils, surface texture [11].

In hybrid journal bearing (HJB), hydrodynamic and hydrostatic physical phenomena are considered simultaneously. HJBs are categorized on different geometry configurations. In plain HJBs, recesses are avoided in the bearing surfaces to maximize the hydrodynamic effect. The plain HJBs can be classified based on lubrication feed to hole-entry and slot-entry restrictor bearings. Slot-entry restrictor has slotted shim, and hole-entry restrictor has holes in a ring form. Hole and slot types of

N. Singh (✉) · P. K. Agarwal
Mechanical Engineering Department, Motilal Nehru National Institute of Technology Allahabad,
Prayagraj, India
e-mail: singhnisha006@gmail.com

P. K. Agarwal
e-mail: pka@mnnit.ac.in

restrictors are arranged in a single row and double rows with the symmetric and asymmetric variety of configurations. The manufacturing of holes is easier in comparison to slots. With an increase in no. of holes, heat dissipation is reduced [1, 2, 11].

In HJBs, different types and number of recesses shape are also taken into account, such as circular, ellipsoidal, rectangular, triangular, shallow and deep pocket-type recess in a single row.

The geometry of HJBs is of three types: cylindrical, conical and lobed. Only the radial direction load is supported by the cylindrical journal bearing, whereas the conical journal bearing can support both radial and axial direction loads. Therefore, these types of bearings are the best substitute for the assemblies made up of journal and thrust bearings where the thrust is stable. Lobed type of bearing is of two-, three- and four-lobed in bearing design. Non-circular bearing {two-lobe (lemon), three-lobe and four-lobes} is implemented to overcome the issue of whirl and whip due to high speed and high loads during the operation. Two-lobe hybrid bearings have better stability and hydrodynamic performances.

Grooves are also used in HJB in the axial and circumferential directions. The axial grooves provide better lubrication for the load-carrying film. Lubricant is distributed around the journal by the circumferential grooves. Circumferential grooves are preferred because of reduced side leakage rates and the ability to minimize self-excited whirl for dynamically loaded conditions. Different types of combination of recess and grooves are used for HJBs.

Surface textures are also used for HJBs. Surface texture is the micro-cavity on the bearing surface to provide micro-lubrication in various micro-shapes such as rectangular, circular, triangular and many others. Surface texturing is provided in bearing surface because of its friction and wear-resistant properties. The surface texture is used to improve tribological properties [32].

HJBs have advantages over hydrodynamic bearing in avoiding wear in starting and stopping conditions and can tolerate designed loads over and above the usual design load in comparison to the hydrostatic bearing. The features of this bearing are discussed in Sect. 2.1.

Hybrid conical journal bearing (HCJB) is the combination of conical bearing and hydrodynamic–hydrostatic bearing to overcome individual bearing limitations and have excellent performance both in starting and stopping conditions. Further, these bearings can support both radial and axial loads. HCJB features and performance are described in Sect. 2.2.

Hybrid lobed journal bearing (HLJB) consists of lobed bearing and hydrostatic–hydrodynamic combination. It has high stiffness and excellent damping characteristics and can support loads with low-viscosity fluids. The performance and features are described in Sect. 2.3.

Hybrid foil journal bearing (HFJB) combines the hydrostatic lift with the hydrodynamic pressure. It can reduce or remove the wear problem occurring in the starting and stopping of the bearing operation. Features of these bearing are described in Sect. 2.4.

Hybrid magnetic journal bearing (HMJB) combines both hydrodynamic and magnetism mechanisms simultaneously to take the benefits of both and limits the

demerits. Magnetism is applied in two ways: active and passive magnetism. The active magnetic technology is mostly used in various applications. These bearings exhibit the advantages of both bearings, such as high load capacity with higher stiffness. These bearings also avoid the starting and stopping wear and provide higher load-carrying capacity, and its features are described in Sect. 2.5.

Hybrid foil magnetic bearing (HFMB) combines compliant foil structure bearing and active magnetic bearing (AMB). These demonstrate the features of the high load-carrying capacity of the compliant foil bearing and high stiffness and control versatility of AMB. This bearing is the solution for wear and friction of foil bearings at starting speed and provides greater load-carrying capacity at high speeds than AMB. The salient features of this bearing are described in Sect. 2.6.

2 Classification of Hybrid Bearings

One key issue of hybrid bearings is to design the topological structures, which affect the performance of the hybrid bearing system.

2.1 Hybrid Journal Bearing (HJB)

HJB is developed to employ the hydrostatic and hydrodynamic characteristics to provide a cheaper bearing with adorable features in respect of less friction and wear, more precise rotor location, greater overload capacity, higher minimum film thickness, film stiffness and damping for different load orientations. Figures 1 and 2 show the general structure of non-recessed and recessed HJB.

The optimization of HJBs, based on varying clearance and varying viscosity, was proposed by Rowe and Koshal [1]. It was shown that plain HJB is more economical when compared with a recessed hydrostatic bearing. Results showed that for hybrid operation, increased load support could be achieved at the expense of total power dissipation.

Koshal and Rowe [2] performed theoretical and experimental investigations for oil-lubricated slot-type plain HJBs to determine its performance. It was described that

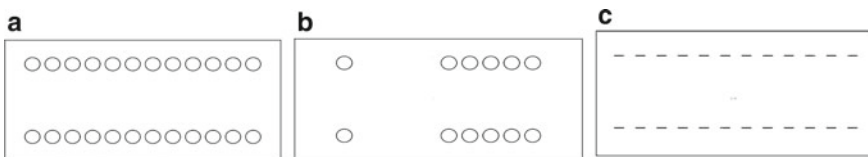


Fig. 1 A non-recessed hybrid journal bearing **a** symmetric hole-entry, **b** asymmetric hole-entry, **c** slot-entry

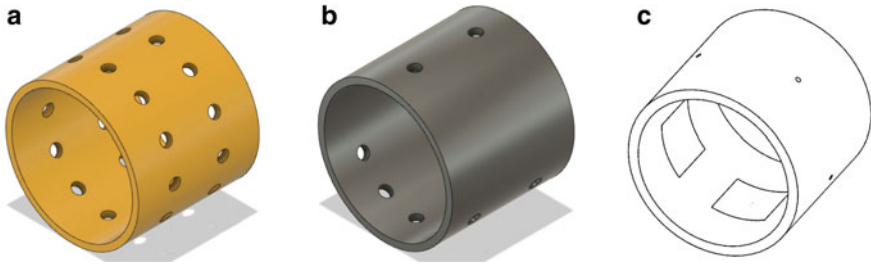


Fig. 2 HJB **a** symmetric hole-entry, **b** asymmetric hole-entry, **c** recess type

hybrid bearings have better features of both hydrostatic and hydrodynamic bearings, and these are more efficient on the basis of load and power.

Rowe et al. [3] wrapped up the performance of non-recessed journal bearings, and they concluded that bearing performed better than the recessed bearing. The efficiency of hole-entry bearings was reported at zero and high-speed operations by comparing with different configurations (such as plain slot-entry HJB, circumferential groove hydrodynamic bearing, axial groove hydrodynamic bearing, 4-recess hydrostatic bearing and non-uniform hole-entry HJB) for heavy load support and reduced energy consumption. Further, for the plain hybrid bearing with two rows of inlets for lubricant, enhanced load-carrying capacity was obtained for the lubrication entries near the bearing end. For asymmetric hole-entry journal bearing, a hole diameter ratio ($c < 1$) is beneficial for pure hydrostatic bearing. In contrast, for high-speed operation with a high eccentricity ratio, a hole diameter ratio ($c > 1$) is beneficial.

Chaomleffel and Nicolas [4] presented pressure distribution with the experimental method in HJBs along with the influence of pressure generation, and inertia forces and results were in good agreement with theoretical results. The first time, it was shown that for small eccentricities (<0.4), bearing behaviour was unloaded, and for large eccentricities (>0.4), hydrodynamic pressure generation was found on circumferential sills.

Yoshimoto et al. [5] presented the theoretical model for hole-entry bearing having capillary restrictor and reported that the pocket dimension highly influenced the load-carrying capacity at zero speed. Effects of bearing flexibility and misalignment on the behaviour of the hole-entry HJBs were also studied.

In non-recessed HJBs, the bearing hub may deform due to the fluid-film pressure under loading conditions, and it may lead to change in the fluid-film profile and the resulting bearing performance characteristics. The investigations were conducted for symmetric and asymmetric hole-entry HJBs [6–9] for investigating the performance characteristics compensated by the orifice and capillary restrictor for a large range of deformation coefficients. These studies also reported a reduced critical journal mass at a given load along with an increased bearing shell flexibility for the symmetric hole-entry-compensated flexible journal bearing.

Standard symmetric and asymmetric configurations were considered in most of the literature related to the non-recessed HJBs. However, most of the configurations

are attainable by altering the location of the hole, which may provide improved performance of the hole-entry journal bearing. Kumar et al. [10] investigated the performance characteristics of hole-entry journal bearing of various configurations and recognized the best configuration.

The influence of restrictor design on the performance and rotordynamic coefficients was presented by Kumar et al. [12]. A capillary restrictor with hole-entry double row (12 holes per row) system was used. Bearing flexibility and change in viscosity due to the rise in temperature of the lubricant were chosen for optimal stiffness and dynamic coefficients. It was shown that variations in flexibility and viscosity affect the design parameters and the stability of the rotor.

Duvedi et al. [14] presented an analytical analysis of non-recessed hole-entry capillary-compensated rigid HJB. Four different types of configuration were analysed. It was found that asymmetric configuration is better than the symmetric configuration concerning load-carrying capacity and stability.

Jadon et al. [15] presented the effects of supply cut-off and geometric parameters on the design of HJB. They reported an increment in the LCC with the plugging of the holes having the presence of the backpressure.

Awasthi et al. [16] showed the effects of wear on the performance of non-recessed hole-entry HJBs. This study was conducted for symmetrical and asymmetric hole-entry bearings. It was shown that wear defects on journal bearing should be minimized with suitable bearing configuration.

Garg et al. [13, 17, 18] thermally analysed the hole-entry HJBs compensated with a constant flow valve and capillary restrictor. It was shown that the performance features were significantly influenced by non-Newtonian and thermal effects of the lubricant. Viscosity variations due to lubricant and temperature rise were considered. The results indicated that the right choice of the value of the restrictor design parameter is mandatory to sustain h_{\min} between journal and bearing.

Garg [19, 20] studied an asymmetric slot-entry HJB system with rheological effects of the lubricant. The finite element method was used in this study. The results showed that a decrease in viscosity reduces h_{\min} and increases the oil requirement. Further, the decreasing viscosity of the lubricant diminishes the attitude angle and enhances the eccentricity ratio. The author also analysed the effects of non-Newtonian lubricant on the hole-entry double row HJB fed with the symmetric constant flow valve. It was shown that due to variation in viscosity, pressure profile gets affected, and the stability of a constant flow valve restrictor (CFV)-compensated hybrid bearing system declined due to viscosity variation of the non-Newtonian lubricant.

Garg and Kumar [21] investigated the analytical analysis of the static performance characteristics of HJB. The authors considered the influence of the plugging of holes of a constant flow valve (CFV)-compensated hole-entry HJB with Newtonian as well as non-Newtonian lubricants. The results showed that the plugged holes would result in sufficient fluid-film thickness with low power requirement and would not cause the failure.

Dwivedi et al. [22, 23] studied the effects of the number and size of recess on the performance of HJB. They reported a minimal effect of the number of recesses on

both load-carrying capacity and oil flow of bearing and also shown a decreased load capacity with an increased L/D ratio. They also showed the study of the lubricant supply arrangement in the non-recessed HJB with single/twin grooves at 30°, 90° and 150° arrangements. In comparison to a single groove, the twin groove caused a decrease in eccentricity, and a small length groove decreased the power loss, and the optimum location of grooves concerning load line were lying between 60° and 90°.

Wang et al. [24] presented water-lubricated HJB, which has circumferential grooves along with shallow and deep recesses. The results showed a decreased average temperature rise with increased flow and improved stability with deep recess depth.

Garg and Kumar [25, 26] analysed the effects of variation in viscosity because of non-Newtonian nature of lubricant and temperature rise on double row hole-entry HJBs compensated with constant flow valve for symmetric/asymmetric configuration. The results showed that a decrease in viscosity is responsible for h_{\min} due to non-Newtonian behaviour, and a rise in temperature improved the eccentricity ratio and declined the values of direct damping coefficients. It was found that a decrease in the viscosity increases the oil requirement and drop in the attitude angle for slot-entry HJB and h_{\min} was also decreased for asymmetric configuration.

Chan [27] presented a multi-objective particle swarm-based optimization algorithm for the design of HJBs. The objective of multi-objective optimization was to minimize the frictional force and maximize stiffness. The size of swarm was used as a variable for the examination of search capability for 2-factor and 4-factor multi-objective bearing optimizations. For the 2-factor case, variables were recess length and radial clearance, and for the 4-factor case, variables were recess length, recess width, radial clearance and orientation angle.

Ram and Sharma [28] investigated the effect of micro-polar lubricants on asymmetric-type slot-entry HJB. Hybrid bearing operating under micro-polar lubricant has higher fluid-film stiffness and damping coefficients. For constant load, the flow value was less for the HJB.

Ram et al. [29] presented the performance of slot-entry symmetric HJB in the turbulent regime. The results were evaluated in laminar as well as turbulent regions. The stiffness of fluid film decreased in the turbulent regime. Further, the damping coefficient increased in the laminar regime, and h_{\min} increased in the turbulent regime for the constant load.

Lin et al. [30] studied the effect of recess configuration on the behaviour of high-speed HJB and reported the combined effects of temperature, turbulence and convective inertia. The fluid–solid interaction (FSI) between lubricant film, journal and bearing wall was used on three HJB systems with different recess configurations such as shallow, deep and ladder-type recess.

Gen et al. [31] analysed the effects of the various recess shapes on the performance of 5 pockets HJB under similar loading conditions. The rectangular, triangular, circular, elliptical and annular shapes were considered. The authors used the response surface model-based method to find out the equilibrium for the journal position.

Khatri and Sharma [32] analysed the significance of surface texturing on the effectiveness of non-recessed HJB with non-Newtonian lubricant. The authors analysed the different configurations of HJB. Results showed that h_{\min} was reduced by surface texturing, and fully textured and dilatant fluid offered the lowest frictional torque. It was found that direct film stiffness coefficients and pseudoplastic fluid have greater values for the fully textured configuration, whereas direct damping coefficients and pseudoplastic fluid have greater values for the non-textured configuration. Further, the stability of the fully textured configuration was found to be greater than that of other configurations.

Ram [33, 36] investigated the performance of micro-polar lubricant on hole-entry HJB (symmetric/asymmetric) with capillary compensated. The results showed that for HJB with micro-polar lubricant, damping and stiffness coefficients were increased, and stability increased for the symmetric bearing configuration. The author also investigated symmetric hole-entry HJB fed by couple stress lubricant. The bearing had better fluid-film thickness and rotordynamic coefficients and exhibited improved stability. Further, h_{\min} was found to be more, and lower values of friction coefficient and lubricant flow were achieved.

Khatak and Garg [34] presented a theoretical analysis of the performance of capillary-compensated HJB considering the combined effect of thermal effects and micro-polar lubricants. Bearing performance gets degraded with consideration of thermal effects and micro-polar lubricants simultaneously.

Untaroiu and Fu [35] presented a complete analysis for the effect of recess shape on HJB with CFD, the design of experiments and optimization. The results showed the optimum size of the rectangular recess and the location of an orifice.

Song et al. [37] experimentally investigated the performance of discharge coefficients in FEM modelling of the hybrid bearing. The results indicated that journal speed was increased, and air-film thickness and high eccentricity ratios were also increased.

Khatak and Garg [38] presented a theoretical analysis of capillary-compensated HJB with the combined effect of thermal and micro-polar lubricant. The results indicated that the increase in micro-polar effects enhances the bearing performance. The stability of HJB was affected by thermal effects.

Chien et al. [39] presented the simulation of the performance of adaptive lubricants in an HJB with five rectangular recesses. This study used a 3D CFD model for HJB operated with fully saturated adaptive lubricants. The result showed that the PAG/CO₂ mixture provided a 19.6% greater load capacity.

Linjamaa et al. [40] analysed the thermal and elastic deformations of an HJB. The results indicated that compliant polymer layer hybrid bearing had suitable performance parameters such as P_{\max} and h_{\min} , and it reduced the maximum edge pressure in the shaft misalignment case.

2.2 Hybrid Conical Journal Bearing (HCJB)

Hybrid conical journal bearings (HCJB) can eliminate thrust bearing in rotor-bearing assemblies. These are used in precision machine tool applications such as high-speed and high-load lathes and grinding machines. Figure 3 shows the structure of hybrid conical journal bearing.

Srinivasan and Prabhu [41] presented the steady-state characteristics of externally pressurized inlet gas-lubricated conical hybrid bearing, which was finite and cone angle varied from 10° to 40° . The bearing had two rows of orifices having eight orifices each around the circumference at quarter division from the end of bearing. The theoretical estimation of pressure, load capacity, attitude angle, stiffness and friction moment were obtained. The results showed that the radial LCC of the tapered journal was higher at higher eccentricity ratios and frictional power loss increased with cone angle.

Hong et al. [42] presented the theoretical as well as experimental method for the dynamic performance of four deep and shallow pockets HCJB with capillary restrictors. The results demonstrated the good features of the bearing in terms of load capacity (LCC) and stability with small eccentricity.

Sharma et al. [43] analysed the behaviour of a multi-recess conical four-pocket HJB with orifice-compensated restrictor. This bearing was analysed for 10° – 40° semi-cone angles having the 10° difference. The stability of this bearing for the higher semi-cone angle was higher. The results exhibited the effect of wear on maximum fluid-film pressure, h_{\min} , bearing flow, direct fluid-film stiffness and damping coefficients and stability threshold speed margin. h_{\min} was decreased when bearing gets deteriorated. And for a 40° semi-cone angle, less lubricant flow was found in the worn-out condition. Direct film stiffness and damping coefficients were reduced as the bearing gets worn, and these coefficients had the most significant values for a 40° semi-cone angle.

Sharma and Rajput [44] theoretically analysed a 4-pocket conical hybrid bearing with capillary compensated fed with micro-polar lubricant. It was shown that if the micro-polar effect is increased, it resulted in increased h_{\min} , reduced bearing flow, increased direct fluid-film stiffness and damping coefficients and increased stability in comparison with Newtonian lubricant. Stability was greater for the higher values of semi-cone angle.

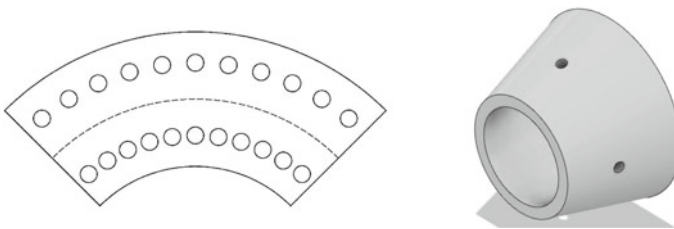


Fig. 3 Conical hybrid journal bearing

Khakse et al. [45] presented the analytical method to determine the static and dynamic performances of a non-recess hole-entry HCJB, and it was compensated with the capillary restrictor and had 12 holes in every two rows and analysed the effect of a semi-cone angle. With the increase in the rotary speed of shaft, P_{\max} was decreased for all semi-cone angle, h_{\min} and bearing flow increase, and direct fluid-film stiffness increases and damping coefficient decreases and stability was little less.

Khakse et al. [46] presented the analysis of a non-recessed HCJB with two rows, and each row consisted of 12 holes, and semi-cone angles were taken as 5° , 10° , 20° and 30° . The results showed that with an increment in semi-cone angles, direct fluid-film stiffness and damping performances increased for both non-recesses hydrostatic and hybrid bearings. HCJB showed better performance for a small cone angle.

Pawar and Phalle [47] presented a detailed study of the effects of wear on the behaviour of capillary-compensated hole-entry HCJB. The simulated outcome showed that if the wear depth was increased, it led to increased eccentricity, and h_{\min} was reduced with wear defect. Damping coefficients were reduced by 24.6% for a 25° semi-cone angle.

Phalle et al. [48] investigated the effect of speed of non-recessed worn HCJB (24 holes were symmetrically arranged in two rows) for different semi-cone angles (10° , 20° , 30° and 40°). The numerically simulated results showed that P_{\max} was increased by about 17.06% for 10° semi-cone angle. Stiffness coefficient increased drastically with an increase in speed, and stability was initially increased, then it was reduced with an increase in speed.

Kumar and Sharma [49] showed the textured conical HJB with smart lubricants fed by capillary restrictors with two numbers of rows and 12 numbers of holes per row. In this model, micro-textures were modelled at the end of the capillary restrictor in the convergent zone, and geometric shapes of micro-texture were rectangular and spherical. The results showed that rectangular dimple takes maximum enhancement in axial load, which was further enhanced by the use of smart lubricants. Partial texturing was good in comparison with full texturing and produced an excellent performance. ER lubricants and micro-textures increased h_{\min} , but micro-dimples increased the lubricant flow rate, and it reduced the electric field. Stiffness coefficients were improved with the combined effect of micro-dimples, and ER lubricants and damping coefficients were reduced in comparison to the circular bearings, and electro-rheological oils compensated this. The analysis showed that a semi-cone angle 30° was suitable for the enhanced value of the axial load, stiffness (axial) and damping coefficient, and 10° semi-cone angle gave better results for fluid-film thickness, friction force, lubricant flow and radial stiffness.

2.3 Hybrid Lobed Journal Bearing

Hybrid lobed journal bearing (HLJB) is designed for high-speed applications. These bearing offer admirable characteristics like favourable dynamic performance along

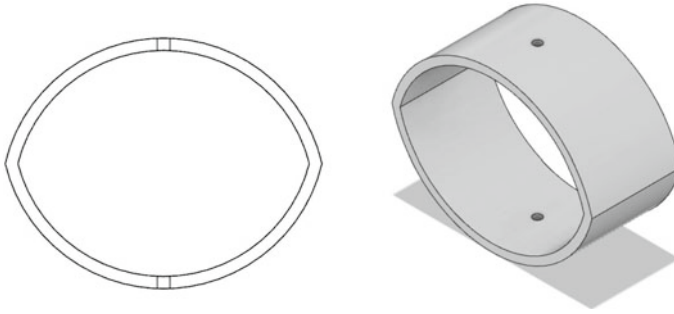


Fig. 4 Lobed-type hybrid journal bearing

with improved shaft stability due to non-circular geometry. HLJB is used to overpower the unfavourable issues of circular journal bearing, such as low stability including self-excited vibration and are being used in the industry considering their ease, effectiveness and less cost. The general configuration of hybrid lobed-type journal bearing is shown in Fig. 4.

Ghosh and Nagraj [50] showed the rotordynamic behaviour of four-lobe orifice-compensated HJB. The results showed that multi-lobe hybrid bearings provided a better substitute for high-speed turbopump. Stability was increased with the offset factor as the speed was increased. Low offset ($\delta = C_1/C_2 < 1.0$) gave improved stability at low speed and vice versa.

Jain et al. [51] analysed the two-lobe 4-recessed HJB with capillary and orifice restrictor, and performance characteristics were shown for different offset factors. It was found that this bearing is better for the direct damping coefficient, and it provided better stability and required less pumping power.

Phalle et al. [52] investigated the two-lobe four-pocket HJB with membrane-compensated restrictor. In this study, wear defect and offset factors were considered, and wear depth parameters were obtained for different values of offset factors and membrane compliance. With the increase in load factor and offset factors, h_{\min} was reduced. h_{\min} was the maximum for membrane restrictor. Wear caused a decrease in values of dynamic coefficients. Rotordynamic coefficients had higher values for membrane restrictor. It was found that the bearing performance with membrane restrictor was more sensitive to change in the wear height.

Sharma et al. [53] theoretically analysed a two-lobe four-recessed HJB with constant flow valve restrictor and defects caused by wear, focused on the load line. Numerically simulated results showed that load-carrying capacity and damping coefficient values were higher for larger offset values, and small values of wear defect were found to have no impact on P_{\max} . If the wear defect was greater than 20%, P_{\max} affected direct stiffness value. The stability threshold speed margin was diminished by wear.

Jain and Sharma [54] presented the performance of four pockets two-lobe HJB with the capillary-compensated restrictor. Different types of journal's geometric imperfections such as barrel, bellmouth and circumferential waviness were analysed,

and the bearing performance was compared with Newtonian and non-Newtonian lubricants with varying defects of the journal. The stiffness and damping coefficients had a higher value in the two-lobe case. h_{\min} and threshold speed have higher values for six-pocket two-lobe bearing configuration in comparison to 4-pocket and barrel, and undulation type of irregularities obtain better dynamic performance.

Sharma and Kushare [55] analysed the comparative study of two-lobe non-recessed roughed HJB. The performance of HJB was analysed with surface roughness, and various types of flow control devices were extended for various configurations of roughness as isotropic, transverse, longitudinal and smooth surfaces. As the surface roughness parameter decreased, it led to reduced h_{\min} . CFV restrictors provided the most significant value of direct film stiffness coefficients. The direct damping coefficient was higher for longitudinal roughness pattern.

Sharma and Khatri [56] analysed the effect of the ER oil-lubricated textured tribus-lobe hole-entry HJB system. This investigation included a comparative analysis of three-lobe HJB and textured three-lobe HJB. The results exhibited that the bearing can sustain a higher external load. The presented geometry of HLJB had improved stability, gave a higher h_{\min} , lower attitude angle, reduced frictional power loss and provide damped-out vibrations.

Khatri and Sharma [57] investigated the effects of couple stress lubricant on the behaviour of a textured duplet lobe slotted HJB. This study compared the results of non-textured slot-entry and textured slot-entry configuration. This bearing is beneficial from the lubricant requirement. Frictional torque is reduced, and rotor dynamic coefficient values increased due to couple stress lubricant.

Sharma and Kushare [58] investigated the nonlinear transient response of the two-lobe symmetric hole-entry HJB structure. The stability of hole-entry HJB changed with the change in surface roughness patterns. The authors investigated the nonlinear journal centre motion trajectory for three different roughness patterns, such as transversely oriented roughness pattern, isotropic pattern and longitudinally oriented roughness pattern for three conditions where journal mass was greater, equal and below the critical mass. When journal mass was similar to critical mass, the most significant value of the threshold speed margin was found for the longitudinal roughness pattern.

Khatri and Sharma [59] analysed the multi-lobe non-recessed textured HJBs with different restrictors and presented the comparative study of the combined effect of electro-rheological lubricants and spherical surface texturing on the performance of twin lobe/circular HJBs. The results exhibited that surface texturing improved the results of all restrictors except CFV. ER fluid gave a better performance with higher frictional torque. CFV was beneficial than the other bearings by considering frictional power losses, and it improved the stiffness coefficients and threshold speed margin parameters. CFV-compensated non-recessed bearing with ER lubricant gave overall best bearing performance characteristics, and it has a small radius of whirl orbit.

2.4 Hybrid Foil Journal Bearing (HFJB)

Hybrid foil journal bearing (HFJB) has provided significant advancement in oil-free rotating machinery. These bearings have no designed speed limit. These bearings can provide support in the high-temperature range, need less maintenance and have high efficiency with less operating costs. But it has lower load capacity in comparison to HJBs. Schematic and solid modelling structure of hybrid foil journal bearing is shown in Fig. 5.

Kumar and Kim [60] analysed the dynamic performance of hybrid air foil bearing (HAFB) including single top foil along with two bump foil and four feed tubes with 72° , 166° , 247° and 341° . It was found that the increase in supply pressure or feed parameter resulted in diminished direct and cross-coupled stiffness, moreover increased direct damping.

Kim and Lee [61] experimentally investigated the static performance of pre-loaded three-pad HAFB at zero running speed for midsized airborne turbomachinery applications. In this work, both simulation and experimental work were compared at zero speed. With the increase in the feed parameter, stiffness is decreased along with the increase in damping. Subsynchronous vibrations for hybrid air foil bearing appeared at higher speeds. Static stiffness increased with the applied load, and natural modal frequency increased with running speed.

Kim and Varrey [62] experimentally analysed rotordynamic performance. In this work, HAFB had three top foils with clearance distributed hydrodynamic preload. Imbalance responses in the cylindrical mode were showed for different pressure supply (2.67–4.67 bar). Imbalance response did not show the effect of increment in pressure near the critical speeds on natural frequency, bearing stiffness and damping. While with a slight increase in supply pressure, the subsynchronous vibrations were suppressed at high speed (34,000 rpm) without affecting the natural frequencies and modal stiffness.

Wang and Kim [63] experimentally showed the dynamic characteristics of a three-pad HAFB with a large diameter of 101.6 mm and 82.6 mm length. In this work, the stiffness coefficient was measured with both time and frequency domain, and it was found that results are close to each other, and coefficient depended on speed,

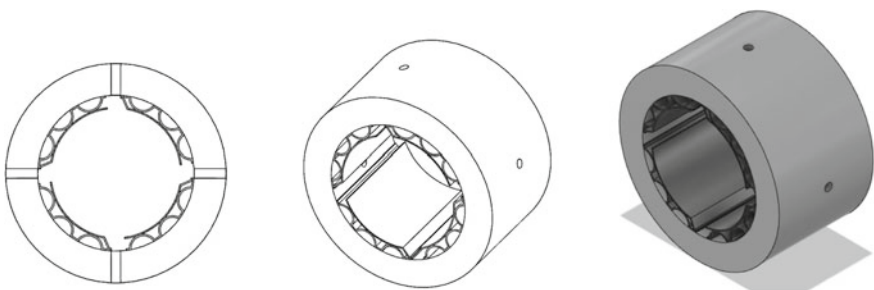


Fig. 5 Hybrid foil journal bearing

pressure (supply) and speed. The frequency domain method gave a larger deviation in results. Damping coefficients were measured only with the impulse response, and these results were compared with the linear perturbation method and showed good agreement.

Feng et al. [64] presented hybrid bump metal mesh foil bearing, which consisted of bump foil along with metal mesh bars in a supporting configuration. This bearing showed excellent damping. A metal mesh density of 36% provided improved damping coefficient, which was twice in comparison to bump foil bearing. This bearing possessed higher accuracy, better stability, improved precision and increased stiffness. With a decrease in density, the loss factor was increased.

Yazdi and Kim [65] analytically and experimentally analysed the rotordynamic performance of three-pad HAFB with top and bump foils. The controlled hybrid-mode eliminated subsynchronous vibrations and showed higher stability than full hybrid mode and hydrodynamic mode. Large eccentricities and small attitude angles provided higher stability.

Kim et al. [66] analysed the rotordynamic behaviour of three-pad HFB under forced vibration input. It had a higher impulse load capability up to 10 g and rotordynamic stability for 30,000 rpm under subsynchronous excitation.

2.5 Hybrid Magnetic Journal Bearing (HMJB)

Hybrid magnetic journal bearing (HMJB) is designed to get better results of both hydrodynamic and magnetic bearings technologies. It can compensate for the extremity of the permanent magnetic bearing breakdown and rotor fracture and can lead to lower wear of journal and stator as a result of the hydrodynamic operation.

Tan et al. [67] investigated hybrid bearing based on a combined permanent magnet and hydrodynamic configuration. The bearing force was generated from both hydrodynamic film and the permanent magnetic field. When the film was not formed, the magnetic force supported the rotor system. Experiment analysis showed that magnetic force and hydrodynamic film force are uncoupled.

Hirani and Samanta [68] presented different HMJB configurations (hydrodynamic + permanent magnetism). The experimental results indicated that hybrid bearing operated with low viscosity. Further, the hydrodynamic part was used to support the dynamic load, and the magnetic part was designed to hover the dead weight.

Muzakkir et al. [69] investigated the heavy loaded slow-speed HJB (magnetic arrangement with conventional journal bearing) with tribological failure analysis. Here, the circular arc (180°) magnetic arrangement and cylindrical (360°) magnetic bearing arrangement were compared. The circular arc magnetic bearing was found to have a higher static load-carrying capacity. The HMJB restrained the negative effects of the magnetic bearing breakdown.

Lijesh et al. [70] presented different configurations of hydrodynamic bearing with permanent magnetic bearing using a 3D Colombian model to avoid the wobbling of the rotor, metal-metal contact at start/stop, bearing wear and excessive power loss.

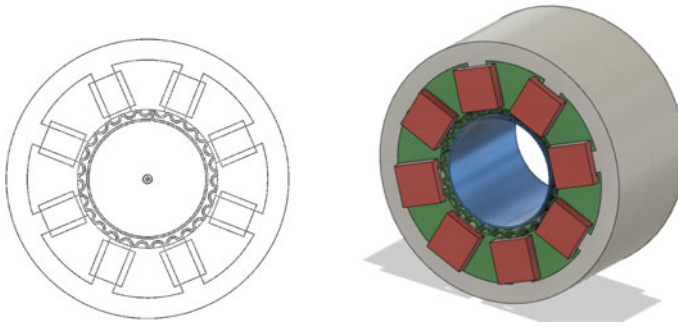


Fig. 6 Hybrid foil magnetic bearing

Here, the static and the dynamic loads were supported by the magnetic and the hydrodynamic bearings, respectively.

Lijesh and Hirani [71] presented the performance of HJB comprising of fluid-film bearing (FFB) + Halbach magnetic bearing under enormous operating conditions such as low-speed and high-load FFB. The results indicated that the bearing showed better performance compared to FFB. This bearing was proposed to reduce the wear in FFB, and theoretical analysis was proposed for sugar mill bearing. The results showed that load capacity was not affected by the eccentricity ratio, and a higher load-carrying capacity was achieved.

2.6 Hybrid Foil Magnetic Bearing (HFMB)

A hybrid foil magnetic bearing (HFMB) is a merger of a compliant foil bearing (CFB) and AMB. It grasps the advantage of both technologies while compensating for individual limitations. The general structure of HFMB is shown in Fig. 6.

Heshmat et al. [72] presented the HFMB (AMB and CFB) to take the maximum advantage of foil bearing and AMB. The authors developed an analysis technique to determine the behaviour of a gas-lubricated journal bearing. The function of AMB in hybrid bearing was set to minimize rubbing between foil and journal at starting and during low speed and after that release the load to compliant foil bearing and it provided synchronous balancing forces and additional damping for high rotational speed rotor stability.

Swanson et al. [73] investigated the HFMB system for a small gas turbine engine. HFMB was configured as a nested design, by inserting a bump foil bearing component in the radial gap between AMB and the rotor. Experiments showed that the foil component acted as a backup for AMB failure, and the hybrid system is used to increase the load capacity of AMB three times with reduced weight.

Heshmat et al. [74] experimentally investigated the coatings for a large HFMB. They showed that KOROLON coating on the top foil and a thin and dense chrome

coating on the shaft provided suitability for high-temperature operation (650 °C) and PS304 coating was not allowable for the severe operating condition.

Tian et al. [75] investigated the steady-state control of HFMB. The HFMB consisted of bump foil bearing (a top foil with four number of bump foils) and AMB. Foil bearing was attached in the space between the poles and the shaft. The results showed that the controller by the area searching algorithm identified the steady-state location of HFMB within 100 s in various situations.

Pham and Ahn [76] experimentally investigated HFMB to determine that the unbalance response was more suppressed. The optimized controller improved the vibration behaviour by 26% at bending critical speed and reduced the power utilization of propulsive motor by 50% compared to the AFB.

Jeong et al. [77] showed the rotor dynamic behaviour and the performance of controllable HFMB experimentally. By modulating the control gain of HFMB, the rotor position was altered, resulting in the controlled vibration and rotordynamic behaviour. For the rotational speeds up to 10,000 rpm, lower stiffness produced better performance. However, with the higher rotational speed, control with higher stiffness gave a better result.

Further, Joeng and Lee [78] showed the influence of eccentricity and variation response on a high-speed rigid rotor supported by HFMB. The results showed that subsynchronous vibration was remarkably decreased and the controlling of the eccentricity resulted in the improved performance of HFMB. This bearing showed the bearing preload could reduce optimal load results for the corresponding eccentricity in the range of (0.2–0.5) and asynchronous vibration.

Jeong and Lee [79] researched the vibrational control of high-speed rotor supported by HFMB with sudden imbalance. The results indicated a 30% reduced $1 \times$ vibration.

Jeong et al. [80] investigated experimentally and analytically the stability of the 225 KW turboblower with HFMB. The results showed more excellent vibration stability with HFMB for unbalance vibration and improved performance by reducing vibration in the low-speed region.

Tian et al. [81] presented an adaptive controller for HFMB (gas foil bearing + eight-pole heteropolar AMB). Simulation results showed excellent performance of the adaptive controller in comparison to a PID controller in the presence of parametric variations of the GFB.

3 Concluding Remarks

Hybrid bearings are the combination of two or more bearing technologies and take benefit of the assets of each technology while neutralizing for individual limitations. These bearings have been proposed for different areas because of their long life, less wear and friction, good static and dynamic forces response characteristics. Such a hybrid bearing system represents a substantial technological advancement with respect to the range of operation and reliability.

Revolutionary development has taken place in the era of hybrid bearings. Hybrid bearings are subject to attention because of their various applications in different operating conditions. Its attractive features are used in multiple applications such as air cycle machines, turbocompressors, turbogenerators, machine tool spindles, reactor coolant pumps, liquid rocket engine turbopumps, precision grinder spindles, ultra-precision machine tools, turbochargers and gas turbine engines.

In this paper, a comprehensive review of various types of HBs is presented. These bearings have a difference in cost, load-carrying capacity, stability, performance and applications. The performances of these HBs in different situations, as reported in the literature, are discussed. Furthermore, different types of variations of HBs of each category available in the literature are also presented. The discussion also includes the possible directions of the future work for the hybrid bearings, which may include different structures and optimum designs.

4 Opportunities for Future Research

Future work requires to include different design variables, to attain more accurate predictions for increased applications of these bearings in different machines. Hence, more analytical and experimental investigations are needed to improve the development of these bearings for high rotational speed, high-load and high-temperature applications.

Apart from these interesting features and discussed results, there are many unanswered questions related to the development of hybrid bearings. The main focus of hybrid bearings is to be free from any design flaws and to be maintenance-free, along with being cost-effective and very reliable. These types of bearings should be designed for more realistic data. Moreover, it should achieve great performance for a more extended duration. Hence, studies are needed to be done on design modifications, both for journals as well as bearings to get invariable performance along with high reliability and increased productivity.

References

1. Rowe WB, Koshal D (1980) A new basis for the optimization of hybrid journal bearings. In: 4th international conference on tribology. Paisley, pp 115–131. [https://doi.org/10.1016/0043-1648\(80\)90097-6](https://doi.org/10.1016/0043-1648(80)90097-6)
2. Koshal D, Rowe WB (1981) Fluid-film journal-bearings operating-in a-hybrid mode: part I—theoretical analysis and design. *J Lubr Technol* 103:558–565. <https://doi.org/10.1115/1.3251737>
3. Rowe WB, Xu SX, Chong FS, Weston W (1982) Hybrid journal bearings with particular reference to hole-entry configurations. *Tribol Int* 2:339–348. [https://doi.org/10.1016/0301-679X\(82\)90143-8](https://doi.org/10.1016/0301-679X(82)90143-8)
4. Chaomleffel JP, Nicolas D (1986) Experimental investigation of hybrid journal bearings. *Tribol Int* 19:253–259. [https://doi.org/10.1016/0301-679X\(86\)90004-6](https://doi.org/10.1016/0301-679X(86)90004-6)

5. Yoshimoto S, Rowe WB, Ives D (1988) A theoretical investigation of the effect of inlet pocket size on the performance of hole entry hybrid journal bearings employing capillary restrictors. *Wear* 127:307–318. [https://doi.org/10.1016/0043-1648\(88\)90162-7](https://doi.org/10.1016/0043-1648(88)90162-7)
6. Sharma SC, Sinhasan R, Jain SC (1990) Elasto-hydrostatic analysis of orifice compensated multiple hole-entry hybrid journal bearings. *Int J Mach Tools Manufact* 30:111–129. [https://doi.org/10.1016/0890-6955\(90\)90046-L](https://doi.org/10.1016/0890-6955(90)90046-L)
7. Jain SC, Sinhasan R, Sharma SC (1992) Analytical study of a flexible hybrid journal bearing system using different flow control devices. *Tribol Int* 25:387–395. [https://doi.org/10.1016/0301-679X\(92\)90076-Y](https://doi.org/10.1016/0301-679X(92)90076-Y)
8. Sharma SC, Sinhasan R, Jain SC (1993) An elasto-hydrostatic study of hole-entry hybrid flexible journal bearings with capillary restrictors. *Tribol Int* 26:93–107. [https://doi.org/10.1016/0301-679X\(93\)90017-U](https://doi.org/10.1016/0301-679X(93)90017-U)
9. Sharma SC, Kumar V, Jain SC et al (1999) A study of slot-entry hydrostatic/hybrid journal bearing using the finite element method. *Tribol Int* 32:185–196. [https://doi.org/10.1016/S0301-679X\(99\)00032-8](https://doi.org/10.1016/S0301-679X(99)00032-8)
10. Kumar V, Sharma SC, Jain SC (2004) Stability margin of hybrid journal bearings: influence of thermal and elastic effects. *J Tribol* 126:630–634. <https://doi.org/10.1115/1.1759343>
11. Garg HC, Sharda HB, Kumar-V, (2006) On the design and development of hybrid journal bearings: a review. *Tribotest* 12:1–19. <https://doi.org/10.1002/tt.1>
12. Kumar V, Sharma SC, Jain SC (2006) On the restrictor design parameter of hybrid journal bearing for optimum rotordynamic coefficients. *Tribol Int* 39:356–368. <https://doi.org/10.1016/j.triboint.2005.03.015>
13. Garg HC, Kumar V, Sharda HB (2009a) Nonnewtonian and thermal effects in constant flow valve compensated symmetric hole-entry hybrid journal bearing. *Lubr Sci* 19:269–286. <https://doi.org/10.1002/lis.48>
14. Duvedi RK, Singh M, Jadon VK (2007) FEM analysis for different configurations of non-recessed hole entry hybrid journal bearings for non-Newtonian lubricants. *Industrial Lubrication and Tribology* 59:266–277. <https://doi.org/10.1108/00368790710820865>
15. Jadon VK, Singh M (2007) Study of supply cut-off and bearing geometric parameters on design of hybrid journal bearing. *Industr Lubric Tribol* 59:92–102. <https://doi.org/10.1108/00368790710731909>
16. Awasthi RK, Sharma SC, Jain SC (2007) Performance of worn non-recessed hole-entry hybrid journal bearings. *Tribol Int* 40:717–734. <https://doi.org/10.1016/j.triboint.2006.05.012>
17. Garg HC, Kumar V, Sharda HB (2009b) Thermohydrostatic analysis of capillary compensated symmetric hole entry hybrid journal bearing operating with non-Newtonian lubricant. *Industr Lubric Tribol* 61:11–21. <https://doi.org/10.1108/00368790910929485>
18. Garg HC, Kumar V, Sharda HB (2010) A comparative thermal analysis of slot-entry and hole-entry hybrid journal bearings lubricated with non-Newtonian lubricant. *J Tribol* 132:1–11. <https://doi.org/10.1115/1.4002034>
19. Garg HC (2011a) Performance of asymmetric slot-entry hybrid journal bearing operating with non-Newtonian lubricant. *J Eng Technol* 1:16–23. <https://doi.org/10.4103/0976-8580.74533>
20. Garg HC (2011b) Influence of non-Newtonian behaviour of lubricant on performance of hole entry hybrid journal bearings employing constant flow valve restrictors. *Industr Lubric Tribol* 63:373–386. <https://doi.org/10.1108/00368791111154995>
21. Garg HC (2013) Static performance characteristics of hybrid journal bearings with plugged entry holes. *Industr Lubric Tribol* 65:333–340. <https://doi.org/10.1108/ILT-10-2012-0116>
22. Dwivedi VK, Chand S, Pandey KN (2013) Effect of number and size of recess on the performance of hybrid (hydrostatic/hydrodynamic) journal bearing. In: *Procedia engineering*. Elsevier B.V., pp 810–817. <https://doi.org/10.1016/j.proeng.2013.01.116>
23. Dwivedi VK, Chand S, Pandey KN (2013) Analysis hybrid (Hydrodynamic/Hydrostatic) journal bearing. *Adv Mater Res* 650:385–390. <https://doi.org/10.4028/www.scientific.net/amr.650.385>
24. Wang L, Pei S, Xiong X, Xu H (2013) Study on the static performance and stability of a water-lubricated hybrid bearing with circumferential grooves and stepped recesses considering

- the influence of recess sizes. *Tribol Trans* 57:36–45. <https://doi.org/10.1080/10402004.2013.840407>
25. Garg HC, Kumar V (2014a) Thermohydrostatic rheological analysis of constant flow valve compensated multiple hole-entry hybrid journal bearings. *Industr Lubric Tribol* 66:244–259. <https://doi.org/10.1108/ILT-10-2012-0114>
 26. Garg HC, Kumar V (2014b) Comparison of static performance characteristics of different configurations of slot-entry hybrid journal bearing operating with non-Newtonian lubricants. *Industr Lubric Tribol* 66:38–45. <https://doi.org/10.1108/ILT-10-2012-0113>
 27. Chan C (2015) Modified particle swarm optimization algorithm for multi-objective optimization design of hybrid journal bearings. *J Tribol* 137:1–7. <https://doi.org/10.1115/1.4028606>
 28. Ram N, Sharma SC (2015) Influence of micropolar lubricants on asymmetric slot entry journal bearings. *Tribol Online* 10:320–328. <https://doi.org/10.2474/trol.10.320>
 29. Ram N, Sharma SC, Yadav S (2015) Performance of symmetric slot-entry hybrid journal bearing in turbulent regime. In: 2015 STLE annual meeting & exhibition, pp 2–4
 30. Lin Q, Wei Z, Wang N, Zhang Y (2016) Effect of recess configuration on the performances of high-speed hybrid journal bearing. *Industr Lubric Tribol* 68:301–307. <https://doi.org/10.1108/ILT-07-2015-0115>
 31. Fu G, Untaroiu A (2016) A study of the effect of various recess shapes on hybrid journal bearing. In: Proceedings of the ASME 2016 fluids engineering division summer meeting FEDSM2016, pp 1–12. <https://doi.org/10.1115/1.4035952>
 32. Khatri CB, Sharma SC (2016) Influence of textured surface on the performance of non-recessed hybrid journal bearing operating with non-Newtonian lubricant. *Tribol Int* 95:221–235. <https://doi.org/10.1016/j.triboint.2015.11.017>
 33. Ram N (2016) Numerical analysis of capillary compensated micropolar fluid lubricated hole entry journal bearings. *Jurnal Tribologi* 9:18–44
 34. Khatak P, Garg HC (2016) Performance analysis of capillary compensated hybrid journal bearing by considering combined influence of thermal effects and micropolar lubricant. *ASME J Tribol* 139:1–33. <https://doi.org/10.1115/1.4033715>
 35. Untaroiu A, Fu G (2017) Effect of recess shape on the performance of a high-speed hybrid journal bearing. *J Eng Gas Turbines Power* 139:1–10. <https://doi.org/10.1115/1.4036946>
 36. Ram N (2017) Effect of couple stress lubrication on symmetric hole-entry hybrid journal bearing. *Tribol Online* 12:58–66. <https://doi.org/10.2474/trol.12.58>
 37. Song L, Cheng K, Ding H, Chen S (2017) Analysis on discharge coefficients in FEM modeling of hybrid air journal bearings and experimental validation. *Tribol Int* 1–28. <https://doi.org/10.1016/j.triboint.2017.11.002>
 38. Khatak P, Garg HC (2017) Performance analysis of capillary compensated hybrid journal bearing by considering combined influence of thermal effects and micropolar lubricant. *J Tribol* 139:1–12. <https://doi.org/10.1115/1.4033715>
 39. Chien S-Y, Cramer MS, Fu G, Untaroiu A (2018) Performance of adaptive lubricants in a hybrid journal bearing operating under fully saturated conditions. *J Eng Gas Turbines Power* 140:1–7. <https://doi.org/10.1115/1.4038551>
 40. Linjamaa A, Lehtovaara A, Larsson R et al (2018) Modelling and analysis of elastic and thermal deformations of a hybrid journal bearing. *Tribol Int* 118:451–457. <https://doi.org/10.1016/j.triboint.2017.02.029>
 41. Srinivasan K, Prabhu BS (1983) Steady state characteristics of conical hybrid bearings. *Wear* 89:57–67. [https://doi.org/10.1016/0043-1648\(83\)90214-4](https://doi.org/10.1016/0043-1648(83)90214-4)
 42. Hong G, Xinmin L, Shaoqi C (2009) Theoretical and experimental study on dynamic coefficients and stability for a hydrostatic/hydrodynamic conical bearing. *J Tribol* 131:1–7. <https://doi.org/10.1115/1.3176991>
 43. Sharma SC, Phalle VM, Jain SC (2011) Influence of wear on the performance of a multirecess conical hybrid journal bearing compensated with orifice restrictor. *Tribol Int* 44:1754–1764. <https://doi.org/10.1016/j.triboint.2011.06.032>

44. Sharma SC, Rajput AK (2012) Influence of micropolar lubrication on the performance of 4-pocket capillary compensated conical hybrid journal bearing. *Adv Tribol* 2012:1–18. <https://doi.org/10.1155/2012/898252>
45. Khakse PG, Phalle VM, Mantha SS (2015) Influence of semi cone angle on performance of a non-recessed-hybrid conical-journal bearing. In: *Proceedings-of-the-ASME 2015 international-mechanical-engineering-congress and-exposition IMECE2015*, pp 1–8. <https://doi.org/10.1115/IMECE2015-50877>
46. Khakse PG, Phalle VM, Mantha SS (2016) Performance analysis of a nonrecessed hybrid conical journal bearing compensated with capillary restrictors. *J Tribol* 138:1–9. <https://doi.org/10.1115/1.4030808>
47. Pawar SR, Phalle VM (2018) Influence of wear on the performance of capillary compensated hole entry hybrid conical journal bearing. *Industr Lubric Tribol* 1–9. <https://doi.org/10.1108/ILT-05-2018-0191>
48. Phalle VM, Pawar SR, Patil SS (2018) Effect of speed on the performance characteristics of non-recessed worn hybrid conical journal bearing for different semi cone angles. In: *Proceedings of the ASME 2018 international mechanical engineering congress and exposition IMECE2018*, pp 1–7. <https://doi.org/10.1115/IMECE2018-87734>
49. Kumar-A S-SC (2019) Textured conical hybrid journal bearing with ER lubricant behavior. *Tribol Int* 129:363–376. <https://doi.org/10.1016/j.triboint.2018.08.040>
50. Ghosh MK, Nagraj A (2004) Rotordynamic characteristics of a multilobe hybrid journal bearing in turbulent lubrication. *J Eng Tribol* 218:61–67. <https://doi.org/10.1243/135065004322842843>
51. Jain S, Sharma S, Basavaraja JS, Kushare P (2010) Study of two-lobe four recessed hybrid journal bearing. *Industr Lubric Tribol* 62:332–340. <https://doi.org/10.1108/00368791011076227>
52. Phalle VM, Sharma SC, Jain SC (2011) Influence of wear on the performance of a 2-lobe multirecess hybrid journal bearing system compensated with membrane restrictor. *Tribol Int* 44:380–395. <https://doi.org/10.1016/j.triboint.2010.11.011>
53. Sharma SC, Phalle VM, Jain SC (2012) Performance of a noncircular 2-lobe multirecess hydrostatic journal bearing with wear. *Industr Lubric Tribol* 64:171–181. <https://doi.org/10.1108/00368791211218704>
54. Jain-D, Sharma-SC (2014) Two lobe geometrically imperfect hybrid journal bearing operating with power law lubricant. *J Eng Tribol* 0:1–17. <https://doi.org/10.1177/1350650114541252>
55. Sharma SC, Kushare PB (2015) Two lobe non recessed roughened hybrid journal bearing—a comparative study. *Tribol Int* 83:51–68. <https://doi.org/10.1016/j.triboint.2014.10.024>
56. Sharma SC, Khatri CB (2017) Electro-rheological fluid lubricated textured multi-lobe hole-entry hybrid journal bearing system. *J Intell Mater Syst Struct* 00:1–20. <https://doi.org/10.1177/1045389X17742731>
57. Khatri CB, Sharma SC (2017) Influence of couple stress lubricant on the performance of textured two-lobe slot-entry hybrid journal bearing system. *J Eng Tribol* 231:366–384. <https://doi.org/10.1177/1350650116658377>
58. Sharma SC, Kushare PB (2017) Nonlinear transient response of rough symmetric two lobe hole entry hybrid journal bearing system. *J Vib Control* 23:190–219. <https://doi.org/10.1177/1077546315575831>
59. Khatri CB, Sharma SC (2018) Analysis of textured multi-lobe non-recessed hybrid journal bearings with various restrictors. *Int J Mech Sci* 17:1–64. <https://doi.org/10.1016/j.ijmecsci.2018.07.014>
60. Kumar M, Kim D (2008) Parametric studies on dynamic performance of hybrid airfoil bearing. *J Eng Gas Turbines Power* 130:1–8. <https://doi.org/10.1115/1.2940354>
61. Kim D, Lee D (2010) Design of three-pad hybrid air foil bearing and experimental investigation on static performance at zero running speed. *J Eng Gas Turbines Power* 132:1–10. <https://doi.org/10.1115/1.4001066>
62. Kim D, Varrey MK (2012) Imbalance response and stability characteristics of a rotor supported by hybrid air foil bearings. *Tribol Trans* 55:529–538. <https://doi.org/10.1080/10402004.2012.681341>

63. Wang YP, Kim D (2014) Experimental identification of force coefficients of large hybrid air foil bearings. *J Eng Gas Turbines Power* 136:1–8. <https://doi.org/10.1115/1.4025891>
64. Feng K, Liu Y, Zhao X, Liu W (2016) Experimental evaluation of the structure characterization of a novel hybrid bump-metal mesh foil bearing. *J Tribol* 138:1–9. <https://doi.org/10.1115/1.4031496>
65. Yazdi BZ, Kim D (2018) Rotordynamic performance of hybrid air foil bearings with regulated hydrostatic injection. *J Eng Gas Turbines Power* 140:1–8. <https://doi.org/10.1115/1.4037667>
66. Kim D, Nicholson B, Rosado L, Givan G (2018) Rotordynamics performance of hybrid foil bearing under forced vibration input. *J Eng Gas Turbines Power* 140:1–12. <https://doi.org/10.1115/1.4037624>
67. Tan Q, Li W, Liu B (2002) Investigations on a permanent magnetic—hydrodynamic hybrid journal bearing. *Tribol Int* 35:443–448. [https://doi.org/10.1016/S0301-679X\(02\)00026-9](https://doi.org/10.1016/S0301-679X(02)00026-9)
68. Hirani H, Samanta P (2007) Hybrid (hydrodynamic + permanent magnetic) journal bearings. *J Eng Tribol* 221:881–891. <https://doi.org/10.1243/13506501JET282>
69. Muzakkir SM, Lijesh KP, Hirani H (2014) Tribological failure analysis of a heavily-loaded slow speed hybrid journal bearing. *Eng Fail Anal J* 40:97–113. <https://doi.org/10.1016/j.engfailanal.2014.02.016>
70. Lijesh KP, Hirani H, Samanta P (2015) Theoretical and experimental study for hybrid journal bearing. *Int J Sci Eng Res* 6:133–139. <https://doi.org/10.14299/ijser.2015.02.002>
71. Lijesh KP, Hirani H (2015) The performance of hybrid journal bearing under extreme operating conditions. *Int J Current Eng Technol* 5:277–282
72. Heshmat H, Chen HM, Walton JF (2000) On the performance of hybrid foil-magnetic bearings. *J Eng Gas Turbines Power* 122:73–122. <https://doi.org/10.1115/1.483178>
73. Swanson EE, Heshmat H, Walton J (2002) Performance of a foil-magnetic hybrid bearing. *J Eng Gas Turbines Power* 124:375–382. <https://doi.org/10.1115/1.1417485>
74. Heshmat H, Jahanmir S (2006) Evaluation of coatings for a large hybrid foil/magnetic bearing. In: Proceedings of IJTC2006 STLE/ASME international joint tribology conference IJTC2006–12328. pp 1–2. <https://doi.org/10.1115/IJTC2006-12328>
75. Tian Y, Sun Y, Yu L (2012) Steady-state-control of hybrid foil-magnetic bearings. *Proc ASME Turbo Expo 2012(GT2012)*:1–9. <https://doi.org/10.1115/GT2012-68394>
76. Pham MN, Ahn H (2014) Experimental optimization of a hybrid foil—magnetic bearing to support a flexible rotor. *Mech Syst Signal Process* 46:361–372. <https://doi.org/10.1016/j.ymsp.2014.01.012>
77. Jeong S, Choe BS, Lee YB (2015) Rotordynamic behavior and performance of controllable hybrid foil-magnetic bearing. In: *Mechanisms and machine science*, pp 1465–1476. https://doi.org/10.1007/978-3-319-06590-8_120
78. Jeong S, Lee YB (2016) Effects of eccentricity and vibration response on high-speed rigid rotor supported by hybrid-foil-magnetic bearing. In: Proceedings of the institution of mechanical engineers, part C: journal of mechanical engineering science, pp 994–1006. <https://doi.org/10.1177/0954406215619449>
79. Jeong S, Lee YB (2017) Vibration control of high-speed rotor supported by hybrid foil-magnetic bearing with sudden imbalance. *J Vib Control* 23:1296–1308. <https://doi.org/10.1177/1077546315592531>
80. Jeong S, Jeon D, Lee YB (2017) Rigid mode vibration control and dynamic behavior of hybrid foil–magnetic bearing turbo blower. *J Eng Gas Turbines Power* 139:1–12. <https://doi.org/10.1115/1.4034920>
81. Tian Z, Wei Z, Sun Y (2017) Nonlinear adaptive control for hybrid foil-magnetic bearing. In: 2017 IEEE international conference on mechatronics and automation, ICMA 2017, pp 81–86. <https://doi.org/10.1109/ICMA.2017.8015793>

Shape and Vibration Control of Spherical Shell Using Functionally Graded Piezoelectric Materials



Chanderkant Susheel

1 Introduction

Spherical shell structures have been abundantly used in the aerospace industry in the form of space antenna, aerospace plane body, etc. The aerospace industry needs structures which can withstand extreme environmental conditions, as well as, it needs structures which are light and tough. A small change in the shape of these structures leads to significant error in their working. In order to control the shape and vibrations in such structures, piezolaminated structures have been used for many years. However, due to environmental disturbances and manufacturing imperfections, the performance of such structures deteriorates [1]. It has also been observed that sensing and actuation capabilities of piezoelectric patches are influenced significantly due to high thermal gradients applied to structures and lead to geometric and material nonlinearity, and it cannot be neglected particularly for space application [1]. Barut et al. [2] studied the response using nonlinear analysis. It was assumed that the moderately thick laminated panels were undergoing large displacements and rotations when thermal loading was applied to it. The equations of motion were derived for these large deformations and rotations by applying Total Lagrangian formulation and the virtual work principle. Ye and Tzou [3] developed a new triangular finite element, which was used to incorporate the properties of a piezo-thermo-elastic composite shell. They performed various investigations that include temperature variation, different mechanical loading and control interactions of piezolaminated composites. Jiang et al. [4] discussed the mathematical model for a composite beam which has a number of distributed piezoelectric sensors and actuators. The model was based on high-order-theories and incorporated a nonlinear electrical potential field across the thickness of the composite. The analysis shows the results of a

C. Susheel (✉)

Mechanical Engineering Department, Punjab Engineering College, Chandigarh, India
e-mail: cksusheel@gmail.com

piezo-thermo-elastic composite beam under a linear temperature field. The piezo-laminated structures can be modelled as an equivalent single layer or as a layer-wise model [5]. Other than the effect of layers, they also studied the effect of higher-order and lower-order expansion under the thermal loading. All the investigations were performed assuming shells with constant radii of curvature. An eight noded finite element was used by Tarapada et al. for the analysis of the smart composite structure. The developed element was an improved element which was capable of incorporating layered composite shell structures. The piezo-thermo-elastic analysis was performed on composite shell structures sandwiched with piezoelectric sensors and actuators [6, 7]. However, different material properties and high thermal gradient across these two materials result in delamination and interface failure due to high-stress concentration. To overcome these shortcomings, functionally graded materials (FGM) were used as a means of stress relaxation to defuse high residual stress at the interface of dissimilar materials. The concept of FGM was first presented by a group of scientists from Japan in 1984 while they were working on some space project fabricating materials which were resistant to high temperatures for aerospace applications [8]. Zhu and Sankar [9] applied Galerkin method to analyse functionally graded structures with a polynomial variation of mechanical properties. The exact solution of shear deformable FG plate for nonlinear bending responses was studied by Navazi and Haddadpour [10]. The first-order shear deformation theory (FSDT), which is also referred to as Mindlin–Reissner theory of plates that consider normal to the mid-surface to remain straight, but not necessarily normal after deformation, and von Karman nonlinearity was used in the mathematical model. Cinefra et al. [11] investigated the transverse deformation of simply supported FG shells using higher-order kinematic models under thermo-mechanical loading.

Kiani et al. [12] investigated FG doubly curved panels for static and dynamic responses using modified Sander's shell theory. Upadhyay and Shukla [13] studied the nonlinear responses using the higher-order shear deformation theory (HSST). Instead of full geometrical nonlinearity, von Karman nonlinearities were considered for analysis of functionally graded skew flat panel. Both static and dynamic analysis was performed. Sharma et al. [14] displayed the capabilities of PZT-Pt-based FGPM in vibration suppression, considering linear conditions. Susheel et al. [15] carried out a similar study by considering nonlinear geometrical conditions for shape and vibration control of antenna reflector in the aerospace application.

In this study, full geometric nonlinearity is used in the analysis for large deformation and rotations in piezolaminated thin structures instead of von Karman-type nonlinearity. The material properties are graded in thickness direction using power-law distribution. The finite element formulation is derived based on FSDT using piezo-thermo-elastic shell element. The obtained equilibrium equations are solved using a modified Newton–Raphson method. Structural control of the spherical shell is depicted using geometric nonlinearity which gives better control as compared to linear. Dynamic analysis is also studied for various loading conditions and shows that the amplitude and period of the response decrease due to the geometric nonlinearities as compared to linear analysis.

2 Functionally Graded Materials (FGM)

The functionally graded materials are heterogeneous materials that usually consist of multiple materials or embedded components, mostly consist of metal and ceramics constituents. The properties of these materials change from the top surface to the bottom according to some function based on the location along with the thickness of the material. The surface with pure metal provides toughness to the structure while the surface with pure ceramic or a majority ceramic acts as a thermal barrier when subjected to higher environmental temperatures. When the properties of the material are varying with the change in thickness, the effective properties need to be calculated. It is assumed that the effective properties vary uniformly according to a simple power-law distribution. The schematic drawing of piezolaminated structure is shown in Fig. 1. It is assumed that both the substructure layer and the piezoelectric layer are functionally graded in the thickness direction. In the case of graded structures, the volume fraction distribution is obtained using power-law distribution and utilized to investigate the effective material properties. According to simple power-law distribution given by He et al., the volume fraction is given as

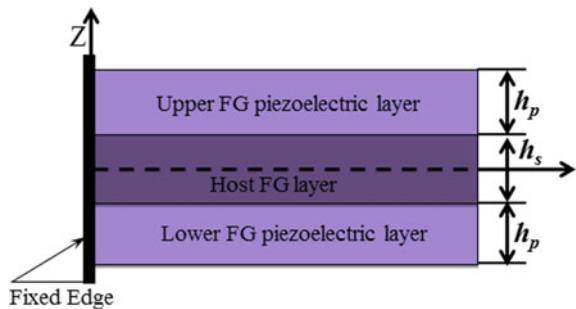
$$V = \left(\frac{1}{2} + \frac{z}{h} \right)^n \tag{1}$$

where the exponent n (varies as $0 \leq n \leq \infty$) defines the profile of material properties across the thickness of FGM, h is the thickness of FGM layer. The effective properties such as density, elastic modulus and thermal expansion coefficient of FGM can be expressed as

$$\begin{aligned} P_{\text{eff}}(z) &= P_T V_T + P_B V_B \\ V_T + V_B &= 1 \end{aligned} \tag{2}$$

where P_T and P_B are properties of top and bottom layers of FGM, respectively, P_{eff} is effective property of FGM, V_T and V_B are volume fractions, respectively. In the area

Fig. 1 Schematic of host FG layer which is sandwiched between FG piezoelectric layers



of smart structures, a functionally graded host structure is sandwiched between two functionally graded piezoelectric material (FGPM) layers. The top layer of FGPM acts as a sensor, and the bottom layer acts as an actuator.

$$\begin{aligned}
 P_{\text{eff}}^s(z) &= (P_T^s - P_B^s) \left(\frac{1}{2} + \frac{z}{h_s} \right)^{n_1} + P_B^s, \quad -\frac{h_s}{2} \leq z \leq \frac{h_s}{2} \\
 P_{\text{eff}}^{PT}(z) &= (P_T^{PT} - P_B^{PT}) \left(\frac{2z - h_s}{2h_{PT}} \right)^{n_2} + P_B^{PT}, \quad \frac{h_s}{2} \leq z \leq \frac{h_s}{2} + h_p \quad (3) \\
 P_{\text{eff}}^{PB}(z) &= (P_T^{PB} - P_B^{PB}) \left(1 + \frac{2z + h_s}{2h_{PB}} \right)^{n_3} + P_B^{PB}, \quad -\frac{h_s}{2} - h_p \leq z \leq -\frac{h_s}{2}
 \end{aligned}$$

Equation 3 can be used to find effective properties of the functionally graded materials which are entirely dependent on the position in the thickness direction. The method discussed above is simple in the formulation and convenient in application to determine the effective properties of functionally graded materials.

3 Finite Element Formulation

The most commonly used approach for analysis of complex structures is the finite element method. A piezoelectric shell element used is shown in Fig. 2. The four-node piezolaminated element used was first developed by Dvorkin and Bathe. In the analysis of thin structures, elements exhibit very stiff behaviour which is generally

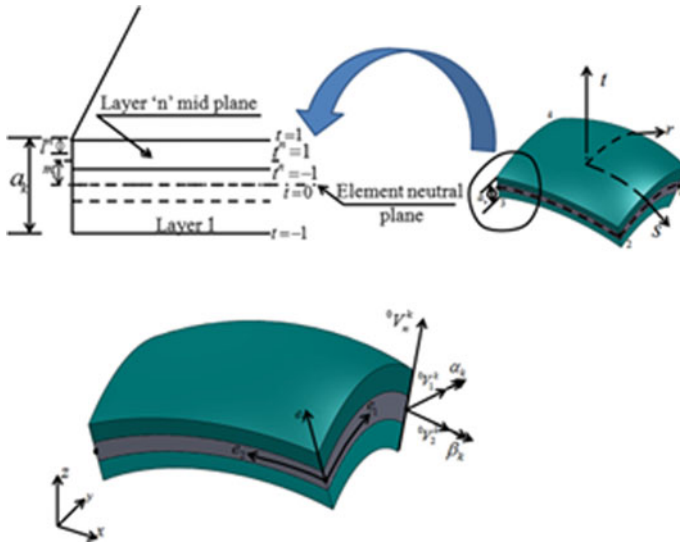


Fig. 2 Piezolaminated shell element

referred to as element locking. In this paper, a mixed interpolation procedure is used to interpolate the transverse shear strain components independently and tie these interpolations to the strains calculated using usual displacement interpolations as described by Dvorkin and Bathe. Using the finite element formulation, the set of linear equations for the functionally graded structure on the elemental level can be obtained. The equation can be represented in terms of a modified Newton–Raphson method incorporating the iterative procedure [15] as

$$[M]\{^{t+\Delta t}\ddot{u}^k\} + [C]\{^{t+\Delta t}\dot{u}^k\} + {}^t_0[K_{uu}]\{u_e^k\} + {}^t_0[K_{u\phi}]\{\Delta\phi_e^k\} = {}^{t+\Delta t}\{R\} - {}^t_0\{f_{int_e}^k\} \quad (4)$$

where $^{t+\Delta t}\ddot{u}$, $^{t+\Delta t}\dot{u}$ are acceleration and velocity at time $t + \Delta t$ M is the mass matrix, and C is the damping matrix. Using Newmark's method, the acceleration and velocity for the modified Newton–Raphson iteration are obtained. For convergence of the iteration scheme, incremental internal energy criterion is used.

4 Numerical Investigation

4.1 Shape Control of Spherical Shell

In this study, a spherical shell panel made of functionally graded material laminated with FGPM is considered. In the shape control application, both the functionally graded piezoelectric layers act as an actuator. The host structure is made of two components, i.e. zirconia and aluminium. The material properties change in the direction of thickness, and the effective properties are calculated using simple power-law distribution. The idea is to decrease stresses at the interfaces in the laminated structure. Thus, the host layer should be functionally graded in such a way that it has the properties of ceramic at the top and the bottom side, whereas in the middle it should have the properties of the metal. The material properties of both host and piezolaminated structures are given in our earlier paper [15]. A functionally graded spherical shell laminated with FGPM layers is shown in Fig. 3 having a radius, R_x of 100 m.

The length and width (a) of the spherical shell are 3 m making the aspect ratio equal to unity. The thickness of the FGM host layer is 2 mm, and the thickness of each FGPM layer is 0.5 mm, which makes the complete spherical panel with the thickness (t) of 3 mm. For shape control, the spherical shell is acted upon by mechanical loading of 100 N/mm² on the upper surface of the shell. Due to symmetric loading and boundary conditions, only quarter part of the spherical shell is used. The boundary condition used is shown below

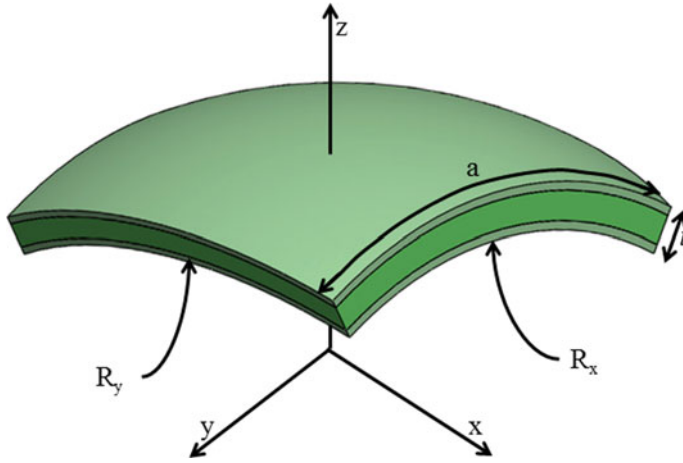


Fig. 3 Functionally graded spherical shell integrated with FGPM

$$v = \theta_x = 0, \text{ at } x \text{ - axis; } y = 0 \quad u = \theta_y = 0, \text{ at } y \text{ - axis; } x = 0$$

$$v = w = \theta_y = \theta_z = 0, \text{ at } y \text{ - axis; } x = a \quad u = w = \theta_x = \theta_z = 0, \text{ at } x \text{ - axis; } y = a$$

For shape control analysis, the centreline deflection of the structure mentioned above along the length of the shell at different gradient indexes of host structure is shown in Fig. 4. The application of mechanical load leads to deformation in the shape of FG spherical shell. This change in the shape can be nullified if an appropriate voltage is applied to FGPM layers. The applied voltage should be less than the threshold value of piezoelectric. Figure 5 shows the shape control of spherical panel at a material index of 1 at the applied voltages of 0–300 V.

4.2 Active Vibration Suppression of Spherical Shell Panel

Active vibration suppression of functionally graded spherical shell is studied for a thermal gradient across the thickness. Active control needs sensor and actuator for proper suppression of vibration-induced due to applied loading. Here, the top layer of FGPM piezoelectric layer acts as a sensor and the bottom layer behaves as an actuator which covers the host structure entirely from top to bottom. As done in the case of shape control, only a quarter part of the spherical shell structure is modelled. First, the frequency analysis of the functionally graded spherical shell is performed at different values of volume fraction exponents.

As expected, the frequency of the pure ceramic case is higher than the pure metallic case due to higher stiffness. The frequencies (F) of the functionally graded spherical structure are shown in Table 1. In this table, higher frequencies are neglected, and only a few first natural frequencies are considered for analysis. The ratio (R) of the

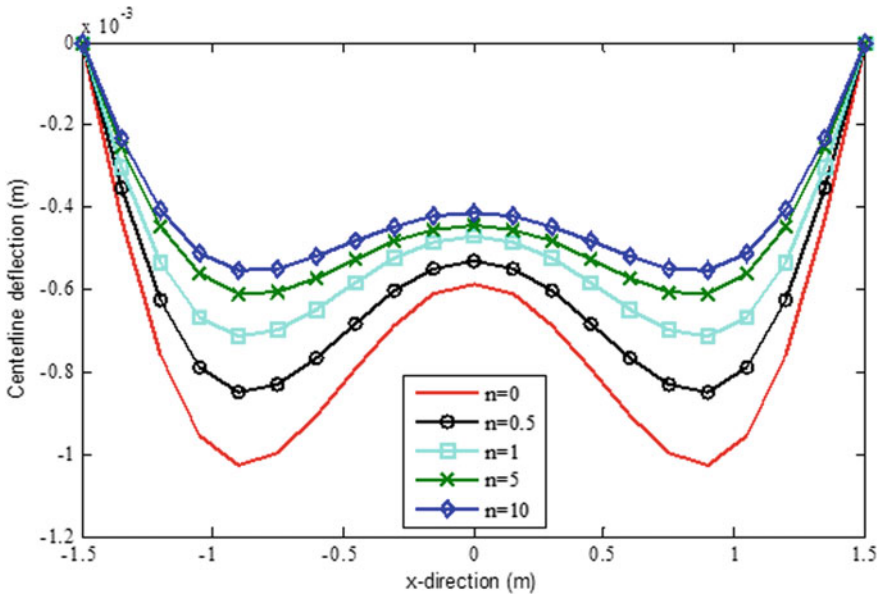


Fig. 4 Mid-surface deformation of simply supported spherical shell at various volume fraction exponents

radius of curvature to arc length is increased from 1 to 10. From Table 1, it can be concluded that the frequency of the spherical panel reduces as the length to width ratio increases. Another observation that can be made from Table 1 is that the natural frequency of the spherical shell rises with a rise in the material gradient exponent from 0 to 10. This variation is pictorially shown in Fig. 6, where frequencies of the structure are shown inordinate direction, and the ratio of length to width is presented in abscissa for volume fraction exponent of $n = 1$. It can be seen from Fig. 6 as the curvature to arc length ratio increases the frequency of the system decrease. However, there is no further change in the frequency of the system when this ratio reaches 20.

Next, the active vibration control of the FG spherical panel under thermal loading is considered. The thermal gradient of $10\text{ }^\circ\text{C}/\text{thickness}$ is applied across the thickness of the structure. The thermal gradient is applied as impact loading, which results in vibrations due to the sudden change in the temperature. First, the open-loop dynamic response of the spherical shell is presented in Fig. 7 for various material gradient indexes under thermal loading. It is observed that, as the material gradient changes from metallic to the ceramic material, the amplitude of the vibrations decreases. After that, active vibration control of the spherical shell is shown for a material gradient of $n = 1$ under the impact loading.

The vibration generated due to the loading is suppressed using various controllers and is shown in Fig. 8. Newmark’s method is used to obtain the time-history response of the plate panel with a coefficient $\alpha = 0.5$ and $\beta = 0.25$. The control force obtained from the fuzzy logic controller is used to attenuate the unwanted vibrations. It is

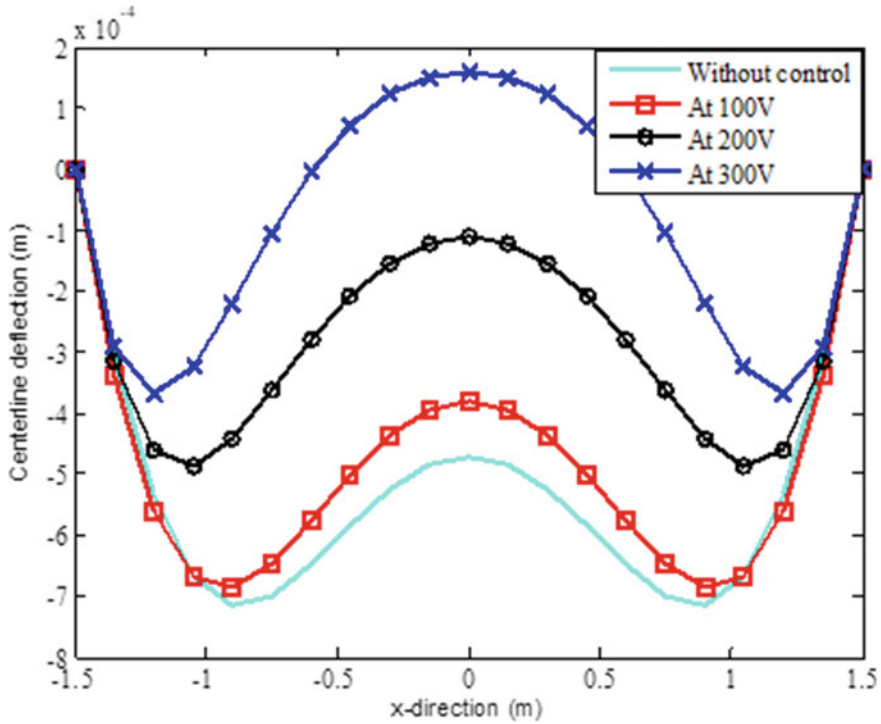


Fig. 5 Shape control of simply supported spherical shell with FGPM at $n = 1$

observed that the fuzzy logic controller attenuates the structural vibration more effectively than other controllers. Figure 9 shows the three-dimensional plot of the spherical panel for both controlled and uncontrolled vibrational response. Figure 10 shows the value of actuation voltage required for suppression of the spherical panel vibrations. The voltage is obtained from the fuzzy logic controller. The vibration suppression is depicted for volume fraction exponent of 1. The voltage provided to the piezoelectric actuators from a nonlinear fuzzy controller is well within the breakdown voltage of the piezoelectric actuator.

5 Conclusion

In this paper, the numerical investigation is performed on FG spherical panel, which shows shape control capabilities of actuators and vibration suppression capabilities of the FG spherical shell structure using a fuzzy logic controller. Different boundary conditions and loading conditions (mechanical and thermal) are considered to carry out numerical simulations. The open-loop and closed-loop vibration control results are presented in the time domain. The stability of the spherical structure is presented

Table 1 Natural frequencies (in Hz) of the FG spherical panel at various gradient indexes

R/F	1	5	10	20	40	80	1	5	10	20	40	80
	$n = 0$											
1	595.25	123.91	62.73	32.85	19.12	13.67	691.70	143.90	72.65	37.69	21.36	14.67
2	620.68	136.97	84.78	65.55	59.78	58.25	720.54	156.14	93.48	69.51	62.09	60.09
3	627.92	137.00	84.79	65.55	59.79	58.25	728.25	156.18	93.48	69.51	62.09	60.09
4	648.62	164.73	121.95	108.70	105.13	104.21	749.06	183.11	130.17	113.18	108.52	107.32
5	649.44	201.24	169.72	160.89	158.61	158.04	752.49	217.90	177.90	166.43	163.44	162.68
	$n = 5$											
1	748.21	155.63	78.55	40.70	22.98	15.68	773.25	160.84	81.18	42.06	23.74	16.20
2	779.27	168.42	100.33	74.12	65.96	63.76	805.33	174.03	103.65	76.55	68.11	65.83
3	787.49	168.47	100.33	74.12	65.96	63.76	813.82	174.08	103.65	76.55	68.11	65.83
4	809.50	196.78	138.96	120.30	115.16	113.84	836.54	203.30	143.52	124.22	118.91	117.54
5	813.61	233.18	189.31	176.68	173.38	172.55	840.81	240.86	195.50	182.43	179.02	178.16
	$n = 10$											

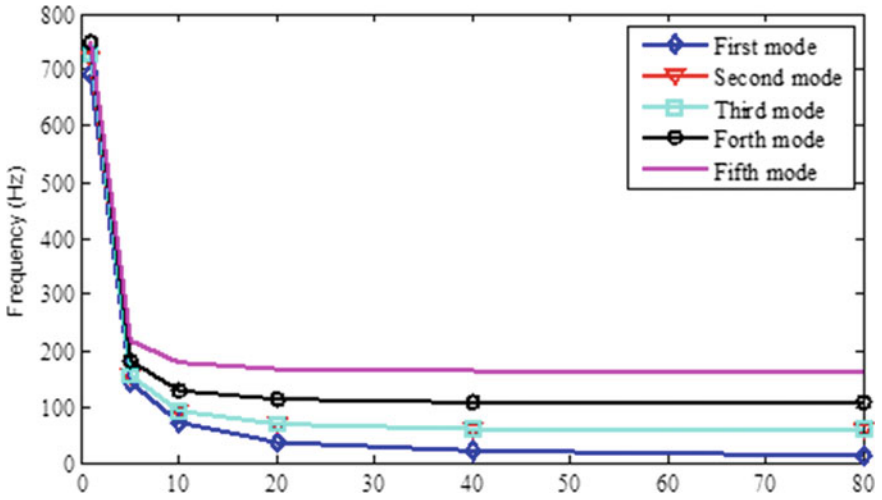


Fig. 6 Graphical representation of frequencies of FG spherical panel with the ratio (R) for material gradient index of $n = 1$

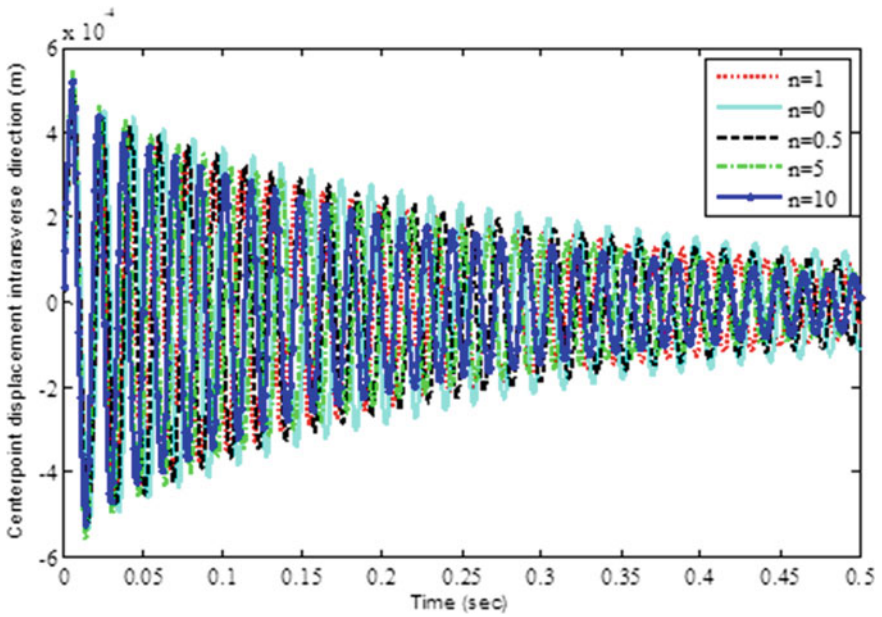


Fig. 7 Open-loop dynamic response of piezolaminated FG spherical shell under the application of thermal load at various materials gradient indexes

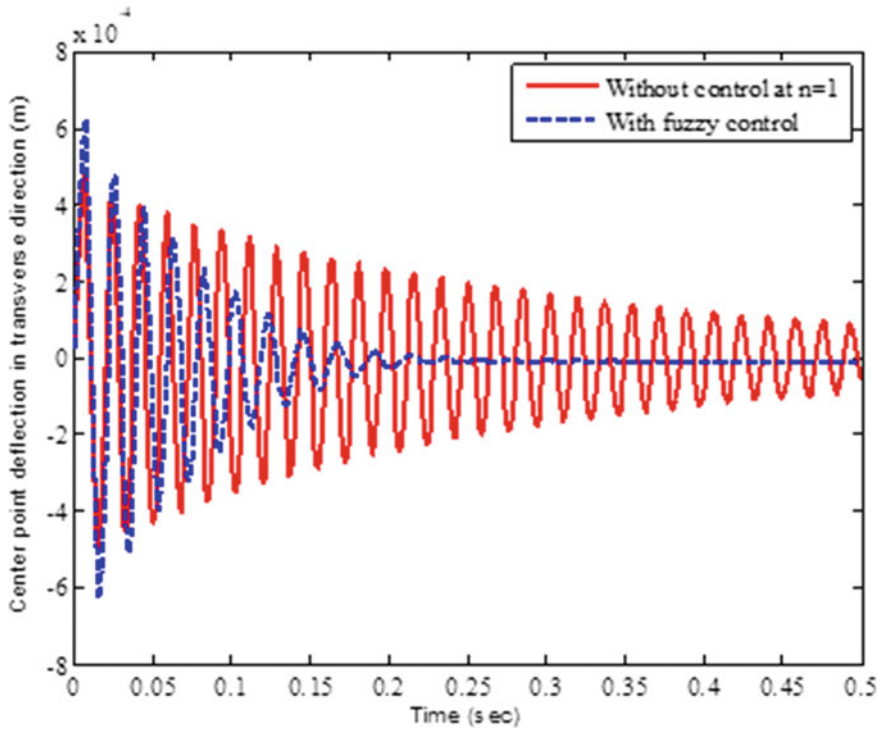


Fig. 8 Uncontrolled and controlled dynamic response of piezolaminated FG spherical shell at $n = 1$ with the fuzzy logic controller

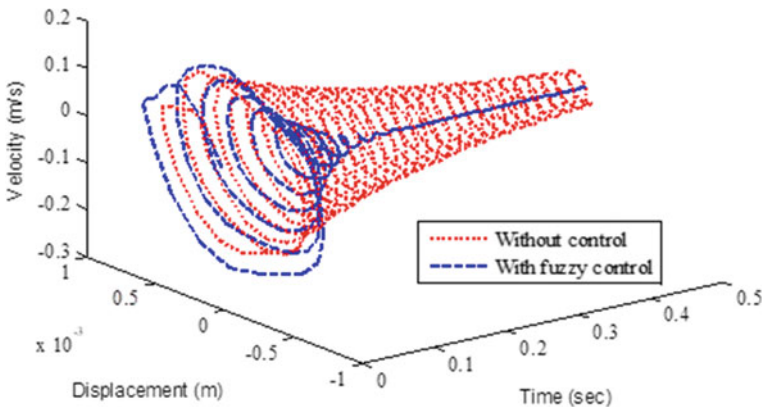


Fig. 9 3-D phase plot of the controlled and uncontrolled structure for $n = 1$

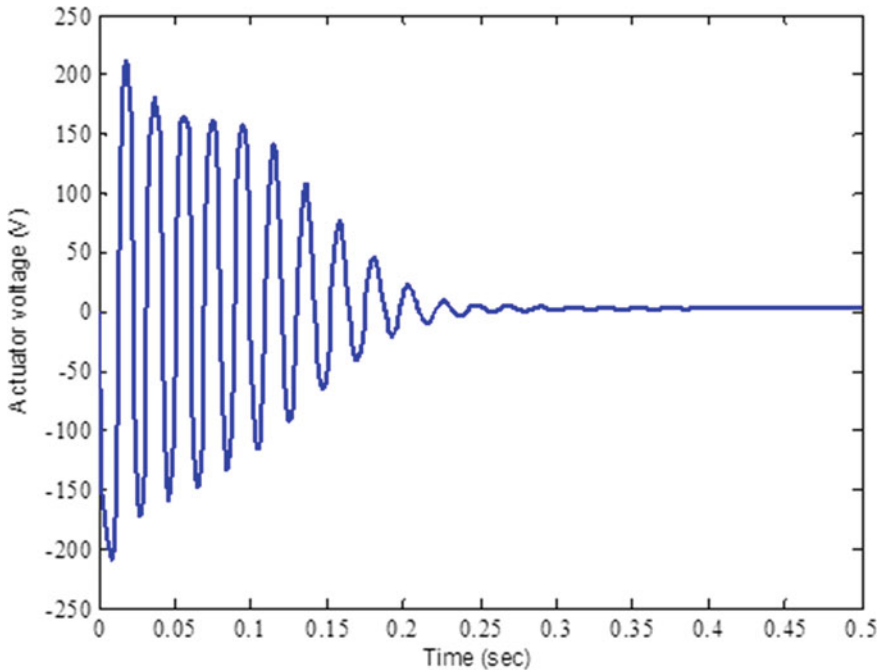


Fig. 10 Actuator voltage obtained from the fuzzy controller during vibration suppression of spherical panel

with the help of a 3-D plot for various actuator voltages. All the numerical simulations are performed by considering the material properties at room temperature only. However, in real-life applications, the structures are vulnerable to very severe environmental conditions which influence the material properties. Also, the piezoelectric patches attached to the whole surface of the structure are not feasible.

References

1. Agrawal BN, Elshafei MA, Song G (1981) Adaptive antenna shape control using piezoelectric actuators. *Acta Astronaut* 40(1):821–826. [https://doi.org/10.1016/S0094-5765\(97\)00185-9](https://doi.org/10.1016/S0094-5765(97)00185-9)
2. Barut A, Madenci E, Tessler A (2000) Nonlinear thermoelastic analysis of composite panels under non-uniform temperature distribution. *Int J Solids Struct* 37(27):3681–3713. [https://doi.org/10.1016/S0020-7683\(99\)00119-5](https://doi.org/10.1016/S0020-7683(99)00119-5)
3. Ye R, Tzou HS (2000) Control of adaptive shells with thermal and mechanical excitations. *J Sound Vib* 231(5):1321–1338. <https://doi.org/10.1006/jsvi.1999.2734>
4. Jiang JP, Dong Li XL (2007) A new finite element model for piezothermoelastic composite beam. *J Sound Vib* 306(3):849–864. <https://doi.org/10.1016/j.jsv.2007.06.023>
5. Brischetto S, Carrera E (2008) Thermal stress analysis by refined multilayered composite shell theories. *J Therm Stresses* 32:165–186. <https://doi.org/10.1080/01495730802540882>

6. Roy T, Manikandan P, Chakraborty D (2010) Improved shell finite element for piezothermoelastic analysis of smart fiber reinforced composite structures. *Finite Elements Anal Design* 46(9):710–720. <https://doi.org/10.1016/j.finel.2010.03.009>
7. Dvorkin EN, Bathe KJ (1984) A continuum mechanics based four-node shell element for general non-linear analysis. *Eng Comput* 1:77–88
8. Koizumi M, Niino M (1995) Overview of FGM research in Japan. *MRS Bull* 20(1):19–21. <https://doi.org/10.1557/S0883769400048867>
9. Zhu H, Sankar BV (2004) A combined Fourier series–Galerkin method for the analysis of functionally graded beams. *J Appl Mech* 71(3):421–424. <https://doi.org/10.1115/1.1751184>
10. Navazi HM, Haddadpour H (2008) Nonlinear cylindrical bending analysis of shear deformable functionally graded plates under different loadings using analytical methods. *Int J Mech Sci* 50(12):1650–1657. <https://doi.org/10.1016/j.ijmecsci.2008.08.010>
11. Cinefra M et al (2008) Thermo-mechanical analysis of functionally graded shells. *J Therm Stresses* 33(10):942–963. <https://doi.org/10.1080/01495739.2010.482379>
12. Kiani Y, A, H, Akbarzadeh, Z.T. Chen, and Eslami, M. R. (2012) Static and dynamic analysis of an FGM doubly curved panel resting on the Pasternak-type elastic foundation. *Compos Struct* 94(8):2474–2484. <https://doi.org/10.1016/j.compstruct.2012.02.028>
13. Upadhyay AK, Shukla KK (2013) Geometrically nonlinear static and dynamic analysis of functionally graded skew plates. *Commun Nonlinear Sci Numer Simul* 18(8):2252–2279. <https://doi.org/10.1016/j.cnsns.2012.12.034>
14. Sharma A, Kumar A, Kumar R, Vaish R, Chauhan VS (2016) Finite element analysis on active vibration control using lead zirconate titanate–Pt–based functionally graded piezoelectric material. *J Intel Mater Syst Struct* 27:490–499. <https://doi.org/10.1177/1045389X15572012>
15. Susheel CK, Sharma A, Kumar R, Chauhan VS (2018) Geometrical nonlinear characteristics of functionally graded structure using functionally graded piezoelectric materials. *J Sandwich Struct Mater* 2018:1099636217752114. <https://doi.org/10.1177/1099636217752114>

Development of Aluminum Matrix Composite Through Microwave Stir Casting



Ganesh R. Panchal and M. S. Srinath

1 Introduction

Aluminum matrix infused with ceramic particles offers higher strength and better mechanical properties than monolithic metals. Aluminum matrix composites (AMCs) are popular composite materials used in the aerospace and automobile industry because of their superior mechanical properties. The methods for developing AMCs include centrifugal casting, stir casting, compocasting, rheocasting, infiltration, powder metallurgy, etc. Among the existing methods, stir casting is widely used because of its low investment cost.

A material processing route plays a vital role in developing defect free AMCs. AMCs are being produced using a stir casting route employing conventional heating sources like resistance furnace or other furnaces, which consume more time and energy. The conventional stir casting methods have many drawbacks: long processing time, inferior microstructure and mechanical properties, non-uniform heating, wettability, porosity, etc. [1–6].

Attempts are being made to investigate material processing using microwaves to overcome the issues related to conventional processing methods. Microwave's popularity has been increasing due to its attributes, such as uniform and volumetric heating in short processing time. Processing of materials using microwaves is an attractive and alternate route because it is fast, eco-friendly, and economical. The fabrication route using microwaves enhances the physical and mechanical properties of metals. However, metals reflect microwaves at room temperature at 2.45 GHz. Research and development in the area of microwave material processing have made

G. R. Panchal (✉) · M. S. Srinath
Department of Industrial and Production Engineering, Malnad College of Engineering, Hassan,
Karnataka 573202, India
e-mail: ganesh9538@gmail.com

M. S. Srinath
e-mail: srinadme@gmail.com

it possible to process bulk metal by applying microwave hybrid heating (MHH) principle. MHH technique employs susceptor material to accelerate the heating of the metal. MHH route has motivated several researchers toward its application in various processes: joining, sintering, cladding, heat treatment, melting, in-situ casting, and drilling [7–9].

The development of alloys and composites by employing microwaves is still at the development stage. MHH route has been explored to melt metals in powder form and to develop alloys and composites [10–13]. Metals in the bulk form are successfully melted by employing the MHH route [14–16]. An attempt to investigate the joining of alloys revealed that the joint was free from defects and showed better mechanical properties [17]. It was reported that cellular grain structure was observed at the joint using MHH [18]. Metal matrix composite (MMC) clads were developed successfully by varying exposure time using microwave irradiation at 2.45 GHz frequency [19]. The various processes using microwaves used fine particles [20]. It was observed from the studies that there exists a spot inside the microwave cavity, where heat generation is more in the microwave absorbing material [12, 21]. Coatings developed through microwave irradiations show better mechanical properties over the sprayed coatings. Microwave irradiation helps in achieving homogeneous structure and better metallurgical bonding between substrate and coating materials. Microwaves remove pores, cracks, and voids by remelting the particles, which remained unmelted through spray technique [22].

Several authors compared conventional sintering with microwave sintering and reported that the sintering by microwave irradiation consumes less time than conventional sintering. The fundamentals and applications of microwave sintering were discussed. The distinguishing attributes and future of material processing through microwaves sintering were markedly presented [8, 9, 23]. The uniform and rapid heating were observed during microwave irradiation when the temperature reaches nearly 50% of the melting point of bulk metal [24].

Compared to sintering, joining, cladding, and melting using microwaves, the development of metal matrix composites (MMCs) using microwave energy is at the immature stage. This provides an option to apply microwave energy to synthesis AMC through stir casting. This method could reduce the processing time and energy requirement. However, the development of AMCs via stir casting technique using microwaves as a heating source has not been reported [2, 7, 25]. The present work is an attempt to use microwave energy as a heating source for producing AMC using a stir casting route. The procedure and preliminary results of the development of AMC through the microwave stir casting route are reported in this paper.

Table 1 Chemical composition of as-received AA6061

S. No.	Elements	Weight (%)
1	Si	0.62
2	Fe	0.7
3	Cu	0.39
4	Mn	0.24
5	Mg	0.8
6	Cr	0.25
7	Zn	0.35
8	Ti	0.18
9	Al	Remaining

2 Experimentation

2.1 Material Details

In the present work, aluminum alloy 6061 (AA6061) in the bulk form was used as matrix material. Silicon carbide (SiC) particles (10–80 μm) were used as reinforcement. The chemical composition of the AA6061 is represented in Table 1.

2.2 Fabrication Process

The experiment was performed under atmospheric conditions in a 3.3 kW industrial microwave furnace at a frequency of 2.45 GHz. The schematic experimental setup of a microwave stir casting used in this study is shown in Fig. 1. Table 2 summarizes the processing parameters used in this study. A graphite clay crucible was filled with about 230 g of AA6061. The crucible, susceptor, and refractory brick were insulated and placed inside the microwave furnace. Alumina was used as an insulating material because it is transparent to microwaves. The MHH technique was applied to melt the AA6061, using SiC block as a susceptor material.

A K-type thermocouple was introduced into the crucible such that it touches the metal for temperature indication during the melting of the metal. The heat was generated rapidly within susceptor material by microwaves and transferred to the metal through the crucible wall. The AA6061 was melted within 1,200 s via the MHH technique. Figure 2 shows the arrangement for processing the material. After reaching 700 °C, the top layer of the slag was removed followed by stirring. About 1 wt.% of magnesium chips were introduced into the liquid metal for wettability between the matrix and reinforcement. Further, 2 wt.% of SiC particles were incorporated slowly while the slurry was solidifying, favoring mixing of all reinforcement in the slurry.

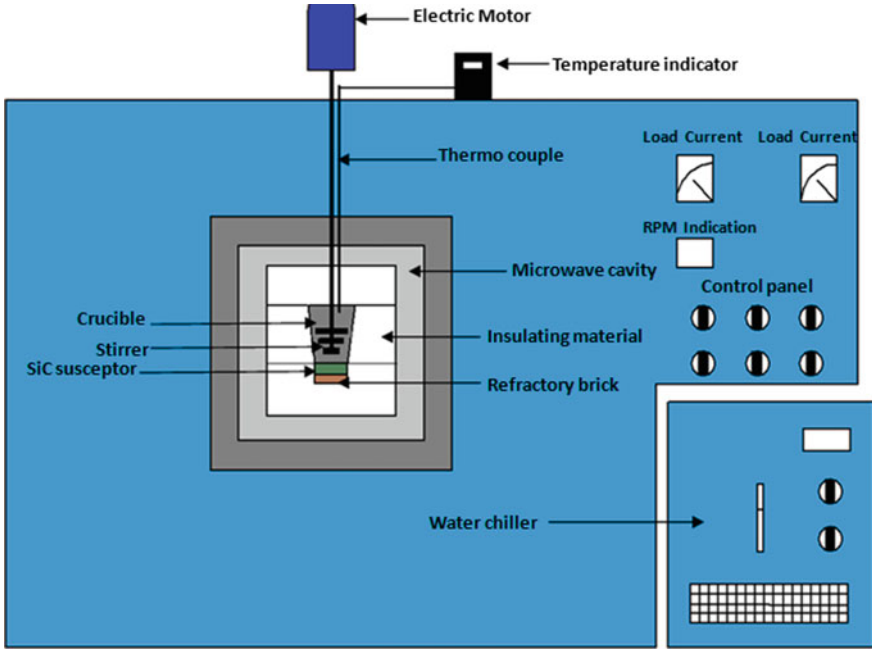


Fig. 1 Schematic diagram of the microwave stir casting setup

Table 2 Details of process parameters

S. No.	Parameters	Description
1	Furnace	Industrial microwave furnace
2	Power	3.3 kW
3	Frequency	2.45 GHz
4	Matrix	AA6061
5	Reinforcement	SiC particles (10–70 μm)
6	Susceptor material	SiC
7	Insulation	Alumina casket
8	Stirrer speed	30 RPM
9	Stirring time	300 s

The temperature of the slurry was increased to 730 °C, and subsequently, the liquid mixture was poured in a graphite mold and allowed for natural cooling. The casted AMC is shown in Fig. 3.



Fig. 2 View of the processing setup

Fig. 3 Developed as-cast AMC



3 Results and Discussions

3.1 Microstructural Study

In the present work, SiC particles were mixed into the AA6061 using the microwave stir casting method. Microstructural study was carried out on as-cast AMC samples to examine the presence and dispersion of SiC particles. The scanning electron microscopy (SEM) micrographs of the composite samples, which are prepared by metallographic procedures, are shown in Fig. 4. The gray area represents the AA6061 matrix. The dark-colored SiC particles are dispersed uniformly in the AA6061 matrix. The accommodation of SiC particles at the grain boundaries can also be observed.

Figure 5 shows dense microstructure, which could be attributed to uniform heating through microwaves. The energy dispersive spectroscopy (EDS) spectrum of the

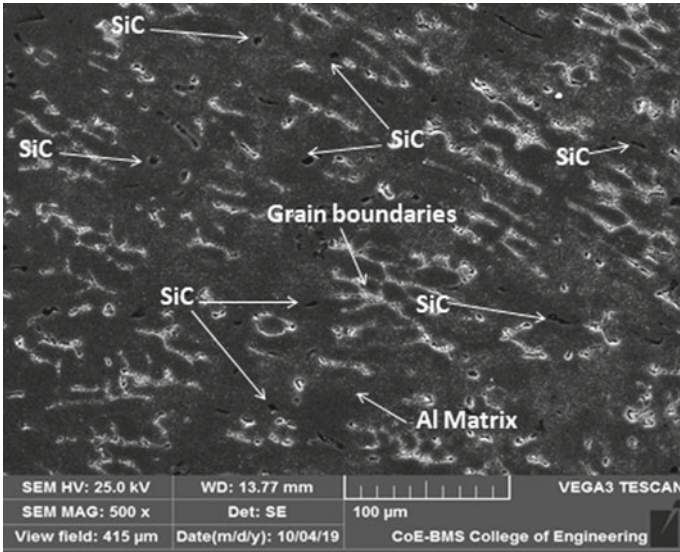


Fig. 4 SEM micrograph of as-cast AMC at 500 X

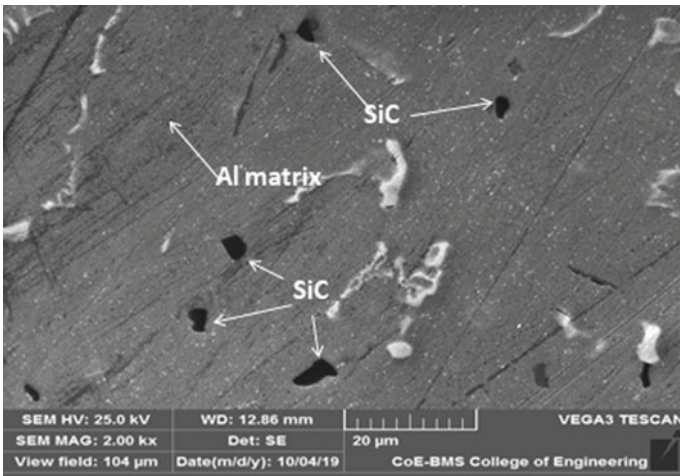


Fig. 5 SEM micrograph of as-cast AMC at 2.00 KX

developed composite is displayed in Fig. 6. The EDS pattern of the composite confirms the presence of the reinforcement in the dominant aluminum alloy matrix.

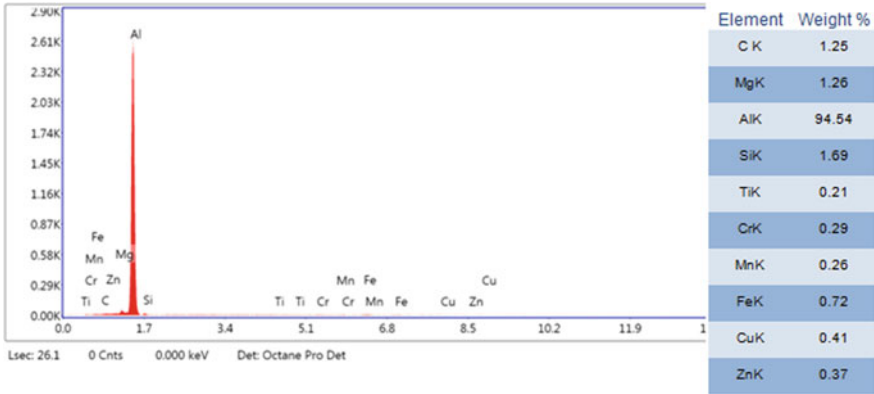


Fig. 6 EDS spectrum of as-cast AMC

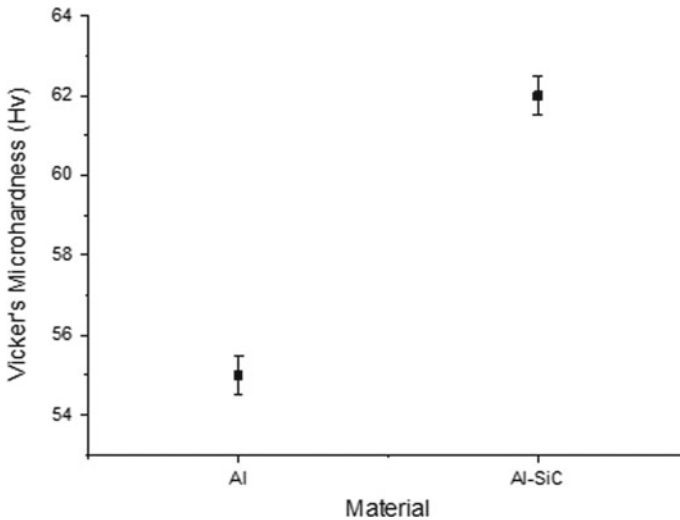


Fig. 7 Microhardness of the AA6061 and AA6061-SiC

3.2 Vicker's Microhardness Test

Vicker's microhardness test was performed using a hardness tester (HIGHWOOD HWMMT-X7). A load of 1 Kgf was applied for 10 s. Microhardness of the as-received AA6061 and the AMC is illustrated in Fig. 7. The average microhardness value of as-received AA6061 and as-cast AMC was found to be 55 Hv and 62 Hv, respectively. It was observed that the hardness value of base alloy increased by 12%, which could be due to microwave heating and the uniform dispersion of SiC particles in the composite.

4 Conclusion

Components of automobiles and aircraft are being fabricated by AMCs. AMCs are produced commonly through conventional stir casting methods. In the conventional stir casting process, the maximum amount of time is consumed in the melting of metals, and the developed composites have defects due to non-uniform heating and pollution. In the present work, the AA6061-SiC composite has been synthesized by a novel microwave stir casting route. The developed fabrication method consumes less time than the conventional stir casting process. The reduction in processing time is attributed to MHH. Moreover, the composite prepared through this method is free from defects due to uniform heating by microwaves. The SEM micrographs show the uniform distribution of reinforcements and dense microstructure. Further, the presence of reinforcement in the matrix was confirmed by EDS. The prepared AA6061-SiC composite is found to have a hardness of 62 Hv, increased by 12% compared with as-received AA6061. The illustrated microwave stir casting process is found to be promising and could be an alternative route for producing AMCs.

References

1. Moona G, Walia RS, Rastogi V (2018) Aluminium metal matrix composites: a retrospective investigation. *Indian J Pure Appl Phys (IJPAP)* 56:64–75. <https://nopr.niscair.res.in/handle/123456789/43556>
2. Ramanathan A, Krishnan PK, Muraliraja R (2019) A review on the production of metal matrix composites through stir-casting furnace design, properties, challenges, and research opportunities. *J Manuf Process* 42:213–245. <https://doi.org/10.1016/j.jmapro.2019.04.017>
3. Kumar M, Gupta RK, Pandey A (2018) A review on fabrication and characteristics of metal matrix composites fabricated by stir casting. *IOP Conf Ser Mater Sci Eng* 377:012125. <https://doi.org/10.1088/1757-899X/377/1/012125>
4. Mistry JM, Gohil PP (2018) Research review of diversified reinforcement on aluminum metal matrix composites: fabrication processes and mechanical characterization. *Sci Eng Composite Mater* 25:633–647. <https://doi.org/10.1515/secm-2016-0278>
5. Pawar PB, Utpat AA (2014) Development of aluminium-based silicon carbide particulate metal matrix composite for spur gear. *Proc Mater Sci* 6:1150–1156. <https://doi.org/10.1016/j.mspro.2014.07.187>
6. Kala H, Mer KK, Kumar S (2014) A review on mechanical and tribological behaviors of stir cast aluminum matrix composites. *Proc Mater Sci* 6:1951–1960. <https://doi.org/10.1016/j.mspro.2014.07.229>
7. Mishra RR, Sharma AK (2016a) A review of research trends in microwave processing of metal-based materials and opportunities in microwave metal casting. *Crit Rev Solid State Mater Sci* 41:217–255. <https://doi.org/10.1080/10408436.2016.1142421>
8. Mishra RR, Sharma AK (2016b) Microwave–material interaction phenomena: heating mechanisms, challenges, and opportunities in material processing. *Compos Appl Sci Manuf* 81:78–97. <https://doi.org/10.1016/j.compositesa.2015.10.035>
9. Agrawal D (2006) Microwave sintering, brazing, and melting of metallic materials. In: Sohn international symposium; advanced processing of metals and materials volume 4: new, improved and existing technologies: non-ferrous materials extraction and processing, vol 4, 183–192. https://www.mri.psu.edu/sites/default/files/file_attach/135.pdf

10. Mishra RR, Sharma AK (2016c) On the mechanism of in-situ microwave casting of aluminum alloy 7039 and cast microstructure. *Mater Des* 112:97–106. <https://doi.org/10.1016/j.matdes.2016.09.041>
11. Mishra RR, Sharma AK (2017a) Structure-property correlation in Al–Zn–Mg alloy cast developed through in-situ microwave casting. *Mater Sci Eng A* 688:532–544. <https://doi.org/10.1016/j.msea.2017.02.021>
12. Mishra RR, Sharma AK (2017b) On melting characteristics of bulk Al-7039 alloy during in-situ microwave casting. *Appl Therm Eng* 111:660–675. <https://doi.org/10.1016/j.applthermaleng.2016.09.122>
13. Singh S, Gupta D, Jain V (2016) Novel microwave composite casting process: theory, feasibility, and characterization. *Mater Design* 111:51–59. <https://doi.org/10.1016/j.matdes.2016.08.071>
14. Lingappa MS, Srinath MS, Amarendra HJ (2017) Microstructural and mechanical investigation of aluminum alloy (Al 1050) melted by microwave hybrid heating. *Mater Res Express*. 4:076504. <https://doi.org/10.1088/2053-1591/aa7aaf>
15. Chandrasekaran S, Basak T, Ramanathan S (2011) Experimental and theoretical investigation on microwave melting of metals. *J Mater Process Technol* 211:482–487. <https://doi.org/10.1016/j.jmatprotec.2010.11.001>
16. Shashank LM, Srinath MS, Amarendra HJ (2017) Microstructural investigation and characterization of bulk brass melted by conventional and microwave processing methods. *Mater Sci Forum Trans Tech Publ* 890:56–361. <https://doi.org/10.4028/www.scientific.net/MSF.890.356>
17. Bansal A et al (2019) Investigation on the effect of post-weld heat treatment on microwave joining of the alloy-718 weldment. *Mater Res Express* 6:086554. <https://doi.org/10.1016/j.jestch.2018.10.012>
18. Singh S et al (2019) Development and characterization of microwave processed cast iron joint. *Eng Sci Technol Int J* 22:569–77. <https://doi.org/10.1016/j.jestch.2018.10.012>
19. Singh B, Zafar S (2019) Effect of microwave exposure time on microstructure and slurry erosion behavior of Ni+ 20% Cr7C3 composite clad. *Wear* 426–427:491–500. <https://doi.org/10.116/j.wear.2018.12.016>
20. Sharma AK, Mishra RR (2018) Role of particle size in microwave processing of metallic material systems. *Mater Sci Technol* 34:123–137. <https://doi.org/10.1080/02670836.2017.1412043>
21. Mishra RR, Sharma AK (2017c) Effect of susceptor and mold material on the microstructure of in-situ microwave casts of Al-Zn-Mg alloy. *Mater Des* 131:428–440. <https://doi.org/10.1016/j.matdes.2017.06.038>
22. Prasad CD, Joladarashi S, Ramesh MR (2019) Effect of microwave heating on microstructure and elevated temperature adhesive wear behavior of HVOF deposited CoMoCrSi-Cr3C2 coating. *Surf Coat Technol* 374:291–304. <https://doi.org/10.1016/j.surfcoat.2019.05.056>
23. Oghbaei M, Mirzaee O (2010) Microwave versus conventional sintering: a review of fundamentals, advantages, and applications. *J Alloy Compd* 494:175–189. <https://doi.org/10.1016/j.jallcom.2010.01.068>
24. Lingappa SM, Srinath MS, Amarendra HJ (2017) An experimental investigation to find the critical (coupling) temperature in microwave hybrid heating of bulk metallic materials. *Mater Res Express* 4:106521. <https://doi.org/10.1088/2053-1591/aa931e>
25. Singh S, Gupta D, Jain V (2015) Microwave processing of materials and applications in manufacturing industries: a review. *Mater Manuf Process* 30:1–29. <https://doi.org/10.1080/10426914.2014.952028>

Process Optimization of WEDM for Machining of Aluminum (6063)/Graphite Metal Matrix Composites



Tejas Pramod Naik, Promod Kumar Patowari, Kassahun Gashu Melese, Ram Singh Rana, Inderdeep Singh, and Apurbba Kumar Sharma

1 Introduction

In the field of cutting edge assembling and designing, composite materials are now playing an important role. Due to increasing demand from technological advancements in the field of aerospace, aircraft, and automobile industries, there is a need for smart and advanced materials [1]. Metal matrix composite (MMC) has always been attractive to researchers as a substitution for pure metallic materials because of its low specific gravity without compromising its strength. It has been conceivable to create novel composite materials with improved physical and mechanical properties in light of countless investigations occurring into the basic idea of materials and a superior comprehension of their structure–property relationship [2]. The traditional way of

T. P. Naik (✉) · I. Singh · A. K. Sharma

Design Innovation Center, Indian Institute of Technology Roorkee, Roorkee, Uttarakhand 247667, India

e-mail: tejasnit@gmail.com

I. Singh

e-mail: inderdeep.singh@me.iitr.ac.in

A. K. Sharma

e-mail: aks@me.iitr.ac.in

P. K. Patowari

Department of Mechanical Engineering, National Institute of Technology Silchar, Assam 788010, India

e-mail: ppatowari@yahoo.com

T. P. Naik · K. G. Melese · R. S. Rana · I. Singh · A. K. Sharma

Mechanical and Industrial Engineering Department, Indian Institute of Technology Roorkee, Roorkee, Uttarakhand 247667, India

e-mail: kassahun28@yahoo.com

R. S. Rana

e-mail: ramsingh.mech17@gmail.com

machining of these advanced materials is difficult; therefore, to overcome these challenges, wire-EDM, which is a non-conventional process, is gaining importance these days. WEDM is a thermo-electrical procedure in which material is removed from the workpiece by the arrangement of discrete sparks among workpiece and wire. While machining, there is no physical contact between tool and workpiece [3]. Therefore, the tool in this process is not eroded, and the finish on the workpiece surface is also very high compared to any conventional machining process. The schematic picture of WEDM appears in Fig. 1. This paper considers four control parameters, in particular, pulse on time (T_{on}) (μs), pulse off time (T_{off}) (μs), peak current (I_p) (A), and table feed (S) ($\mu m/s$), while rest of the parameters are kept steady. Taguchi L16 symmetrical cluster has been intended to carry out the investigation study [4]. Yigezu et al. [5] have investigated the ceramic particle reinforced aluminum composites. It was reported that for the fabrication of the metal matrix composites, stir casting route is cost effective and straightforward. Mazahery and Shabani [6] have researched the mechanical properties of B_4C fortified A356 composite. It was discovered that the porosity, rigidity, and hardness are higher than the Al compound and increment with an increase in the B_4C content. Rahman et al. [7] have determined the impact of EDM input responses on the MRR of titanium (Ti) alloy. They have concluded that current and T_{on} were the most influencing parameters affecting MRR. Liu et al. [8] utilized wire electrochemical discharge machining to study the machining characteristics of Al_2O_3 /aluminum composites. They found that material removal rate increases with high current.

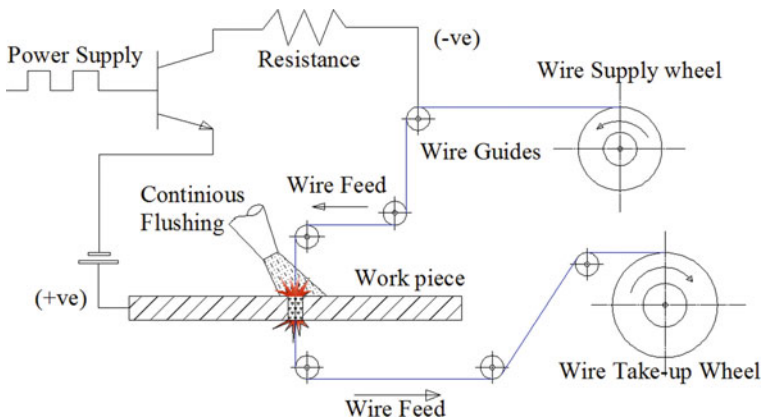


Fig. 1 Schematic diagram of CNC WEDM [9]



Fig. 2 Wire electrical discharge machine

2 Experimental Investigations

2.1 Materials and Method

The aluminum (6063) rods supplied by Madhab and Company, Kolkata, West Bengal, India, and Graphite powder of mesh size 60 was used for the fabrication of metal matrix composites. The investigations were done on a CNC WEDM machine located at NIT Silchar (Make: Ratnaparkhi Electronics (I) Pvt Ltd.) which is shown in Fig. 2. The dielectric fluid used for the study was de-ionized water which is continuously flushed at the machining zone to remove the debris produced during the machining.

2.2 Design of Experiments

Input parameters, for example, pulse on time (T_{on}), pulse off time (T_{off}), peak current (I_p), and table feed (S) utilized in this investigation study are given in Table 1. Each factor is examined at four levels to decide the ideal settings for the WEDM procedure. These parameters and their levels have been picked dependent on the Taguchi investigation for the tests to be directed. The Design of experiment (DOE) with Taguchi's L16 symmetrical cluster dependent on four information parameters having four distinct levels appears in Table 2.

Table 1 Input parameters

Symbol	Input parameters	Unit	Value 1	Value 2	Value 3	Value 4
T_{on}	Pulse on time	μ s	25	35	45	55
T_{off}	Pulse off time	μ s	8	10	12	14
I_p	Peak current	A	2	3	4	5
S	Table speed	μ m/s	46.70	55.60	60.00	69.90

Table 2 Taguchi L16 design of experiment

Exp. no	T_{on} (μ s)	T_{off} (μ s)	I_p (A)	S (μ m/s)
1	25	8	2	46.7
2	25	10	3	55.6
3	25	12	4	60.0
4	25	14	5	69.9
5	35	8	3	60.0
6	35	10	2	69.9
7	35	12	5	46.7
8	35	14	4	55.6
9	45	8	4	69.9
10	45	10	5	60.0
11	45	12	2	55.6
12	45	14	3	46.7
13	55	8	5	55.6
14	55	10	4	46.7
15	55	12	3	69.9
16	55	14	2	60.0

2.3 Experimental Results

The tool utilized during the tests was a brass wire of 0.22 mm diameter. The workpiece picked was a composite of measurements 30 mm \times 24 mm \times 5 mm. The cutting length in all the tests was fixed; equivalent to 5 mm. Dielectric utilized was deionized water, which is flushed continuously to the machining zone to divert the debris particles. The whole arrangement of investigations has been completed three times. While performing out each arrangement of analysis, values for MRR and CR have been determined, and KW was seen on a microscope. Finally, the average estimations of MRR, CR, and KW have been determined and are given in Table 3. Figure 3a–d shows the figure of a composite workpiece reinforced with graphite with two distinctive wt. percentage (5 and 10%) alongside its optical pictures of kerf width.

The kerf width (in μ m), of each experimental, has been seen by the metallurgical microscope model number DM 2500M (Make: Leica). The material removal rate

Table 3 Values of response measures using WEDM in Al-Graphite (5 and 10%) composite

Exp. no	5% by wt			10% by wt		
	MRR (mg/s)	Cutting rate (μm/s)	Kerf width (μm)	MRR (mg/s)	Cutting rate (μm/s)	Kerf width (μm)
1	0.1874	46.30	420.65	0.3248	45.87	413.51
2	0.1765	51.02	427.05	0.3316	52.63	445.03
3	0.3149	57.47	443.84	0.4695	60.98	474.7
4	0.3197	70.42	441.62	0.5873	70.42	452.45
5	0.3544	55.56	431.61	0.4107	59.52	452.45
6	0.4289	69.44	428.23	0.5813	66.67	445.03
7	0.4413	45.87	493.95	0.3714	47.62	482.12
8	0.2917	52.08	471.53	0.3691	51.55	489.54
9	0.4726	68.49	475.01	0.5600	66.67	470.99
10	0.4145	60.24	485.08	0.4488	59.52	519.21
11	0.3908	52.08	444.88	0.3626	50.51	437.62
12	0.2563	44.64	452.01	0.3914	47.62	489.54
13	0.3447	52.63	496.00	0.4583	52.08	519.21
14	0.3176	47.17	476.11	0.4355	45.45	500.66
15	0.6108	66.67	456.93	0.6014	70.42	470.99
16	0.2732	60.24	442.58	0.4512	58.14	429.07

(mg/s) is calculated utilizing equation 1.

$$MRR = \frac{\text{weightloss}}{\text{machining time}} \tag{1}$$

where weight loss = difference between the initial and final weights of the composite sample.

Cutting rate (μm/s) is determined to utilize equation 2.

$$CR = \frac{\text{Cuttinglength(fixed5mm)}}{\text{machining time}} \tag{2}$$

For the most part, OEC is performed while the clashing measure is available in the investigation, and it is calculated using equation 3 [9]. As in this investigation, the requirement is of having kerf width of the slot as minimum and MRR and cutting rate as maximum, so equal weightage has been given to all the output responses, i.e., 33.33%.

$$OEC = \left(\frac{X - X_{min}}{X_{max} - X_{min}} \times W_x \right) + \left(\frac{Y - Y_{min}}{Y_{max} - Y_{min}} \times W_y \right)$$

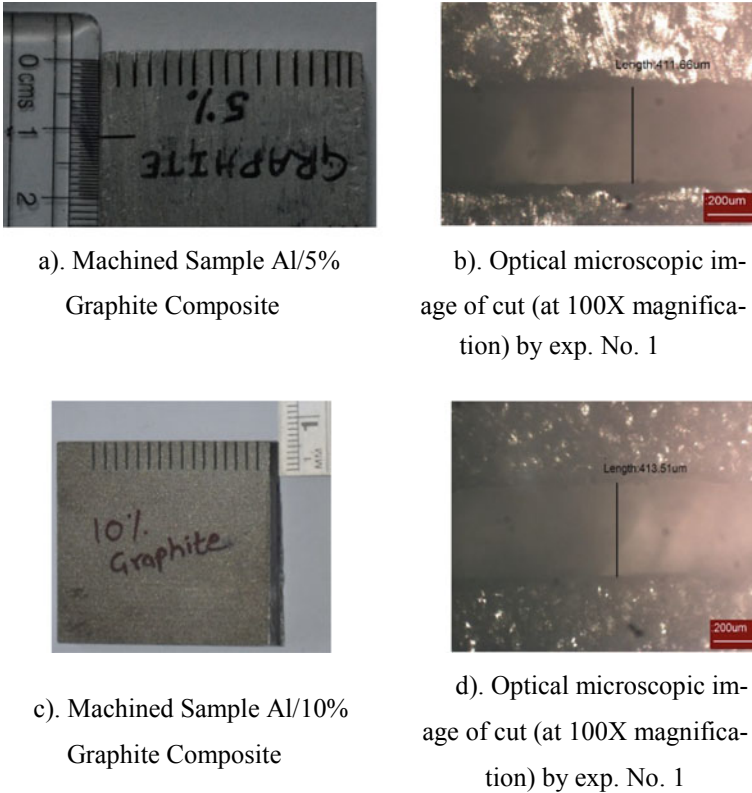


Fig. 3 Machined composites and microscopic image

$$+ \left(\left(1 - \frac{Z - Z_{\min}}{Z_{\max} - Z_{\min}} \right) \times W_z \right) \tag{3}$$

where

- $X, Y,$ and $Z =$ test value of MRR, CR, and KW respectively.
- $X_{\max}, Y_{\max},$ and $Z_{\max} =$ best values of MRR, CR, and KW respectively.
- $X_{\min}, Y_{\min},$ and $Z_{\min} =$ worst values of MRR, CR, and KW respectively.
- $W_x, W_y,$ and $W_z =$ equal weightage, i.e., 33.33%.

3 Results and Discussion

Figure 4 shows the impact of $T_{\text{on}}, T_{\text{off}}, I_p,$ and S on MRR. It is obvious from the figure that MRR increases with an increase in T_{on} this is a direct result of an increasingly large number of pulses striking the workpiece that progressively removes material

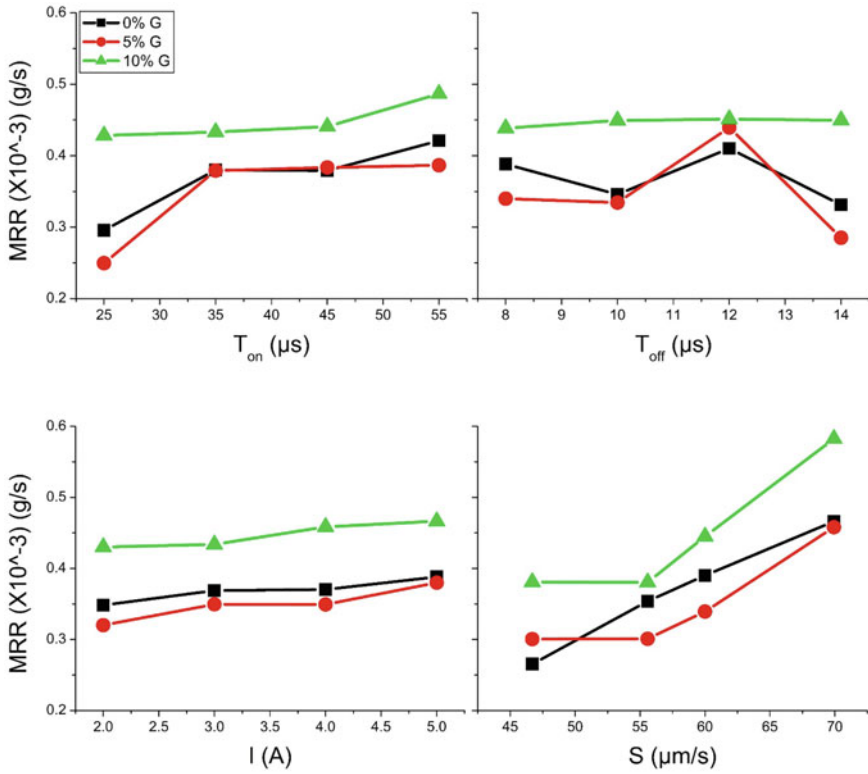


Fig. 4 Effect of input parameters on MRR for different reinforcing graphite content

and prompts higher MRR. If T_{on} is high, more time will be provided for the material to receive heat, to get vaporized, which will increase the MRR. However, as T_{on} decreases, MRR decreases because the pulses will strike the workpiece for less amount of time, and suddenly T_{off} will start, which will not allow the vaporization of the material. As I_p increase, more energy is supplied, which increases MRR. Moreover, it is seen that with increasing S , MRR increases because of the rapid movement of the table.

Figure 5 shows the impact of T_{on} , T_{off} , I_p , and S on cutting rate. It is obvious from the figure that S is a most important factor when contrasted with other responses. As S increases, the cutting rate increases due to the quick movement of the table. Also, it is seen that the cutting rate for pure aluminum is more compared to the composite material because the graphite particles which are used as reinforcement has a higher melting point, and so it obstructs the rate of cutting as it takes time to melt the graphite particle. Likewise, no significant distinction is seen in the cutting rate for both 5 and 10% graphite-reinforced composites.

Figure 6 shows the impact of T_{on} , T_{off} , I_p , and S on KW. By and large, it is obvious from figure that with an increase in T_{on} , kerf width increases since progressively

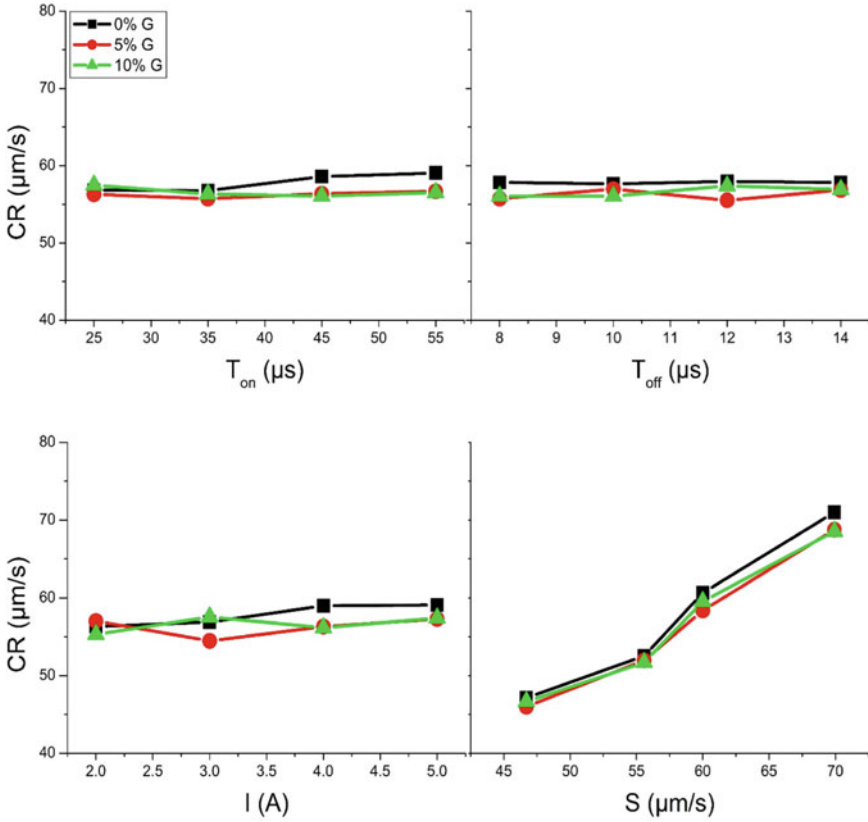


Fig. 5 Effect of input parameters on cutting rate for different reinforcing graphite content.

more material removal prompts higher KW. However, T_{off} does not significantly influence the KW. Because of increase in I_p , kerf width increases since more energy is provided, which prompts a higher concentration of release energy in the spark gap which brings about more significant cavity development. However, an increase in S decreases the kerf width as the table moves at a faster rate. It is observed that while machining in the composite material, brass wire (tool) faces graphite particles in between, which acts like a boundary for the wire while machining, thus results in narrow kerf width as compared to kerf width in the unreinforced material.

Table 4 depicts the OEC values for each experimental run, and it is found out that maximum OEC in case of Al-5% Graphite is 81.42, and in the case of Al-10% Graphite is 86.42.

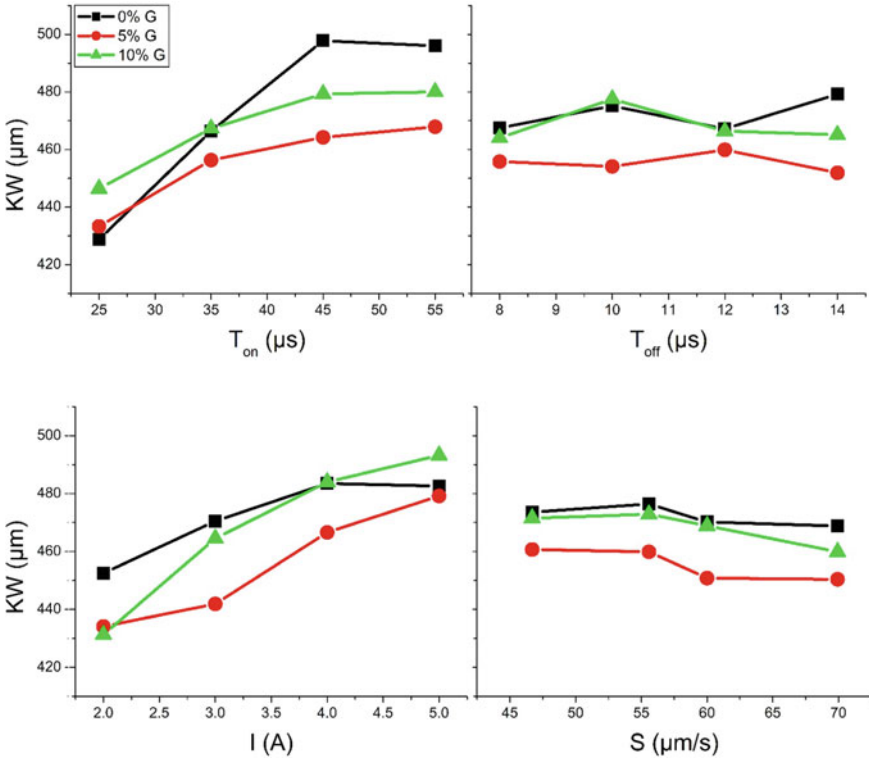


Fig. 6 Effect of input parameters on kerf width for different reinforcing graphite content.

3.1 Confirmation Test

Based on the OEC values, the graph has been plotted using Minitab software, and the optimum parametric conditions have been observed. Based on these conditions, experiments were again conducted three times, and the average values of the MRR, CR, and KW have been obtained. The predicted OEC value for the optimal condition is obtained using Minitab software. The actual OEC value for the optimum values of the output conditions has been calculated using the same equation 3. This actual OEC value and the predicted value are compared, and the % deviation is found out, which is given in Table 5.

4 Conclusions

The key results are summarized as follows:

Table 4 Overall evaluation criteria

Exp. no	Al-5% Graphite	Al-10% Graphite
1	36.31	33.89
2	38.75	33.79
3	50.29	52.20
4	68.38	86.02
5	56.25	50.19
6	81.42	82.62
7	22.82	20.21
8	29.29	22.83
9	62.85	71.87
10	43.26	33.73
11	48.68	37.03
12	25.58	20.28
13	23.24	24.94
14	22.90	19.19
15	79.09	81.87
16	51.22	60.59

Table 5 Confirmation test results

Composites	Observed OEC	Predicted OEC	% Deviation
Al-5% Graphite	87.86	87.18	0.77
Al-10% Graphite	87.45	96.32	10.14

- During the machining of Al-5% Graphite composites, the highest MRR was found to be 0.6108 mg/s, and the lowest MRR was 0.1765 mg/s. The highest cutting rate was found to be 70.42 $\mu\text{m/s}$, and the lowest was found to be 44.64 $\mu\text{m/s}$. The minimum kerf width obtained was 420.65 μm , and the largest was 496.00 μm .
- The optimum parametric conditions after the application of OEC in the case of 5% reinforced graphite composite were found to be $T_{\text{on}} = 25 \mu\text{s}$, $T_{\text{off}} = 12 \mu\text{s}$, $I_p = 2 \text{ A}$, and $S = 69.9 \mu\text{m/s}$. After performing OEC, the % deviation between observed and predicted OEC was found to be 0.77%.
- However, in Al-10% Graphite composites, the highest MRR was found to be 0.6014 mg/s, and the lowest MRR was 0.3248 mg/s. The highest cutting rate was found to be 70.42 $\mu\text{m/s}$, and the lowest was found to be 45.45 $\mu\text{m/s}$. The minimum kerf width obtained was 413.51 μm , and the largest was 519.21 μm .
- The optimum parametric condition after the application of OEC in the case of 10% reinforced graphite composite was found to be $T_{\text{on}} = 25 \mu\text{s}$, $T_{\text{off}} = 12 \mu\text{s}$, $I_p = 2 \text{ A}$, and $S = 69.9 \mu\text{m/s}$. After performing OEC, the % deviation between observed and predicted OEC was found to be 10.14%.

Acknowledgements The author, Tejas Pramod Naik, gratefully acknowledges the Design Innovation Center (DIC), Ministry of Human Resource and Development (MHRD), Government of India, for providing fellowship for the Ph.D. work.

References

1. Surappa MK (2003) Aluminium matrix composites: challenges and opportunities. *Sadhana* 28:319–334
2. Kala H, Mer KKS, Kumar S (2014) A review on mechanical and tribological behaviors of stir cast aluminum matrix composites. *Proc Mater Sci* 6:1951–1960. <https://doi.org/10.1016/j.mspro.2014.07.229>
3. Ramakrishnan R, Karunamoorthy L (2006) Multi response optimization of wire EDM operations using robust design of experiments. *Int J Adv Manuf Technol* 29:105–112. <https://doi.org/10.1007/s00170-004-2496-6>
4. Mahapatra SS, Patnaik A (2006) Parametric optimization of wire electrical discharge machining (WEDM) process using Taguchi method. *J Brazilian Soc Mech Sci Eng* 28:422–429. <https://doi.org/10.1590/S1678-58782006000400006>
5. Yigezu BS, Jha PK, Mahapatra MM (2013) The key attributes of synthesizing ceramic particulate reinforced Al-based matrix composites through stir casting process: a review. *Mater Manuf Process* 28:969–979. <https://doi.org/10.1080/10426914.2012.677909>
6. Mazahery A, Shabani MO (2012) Mechanical properties of squeeze-cast A356 composites reinforced with B 4C particulates. *J Mater Eng Perform* 21:247–252. <https://doi.org/10.1007/s11665-011-9867-6>
7. Rahman MM, Khan MAR, Kadrigama K (2010) Modeling of material removal on machining of Ti-6Al-4V through EDM using copper tungsten electrode and positive polarity. *World Acad Sci Eng Technol* 71:576–581
8. Liu JW, Yue TM, Guo ZN (2009) Wire electrochemical discharge machining of Al₂O₃ particle reinforced aluminum alloy 6061. *Mater Manuf Process* 24:446–453. <https://doi.org/10.1080/10426910802714365>
9. Naik TP, Debnath T, Patowari PK (2018) Machinability study on German silver using wire-EDM. *AIP Conf Proc* 1998:1–8. <https://doi.org/10.1063/1.5049100>

Enhanced Mechanical Properties of h-BN Nanosheets via Edge Passivation Using Various Radicals



Bharat Bhushan Sharma and Avinash Parashar

1 Introduction

In the last few years, various two-dimensional (2D) nanomaterials such as graphene [1, 2], h-BN [3], and MoS₂ [4] have been widely synthesized and considered in both numerical and experimental analysis. Hexagonal boron nitride is one of the 2D single atomic layered materials very similar to graphene having sp² hybridized hexagonal lattice with an equal number of B and N atoms [5]. This sp² hybridized hexagonal lattice of h-BN nanosheets attributed to exceptional mechanical [6] and thermal properties [7]. In addition to these exceptional properties, h-BN also possesses some unique properties such as high thermal stability [6], chemical inertness [8], biological compatibility [9], and good electrical insulation [5] as compared to graphene due to their ionic nature of bonding. These unique and exceptional properties make h-BN as a potential candidate for nanocomposite [10], biomedical [11], electronic packaging [12], nanoelectromechanical (NEMS) [13], nanofluidic, and water desalination [14, 15]. Further, selective chemical functionalization in their quantum domain has greatly modified the properties of h-BN [16–18].

To enhance the properties of 2D nanomaterials such as graphene and h-BN, researchers are trying to chemically functionalize their quantum domain with various radicals [16, 19–22]. Lots of research article had already been published on h-BN functionalization by various radicals such as hydrogen [16], hydroxyl [20], fluorine [21], CH₃ [21], and CHO [21] and concluded that functionalization alters the properties of h-BN nanosheets. Hydrogenated and hydroxyl functionalized h-BN nanosheets had already been analyzed using experimental and numerical techniques

B. B. Sharma · A. Parashar (✉)

Department of Mechanical and Industrial Engineering, Indian Institute of Technology Roorkee, Roorkee, Uttarakhand 247667, India

e-mail: avinash.parashar@me.iitr.ac.in

B. B. Sharma

e-mail: bsharma@me.iitr.ac.in

for tailoring selective properties [16–23]. In 2012, Sainsbury et al. [23] synthesized the OH functionalized h-BN using solution-phase oxygen radical functionalization techniques. In 2016, Kumar et al. [16] predicted the uniaxial tensile strength and fracture morphology of hydrogen functionalized h-BN nanosheets using MD-based simulations. Apart from this fully functionalized h-BN, Kumar et al. [22] also investigated the effect of functionalization of crack edge atoms on the fracture toughness of h-BN using classical mechanics-based simulations. Xiao et al. [24] exfoliated the edge-hydroxylated h-BN by an experimental-based steam treatment method and investigated that edge-functionalized h-BN used as an additive to enhance the thermal conductivity of hydrogels.

Based on the literature that is available on H and OH functionalized h-BN, a lot of articles had already been published on synthesizing techniques, dispersion properties, stability, mechanical properties, and thermal properties. Despite a lot of research, literature is almost silent on the effect of edge functionalization on the mechanical characterization of h-BN containing free edges. In this research paper, the effects of edge passivation on the uniaxial tensile strength of h-BN are investigated. In this research work, classical mechanics-based MD simulations have been executed using reactive force field (ReaxFF) [25], to predict the uniaxial tensile strength of edge-passivated h-BN nanosheets.

2 Computational Details

Classical mechanics-based MD simulations were executed using LAMMPS, while post-processing was done using the OVITO. The exactitude of the results in MD depends upon the potential that was utilized in the simulations. In this article, computationally intensive, but more accurate ReaxFF potential [25] was used in order to capture the atomistic interactions in edge-passivated h-BN. ReaxFF parameters proposed by Paupitz et al. [26] were utilized in this work. In ReaxFF potential, the total energy is the summation of the various partial energies and expressed as in Eq. (1).

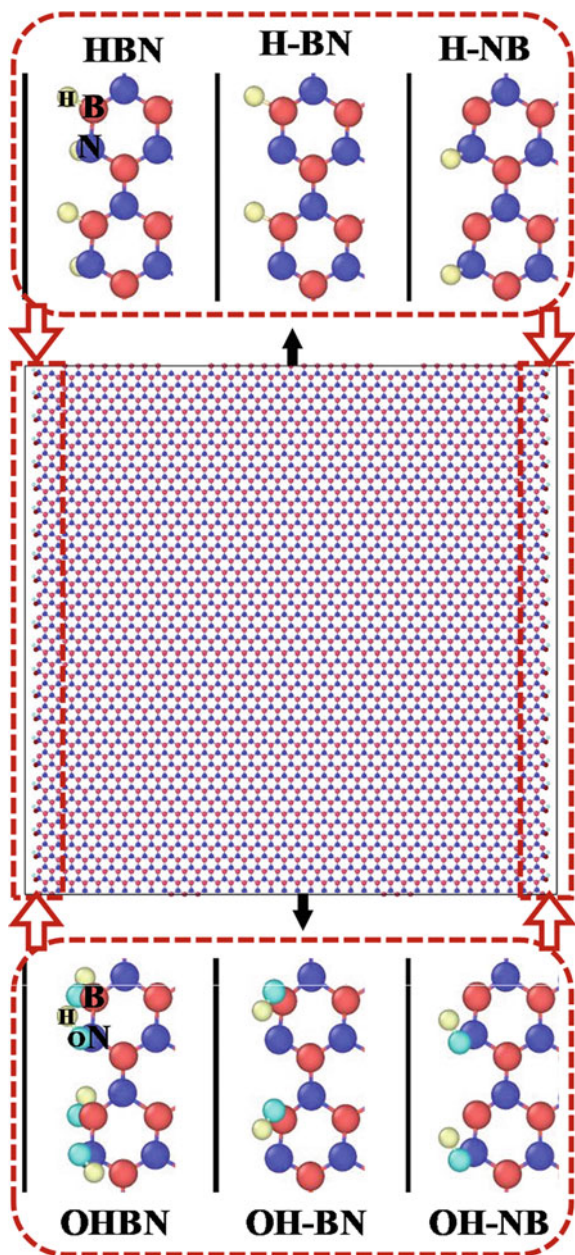
$$E_{\text{system}} = E_{\text{bond}} + E_{\text{over}} + E_{\text{under}} + E_{\text{lp}} + E_{\text{val}} + E_{\text{pen}} + E_{\text{tors}} + E_{\text{conj}} + E_{\text{vdWaaals}} + E_{\text{Columb}} \quad (1)$$

Where E_{bond} = bond order energy; E_{over} and E_{under} are the energies because of over- and under-coordination of the atoms; E_{lp} = lone pairs energy on N atoms; E_{val} = valence angle distortion energy; E_{pen} = penalty energy; E_{tors} = energy related to the torsion angle; E_{conj} = conjugation energy; and E_{vdWaaals} and E_{Columb} are the potential of energies for van der Waals and Coulomb interactions.

In this research paper, the size of nanosheets was kept constant at $100\text{\AA} \times 100\text{\AA}$ along with both the directions. In order to create the free edges, size of the nanosheets was reduced to 94\AA along the transverse direction to the loading, which

help in averting the image interaction in the simulation box as illustrated in Fig. 1. Herein, periodic boundary conditions were applied in in-plane directions, while fixed boundary condition was applied in out of the plane direction. To avert the thermal

Fig. 1 Various configurations of hydrogen and hydroxyl edge-functionalized h-BN subjected to loading in AC direction



disorder, simulations were executed at a very low temperature of 1 K. To analyze the effect of edge passivation, six different types of configurations were considered: fully passivated when H or OH radicals were attached to both *sp* hybridized N and B atoms (HBN or OHBN) and partially passivation when H or OH radicals were attached either to *sp* hybridized B (H-BN or OH-BN) or *sp* hybridized N (H-NB or OH-NB), which are shown in Fig. 1.

After generating the atomistic configurations of edge-passivated h-BN in the simulation box, the atomic configurations were equilibrated using NPT ensemble for 20 ps with an integrating time step of 0.25 fs. To analyze the tensile behavior of passivated and non-passivated h-BN, the uniaxial tensile strain was applied on the equilibrated structures at a strain rate of 0.001 ps⁻¹ with NVT ensemble. The coordinates of atoms were updated using velocity–verlet integration scheme with an integration time step of 0.25 fs. The atomic virial stresses were calculated with the help of Eq. (2).

$$\sigma_{ij}^{\alpha} = \frac{1}{\varphi} \left(\frac{1}{2} m^{\alpha} v_i^{\alpha} v_j^{\alpha} + \sum_{\beta=1, n} r_{\alpha\beta}^j f_{\alpha\beta}^i \right) \quad (2)$$

Where *i* and *j* are indices of the Cartesian coordinates system, α and β are the atomic indices, m_{α} and v_{α} = mass and velocity of atom α , $r_{\alpha\beta}$ = distance between atoms α and β , and φ = atomistic volume of h-BN.

3 Results and Discussion

Initially, the accuracy of ReaxFF potential was validated by predicting the value of tensile strength of pristine h-BN. Snapshot of pristine as well as h-BN nanosheets with free edges subjected to AC loading direction is shown in Fig. 2. The predicted value of tensile strength in the AC loading direction is 170 GPa, which is close to the value reported in the article [27].

After investing the value of mechanical strength of pristine h-BN, next set of simulations were executed to predict the effect of H and OH edge functionalization on the uniaxial tensile strength of h-BN containing free edges. Stress–strain plots investigated in the AC loading direction for various configurations are shown in Fig. 3. It can be investigated from Fig. 3 that in all the passivated configurations, fully edge-passivated configurations represent the maximum enhancement, while partially passivated configurations have no significant effect on the uniaxial tensile strength of h-BN.

To further analyze the effect of edge functionalization on the uniaxial tensile strength, snapshots of fracture initiation site in pristine as well as h-BN nanosheet with free edges are shown in Fig. 4. It can be seen from Fig. 4 that fracture always initiates from the free edges in h-BN nanosheets containing free edges, while a shift in fracture initiation was observed in fully periodic h-BN nanosheets (no free edges present). These free edges are one type of geometrical defects in h-BN nanosheets,

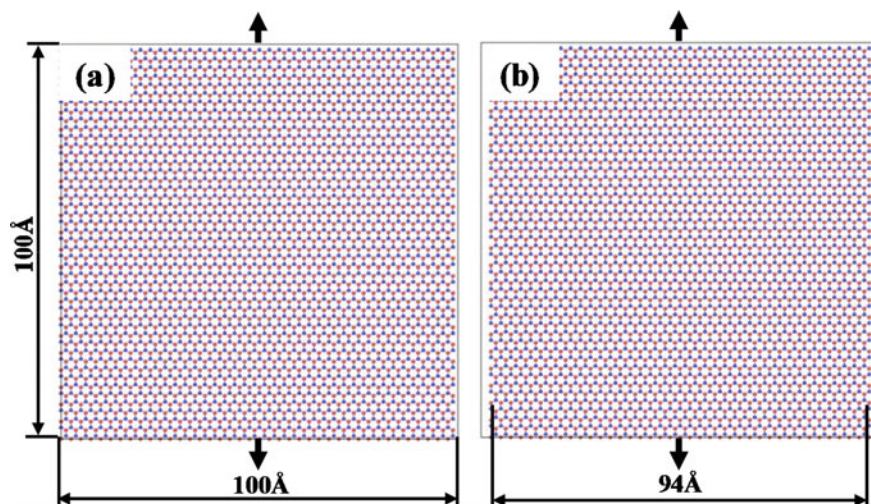
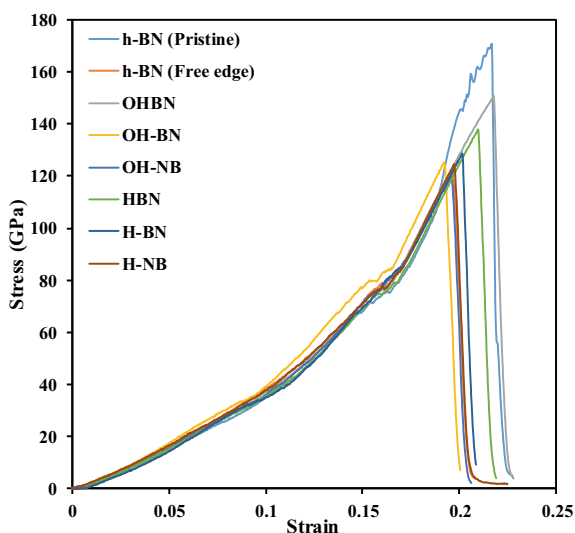


Fig. 2 Schematic of **a** h-BN nanosheet (pristine) and **b** h-BN nanosheet containing free edges subjected to loading in AC direction

Fig. 3 Stress–strain plot for different configurations of hydrogen and hydroxyl edge passivation subjected to loading in AC direction



which significantly reduce the overall mechanical strength of h-BN. In full edge passivation, all the sp hybridized atoms at the edges were shifted to a more stable sp^2 hybridized state, which ultimately shifts the failure initiation site from the free edges, and hence, the tensile strength of h-BN nanosheets was improved. While in partial edge passivation, fracture initiation from the free edges is not fully restricted, as all the sp hybridized atoms on the free edges are not shifted to a more stable sp^2

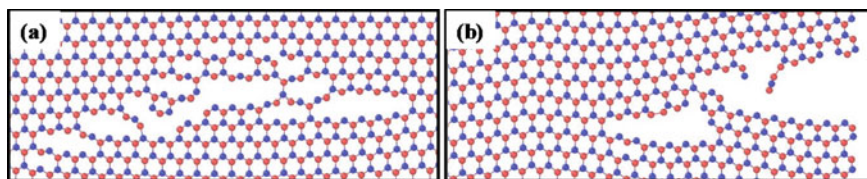


Fig. 4 Snapshot of **a** h-BN nanosheet (pristine) and **b** h-BN containing free edges at the beginning of fracture when subjected to loading in AC direction

hybridized state, and hence, negligible enhancement in the uniaxial strength of h-BN was investigated in partial edge functionalization.

4 Conclusion

Classical mechanics-based MD approach was executed to predict the effect of edge functionalization on the mechanical strength of h-BN nanosheets with free edges. It can be deduced from the simulations that the full edge functionalization with hydrogen and hydroxyl groups has improved the fracture toughness up to 25% in AC loading direction, while partially edge passivation had no significant effect on the uniaxial tensile strength of h-BN. Results observed from this study will help in utilizing the full capacity of h-BN nanosheets in various applications such as nanomembrane for ion separation, drug delivery, and nanocomposite.

References

1. Verma PK, Sharma BB, Chaurasia A, Parashar A (2020) Inter-granular fracture toughness of bi-crystalline graphene nanosheets. *Diam Relat Mater* 102:107667
2. Sharma SS, Sharma BB, Parashar A (2019) Defect formation dynamics in dry and water submerged graphene nanosheets. *Mater Res Express* 6:075063
3. Sharma BB, Parashar A (2020) Mechanical and fracture behaviour of hydroxyl functionalized h-BN nanosheets. *J Mater Sci* 55:3228–42
4. Radisavljevic B, Radenovic A, Brivio J, Giacometti V, Kis A (2011) Single-layer MoS₂ transistors. *Nat Nanotechnol* 6:147–50
5. Sharma BB, Parashar A (2020) A review on thermo-mechanical properties of bi-crystalline and polycrystalline 2D nanomaterials. *Crit Rev Solid State Mater Sci* 45:134–70
6. Sharma BB, Parashar A (2019) Atomistic simulations to study the effect of grain boundaries and hydrogen functionalization on the fracture toughness of bi-crystalline h-BN nanosheets. *Phys Chem Chem Phys* 21:13116–25
7. Mortazavi B, Pereira LFC, Jiang JW, Rabczuk T (2015) Modelling heat conduction in polycrystalline hexagonal boron-nitride films. *Sci Rep* 5:1–11
8. Golberg D, Bando Y, Tang CC, Zhi CY (2007) Boron nitride nanotubes. *Adv Mater* 19:2413
9. Chen X, Wu P, Rousseas M, Okawa D, Gartner Z (2009) Boron nitride nanotubes are nontoxic and can be functionalized for interaction with proteins and cells. *J Am Chem Soc* 131:890–1

10. Chaurasia A, Verma A, Parashar A, Mulik RS (2019) Experimental and computational studies to analyze the effect of h-BN nanosheets on mechanical behavior of h-BN/polyethylene nanocomposites. *J Phys Chem C* 123:20059–70
11. Roosta S, Nikkhah SJ, Sabzali M, Hashemianzadeh SM (2016) Molecular dynamics simulation study of boron-nitride nanotubes as a drug carrier: from encapsulation to releasing. *RSC Adv* 6:9344–51
12. Lin Z, Liu Y, Raghavan S, Moon KS, Sitaraman SK, Wong CP (2013) Magnetic alignment of hexagonal boron nitride platelets in polymer matrix: toward high performance anisotropic polymer composites for electronic encapsulation. *ACS Appl Mater Interfaces* 5:7633–40
13. Ghorbanzadeh Ahangari M (2015) Modeling of the interaction between polypropylene and monolayer sheets: a quantum mechanical study. *RSC Adv* 5:80779–85
14. Sharma SS, Sharma BB, Parashar A (2019) Mechanical and fracture behavior of water submerged graphene. *J Appl Phys* 125:215107
15. Lei W, Portehault D, Liu D, Qin S, Chen Y (2013) Porous boron nitride nanosheets for effective water cleaning. *Nat Commun* 4:1777
16. Kumar R, Mertiny P, Parashar A (2016) Effects of Different hydrogenation regimes on mechanical properties of h-BN: a reactive force field study. *J Phys Chem C* 120:21932–8
17. Sharma BB, Parashar A (2019) Atomistic simulations to study the effect of water molecules on the mechanical behavior of functionalized and non-functionalized boron nitride nanosheets. *Comput Mater Sci* 169:109092
18. Kong D, Zhang D, Guo H, Zhao J, Wang Z, Hu H, Xu J, Fu C (2019) Functionalized boron nitride nanosheets/Poly(l-lactide) nanocomposites and their crystallization behavior. *Polymers (Basel)* 11:440
19. Sharma BB, Parashar A (2020) Mechanical strength of a nanoporous bicrystalline h-BN nanomembrane in a water submerged state. *Phys Chem Chem Phys* 22:20453–65
20. Chaurasia A, Parashar A, Mulik RS (2020) Effect of hexagonal boron nitride nanoplatelet on crystal nucleation, mechanical behavior, and thermal stability of high-density polyethylene-based nanocomposites. *Macromol Mater Eng* 305:2000248
21. Sharma BB, Parashar A (2021) Fracture behaviour of pristine and defective form of water submerged h-BN nanosheets. *J Phys D: Appl Phys* 54:035306
22. Kumar R, Parashar A (2017) Fracture toughness enhancement of h-BN monolayers via hydrogen passivation of a crack edge. *Nanotechnology* 28:165702
23. Sainsbury T, Satti A, May P, Wang Z, McGovern I, Gun'ko YK, Coleman J (2012) Oxygen radical functionalization of boron nitride nanosheets. *J Am Chem Soc* 134:18758–71
24. Xiao F, Naficy S, Casillas G, Khan MH, Katkus T, Jiang L, Liu H, Li H, Huang Z (2015) Edge-hydroxylated boron nitride nanosheets as an effective additive to improve the thermal response of hydrogels. *Adv Mater* 27:7196–203
25. Van Duin ACT, Dasgupta S, Lorant F, Goddard WA (2001) ReaxFF: A reactive force field for hydrocarbons. *J Phys Chem A* 105:9396–409
26. Paupitz R, Junkermeier CE, van Duin ACT, Branicio PS (2014) Fullerenes generated from porous structures. *Phys Chem Chem Phys* 16:25515–22
27. Mortazavi B, Re Y (2012) Investigation of tensile response and thermal conductivity of boron-nitride nanosheets using molecular dynamics simulations 44:1846–52

Evaluation of Interfacial Shear Strength of h-BN/PE Nanocomposites Using Molecular Dynamics



Ankur Chaurasia , Avinash Parashar , and Rahul S. Mulik

1 Introduction

Since last few years, research fraternity has been attracted towards two-dimensional nanofiller such as graphene and hexagonal boron nitride nanosheet (isoelectric analogous to graphene) as reinforcement in polymers [1–3]. This nanomaterial exhibits excellent thermal and mechanical properties. BNNS is thermally and chemically stable at high temperature [4]. These excellent properties of BNNS claim it, potential candidate, among 2-D nanofillers. Polyethylene (PE) is widely used in diversified application due to its lightweight (due to the low mass of hydrogen) [5, 6]. Neat high-density polyethylene (HDPE) lacks in mechanical and thermal properties such as tensile strength, thermal conductivity [7] and high-temperature thermal stability. h-BN nanofiller (BNNS, BNNT) is the suitable nanofiller for enhancing the mechanical properties of the neat PE-based nanocomposites. Several literatures on interfacial interaction between nanofiller and PE matrix have been reported. Few of them have modelled the matrix and nanofiller using different pair potentials, i.e. DRIEDING, PCFF, CVFF and Tersoff in conjunction with molecular dynamics [8–11].

Li et al. have [12] studied the mechanical behaviour of multilayer graphene sheet in the epoxy matrix. They reported that nanovoid and strain localization were observed in the bulk polymer while interfacial debonding was observed in the case of perpendicular graphene sheets. The effect of pulling velocity, graphene with wavy structure and matrix on the interfacial mechanical properties of polymethyl methacrylate and

A. Chaurasia · A. Parashar (✉) · R. S. Mulik
Department of Mechanical and Industrial Engineering, Indian Institute of Technology Roorkee,
Roorkee, Uttarakhand 247667, India
e-mail: avinash.parashar@me.iitr.ac.in

A. Chaurasia
e-mail: achaurasia@me.iitr.ac.in

R. S. Mulik
e-mail: rsmulfme@iitr.ac.in

polyethylene nanocomposites has been studied by Liu and his team [13]. Pulling velocity and graphene with wavy edges significantly affects the interfacial properties of graphene-based nanocomposites. Hadden and his team [14] have contemplated the impact of cross-link density on the interface region of the graphite/epoxy composite material. Hadden and his team have modelled the hybrid composites that consist of graphene nanoplatelet and carbon fibre/epoxy using multiscale modelling. Meng et al. [15] predicted the work required for the exfoliation of BNNS from the h-BN/PE fibre and validated with the experimental results. Kumar and Parashar [5] have worked on the effect of hydrogenated and defected h-BN nanofiller on mechanical properties of h-BN/PE nanocomposites. Verma et al. [16] have also calculated the interfacial strength of the defective graphene nanosheets in the polyethylene matrix.

Synthesis of BNNS with required morphology is not possible practically. Naturally, two-dimensional BNNS is synthesized in various morphologies such as circular, triangular, rectangular and polygon. In this present study, authors have attempted to predict the interfacial strength of h-BN/PE nanocomposites with rectangular and triangular morphology. In addition to this, authors have also studied the effect of stacked rectangular BNNS on interfacial strength of h-BN/PE nanocomposites.

2 Computational Details

Molecular dynamics (MD) simulation is a tool for analysing the material at the atomistic scale without synthesizing them. One of the important goals of atomistic modelling is to understand the physical phenomenon of material at the atomistic scale. Molecular dynamics theory is based on Newton's equation of motion. After each time step, the velocity and position of each atom are computed and then combined with the existing velocity and position using velocity Verlet algorithm. In this present study, reaction force field (Reaxff) [17, 18] potential is used for analysing the interatomic interaction between the pair of atoms. Charge polarization and bond order formalism allow reaction force field potential to model covalent as well as electrostatic interaction for the variety of materials [19]. The energy component of the reaction force field outlined by Eq. (1) [20];

$$E_{\text{system}} = E_{\text{angle}} + E_{\text{tors}} + E_{\text{bond}} + E_{\text{over}} + E_{\text{vdwall}} + E_{\text{coulomb}} + E_{\text{specific}} \quad (1)$$

where E_{tors} and E_{angle} described as energy relate with 4-body torsional angle strain and 3-body valence angle strain E_{bond} ; is continuous function of interatomic distance; E_{over} over coordination penalty energy of atoms; E_{specific} system-specific energy terms to the system of interest such as conjugate bond correction, lone pair and hydrogen binding; E_{vdwalls} and E_{coulomb} are the energy that relate the van der Waals and coulombic interaction between all atoms.

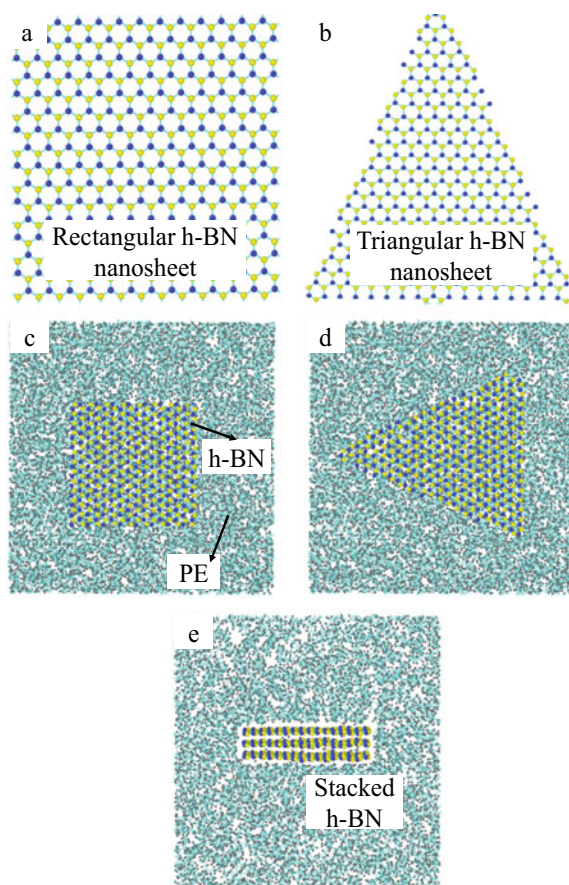
High-density polyethylene coordinates are created in material studio software. MD simulation was performed using open-source large atomic/molecular massively parallel simulator (LAMMPS) developed by SNL [21, 22]. For the interatomic pair

Table 1 Lennard–Jones potential parameter

S. No.	LJ potential parameter	Distance constant σ (Å)	Energy constant ϵ (Kcal/mole)
1	N	3.365	0.1448671
2	B	3.453	0.094988
3	H	2.958	0.071659
4	C	3.400	0.056039

interaction between hydrogen (H), carbon (C), boron (B) and nitrogen (N), atoms are simulated with ReaxFF potential parameter developed by Han et al. [23]. However, the interface between BNNS and PE is modelled with Lennard–Jones potentials (L-J potentials) parameter [24] given in Table 1. In this present study, two morphologies of BNNS are studied, i.e. rectangular and triangular. These BNNSs were incorporated in neat PE at the middle position of the simulation box (as shown in Fig. 1). The weight

Fig. 1 Schematic diagram of **a** rectangular h-BN, **b** triangular h-BN, **c** rectangular h-BN in PE matrix, **d** triangular h-BN in PE matrix and **e** stacked combination of rectangular BNNS



percentage of both rectangular and triangular BNNS was controlled very close to 3wt. % of neat PE, whereas in case of stacked rectangular BNNS, three layers of BNNS are stacked together with the interlaminar distance of 3.33 Å at the middle position of the simulation.

The simulation was performed at 100 K for all configurations. For relaxation of PE chains and BNNS, system is equilibrated with NVE ensembles at 500 K along with the langvin thermostat. In the very next phase of the simulation, whole system is relaxed for 40 ps with NPT ensembles later on it cools down to 100 K using NPT ensembles. In the last stage of the simulation, the system is relaxed at 100 K for 25 ps using NPT ensembles.

In-plane mechanical properties of the BNNS are much higher than that of PE matrix; therefore, in this present study, BNNS is assumed as a rigid body in the PE matrix. The BNNS is pulled out from the PE matrix with a velocity of 0.01 Å/fs. The maximum interfacial shear stress observed by the BNNS can be calculated by Eq. (2)

$$\tau_{xy-\max} = \frac{F_{x-\max}}{2A}. \quad (2)$$

where A is the in-plane surface area of rectangular and triangular BNNS, and $F_{x-\max}$ is the maximum force on BNNS during the pull-out. Periodic boundary conditions were kept in two principal directions only, while the third direction (non-periodic) was utilized for pulling direction of BNNS from PE matrix (refer Fig. 2). Both morphologies of the BNNS were pulled in a non-periodic direction, and maximum shear strength was calculated.

3 Results and Discussion

Validating the force field pair potential parameter and developed model the authors have performed the simulation of uniaxial tensile testing of pure PE and h-BN/PE nanocomposites. The stress–strain output of the pure PE, pristine BNNS and h-BN/PE nanocomposites are in strong agreement with the previous literature [16, 25–27]. Interfacial shear strength of all combination of h-BN/PE systems is calculated and discussed in two sections.

3.1 *Effect of Different Morphology on Interfacial Shear Strength of h-BN/PE Nanocomposites*

In the first section, authors have performed the simulation to evaluate the interfacial shear strength of the rectangular and triangular h-BN/PE nanocomposites. The snapshot of pull out is shown in Fig. 2.

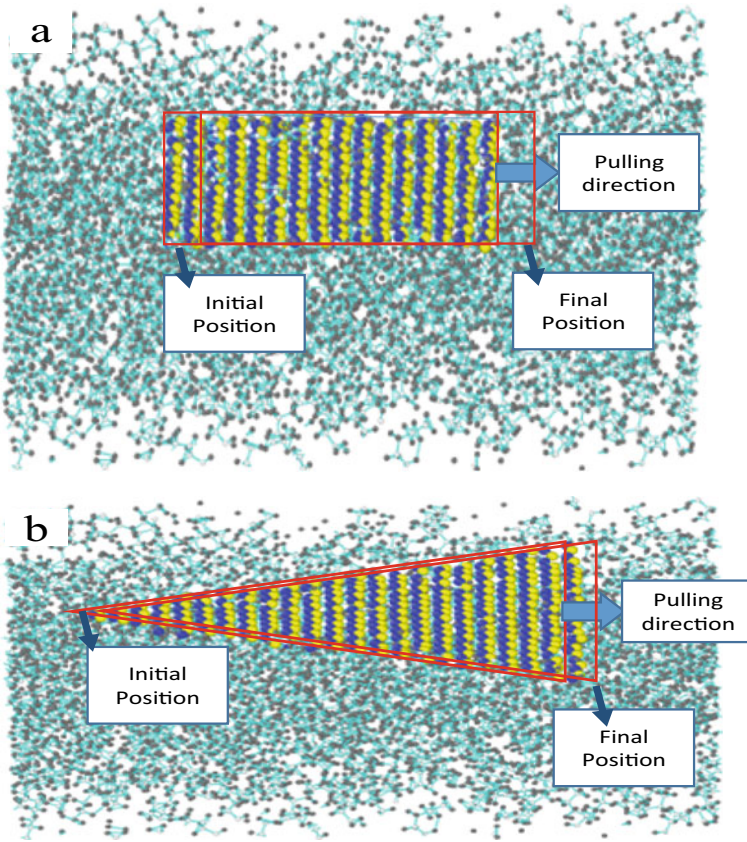


Fig. 2 Snapshot of pull out **a** rectangular BNNS and **b** triangular BNNS

It can be observed from Fig. 3 that interfacial shear strength of the rectangular h-BN/PE systems (348.58 MPa) is higher than that of triangular h-BN/PE system (310.65 MPa). The interfacial shear strength of all systems is tabulated in Table 2.

The interaction energy of rectangular BNNS (238 kcal/mol) is higher than that of triangular BNNS (230 kcal/mol) due to the larger surface area of rectangular BNNS. In addition to this, higher interaction energy between matrix and reinforcement leads to better interfacial strength and load transfer capability. This results in higher interfacial strength of rectangular h-BN/PE system.

Fig. 3 Interfacial shear stress of rectangular and triangular BNNS

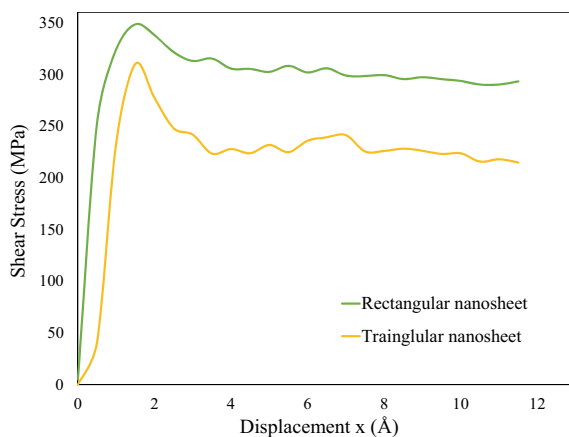


Table 2 Interfacial shear strength of the rectangular, triangular and stacked combination of h-BN/PE system

S. No.	Regular	Interfacial shear strength (MPa)
1	Rectangular h-BN/PE system	348.58
2	Triangular h-BN/PE system	310.65
3	Stacked rectangular h-BN/PE system	313.67

3.2 Effect of Stacked Rectangular BNNS on Interfacial Shear Strength of h-BN/PE Nanocomposites

In the second section, the authors have discussed the interfacial strength of the stacked rectangular h-BN/PE system. In nature, BNNS is naturally stacked to each other due to their high surface energy. They stick together due to weak van der Waal and electrostatic forces. Therefore, authors have also predicted the interfacial shear strength of the stacked rectangular h-BN/PE nanocomposites.

It can be deduced from Fig. 4, interfacial shear strength of stacked rectangular h-BN/PE system is lower (313.67 MPa) than that of a single rectangular h-BN/PE system. In the case of a stacked combination of rectangular BNNS, one surface of BNNS is exposed to PE matrix while other surface exposed to the other BNNS (as shown in Fig. 5). This phenomenon reduces the interfacial interaction between BNNS and PE matrix, therefore lowering interfacial shear strength.

Fig. 4 Interfacial shear strength of stacked rectangular BNNS with top and middle layer pull out

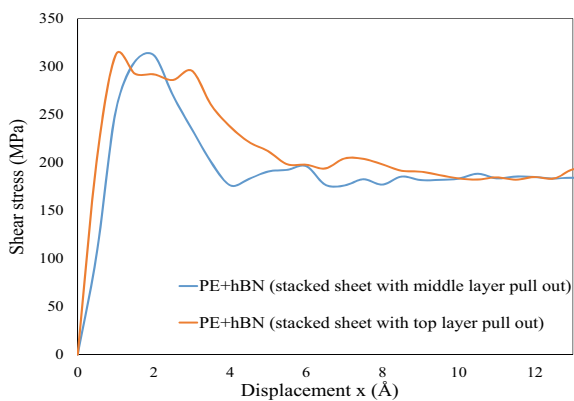
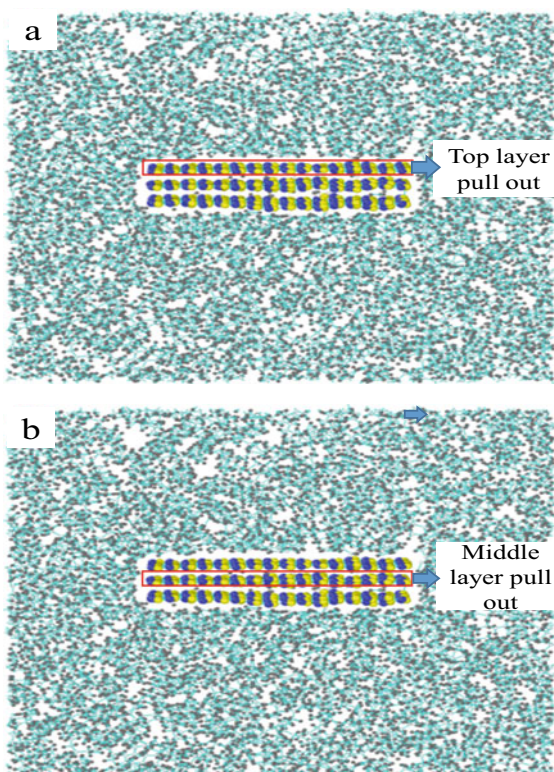


Fig. 5 Interfacial shear strength of stacked rectangular BNNS with top and middle layer pull out



4 Conclusion

In this present study, reaction force field potential is used and validated with the previous literature. It was observed that interfacial shear strength significantly depends on the morphology of BNNS. Interfacial shear strength of rectangular h-BN/PE system is higher than triangular h-BN/PE system. However, interfacial shear strength of stacked rectangular h-BN/PE system is lower than the single rectangular h-BN/PE system.

References

1. Sharma SS, Sharma BB, Parashar A (2019) Defect formation dynamics in dry and water submerged graphene nanosheets. *Mater Res Express* 6:075063
2. Sharma BB, Parashar A (2019) Atomistic simulations to study the effect of water molecules on the mechanical behavior of functionalized and non-functionalized boron nitride nanosheets. *Comput Mater Sci* 169:109092
3. Sharma SS, Sharma BB, Parashar A (2019) Mechanical and fracture behavior of water submerged graphene. *J Appl Phys* 125:215107
4. Sharma BB, Parashar A (2020) Review on thermo-mechanical properties of bi-crystalline and polycrystalline 2D nanomaterials. *Crit Rev Solid State Mater Sci* 45:134–170
5. Kumar R, Parashar A (2018) Effect of geometrical defects and functionalization on the interfacial strength of h-BN/polyethylene based nanocomposite. *Polymer* 146:82–90
6. Chaurasia A, Verma A, Parashar A, Mulik RS (2019) Experimental and Computational Studies to Analyze the Effect of h-BN Nanosheets on Mechanical Behavior of h-BN/Polyethylene Nanocomposites. *J Phys Chem C* 123:20059–20070
7. Yu C, Zhang J, Tian W, Fan X, Yao Y (2018) Polymer composites based on hexagonal boron nitride and their application in thermally conductive composites. *RSC Adv* 8(39):21948–21967
8. Nasrabadi AT, Foroutan M (2010) Interactions between polymers and single-walled boron nitride nanotubes: a molecular dynamics simulation approach. *J Phys Chem B* 114(47):15429–15436
9. Yuan Z, Lu Z, Yang Z, Sun J, Xie F (2016) A criterion for the normal properties of graphene/polymer interface. *Comput Mater Sci* 120:13–20
10. Zaminpayma E (2014) Molecular dynamics simulation of mechanical properties and interaction energy of polythiophene/polyethylene/poly(p-phenylenevinylene) and CNTs composites. *Polym Compos* 35(11):2261–2268
11. Verma PK, Sharma BB, Chaurasia A, Parashar A (2019) Inter-granular fracture toughness of bi-crystalline graphene nanosheets. *Diam Relat Mater* 102:107667
12. Li C, Browning AR, Christensen S, Strachan A (2012) Atomistic simulations on multilayer graphene reinforced epoxy composites. *Compos Part A Appl Sci Manuf* 43(8):1293–1300
13. Liu F, Hu N, Ning H, Liu Y, Li Y, Wu L (2015) Molecular dynamics simulation on interfacial mechanical properties of polymer nanocomposites with wrinkled graphene. *Comput Mater Sci* 108:160–167
14. Hadden CM, Klimek-Mcdonald DR, Pineda EJ, King JA, Reichanadter AM, Miskioğlu I, Gowtham S, Odegard GM (2015) Mechanical properties of graphene nanoplatelet/carbon fiber/epoxy hybrid composites: Multiscale modeling and experiments. *Carbon N. Y.* 95:100–112
15. Meng J, Tajaddod N, Cranford SW, Minus ML (2015) Polyethylene-assisted exfoliation of hexagonal boron nitride in composite fibers: a combined experimental and computational study. *Macromol Chem Phys* 216(8):847–855

16. Sharma BB, Parashar A (2020) Fracture behaviour of pristine and defective form of water submerged h-BN nanosheets. *J Phys D: Appl Phys* 54:035306
17. Van Duin ACT, Dasgupta S, Lorant F, Goddard WA (2001) ReaxFF: A reactive force field for hydrocarbons. *J Phys Chem A* 105(41):9396–9409
18. Chaurasia A, Parashar A, Mulik RS (2020) Effect of hexagonal boron nitride nanoplatelet on crystal nucleation, mechanical behavior, and thermal stability of high-density polyethylene-based nanocomposites. *Macromol Mater Eng* 305:2000248
19. Senftle TP, Hong S, Islam MM, Kylasa SB, Zheng Y, Shin YK, Junkermeier C, Engel-Herbert R, Janik MJ, Aktulga HM, Verstraelen T, Grama A, Van Duin ACT (2015) The ReaxFF reactive force-field: Development, applications and future directions. *npj Comput Mater* 2(November):2016
20. Sharma BB, Parashar A (2020) Mechanical strength of a nanoporous bicrystalline h-BN nanomembrane in a water submerged state. *Phys Chem Chem Phys* 22:20453–20465
21. Plimpton S (1995) Fast parallel algorithms for short-range molecular dynamics. *J Comput Phys* 117(1):1–19
22. Kumar R, Mertiny P, Parashar A (2016) Effects of different hydrogenation regimes on mechanical properties of h-BN: a reactive force field study. *J Phys Chem C* 120(38):21932–21938
23. Han SS, Kang JK, Lee HM, Van Duin ACT, Goddard WA (2005) Theoretical study on interaction of hydrogen with single-walled boron nitride nanotubes. II. Collision, storage, and adsorption. *J Chem Phys* 123(11)
24. Ahadi Z, Shadman M, Yeganegi S, Asgari F (2012) Hydrogen adsorption capacities of multi-walled boron nitride nanotubes and nanotube arrays: A grand canonical Monte Carlo study. *J Mol Model* 18(7):2981–2991
25. Liao L, Huang C, Meng C (2018) Study on mechanical properties of polyethylene with chain branching in atomic scale by molecular dynamics simulation. *Mol Simul* 44(12):1016–1024
26. Sharma BB, Parashar A (2019) Atomistic simulations to study the effect of grain boundaries and hydrogen functionalization on the fracture toughness of bi-crystalline h-BN nanosheets. *Phys Chem Chem Phys* 21:13116–13125
27. Sharma BB, Parashar A (2020) Mechanical and fracture behaviour of hydroxyl functionalized h-BN nanosheets. *J Mater Sci* 55:3228–3242

Effect of the Material Hardness and Operating Conditions on the Friction and Wear During Lubricated Sliding



Amar Kumar Jain, Manoj Kumar, and Gananath Doulat Thakre

1 Introduction

Friction and wear are two integral parts of the tribological study of any lubricated contact. Wear is a process by which material gradually removed from the surfaces in contact. It is inevitable when the surfaces are in relative motion. Wear in mechanical systems is evaluated using Archard's law. However, wear of materials is a complex phenomenon and is a function of operating parameters, the environment of operation, material hardness, etc. Friction is the resistive force arising due to the resistance offered by the contacting bodies against the motion. Friction has two basic components, i.e. static and kinetic friction. The friction theories in general state that friction is affected by the applied load and the real area of contact. These theories have been in use since the ages and have formed the basis for the designing of the mechanical systems. However, friction in lubricated contacts is a complex function of, material hardness, surface roughness, lubricant film, operating conditions, etc. In a well-designed tribological system, both friction and wear are assumed to be minimal. However, in real-life situations, both friction and wear are of prominence and detrimental to the system life expectancy. Hence, for thorough know-how of tribo-phenomena occurring inside a contact, it is essential to understand the parameters that influence the tribo-performance of the contact. The studies in the area of

A. K. Jain · G. D. Thakre (✉)
CSIR-Indian Institute of Petroleum, Dehradun 248005, India
e-mail: gdthakre@iip.res.in

A. K. Jain
e-mail: amarkumarjain@yahoo.co.in

M. Kumar
Mechanical Engineering Department, DIT University, Dehradun 248009, India
e-mail: kmanoj1947@gmail.com

tribology have revealed that the material hardness, along with the operating parameters has a profound influence on the tribo-performance behaviour of the contact [1].

Hokkirigawa et al. [2] with the help of Scanning Electron Microscope (SEM) reported in-situ wear in single point scratch test. The study revealed that the wear mode changed sequentially from ploughing to wedging and then cutting with an increase in penetration. Furthermore, the extent of wear in cutting enhanced with increase in hardness. Kayaba and Iwabuchi [3] reported that in the case of fretting wear, hardness had a minor influence on wear phenomenon. On the contrary, the oxide produced during the process protected the parent surface from wear damage, but caused wear of opposing surface. Adachi and Hutchings [4] observed that in a micro-scale abrasion test, wear rates are insensitive to test conditions in case of rolling particles and the variation in wear resistance is insignificant with hardness. Fang et al. [5] through a three-body abrasion study revealed co-existence of cutting and plastic deformation wear, and the material hardness influenced it. Ajayi et al. [6] proposed that as heat generation exceeds the heat dissipation, the scuffing wear propagates; otherwise, it gets quenched.

Along with material hardness, wear is also influenced by the load and the distance traversed. The study revealed that the contact wears increased with the load. With the increase of load, the actual area of contact increases, thereby increasing the wear. Sudin et al. [7] studied wear in ABS and ABS composite parts and revealed that the applied load and the run time significantly affected the rate of wear and the contact friction. Wear also gets enhanced with enhancement in the sliding distance. Cozza [8] investigated the influence of sliding distance on the abrasive wear. It was reported that an increase in sliding distance resulted in a transition from grooving abrasion to rolling abrasion. Similarly, Okonkwo et al. [9] studied the influence of sliding speed on adhesive wear. The study revealed that the rate of wear is sensitive to the sliding speeds, specifically at lower speeds, but it becomes insensitive with an increase in sliding speeds.

The research studies undertaken in the area of contact friction reveal that the friction decreases with a decrease in applied load and an increase in sliding speeds [10]. Bhushan and Kulkarni [11] reported that friction coefficient starts to increase at critical load, and it also corresponds to the hardness of the specimen. Recently, Thakre et al. [12] investigated the influence of operating parameters on the performance of micro EHL contact. The study revealed that the lube film thickness and contact friction is not only influenced by the load, speed, temperature, but also by the slide-to-roll ratio and the lubricant rheology. Investigations pertaining to the effect of texture on tribo-performance of the contact have been undertaken by various researchers [13–16]. The studies have revealed that the roughness parameters, along with the small and shallow cavities, significantly reduce the contact friction.

The contact friction and wear in lubricated contact is a complex function of lubricant film thickness, interlayer shearing of lubricating film and the material characteristics and operating conditions. In the study undertaken by Kimura and Sugimura [17], it has been concluded that the fatigue of ridges in the sliding direction results into flake-like wear particles. Moreover, the acids and peroxides present in the lubricant

influence wear of the lubricated contact [18]. Recently the influence of nanoparticles and ionic liquids on the friction and wear behaviour of the lubricated contact was investigated [19, 20].

The literature review reveals that a large number of studies have been undertaken to study the effect of the material hardness and the operating parameters on the performance of dry contacts. However, the studies considering the combined effect of hardness and operating parameters in case of lubricated contacts are very limited. In order to have in-depth information on the dependence of the input design parameters on the tribological studies, it is very much essential to utilize the robust statistical tool to generate a reliable correlation. Hence, the present study attempts, investigating the dependency of the material hardness and the operating parameters on the tribology of lubricated contact using the Taguchi method of experiment design. The study undertaken will be of significant importance to design engineers in designing the engineering components.

2 Experimental

The experimental investigations were performed on a pin-on-roller tribo-tester shown in Fig. 1. The tribo-tester utilizes a cylindrical flat-ended pin in contact with the cylindrical roller. The flat surface of the pin is mated with the cylindrical surface of the roller in such a way that the axis of pin and roller are perpendicular to each other. The pin was loaded by a pneumatic loading system on the top of the pin. The roller is partially submerged into the lubricant reservoir housed at the bottom of the roller. The roller while in motion builds the lubricating film on its surface.

The contact is lubricated with commercial lubricating oil having physico-chemical characteristics as tabulated in Table 1. The pin is lowered on the roller surface, and the load applied. The experiments were carried out on cylindrical flat-end pins of $\Phi 8$ mm and 12 mm length fabricated from materials of different hardness, i.e. spring steel, EN31 and Gun-metal. The contact surface of the pins was mated with a polished EN31 cylinder of $\Phi 50$ mm and 20 mm width. The contact friction in terms of friction force and the friction coefficient is thus continuously monitored. The wear of the contact was measured by weight loss technique at the end of the test.

The tribological performance of a lubricated contact depends on a large number of parameters viz. material parameters, operating conditions, lubrication, etc. Based on the literature review, the cause and effect diagram has been constructed, as shown in Fig. 2. Among the various influencing parameters, the operating conditions and the material hardness has been selected to investigate their influence on the tribo-performance. The experiments were performed as per the L9 Taguchi orthogonal array. The design parameters selected were applied load, test/sliding duration and the material hardness. The contact friction and the wear were selected as the output parameters. The L9 Orthogonal Array for three input design parameters for three levels is given in Table 2.

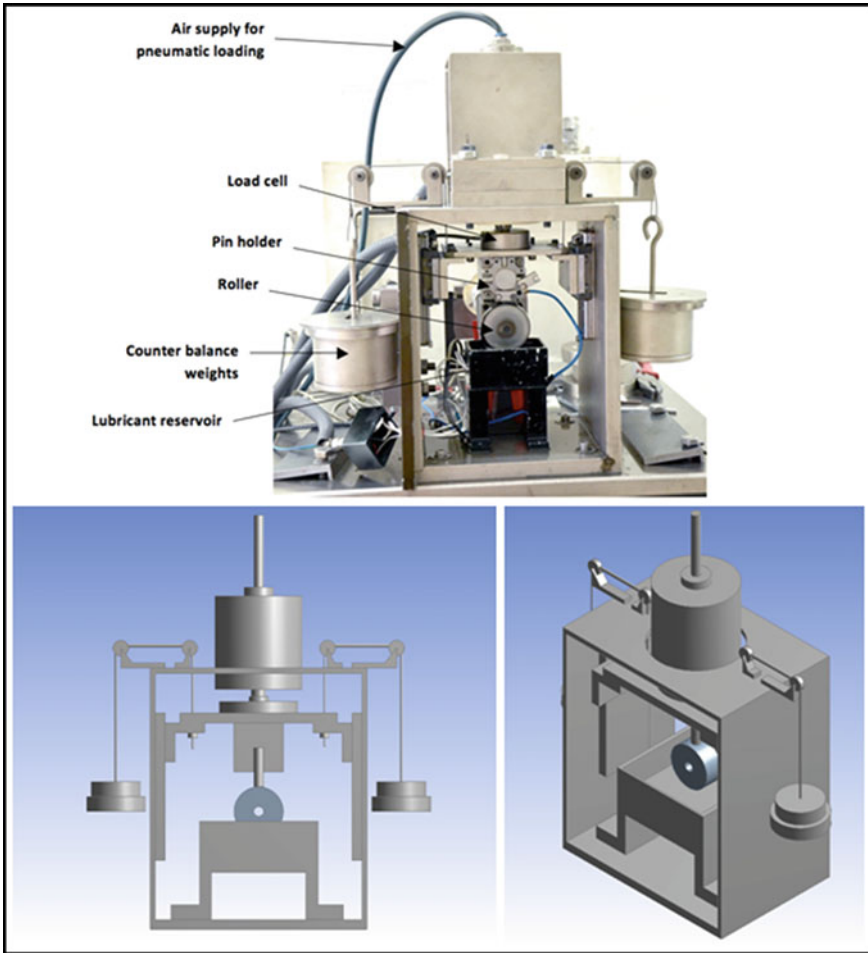


Fig. 1 Pin-on-Roller tribo-tester

Table 1 Lubricant properties

Kinematic viscosity (cSt)		Density @15 °C (kg/l)	Pour point (°C)	Flash point (°C)
@40 °C	@100 °C			
74.4	13.1	0.840	-39	215

The experimental results thus obtained were then subjected to statistical analysis and signal/noise (S/N) ratio determined. The S/N ratio is given by;

$$S/N = -10 \log_{10} \frac{1}{a} \sum_{i=1}^a b^2 \tag{1}$$

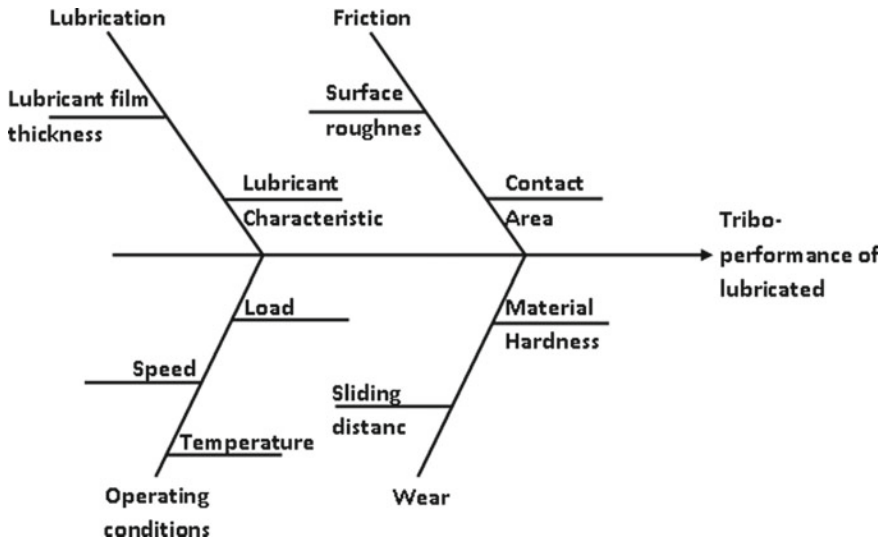


Fig. 2 The cause and effect diagram

Table 2 Experimental design matrix

Experiment No.	Load (N)	Time (min)	Hardness (HRC)
01	100	30	27.96
02	200	60	27.96
03	300	120	27.96
04	100	60	34.29
05	200	120	34.29
06	300	30	34.29
07	100	120	58.59
08	200	30	58.59
09	300	60	58.59

where ‘a’ represents a number of experiments, and ‘b’ is the number of the response value. The ratio is used to optimize the quality characteristics. In the present case, the criterion of smaller the S/N ratio better will be the tribological performance has been considered.

Subsequently, Analysis of Variance (ANOVA) was performed to determine the input factors that significantly influence the performance characteristics. The domain was established for lower values of output parameters in the entire factor space. The data obtained were further analysed using normal probability plots. The regression analysis was performed on experimentally obtained results to establish the quadratic equations for friction and wear prediction. The experiments were designed using Minitab v17 software.

3 Results and Discussion

The contact friction along with wear for different operating conditions as per the Taguchi experimental design is given in Table 3. The results reveal that the coefficient of friction and the weight loss due to wear varies with input design parameters of the experimental design. The contact wear is directly proportional to the applied load and distance travelled.

However, material hardness has a reverse impact on wear. With an increase of load, the actual contact area increases and the lubricant film thickness decreases. Therefore, the metal-to-metal contact increases resulting in an increase in wear. Same is the case with the sliding time. As the contact traverses longer distance with time, the wear of the contact increases with time. However, in the case of hardness, the wear decreases with hardness. As the hardness increases, the material becomes more brittle, and its wear due to adhesive mechanism becomes negligible.

The probability of abrasive wear increases, but due to the presence of lubricant film this chance diminishes. Hence, wear decreases with an increase in hardness. As per the classical theories of friction, the contact friction increases with load and hardness and decrease with sliding distance.

However, the values of S/N ratio can provide a better understanding of the design parameters and friction/wear behaviour of the contact. The values of S/N ratio in graphical form are shown in Fig. 3. Considering the criterion of smaller the better, the parameter setting for lower wear and fiction are H3-L1-T2 and H2-L1-T3, respectively.

The results indicate that by increasing the material hardness, wear gets reduced. A lower load and moderate sliding distance too results in lower wear. In the case of friction, it is observed that moderate material hardness results in lower friction. Friction increases at the higher hardness and also a lower material hardness result in higher friction because of the increase in adhesive forces. The friction decreases with rising in load and sliding distance. As the sliding distance increases, smoothening of asperities takes place, which in turn results in lower friction values.

Table 3 Friction and wear of the contact

Experiment No.	Coeff. of friction	Weight loss due to wear (mg)
01	0.085	0.25
02	0.103	0.25
03	0.069	4.9
04	0.056	21.1
05	0.051	57.2
06	0.111	27.9
07	0.080	0.25
08	0.076	0.1
09	0.072	0.17

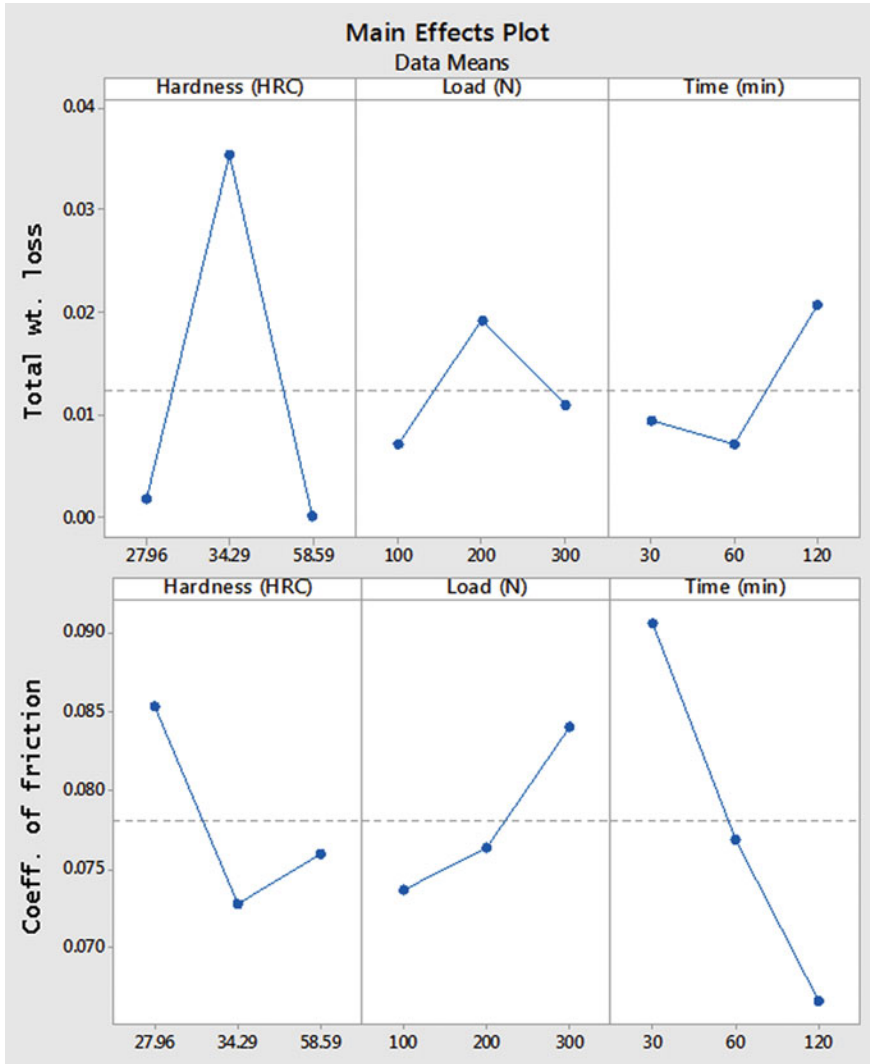


Fig. 3 Main effects plot for wear and friction

Figures 4 and 5 represent the response surface plots for the wear and contact friction over the input parameters. The surface plots confirm the findings observed from the principle effect analysis. The normal probability plots for the residuals and the predicted response of wear and friction are shown in Figs. 6 and 7. When the normal probability plots closely follow the mean line, this represents a good agreement between the experimental findings. Figures present the agreement with those of mean line.

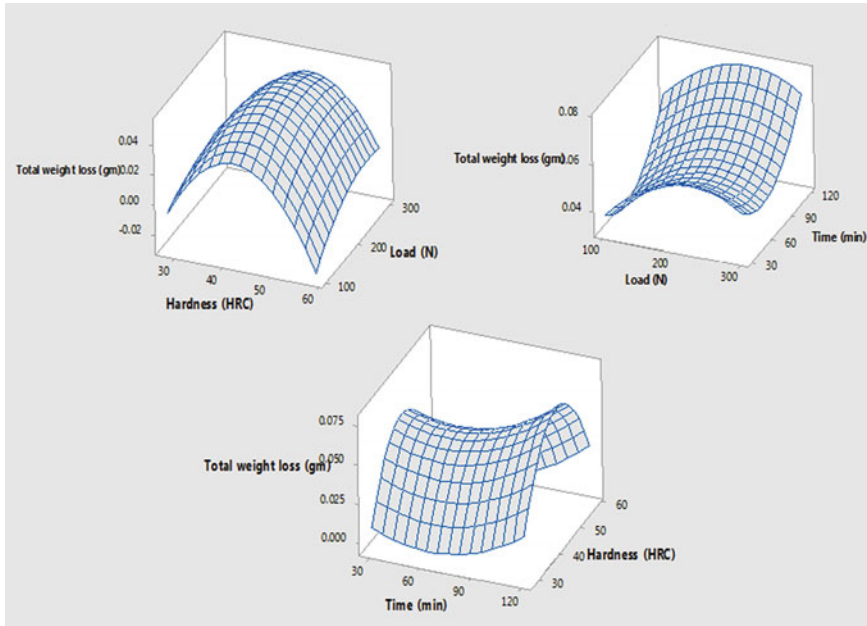


Fig. 4 Response surfaces for wear behaviour versus input parameters

Subsequently, with the use of regression analysis quadratic equations for the contact friction and wear with input parameters as variables have been determined. The regression equations thus obtained are;

$$\begin{aligned} \mu = & 0.1708 - 0.006570H + 0.000956W - 0.001309t \\ & + 0.000069H^2 - 0.000001W^2 - 0.000002t^2 - 0.000009H*W \\ & + 0.000030H*t \end{aligned} \tag{2}$$

$$\begin{aligned} \text{Wt.loss} = & -0.03245 + 0.01734H + 0.000276W - 0.001063t \\ & - 0.000221H^2 - 0.000001W^2 + 0.000007t^2 - 0.000007H*W \\ & + 0.000006H * t \end{aligned} \tag{3}$$

In the above equations, H = hardness of the material in HRC, t = time in minutes and W = load in Newton.

A comparative assessment of the results obtained from the experiments and those obtained from the regression equation is shown in Fig. 8. The comparison reveals that the developed equation can predict the tribo-performance of lubricated point contact efficiently.

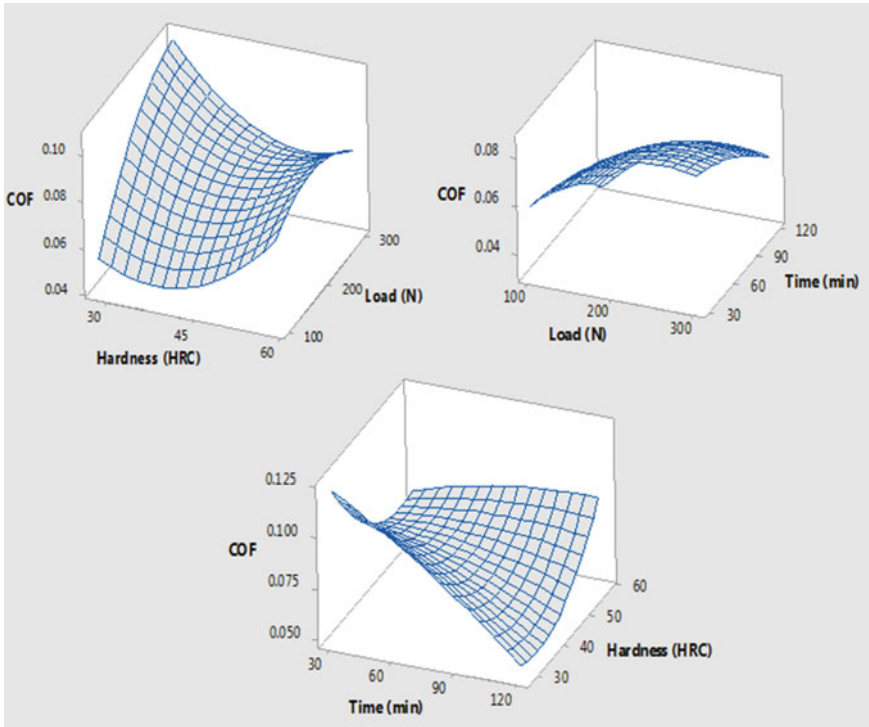


Fig. 5 Response surfaces for friction behaviour versus input parameters

4 Conclusions

An experiment-based study utilizing the concept of Taguchi design of experiments has been performed to study the influence of operating and material parameters on tribo-performance behaviour of the lubricated contact in sliding. Concerning the study undertaken following salient conclusions have been made;

- The contact wear is influenced by applied load, distance traversed and the material hardness. Wear decreases with an increase in hardness. Lower wear can be observed at lower loads and moderate sliding distances.
- A lower value of contact friction is obtained at lower loads and higher sliding distances. However, in order to have lower friction, the material hardness has to be moderate.
- The empirical relations for the contact wear and friction with applied load, sliding distance and material hardness as input variables have been presented. The empirical relations can provide useful information on the contact friction wear for the considered design parameters.

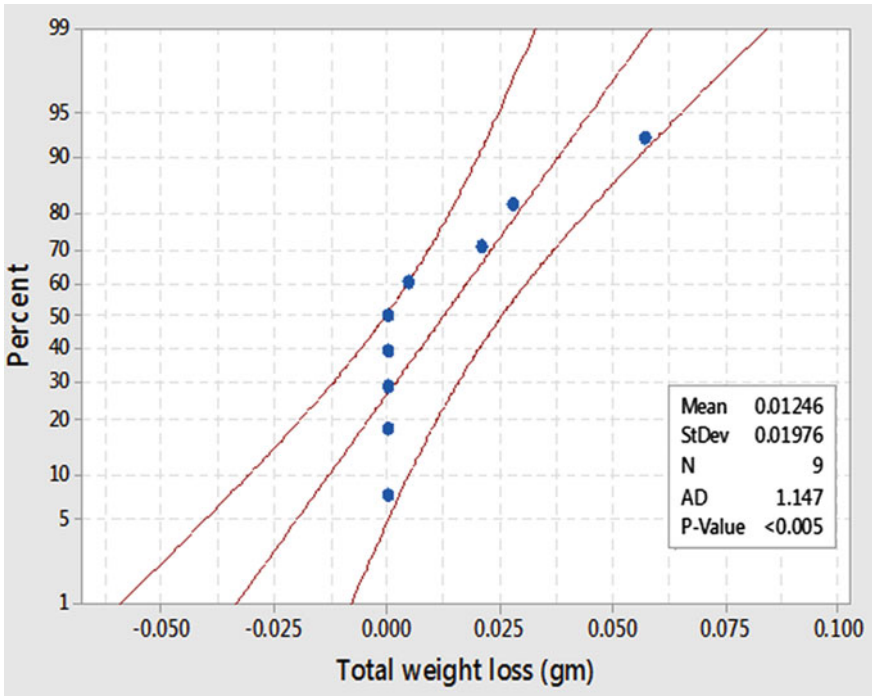


Fig. 6 Normal probability plot for wear response of the contact

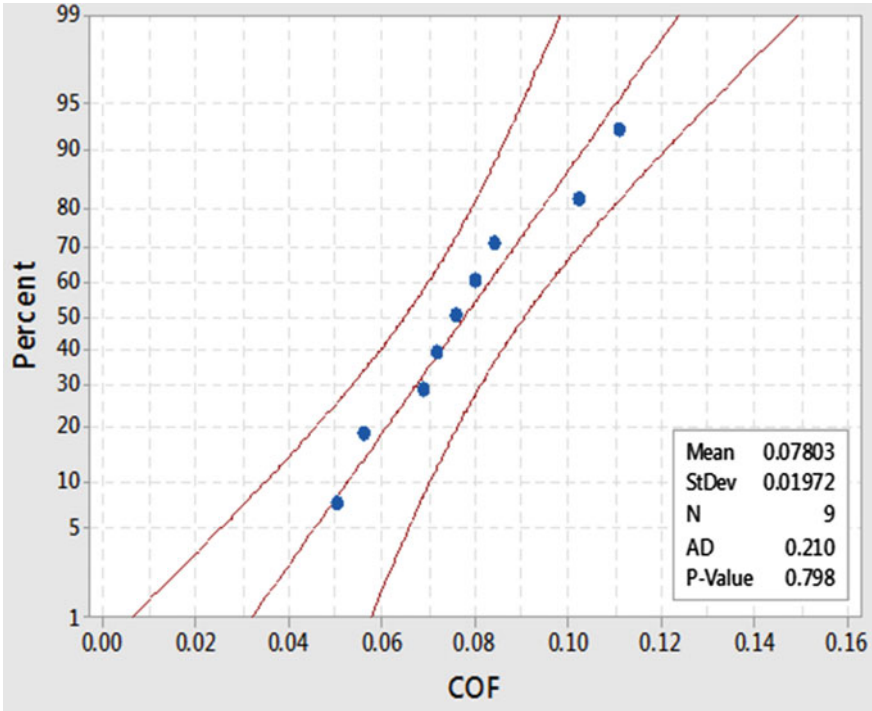


Fig. 7 Normal probability plot for friction response of the contact

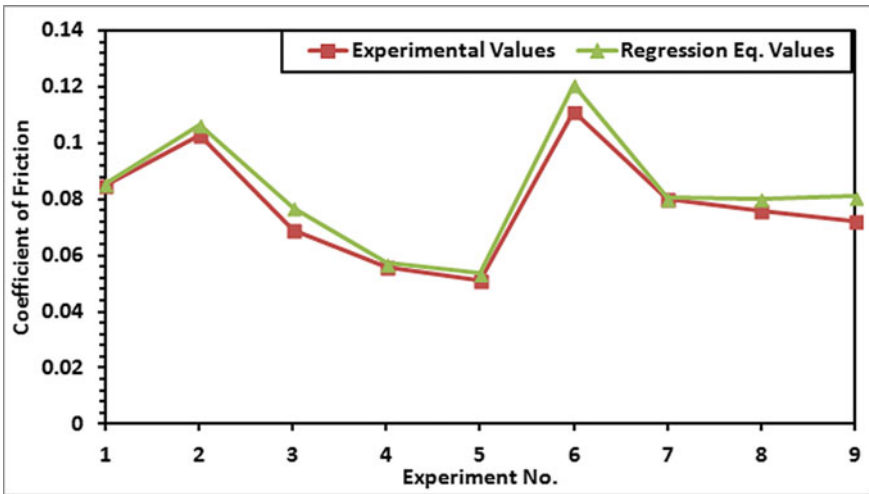


Fig. 8 Comparative assessment of experimental and regression values

Acknowledgements The authors thank Director, CSIR-Indian Institute of Petroleum, Dehradun, India for the financial support to carry out the experimental work and also to publish the findings.

References

1. Stachowiak G, Batchelor AW (2013) Engineering tribology. Butterworth-Heinemann
2. Hokkirigawa K, Kato K, Li ZZ (1988) The effect of hardness on the transition of the abrasive wear mechanism of steels. *Wear* 123(2):241–251
3. Kayaba T, Iwabuchi A (1981) Effect of the hardness of hardened steels and the action of oxides on fretting wear. *Wear* 66(1):27–41
4. Adachi K, Hutchings IM (2005) Sensitivity of wear rates in the micro-scale abrasion test to test conditions and material hardness. *Wear* 258(1–4):318–321
5. Fang L, Zhou QD, Li YJ (1991) An explanation of the relation between wear and material hardness in three-body abrasion. *Wear* 151(2):313–321
6. Ajayi OO, Lorenzo-Martin C, Erck RA, Fenske GR (2011) Scuffing mechanism of near-surface material during lubricated severe sliding contact. *Wear* 271(9–10):1750–1753
7. Sudin MN, Ramli FR, Alkahari MR, Abdullah MA (2015) Comparison of wear behavior of ABS and ABS composite parts fabricated via fused deposition modelling. *Int J Adv Appl Sci* 5(1):164–169
8. Cozza RC (2015) Effect of sliding distance on abrasive wear modes transition. *J Mater Res Technol* 4(2):144–150
9. Okonkwo PC, Kelly G, Rolfe BF, Pereira MP (2016) The effect of sliding speed on the wear of steel–tool steel pairs. *Tribol Int* 97:218–227
10. Kakaš D, Škorić B, Mitrović S, Babić M, Terek P, Miletić A, Vilotić M (2009) Influence of load and sliding speed on friction coefficient of IBAD deposited TiN. *Tribol Ind* 31(3–4):3–10
11. Bhushan B, Kulkarni AV (1996) Effect of normal load on microscale friction measurements. *Thin Solid Films* 278(1–2):49–56
12. Thakre GD, Sharma SC, Harsha SP, Tyagi MR (2015) A parametric investigation on the microelastohydrodynamic lubrication of power-law fluid lubricated line contact. *Proc Inst Mech Eng, Part J: J Eng Tribol* 229(10):1187–1205
13. Sedlaček M, Podgornik B, Vižintin J (2009) Influence of surface preparation on roughness parameters, friction and wear. *Wear* 266(3–4):482–487
14. Chouquet C, Gavillet J, Ducros C, Sanchette F (2010) Effect of DLC surface texturing on friction and wear during lubricated sliding. *Mater Chem Phys* 123(2–3):367–371
15. Tang W, Zhou Y, Zhu H, Yang H (2013) The effect of surface texturing on reducing the friction and wear of steel under lubricated sliding contact. *Appl Surf Sci* 273:199–204
16. Thakre GD, Sharma SC, Harsha SP, Tyagi MR (2016) A theoretical study of ionic liquid lubricated μ -EHL line contacts considering surface texture. *Tribol Int* 94:39–51
17. Kimura Y, Sugimura J (1984) Microgeometry of sliding surfaces and wear particles in lubricated contact. *Wear* 100(1–3):33–45
18. Newley RA, Spikes HA, Macpherson PB (1980) Oxidative wear in lubricated contact. *J Lubr Technol* 102:539–544
19. Sharma V, Timmons R, Erdemir A, Aswath PB (2017) Plasma-functionalized polytetrafluoroethylene nanoparticles for improved wear in lubricated contact. *ACS Appl Mater Interfaces* 9(30):25631–25641
20. Mu Z, Zhou F, Zhang S, Liang Y, Liu W (2005) Effect of the functional groups in ionic liquid molecules on the friction and wear behavior of aluminum alloy in lubricated aluminum-on-steel contact. *Tribol Int* 38(8):725–731

Investigation on Microwave Joining of Mild Steel Plates at 2.45 GHz and Joint Characterization



Gaurav Kumar, Dungali Sreehari, Radha Raman Mishra, Viveksheel Yadav, and Apurbba Kumar Sharma

1 Introduction

Joining is one of the essential processes in assembling of complex and big parts such as ships, aeroplanes, building construction, bridges, etc. It plays an important part in the strength of the big structure because many big structures may fail due to the improper joining. Microwave heating found its origin in the middle of the 1940s after the evolution of Maxwell electromagnetic theory in 1864 [1]. Microwave processing of material uses electromagnetic waves in the frequency ranges of 300 MHz to 300 GHz [2]. In this technique, materials to be processed are exposed to electromagnetic radiation which vibrates the molecules of the material and results in the heat generation inside the material. In microwave heating, the microwave comes directly in contact with the material which causes volumetric heating of the material. Materials processed through microwave have better microstructure than conventional processes. Although the processing of metal with microwave is very much challenging task, many researchers had successfully demonstrated the processing of metals using the microwave. Roy et al. [3] reported sintering of metallic material in 1999. After that, various works had been reported on joining of metals through microwave in 2009. Sharma et al. [4] successfully joined bulk metallic material using a domestic microwave oven in 2009. Srinath et al. [5] carried out the joining of copper plates using microwave radiation. The results revealed that the joint interface has 78

G. Kumar (✉) · D. Sreehari · V. Yadav

Department of Mechanical Engineering, National Institute of Technology, Uttarakhand, Srinagar (Garhwal) 246174, India

e-mail: grv.kmr2015@gmail.com

R. R. Mishra · A. K. Sharma

Design Innovation Center, Indian Institute of Technology Roorkee, Roorkee 247667, India

A. K. Sharma

Department of Mechanical and Industrial Engineering, Indian Institute of Technology Roorkee, Roorkee 247667, India

Hv of hardness which is higher than the base material. Joining of steel plates using microwave has been reported. The results indicated that the joint strength is much higher than the base material hardness [6]. The tensile strength at the joint interface was 425 MPa, with an average elongation of 9.44% [7]. Singh et al. carried out the joining of aluminium metal plates through microwave radiation. The results showed that the joint strength at the joint interface was 72.4 Hv [8]. Gamit et al. successfully joined mild steel pipes using microwave energy. The result revealed that the joint efficiency was mainly depending on the exposure time [9]. Srinath et al. successfully joined two different metals using nickel powders as an interfacing material between two dissimilar metal plates. The microhardness of 133 Hv and porosity of 0.58% was reported during mechanical characterization [10]. Bajpai et al. evaluated the joining strength of natural fibre joined by microwave heating. The results revealed that microwave processing provides better joint strength [11]. Bansal et al. investigated the joining of Inconel 718 using nickel powder as an interfacing layer between them. Tensile strength of 400 MPa with a percentage elongation of 6% at the joint was reported [12]. Ahmed and Siores investigated microwave heating of alumina–zirconia–silica ceramics. The results showed improved strength of joint specimen as compared to base material [13].

Therefore, it is found from the literature review that the electromagnetic energy can be utilized for high-temperature applications such as joining of ceramics and metals. The objective of the present work is to join mild steel plates using microwave and simulate the joining process through COMSOL Multiphysics 5.2. The study on microstructure analysis of the joint has been done using EDS and FESEM test.

2 Materials and Method

Mild steel is commonly used in an industrial and commercial application such as in making engineering equipments, automobile industries, building construction and various home appliances. It is also called ‘low carbon steel’ (0.05–0.25% carbon). It has ductile property and is not easily tempered, but possesses high strength. Commercially available mild steel plates of $34 \times 12 \times 4 \text{ mm}^3$ (L \times W \times D) were used in present work. The optical image of as-received the mild steel plate has been shown in Fig. 1. The chemical composition of mild steel is shown in Table 1. The EDS analysis (Table 1) of mild steel base material shows 96% iron with 1.96% cobalt, 0.69% chromium and 0.25% carbon in it. Figure 1b shows the SEM image of the SiC particles.

Microwave joining uses a hybrid heating technique for the developing joint in which a susceptor material (SiC) is used for heating metallic powder initially as metals reflect the electromagnetic waves at room temperature. When metallic powder reaches its elevated temperature, it starts absorbing the microwave radiation and melting of metal powder starts. As the metal reaches its melting point, the joining of metals is performed and left for cooling in air. The schematic and actual diagram of microwave hybrid heating experimental set-up for joining metallic material has

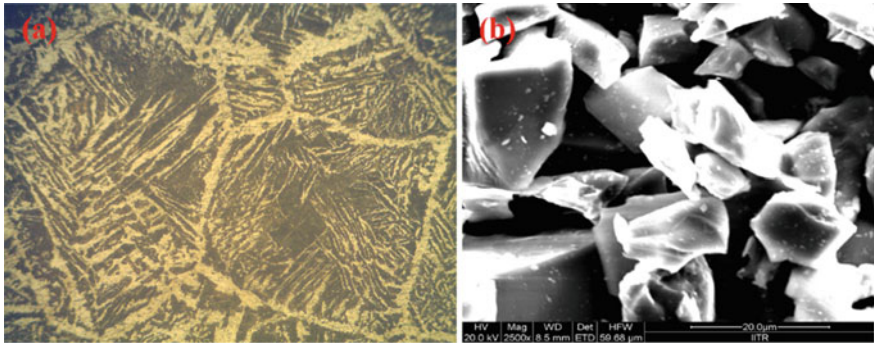


Fig. 1 Optical image of the as-received mild steel plate **b** SEM image of the SiC powder particles

Table 1 Chemical composition (% wt.) of mild steel

Element	C	Fe	Ni	Co	Cr
% wt	0.25	96.0	0.81	1.96	0.69

been shown in Fig. 2a, b. The surface of the plates was cleaned with acetone and sandpaper prior to applying the interface layer. Nickel powder was placed at the interface surface between the two plates, maintaining a fine thickness. After that, separator plate was placed over the surface above the joint zone to avoid contact of nickel powder with susceptor material. Susceptor material was used to avoid direct exposure of metals with a microwave. The specimen is placed into a microwave oven where it was heated under controlled timing and temperature mode. The experiments are carried out in atmospheric conditions. The experiment is performed at constant input power and a frequency of 2.45 GHz inside a domestic microwave oven. The experimental process parameters of microwave hybrid heating are given in Table 2.

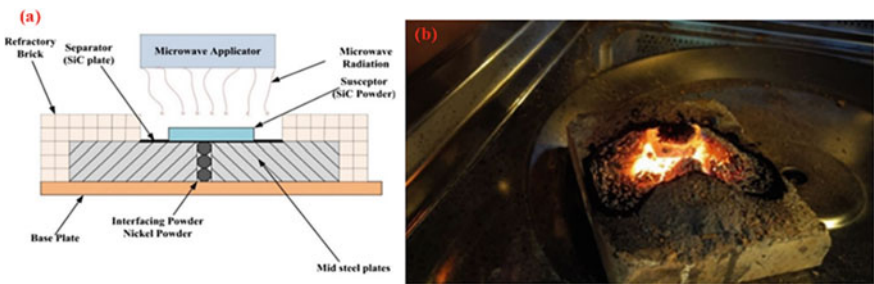


Fig. 2 **a** Schematic diagram of microwave joining of metals; **b** Actual experimental set-up of microwave hybrid heating of metals

Table 2 Process parameters for microwave hybrid heating of materials

Parameter	Statement
Power	900 W
Exposure time	8 min, 10 min
Susceptor material	Charcoal, SiC powder
Interfacing powder	Nickel powder
Separator	SiC plate
Work piece	Mild steel

3 Modelling and Simulation

This section illustrates the simulation of microwave joining of mild steel plates. A 3D model of microwave cavity having dimension $530 \times 315 \times 520 \text{ mm}^3$ ($W \times H \times D$) was created as shown in Fig. 3a. A rectangular waveguide having dimension $70 \times 98 \times 28 \text{ mm}^3$ ($W \times H \times D$) and operating in a transverse electric TE_{10} mode was created on the right side of the cavity. The mild steel plates were placed at the centre, and nickel powder was placed in between the plates as an interfacing material. Susceptor material (silicon carbide powder) has been assumed as a metallic plate of dimension $12 \times 3 \times 0.2 \text{ mm}^3$ ($W \times D \times H$). Physics controlled meshing was used to mesh the microwave cavity and the joint area (Fig. 3b, c). Table 3 shows the details of the mesh.

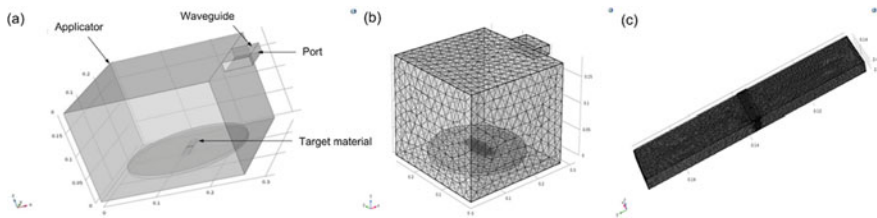


Fig. 3 a 3D geometry of microwave heating of metals b Image showing meshing of the whole domain c Image showing fine meshing of the workpiece

Table 3 Mesh detail

S. No	Elements detail	No. of elements
1	Tetrahedral elements	407,590
2	Triangular elements	26,250
3	Edge elements	1204
4	Vertex elements	48
5	Element volume ratio	$1.572e-7$
6	Mesh volume	0.01362 m^3
7	Maximum growth rate	5.66
8	Average growth rate	2.035

The geometry is solved by applying various boundary conditions in the domain. Transverse electric waves are generated through a rectangular port. The electric field distribution inside a microwave cabin is determined by Maxwell's equation [14]:

$$\nabla \times \left(\frac{1}{\mu} \nabla \times \vec{E} \right) - \frac{\omega^2}{C} (\varepsilon' - i\varepsilon'') \vec{E} = 0 \quad (1)$$

where \vec{E} is an electric field, ε' is dielectric constant, ε'' is the dielectric loss or imaginary part of relative permittivity, ω is angular wave frequency, μ' is relative permeability and c is the light speed.

The dissipated power per unit volume is calculated using

$$P(r) = -\text{Re}(\nabla \cdot S) = \frac{1}{2} \omega \varepsilon_0 \varepsilon'' |E|^2 \quad (2)$$

Transient temperature profile at the joint interface exposed to electromagnetic energy is obtained by the heat conduction equation:

$$\rho c_p \frac{\partial T}{\partial t} - \nabla \cdot (k \nabla T) + p(r) \quad (3)$$

where ρ is the material density, c_p is specific heat capacity, and k is a thermal conductivity of the given material.

4 Results and Discussion

This section includes various results obtained from simulation and characterization study obtained from FESEM and EDS of the joint zone of mild steel.

4.1 Electric Filed Distribution

Figure 4a shows the distribution of the electric field inside the microwave oven cavity. The results show the various hot spot region inside the cavity where the electric field is maximum. A maximum electric field of 4×10^4 V/m was obtained (Fig. 4a). The joining experimental set-up was placed at the hot spot obtained (Fig. 4b) using simulation inside the microwave oven during experimentation.

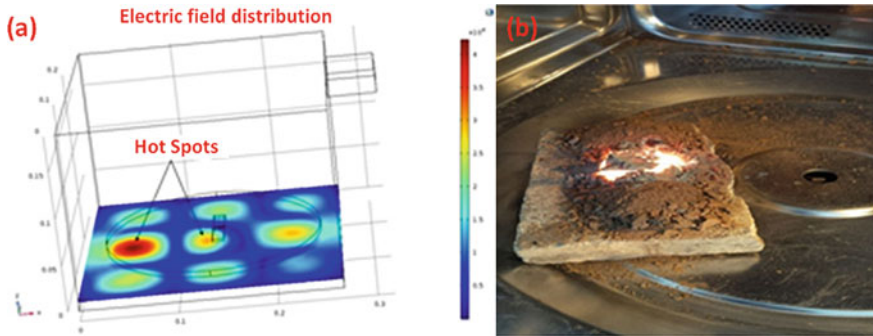


Fig. 4 a Electric field distributions inside microwave oven b Image of the joining experimental set-up placed at the position of maximum electric field strength inside the microwave oven

4.2 Temperature Distribution

Figure 5 shows the distribution of temperature over the mild steel plate during microwave joining. It is observed that the maximum temperature above $1400\text{ }^{\circ}\text{C}$ was obtained at joint zone after exposing the specimen for 600 s inside a microwave oven. Figure 6 shows the optical image of a mild steel plate joined using microwave energy. During experimentation, the joint was exposed to microwave radiation for different periods. The sample exposed to microwave radiation for 8 min got separated in two pieces during sample preparation due to improper fusion of nickel powder with mild steel in the joint zone, as shown in Fig. 6b. Thus, it implies that the sample

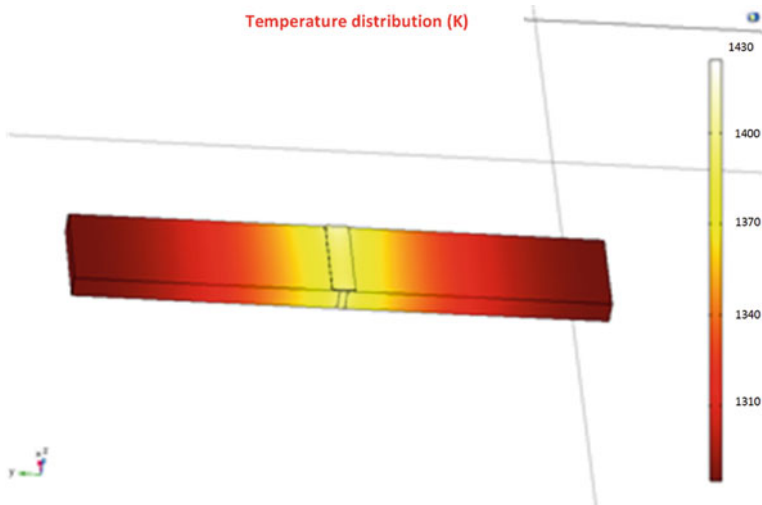


Fig. 5 Temperature distribution over mild steel joint specimen

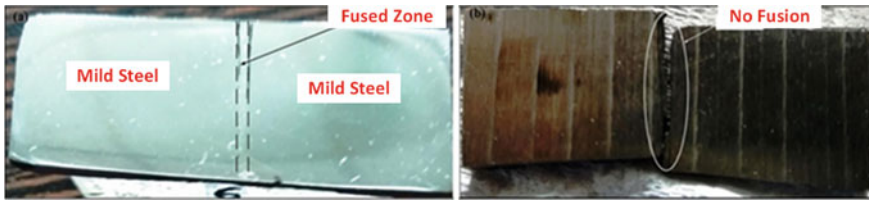


Fig. 6 Optical image showing **a** complete fusion along the joint zone of mild steel plate specimen at 10 min **b** improper joining along the joint zone of mild steel plate specimen at 8 min

should be exposed for a certain minimum time duration which is essential for the complete melting of nickel powder and its subsequent fusion with the adjacent base metal of the sample to be joined. Thus, the sample was exposed for 10 min. At this time duration, a successful butt joint between two mild steel plates having sufficient strength was developed as shown in Fig. 6a. The successful joining of the mild steel plates has been validated with characterization techniques, as discussed in the subsequent section.

4.3 Microstructural Investigation of Joints

Figure 7 shows the optical and microscopic image of the developed mild steel joint. The developed joint shows complete melting and fusion of nickel powder with the adjacent surface of the base metal. The wavy interface at the joint interface (Fig. 7c) shows that the nickel powder is completely fused with the base material. It is evident from Fig. 8 that porosity and various phases like carbide, oxide, etc., are present in the joint zone. The presence of porosity in the joint zone can be attributed to the presence of air during the start of the experimentation as the pressure inside the cavity is similar to atmospheric pressure. However, as the heating of the powder in the joint zone takes place, the entrapped air comes out from the joint zone leaving behind a pinhole porosity which can be seen from the SEM images as shown in Fig. 8.

The porosities present in the joint zone, as shown in Fig. 8, are having sharp edges, and the shape is not circular. The electric field strength is very high around the sharp corners of the porosity, which produces microplasma around the corners; thus, a high temperature. Due to high temperature, the diffusion of the nickel powder takes place to a greater distance in the mild steel plate around the joint interface. It is clear from Fig. 8 that the concentration of iron is about 75% and the concentration of nickel is about 24%, and the rest is other metals. The presence of nickel indicates its complete fusion with the adjacent surface of mild steel. This indicates the successful joining of mild steel plates. EDS also shows the presence of Cobalt in few amounts in the joint zone, which was present in base metal as evident from Fig. 8. Figure 8 shows the EDS analysis of the white phase (Spot 1) present in the joint zone. The results show the presence of iron, nickel and oxygen (14.39%). The presence of oxygen in

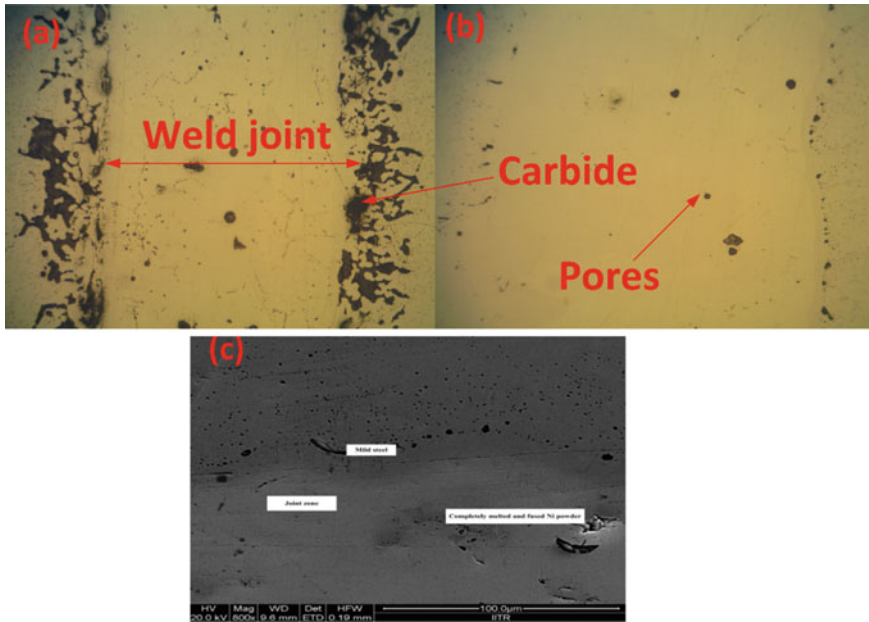


Fig. 7 Optical and SEM image of mild steel joint

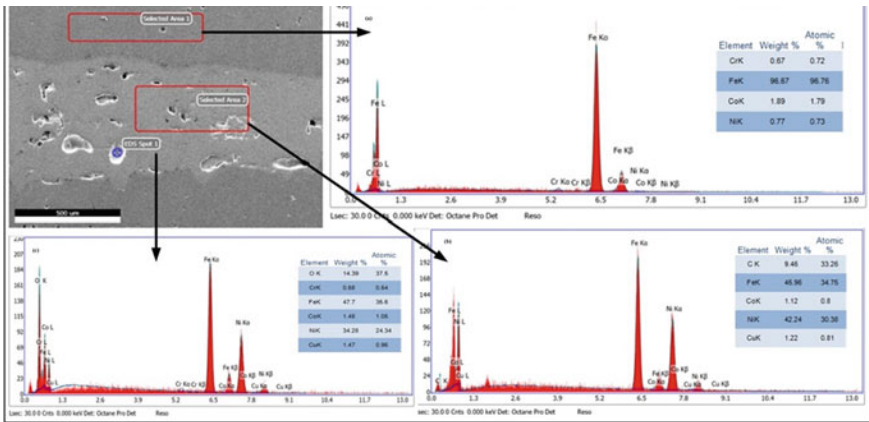


Fig. 8 EDS spectra of region a Selected area 1 b Selected area 2 c EDS spot 1 near joint zone

large amount is due to the oxide formation. The reason behind the oxide formation in that region is the oxygen present in air entrapped between the nickel powders, which were placed in the joint zone. The air entrapped between the nickel powder escapes at high temperature, and oxygen at high temperature reacts with iron to form oxides like Fe_2O_3 . These oxides help in microwave heating which can be validated from

the diffusion of nickel to a greater distance along the joint zone, as shown in Fig. 8. Further EDS analysis of spot 1 and selected area 2 shows the presence of iron in a very large amount (~46%). This confirms that the temperature around the joint zone is 1400 °C which has been shown in Fig. 5. Further, molten part of the edge of the specimen to be joined diffuses in the Ni reach the region to form a strong joint. EDS result of the selected area 2 shows the presence of carbon besides iron and nickel. This is due to the formation of carbide, shown as a black phase in the selected area 2. The carbon present in the separator plate made up of silicon carbide reacts with iron at high temperature to form hard carbide phases like Fe_2C_3 . These carbide phases are very good absorber of the microwave, which increases the temperature around the region of these phases. High temperature around the carbide phase present in the joint zone enhances the diffusion rate, which is evident from Ni present inside a mild steel base plate, as shown in the EDS of selected area 1. Besides it, these phases increase the hardness of the joint zone ($405 \pm 12 \text{ Hv}$) as compared to the hardness of base metal ($211 \pm 12 \text{ Hv}$).

5 Conclusions

Microwave joining of mild steel plates at an input power of 900 W has been successfully demonstrated using experimental and simulation study. However, the efficiency of joint developed using microwave energy decreases as the thickness of the sample to be joined increases. Besides it, contamination of the joint zone due to the use of susceptor material seems to be a major drawback of this process as diffusion of carbon in the joint zone decreases the ductility of joint. Based on the above study, it has been found that:

- The joining of mild steel using nickel as an interface powder was successfully done in domestic microwave applicator through microwave hybrid heating.
- Simulation carried out using COMSOL Multiphysics 5.2 software revealed that electric field plays a more prominent role in microwave heating.
- Simulation helps in identification of hot spot inside the resonating cavity of microwave applicator.
- Nickel powder couples very well with microwave as it was completely melted and fused very well with the surface of the mild steel plate to be joined.
- SEM image and EDS results also revealed that the temperature around the joint zone is above 1400 °C as the iron was present in a very large amount in the Nickel rich region which confirms that the melting of mild steel.
- SEM image shows the presence of porosity, oxides and carbide phase in and around the joint zone, which has been confirmed by energy dispersive X-ray diffraction test.
- Presence of porosity, oxides and carbide phase enhances the microwave heating as these are very good absorber of a microwave.

References

1. Sobol H, Tomiyasu K (2002) Milestones of microwaves. *IEEE Trans Microw Theory Tech* 50(3):594–611
2. Sun J, Wang W, Yue Q (2016) Review on microwave-matter interaction fundamentals and efficient microwave-associated heating strategies. *Materials* 9(4):231
3. Roy R, Agrawal D, Cheng J, Gedevanishvili S (1999) Full sintering of powdered-metal bodies in a microwave field. *Nature* 399(6737):668
4. Sharma AK, Srinath MS, Kumar P (2009) Microwave joining of metallic materials. Indian patent application no. 1994/Del
5. Srinath MS, Sharma AK, Kumar P (2011a) A new approach to joining of bulk copper using microwave energy. *Mater Des* 32(5):2685–2694
6. Bansal A, Sharma AK, Das S (2013) Metallurgical and mechanical characterization of mild steel-mild steel joint formed by microwave hybrid heating process. *Sadhana*. 38(4):679–686
7. Bansal A, Sharma AK, Kumar P, Das S (2014) Characterization of bulk stainless steel joints developed through microwave hybrid heating. *Mater Charact* 91:34–41
8. Singh S, Suri NM, Belokar RM (2015) Characterization of joint developed by fusion of aluminum metal powder through microwave hybrid heating. *Mater Today: Proc* 2(4–5):1340–1346
9. Gamit D, Mishra RR, Sharma AK (2017) Joining of mild steel pipes using microwave hybrid heating at 2.45 GHz and joint characterization. *J Manuf Process* 27:158–168
10. Srinath MS, Sharma AK, Kumar P (2011b) Investigation on microstructural and mechanical properties of microwave processed dissimilar joints. *J Manuf Process* 13(2):141–146
11. Bajpai PK, Singh JM (2012) Joining of natural fiber reinforced composites using microwave energy: experimental and finite element study. *Mater Des* 35:596–602
12. Bansal A, Sharma AK, Kumar P, Das S (2012) Application of electromagnetic energy for joining Inconel 718 plates. *i-Manager's. J Mech Eng* 2(4):18
13. Ahmed A, Siores E (2001) Microwave joining of 48% alumina–32% zirconia–20% silica ceramics. *J Mater Process Technol* 118(1–3):88–94
14. Mishra RR, Sharma AK (2016) Microwave–material interaction phenomena: heating mechanisms, challenges and opportunities in material processing. *Compos a Appl Sci Manuf* 81:78–97

Effects of Tool Pin Profiles on Mechanical Properties of Al/TiB₂ Surface Composite Fabricated by Friction Stir Process



Manoj Kumar Gupta, Brijesh Gangil, Lalit Ranakoti,
Pawan Kumar Rakesh, and Vinay Kumar Patel

1 Introduction

In the current scenario, industries required more durable, lighter and less expensive materials. The broad spectrum of mechanical properties of monolithic material systems is quite challenging [1, 2]. The composite materials have superior mechanical and wear resistance properties than solid material. A combination of improved surface properties and toughness in the interior bulk material is not achievable in monolithic materials [3, 4]. In surface composite, the ceramic particles were reinforced only on the surface of matrix material while properties of the bulk material remain unchanged. The surface composites can be fabricated by various techniques like a high energy laser beam; the laser melts injection, thermal spraying, cast sinter and coating [5, 6]. Mainly the techniques which are implemented to modify the surface of materials are based on the liquid state processing methods which have high processing temperature, where it is challenging to control interfacial reaction between matrix and reinforcement as well as the formation of a specific deleterious

M. K. Gupta (✉) · B. Gangil
Mechanical Engineering Department, H.N.B Garhwal University, Srinagar, Uttarakhand, India
e-mail: gupta_291@rediffmail.com

B. Gangil
e-mail: brijeshgangil@gmail.com

L. Ranakoti · P. K. Rakesh
Mechanical Engineering Department, National Institute of Technology Uttarakhand, Srinagar,
Uttarakhand 246174, India
e-mail: lalit_9000@yahoo.com

P. K. Rakesh
e-mail: pawanrakesh@nituk.ac.in

V. K. Patel
Mechanical Engineering Department, G.B.P.I.E.T, Pauri Garhwal, Uttarakhand, India
e-mail: vinaykrpatel@gmail.com

Table 1 Chemical constituents of Al-1120

Material	Constituents (Wt. %)						
Al 1120	Si	Mg	Ca	Fe	Cu	Mn	Al
	0.18	0.26	0.12	0.43	0.22	0.03	98.76

state. Furthermore, controlling the process parameters is also a difficult task. To overcome these problems, a solid-state processing method, i.e., friction stir process, was recommended for the fabrication of surface composites. In this paper, aluminum surface composites were reinforced by TiB_2 particulate on the surface of Al-1120 alloy plate through the friction stir process using a taper and threaded pin tools. The effects of tool pin and reinforcement on the mechanical properties of surface composites were reported.

2 Materials and Methods

Surface composites consist of matrix and reinforcement materials. The selection of these materials depends upon the compatibility between matrix and reinforcement, fabrication process, the properties required for composites and their applications.

2.1 Matrix and Reinforcement Material

Al-1120 flat of thickness 10 mm was used as a matrix material, and its composition is depicted in Table 1.

The titanium diboride (TiB_2) having a particle size of 325 meshes was used as reinforcement materials. The purity of TiB_2 particles was 99.9%.

2.2 Experimental Setup and Process Parameters

Friction Stir Process setup was prepared on the vertical milling machine as depicted in Fig. 1. The FSP process parameters determine the composite's properties. The major process parameters which are significantly influenced by the properties of the surface composites are identified as rotational tool speed, feed rate, groove size, reinforcing techniques and type of ceramic particles [7]. Several trial experiments were initially conducted to set the process parameters. In the friction stir process, the tool profiles are the most important parameter that controls the material flow. The main function of the tool shoulder is to generate heat and plasticized matrix material, and the tool pin mixes the reinforcement material in the stir zone. The aluminum

Fig. 1 Friction stir process setup



surface composites were fabricated using a pinless, tapered and threaded pin profile FSP tool made of H-13 tool steel. The FSP tool shape and their dimensions are depicted in Fig. 2a-c.

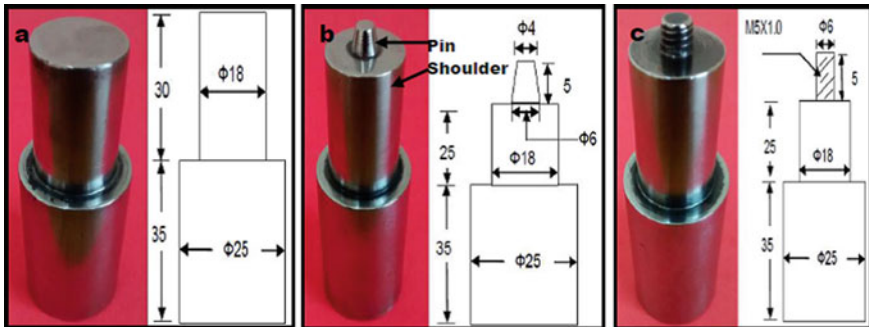


Fig. 2 a Pinless tool, b Taper pin tool, c Threaded pin tool

2.3 Fabrication of Surface Composites

The matrix material aluminum alloys Al-1120 plate was cut into a size of $250 \times 38 \times 10 \text{ mm}^3$ for sample preparation. The grooves of $2 \times 2 \text{ mm}^2$ were cut on the top surface of sample pieces, and TiB_2 was filled in the grooves. The samples were kept on the backing plate and firmly clamped into the machine vice. The FSP tool was mounted in the spindle of the milling machine. Initially, several experiments were conducted to optimize the FSP process parameters for the development of defect-free composites. The rotational tool speed of 1400 rpm and feed rates of 56 mm/min were selected for making composites. The tilt angle of the spindle was set at 2.5° for better cutting and mixing action during the stirring process for all sample preparation. Firstly, FSP was carried out by the pinless tool, as shown in Fig. 3a to pack reinforcement particles effectively in the groove. The second FSP passes were carried out by the taper and threaded pin tool profile, as shown in Fig. 3b, c to disperse reinforcement particles in surface composites.

The stirred zone material was cut for the preparation of testing samples. The hardness of composites was tested at the load of 100 g and dwell time of 30 s using Micro Vickers Hardness Tester (MV1-PC, FIE) having a maximum capacity of 1000 g as shown in Fig. 4a.

The Charpy test was conducted using the impact testing machine, as shown in Fig. 4b to test the impact strength of surface composites. The tensile test was carried out as per the ASTM standard E8/E8M-09 using a computerized universal testing machine (UNITEK 94,100, FIE) as shown in Fig. 5.

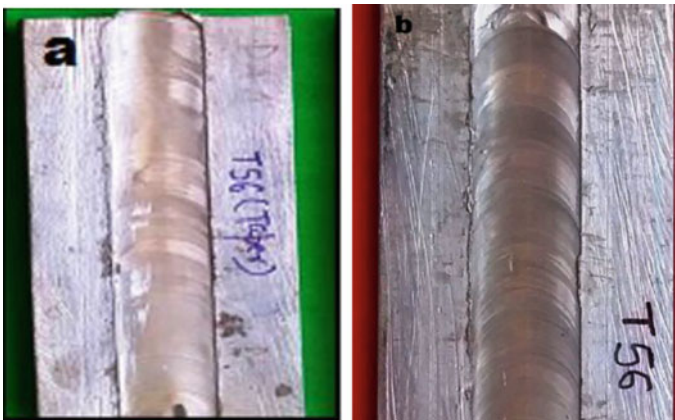


Fig. 3 a Surface composites using, a Taper, b Threaded pin tool



Fig. 4 a Micro Vickers hardness test, b Impact testing machine

Fig. 5 Universal testing machine



3 Results and Discussion

3.1 Microstructure Characterization

The SEM image of the top surface of composites was depicted in Fig. 6. It was observed that the reinforcement particles were uniformly distributed on the matrix surface. The XRD test identified the phase formed in composites. The XRD analysis of TiB_2 reinforced surface composites is shown in Fig. 7. The peaks of reinforcement

Fig. 6 SEM image of TiB_2 reinforced composite

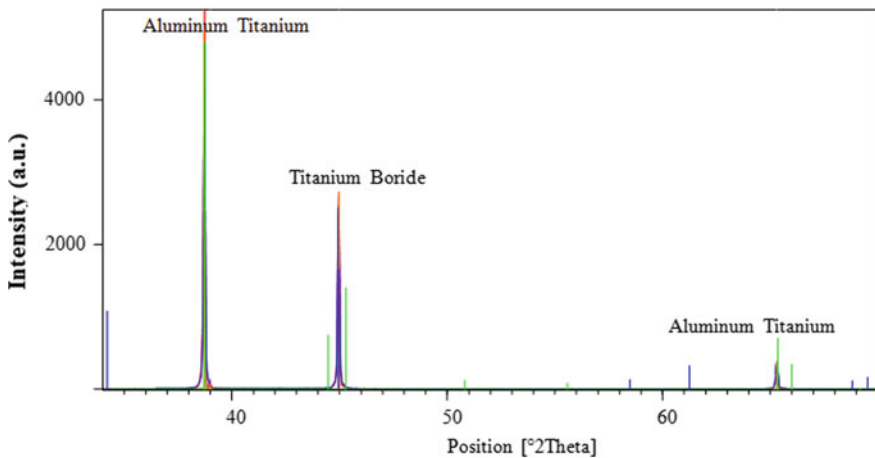
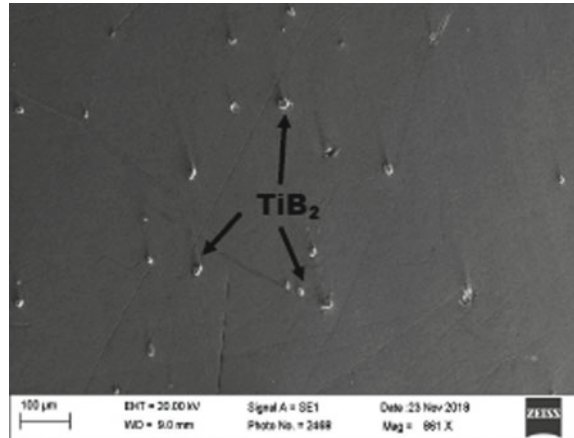


Fig. 7 XRD of TiB_2 reinforced surface composite

element Ti and matrix material elements Al and phases of Al- TiB_2 , which confirmed the presence of reinforcement in the matrix material.

3.2 Tensile Strength Analysis

The tensile strength and percentage elongation of surface composites were evaluated and reported in Table 2. It was observed that the tensile strength surface composites improved due to the presence of hard particles of TiB_2 in the matrix [8–12]. Table 2 shows that surface composite fabricated with threaded pin tool exhibited better tensile strength and percentage elongation as compared to the taper tool. The tensile

Table 2 Tensile strength of surface composites

S. No.	Material	Tensile strength (MPa)	% Elongation
1	Aluminum (Al 1120)	98	27.18
2	TiB ₂ reinforced composite with Taper tool	161	37.17
3	TiB ₂ reinforced composite with Threaded Tool	166	37.86

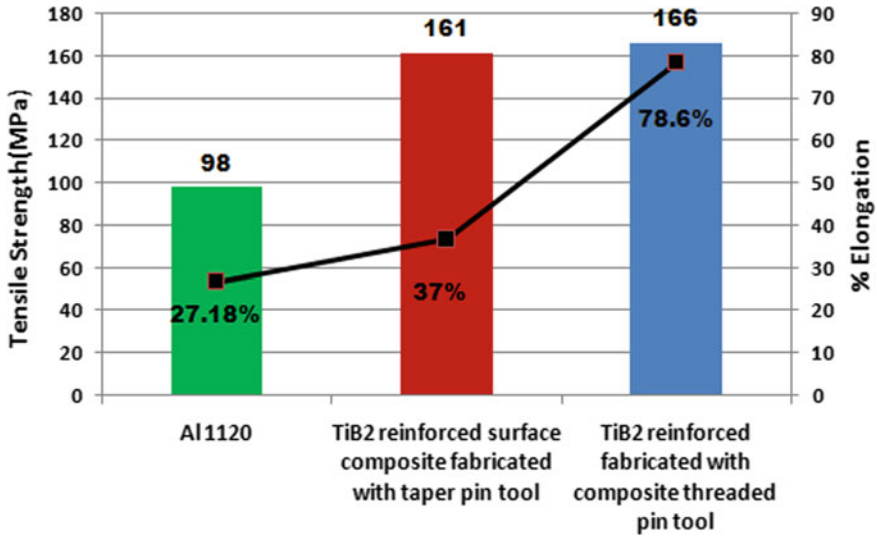


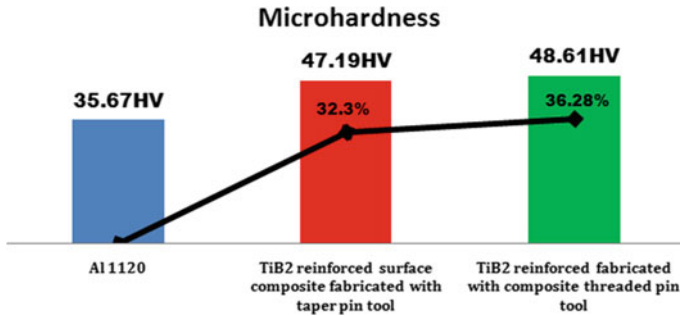
Fig. 8 Tensile strength and percentage elongation of surface composites

strength and percentage elongation of all processed surface composites are depicted in Fig. 8.

The experimental results revealed that TiB₂ reinforced composites processed with a taper pin tool experienced 66.32% higher tensile strength as compared to Al 1120 matrix. However, composite fabricated with threaded pin tool showed 69.38% higher as compared to the matrix material. The composites fabricated with the threaded tool showed 3.06% higher tensile strength as compared to a taper pin profile tool. The percentage elongation of TiB₂ reinforced surface composite fabricated with a taper and threaded pin tool showed 35% and 75% higher elongation as compared to the matrix material. Furthermore, the percentage elongation of TiB₂ reinforced is higher due to the TiB₂ particles are thermally conductive and finer grain size of PNA [13–16]. It was also observed that pin profiles affect the elongation properties of surface composites [17–20]. In a nutshell, composite fabricated with threaded pin tool showed superior tensile and elongation properties as compared to taper pin tool.

Table 3 Microhardness of surface composites

S. No.	Material	Hardness (HV)
1	Al 1120	35.67
2	TiB ₂ reinforced surface composite with a taper pin tool	47.19
3	TiB ₂ reinforced surface composite with a threaded pin tool	48.61

**Fig. 9** Microhardness of composites fabricated with a Taper and Threaded pin tool

3.3 Hardness Analysis

The microhardness test results of all fabricated composites are tabulated in Table 3. It was found that the hardness of composites was extensively improved due to the presence of TiB₂ particles in the matrix material. The microhardness of composites fabricated through a taper pin and threaded pin tool is depicted in Fig. 9. It was also observed that the hardness of surface composites with a taper and threaded pin tool increased by 32.30% and 36.28%, respectively. Furthermore, composites fabricated with the threaded pin showed the highest microhardness, and tensile strength of surface composite increases with the increase of hardness.

3.4 Impact Strength Analysis

The impact strength of matrix material and TiB₂ reinforced surface composites with a taper and threaded pin tool was tested, and results are tabulated in Table 4. The impact strength of TiB₂ reinforced surface composite with taper tool was increased by 15.13%. However, the impact strength of surface composite with threaded pin tool increased by 17.93% as depicted in Fig. 10. The surface composite with threaded pin tool showed as 2.80% higher impact strength as compared to taper pin tool.

The experimental result revealed that the impact of TiB₂ reinforced surface composite substantially improved as compared to the matrix material. The composite

Table 4 Impact strength of composites with a Taper & Threaded pin tool

Materials	Impact strength		Average impact strength	
	Energy (Joule)	Strength (J/cm ²)	Energy (Joule)	Strength (J/cm ²)
Al Alloy 1120 (Matrix material)	28.20	36.40	29.53	36.80
	30.60	38.70		
	29.80	35.20		
TiB ₂ reinforced surface composite with taper tool	38.20	41.20	38.04	42.37
	36.70	43.70		
	39.30	43.30		
TiB ₂ reinforced surface composite with a threaded tool	39.30	42.20	39.13	43.40
	37.50	43.80		
	40.60	44.10		

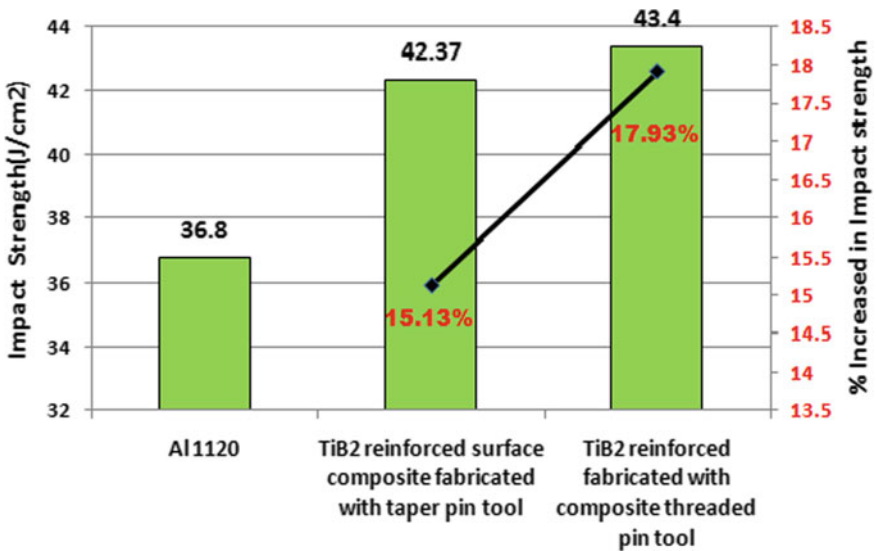


Fig. 10 Impact strength and the percentage increase of impact strength composites

processed with threaded pin exhibited better properties as compared to fabricate with a taper pin tool.

4 Conclusions

The surface composites of Al1120/TiB₂ were fabricated through a friction stir process (FSP) at constant processing machine parameters using a taper and threaded pin profile tools. The effect of reinforcing particle and tool pin geometry on the micro-hardness, impact strength, and tensile strength were investigated. The XRD spectrum of surface composites exhibited the peaks of reinforced particles, which were observed in the presence of matrix material. The SEM images of surface composites confirmed the presence of reinforcement on the surface of the material. The tool shape and size have been recognized that an effective strategy for the improvement of surface properties of surface composites in FSP. The properties of surface composites fabricated with threaded tool showed superior properties as compared to the taper tool. The composites fabricated with the taper and threaded pin tool showed a tensile strength of 66% and 69% higher, respectively as compared to the matrix material. The percentage increase of the micro-hardness of surface composites reinforced with the threaded tool improved by 36.27%. The impact strength of the surface composite was increased by 17.93% as compared to the matrix material.

References

1. Rino JJ, Chandramohan D, Sucitharan KS, Jebin VD (2012) An overview on development of aluminium metal matrix composites with hybrid reinforcement. *IJSR* 23(19):7064–7078
2. Gupta MK (2018) Controlling factors in aluminum matrix composites fabrication. *Anusandhan* 5(15):141–151
3. Sharma V, Prakash U, Manoj Kumar BV (2015) Surface composites by friction stir processing: a review. *J Mater Process Technol* 224:117–134
4. Gupta MK, Rakesh PK (2019) Application of industrial waste in metal matrix composite. *J Polym Compos* 4(3):27–34
5. Hong T, Ngo A, The D, Dinh K, Thi T, Nguyen M (2016) Surface modification of polyamide thin Fi Lm composite membrane by coating of titanium dioxide nanoparticles. *J Sci Adv Mater Devices* 1(4):468–475
6. Nattapat M, Marimuthu S, Kamara AM, Esfahani MRN, Nattapat M, Marimuthu S, Kamara AM, Esfahani MRN (2015) Laser surface modification of carbon fiber reinforced composites laser surface modification of carbon fiber reinforced composites. *Mater Manuf Process* 6914:1450–1456
7. Asadi P, Faraji G, Besharati MK (2010) Productions of AZ91/SiC composite by friction stir processing (FSP). *Int J Adv Manuf Technol* 51:247–260
8. Gupta MK, Ranakoti L, Rakesh PK (2019) Effects of reinforcement on tribological behaviour of aluminium matrix composites. *Automotive Tribology*. Springer, Singapore, pp 131–143
9. Tio M, Wang L, Lu W (2016) Communication effects of friction stir processing on the phase transformation. *Metall Mater Trans A* 47(12):5675–5679
10. Shojaeefard MH, Akbari M, Asadi P (2017) The effect of reinforcement type on the microstructure, mechanical properties, and wear resistance of A356 matrix composites produced by FSP. *Int J Adv Manuf Technol*, 1391–1407
11. Anvari SR, Karimzadeh F, Enayati MH (2013) Wear characteristics of Al–Cr–O surface nanocomposite layer fabricated on Al6061 plate by friction stir processing. *Wear* 304(12):144–151

12. Alaneme KK, Olubambi PA, Afolabi AS, Bodurin MO (2014) Corrosion and tribological studies of bamboo leaf ash and alumina reinforced Al-Mg-Si alloy matrix hybrid composites in chloride medium. *Int J Electrochem Sci* 9:5663–5674
13. Yuvaraj N, Arvidham S (2017) Wear characteristics of Al5083 surface hybrid nanocomposites by friction stir processing. *Trans Indian Inst Met* 70(4):1111–1129
14. Swamy ARK, Ramesha A, Kumar GBV, Prakash JN (2011) Effect of particulate reinforcements on the mechanical properties of Al6061-WC and Al6061-Gr MMCs. *J Miner Mater Character Eng* 10(12):1141–1152
15. Karthikeyan L, Kumar VSS, Padmanabhan KA, Karthikeyan L, Padmanabhan KA (2015) Investigations on superplastic forming of friction stir-processed AA6063-T6 aluminum alloy investigations on superplastic forming of friction. *Mater Manuf Process* 6914:294–298
16. Behnagh RA, Givi MKB, Akbari M (2015) Mechanical properties, corrosion resistance, and microstructural changes during friction stir processing of 5083 aluminum rolled plates mechanical properties, corrosion resistance, and microstructural changes during friction stir processing of 5083 aluminum rolled plates. *Mater Manuf Process*, 636–640
17. Amirtharaj D, Rajamurugan G, Sivachidambaram S, Dinesh D (2015) Effect of tool geometry on surface modification of aluminium 6063 by friction stir processing. *ARPN J Eng Appl Sci* 10(12):5391–5394
18. Gerlich AP (2017) Critical assessment friction stir processing potential, and problems critical assessment: friction stir processing, potential, and problems. *Mater Sci Technol* 0836:1139–1144
19. Dolatkhan A, Golbabaee P, Givi MKB, Molaiekiya F (2012) Investigating effects of process parameters on micro structural and mechanical properties of Al5052/SiC metal matrix composite fabricated via friction stir processing. *Mater Des* 37:458–464
20. Dinaharan I (2018) Influence of ceramic particulate type on microstructure and tensile strength of aluminum matrix composites produced using friction stir processing. *Integr Med Res* 4(2):209–218

Designing of an Electromagnet Producing Gradient MF and Its Effect on Water Properties



Ashish Kumar, Apurba Mandal, and T. Sudhakar

1 Introduction

The molecular construction of water has been under inspection for almost a century and is persuaded by various factors. The features and duration of this region of 'structured' water have been a matter of debate. It has been provided with evidence that magnetic fields strengthen hydrogen bonds along with the basic properties of water. The MF impact on hydrogen bonds is also a source of discussion with much confirmation. However, Feng [1], has granted what appears to be strong support for the magnetic treatment of water. Amiri et al. [2] discovered that adjustments in surface pressure of water with time could be a crucial point in following debasements in water. Cai et al. [3] broke down the adjustment in the physicochemical properties of water when coursed at a consistent stream rate. Additionally, demonstrating a lessening of surface strain and the expansion of thickness over the treatment time; the two-stage model was built up. The outcomes prescribed that the normal size of water bunches become bigger by attractive medicines.

Holysz et al. [4] exhibited the dissipation measure of water expanded when presented to a static MF, and it reasoned that the MF caused variation in hydration framework of molecules. Chang et al. [5] studied the progression of subatomic elemental recreations depending upon the adaptable 3-focused model of the water system. The examination shows basic changes in the fluid by utilization of MF with a quality range (1–T). Guo et al. [6] examined the vanishing of water in MF of the

A. Kumar · A. Mandal (✉) · T. Sudhakar
Mechanical Engineering Department, National Institute of Technology Uttarakhand, Srinagar,
Uttarakhand 246174, India
e-mail: mandal@nituk.ac.in

A. Kumar
e-mail: ashishkr.iitbhu@gmail.com

T. Sudhakar
e-mail: sudhakar@nituk.ac.in

high gradient (from utilizing the super magnet and reproduced gravity. Wang et al. [7] studied the impact of the attractive static field on the hydrogen holding in water utilizing a frictional examination. Gabrielli et al. [8] built a device to treat scales present in water using magnets (permanent). Wang et al. [9] investigated physical properties after MF exposor on various types of test water samples and concluded the results in affirmation. The ideal polarization MF strength was reduced to 300 mT. They examined the maximum evaporation and least B.P. at 300 mT. Until now, researches have studied the effect of static magnetic field on the water properties. However, a study on the effect of the gradient magnetic field is still in dew. In this work, the varying magnetic field by the tapered solenoid and its effect on the water properties is studied.

2 System Modelling

The actual model is represented schematically in Fig. 1.

The experimental set up designed for testing of the evaporation rate of water under the influence of the gradient magnetic field mainly consists of: Auto-Transformer, Tapered solenoid, Graduated cylinder, Resistance coil, NI cDAQ-9178, K-type thermocouple, and NI-9213 C Series Temperature Input Module.

The main part of the setup is the tapered solenoid which will be able to generate the gradient magnetic field along the axis of the solenoid. The tapered solenoid of length 150 mm having one end diameter of 50 mm and another end diameter of 100 mm is made of insulated copper wire is considered. Effect of copper wire diameter on the magnetic field is considered. Two sets of dia are considered, as mentioned in Table 1. Due to more diameters in the 2nd model number of layers of winding is increased as the length of the wire is constant for both cases. Design of the tapered solenoid in the first model and the second model is represented in Fig. 2a, b.

Because of linear change in diameter along the axis of the solenoid, the gradient magnetic field can be generated based on the concept of simple Biot-Savart's Law of electromagnetism. The actual set up of this model is shown in Fig. 2c.

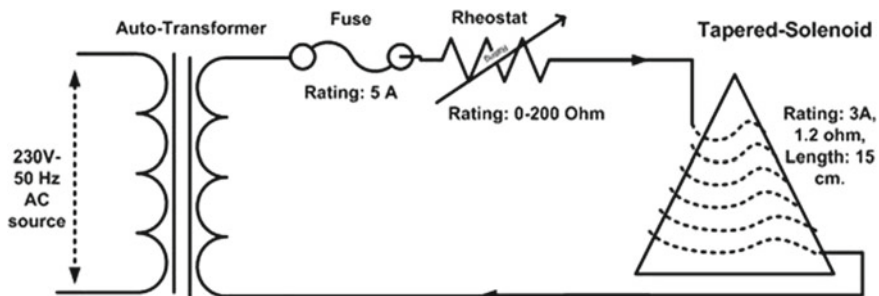
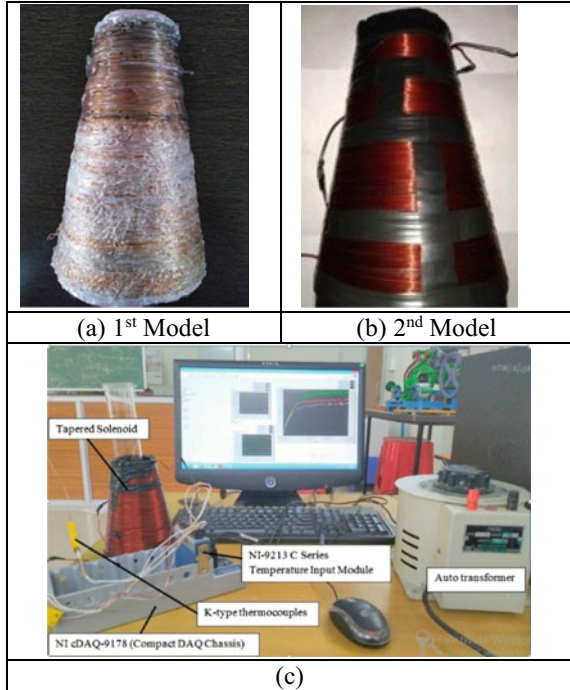


Fig. 1 Schematic representation of the actual model

Table 1 Detail description of the models

Description	1st model	2nd model
Diameter of copper wire	22 gauge	18 gauge
Length of copper wire	60 cm	60 cm
Number of turns	300	300
Number of layer winding	1	2
Winding connection	Series	Series

Fig. 2 a, b Design of tapered solenoid; c Actual set up of model



2.1 Derivation of the Magnetic Field Along the Axis of the Solenoid

The intrinsic magnetic moment of particles and currents (moving charges) are the main reasons for the generation of magnetic fields. In the present work, the relationship between current and magnetic field is evaluated. To study the effect of the magnetic field produced due to the element is determined by considering a point P at a distance of D along the solenoid axis. The point P is making an angle θ with the solenoid axis with the line joining the solenoid surface, as shown in Fig. 3c.

Z = radius of the ring which is at a distance x from the near edge

R_1 = radius of the near edge (smaller radius of the tapered solenoid)

R_2 = radius of the far edge (bigger radius of the tapered solenoid)

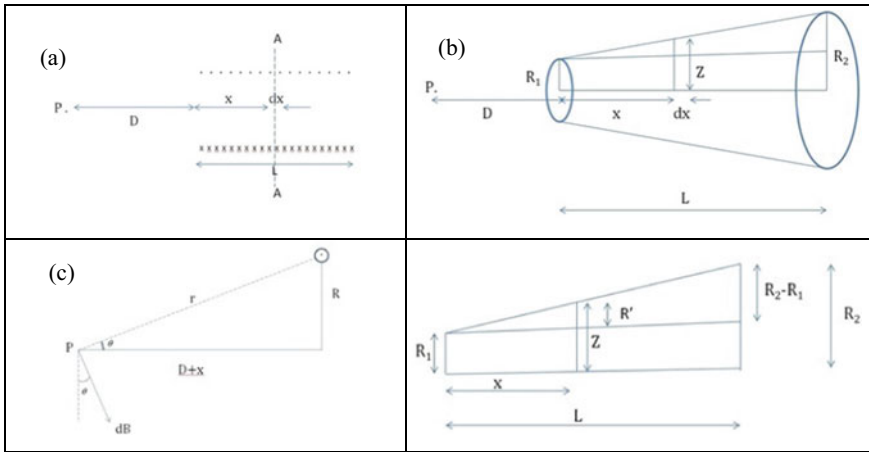


Fig. 3 Graphical representation of the tapered solenoid model

From the similar triangle rule,

$$x = \frac{LR'}{(R_2 - R_1)} \tag{1}$$

Then, the radius of the ring of the tapered solenoid at a distance x from the near edge

$$Z = R_1 + \frac{x}{L}(R_2 - R_1) \tag{2}$$

By differentiating the above the equation

$$dx = \frac{LdZ}{(R_2 - R_1)} \tag{3}$$

Then from Biot–Savart’s law and Eq. (2), for a single loop at the distance x from the near edge of the tapered solenoid, the magnetic field will be,

$$dB = \frac{\mu_0 In}{4\pi} \frac{Z}{[(D + x)^2 + Z^2]^{3/2}} ds \tag{4}$$

Since, s = the perimeter of the ring situated at a distance from the ear edge having radius Z , then

$$\begin{aligned} s &= 2\pi Z \\ ds &= 2\pi dZ \end{aligned} \tag{5}$$

Then, by substituting the value of ds into Eq. (4), we get,

$$dB = \frac{\mu_0 In}{2} \frac{Z}{[(D+x)^2 + Z^2]^{3/2}} dZ \quad (6)$$

Differentiating equation 2,

$$dZ = \frac{(R_2 - R_1)}{L} dx \quad (7)$$

By substituting equation 2 and 7 in Eq. 6, the Gradient Magnetic Field at point 'P', the tapered solenoid of length 'L' the axis of the tapered solenoid at a distance $(D+x)$ from the near edge equals to:

$$\frac{dB}{dx} = \frac{\mu_0 In}{2} \frac{R_1 + \frac{x}{L}(R_2 - R_1)}{[(D+x)^2 + \{R_1 + \frac{x}{L}(R_2 - R_1)\}^2]^{3/2}} \frac{(R_2 - R_1)}{L} \quad (8)$$

2.2 Calculation of Gradient Magnetic Field for a Proposed Design

The experimental setup is expected to be kept in ideal condition. The working temperature is kept constant at 25 °C with a continuous flow of the current of 5 A. Prior to the experiments, the test structure was carefully observed for testing of the solenoid copper coil. The calculated gradient MF for both models is shown in Fig. 4. As the distance increases the magnetic field decreases. In the 2nd model, the magnetic field is very high at the near end. But the rate of decrease in the magnetic field is higher in the 2nd model.

3 Experimental Results

Initially, 100 ml of untreated water (13 °C) without the influence of the magnetic field is heated. Evaporation time and rate of the water has found as 24:40 min and 0.0675 ml/s, respectively. The boiling point of the water is 99.2 °C. It has performed the experiments for River water, RO water and Tap water under the GMF for both models. In the 1st model, with the effect of the magnetic field, the evaporate rate increases, and the boiling point of the water is decreased. Tap water is evaporating at a faster rate than river water and RO water. But the boiling point is the same for all the cases. The experimental results for the 1st model are mentioned in Table 2.

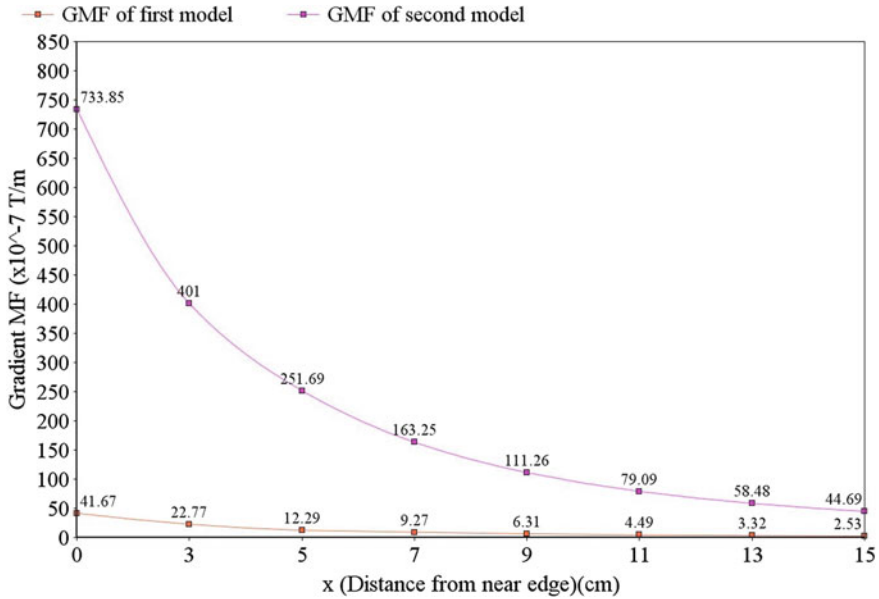


Fig. 4 Variation of the magnetic field in a new design

Table 2 Experimental results for water samples at various parameter for 1st model

Experimental parameter	River water	RO water	Tap water
Water initial temp. (°C)	12	13	13
Final temp. after GMF	32	30	31
Atm. temperature (°C)	13	13	12
GMF exposer time (min)	50	50	50
Evaporation time (min)	22:35	22:50	22:20
Sample amount (ml)	100	100	100
Evaporation rate (ml/sec)	0.0738	0.0729	0.0746
BP after GMF (°C)	96	96	96

In the 2nd model, also the evaporation rate is faster for the tap water than the river water and RO water. In RO water, due to the removal impurities, the magnetic particles will be separated. This causes a reduction in the evaporation rate. The boiling point of water is the same all cases but little higher than the 1st model. The experimental results for the 2nd model are mentioned in Table 3.

It shows that decreasing of insulated copper wire dia, for the same length, the magnetic field produced more. Fig. 5 represents the evaporation rate comparison for untreated test samples with treated (magnetized) water samples for both models. It shows that under the influence of the more magnetic field, the evaporation rate is high.

Table 3 Experimental results for water samples at various parameter for the 2nd model

Experimental parameter	River water	RO water	Tap water
Water initial temp. (°C)	12	13	13
Final temp. after GMF	40	38	39
Atm. temperature (°C)	15	15	14
GMF exposer time (min)	50	50	50
Evaporation time (min)	21:01	21:34	20:49
Sample amount (ml)	100	100	100
Evaporation rate (ml/sec)	0.0793	0.0781	0.0804
BP after GMF (°C)	96.5	96.5	96.5

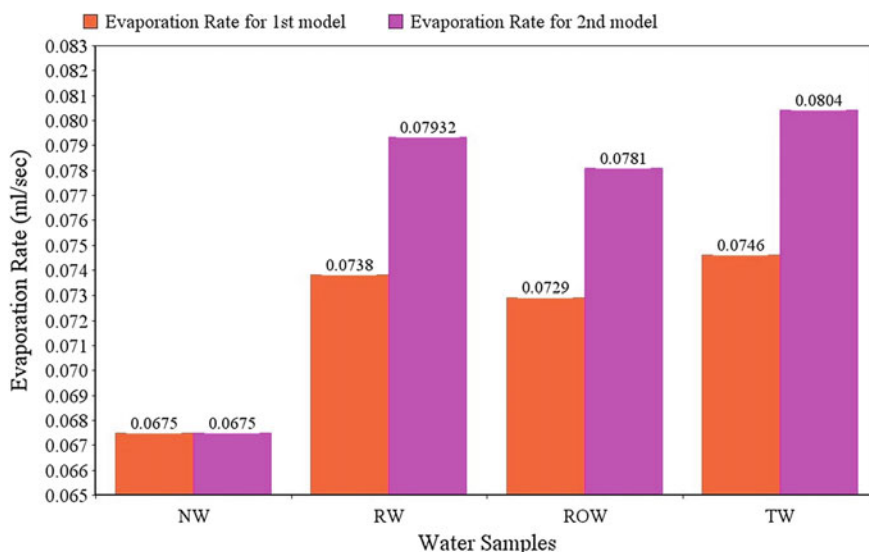


Fig. 5 Evaporation rate of normal water (untreated) with treated samples (RW, ROW and TW)

4 Results on Resistance and Conductivity Test of Water Samples under Gradient MF

Further, it has calculated the resistance and conductivity of the water samples with the designed 2nd model of the tapered solenoid. To calculate the resistance and conductivity of the water samples, it has kept them in the gradient MF for a total experimental time of 2 h 30 min. Figure 6 shows the change in the resistance of the water samples with respect to the time of exposing to the gradient MF. It can be observed that the resistance is continuously decreasing with the increase of time of gradient MF exposure. In the case of RW, the resistance is high as compared to TW and ROW. This is maybe due to more impurities in water samples. The

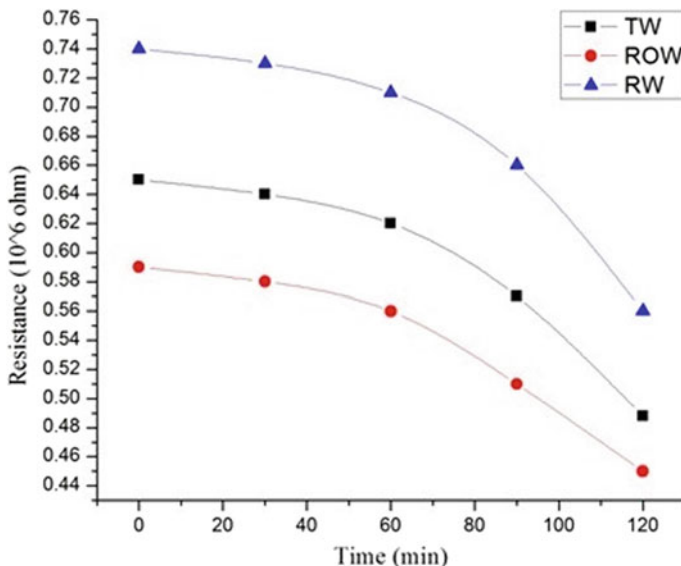


Fig. 6 The resistance of different water sample under GMF versus Time plot

resistivity/specific resistance of absolutely pure water is about $18.2 \text{ M}\Omega \text{ cm}$ at 25°C . But as the time of exposure of gradient MF increases, all samples experienced the flow of its movable charges and resulted in gives lowering electric resistance.

Conductivity is defined as the inverse of resistivity (SI units of Siemens per meter (S/m)). Fig. 7 shows the variation of conductivity of different water samples in the gradient MF with respect to the time. It shows that the conductivity of water is increasing continuously with time is due to more prolonged exposure to the gradient.

5 Conclusion

From the above experiments, certain conclusions were made. Detailed investigation shows that enhanced the properties of water. The designed setup gives a desirable continuous gradient magnetic field. When GMF was applied perpendicularly on the water surface, change in a property of water, e.g. change in boiling point, evaporation rate was observed. Under the exposure of MF, the boiling point of water is decreased from 99.2 to 96.5°C . It also improved the evaporation rate of water samples. Experimental studies have been determined the changes in conductivity and resistance of water samples. As the time of exposure to gradient MF is increased, the flow of its movable charges enables water samples to improve the conductivities.

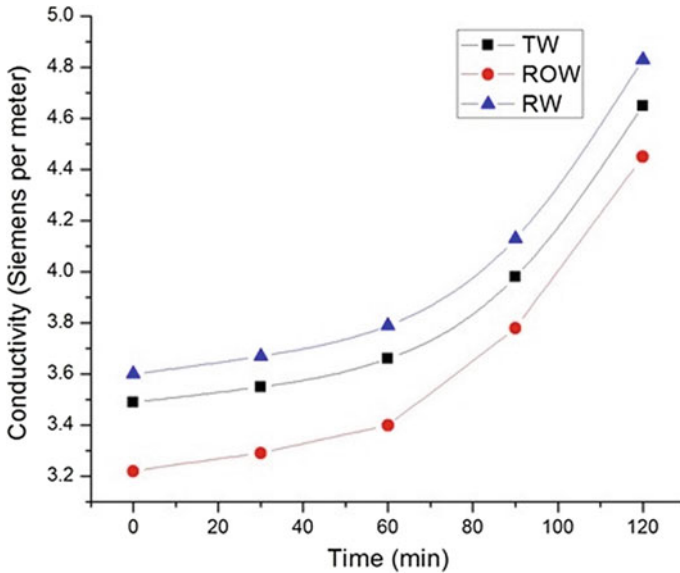


Fig. 7 Conductivity variation of magnetized water samples under GMF

Acknowledgements We would like to thanks Shri Proloy Jyoti Naskar, Principal Engineer (System Engineering and Development), Rolls Royce India Private Ltd., Bangalore, for helpful suggestions on current works. Authors of this paper gratefully acknowledge the guidance and technical suggestion provided by Shri P. J. Naskar.

References

1. Pang X-F, Deng B (2008) The changes of macroscopic features and microscopic structures of water under the influence of the magnetic field. *Phys B: Condensed Matter* 403(19–20):3571–3577
2. Amiri M, Dadkhah AA (2006) On reduction in the surface tension of water due to magnetic treatment. *Colloids Surfaces A: Physicochem Eng Aspects* 278(1–3):252–255
3. Cai R, Yang H, He J, Zhu W (2009) The effects of magnetic fields on water molecular hydrogen bonds. *J Mol Struct* 938(1–3):15–19
4. Holysz L, Szczes A, Chibowski E (2007) Effects of a static magnetic field on water and electrolyte solutions. *J Colloid Interface Sci* 316(2):996–1002
5. Chang K-T, Weng C-I (2006) The effect of an external magnetic field on the structure of liquid water using molecular dynamics simulation. *J Appl Phys* 100(4):043917
6. Guo Y-Z, Yin D-C, Cao H-L, Shi J-Y, Zhang C-Y, Liu Y-M, Huang H-H, Liu Y, Wang Y, Guo W-H (2012) Evaporation rate of water as a function of a magnetic field and field gradient. *Int J Mol Sci* 13(12):16,916–16,928
7. Wang Y, Zhang B, Gong Z, Gao K, Ou Y, Zhang J (2013) The effect of a static magnetic field on the hydrogen bonding in water using frictional experiments. *J Mol Struct* 1052:102–104
8. Gabrielli C, Jaouhari R, Maurin G, Keddad M (2001) Magnetic water treatment for scale prevention. *Water Res* 35(13):3249–3259

9. Wang Y, Wei H, Li Z (2018) Effect of magnetic field on the physical properties of water. *Res Phys* 8:262–267

Thermal and Thermo-Mechanical Analysis of Vinyl-Ester-Carbon/CBPD Particulate-Filled FGMS and Their Homogenous Composites



Brijesh Gangil, Manoj Kumar Gupta, Lalit Ranakoti, and Tej Singh

1 Introduction

Polymer composite materials are extensively subjected to static loading applications. This is because of the strength of the product, which comprises mainly fiber and matrix. Thus, the strength of the polymer composites is henceforth solely depending on the strength of fibrous and matrix materials [1, 2]. On the other hand, conventional materials like iron ore and its alloys are far stronger than the polymer composites, but gradually reducing in quantities. Polymer composites are then coming into the picture to fulfill the dearth of conventional materials. Not in every sector, but in few, conventional materials can be replaced by polymers composites [3]. Although composites have many benefits over monolithic materials, composite materials fail under extreme working conditions through a process called delamination which can be resolved by graded composites. Functionally graded material (FGM) has been classified under those new engineering composites where a gradient in microstructure/morphology is intentionally formed to get the desired properties and to get better performance levels than their homogeneous counterpart. A functionally graded material (FGMs) which is generally applied in the applications where the requirement

B. Gangil (✉) · M. K. Gupta
Mechanical Engineering Department, H.N.B Garhwal University, Srinagar, Uttarakhand, India
e-mail: brijeshgangil@gmail.com

M. K. Gupta
e-mail: gupta_291@rediffmail.com

L. Ranakoti
Mechanical Engineering Department, National Institute of Technology Uttarakhand, Srinagar,
Uttarakhand, India
e-mail: lalit_9000@yahoo.com

T. Singh
Savaria Institute of Technology, Eötvös Loránd University, Szombathely, Hungary
e-mail: tejschauhan@gmail.com

of strength in a certain material is layer by layer or properties vary with respect to materials dimension [4] is required. Due to its special characteristics, FGMs are now becoming one the attractive areas of research in the domain of materials. A lot of research has been undergoing in the field of FGMs, the material of FGMs and the evolution of technique for the manufacturing of FGMs.

Chemical vapor deposition (CVD) a very well-known technique had been utilized to manufacture the functionally graded Si/C material [5]. It was found that the crack propagation property of the material gets substantially enhanced. With the help of the same technique, i.e., CVD, deposition of C on to the SiC had been analyzed and reported that further improvement in the cracks propagation can be achieved [6]. For instance, the effects of change in the parameters like gas flow rate and reaction source ratio of CVD for the FGMs result in better UV emission intensity ratio and good physical property [7]. Changing the parameters also helps in the controlled growth of microstructure [8]. With the help of thermal spray technique (used to deposit material at the surface of another), large numbers of FGMs are being manufactured for the research purposes [9]. Various issues like crystallinity, hardness, surface cracks, fatigue, thermal shock, mechanical behavior, interfacial adhesion, etc., had been raised and investigated for the FGMs [10–13]. For the manufacturing of FGMs in bulk form, centrifugal casting has been generally preferred. Short kevlar fiber, carbon fiber, bagasse fiber, etc., based polymer matrix FGMs had been fabricated, tested for various parameters such as physical-mechanical and wear and compared with homogeneous composite materials via centrifugal casting. The author had recommended FGMs over homogeneous for the various tested parameters and duly suggested for the further potential in FGMs [14–17]. Currently, FGMs are exploited to the various applications, whereas high endurance, thermal, corrosion resistance are required. Increasing the range of applications in this dynamic world can be a challenge but not impossible. The dynamic application requires a material which is well sound in variable loading conditions such as a change in temperature and change in load. TGA and DMA are the test apparatus which give us access to analyze the material with varying loading condition. Taking into consideration, the present study is focused on the dynamic mechanical analysis (DMA) and thermal gravimetric analysis (TGA) of the carbon bypass dust (CBPD) filled, carbon fiber/vinyl-ester FGM. Centrifugal casting has been utilized for the manufacturing of FGMs, and the DMA and TGA results are compared with the homogeneous composites.

2 Materials and Method

The material used in the study mainly consists of CBPD, which is a by-product of Portland cement constitute CaO in major and other components are SiO₂, Al₂O₃, Fe₂O₃, K₂O, Na₂O, Cl⁻, etc., purchased from the local vendor in Srinagar. The fiber material, i.e., short carbon fiber was supplied by St. Gobain Ltd. India. Owing to its phenomenal reinforcing properties, carbon fiber is selected rather than glass or Kevlar. The matrix material is used as vinyl-ester which is a thermoset resin

was supplied by Amtech ester Pvt. Ltd. A thermal analyzer DTG-60 model of Shimadzu Corporation is used for TG analysis. The thermogravimetric analyses were carried out on approximately 20 ± 0.1 mg of fabricated composite material, while for the thermo-mechanical characterization of the composite, specimens are performed on NETZSCH DMA 242 C having a temperature range of -170 to 600 °C; heating/cooling rates of $0.01/20$ K/min.; modulus range of 10^{-3} to 106 MPa; frequency range of 0.01 – 100 Hz; $\tan \delta$ range of 0.00006 – 10 . The testing parameters are specimen dimensions = $40 \times 12 \times 4$ mm³ in three-point bending test; frequency = 1 Hz; heating rate = 2 K/min.; temperature range = 25 – 200 °C.

2.1 Manufacturing Method

The technique used in the manufacturing of homogeneous and FGMs is gravity casting and centrifugal casting, respectively. The percentage of CBPD was varied in the composition from 0 to 12 wt% for both homogeneous and FGMs keeping the short carbon fiber constant in the matrix material. For the preparation of homogeneous composite, the liquid resin of vinyl-ester was mixed with short carbon fiber and CBPD. Cobalt naphthenate and methyl-ethyl-ketone-peroxide were used as the accelerator and hardening agent. The composition was mechanical stirred to mix the ingredients. For homogenous composites, the stirred mixture was carefully poured in the glass tube of size 10 mm diameter and 120 mm length, and the mixture was then left in a test tube for cooling about 48 h. While vertical centrifugal casting was used for FGMs with the rotating speed of 1000 rpm for 30 min as reported in the literature [18]. The fabricated composites are shown in Fig. 1. Thereafter, specimens are cut from the homogeneous and FGMs composites for characterization. The details of the fabricated composites are shown in Table 1.

3 Results and Discussion

3.1 TG Analysis

Figure 2 shows the TGA analysis of CBPD filled, short carbon fiber vinyl-ester composites. It can be seen that for both homogeneous and FGMs, the weight loss occurred during the experiment, and the weight loss occurred in three-stage. In the first stage, only 1 – 2% weight loss is observed in the range of temperature 30 – 210 °C, and this happens due to the combined effect of burning out of moisture and evaporation of the component of vinyl-ester, i.e., solvent and styrene. On further increasing the temperature beyond 200 °C, i.e., in the second phase, the weight loss is observed to be approximately 15% of the total weight loss. It is noticeable that the composite undergoes degradation and rupture of the fiber–matrix chain starts. The important

Fig. 1 Fabricated homogenous and graded polymer composite



Table 1 Percentage of short carbon fiber, CBPD and vinyl-ester for homogeneous and FGMs

S. No.	Designation	Composition
1	HCBPD-0	Vinyl-ester (90 wt%) + Carbon fiber (10 wt%)
2	HCCBPD-1	Vinyl-ester (86 wt%) + CBPD Filler (4 wt%) + carbon fiber fixed (10 wt%)
3	HCCBPD-2	Vinyl-ester (82 wt%) + CBPD Filler (8 wt%) + carbon fiber fixed (10 wt%)
4	HCCBPD-3	Vinyl-ester (78 wt%) + CBPD Filler (12 wt%) + carbon fiber fixed (10 wt%)
5	GCBPD-0	Vinyl-ester (90 wt%) + Carbon fiber (10 wt%)
6	GCCBPD-1	Vinyl-ester (86 wt%) + CBPD Filler (4 wt%) + carbon fiber fixed (10 wt%)
7	GCCBPD-2	Vinyl-ester (82 wt%) + CBPD Filler (8 wt%) + carbon fiber fixed (10 wt%)
8	GCCBPD-3	Vinyl-ester (78 wt%) + CBPD Filler (12 wt%) + carbon fiber fixed (10 wt%)

role CBPD plays in the composite is to reduce the mobility of fiber–matrix chain; thus, the tension induced in the carbon–carbon bond decreases and results in low degradation [19]. At the temperature greater than 300 °C, rapid degradation of the composites take place and due to which 40–65% of the total weight loss take place. Evaporation of styrene and loss of hydrogen bonding present in the vinyl-ester starts to decompose at this stage and thus leads to higher degradation. The weight loss continues to after 4000 °C but almost gets constant at 5000 °C. Around 10–30%

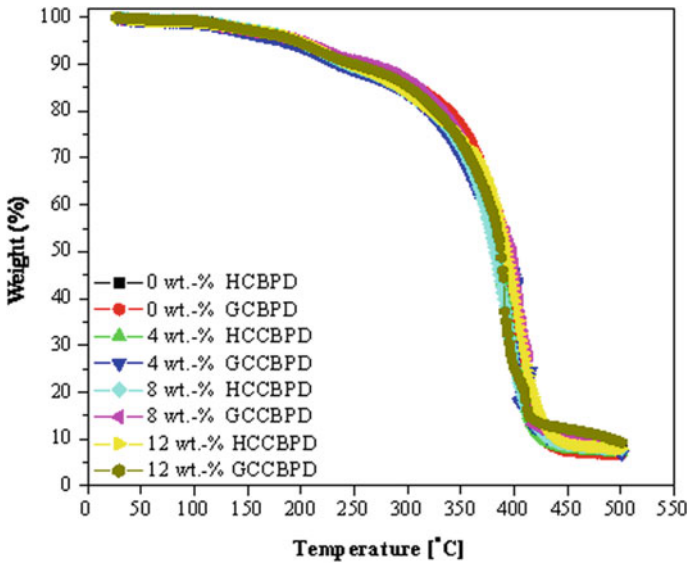


Fig. 2 TG analysis of carbon/CBPD filled homogenous and graded composites

weight loss is observed in this range of temperature 4000–5000 °C. Table 2 shows that composites with increased CBPD content are more thermally stable than those with lower CBPD content. On the one hand, the degradation of CBPD is activated at a higher temperature. Overall, from the graph and table, it can be observed that FGMs are superior to homogeneous at elevated temperature. The details of weight loss at a particular temperature for each sample have been shown in Table 2.

Table 2 TG analysis of CBPD/carbon-filled graded and homogenous composites N₂ atmosphere

Composite	Weight loss (%) with respect to temperature (°C)		
	30–300	300–400	400–500
0 wt% HCBPD	15.04	54.99	21.98
0 wt% GCBPD	13.60	52.90	26.95
4 wt% HCCBPD	14.31	57.97	20.70
4 wt% GCCBPD	16.26	38.47	38.47
8 wt% HCCBPD	16.28	57.23	18.72
8 wt% GCCBPD	13.66	39.15	38.51
12 wt% HCCBPD	15.76	43.45	32.93
12 wt% GCCBPD	14.69	65.06	9.90

3.2 Thermo-Mechanical Analysis of Vinyl-Ester-Carbon/CBPD Particulate Filled FGMs and Their Homogenous Composites

To characterize the thermal mechanical behavior of the composite, DMA has been used. Storage modulus (E'), loss modulus (E'') and damping factor ($\tan \delta$) as a function of temperature have been evaluated for different compositions of homogeneous and FGMs. As shown in Fig. 3, the E' remains constant up to the temperature 30 °C. As the temperature increases from 30 °C, a sudden decline is observed in E' till the temperature reaches 90 °C. Highest value for E' is achieved for the sample 8 wt% CBPD and lowest is observed for 12 wt% CBPD. The E' tends to increase as the percentage of CBPD increases to 8 wt% and then decreases. The phase transformation due to thermal induction in the composite leads to hardening of composition, thus results in shifting of glass transition temperature to higher values [20]. At higher temperature, i.e., beyond 40 °C, the E' starts to decrease due to the rubber formation and coincidence of mechanical deformation and internal frictional provided by the oscillatory motion. Carbon/CBPD filled homogenous and graded composites. The energy dissipation, i.e., loss modulus E'' has been shown in Fig. 4.

It can be observed that 8 wt% GCCBPD shows the highest capability of energy dissipation among all the fabricated composites for the range of temperature. This may be attributed to the presence of CBPD and the centrifugal technique applied

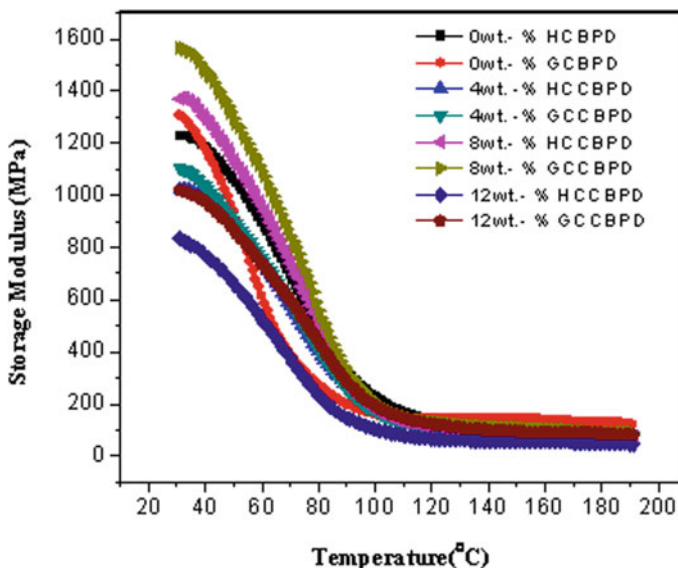


Fig. 3 Storage modulus (E') versus temperature of carbon/CBPD filled homogenous and graded composites

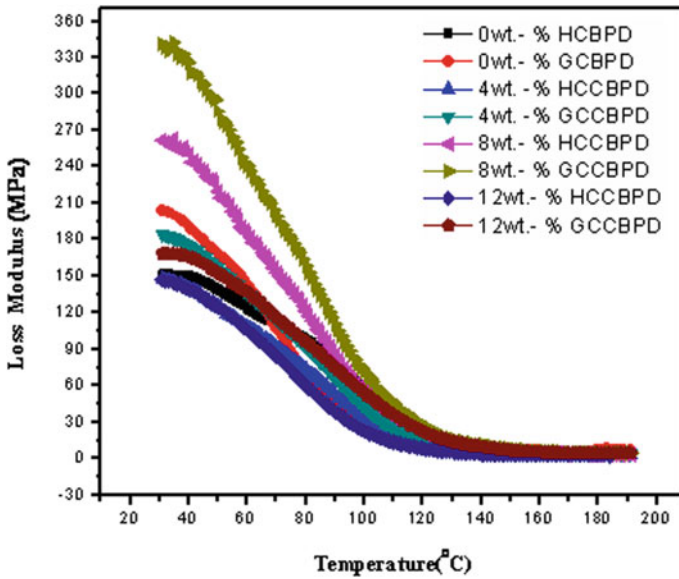


Fig. 4 Loss Modulus (E'') versus temperature of carbon/CBPD filled homogenous and graded composites

in the manufacturing of the graded material. The presence of higher density at the surface of FGMs makes it better material to withhold higher temperature.

The damping factor ($\tan \delta$) of FGMs and homogeneous has shown in Fig. 5. Similar trends can be observed for $\tan \delta$ also as obtained for E' and E'' . It is highest for 8 wt% GCCBPD and lowest for 4 wt% HCBPD. Glass transition temperature for neat carbon fiber vinyl-ester FGMs is observed to be 78 °C, and for homogeneous material, the same is noticed at 90 °C. On adding the CBPD to both FGMs and homogeneous material, the glass transition temperature shows significant improvement for the FGMs, i.e., 90 ± 5 °C for homogeneous material and 95 ± 5 °C for FGMs. This makes it clear that FGMs are more prominent than homogeneous material at elevated temperature. Moreover, the presence of CBPD in both homogeneous and FGMs is more beneficial in FGMs due to the centrifugal effect of the casting method, which makes them segregated at the surface of the material.

4 Conclusion

In the present investigation, CBPD an industrial waste is used as a potential filler material in vinyl-ester matrix composites. Inclusion of CBPD has a significant effect on the thermal and thermo-mechanical analysis of Vinyl-Ester-Carbon/CBPD particulate filled FGMS and their homogenous composites. From the TGA result, it is clear

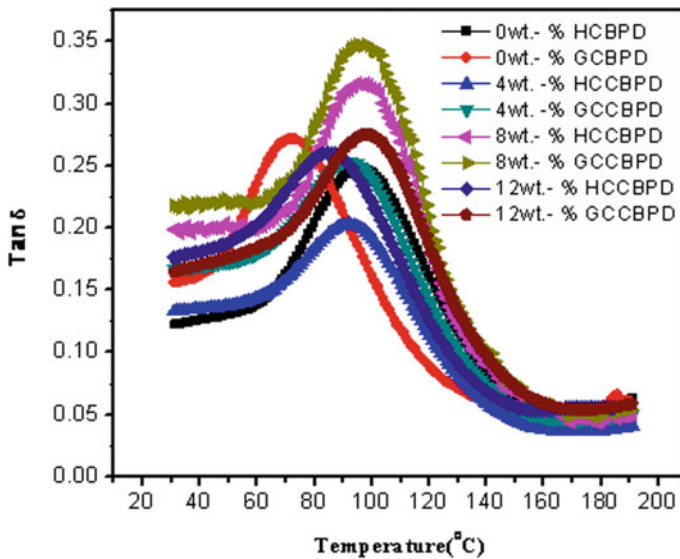


Fig. 5 Loss-tangent factor ($\tan \delta$) versus Temperature of CBPD/carbon-filled homogenous and graded composites

that the thermal stability of graded composites shows better stability among all the fabricated samples. TGA curves also demonstrate the lower reduction in weight percentage for FGMs as compared with homogeneous.

The dynamic mechanical properties of investigated homogenous and graded composites (viz. storage modulus (E'), loss modulus (E'') and loss-tangent factor ($\tan \delta$) are studied to investigate stiffness and damping characteristics. The DMA test reveals that the addition of fiber/filler in the matrix enhances the storage modulus as compared with neat composites. Graded composites have much higher damping capacities than homogenous and unfilled CBPD composites. A maximum $\tan \delta$ has been observed for 4wt% GKCBPD, followed by the composite with 8 wt% GKCBPD. As FGMs are found to have higher storage modulus than homogeneous, it would be worth saying that centrifugal technique for the FGMs can be preferred rather than hand layup method.

References

1. Mohammed L, Ansari MN, Pua G, Jawaid M, Islam MS (2015) A review on natural fiber reinforced polymer composite and its applications. *Int J Polym Sci*
2. Lalit R, Mayank P, Ankur K (2018) Natural fibers and biopolymers characterization: a future potential composite material. *Strojníckycasopis J Mech Eng* 68(1):33–50
3. Friedrich K, Almajid AA (2013) Manufacturing aspects of advanced polymer composites for automotive applications. *Appl Compos Mater* 20(2):107–128

4. Mahamood, R. M., Akinlabi, E. T., Shukla, M., & Pityana, S. (2012). Functionally graded material: an overview
5. Sasaki M, Hirai T (1994) Thermal fatigue resistance of CVD SiC/C functionally gradient material. *J Eur Ceram Soc* 14(3):257–260
6. Kawase M, Tago T, Kurosawa M, Utsumi H, Hashimoto K (1999) Chemical vapor infiltration and deposition to produce a silicon carbide–carbon functionally gradient material. *Chem Eng Sci* 54(15–16):3327–3334
7. Wang X, Chu X, Zhao H, Lu S, Fang F, Li J, Wang X, Du P, Wang X (2014) Controllable growth of functional gradient ZnO material using chemical vapor deposition. *Integr Ferroelectr* 151(1):1–6
8. Seifried S, Winterer M, Hahn H (2001) Nanocrystalline gradient films through chemical vapor synthesis. *Scriptamaterialia* 44(8–9):2165–2168
9. Heimann RB (2008) *Plasma-spray coating: principles and applications*. Wiley, Boca Raton
10. Cannillo V, Lusvardi L, Sola A (2008) Production and characterization of plasma-sprayed TiO₂–hydroxyapatite functionally graded coatings. *J Eur Ceram Soc* 28(11):2161–2169
11. Ivošević M, Knight R, Kalidindi SR, Palmese GR, Sutter JK (2005) Adhesive/cohesive properties of thermally sprayed functionally graded coatings for polymer matrix composites. *J Therm Spray Technol* 14(1):45–51
12. Han Z, Xu B, Wang H, Zhou S (2007) A comparison of thermal shock behavior between currently plasma spray and supersonic plasma spray CeO₂–Y₂O₃–ZrO₂ graded thermal barrier coatings. *Surf Coat Technol* 201(9–11):5253–5256
13. Stewart S, Ahmed R, Itsukaichi T (2004) Contact fatigue failure evaluation of post-treated WC–NiCrBSi functionally graded thermal spray coatings. *Wear* 257(9–10):962–983
14. Gangil B, Patnaik A, Kumar A, Biswas S (2013) Thermo-mechanical and sliding wear behaviour of vinyl ester–cement by-pass dust particulate-filled homogenous and their functionally graded composites. *Proc Inst Mech Eng Part J: J Eng Tribol* 227(3):246–258
15. Gangil B, Patnaik A, Kumar A (2013) Mechanical and wear behavior of vinyl ester-carbon/cement by-pass dust particulate filled homogeneous and their functionally graded composites. *Sci Eng Compos Mater* 20(2):105–116
16. Gangil B, Patnaik A, Kumar A (2013) Evaluation of thermo-mechanical and wear behavior of short carbon fibre vinyl-ester filled homogenous and their functionally graded composites. *Int Polym Proc* 28(2):207–220
17. Singh T, Gangil B, Singh B, Verma SK, Biswas D, Fekete G (2019) Natural-synthetic fiber reinforced homogeneous and functionally graded vinylester composites: effect of bagasse-Kevlar hybridization on wear behavior. *J Mater Res Tech*
18. Singh Y, Gangil B, Patnaik A, Kumar S, Rishiraj A, Fekete G (2018) Physico-mechanical, thermal and dynamic mechanical behaviour of natural-synthetic fiber reinforced vinyl-ester based homogenous and functionally graded composites. *Mater Res Expr* 06(02):025704
19. Yao F, Wu Q, Lei Y, Guo W, Xu Y (2008) Thermal decomposition kinetics of natural fibers: activation energy with dynamic thermogravimetric analysis. *Polym Degrad Stab* 93(1):90–98
20. Kumar S, Satapathy BK, Patnaik A (2011) Thermo-mechanical correlations to erosion performance of short carbon fibre reinforced vinyl ester resin composites. *Mater Des* 32(4):2260–2268

Experimental Investigation for Quality of Micro-holes Machined Using Electrochemical Discharge Machining Process



Mohinder Pal Garg, Manpreet Singh, and Sarbjit Singh

1 Introduction

The leading-edge materials such as glass, composites and ceramics have attracted the interest of research society owing to their foremost chemical and mechanical properties. The machining of these materials with conventional machining processes is challenging to researchers due to damages during machining, such as chipping, delamination and cracks. In advanced machining processes, the electrochemical discharge machining (ECDM) has risen as a fabulous machining process for the processing of difficult to cut materials regardless of their properties [1]. More importantly, the ECDM process has extremely endeavoured for processing of non-conductive materials. The basic ECDM set-up includes two electrodes: (1) cathode, (2) anode and named as tool electrode and auxiliary electrode, respectively, as shown in Fig. 1. While machining, the workpiece is dipped in electrolyte, and tool electrolyte is partially immersed in an electrolyte. A DC power source is used for supply of voltage to cathode and anode electrodes of ECDM set-up. The regulation of voltage supply to respective electrodes yields the electrolysis process. This tends to generate hydrogen bubbles in the vicinity of the tool electrode and combines to form a thin gas layer which acts as insulation in between the tool electrode and electrolyte [2]. When the applied potential surpasses, the critical value of gas film and spark is produced in front of the tool and sides of the tool electrode. The heating and thermal energy of

M. P. Garg · S. Singh (✉)

Department of Mechanical Engineering, DAV University, Jalandhar, India

e-mail: sarb1234.iitroorkee@gmail.com

M. P. Garg

e-mail: mpgargacad@gmail.com

M. Singh

Department of Mechanical Engineering, Punjab Engineering College, Chandigarh, India

e-mail: gurayamanpre5800@gmail.com

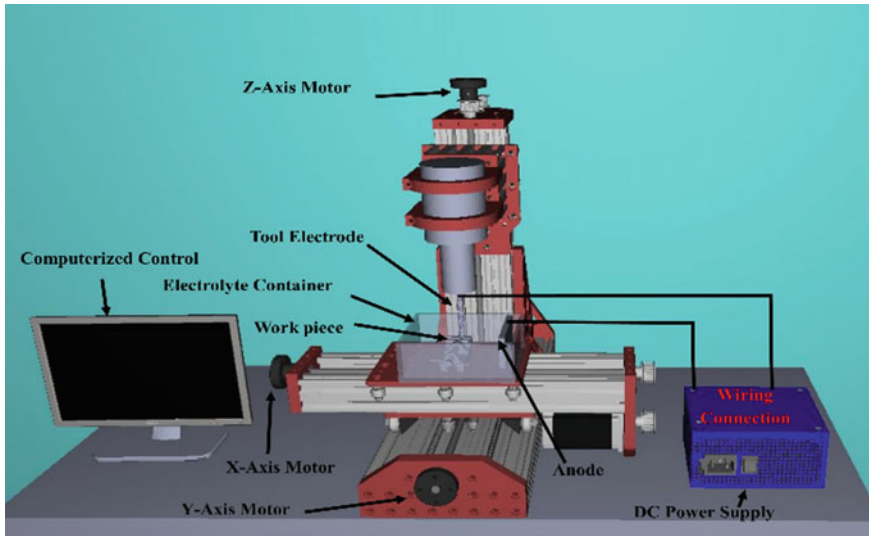


Fig. 1 Schematic of ECDM set-up installed on CNC machine

sparking at the tool electrode tip tends to machine workpiece material. In the beginning period, the ECDM procedure is used for machining of glass, and later on, the machining of ceramics, composites and alloys was effectively performed. Wuthrich et al. [3] characterized the micro-drilling of glass into two phases; (1) discharge regime with depth up to 300 μm , (2) hydrodynamic regime with a depth higher than 300 μm . The machining features of the second phase of the regime were outrageous due to limited supply and flushing of machined products at greater machining depth.

Chak and Rao [4] studied the trepanning of Al_2O_3 ceramic using abrasive particles coated tool electrode. They concluded that incorporation of abrasive particles coated tool electrode yields superior results in terms of machining quality in comparison with the copper tool. The abrasive particles coated tool electrode produces spark in front of tool electrode irrespective to sides of the tool electrode. Therefore, the side cutting is successfully eliminated with the use of particles coated tool in ECDM process. Liu et al. [5] studied machining behaviour of metal-based composite with the incorporation of diamond particles coated tool during ECDM. The diamond particles coated tool provides superior results in comparison with without coating tool electrode. The surface integrity of the machined sample is significantly improved due to additional grinding action. The morphology of machined holes exhibits HAZ and cracks around the periphery of holes. Sundaram et al. [6] explored the machining features of fibre epoxy-based composite using pulsed ECDM process. They concluded that the input of low pulsed supply reduced the diameter of the machined hole due to the reduction of gas layer size. The higher electrolyte level disperses the gas layer formed during machining and causes more diameter of the hole.

Moreover, there exists the best grouping of pulsed supply and electrolyte level for the generation of a precise hole with minimum HAZ. Kang and Tang [7] investigated the machining mechanism for ceramic coated Ni-based super-alloy using ECDM process. Based on the current waveform, the authors concluded that machining of coating is occurred due to electrochemical discharge. At the same time, the super-alloy substrate is machined due to the combination of electrochemical discharges and electrical discharges. Moreover, the surface roughness of the hole sidewall with ECDM is $5.6 \mu\text{m}$ as compared to $10.9 \mu\text{m}$ by EDM process. Singh et al. [8] explored the machinability of the silicon wafer during ECDM. They concluded that applied potential and tool travel rate are energetic input parameters which dominantly affect surface characteristics of a machined sample. Apart from these studies, the machining of carbon fibre-reinforced polymer (CFRP) composite is least reported in the literature using the ECDM process. Therefore, the present study describes the micro-manufacturing of holes on CFRP composite.

2 Methodology and Experimentation

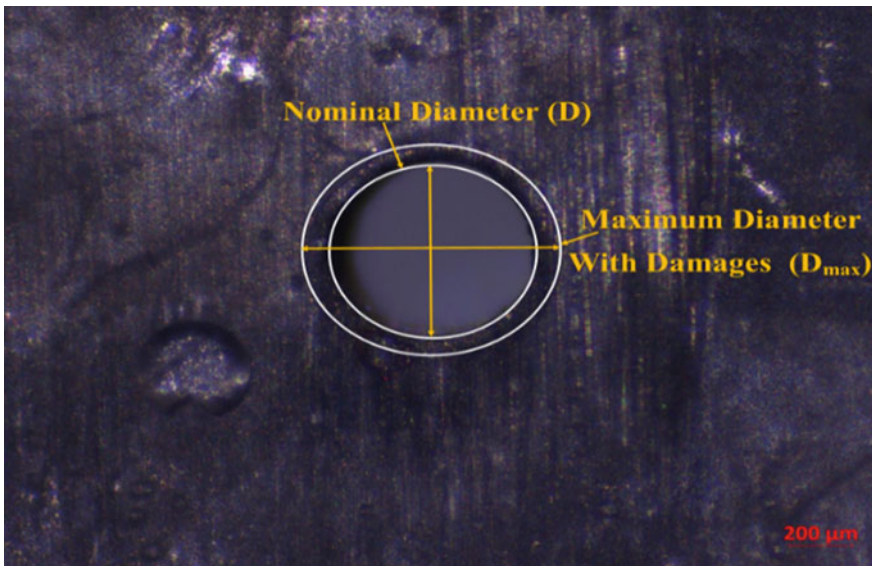
The leading-edge materials such as glass and composites have attracted the interest of research fraternity due to their superior chemical and mechanical properties. The micro-manufacturing CFRP composite has been attempted using house in developed ECDM set-up attached to HY3040 CNC machine (Fig. 1). This machine provides accurate movements to machining platform in the X, Y and Z directions. Taguchi's L_9 orthogonal array was used to conduct the experiments with input parameters as applied voltage, electrolyte concentration and duty cycle. The experimental conditions are applied voltage of 50–70 V, the concentration of electrolyte from 20% to 40% and a duty cycle of 60–80%. The other experimental conditions include NaOH electrolyte, tool electrode, i.e. tungsten carbide drill bit of $450 \mu\text{m}$ and gap in between the tool and auxiliary electrode of 40 mm. The thickness of the surface damaged zone (TSDZ) was observed as response characteristics. Experimental results with several trails of Taguchi's L_9 orthogonal array are shown in Table 1. The TSDZ around the periphery of the machined hole is measured using a Zeiss optical microscope of high magnification. The TSDZ is measured as the difference between maximum hole diameter with damages and nominal hole diameter [9]. The maximum diameter with damages and a nominal diameter of the hole are represented in Fig. 2. The TSDZ is measured using this Eq. (1):

$$\text{TSD} = (D_{\text{max}} - D)/2 \quad (1)$$

where D_{max} stands for the maximum diameter of the hole with surface damages and D stands for the nominal diameter of the hole.

Table 1 Experimental results for TSDZ

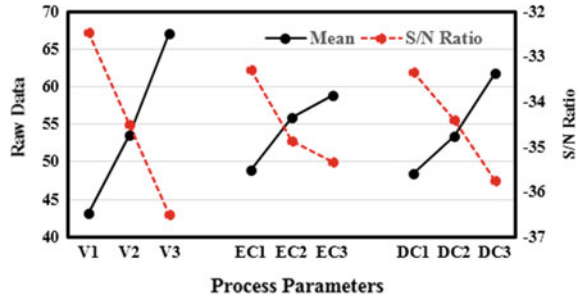
S. No.	Voltage (V)	Electrolyte concentration (%)	Duty cycle (%)	TSDZ (mean) (μm)	S/N ratio
1	50	20	60	30.25	-29.6145
2	50	30	70	45.67	-33.1926
3	50	40	80	53.56	-34.5768
4	60	20	70	45.78	-33.2135
5	60	30	80	60.78	-35.6752
6	60	40	60	53.98	-34.6447
7	70	20	80	70.89	-37.0117
8	70	30	60	61.23	-35.7393
9	70	40	70	68.94	-36.7694

**Fig. 2** Optical image for a description of maximum and the nominal diameter of the hole

3 Results and Discussions

The behaviour of input parameters such as applied voltage, electrolyte concentration and duty cycle on the thickness of surface damage zones (TSDZ) is presented in Fig. 3. It is concluded that the TSDZ increases with the increase of applied potential. The TSDZ increases from 43.16 to 67.02 μm with the rise in applied potential from 50 V (V1) to 70 V (V3). The higher voltage of the ECDM process boosts the spark intensity and generates an excess amount of thermal energy in the machining regime.

Fig. 3 The behaviour of process parameters on TSDZ



The excess thermal energy tends to produce heat-affected area around the periphery of the hole. The excess heat conducted to composite material produces uneven streaks on the surface of the machined sample, as shown in Fig. 4. Moreover, the TSDZ is more severe in CFRP composite material due to low-temperature resistant properties of epoxy. Likewise, the TSDZ significantly increases with the increase of electrolyte concentration of ECM process. The TSDZ increases from 48.97 to 58.82 μm with an increase in the concentration of electrolyte from 20% (EC1) to 40% (EC3). The higher concentration of electrolyte promotes the kinetics of electrochemical reactions and causes ECM action is more dominating in the machining of ECM. The

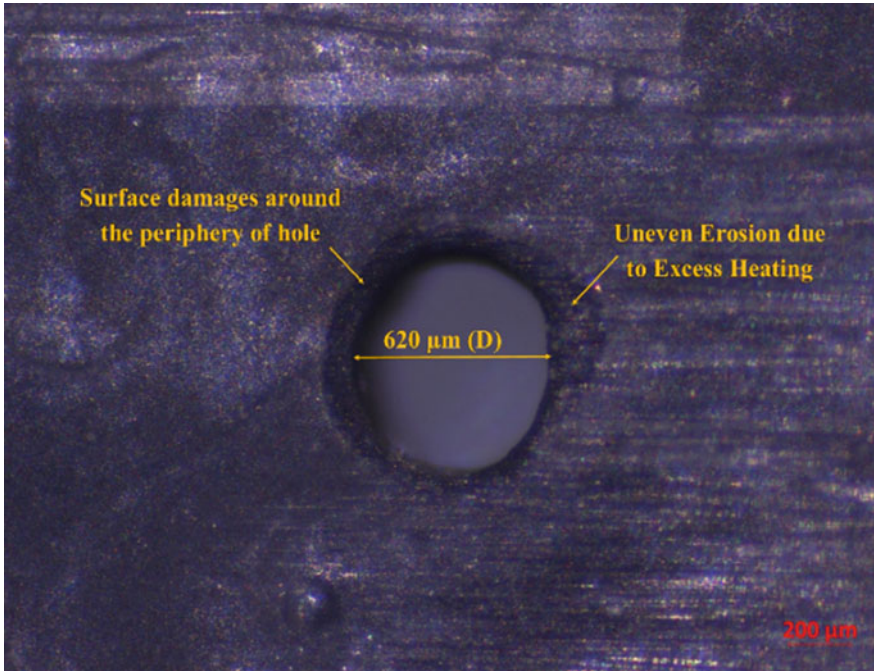


Fig. 4 Optical image of a micro-hole machined using ECM

stepped-up electrochemical reactions produce intense heat in the machining zone. The generated heat is transferred to surrounding of machined hole and electrolyte by convection. Therefore, the transferred heat is responsible for uneven burn, surface damages and HAZs around the machined hole.

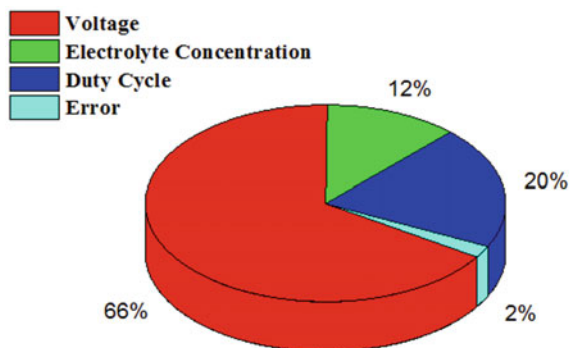
The TSDZ dominantly increases with the rise of the duty cycle of the ECDM process. TSDZ increases from 48.48 to 61.74 μm with an increase of duty cycle from 60% (DC1) to 80% (DC3). The duty cycle is incorporated to promote the cooling of machining products and electrolyte solution during the machining mechanism. At higher duty cycle, i.e. 80%, the time for cooling of machining products and the electrolyte solution is minimum. Therefore, the excess heat generated during machining is transferred to machined sample and produces uneven melting and HAZs around the periphery of the hole. On the other hand, at a low duty cycle, i.e. 60%, the excess heat generated is cooled down due to the availability of a long time for the next spark to have occurred. Therefore, the low duty of ECDM process produces better quality machined surface with least TSDZ.

According to S/N ratio, the optimal process parameters for TSDZ have applied voltage of 50 V (V1), the concentration of electrolyte, i.e. 20% (EC1) and duty cycle of 60% (DC1). The analysis of variance (ANOVA) for TSDZ is represented in Table 2 and concluded that TSDZ is dominantly affected by the applied voltage and followed by duty cycle and electrolyte concentration. The statistical analysis of input parameters on TSDZ is presented in Fig. 5. These results are justified from previous

Table 2 Analysis of variance for TSDZ

Source	DF	Adj SS	Adj MS	F value	P-value	% contribution
Voltage	2	858.92	429.4	36.55	0.027	66
Electrolyte concentration	2	153.58	76.79	6.54	0.133	12
Duty cycle	2	269.06	134.53	11.45	0.080	20
Error	2	23.50	11.75			2
Total	8	1305				

Fig. 5 Statistical analysis of process parameters on TSDZ



research in machining behaviour of the epoxy-based composite using ECDM process [10].

4 Conclusions

The conclusions explored from the findings of the present research problem were observed as

- The thickness of the surface damaged zone (TSDZ) during ECDM of CFRP composite was significantly affected by an applied voltage, electrolyte concentration and duty cycle of the ECDM process.
- The micro-images of machined hole signify the presence of TSDZ and uneven erosion of material around the periphery of the hole.
- The optimal process parameters for TSDZ have applied voltage of 50 V, concentration of electrolyte, i.e. 20% and duty cycle of 60%.
- The ANOVA analysis of TSDZ reveals the percentage contribution of applied voltage of 66%, duty cycle of 20%, electrolyte concentration of 12% and an error of 2%.
- The ECDM process is an imperious machining process for micro-machining of polymer matrix-based composites.

Acknowledgements The authors highly acknowledge the Science and Engineering Research Board (SERB), DST, Govt. of India, New Delhi, India, for providing the financial support under this work grant no. EMR/2016/005352.

References

1. Mehrabi F, Farahnakian M, Elhami S, Razfar MR (2018) Application of electrolyte injection to the electrochemical discharge machining (ECDM) on the optical glass. *J Mater Process Technol* 255:665–672. <https://doi.org/10.1016/j.jmatprotec.2018.01.016>
2. Singh M, Singh S (2019) Electrochemical discharge machining: a review on preceding and perspective research. *Proc Inst Mech Eng Part B: J Eng Manuf* 233(5):1425–1449. <https://doi.org/10.1177/0954405418798865>
3. Wuthrich R, Hof LA, Lal A, Fujisaki K, Bleuler H, Mandin P, Picard G (2005) Physical principles and miniaturization of spark assisted chemical engraving (SACE). *J Micromech Microeng* 15(10):S268. <https://doi.org/10.1088/0960-1317/15/10/S03>
4. Chak SK, Rao PV (2008) The drilling of Al₂O₃ using a pulsed DC supply with a rotary abrasive electrode by the electrochemical discharge process. *Int J Adv Manuf Tech* 39(7–8):633–641. <https://doi.org/10.1007/s00170-007-1263-x>
5. Liu JW, Yue TM, Guo ZN (2013) An analysis of the discharge mechanism in electrochemical discharge machining of particulate reinforced metal matrix composites. *Int J Adv Manuf Tech* 68(9–12):2349–2357. <https://doi.org/10.1016/j.ijmachtools.2009.09.004>
6. Sundaram M, Chen YJ, Rajurkar K (2019) Pulse electrochemical discharge machining of glass-fiber epoxy reinforced composite. *CIRP Ann.* <https://doi.org/10.1016/j.cirp.2019.04.113>

7. Kang X, Tang W (2018) Micro-drilling in ceramic-coated Ni-superalloy by electrochemical discharge machining. *J Mater Process Technol* 255:656–664. <https://doi.org/10.1016/j.jmatprotec.2018.01.014>
8. Singh M, Singh S, Kumar S (2019) Experimental investigation for generation of micro holes on silicon wafer using electrochemical discharge machining process. *Silicon* 1–7. <https://doi.org/10.1007/s12633-019-00273-8>
9. Gupta PK, Debnath K (2019) Electrochemical discharge machining of glass fiber-reinforced epoxy composites: a challenging approach. *J Phys IOP Publ Conf Ser* 1240(1):012044. <https://doi.org/10.1088/1742-6596/1240/1/012044>
10. Sabahi N, Razfar MR (2018) Experimental study on the heat-affected zone of glass substrate machined by electrochemical discharge machining (ECDM) process. *Int J Adv Manuf Tech* 95(1–4):643–657. <https://doi.org/10.1007/s00170-018-2027-5>

Influence of Parameters on Powder Mixed Electric Discharge Machining of EN-31 Tool Steel



Sharanjit Singh and Pawan Kumar Rakesh

1 Introduction

EDM is a process which is broadly used to work on the conductive materials irrespective of their toughness and hardness. It is specially employed for a generation of intricate shapes in moulds and dies, which are else tough to produce with other normal machining processes. EDM can machine the hard material like tool steels. But its lower MRR and lower surface finish affect its applications. In past years, to enhance the capabilities of EDM, a fine powder (silicon carbide, aluminium, copper or chromium, etc.) is put in the dielectric oil of EDM [1, 2]. This process is familiar with the name of powder mixed EDM (PMEDM). In PMEDM, powder is mixed into dielectric oil up to some known level, which will affect the capability of the EDM process. When the electrically conductive powder is added to dielectric oil, the method behaves more stable due to lower insulating provided by dielectric oil. Therefore, there is an improvement in MRR and surface finish and a reduction in tool wear rate (TWR). The influence of materials (impurities) like (iron, carbon, copper and aluminium) in dielectric oil used in EDM was investigated by Erden and Bilgin [3]. They concluded that the MRR rises with the rise in the concentration of the powder because of lower time lag. It was also found with the application of graphite, and aluminium powder in dielectric oil demonstrates more enhancement in the surface finish of parts than presented with the use of Si powder [4]. The mixing of metallic powder into dielectric oil enhances the gap distance from 25 to 50 μm to larger value. When the voltage range reaches 80–340 V between tool and workpiece, then

S. Singh (✉)

Department of Mechanical Engineering, DAV University Jalandhar, Punjab 144001, India
e-mail: malhi.sharanjit@gmail.com

P. K. Rakesh

Department of Mechanical Engineering, National Institute of Technology, Uttarakhand, Srinagar (Garhwal), Uttarakhand 246174, India
e-mail: pawanrakesh@nituk.ac.in

the electric field ranges will be between 105 and 107 V/m. It energizes the powder particles and starts moving in a zigzag motion. The metal particles come closer and arrange themselves in clusters under the sparking area. Electric forces arrange these particles in the form of chains at many locations in the sparking zone. The bridging effect is created that disperses the discharge in several trajectories. Insulating strength and gap voltage are also lower because of the bridging effect. Now with one input impulse generates several discharge trajectories/spot, which enhances surface finish and MRR of the parts [5].

2 Literature Review

In the previous years, comparatively limited work has been published on PMEDM. It was noticed that significant work had been intended to reduce the surface roughness by mixing the powder in dielectric oil [6, 7]. In 1980, Bilgin and Erden examined the MRR for mild steel [3]. They found that the addition of powder (carbon, copper, iron and aluminium) improves the breakdown strength of the dielectric oil and improves the MRR. It was further noticed that short-circuiting occurs with high powder concentration leads towards instability in the process. Jeswani found the influence of the inclusion of graphite powder into dielectric oil for tool steels [8]. Mohri et al. described the effect of silicon powder for surface finish of die steel [9], and found that parts generated having fine and a corrosion-resistant surface with a roughness value of 2 μm . It was further concluded that under specific circumstances, graphite and aluminium powders yield an enhanced surface finish than the Si powder. The concentration of powder lies between 2 and 15 g/l generates surfaces having Ra value less than 2 μm for graphite and aluminium powder particles.

Further, Kansal et al. also analysed the effect of different parameters using die steel using Si powder mixed dielectric oil [10]. They investigated that the MRR rises with Si powder, current and powder concentration are more influencing factors in the process. Assarzadeh and Ghoreishi studied with the use of Al_2O_3 powder in dielectric oil [11]. It has seen that MRR tends to uprise steadily with a higher value of pulse-on time as well as current. Kobayashi et al. found the influence of dielectric oil containing powder for surface roughness of parts [12]. It is investigated that the surface quality of the workpiece is upgraded with the application of Si powder. Chen and Yan noticed the influence of silicon carbide and aluminium powder on EDM of Ti-6Al-4V and SKD11 [13]. Significant enhancement in MRR is noticed with reduced surface quality. He and Ming concluded that the particles (inorganic oxide and conductive particles) lower the TWR, enhance the MRR and SR of the parts effectively [14]. For titanium alloy, Chow et al. studied that the mixing of Al and SiC particles into the dielectric oil enlarges the gap distance, causing high MRR and debris removal rate [15].

From the above literature review on PMEDM, it is obtained that a limited number of investigations have been presented with the use of Si powder in dielectric oil of

EDM. Hence, the focus of the present work is to examine the effect of different parameters with MRR.

3 Development of Model

All the experiments are conducted in machine tool lab having T-3822 EDM set-up fabricated by Electronica India. The tank capacity of the EDM machine accommodates 150 L dielectric oil. It requires a huge quantity of powder for mixing it in dielectric oil, which increases the wastage of kerosene oil as well as metal powder. Therefore, additionally developed circulation system is used for experimentation. According to the requirements, this experimental set-up designed and fabricated in the laboratory for PMEDM, as shown in Fig. 1. We divide the machining tank into subpart by placing a transparent glass sheet in it. This new machining set-up has a capacity of 20 L of dielectric oil for experimentation. A workpiece holding device is employed in the machining tank for holding the workpiece. The tank is filled up with powder mixed dielectric oil. The stirring system is used to keep circulation powder particles in the tank. Machining tank is equipped with a pump as well as a stirrer. To enhance the suspension of powder properly in discharge gap, distance among dielectric suction point and nozzle outlet kept low as possible. Magnetic forces are provided by permanent magnets located in the machining tank to distinct the impurities and debris from the dielectric oil. EN-31 tool steel with a fully annealed condition is taken as the work material having an average hardness of 59 HRC and widely used in ball bearings and valves. A tubular copper electrode having dia. of 10 mm is used as an electrode. The machining is carried out with commercial kerosene oil by mixing silicon powder into it.

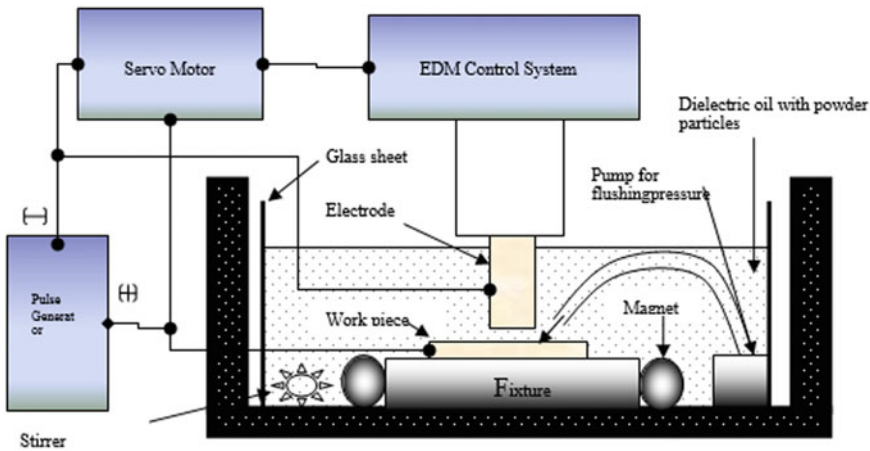


Fig. 1 Block diagram of powder mixed EDM experimental set-up

4 Process Parameters and Experimental Design

To investigate different parameters that affect performance and parts quality produced by PMEDM, cause and effect diagram is created, as shown in Fig. 2.

Table 1 presents the levels of selected parameters. In every test, the MRR is taken by the formula shown below:

$$MRR(mm^3/min) = \text{Total volume removed from the workpiece}/\text{machining time}$$

The experiments are designed to study the influence of parameters viz abrasive size, the concentration of powder, current and pulse-on time for MRR of the process. Response surface methodology is employed for the development of face-centred central composite design (CCD). Total of 30 experiments is performed with four input parameters. The design factors and the response used for the study are presented in Table 2.

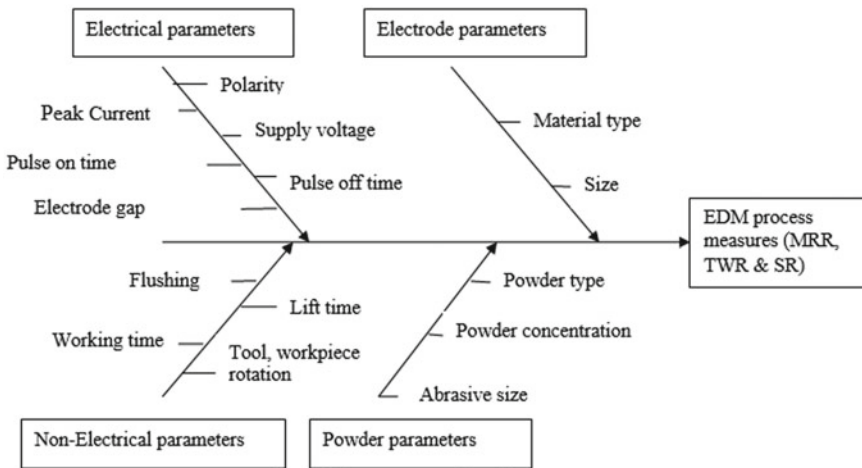


Fig. 2 Ishikawa cause-effect diagram

Table 1 Different experimental settings

S. No.	Fixed parameters	Values	Variable parameters	Range/level
1	Polarity	+ve	Abrasive size (μs)	200, 400, 600
2	Electrode lift time	0.2 s	Conc. of powder (g/l)	2, 3, 4
3	Dielectric flow rate	25/min	Current (A)	6, 8, 10
4	Dielectric pressure	0.5 kg/cm ²	Pulse-on time (μs)	6, 8, 10
5	Machining time	15 min	–	–

Table 2 Experimental design matrix and collected data

S. No.	A	B	C	D	Abrasive size (μs)	Powder conc. (g/l)	Current (A)	Pulse-on time (μs)	MRR
1	1	1	1	1	600	4	10	10	3.31
2	0	-1	0	0	400	2	8	8	1.69
3	-1	1	1	1	200	4	10	10	2.415
4	1	-1	1	1	600	2	10	10	2.38
5	1	0	0	0	600	3	8	8	1.99
6	1	-1	-1	1	600	2	6	10	1.62
7	1	1	1	-1	600	4	10	6	1.9
8	-1	-1	-1	-1	200	2	6	6	1.5
9	-1	-1	-1	1	200	2	6	10	1.6
10	0	1	0	0	400	4	8	8	2.2
11	0	0	0	-1	400	3	8	6	1.75
12	0	0	0	1	400	3	8	10	2.1
13	-1	1	1	-1	200	4	10	6	2.1
14	1	-1	-1	-1	600	2	6	6	1.61
15	0	0	0	0	400	3	8	8	1.97
16	0	0	0	0	400	3	8	8	1.96
17	0	0	-1	0	400	3	6	8	1.6
18	1	1	-1	-1	600	4	6	6	1.57
19	0	0	0	0	400	3	8	8	1.94
20	-1	1	-1	-1	200	4	6	6	1.4
21	0	0	0	0	400	3	8	8	1.97
22	0	0	0	0	400	3	8	8	1.96
23	-1	-1	1	1	200	2	10	10	1.6
24	-1	0	0	0	200	3	8	8	1.89
25	1	-1	1	-1	600	2	10	6	1.98
26	-1	1	-1	1	200	4	6	10	1.57
27	0	0	1	0	400	3	10	8	2.3
28	-1	-1	1	-1	200	2	10	6	1.91
29	0	0	0	0	400	3	8	8	1.92
30	1	1	-1	1	600	4	6	10	1.7

5 Results and Discussion

5.1 Analysis of Variance

ANOVA for MRR on collected data has been performed to check the significance of the generated model and its coefficients. The 2FI model was used to fit the data appropriately. As seen in Table 3, the F-value of a model (16.52) implies the model is significant. In this model, A, B, C, D, AD, BC, BD, CD are significant terms. The final model, in coded factors, is presented by the following second-order polynomial Eq. (1):

$$\begin{aligned} \text{MRR}(\text{mm}^3/\text{min}) = & 1.91 + 0.12A + 0.13B + 0.32C + 0.14D \\ & + 0.12BC + 0.11BD + 0.088CD \end{aligned} \tag{1}$$

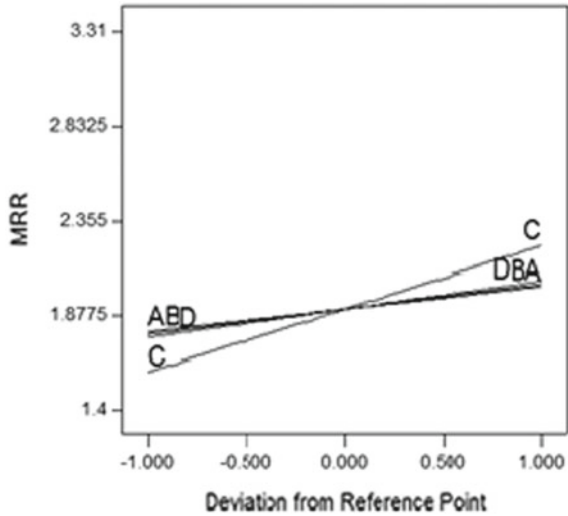
In terms of actual factors, the relationship between MRR and parameters is presented in second-order polynomial Eq. (2):

$$\begin{aligned} \text{MRR}(\text{mm}^3/\text{min}) = & 1.91350 + 0.11528A + 0.12639B + 0.31806C + 0.14306D \\ & + 0.10469AD + 0.12156BC + 0.11406BD + 0.87813CD \end{aligned} \tag{2}$$

Table 3 ANOVA of the model after backward elimination

Source	Sum of squares	DF	Mean square	F value	Prob > F	
Model	3.46	8	0.43	16.52	<0.0001	Significant
A	0.24	1	0.24	9.14	0.0065	
B	0.29	1	0.29	10.99	0.0033	
C	1.82	1	1.82	69.58	<0.0001	
D	0.37	1	0.37	14.08	0.0012	
AD	0.18	1	0.18	6.7	0.0171	
BC	0.24	1	0.24	9.03	0.0067	
BD	0.21	1	0.21	7.95	0.0102	
CD	0.12	1	0.12	4.71	0.0415	
Residual	0.55	21	0.026			
Lack of fit	0.55	16	0.034	88.52	< 0.0001	significant
Pure error	1.93E-03	5	3.87E-04			
Cor total	4.01	29				
Std. dev.	0.16				R-squared	0.8629
Mean	1.91				Adj R-squared	0.8107
C.V.	8.45				Pred R-squared	0.4853
Press	2.06				Adeq precision	19.554

Fig. 3 Perturbation plot for MRR



5.2 Influence of Input Variables on MRR

The generated chart as in Fig. 3 displays the comparative effects of all independent parameters on MRR in a specific pattern as the level of one parameter is changed, avoiding the change in the level of other parameters.

The perturbation plot displays the response of each parameter level. Figure 3 shows the effect on MRR with a change in the size of silicon particle present into the dielectric oil. When the size of particles increases from 200 to 600 μs , the MRR also increases. An increase in MRR from workpiece is due to high bridging effect (number of discharges) among them. Further, the difference in abrasive powder concentration also shows a variation towards MRR. The increase in the concentration of power from the lower level to high level MRR increases continuously. From this trend, it is observed that the addition of an appropriate quantity of powder in the dielectric oil of EDM causes higher erosion of the metal because the breakdown strength of the dielectric oil lowers due to conductive powder particles suspended into dielectric oil. The spark gap increases result in broader discharge routes. The particles in powder get energized and occur in a zigzag motion. The particles gather in a cluster in spark zone. These particles bridge the discharge gap between work and electrode. Due to this, discharge is dispersed in several increments (discharging frequency increases), and therefore, MRR increases.

Further in this plot, the change in the level of electric current also shows a variation in MRR. It is observed that when current increases from a low level towards a higher level, the MRR gradually increases. This is because the current directly relates to the input energy, with an increase in current, the energy provided by every pulse in the spark gap zone also increases, which leads to bust up the movement of ions towards electrodes. This increases in discharge result in the high frequency of sparking in

the gap, MRR rises with a rise in current. Next, with a rise in pulse-on time, MRR also enhanced. This can be endorsed to the fact that a long pulse span causes more vaporization on the workpiece surface and results in higher MRR.

The effect and interaction between variables can be visualized with interaction and 3D surface plots shown in Fig. 4. Parallel lines in this graph show no interaction, but the increase in the departure of lines from the parallel trend means a high degree of interaction. The first plot presents the interaction between abrasive size and pulse-on time. It is observed that there is a strong interaction between these parameters at a higher level. Same interaction also was seen between abrasive concentration and current as well as abrasive concentration and pulse-on time at a higher level. Further, in case of interaction plot between current and pulse-on time, higher MRR is obtained when the level of both parameters increases.

6 Optimization

In optimization, the most suitable set of selected parameters are obtained for maximum MRR. For this, all parameters are selected within range, and MRR is set at maximum. The number of conditions possessing peak desirability value is set as an optimum situation for the compulsory output. As shown in Table 4, the optimum MRR is achieved when abrasive size is 200 μs , abrasive concentration is 2 g/l, the current is 8A, and pulse-on time is 6 μs , with desirability function value of 0.5. Confirmation experiments are performed to test the generated model; the MRR value 1.84 is obtained, which shows that the generated model can be used for machining.

7 Conclusion

It is found that EDM a promising machining process for machining and generating preferred accuracy from EN-31 tool steel. The addition of powder into the dielectric oil of EDM enhances machining rates. The outcome of this work identifies the significant effects of variables on the Si powder in the dielectric oil to obtain maximum MRR from EN-31 tool steel. Following are the conclusions made:

- Current, abrasive size, the concentration of the powder and pulse-on time significantly affect the MRR in PMEDM.
- MRR enhanced with a rise in the abrasive size, abrasive concentration and pulse-on time.
- Current is the key influential parameter for causing MRR as its level progresses for low level towards high level.
- The presence of Si powder into the dielectric oil of EDM significantly increases MRR because silicon powder creates more discharge between the electrode

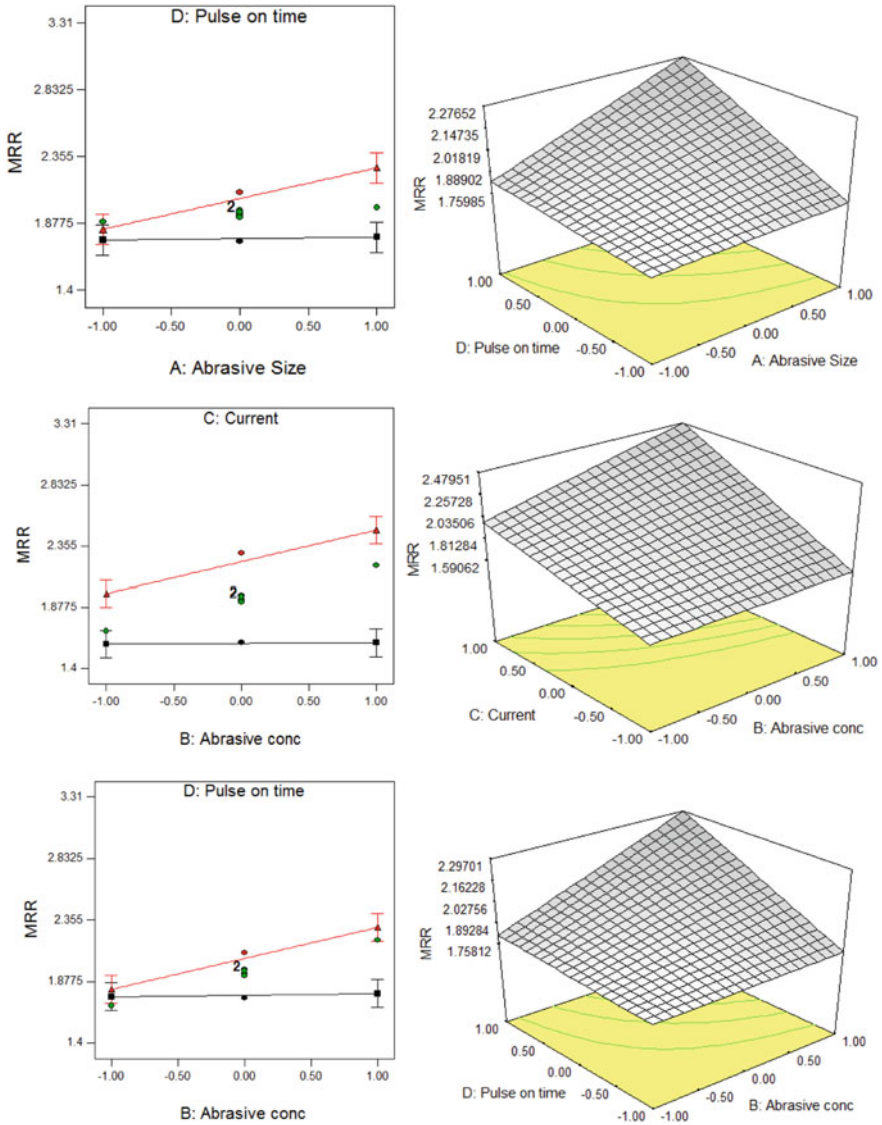


Fig. 4 Interaction and 3D response surface plot for MRR and abrasive size versus pulse-on time; abrasive concentration versus current; abrasive concentration versus pulse-on time; current versus pulse-on time

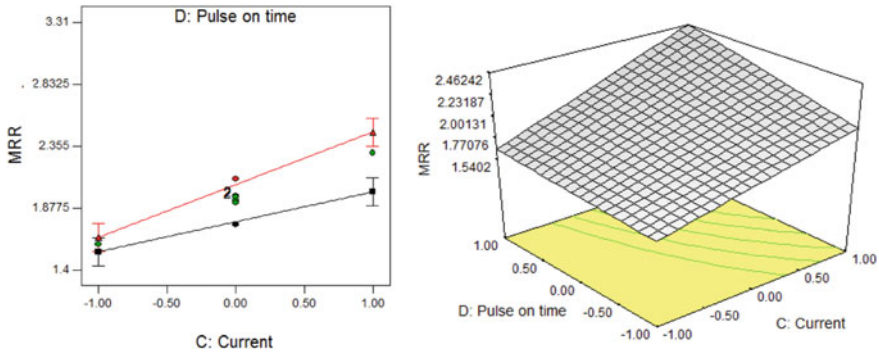


Fig. 4 (continued)

Table 4 Optimization results for minimizing

S. No.	Abrasive size	Abrasive Conc	Current	Pulse-on time	MRR	Desirability
1	-0.99	-1	1	-0.95	1.85691	0.511
2	-1	-1	0.98	-0.83	1.85573	0.508
3	-1	-1	1	-0.62	1.86045	0.505
4	-1	-1	1	-0.56	1.86162	0.503
5	-0.74	-1	1	-1	1.85876	0.484
6	1	1	-1	0.96	1.97785	0.466
7	-1	-0.73	1	-1	1.89237	0.466
8	1	1	-0.88	1	2.05244	0.464
9	1	1	-0.65	1	2.17227	0.449
10	1	0.99	0.93	1	3.00536	0.423

compressive action of tool which will cause the material to flow plastically from the peaks to fill the valleys of the surface.

References

1. Wong YS, Lim LC, Tee RI (1998) Near mirror finish phenomenon in EDM using powder mixed dielectric. *J Mater Process Tech* 79:30–40
2. Zhao WS, Meng QG, Wang ZL (2002) The application of research on powder mixed EDM in rough machining. *J Mater Process Tech* 129:30–33
3. Erden A, Bilgin S (1980) Role of impurities in electric discharge machining. In: *Proceedings of the 21st international machine tool design and research conference*. Macmillan, London, pp 345–350
4. Uno Y, Okada (1997) A surface generation mechanism in electrical discharge machining with silicon powder mixed oil. *Int J Electro-Mech* 13–18

5. Chow HM, Yan BH, Huang FY, Hung JC (2000) Study of added powder in kerosene for the micro-slit machining of titanium alloy using electro-discharge machining. *J Mater Process Tech* 101:95–103
6. Kansal HK, Singh S, Kumar P (2007) Technology and research developments in powder mixed electric discharge machining (PMEDM). *J Mater Process Tech* 184:32–41
7. Garg RK, Singh KK, Sachdeva A, Sharma VS, Ojha K, Singh S (2010) Review of research work in sinking EDM and WEDM on metal matrix composite materials. *Int J Adv Manuf Tech* 50(5–8):611–624
8. Jeswani ML (1981) Effects of the addition of graphite powder to kerosene used as the dielectric oil in electrical discharge machining. *Wear* 70:133–139
9. Mohri N, Saito N, Higashi MA (1991) A new process of finish machining on free surface by EDM methods. *Ann CIRP* 40(1):207–210
10. Kansal HK, Singh S, Kumar P (2007) Effect of silicon powder mixed EDM on machining rate of AISI D2 die steel. *J Manuf Process* 9:13–22
11. Assarzadeh S, Ghoreishi M (2013) A dual response surface desirability approach to process modelling and optimization of Al_2O_3 powder mixed electrical discharge machining parameters. *Int J Adv Manuf Tech* 64:1459–1477
12. Kobayashi K, Magara T, Ozaki Y, Yatomi T (1992) The present and future developments of electrical discharge machining. In: *Proceedings of 2nd international conference on die and mould technology*. Singapore, pp 35–47
13. Yan BH, Chen SL (1993) Effects of dielectric with suspended aluminum powder on EDM. *J Chin Soc Mech Eng* 14(3):307–312
14. Ming QY, He LY (1995) Powder-suspension dielectric oil for EDM. *J Mater Process Tech* 52:44–54
15. Chow HM, Yang LD, Lin CT, Chen FY (2008) The use of SiC powder in water as dielectric for the micro-slit EDM machining. *J Mater Process Tech* 195:160–170

Joint Design for Adhesive Joining of Sisal/Epoxy Composite Laminates



Kassahun Gashu Melese , Tejas Pramod Naik , Ram Singh Rana , and Inderdeep Singh 

1 Introduction

Natural fiber-based polymer composites have drawn the first-rate appeal due to the fact of low price, environment-friendship, and an opportunity of the alternate synthetic (artificial) fiber-reinforced plastic. Sisal woven mat epoxy composite is a family of natural fiber polymer-based composite; it has higher fiber content for the equivalent performance of artificial fibers, which reduces the amount of more contaminating base polymers [1, 2]. The assembly of structural construction from different components needs some means of joining. In this context, bonding with adhesives has many compensational compared to traditional joining methods, e.g., reduced the concentration of stresses on joined area, increased uniform distribution of stresses, minimized weight, and easy fabricating [3, 4]. Adhesive joining is used for most of the epoxy polymer composite material. Making holes and inserting small Teflon sheet in the adhesively joined area of sisal mat epoxy fibers, it increased the load-carrying capacity of the lap joining. Esteves and Romão [5] studied the joining behavior of adhesively joined sisal-epoxy composite. Sisal fiber was treated with sodium hydroxide (NaOH) solution (4 and 8% w:v) and for two different treatment times (1 and 2 h). Lap joint was made to characterize the joint strength. Treatment of fiber was reported an enhancement of joint strength. Gonzalez-Murillo et al. [6]

K. G. Melese (✉) · T. P. Naik · R. S. Rana · I. Singh
Mechanical and Industrial Engineering Department, Indian Institute of Technology Roorkee,
Roorkee 247667, India
e-mail: kassahun28@yahoo.com

T. P. Naik
e-mail: tejasnit@gmail.com

R. S. Rana
e-mail: ramsingh.mech17@gmail.com

I. Singh
e-mail: inderdeep.singh@me.iitr.ac.in

studied lap shear strength of henequen and sisal fiber-reinforced epoxy composite with three different joint configurations, including single lap joints, intermingled fiber joints, and laminated fiber joints. Joint strength was determined for overlap length varying from 5 to 50 mm. Joint strength of single lap was reported lower than intermingled fiber joints and laminated fiber joints. In laminated fiber joints, joint strength was reached to 92% of plain composite strength. FEM analysis of single lap joints was reported high-value stress generation near the end of the lap joint. Analytical and numerical analyses were showed cohesive failure in adherends. The high quality bonded joint region is very important for the integrity of structures involving composites as unless all the parts are co-cured simultaneously [7, 8].

2 Experimental Investigations

2.1 Materials (Specimen Composition)

The composite specimens used as adherends were fabricated by using the hand layup technique. Hand layup is an open mold process where fiber reinforcements are placed by hand then wet with epoxy resin. Sisal fiber in the woven mat form was used to reinforcement, and the polymer-based epoxy material (Type: LY-556 with hardener HY-951 in the 10:1 ratio Make: Araldite) was used to matrix manufactured and marketed by Huntsman International (India) Pvt. Ltd, Mumbai, India. The matrix and fiber have a density of 1.16 and 1.45 g/cm³, respectively, at room temperature. Sisal fiber in the form of woven fabric was supplied with the aid of the Women's Development Organization (WDO), Dehradun, Uttarakhand, India.

2.2 Mechanical Behavior of Developed Composites

From Table 1, it has shown that the mechanical characterization of pure sisal mat fiber, sisal/epoxy adherend, and the LY-556 pure epoxy adhesive with HY-951 hardener were chosen. The tensile and flexural properties of fiber, adhesive, and adherends tested on the INSTRON 5982 by ASTM D1683, D3039, and D7264, respectively.

2.3 Composite Fabrications

In the current study, as shown in Fig. 1, sisal-epoxy polymer composite material was fabricated by the hand layup method. Four consecutive sisal mat fiber layers had been prepared as per dimensions of mold plate size of 300 × 300 × 4 mm³ was used to make the specimen. The composite specimen contains completely four layers of

Table 1 Tensile and flexural properties of adhesive and adherends

Material	Maximum load (N)	Stress at maximum load (MPa)	Stress at the yield point (MPa)	Modulus (E-modulus) (MPa)	Flexure stress at maximum load (MPa)	Young's modulus (MPa)	Flexure strain (extension) at maximum load (mm/min)
Epoxy LY-556 Hardener HY-951	1747.98	29.13	24.97	4713.69	56.55	4225.58	0.01
Pure Sisal Woven Fiber	2054.72	34.24	33.04	6840.86	–	–	–
Sisal/Epoxy	2197.82	36.63	39.877	8641.18	103.18	8298.71	0.015

Fig. 1 Four layers sisal/epoxy polymer composite by a hand layup fabrication process

the sisal arrangement of fibers. The amount of epoxy is taken for a specific weight fraction of fiber and matrix with mixed the hardeners in the ratio of 10:1 after the woven fibers were wide-open to sunlight for two days.

Figures 2 and 3 show the mechanical properties of sisal-epoxy composite better than the pure epoxy polymer, indicated that making composite by the combination of sisal and epoxy is advantageous for further investigations such as joining.

2.4 Preparation of Single Lap Joints

Preparation of composite specimens as shown in Fig. 4, it is encouraged that a diamond-tipped circular saw wood cutting machine (Make: Dewalt Circular Saw Machine, Type: DW745-KR), that is capable of producing sharp cut edges as per

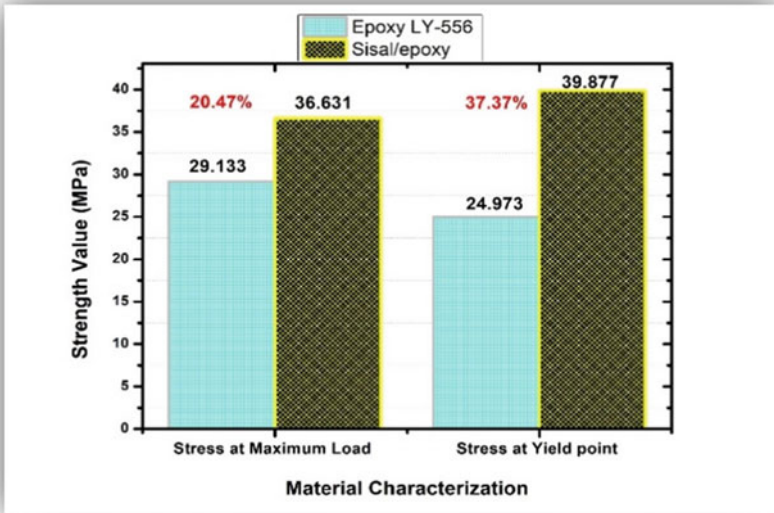


Fig. 2 Sisal/epoxy and pure epoxy stress at maximum load

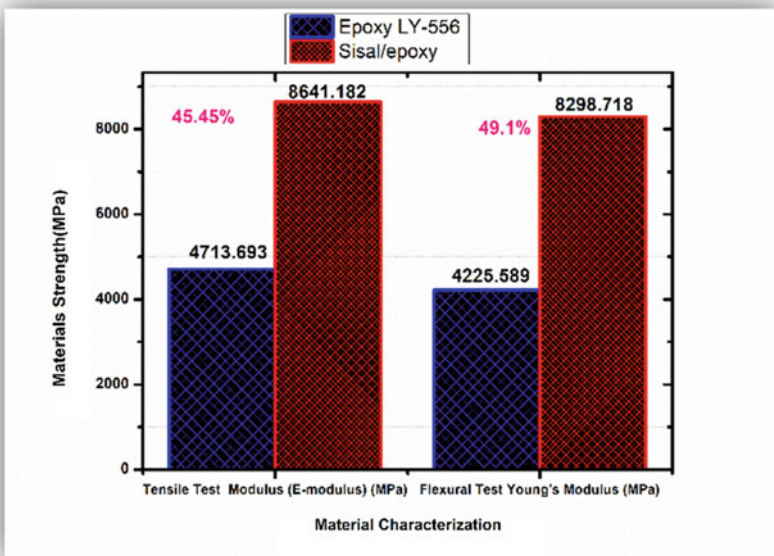


Fig. 3 Sisal/epoxy and pure epoxy tensile and flexural modulus



Fig. 4 Specimens cutting preparation by power circular saw machine

ASTM standard for different testing such as; D3039 for tensile, D7264 for flexural, D3410 compression and D5868 single-lap share testing.

The specimens to be used as adherends were cut from a fabricated composite laminate as per ASTM D5868-01 standard [9]. The ASTM standard dimensions of the composite test specimen are given in Fig. 5. The holes were drilled in the composite adherends as per different configurations at the spindle speed of 1087 rpm with a standard twist drill.

Four types of hole arrangements have been chosen, and the hole diameter used is 2 mm, and the depth of the hole is equal to the adherend thickness (through-hole), as shown in Fig. 5. The standard adhesive joint preparation protocol was adopted for joint preparation before applying the adhesive. All the testing specimens were tested after a curing period of 14 days under room temperature in order to gain the best joint performance [2, 10]. Four types of hole arrangements were drilled out in the joint overlap area in both the adherends. The holes were subsequently filled with adhesive and left for room temperature curing. The adhesive filled in the holes is expected to act as hinged support, capable of resisting forces acting in shear mode. Mechanical behavior of the adhesively joined test specimens was tested using the universal testing machine (UTM, Make: Instron, Type: 5982).

3 Results and Discussion

3.1 Mechanical Properties

As discussed earlier, holes were drilled in the adherends in different arrangements for investigating their influence on the tensile behavior of adhesively bonded composite joints. Figure 6 shows the load–displacement curves of sisal/epoxy with different hole

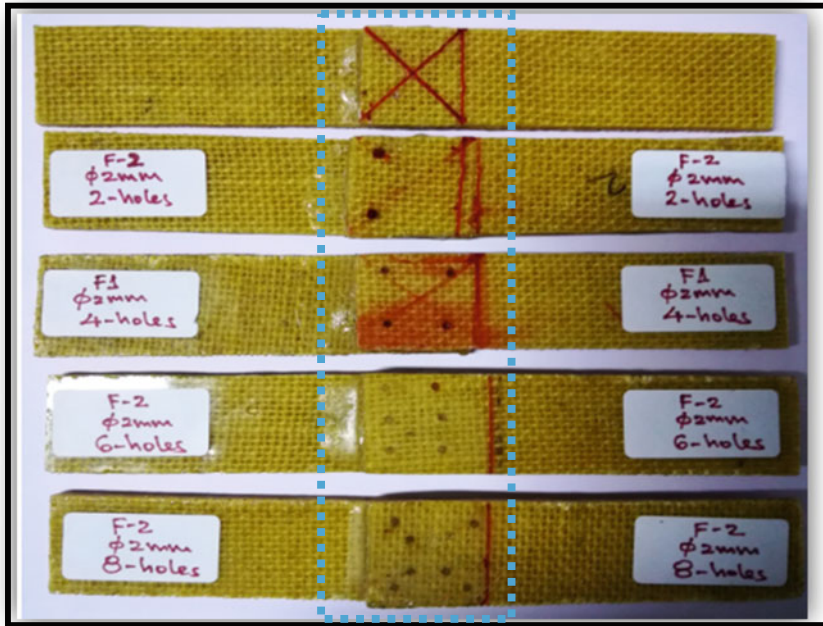


Fig. 5 Single lap adhesive joining of sisal-epoxy composite with four different hole arrangements

arrangements used in the current investigation. The adherends were tested without holes and with four different hole arrangements.

3.2 Sisal/Epoxy Single-Lap Holes Arrangement

The maximum displacement and failure load values after tensile testing are given in Fig. 6 at the load versus displacement curves of sisal-epoxy polymer composite, for eight-hole arrangement. Since the location of the eight holes on the cross diagonal of the joined area and all are symmetric as shown in Fig. 5 and the area percentage covered by the eight holes 10.78% of the total area of the lap joined it can affect the values of load and displacement on the given sisal-epoxy polymer composites, on the other hand, the minimum failure load of 1977 N and a 0.9 mm of elongation observed in six-hole arrangement. These types of holes location arrangements are very helpful for sisal fiber, and it is determined as a load of 2688.8 N and a 1.6 mm elongation. Lap shear strengths as a function of hole arrangement are shown in Fig. 7. This figure represents the result of the maximum shear stress for the different arrangements at different holes in composites. The shear stress in arrangements 2-holes and 6-holes (i.e., 10.90 MPa and 11.09 MPa, respectively) decreased related to pure lap

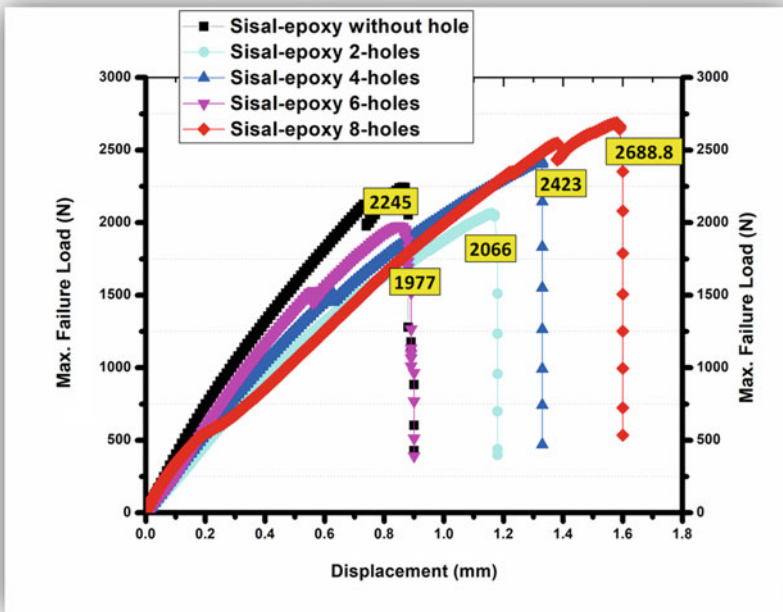


Fig. 6 Load–displacement curves for adhesively bonded joints with different hole arrangements

arrangement of the composite, but it increased at arrangements 4-holes and 8-holes (i.e., 12.06 MPa and 13.65 MPa, respectively). The lowest value of the shear stress of sisal mat composites was observed in the arrangement of 2-hole. The exact location of the four holes is on the parallel edge of the joint area, as shown in Fig. 5. Due to the symmetric arrangements of four and eight-hole, it is known that the failure occurred at the end of the overlapped area [1]. The outcomes of an experimental study making holes have little effect on the failure load of pure lap arrangement; however, there is a positive contribution at 4-holes and 8-holes arrangements.

The morphological structure of the sisal-epoxy mat composites is shown in Fig. 8. The composite samples after the tests have been cut to specified dimensions cleaned properly and mounted cross section-wise on the FE-SEM setup [11]. Among individual types of structural behavior, the matrix cracked without stretching on the surface of the composite, then again because of the applied tensile load, the sisal mat fibers are highly stretching and breakage.

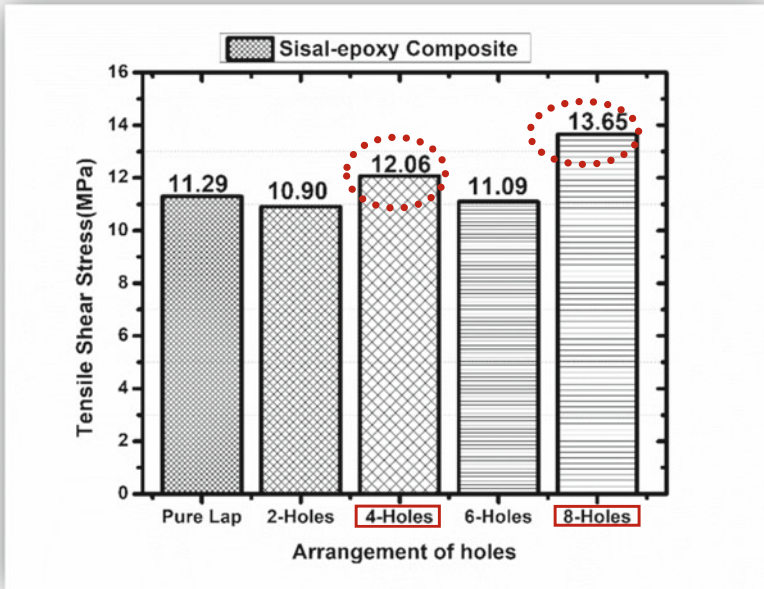


Fig. 7 Tensile shear strengths as a function of sisal-epoxy composite and arrangement of holes

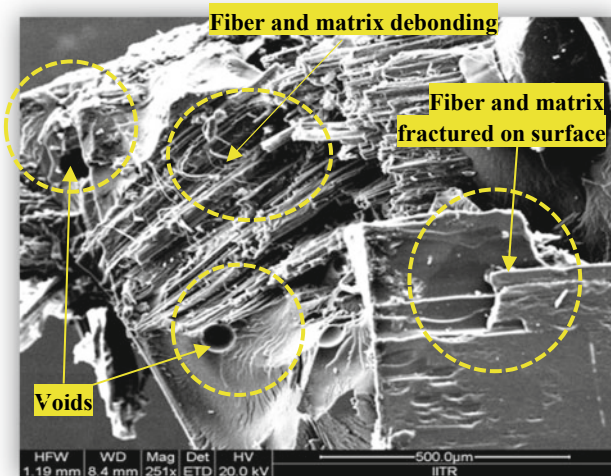


Fig. 8 FE-SEM images of woven sisal-epoxy composites under tensile failure mode methods

4 Conclusions

Based on the experimental investigation on the load-carrying capacity of a single-lap adhesive joint of woven sisal/epoxy composites having performed the tensile and morphological analysis.

The outcomes of this experimental study the following conclusions had been obtained:

- After tensile testing on UTM, it observed almost all a stock-break type of failure, because it created the strong adhesive bonding between the adherends.
- The maximum shear strength and failure load existed at four- and eight-hole arrangements.
- The increment of holes on the lap joint affected the smoothness of the bonded area.
- Symmetric hole arrangements of composite have a quite better adhesive bonding of a single lap joint.
- The FE-SEM images of the tensile fracture surface morphologies of sisal-epoxy composites reveal that relatively fewer fiber breakouts and de-bonding have been detected strong adhesion between matrix and fiber reinforcement.

References

1. Ghanbari E, Sayman O, Pekbey Y, Ozdemir O (2016) Experimental analysis of single-lap composite joints with two different adhesives at various conditions. *J Compos Mater* 50:1709–1715. <https://doi.org/10.1177/0021998315595532>
2. Arikan V, Sayman O (2015) Comparative study on repeated impact response of E-glass fiber reinforced polypropylene and epoxy matrix composites. *Compos Part B: Eng* 83. <https://doi.org/10.1016/j.compositesb.2015.08.051>
3. Campilho RDSG, Fernandes TAB (2015) Comparative evaluation of single-lap joints bonded with different adhesives by cohesive zone modelling. *Proc Eng* 114:102–109. <https://doi.org/10.1016/j.proeng.2015.08.047>
4. Parashar A, Mertiny P (2012) Adhesively bonded composite tubular joints: Review. *Int J Adhes Adhes* 38:58–68. <https://doi.org/10.1016/j.ijadhadh.2012.05.004>
5. Esteves JL, Romão C (2007) Adhesive joints for vegetal natural fibres reinforced composites. In: IV international materials symposium, 2007. international conference proceedings book, materials, FEUP—PORTO—Portugal. https://sigarra.up.pt/reitoria/en/pub_geral.pub_view?pi_pub_base_id=65215
6. Gonzalez-Murillo C, Ansell MP (2010) Co-cured in-line joints for natural fibre composites. *Compos Sci Tech* 70:442–449. <https://doi.org/10.1016/j.compscitech.2009.11.017>
7. Jagadeesh V, Venkatasubbaiah K, Lakshumu Naidu A (2019) Experimental study on mechanical behavior of natural hybrid composites filled with ground nut shell ash. *Mech Mech Eng* 23:218–227. <https://doi.org/10.2478/mme-2019-0029>
8. Rashed H, Islam M, Rizvi F (1970) Effects of process parameters on tensile strength of jute fiber reinforced thermoplastic composites. *J Naval Architect Mar Eng* 3:1–6. <https://doi.org/10.3329/jname.v3i1.923>

9. Jawaid M, Abdul Khalil HPS, Abu Bakar A (2011) Woven hybrid composites: tensile and flexural properties of oil palm-woven jute fibres based epoxy composites. *Mater Sci Eng, A* 528:5190–5195. <https://doi.org/10.1016/j.msea.2011.03.047>
10. Sayman O, Soykok IF, Dogan T (2015) Effects of axial impacts at different temperatures on failure response of adhesively bonded woven fabric glass fiber/epoxy composite joints. *J Compos Mater* 49. <https://doi.org/10.1177/0021998314533598>
11. Tripathi P, Gupta VK, Dixit A (2018) Development and characterization of low cost jute, bagasse and glass fiber reinforced advanced hybrid epoxy composites. *AIMS Mater Sci* 5:320–337. <https://doi.org/10.3934/MATERSCI.2018.2.320>

Product Development

Influence of Different Tool Profiles and Process Parameters on Mechanical Properties of Dissimilar AA6061 and AA7075 Aluminium Alloys by Friction Stir Welding



Rajeev Rana, D. B. Karunakar, and Anish Karmakar

1 Introduction

Aluminium (Al) alloys can be classified into two broad categories: wrought Al (having less than 4% alloying element composition) and cast Al alloys (having greater than 22% alloying element composition) [1]. Eight different grades of cast Al alloys are available. Two common series of cast Al alloys are 6xxx series has Si and Mg, and 7xxx series has zinc as their main alloying element. Both aluminium alloys series are heat treatable. AA6061 is extensively used for structure, marine and architectural applications. AA7075 is frequently used for aerospace applications due to its higher weight to strength ratio.

The joining of dissimilar aluminium alloys by friction stir welding (FSW) has attracted more attention mainly in automotive, aerospace, marine and structure applications as it could be used only one of the more expensive alloys [2]. It is very difficult to make dissimilar welded joints of AA6061 and AA7075 alloys using conventional welding processes due to the susceptibility of weld defects formation as it formed porosity and cracks [3]. FSW seems to be a new and attractive solid-state joining technique that developed rapidly because of several benefits as compared to fusion welding processes. Figure 1 shows a schematic of the FSW process. FSW includes friction and adiabatic heating, plastic deformation and solid-phase diffusion. It is eco-friendly and energy-efficient technique.

R. Rana · D. B. Karunakar (✉)

Department of Mechanical and Industrial Engineering, Indian Institute of Technology Roorkee, Roorkee 247667, Uttarakhand, India
e-mail: benny.karunakar@me.iitr.ac.in

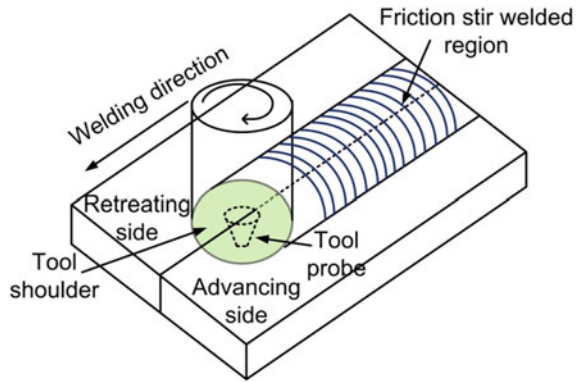
R. Rana

e-mail: rajeevrana027@gmail.com

A. Karmakar

Department of Metallurgical and Materials Engineering, Indian Institute of Technology Roorkee, Roorkee 247667, Uttarakhand, India

Fig. 1 Schematic of FSW process



In 1991, FSW was introduced the first time at The Welding Institute (TWI). FSW used to join high-strength aluminium alloys below their melting temperatures [4]. FSW process is also used to join non-weldable Al alloys, which are difficult to join by other fusion welding processes due to problems of hot cracking and poorly solidified microstructure [5]. The tool pin profile and process parameters are the most influencing factors that change the quality of welded joints and their mechanical properties [6]. The welding speed and tool rotational speed have less effect on tensile strength of A3019 FSW welded joint rather than vertical force [7]. The threaded tool probe formed defect-free weld joints and allowed better material mixing behaviour as well as better tensile strength for dissimilar FSW joints of Al alloys [8]. In this study, the effect of tool probe geometry and influence of tool travel speed has been examined on dissimilar FSW joints of AA6061 and AA7075 Al alloys. Further, microstructural behaviour, defect behaviour in the nugget zone and mechanical properties have been examined.

2 Experimental Procedure

To make dissimilar welded joints, the 6 mm thick plates of AA7075 and AA6061 Al alloys were utilized. The compositions of as-received base materials were analysed using optical emission spectrometers, as depicted in Table 1. FSW process was used to make dissimilar joints. The details process parameters are depicted in Table 2.

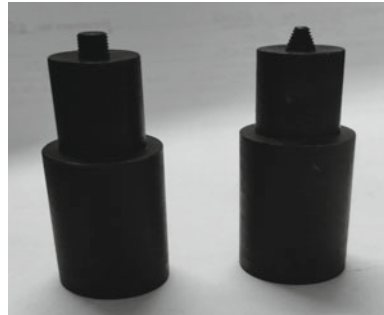
Table 1 Chemical compositions of base alloys

Elements	Si	Fe	Cu	Mn	Mg	Cr	Zn	Al
AA7075	0.04	0.11	1.70	0.62	2.41	0.18	5.61	Balance
AA6061	0.60	0.70	0.25	0.14	1.0	0.16	0.23	Balance

Table 2 FSW process parameters

Rotational speed (rpm)	664	708
Welding speed (mm/min)	20	30
Tool tilt angle	2°	2°

Fig. 2 Photograph of the welding tool



The welding has been performed along the joint line of butt plates whose dimensions were 150 mm × 50 mm × 6 mm.

A 10 kN vertical downward force was applied at the time of welding. AA6061 plate was placed on the advancing side because mixing the material is much more operative. AA7075 was positioned on the retreading side.

The FSW process starts with designing of FSW tool, which would fix on modified vertical milling machine shank (FSW machine). Initially, FSW tool geometry was designed in a simpler way having a cylinder-shaped tool probe. The tool shank diameter and shoulder diameter were designed as 24.8 mm and 20 mm, respectively. The pin diameter and length were taken as 6 and 5.9 mm. Figure 2 shows two different tool geometries.

The generated forces were high during tool penetration with a cylindrical shape pin. The defect in the form of the tunnel was detected with cylindrical shape pin geometry, and heat generation was also high. To reduce friction, heat and penetration force, the probe diameter has been changed to a tapered threaded probe having 6 mm bigger dia. and 3 mm smaller diameter. This designed tool resulted in a defect-free nugget zone with decreased forces. The designed tapered threaded tool had shank dia. of 24.8 mm, shoulder dia. of 20 mm, bigger probe dia. of 6 mm, smaller probe dia. of 3 mm and probe length of 5.9 mm.

In order to characterize the welded specimens for optical microscope (OM), standard metallographic techniques were used. Initially, samples were polished using silicon carbide papers up to grit size of 2500. After paper polishing, specimens were cloth polished with MgO powder. The samples were etched in modified Keller’s reagent for 8–20 s. The microhardness measurement of welded specimens was carried with Vicker’s hardness tester across the centreline at the load of 100 g with 10 s of

dwel time. Flat sub-size tensile samples were made transversely as per the ASTM-E8 standard. Instron-5982 was utilized for tensile tests with 1 mm/min of cross-head speed.

3 Results and Discussion

3.1 Microstructure Analysis

The optical micrographs of as-received AA6061 and AA7075 alloy are shown in Fig. 3(a and b), respectively. These base alloy micrographs will be used into the account to evaluate the welding parameters effect on the microstructure change in nugget zone (NZ).

Figure 4a shows an optical micrograph of NZ welded at lower heat input (tool rotation speed of 664 rpm and welding speed of 20 mm/min) using a cylindrical threaded tool probe. A triangular-shaped tunnel defect is identified in the centre of NZ. The tunnel defect occurs when the material flow around the tool probe is not adequate. The material flow is governed by the tool probe geometry, heat input and vertical force applied during the FSW process. The optical micrograph of NZ welded at higher heat input (tool rotation speed of 708 rpm and welding speed of 30 mm/min) using a tapered threaded tool probe, as shown in Fig. 4b. Defect-free NZ is identified with increased heat input.

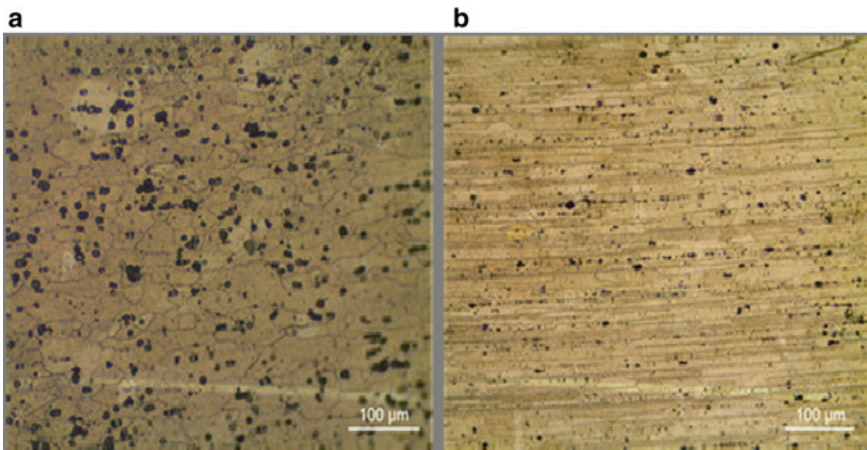


Fig. 3 Optical micrographs of the base alloy: **a** AA6061, **b** AA7075

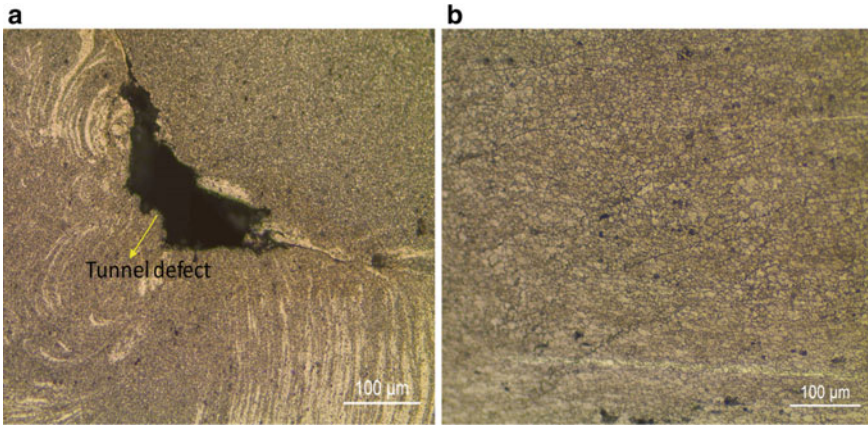


Fig. 4 Optical micrograph of the NZ welded at **a** tool rotation speed 664 rpm and welding speed of 20 mm/min, **b** tool rotation speed of 664 rpm and welding speed of 30 mm/min

Table 3 Tensile properties of dissimilar welded joints

Welding speed (mm/min)	YS (MPa)	UTS (MPa)	TE (%)	Joint efficiency	Failure location
20	112 ± 8	170 ± 10	7 ± 4	58	NZ
30	151 ± 7	230 ± 11	9 ± 5	78	HAZ_6061

3.2 Tensile Test

The ultimate tensile strength (UTS), yield strength (YS), total elongation, joint efficiency and failure locations are depicted in Table 3.

Both YS and UTS were increased due to a defect-free region in NZ with increased heat input, as shown in Fig. 5. The fracture location of sample welded with lower heat input and a cylindrical threaded tool probe is identified as NZ. In higher heat input FSW welded joints, the fracture location shifted to HAZ of softer AA6061 alloy side due to the coarsening of precipitates. The weakening of HAZ due to precipitate coarsening is already reported [9].

3.3 Microhardness Test

Figure 6 shows the Vicker’s microhardness variation of a cross section of dissimilar AA6061 and AA7075 welded joints produced under different process parameters. Both dissimilar welded joints revealed an inevitable decrease in microhardness of corresponding HAZs as compared to their corresponding parent metal. The moderately lower hardness has found in the HAZs of both Al alloys due to precipitates

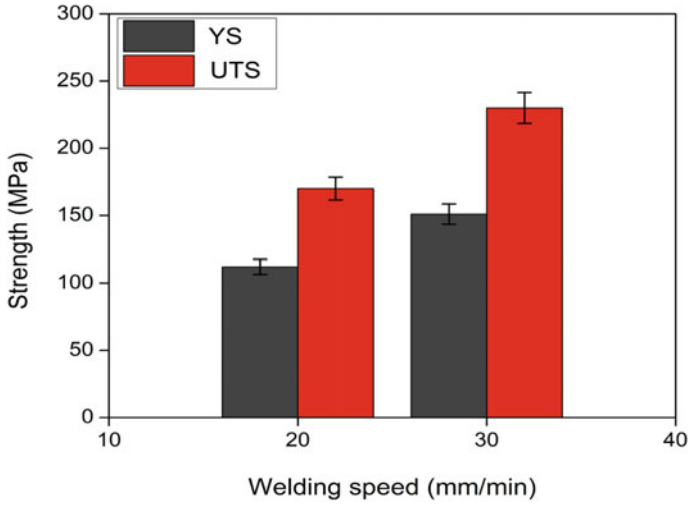


Fig. 5 Variation of YS and UTS of dissimilar AA6061 and AA7075 welded sample with different process parameters

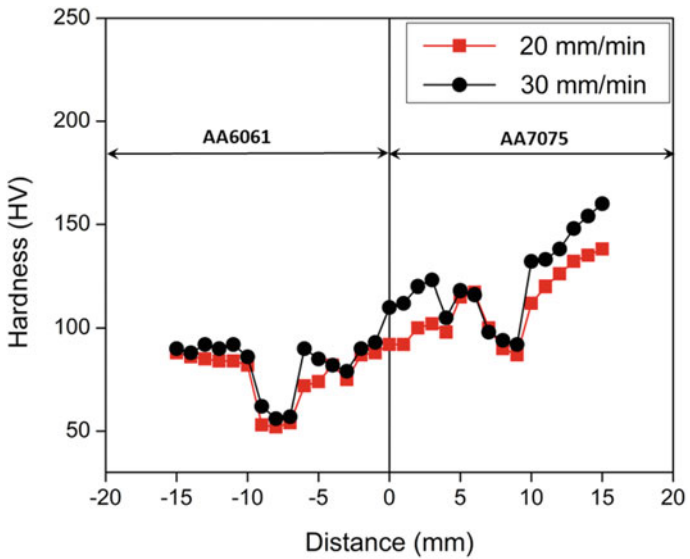


Fig. 6 Vicker's microhardness measurements at the cross section of dissimilar AA6061 and AA7075 welded joints

coarsening (like over-ageing process) and vanishing of GP (Guinier–Preston) zones [10].

4 Conclusion

The following conclusion could be drawn

- AA6061 and AA7075 aluminium alloys were successfully joined defect-free using friction stir welding with higher heat input and tapered threaded tool probe.
- A tunnel defect was observed due to insufficient material flow and less heat input.
- Both YS and UTS were enhanced due to the defect-free region in the NZ with increased heat input and tapered threaded tool probe.
- Both dissimilar welded joints show a decrease in microhardness of HAZs as compared to their corresponding parent metal.

References

1. Davoodi A, Esfahani Z, Sarvghad M (2016) Microstructure and corrosion characterization of the interfacial region in dissimilar friction stir welded AA5083 to AA7023. *Corros Sci* 107:133–144
2. Guo JF, Chen HC, Sun CN, Bi G, Sun Z, Wei J (2014) Friction stir welding of dissimilar materials between AA6061 and AA7075 Al alloys effects of process parameters. *Mater Des* 56:185–192
3. Sinhmar S, Dwivedi DK (2017) 2018 “A study on corrosion behaviour of friction stir welded and tungsten inert gas welded AA2014 aluminium alloy”. *Corros Sci* 133(August):25–35
4. Pouget G, Reynolds AP (2008) Residual stress and microstructure effects on fatigue crack growth in AA2050 friction stir welds. *Int J Fatigue* 30(3):463–472
5. Fresnel RA, Cedex M (2008) Methodology for qualifying a friction stir welding equipment. In: 7th international symposium on friction stir welding—Awaji Island, May, pp 20–22
6. Raturi M, Garg A, Bhattacharya A (2019) Joint strength and failure studies of dissimilar AA6061-AA7075 friction stir welds: Effects of tool pin, process parameters and preheating. *Eng Fail Anal* 96:570–588
7. Kumar S, Kumar S, Kumar A (2013) Optimization of process parameters for friction stir welding of joining A6061 and A6082 alloys by Taguchi method. *Proc Inst Mech Eng Part C J Mech Eng Sci* 227(6):1150–1163
8. Ilangovan M, Boopathy SR, Balasubramanian V (2015) Science direct effect of tool pin profile on microstructure and tensile properties of friction stir welded dissimilar AA 6061 e AA 5086 aluminium alloy joints. *Def Tech* 11(2):174–184
9. Amancio-Filho ST, Sheikhi S, dos Santos JF, Bolfarini C (2008) Preliminary study on the microstructure and mechanical properties of dissimilar friction stir welds in aircraft aluminium alloys 2024-T351 and 6056-T4. *J Mater Process Tech* 206(1–3):132–142
10. Su JQ, Nelson TW, Mishra R, Mahoney M (2003) Microstructural investigation of friction stir welded 7050-T651 aluminium. *Acta Mater* 51(3):713–729

Numerical Analysis of Savonius Vertical Axis Wind Turbine with Dimpled Blades



Paarth Tantia , Pratyush Singh , Punit Prakash , and Nishant Mishra 

1 Introduction

Over the decades, the world is getting a hotter and scientific opinion is human activities, particularly greenhouse gas emissions is the major cause associated with it. The energy sector is by far the largest source of these emissions, and to tackle this situation, research needed to focus on improving the efficiency of renewable energy sources. One such resource for renewable energy is Wind Energy. Wind power is a well-proven and cost-effective technology and is expected to be a dominating energy-producing industry while responding to the government's goals of 60 GW till 2022, i.e. 'world's largest renewable expansion program', the industry needs to increase the installed capacity to achieve this target [1]. India is the fourth-largest alternative energy producer within the world. According to a government, released on 27 December 2017. The country is emerging as a robust manufacturing hub in wind generation with 20 manufactures of 53 different turbine models of international quality ranging three MW in size with exports to Europe, USA, and other countries. Renewable energy also happens to be a specific focus of attention for the government. As per report published by the International Renewable Energy Agency (IRENA) as high as 1 million jobs will generate until 2022, in our country [2].

Wind turbines manufactured broadly in a vertical and horizontal axis type. Larger horizontal axis turbines used for creating contributions to a grid power supply.

P. Tantia (✉) · P. Singh · P. Prakash · N. Mishra
Department of Mechanical Engineering, Shiv Nadar University, Gautam Buddh Nagar, UP, India
e-mail: pt376@snu.edu.in

P. Singh
e-mail: ps512@snu.edu.in

P. Prakash
e-mail: pp431@snu.edu.in

N. Mishra
e-mail: nishant.mishra@snu.edu.in

Vertical axis wind turbine (VAWT) is a form of a turbine that has two or three blades and within which axis of rotation runs vertically. To exploit the low wind speed potential, a design was prepared, which involved some improvisations in a very conventional Savonius Turbine. A Savonius Turbine somewhat resembles a cup anemometer in its design and has many advantages over other turbines; its construction is less complicated and economical. It is independent of the wind direction and encompasses a good starting torque at lower wind speeds. The advent of 3D printing has open new horizons to design more complicated blade profiles that were earlier too complex for the manufacturing industry to develop.

The performance of Savonius VAWT studied by many researchers from 1977 to the present day, optimum design parameters of this rotor is readily available. Various parameters of blade are aspect ratio, overlap, and eccentricity. Alexander and Holownia presented the effect of adding end extensions, endplates on the profile. These test, as mentioned, was performed onto a structure on various Savonius rotor geometries with wind speeds starting from 6 to 9 m/s. They find little improvement in rotor performance with increasing the ratio. Tests by increasing no of blades to 3 and 4 blade geometries gave lower values of efficiency than two blades rotor. Efficiency increases with the rise of the extension. They also stated that the efficiency of the rotor with an endplate and is bigger than that without endplate [3].

The efficiency obtained for a Savonius rotor with endplate found to be greater than that of the rotor without endplate. They also found that increasing the rotor overlap ratio increases rotor efficiency. Modi et al. reported that the optimum values of the aspect and overlap ratios are 0.77 and 0.25, respectively [4]. Majola studied the performance of the Savonius wind rotor using seven different values of the overlap and concluded that the effect of overlap ratio on rotor performance depends on its tip speed ratio [5].

Nobuyuki investigated the aerodynamic performance and the flow fields of Savonius rotors at various overlap ratios. The static torque performance of the rotor, particularly of the returning blade enhanced by the presence of the overlap and the optimum value of the overlap at 0.15 [6]. Naskali studied the effect of dimpling on rotor blades. They concluded that the dimple pattern reduces the resistance of the movement of the blade as passes through the air. A dimpled pattern can include either or both concave or convex dimples of various geometric shapes and sizes [7].

2 Terminologies

2.1 Betz's Law

Betz's law applies to all Newtonian fluids. It indicates that the maximum power that generated from the wind does not depend on the design of wind turbine in open flow. In 1919, Albert Betz gave this theory for wind turbines. The law is based on principles of conservation of mass and momentum of the air stream flowing through an idealized 'actuator disk' that takes energy from the wind stream. It states that maximum energy

that can be generated from the wind turbine is 59.3% of the incoming energy of the wind. Practical utility-scale wind turbines achieve at peak 75–80% of the Betz’s limit [8].

2.2 Tip Speed Ratio

The tip speed ratio is the ratio of the tangential wind speed at the tip of a blade to the speed of the wind. The tip-speed ratio is associated with efficiency, with the optimum value varying with a blade profile. Noise levels increase with greater tip speed values due to the centrifugal force generated by wind levels and because of this needs stronger blades. Tip speed in general represented by letter λ as shown in Eq. (1) stated below.

$$\lambda = \frac{\text{Tip speed of blade}}{\text{Wind speed}} \tag{1}$$

2.3 Coefficient of Power

The coefficient of power demarked as the ratio of the output generated by the blades of the turbine to the power of the incoming wind where Eqs. 2, 3 and 4 represent states the mathematical representation.

$$C_p = \frac{P_m}{P_w} \tag{2}$$

$$P_m = T \times \omega \tag{3}$$

$$P_w = \frac{1}{2} \times \rho \times v^3 \tag{4}$$

where ‘ T ’ is the mechanical torque, ‘ ω ’ is the angular velocity of the rotor blades, ‘ ρ ’ is air density, kg/m^3 , ‘ v ’ is the wind speed, m/s .

2.4 Number of Blade

Deciding the number of blades required for a wind turbine is an important design aspect since wind capture, and transformation of energy takes place at this interface. Mahmoud et al. [9] performed experimental investigations on a Savonius VAWT to optimize a number of blades. Effect on power produced noted with varying wind speeds and a different number of blades. This paper concluded that the two-blade system is an ideal configuration.

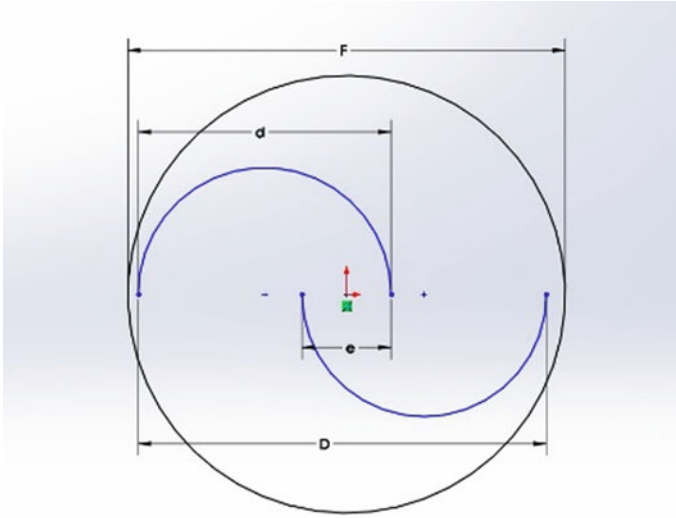


Fig. 1 Top-view of a Savonius turbine with endplates

2.5 Aspect Ratio

Aspect Ratio is a ratio between height and the diameter, and it is directly proportional to the coefficient of performance.

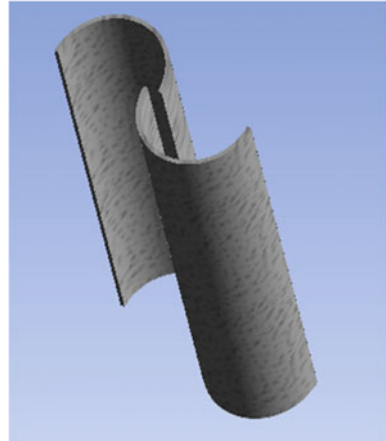
2.6 Overlap Ratio

It is the ratio of eccentricity to the diameter of the rotor blades. In line with the research paper ‘Influence of phase shift and overlap ratio on Savonius wind turbine’s performance’, overlap ratio of 0.167 for single stage rotor is appropriate. Figure 1 shows the top view of a Savonius turbine with endplate where e denotes the eccentricity, d the diameter of the semicircular blade, D is the overall diameter of blades and F is the diameter of the endplates [10].

2.7 Dimple Structure

Dimples increase the length of flow separation as turbulence precedes. The dimples on a sphere induce a turbulent boundary layer that has a larger momentum than laminar boundary layer flow, and thus delays separation and therefore dimpled structure results in a thin wake region [11, 12].

Fig. 2 Single-stage without endplates



3 Methodology

3.1 Turbine Designing

After deciding the configuration of the blades, various computational designs of the turbines are prepared represented as follows:

3.1.1 Single Stage Turbine Without Endplates

Turbine geometry sized according to the specifications and a 3D model, as shown in Fig. 2. The various parameters of a Savonius turbine and various parameters are (Source: ANSYS 2017):

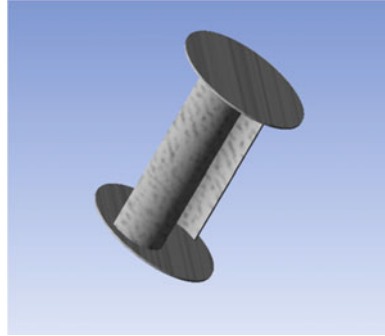
Wingspread of the rotor (D)	15.5 cm	The diameter of turbine blades (d)	8.5 cm
Height of blades/shaft (h)	24 cm	Spacing between blades (e)	2.7 cm

3.1.2 Single Stage Turbine with Endplates

Mishra et al. studied the effect of endplate on the performance of VAWT [14]. A 3D model developed and presented in Fig. 3 and the various parameter listed below (Source: ANSYS 2017):

Wingspread of a rotor (D)	15.5 cm	Spacing between blades (e)	2.7 cm
Height of blades/shaft (h)	24 cm	Diameter of endplates (F)	18.6 cm
The diameter of turbine blades (d)	8.5 cm		

Fig. 3 Single-stage with endplates



3.1.3 Single Stage Turbine with Endplates and Dimples

A 3D blade with dimples [15] developed and endplates added to the geometry as presented in Fig. 4. Various parameters as listed below:

Wingspread of a rotor (D)	14.2 cm	Spacing between blades (e)	2.7 cm
Height of blades/shaft (h)	24 cm	Depth of dimple	0.1 cm
The diameter of turbine blades (d)	8.5 cm	Spacing between dimples	0.3 cm
Pattern of dimples	Uniform	Shape of dimples	Hemispherical

Fig. 4 Single-stage turbine with dimples. *Source* ANSYS (2017)

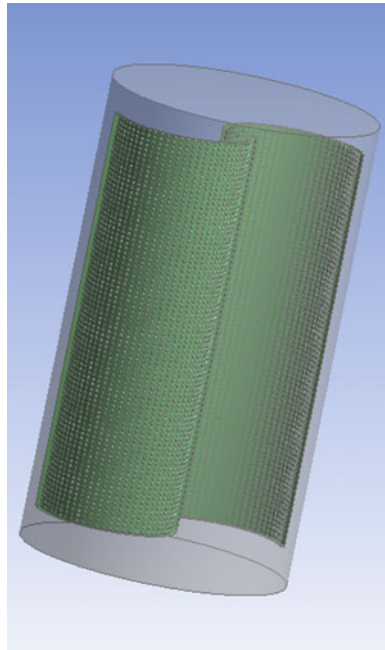
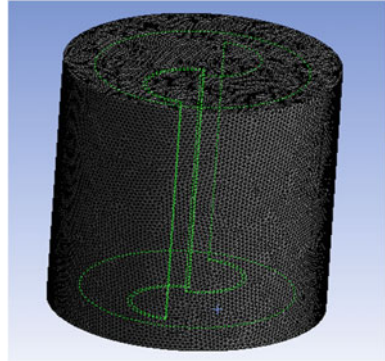


Fig. 5 Meshing of a rotor.

Source ANSYS (2017)



3.2 Meshing

It is an essential part of the simulation process where the geometries discretize into smaller nodes and element; physics applies to all discrete local estimates of the larger domain. The mesh effects the convergence, speed of the simulation and accuracy. The study involves two separate mesh, namely, rotor mesh and stator mesh. Both meshes are finally merged to perform a flow analysis based on Transient Blade Row Model of CFX for generating flow conditions. $K - \epsilon$ model is used for solving physics and generating the solution.

3.2.1 Rotor Meshing

The rotor is one of the rotatory enclosures that incorporate the turbine blade model. The region is where the analysis concentrates. The meshing in this area is very fine, with a smooth transition is allowed. Figure 5 shows the meshing of the rotor.

Parameters:

Physics	CFD	Total elements	690,624
Solver	CFX	Relevance	100
Total nodes	129,355		

3.2.2 Stator Meshing

The enclosure consists of a rectangular domain onto which the boundary conditions are applied. A cavity generated as shown in Fig. 6b such that the rotor meshing fit when imported to the enclosure. The analysis requires joining of the interface of the rotor and stator for analysis to proceed. Boundary condition defined for input, output, the interface of a stator for top-bottom and a cylindrical wall along with boundary

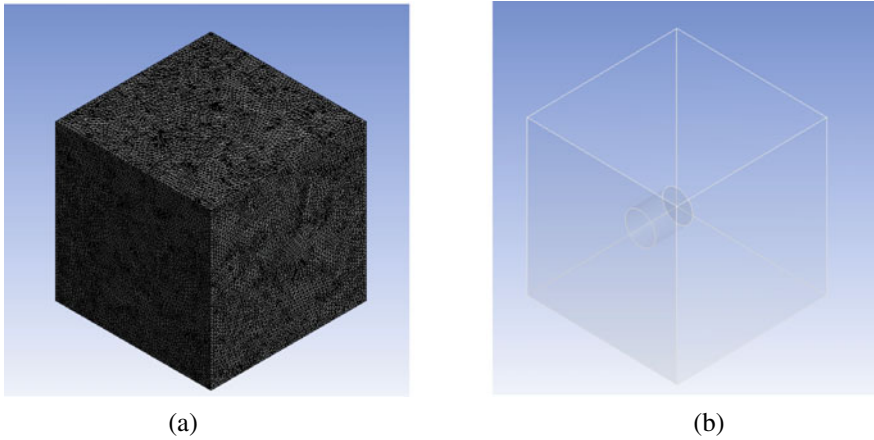


Fig. 6 a Meshing of Stator area, b the geometry of the Stator area

walls, Fig. 6a shows the meshing of the stator and Fig. 6b the geometry of the stator correspondingly.

3.3 Setup: Rotatory Machinery Turbulent Flow— $k - \epsilon$ Turbulent Model

K-epsilon ($k - \epsilon$) turbulence model is the most common model used in Computational Fluid Dynamics (CFD) to simulate mean flow characteristics for turbulent flow conditions. It is a two-equation model that gives a general description of turbulence utilizing two transport equations (PDEs). Figure 7 shows the boundary condition for the geometry of the enclosure; the arrows represent the inlet and outlet [13].

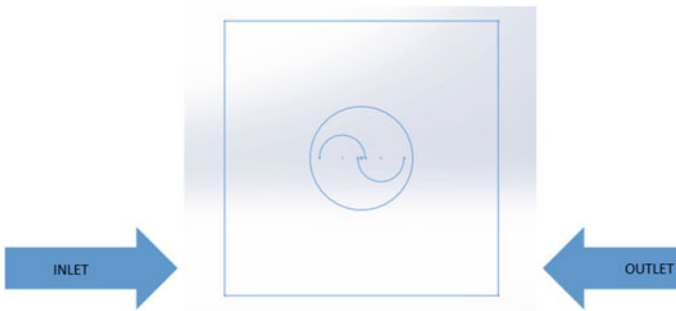


Fig. 7 Boundary conditions for geometry

- The first transported variable in Eq. (5) is the turbulent kinetic energy (k).

$$\frac{\partial(\rho k)}{\partial t} + \frac{\partial(\rho k u_i)}{\partial x_i} = \frac{\partial}{\partial x_j} \left[\frac{\mu_t}{\sigma_k} \frac{\partial k}{\partial x_j} \right] + 2\mu_t E_{ij} E_{ij} - \rho \varepsilon \quad (5)$$

- The second transported variable in Eq. (6) is the rate of dissipation of turbulent kinetic energy (ε).

$$\frac{\partial(\rho \varepsilon)}{\partial t} + \frac{\partial(\rho \varepsilon u_i)}{\partial x_i} = \frac{\partial}{\partial x_j} \left[\frac{\mu_t}{\sigma_k} \frac{\partial \varepsilon}{\partial x_j} \right] + C_{1\varepsilon} \frac{\varepsilon}{k} 2\mu_t E_{ij} E_{ij} - C_{2\varepsilon} \rho \frac{\varepsilon^2}{k} \quad (6)$$

Parameters:

Inlet velocity: (u, v, w)	7,0,0 (m/s)	Time steps/period	100
Rotation axis	Z-axis	Time step	0.6981 ms
Maximum periods	25	Angular velocity (blades)	90 rad/s
Discretization method	Finite volume method	Flow analysis type	Transient blade row model

4 Computational Analysis

4.1 Savonius Turbine Without End Plates Simulation

Figure 8 shows the velocity and Pressure contour for a turbine without endplates and with no dimples. The turbine produces less drag.

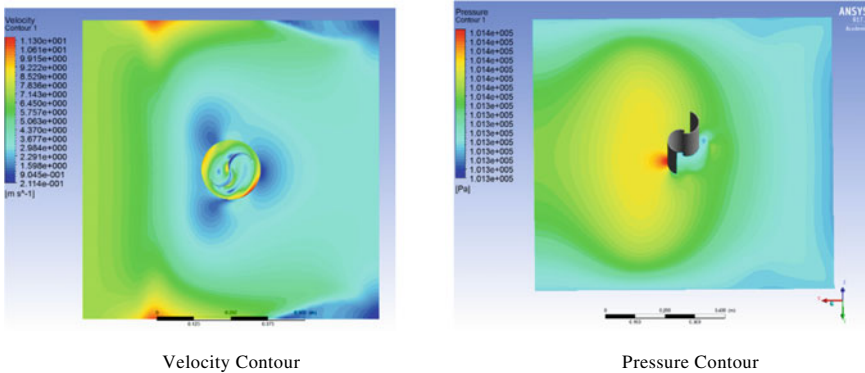


Fig. 8 Without endplate ANSYS simulation

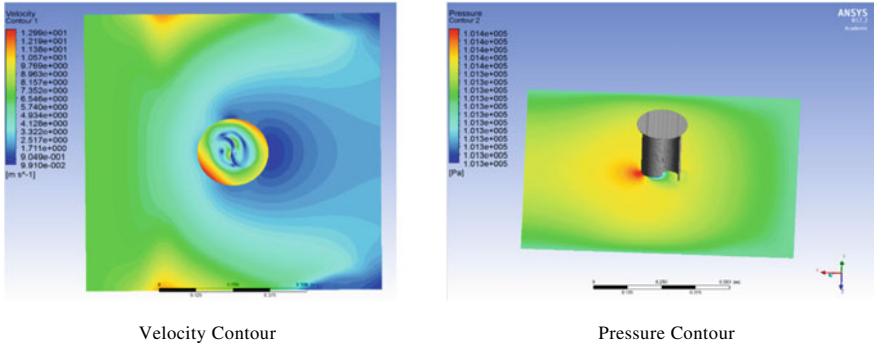


Fig. 9 With endplate ANSYS simulation. Source ANSYS (2017)

4.2 Savonius Turbine with End Plates Simulation

Figure 9 shows the velocity and pressure contour for the turbine with endplates; the drag forces increase as the wake region becomes thinner near the endplate region.

4.3 Savonius Turbine with Endplates and Dimples Simulation

Figure 10 shows, velocity and pressure contour for the turbine with an endplate and with dimples. The wake region decreases and becomes thinner than the above two cases.

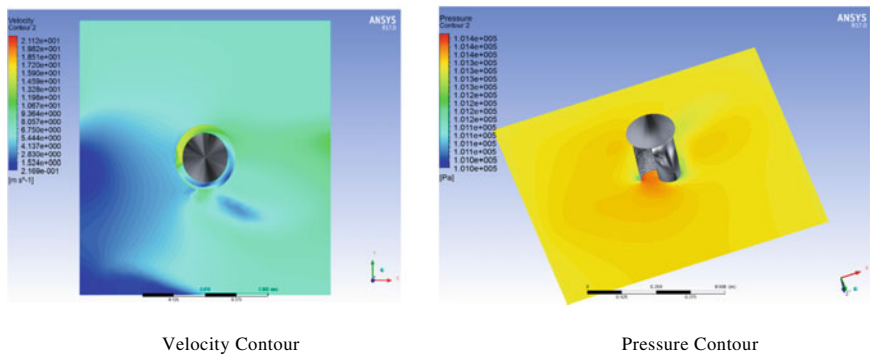


Fig. 10 With dimples ANSYS simulation. Source ANSYS (2017)

5 Results and Discussion

This section describes all the computational observations made using the turbine with different configurations.

5.1 Savonius Turbine Without Endplates

From Fig. 11, it is observed that both the graphs are symmetric because of the symmetry of the turbine and the maximum velocity comes about to be 9 m/s, when the results are viewed near the top end and in the middle of the turbine blade. The discontinuity in the middle is seen because of the overlap ratio of the turbine blade, and it is seen that the pressure difference created on both sides of the turbine at the inlet and outlet boundaries rotates the turbine.

Figure 12 shows that the rate of turbulence eddy dissipation starts gradually increasing and reaches a maximum value of $65 \text{ m}^2/\text{s}^3$. The second figure shows

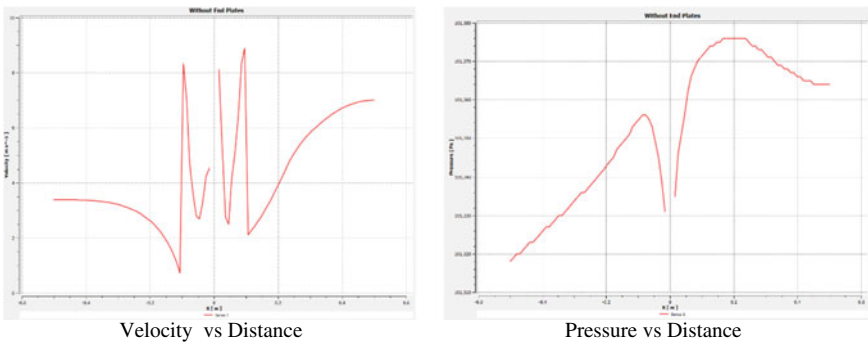


Fig. 11 Graphs ANSYS CFX

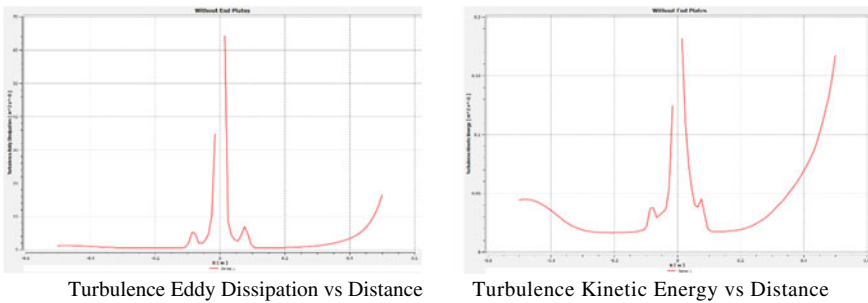


Fig. 12 Graphs ANSYS CFX

the variation of turbulence kinetic energy as the wind approaches the turbine blades and leaves. The max turbulence kinetic energy achieved is about $0.18 \text{ m}^2/\text{s}^2$.

5.2 Savonius Turbine with Endplates

Figure 13 shows that both the graphs are symmetric because of the turbine and the maximum velocity reached about to be 11 m/s due to the presence of endplates when the results are viewed near the top end and in the middle of the turbine blade. The discontinuity in the middle is because of the overlap ratio of turbine blades. The other figure shows the pressure difference created on both sides of the turbine, i.e. at the inlet and outlet boundaries because of which the turbine rotates.

Figure 14 shows the rate of turbulence eddy dissipation starts gradually increasing and reaches a maximum value of $90 \text{ m}^2/\text{s}^3$ more than without endplates, which means eddy currents will dissipate faster than without endplates and the turbine will harness more energy. The other figure shows the variation of turbulence kinetic energy as the wind approaches the turbine blades and leaves. The max turbulence kinetic energy achieved is about $0.18 \text{ m}^2/\text{s}^2$ similar to the case of without endplates.

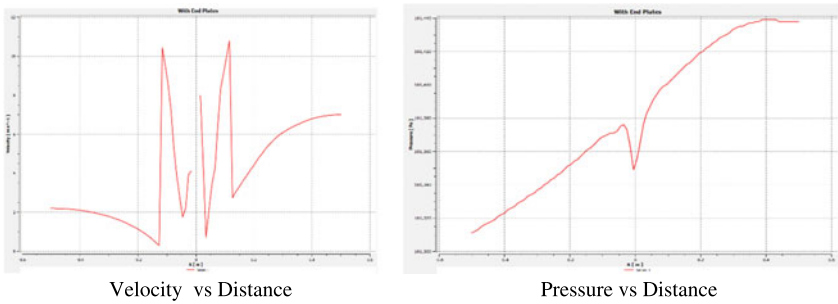


Fig. 13 Graphs ANSYS CFX

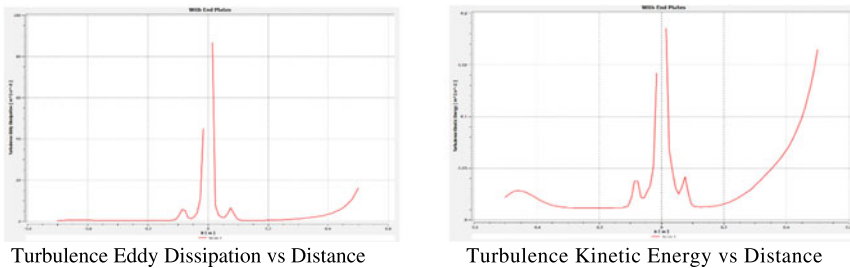


Fig. 14 Graphs ANSYS CFX

5.3 Savonius Turbine with Endplates and Dimples

Figure 15 shows the maximum velocity reached about to be 16.5 m/s due to the presence of dimples when the results are viewed near the top end and in the middle of the turbine blade. The velocity attained higher compared to the other two cases because of the effects of dimples. The other figure clearly shows the pressure difference created on both sides of the turbine, i.e. at the inlet and outlet boundaries because of which the turbine rotates.

Figure 16 shows that the rate of turbulence eddy dissipation shows a sharp increase. The number of surfaces increases due to the presence of dimples and reaches a maximum value of greater than 4000 m^2/s^3 , which is far more than with and without endplates, which means eddy currents will dissipate fast enough and will harness more energy than that of other two turbines. The other shows the variation of turbulence kinetic energy as the wind approaches the turbine blades and leaves. The max turbulence kinetic energy achieved is about 3 m^2/s^2 , which is also much greater than the other two cases.

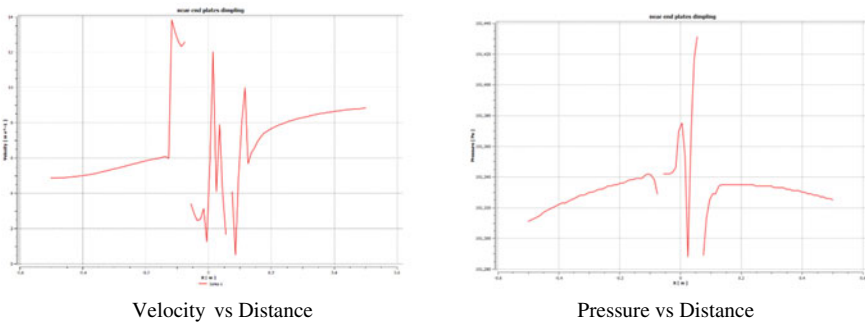


Fig. 15 Graphs ANSYS CFX

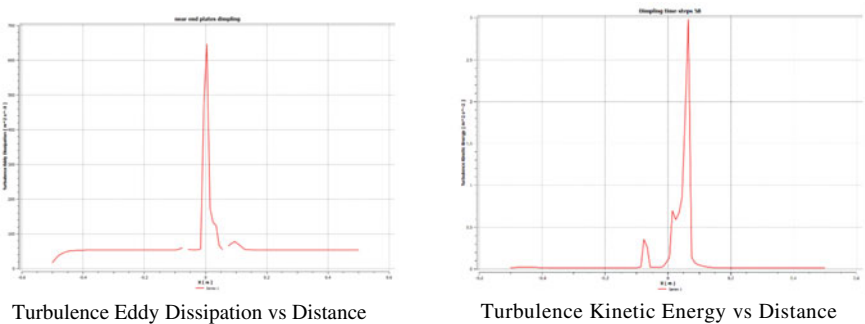


Fig. 16 Graphs ANSYS CFX

Table 1 Numerical results (inlet velocity of 7 m/s, time step of 98)

Parameters	Blade tip velocity (m/s)	Turbulence eddy dissipation (m^2/s^3)	Turbulence kinetic energy (m^2/s^2)
Without end plates	9	65	0.18
With end plates	11	90	0.18
With dimples and endplates	16.5	4000	3

6 Comparative Study

From Table 1, we can infer that outlet velocity, turbulence eddy dissipation and turbulence kinetic energy increases with the addition of endplates to the Savonius turbine. A sharp increase in the outlet velocity and turbulence eddy dissipation observed with the addition of hemispherical dimples onto the turbine blades while keeping all other geometric parameters constant.

7 Conclusion

The objective of the study is to analyze the performance characteristics of a wind turbine designed with dimples to reducing drag. This is an attempt to increase the efficiency of the wind turbines. The motivation in using dimples to modify the surface topology of wind turbines is the functional advantage they provide evidence from the golf balls contributing to torque and eventually improved performance levels.

A single-stage Savonius turbine studied and its performance compared with the addition of endplates and dimples on the blade profile. The study emphasizes the aerodynamic properties, which resulted due to the presence of dimples. It is found that the velocity profile increases near the endplates and profile further increases with the addition of dimples on the blades, obtained by performing computational analysis on ANSYS 17.2 Academic and research license. This simulation also shows that the eddy dissipation rate increases significantly with dimples compared to the other two blade profiles.

Further, analysis shows eddy formed on the surface decreases because of more dissipation rate in case of the dimpled profile, thus the coefficient of drag decreases and flow separation delay. This shows the adverse pressure gradient that develops on the blade profile minimizes due to the addition of dimples on the blade profile. Thus, the inclusion of dimples on blades will enhance the performance levels of the Savonius wind Turbine.

References

1. Ministry of New and Renewable Energy <https://mnre.gov.in/>. Accessed on 25/11/2019
2. International Renewable Energy Agency <http://www.irena.org/>. Accessed on 25/11/2019
3. Alexander AJ, Holownia BP (1978) Wind tunnel tests on a Savonius rotor. *J Industr Aerodyn* 3:343–351. [https://doi.org/10.1016/0167-6105\(78\)90037-5](https://doi.org/10.1016/0167-6105(78)90037-5)
4. Modi VJ, Roth NJ, Fernando MS (1984) Optimum-configuration studies and prototype design of a wind-energy-operated irrigation system. *J Wind Eng Ind Aerodyn* 16:85–96. [https://doi.org/10.1016/0167-6105\(84\)90050-3](https://doi.org/10.1016/0167-6105(84)90050-3)
5. Mojola O (1985) On the aerodynamic design of the Savonius windmill rotor. *J Wind Eng Ind Aerodyn* 21:223–231. [https://doi.org/10.1016/0167-6105\(85\)90005-4](https://doi.org/10.1016/0167-6105(85)90005-4)
6. Nobuyuki F (1992) On the torque mechanism of Savonius rotors. *J Wind Eng Ind Aerodyn* 40:277–292. [https://doi.org/10.1016/0167-6105\(92\)90380-S](https://doi.org/10.1016/0167-6105(92)90380-S)
7. Naskali PH, MacLean A, Gray NCC, Lewis JH, Newall AP (2008) Helical wind turbine. US Patent 7344353B2
8. Proof of Betz Law, Delft University of Technology <http://tudelft.nl/duwind>. Accessed 25th Nov 2019
9. Mahmoud NH, Haroun AAH, Wahba E, Nasef MH (2010) An experimental study on improvement of Savonius rotor performance 51:19–25. <https://doi.org/10.1016/j.aej.2012.07.003>
10. Jian C, Kumburnuss J, Linhua Z, Hongxing LLY (2012) Influence of phase-shift and overlap ratio on Savonius wind turbine's performance. *J Sol Energy Eng* 134:011016. <https://doi.org/10.1115/1.4004980>
11. Griffith TS, Hadhrami LA, Han JC (2003) Heat transfer in rotating rectangular cooling channels ($AR = 4$) with dimples. *J Turbomach* 125(3):555–563. <https://doi.org/10.1115/1.1471525>
12. Arun KK, Navaneeth VR, Vimal KS, Ajay R (2018) Analysing the effect of dimples on wind turbine efficiency using CFD. *Int J Appl Eng Res* 13(6):4484–4489
13. Mishra N, Jain A, Nair A, Khanna B, Mitra S (2019) Experimental investigation on a ducted savonius vertical axis wind turbine and its performance comparison with and without endplates. *Renew Energy Res Appl* 1:1–9
14. Mishra N, Tyagi U, Fayaz H, Jain A (2019) Numerical investigations on performance enhancement of a Savonius wind turbine. In: 2019 ICMechD conference, Chennai, Tamil Nadu
15. Versteeg HK, Malalasekera W (2007) an introduction to computational fluid dynamics: the finite volume method. ISBN 9780131274983

An Effect of Current on Mechanical Properties and SEM Characterization of Butt Joint of Aluminium AA6082 Using GTAW



Sunil Kumar, Prabhkiran Kaur, and Amrik Singh

1 Introduction

Aluminium is one of the most easily available metals at optimum cost. It is very popular in the industry due to many good properties like corrosion resistance, castability and ease of fabrication, etc., required in the end products. Production of aluminium products can be met with the help of many processing and joining methods, such as casting, welding and forging. Welding is an easy method for the production of components, but the problem of oxidation of aluminium is a hindrance while doing the welding as the surface has to be cleaned every time before welding [1]. Welding parameters were studied of Aluminium Alloy AA6082 by several researchers with different conditions [2–11]. Another alloy AA5456 was studied by Kumar et al. [12] regarding the improvement of mechanical properties through pulsed TIG welding. Microstructure and mechanical behaviour characteristics of TIG welds and FSW were studied by Cabello Mun et al. [13]. The butt joining of AA 2024-T3 with TIG and FSW was characterized for corrosion resistance and microstructure by Squillac [14].

Gas metal arc welding of 6082-T6 acquires only 60% of the tensile strength under better welding environment [5] and that is consistent with the indications of design norms [6]. The test material showed a minimum reduction in tensile strength and

S. Kumar (✉) · A. Singh
Mechanical Engineering Department, Sant Longowal Institute of Engineering and Technology,
Longowal, Sangrur, Punjab, India
e-mail: sunil_thappa@yahoo.com

A. Singh
e-mail: hanspalamriksingh@gmail.com

P. Kaur
Mechanical Engineering Department, I. K. Gujral Punjab Technical University, Amritsar Campus,
Amritsar, Punjab 144603, India
e-mail: pkiran_vora@yahoo.co.in

hardness at 6 mm from the weld line in heat-affected zone [5]. Medium strength alloys have achieved a high place in industry due to their properties such as low specific weight and larger strength to weight ratio for structural applications. In the present study, the butt joint welding of AA6082 aluminium with AC mode TIGW was studied. Experiments were carried to find the best current rates of TIGW for better mechanical properties of AA 6082. Further, the effects of current on mechanical properties and SEM characterization were investigated.

2 Experimental Work

The specimen of AA6082 was prepared by cutting the plates from 6-mm thick sheet. Two strips were welded using filler alloy of 4043 material [5].

2.1 Preparation of Test Specimen

In the first step of experimentation, a 6 mm-thick plate of size 300 mm \times 75 mm was cut as shown in Fig. 1, and each cut was machined to form V-groove with 65° of angle and 2 mm root face according to the Bureau of Indian Standards.

Before performing TIGW, grooves of plates were cleaned with wire brush and acetone. Then, butt joints were made only by AC TIG welding technique as per the manual of TIG welding equipment. Argon gas (purity of 99.97%) was used as a shield along with 99.75% pure tungsten electrode of 3 mm diameter. The filler wire of 2.4 diameters was used to weld butt joint. The current for each plate was different, and it ranged from 60 to 300 amp. While welding, it was noticed that welding done with current less than 80 amp, joining was not possible, and with current, more than 250 amp plates were burning. So, accordingly, range of currents considered for welding were 100, 120, 140, 160, 180, 200, 220 and 240 amp.

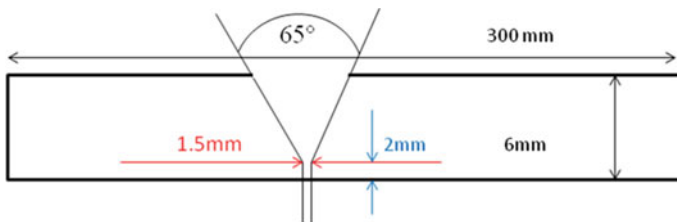


Fig. 1 Specimen for welding

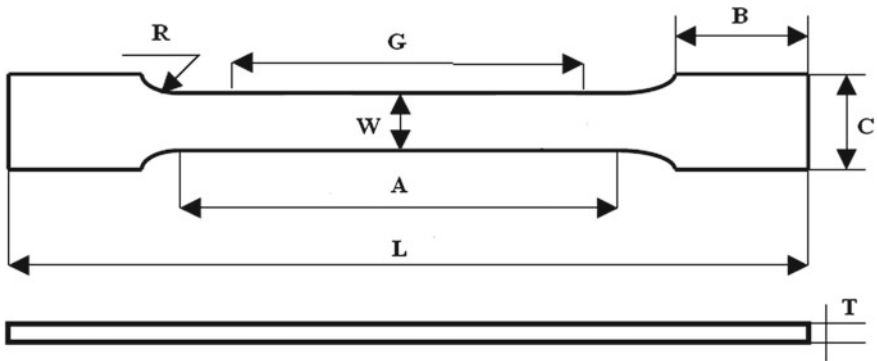


Fig. 2 Standard specimen size for tensile strength testing ($L = 150$ mm, $A = 70$ mm, $B = 40$ mm, $C = 25$ mm, $G = 50$ mm, $W = 15$ mm, $R = 6$ mm, $T = 6$ mm)

2.1.1 Tensile Test

According to ASTM standards, specimens were prepared for the tensile test from weld pads, as shown in Fig. 2. For each current input, two specimens were prepared. The tests were performed on UTM of 400 kN capacity, which was a servo-controlled machine. To study the fracture, scanning electron microscopy (SEM) was carried out on the fractured end.

2.1.2 Charpy Test

The specimens for the Charpy test were prepared for each set as per ASTM [1]. Figure 3 shows the schematic diagram of the specimen for impact checking.

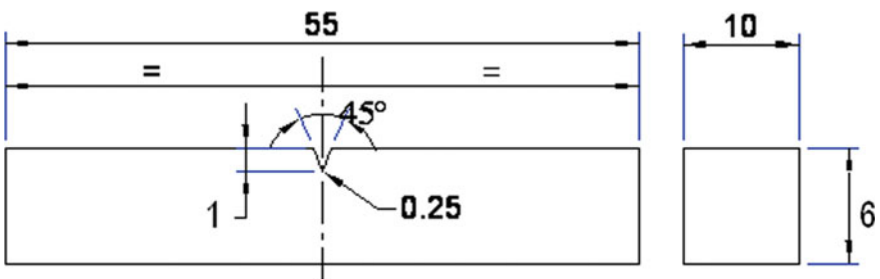


Fig. 3 Standard specimen size for impact testing

3 Results

3.1 An Effect of Current on Tensile Strength

The evaluation of tensile strength for each butt joint was conducted after experimentation. Figure 4 shows tensile strength specimens before the tensile test was done, and Fig. 5 shows the specimens after the tensile test was done. The ultimate tensile strength was measured, and the corresponding variation with the current is plotted in Fig. 6. The plot shown in Fig. 6 was made by taking an average of the tensile strength of two specimens for each set of current, and joint efficiency was calculated for a sample having the highest tensile strength. The results obtained revealed that the highest tensile strength of 210.25 MPa is for the specimens made using a current of 140 amp and followed by 162.41 MPa using high current 240 amp. It was also revealed from Fig. 4 that specimens splintered from the welded area, and thus, it can be assumed that strength obtained of the weld [15].

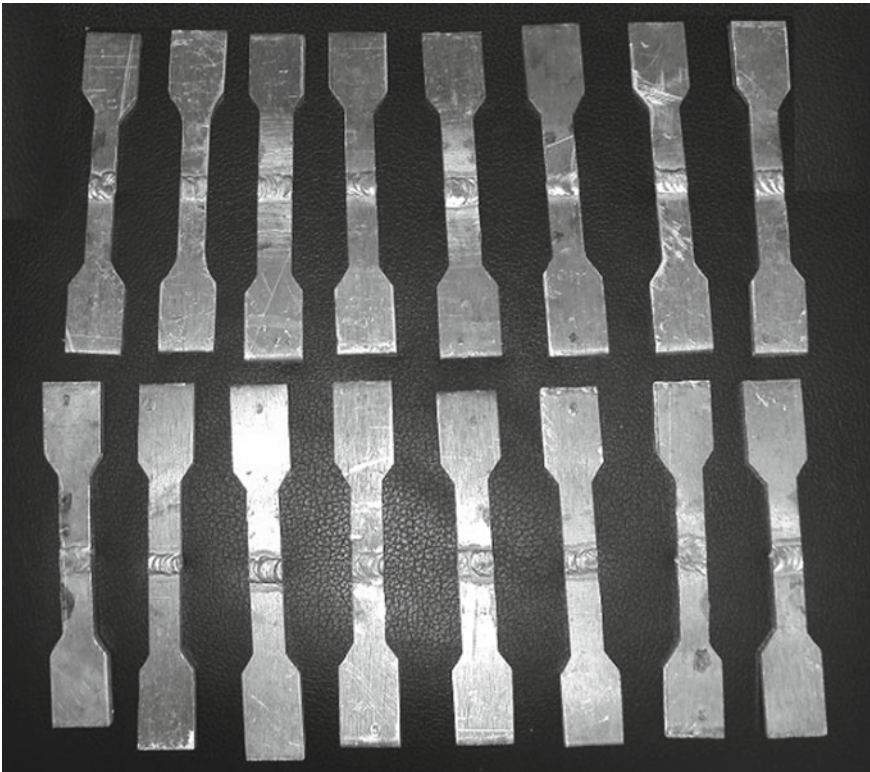


Fig. 4 Tensile specimens before the test

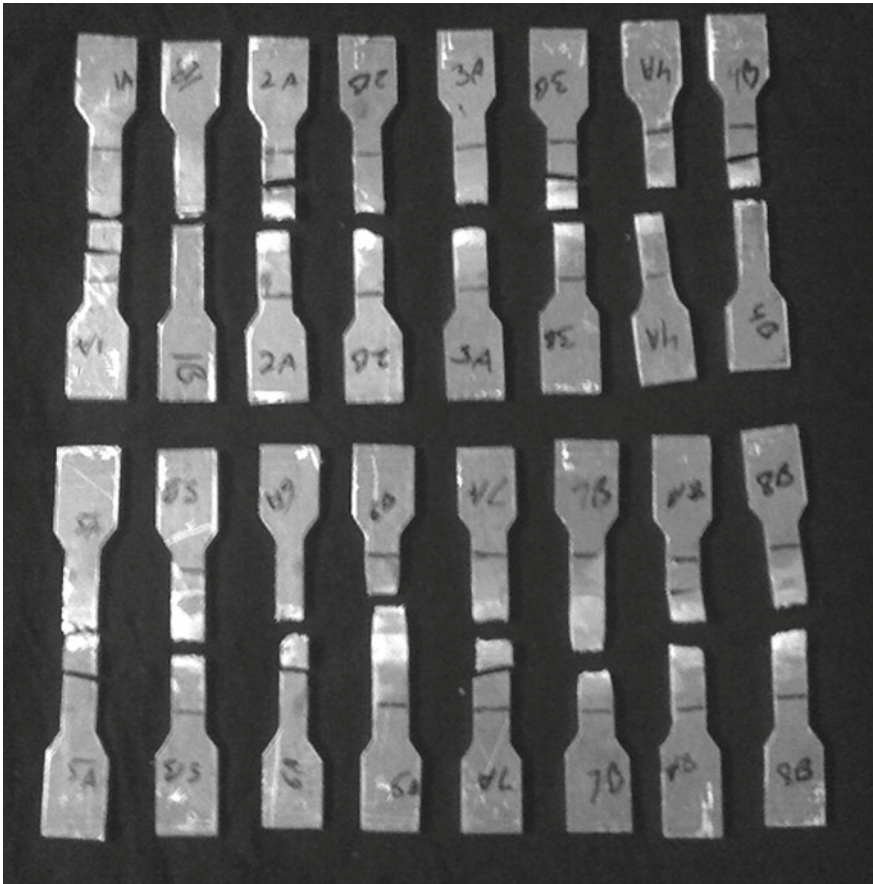
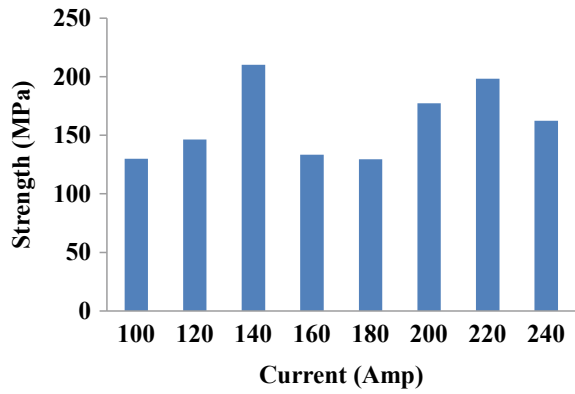


Fig. 5 Tensile specimens after a test

Fig. 6 Tensile strength of all specimens at different currents in amp



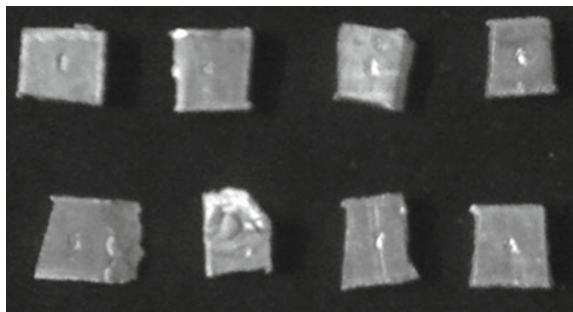
As the current increases, tensile strength starts increasing, but only till a value, i.e. 140 amp, after which it starts decreasing. The obtained strength at all conditions is supported by the SEM fractography of the respective specimens shown in Figs. 8, 9, 10, 11, 12, 13 and 14. With an increase in current beyond certain limit, dimples of different size, blowholes, porosity and distortion were seen. The tensile strength of specimen welded with current 140 amp has attained maximum tensile strength (210.25 MPa) and has a maximum efficiency of the joint, i.e. 65%.

3.2 SEM of Tensile Specimen

SEM characterization of fractured surfaces of various tensile test specimens was investigated. Figure 7 shows tensile tested specimen for SEM. SEM fractography of fractured surfaces for all the specimens of tensile tests is shown in Figs. 8, 9, 10, 11, 12, 13 and 14. SEM shown in Fig. 8 for the specimen made at 100 Amp has large dimples and a small population of grains. Figure 9 also shows that specimen made at 120 amp has some large dimples and also have some blowholes which lead to low tensile strength, but in the case of specimens made at 140 amp (Fig. 10), there are some dimples of small size along with larger diameter shallow dimple which shows ductile fracture which is responsible for higher tensile strength and ductility. Figure 11 shows a small population and large size of grains leading to low strength. Observation made from Fig. 12 concludes that large dimple size and small populations of grains are present. There was the negligible presence of any type of dimple but having some blowholes and large size grain structure for a specimen as Fig. 13.

During welding of the specimen made with current of 220 and 240 amp, some distortion of joint is observed. The SEM shown in Fig. 14 reveals that this specimen contains deep and large size dimples and grain size is not of the same size. The last specimen shown in Fig. 15 contains a very large and deep dimple, a smaller number of grain population and some blowholes. It has been observed from the SEM fractography that the welded joints formed by TIGW acquired best joining properties under the present conditions of welding, i.e. at current 140 Amp. All the

Fig. 7 Tensile test specimens for SEM



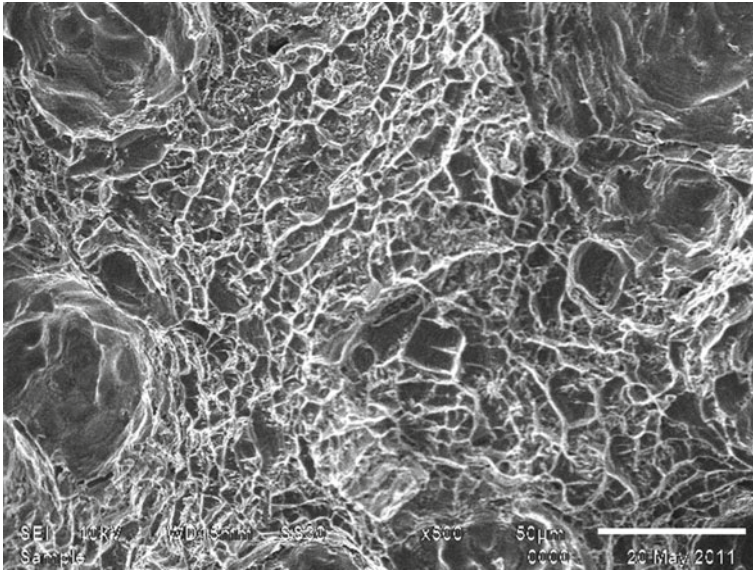


Fig. 8 Tensile test specimen fractograph at current (100 amp)

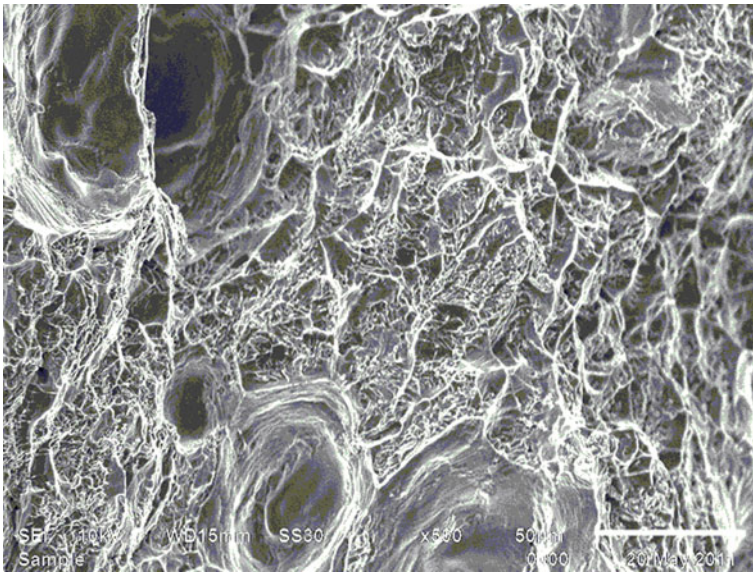


Fig. 9 Tensile test specimen fractograph at current (120 amp)

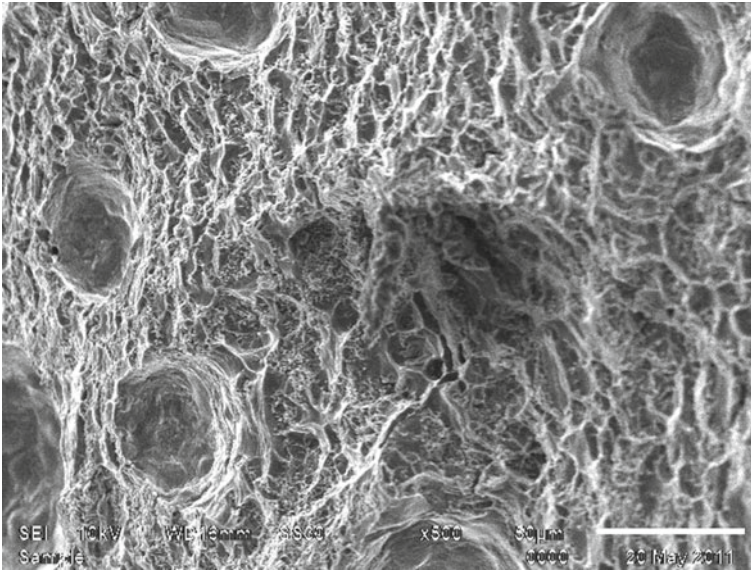


Fig. 10 Tensile test specimen fractograph at current (140 amp)

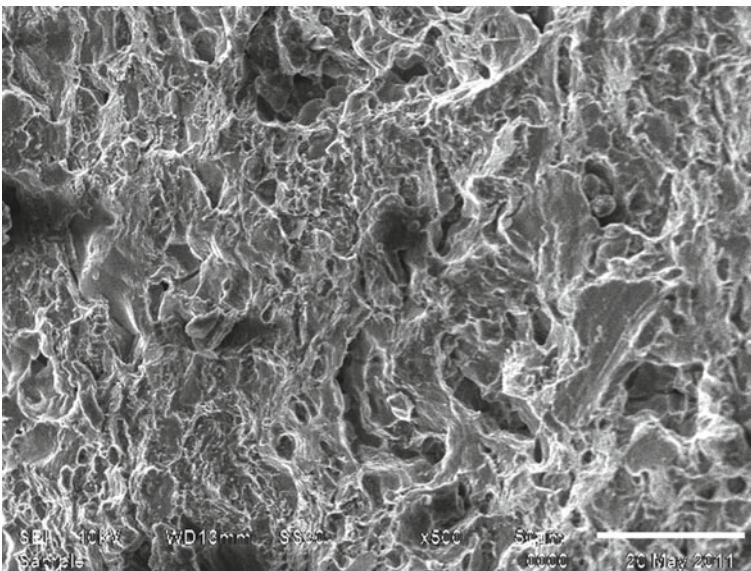


Fig. 11 Tensile test specimen fractograph at current (160 amp)

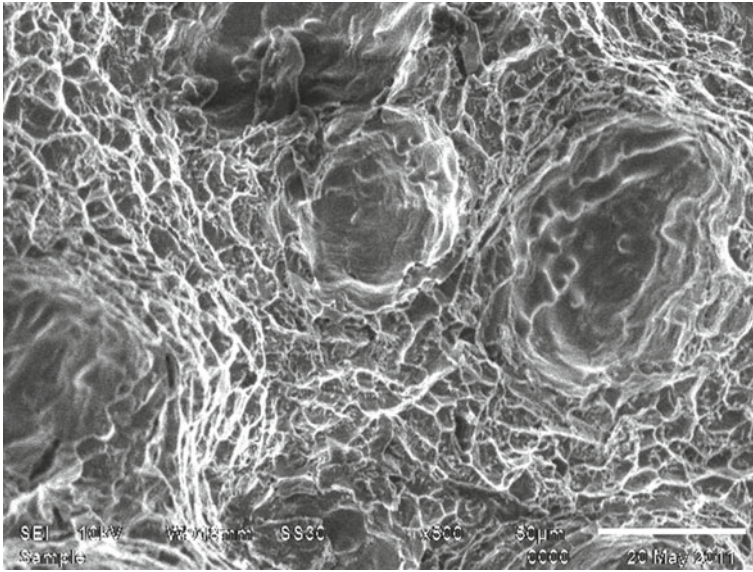


Fig. 12 Tensile test specimen fractograph at current (180 amp)

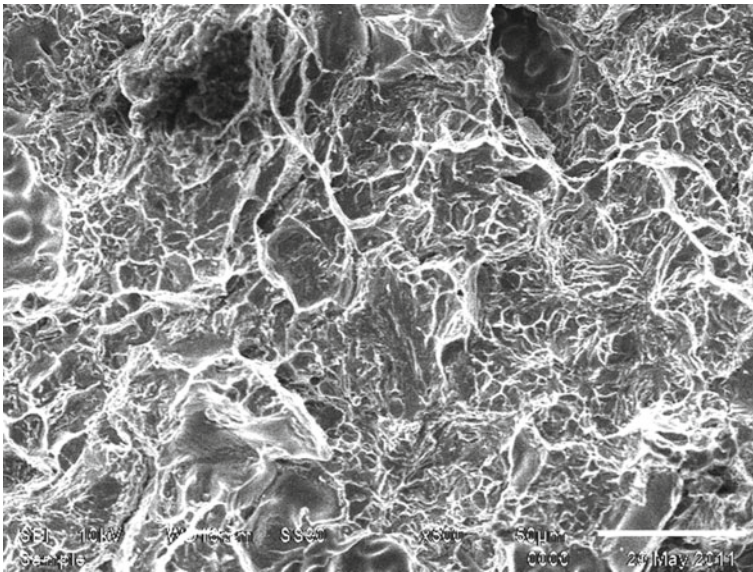


Fig. 13 Tensile test specimen fractograph at current (200 amp)

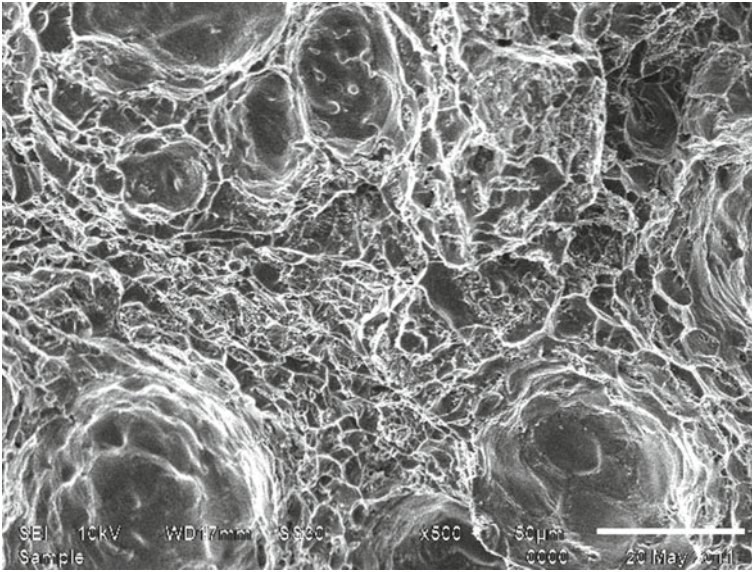


Fig. 14 Tensile test specimen fractograph at current (220 amp)

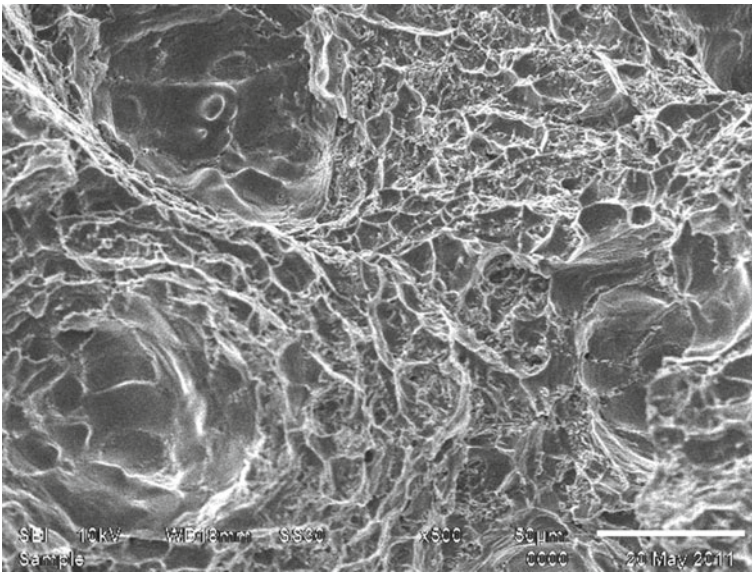


Fig. 15 Tensile test specimen fractograph at the current (240 amp)

fracture surfaces showed mostly cup and cone type of fracture, which is a symbol of ductile behaviour of the joint irrespective of the size of dimples [15, 16].

3.3 Effect of Current on Impact Toughness

The impact test was conducted at different values of AC current. Figure 16 shows all the specimens after performing the impact test. Figure 17 shows the obtained toughness measured for the specimens made with respect to the current. As the current increases, the increase in toughness was not significant, so there was not much effect of increasing the current on impact toughness. The toughness measured for all the specimens was less as compared to the base metal, i.e. 11 J; this indicates that workpiece may fail from joint under impact loading.

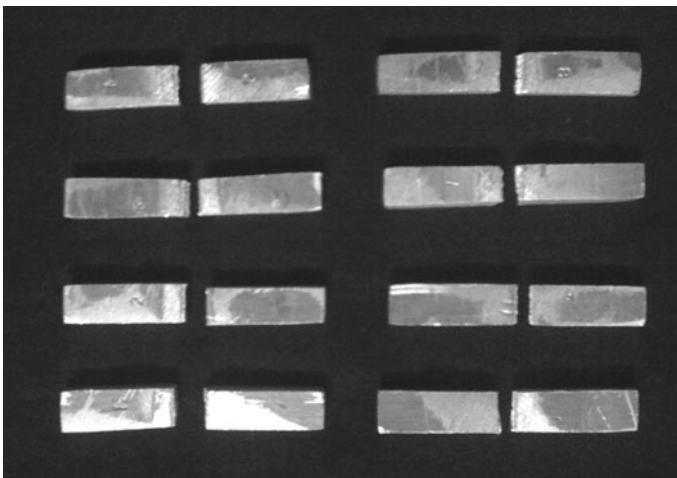
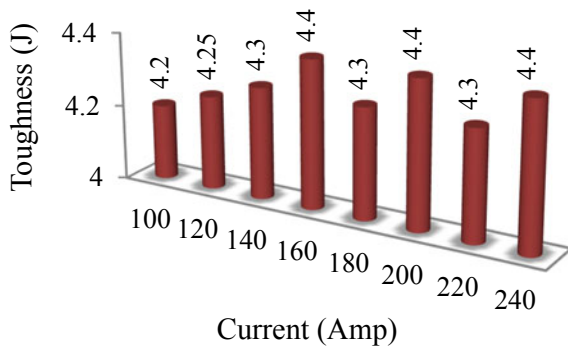


Fig. 16 Impact specimens after the test

Fig. 17 Toughness of all specimens at different currents



4 Conclusions

- It was evident from the SEM at the weld centre of the samples welded by TIG with current 140 amp, achieved sound weld, resulted in fine equiaxed grains compared to other conditions.
- It is evident from cup and cone type of fracture at current 140 amp that the weldment comprises ductile fracture.
- The specimen with the current of 160 Amp has the highest toughness of 4.4.
- The maximum strength of the welded joint achieved is 210 MPa for specimen made with 140 amp current and gas flow rate of 20 l/min. The strength of joint achieved with TIG is 65% of base metal.

References

1. ASM Committee (1990) Metal handbook—properties and selection: Irons, Steels and High-performance alloys, ASM International, ISBN: 978-0-87170-377-4
2. Cavaliere P, Santis A, Panella F (2009) Thermoelasticity and CCD analysis of crack propagation in AA6082 friction stir welded joints. *Int J Fatigue* 31:385–392
3. Ravikumar BVR, Krishna Sai BLN, Rajashekhar S (2014) Evaluation of mechanical properties of AA6082-T6 aluminium alloy using pulse & non-pulse current GTAW process. *Int J Innov Res Sci Eng Technol* 3(12):18139–18146
4. Liu J, Wang L-L, Lee J, El-Fakir O, Chen L, Lin J, Dean TA (2015) Size-dependent mechanical properties in AA6082 tailor welded specimens. *J Mater Process Technol* 224:169–180
5. Missori S, Sili A (2000) Mechanical behavior of 6082-T6 aluminium alloy welds. *J Metallurgical Sci Technol* 18:12–17
6. Cavalier P, Squillace A, Panella F (2008) Effect of welding and microstructural properties of AA 6082 joints produced by friction stir welding. *J Mater Process Technol* 200(1–3):364–372
7. Scialpi A, De Filippis LAC, Cavaliere P (2007) Influence of shoulder geometry on microstructure and mechanical properties of friction stir welded 6082 aluminium alloy. *J Mater Design* 28:1124–1129
8. El-Shennawy M, Abdel-Aziz Kh, Omar AA (2017) Metallurgical and mechanical properties of heat treatable aluminum alloy AA6082 welds. *Int J Appl Eng Res* 12(11):2832–2839
9. Gurjinder S, Sunil K, Amrik S (2013) Influence of current on microstructure and hardness of butt welding aluminium AA 6082 using GTAW Process. *Int J Res Mech Eng Technol (IJRMET)* 3(2):143–146
10. Akinlabi ET, Kailas SV, Brandi SD (2018) Microstructural properties of a dissimilar friction stir welded thick aluminum AA6082-t6 and AA7075-t6 alloy. *Mater Today* 5(9):18297–18306
11. Sameer MD, Anil Kumar B (2019) Mechanical and metallurgical properties of friction stir welded dissimilar joints of AZ91 magnesium alloy and AA 6082–T6 aluminium alloy. *J Magnesium Alloys* 7(2):264–271
12. Kumar A, Sundarajan S (2009) Optimization of pulsed TIG welding process parameters on mechanical properties of AA 5456 aluminium alloy weldments. *J Mater Design* 30:1288–1297
13. Cabello Munoz A, Ruckert G, Huneau B, Sauvage X, Marya S (2008) Comparison of TIG-welded and friction stir welded Al–4.5Mg–0.26Sc alloy. *J Mater Process Technol* 197:337–343
14. Squillac A, De Fenzo A (2004) A comparison between FSW and TIG welding technique modification of microstructure and pitting corrosion resistance in AA 2024-T3 butt joints. *J Mater Process Technol* 152:97–105

15. Senthil Kumar T, Balasubramanian V, Sanavullah MY (2007) Influences of pulsed current tungsten inert gas welding parameters on the tensile properties of AA 6061 aluminium alloy. *J Mater Design* 28:2080–2092
16. Subodh Kumar A, Shahi S (2011) Effect of heat input on the microstructure and mechanical properties of gas tungsten arc welded AISI 304 stainless steel joints. *J Mater Design* 32:3617–3623

Review: Composite Materials for Armour Application



Timo Nieberle, Shiv Ranjan Kumar, Amar Patnaik,
and Chandramani Goswami

1 Introduction

Power armour has an objective to protect the body from injuries caused by direct contact weapon of high-speed projectiles. One can distinguish between body armour and vehicle armour. In order to be feasible for armour application, a material should meet certain requirements. It should be hard and tough, providing penetration resistance and absorbing impact energy while at the same time being lightweight and cost-efficient. Especially in the field of body armour, flexibility in design and manufacturing are also of high interest. In general, the choice of material depends strongly on the specific application, and a compromise between weight, flexibility and protection level has to be taken. In this regard, various materials have been fabricated and tested. The armour materials can be classified as metal and alloys, polymers, ceramic and composite.

1.1 Metals and Alloys

Iron and steel (an alloy of iron with carbon) have been the main material for armours for a long time. They are still used in the field of vehicle armour due to their high strength, easy manufacturing and low cost. Aluminium offers much lower density, but also strength is reduced in comparison with iron. The ballistic impact behaviour

T. Nieberle
Chair of Experimental Physics I, University of Augsburg, Augsburg, Germany

S. R. Kumar (✉)
Mechanical Engineering Department, JECRC University, Jaipur, India
e-mail: ranjan.shiv@gmail.com

A. Patnaik · C. Goswami
Mechanical Engineering Department, Malaviya National Institute of Technology, Jaipur, India

of these materials and their dependence, e.g. on tempering is still part of current investigations [1, 2]. Titanium is as strong as iron with a lower density, but more expensive than iron. In the tank armour, sometimes depleted uranium (by-product of enriched uranium for nuclear reactors) is used due to its very high density.

1.2 Glassy Polymers

Transparent armour can be realized using thermoplastics with high mechanical properties like polycarbonates and acrylic glass. Often laminated glass consists of alternate layers of a polymer in the glassy state (hard and brittle) and plastic state (softer, allows deformation) which are bound by a vinyl adhesion layer.

1.3 Ceramics

Ceramics are inorganic, non-metallic materials that are often produced in a sintering, reaction-bonding or gel casting process [3]. Aluminium oxynitride Al_2O_3 with certain N content (ALON) is available in a polycrystalline (cubic) structure, is transparent for visible light and has enhanced mechanical properties in comparison with glassy polymers, but it is very expensive and therefore, only used for high-end applications. Next to conventional powder processing and sintering, ALON can be produced using a gel casting process resulting in a higher homogeneity and improved mechanical properties [4]. Boron carbide (B_4C) combines low density with being one of the hardest known materials (almost as hard as diamond), but does not provide good energy dispersion of high-velocity impacts due to its brittleness [5]. Silicon carbide (SiC) and titanium diboride (TiB_2) and wolfram carbide (WC) are other established ceramic armour materials. To evaluate their performance in case of ballistic impact, their volume and mass gain compared to rolled homogeneous armour (RHA) made of conventional steel can be investigated. The hybrid armour ceramic plates often have the task to fracture the projectile core into fragments, reducing the effectiveness of the projectile and distributing the impact load on a larger area.

1.4 Composites

The term composite armour often refers to a material combination of woven or unwoven fabrics of yarns, which are embedded in a thermoset or thermoplastic resin matrix. A thermoplastic consists of long-chain polymers that are bound together by intermolecular forces. Heating or cooling leads to reversible melting and solidification. In a thermoset resin, covalent bonds are formed in a chemical reaction between the resin components. A widely used class is so-called epoxy resin, which has highly

reactive characteristic epoxy groups (three-ring of oxygen and two carbon atoms). After mixing the resin with an appropriate hardener (or linker), an exothermic cross-linking reaction is launched, and the resin performs a phase transitions from the liquid to the rubbery to the glassy state. A typical class of hardener is polyfunctional amines that can bind several epoxy molecules by a nucleophile addition reaction. Depending on the used resin system, the curing process might require elevated temperatures. The resulting product shows high mechanical, thermal and chemical stability, but is quite brittle just like thermoplastics. Therefore, it can be very advantageous to strengthen the material, e.g. with meshes of fibres.

Fabrics are available in very different configurations. It can be woven two-dimensional as well as three-dimensional. Either a single yarn material is used or several (hybrid fabric), and for easy manufacturing, fabrics can be pre-impregnated (prepreg) so that heating under pressure is enough to obtain the final component. Classical fibres types like carbon and glass are widely used in aerospace technology and for wind blades, etc. Apart from that for armour application, several other types have been investigated. There are so-called rigid chain aromatics like nylon or aramid (aromatic polyamide) fibres. Nylon is the oldest synthetic fibre, but could not stop bullets effectively. In 1960, an aramid fibre poly (*p*-phenyleneterephthalamid (PPTA)) was developed, which is still widely used and has Kevlar or Twaron as trade names. Another similar aramid is poly (m-phenylenisophthalamid) (PMPI), which is known as Nomex. Vectran is spun from a liquid crystal solution, which leads to high orientation within the resulting fibre. The fibre types have excellent mechanical properties but degrade slowly in case they are exposed to UV-radiation. Another class is especially stable at high temperatures, to which belong polybenzimidazole (PBI) and poly (*p*-phenylen-2,6-benzobisoxazol) (PBO) with trade name Zylon. Finally, there are also thermoplastic fibres made of high-modulus polyethylene (HMPE) or ultra-high molecular weight polyethylene (UHMWP), which have Dyneema and Spectra as trade names. The mechanical properties of various fibre and their historical evaluation are reviewed [6]. The theoretical ballistic limit velocity V50 parameter represents the velocity needed to penetrate the material with a probability of 50%. Synthetic fibres are usually spun to yarns and threads. A measurement quantity to describe the thickness of yarn or thread and to classify them is the linear mass density which can be given in the unit of denier and determines the thickness of the material for a known volume density. Kevlar fabrics often consist of woven yarns, while Dyneema and Spectra are typically used unwoven by placing single sheets of nonwoven fabric over each other with 90° angle. The nonwoven fabrics show a different stress–strain response and depending on the fibre type used can react quicker with laminate stiffness coupled to fibre stiffness. The nonwoven fabrics also may lead to a more global delamination effect. In contrast, the woven fabric is more compliant, which enhances the fibre stretching period before rupture. Different types of nonwoven fabrics, including filaments with resin reinforcement, stitch-bonded, cross lapped and needle punched fabrics, are weaved in different ways [7–9].

1.5 *Advanced Composite Materials*

Apart from conventional synthetic fibres, some other (often nanoscale) materials show great potential to substitute synthetic fibres in composites or be used in combination with them. One of these material classes is shear thickening fluids (STF, dilatant). Shear thickening fluids do not exhibit linear elastic behaviour which is in contrast with Newton Fluids. Instead, their viscosity rises strongly in that case high shear stress is applied, e.g. by a high-velocity impact. Colloidal suspensions, for example, polyethylene glycol with silica particles can show shear thickening properties. Shear thickening fluids are already used to strengthen Kevlar composites by impregnating the fibres prior to composite fabrication [10]. Another similar approach based on a fluid is the so-called magnetorheological fluid (MRF) [11]. MRFs consist of oils with a volume content of 20–40% microscale iron particles that align within less than 0.02 s when a magnetic field is applied and therefore increase the viscosity of the fluid dramatically or even transform it into a solid body. The magnetic field which is needed for the enhanced mechanical properties can be produced by electrical circuits running through the material. Nanofiller materials, which can be added to the epoxy matrix prior to fabrication, are a straightforward, but effective possibility to strengthen the composite. According to Marquis et al. [12], a nanocomposite is a multiphase solid in which one phase has at least one dimension being smaller than 100 nm (nanoplates, nanotubes, nanoparticles). Usually, the content of nanofiller within the polymer is within 1–10 wt%. The most widely used reinforcement is clay due to its natural abundance. Nano-oxides are another class of nanofillers. Titanium oxide (TiO_2) nanoparticles can have different sizes. So-called anatase has a diameter of around 20 nm, while rutile is much bigger (200–300 nm) and is used as a white pigment. Nano alumina is made of spherical crystal particles of Al_2O_3 and is used in a wide range of sizes (20 nm up to several μm). Also, the size of nano-silica varies a lot depending on the way of production or natural origin. Carbon nanotubes (CNT) can have a length in μm scale and a diameter of only several nm. They have extraordinarily high Young's modulus, heat conductivity and electrical conductivity. Also, the relatively low density of carbon nanotubes can be mentioned. The objective of carbon nanotubes within a composite is to maximize the energy dispersion into the matrix [13]. There exist several types of modification to improve the interfacial interactions with the matrix. One possibility is chemical functionalization. The material can bind both the carbon nanotube as well as the polymer matrix, for example, amines or silanes. Plasma etching can produce defects in the carbon nanotubes resulting in the possibility to bind functional groups. Another surface modification can be applied via plasma deposition of a very thin polymer film (2–7 nm) on the surfaces of the CNTs [14].

Cai and Song [15] describe the fabrication of graphene and graphene reinforced polymer nanocomposites. They give evidence that the tensile strength and Young's modulus increase with increasing graphene content and also provide an overview of thermal and electrical properties. Due to lower fabrication cost, graphene might substitute carbon nanotubes, but there are still challenges remaining large scale

usage. Especially better methods to produce the graphene precursor graphite oxide have to be developed, and techniques to functionalize graphene are necessary because of often low polymer graphene interaction. In general, the production of body armour of sufficient thickness based only upon CNTs is still quite costly and challenging [16].

Bhatnagar [7] provides a very detailed overview of several aspects concerning modern composite armour, including bullet characterization and analysis, computational modelling of impact events, types of material with their application and processing. A detailed analytical description of the ballistic impact of a rigid cylindrical projectile into a 2D woven fabric composite is given in Pandya et al. [17]. A variety of energy-absorbing mechanisms are considered including compression close and more distant to the impact area, shear plugging, tensile failure and deformation, matrix cracking and delamination. Experiments with glass and carbon composites showed good agreement with the theoretical ballistic limit velocity V_{50} . Shear plugging, stretching and tensile failure seem to be the most critical energy dissipating mechanisms in the direct surrounding of the projectile. Gibson et al. [18] investigated the performance of a Kevlar epoxy composite with 1.67 wt% added carbon nanotubes (CNTs) or milled fibres. By measuring the residual strain in the Kevlar fibres with Raman spectroscopy, they could estimate the transmitted energy by stress wave propagation. After ballistic tests, they observed an improvement of the behaviour for the component with carbon nanotubes which they traced back to an increase of the critical stress intensity factor of the brittle epoxy polymer. For 0.5 wt% CNTs, they did not detect any improvement which is due to the fact that for such low content the CNTs did not form a good aggregate with the larger milled fibres, and therefore, crack propagation during a ballistic impact was not prevented as efficient as for higher CNT contents.

Fogle [19] worked on how to enhance the absorption of shockwave energy from explosive blasts in thermoplastic polyurethane (TPU) by reinforcement with high-modulus nanoparticles such as fullerene (C60), nano-clay, inorganic disulphide nanotubes and others. Applying different deposition techniques, they found that an ultrasonic spray technique led to the best dispersion. With the lowest tested content of 0.2 wt% C60, the highest strength exceeding the reference sample by a factor of 15 could be obtained.

Monteiro et al. [20] incorporated raw bagasse or extracted bagasse fibres from sugar cane into polymeric composites. They conducted ballistic tests with 30 vol.% bagasse composite plate as a second layer and a ceramic plate as a first layer. While the raw bagasse composite showed worse ballistic performance with almost twice the indentation depth, the indentation depth of the bagasse fibre composite was comparable to the traditional Kevlar composite. A significant advantage of bagasse composites is that they are about 180% less expensive than Kevlar composites and more sustainable as bagasse is a by-product of sugar and ethanol production. Benzait and Levent [6] reported on similar studies and results with Sisal fibres, Curaua, giant bamboo and Jute, among others. Although tensile strength and modulus of the natural fibres are much smaller than the ones of Kevlar, this seems to be not the most critical parameter when the composite is used as a second layer in a multilayered

armour system. In this case, the energy dispersion capacity is more important as the first ceramic layer is first confronted with the projectile and scatters.

Braga et al. [21] conducted ballistic tests with Amazon Curaua nonwoven fabrics as the second layer in a multilayered armour system with ceramic as the front layer. The NIJ standards could still be fulfilled although the back-face damage was more extensive compared to the Kevlar composites. The microscopic analysis confirmed that the same fracture mechanism occurred in both composites.

Randjbaran et al. [22] performed ballistic tests with hybrid composite material consisting of different stacking sequences of carbon, glass and Kevlar fabrics. They deduce that using a glass layer on the front is effective, and the combination of carbon and glass is more efficient to use in the central layers. Also, due to low measured energy absorption in one sample, they do not recommend employing carbon fibres as the last layer [23]. Using a DGEBA-based epoxy resin and hand layup method, they compared reinforcement properties with plain Kevlar fabrics and Kevlar/glass hybrid fabrics. They found that the hybrid structure developed higher tensile and bending strength as well as impact energy absorption.

Bandaru et al. [24] investigated hybrid composites consisting of different meshes (symmetric or unsymmetrical woven, 2D or 3D) within a polypropylene matrix. Applying a material model, they could predict matrix cracking, fibre failure, shear plugging and delamination for ballistic impact. While the impact pattern on the front did not vary with different stacking sequences, the back-face impact pattern and projectile deformation were influenced by the stacking sequence. Udatha et al. [25] used an analytical model to simulate the behaviour of 2D and 3D woven composites during ballistic impact. Experimental results confirmed that the limit velocity for the 2D plain weave composite is lower than that for the 3D woven composite, which is consistent with findings [26] which shows that 3D weaves have higher interlaminar fracture toughness and higher damage tolerance than 2D weaves. However, the weaving process might lead to a degradation of the yarns.

Majumdar et al. [10] analysed the dependency of the impact behaviour of Kevlar composites with respect to padding pressure during processing and nano-silica content in the shear thickening fluid (STF) used. They found that high STF content and pressure can strongly enhance the amount of energy absorbed during impact. Although higher pressure reduces the STF add-on %, it promotes a more uniform distribution of STF resulting in better triggering of the shear thickening behaviour (a strong increase of viscosity in case of high-velocity impact) and therefore higher impact resistance. Shear thickening fluids can also be used to strengthen pure Kevlar fabrics without any polymeric resin component. By impregnating the fabrics with a colloidal solution containing silica particles (diameter around 400 nm), the performance in stab tests could be improved [27]. This can be meaningful, especially for armour which is made to protect neck and joints where certain flexibility of the material is required.

Hetherington [28] investigated two-component vehicle armour consisting of a front ceramic plate and an aluminium 5083 backing plate. A theoretical model was applied to determine the ballistic limit velocity V_{50} in dependence of the plate thickness ratio. Ballistic impact experiments could confirm that there is an ideal thickness

ratio. Sioh [29] also studied composite ceramic consisting of a steel backing layer and ceramic front layer concentrating on the interface properties, as these are the weakest part of the armour.

Reis and Ferreira [30] performed ballistic experiments with Kevlar composites with cork powder and nanoclays Cloisite 30B as nanofiller material. With their experiments, they could enhance the maximum impact load by 16.1% when using clays. Only cork as a filler led to 4.5% enhancement and a combination of both fillers to an increase of impact load of 10.4%. The elastic recuperation for clay-filled composites was found to be 40.1% higher than for unfilled references and the damaged area increased by 29%.

Kaufmann et al. [31] conducted penetration tests with four different commercially available ceramics (silicon carbide, boron carbide, alumina and modified alumina). They state that compressive strength and hardness is important for the initial resistance of a ceramic to penetration. These properties lead to deflection and blunting, which decrease the ability of the projectile to penetrate further into the material. Also, a high bulk, shear and Young's modulus, which are interrelated with the Poisson ratio, help resisting deformation to failure. The penetration tests showed that silicon carbide and boron carbide had better performance than the alumina alloys, which showed similar behaviour.

Silva et al. [32] investigated three compositions of commercial alumina containing 92, 96 and 99.7 wt% Al_2O_3 , regarding their suitability for ballistic ceramics. The plates were tested for hardness and flexural strength. Although the alloys with 92 and 99.7% showed comparable results, the 92% alloy was selected for the ballistic test due to its lower porosity. Five 12 mm thick plates were tested according to AISI 1045, and none of the shots with energy of around 4000 J showed penetration in the used metal backing layer. Azarafza [33] performed mechanical testing and ballistic experiments with pure Al_2O_3 and Al_2O_3 with 5, 10 and 15 wt% added SiC nanoparticles. They detected the best fracture toughness and flexural strength for the 10% compound. This modification of pure Al_2O_3 led to higher impact resistance with a decreased density at the same time. Similar results were obtained when testing laminated structures containing a ceramic front layer with 10 vol.% SiC and 500 ppm MgO nanoscale particles added to conventional Al_2O_3 and a metallic backing layer. For the compound treated with nanofillers, the flexural strength increased by 57% and the hardness by 35%. They measured the amount of bulge and bending of the backing layer and observed a higher energy distribution factor for the 10% SiC treated composite [34]. Gopalakannan and Senthilvelan [35] also worked with SiC nanoparticles. Still, they produced a so-called metal matrix composite to enhance the properties of Aluminium 7075 (Al–Zn–Mg–Cu alloy) instead of aluminium oxide and also applied 0.5 wt% B_4C nanoparticles. Analysing the distribution of nano B_4C and SiC, they found that B_4C particles showed better dispersion and fewer clusters because of their wettability property. Nevertheless, an amplification of tensile strength and hardness was observed for both nanofiller materials.

Park et al. [36] investigated the interfacial properties and micro failure mechanisms for Kevlar and Zylon fibres using micromechanical techniques and non-destructive acoustic emission. They found that the adhesion between the fibres can be enhanced

activating the surface with plasma oxidation as more covalent and hydrogen bonds can be formed between the fibres after plasma treatment. The plasma-treated Kevlar showed the maximum critical surface tension, while the untreated Zylon showed the lowest. It may be attributed to the fact that Kevlar has more hydrophilic functional groups.

Polak et al. [37] investigated three commercially available types of bulletproof vests. They performed ballistic tests in which they analysed the depression depth of a backing layer for various insertion parts of the vests, projectile velocities and environmental circumstances (wet or dry surface). In general, the mechanical properties of the fibre composites can differ for wet or dry circumstances. All the vests could resist the impacts according to the specified standard. The depth of depression was found to be dependent on the part of the vest that was investigated (front, back, abdomen) as different composite inserts were used. The influence of environmental circumstances was not found to be very significant. Further, they also discussed the steps required to produce a bulletproof vest and overviewed the classification of the protection level (depending mainly on the mass and velocity of the projectile) [38]. Zaera pointed out a historical development of armour material and also showed possibilities to model the impact behaviour of composites and ceramics [39].

Njuguna et al. [40] investigated the effect of nanofiller reinforcements on several polymeric composites based on polyesters, polyamides (PAs), polyurethanes (PUs), polypropylenes (PPs), polyimide (PI) and poly p-phenylene benzobisoxazole (PBO). In the study to characterize the effect of nanoparticles and micro-particles on mechanical properties of composite, they point out that while micro-particles almost do not participate in the plastic zone deformation, nanoparticles can contribute stronger to the fracture energy values due to their higher surface per volume fraction. Furthermore, they remind that nanoparticles, as well as colouring pigments, can affect the morphology of the polymer which is obtained during curing, what makes it more challenging to separate the effect of the pure material variation.

In the very recent analysis of the design of body armour, stacked systems of hard armour plates are suggested to be very advantageous for which the newest ultra-high molecular weight polyethylene (UHMWPE) is crucial. It is pointed out that it can be convenient to develop soft and hard body armour as separate clothing which can be combined [41].

2 Conclusions

Modern weapons are becoming more sophisticated and destructive; therefore, there is a strong demand for the improvement in armour material. While conventional materials like metals, alloys and ceramics are mainly used for vehicle armour, body armour requires a material with higher performance, offering impact resistance and being lightweight at the same time. Composite materials seem to be the best option to meet these demands. In this review, possibilities were shown how to improve the

ballistic performance of composites. Adding different kinds of nanofillers is a prevalent and robustly investigated approach. Due to their outstanding properties, carbon nanotubes and graphene seem to be very promising for future armour materials.

References

1. Jena PK, Kumar KS, Krishna VR, Singh AK, Bhat TB (2008) Studies on the role of microstructure on performance of a high strength armour steel. *Eng Fail Anal* 15(8):1088–1096
2. Jena PK, Mishra B, Kumar KS, Bhat TB (2010) An experimental study on the ballistic impact behavior of some metallic armour materials against 7.62 mm deformable projectile. *Mater Design* 31(7):3308–3316
3. Akella K, Naik NK (2015) Composite armour—a review. *J Indian Inst Sci* 95(3):297–312
4. Wang J, Zhang F, Chen F, Zhang H, Tian R, Dong M, Wang S (2014) Fabrication of aluminum oxynitride (γ -AlON) transparent ceramics with modified gelcasting. *J Am Ceram Soc* 97(5):1353–1355
5. Savio SG, Ramanjaneyulu K, Madhu V, Bhat TB (2011) An experimental study on ballistic performance of boron carbide tiles. *Int J Impact Eng* 38(7):535–541
6. Benzait Z, Trabzouk L (2018) A review of recent research on materials used in polymer–matrix composites for body armor application. *J Compos Mater* 52(23):3241–3263
7. Bhatnagar A, Lang D (2006) Military and law enforcement applications of lightweight ballistic materials. In: *Lightweight ballistic composites*. Woodhead Publishing, pp 364–397
8. Thomas HL (2006) Non-woven ballistic composites. In: *Lightweight ballistic composites*. Woodhead Publishing, pp 240–271
9. Song JW (2006) Fabrics and composites for ballistic protection of personnel. In: *Lightweight ballistic composites*. Woodhead Publishing, pp 210–239
10. Majumdar A, Butola BS, Srivastava A (2014) Development of soft composite materials with improved impact resistance using Kevlar fabric and nano-silica based shear thickening fluid. *Mater Des* 1980–2015(54):295–300
11. Olszewska K, Polak J, Zielińska D, Struszczyk MH, Kucińska I, Wierzbicki Ł, Wiśniewski A (2013) Textile multilayered systems with magnetorheological fluids for potential application in multi-threat protections. Preliminary stab-resistance studies. *Fibres & Textiles in Eastern Europe*
12. Marquis DM, Guillaume E, Chivas JC (2011) Nanocomposites and polymers with analytical methods. Intech. ISBN 978-953-307-352-1
13. Treacy MJ, Ebbesen TW, Gibson JM (1996) Exceptionally high Young's modulus observed for individual carbon nanotubes. *Nature* 381(6584):678–680
14. Naghizadeh Z, Faezipour M, Pol MH, Liaghat GH, Abdolkhani A (2018) Improvement in impact resistance performance of glass/epoxy composite through carbon nanotubes and silica nanoparticles. *Proc Inst Mech Eng Part L: J Mater Design Appl* 232(9):785–799
15. Cai D, Song M (2010) Recent advance in functionalized graphene/polymer nanocomposites. *J Mater Chem* 20(37):7906–7915
16. Crouch I (ed) (2016) *The science of armour materials*. Woodhead Publishing
17. Pandya KS, Kumar CVS, Nair NS, Patil PS, Naik NK (2015) Analytical and experimental studies on ballistic impact behavior of 2D woven fabric composites. *Int J Damage Mech* 24(4):471–511
18. Gibson J, McKee J, Freihofer G, Raghavan S, Gou J (2013) Enhancement in ballistic performance of composite hard armor through carbon nanotubes. *Int J Smart Nano Mater* 4(4):212–228
19. Fogle JG (2013) Processing, structure, and properties of nanoparticle reinforced nonwoven sandwich composites. PhD. Dissertation, University of Tennessee, Knoxville

20. Monteiro SN, Candido VS, Braga FO, Bolzan LT, Weber RP, Drelich JW (2016) Sugarcane bagasse waste in composites for multilayered armor. *Eur Polymer J* 78:173–185
21. De Oliveira Braga F, Cabral AC, Lima ÉP, Monteiro SN, de Assis FS (2017) Curaua non-woven fabric composite for ceramic multilayered armors: a lightweight, natural, and low cost alternative for Kevlar TM. In: *Proceedings of the 3rd Pan American Materials Congress*. Springer, Cham, pp 339–346
22. Randjbaran E, Zahari R, Majid DL, Jalil NA, Vaghei R, Ahmadi R (2013) The effects of stacking sequence layers of hybrid composite materials in energy absorption under the high velocity ballistic impact conditions: an experimental investigation. *J Mater Sci Eng* 2(4):1–8
23. Valença SL, Griza S, de Oliveira VG, Sussuchi EM, de Cunha FGC (2015) Evaluation of the mechanical behavior of epoxy composite reinforced with Kevlar plain fabric and glass/Kevlar hybrid fabric. *Compos B Eng* 70:1–8
24. Bandaru AK, Ahmad S, Bhatnagar N (2017) Ballistic performance of hybrid thermoplastic composite armors reinforced with Kevlar and basalt fabrics. *Compos A Appl Sci Manuf* 97:151–165
25. Udatha P, Sessa Kumar CV, Nair NS, Naik NK (2012) High velocity impact performance of three-dimensional woven composites. *J Strain Anal Eng Design* 47(7):419–431
26. Shahkarami A, Cepus E, Vaziri R, Poursartip A (2006) Material responses to ballistic impact. In: *Lightweight ballistic composites*. Woodhead Publishing, pp 72–100
27. Li X, Cao HL, Gao S, Pan FY, Weng LQ, Song SH, Huang YD (2008) Preparation of body armour material of Kevlar fabric treated with colloidal silica nanocomposite. *Plast Rubber Compos* 37(5–6):223–226
28. Hetherington JG (1992) The optimization of two component composite armours. *Int J Impact Eng* 12(3):409–414
29. Sioh EL (2010) Functional graded material with nano-structured coating for protection. *Int J Mater Prod Technol* 39(1–2):136–147
30. Reis PNB, Ferreira JAM, Santos P, Richardson MOW, Santos JB (2012) Impact response of Kevlar composites with filled epoxy matrix. *Compos Struct* 94(12):3520–3528
31. Kaufmann C, Cronin D, Worswick M, Pageau G, Beth A (2003) Influence of material properties on the ballistic performance of ceramics for personal body armour. *Shock Vibr* 10(1):51–58
32. Silva MV, Stainer D, Al-Qureshi HA, Montedo ORK, Hotza D (2014) Alumina-based ceramics for armor application: mechanical characterization and ballistic testing. *J Ceramics*
33. Azarafa R, Arab A, Mehdipoor A (2012) Impact behavior of ceramic-metal armour composed of Al₂O₃-nano SiC composite. *Int J Adv Design Manuf Technol* 5(5):83–87
34. Asadi A, Vanini AS, Jabbari A (2011) Investigation on the impact behavior of Al₂O₃-SiC-MgO nanoceramic/metal laminated composite. *J Mech Sci Technol* 25(9):2179
35. Gopalakannan S, Senthilvelan T (2015) Synthesis and Characterisation of Al 7075 reinforced with SiC and B 4 C nano particles fabricated by ultrasonic cavitation method. *J Sci Ind Res* 74:281
36. Park JM, Kim DS, Kim SR (2003) Improvement of interfacial adhesion and nondestructive damage evaluation for plasma-treated PBO and Kevlar fibers/epoxy composites using micromechanical techniques and surface wettability. *J Colloid Interface Sci* 264(2):431–445
37. Polak J, Kucinska I, Grabowska G, Błaszczuk J, Ledwon E, Romek R, Struszczyk MH (2009) Bullet-proof vests with the ballistic inserts based on the fibrous composites. *Techniczne Wyroby Włókiennicze* 17:95–106
38. Kumar KN (2016) Bulletproof Vest and Its Improvement—a review. *Int J Sci Develop Res (IJS DR)* 1:34
39. Zaera R (2011) Ballistic impacts on polymer matrix composites, composite armor, personal armor. In: *Impact engineering of composite structures*. Springer, Vienna, pp 305–403
40. Njuguna J, Pielichowski K, Desai S (2008) Nanofiller reinforced polymer nanocomposites. *Polym Adv Technol* 19(8):947–959
41. Crouch IG (2019) Body armour—New materials, new systems. *Defence Technol* 15(3):241–253. <https://doi.org/10.1016/j.dt.2019.02.002>

Identification of Effective Potassium Permanganate Fiber Surface Treatments on Mechanical Properties of Epoxy/*Ricinus communis* L Fiber Composites



Rajesh Egala and Srinivasu Gangi Setti

1 Introduction

In modern days, natural fiber reinforced composites have recognized an enhanced number of usages in a global activity specifically for some low load industries involved with natural friendly components, i.e., household and automotive [1–3]. Natural fibers such as bamboo, sisal, coir, kenaf, jute, hemp, flax and abaca fiber have been evidenced to be better reinforcement in thermoplastic and thermoset matrices. The advantages affiliated with the utilization of natural fiber as filler in polymers include their high specific properties, low density, low energy consumption, biodegradability and low cost. These materials discover their way in nonstructural usages such as interior parts of the automobile, the casing of electronic materials. Most of the natural fiber composites formulated so far have mechanical values lower than synthetic fiber composites, which curbs their utilization in high load applications.

However, the drawback of natural fibers is their nature of hydrophilic that degrades the compatibility zone with polymeric hydrophobic matrices during composite fabrication. The mechanical values of natural fiber composite rely on the degree of interfacial shear adhesion between the matrix and natural fiber [4]. Thereby, the inadequate matrix/fiber bonding interface leads to a lower strength composite. In the last years, numerous researchers concentrated on enhancing the adhesion by altering the fiber surface texture via chemical and physical treatments to compose them added compatible with matrix [5].

Various treatments have been researched in present scenarios such as sodium chloride, stearic acid, peroxide, permanganate, acrylation, benzylation, acetylation, silane, alkaline, electric discharge and cyano ethylation. Various surface chemical treatments have been utilized to enhance cellulosic fiber/polymer matrix interfacial

R. Egala · S. Gangi Setti (✉)
Mechanical Engineering Department, National Institute of Technology Raipur, Raipur, India
e-mail: sgsetti.me@nitrr.ac.in

adhesion bond in natural fiber reinforced composites [6–10]. Zhu et al. [11] worked on the effect of alkalization on mechanical properties of flax fiber – tannin resin composite. They represented that the alkalized flax fiber composites have higher tensile, flexural values than untreated ones. Gejo et al. [6] enhanced interfacial shear bonding between jute fiber and polypropylene yarns using four types of fiber surface treatments, namely stearic acid, KMnO_4 , toluene diisocyanate and maleic anhydride-modified polypropylene. It was shown that KMnO_4 treated jute fiber reinforced polypropylene yarns show higher mechanical values when compared to other treatments. Tran et al. [8] enhanced the mechanical values of jute coir/poly(butylene succinate) biodegradable composites by alkali treatment. Bhanu et al. [10] advised that it was reasonable to alter the surface of the jute fibers to enhance the interfacial shear adhesion with the polylactide in order to appreciate the high potential of polylactide/jute composites. Studying the work carried out by different authors, it understood that matrix/fiber interfacial adhesion is the main factor in analyzing the properties of composites. Therefore, an effort is made in this research to enhance the interfacial shear adhesion of the epoxy with the castor oil fiber by potassium permanganate treatment. The present research has demonstrated the result of potassium permanganate treatment on the mechanical performance of composites.

2 Experimental Procedures

2.1 Materials

In the present investigation, Castor oil cortex fiber was obtained [12] by retting and mechanical rolling. The epoxy resin of HY951 and LY556 was utilized as a matrix material [13].

2.2 Chemical Treatment

Potassium Permanganate (KMnO_4) Treatment: In Potassium permanganate (KMnO_4) treatment, castor oil fibers were immersed individually in a chemical solution. The concentration of KMnO_4 is varied from 0.1 to 1% (Fig. 1) with 4 soaking timings of 5, 15, 25, 35 and 50 min. The fibers were cleaned until all fibers were Potassium permanganate free and then dried in an oven at various temperatures from 35 to 110 °C. The feasible list of tests located on the trial and error process is shown in Table 1.

Fabrication of Unidirectional Fiber Reinforced Composites: The composites were fabricated, using castor oil fiber as filler and epoxy as matrix via hand layup method as explained in the previous study [14, 15].

Fig. 1 Potassium permanganate treatment of castor oil fiber



Table 1 Possible list of tests

S. No.	Experiment Number	Concentration (%)	Soaking time (min)	Drying temperature (°C)
1	KMnO ₄ -1	0.1	5	35
2	KMnO ₄ -2	0.3	5	35
3	KMnO ₄ -3	0.5	5	35
4	KMnO ₄ -4	0.8	5	35
5	KMnO ₄ -5	1	5	35
6	KMnO ₄ -6	0.1	25	35
7	KMnO ₄ -7	0.3	25	35
8	KMnO ₄ -8	0.5	25	35
9	KMnO ₄ -9	0.8	25	35
10	KMnO ₄ -10	1	25	35
11	KMnO ₄ -11	0.1	15	35
12	KMnO ₄ -12	0.1	35	35
13	KMnO ₄ -13	0.1	50	35
14	KMnO ₄ -14	0.3	15	35
15	KMnO ₄ -15	0.3	35	35
16	KMnO ₄ -16	0.3	50	35
17	KMnO ₄ -17	0.1	5	50
18	KMnO ₄ -18	0.1	5	70
19	KMnO ₄ -19	0.1	5	90
20	KMnO ₄ -20	0.1	5	110
21	KMnO ₄ -21	0.3	25	50
22	KMnO ₄ -22	0.3	25	70
23	KMnO ₄ -23	0.3	25	90
24	KMnO ₄ -24	0.3	25	110

Testing of Composites: The tensile properties of the composites were measured in correspondence with ASTM: D638-89 [16]. The flexural properties of the composites were measured in agreement with ASTM D790 M [17]. Izod test of the composite was executed as per ASTM D256-88 [18].

3 Results and Discussion

3.1 Tensile, Flexural and Impact Properties of Potassium Permanganate ($KMnO_4$) Treated Composites

The tensile experiment has been worked for the samples with 40% volume fraction by manual hand layup process utilizing $KMnO_4$ treated fiber as mentioned in Table 1. The values of the treated and untreated fiber reinforced composites are presented in Fig. 2a–f. In all the figs, the straight line represents the untreated fiber composites values. Figure 2a presents that strength enhances then decreases as $KMnO_4$ concentration enhances from 0.1 to 1 at 5, 25 min treatment time. Changes in tensile value with alter in concentration represents that as used $KMnO_4$ concentration enhances interfacial strength of samples. $KMnO_4$ -6,7 composites demonstrated better strength values due to 0.1%, 0.3% $KMnO_4$ concentration as consequences of proper concentration causes high rough surface on fiber which cause the best bonding zone between matrix and fiber. Figure 2e demonstrates that tensile modulus increases and decreases as treatment time enhances at 0.1%, 0.3% $KMnO_4$ concentrations at 35°C which shows 0.3% concentration and 25 min treatment time gave high interfacial bond between matrix and fiber. Here $KMnO_4$ -22 fiber-reinforced samples shows 8.5% of the increment in tensile strength and 10% in tensile modulus, alike $KMnO_4$ -21 fibre-reinforced samples represents 5.6% of the increment in tensile strength and 6.5% in tensile modulus, $KMnO_4$ -7 treated fibre-reinforced composites contributes 4.7% of the increment in tensile strength and 0.25% decrement in tensile modulus. $KMnO_4$ -13 treated fiber composite showed 21% decrement over the untreated fiber composite.

The flexural strength value of untreated and treated fiber reinforced samples is shown in Fig. 3. Figure 3a, d shows that flexural value decreases as $KMnO$ concentration enhances at 25 min treatment time. The proper effective chemical treatment of $KMnO_4$ -7 produces better flexural values than $KMnO_4$ -6, 2. Due to proper shear bond between matrix and fiber. The raw fiber sample flexural strength has 121 MPa, $KMnO_4$ -22 and $KMnO_4$ -21 fiber composites have a value of 139 MPa and 136 MPa, respectively. The $KMnO_4$ -22 treated with fiber reinforced composites delivers 15% of the increment in flexural strength and flexural modulus.

Figure 4. shows the impact values of untreated and $KMnO_4$ treated fiber composites. From Fig. 4a, it demonstrated that the impact value is increased with respect to $KMnO_4$ concentration from 0.1 to 0.3 at 35 °C oven temperature. From Fig. 4c, 25-min treatment condition delivered the best impact strength at 0.3% $KMnO_4$

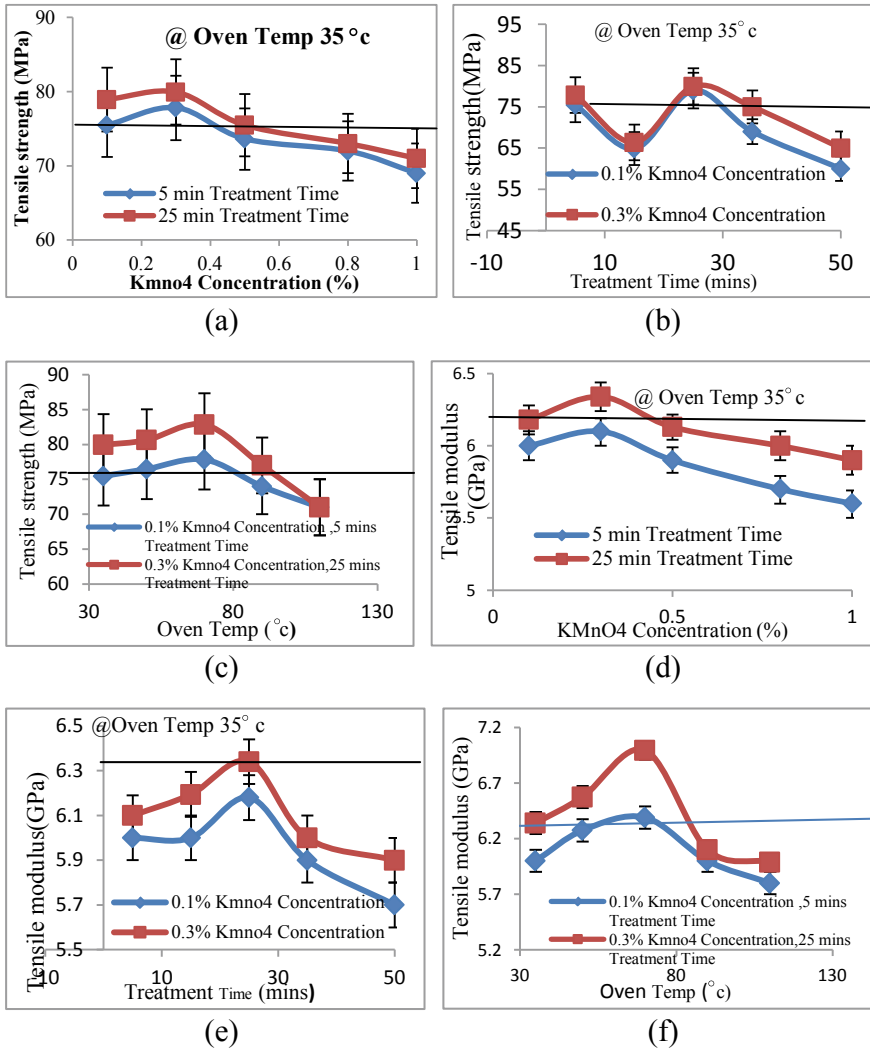


Fig. 2 Tensile strength and Tensile modulus of untreated and different conditions of KMnO₄ treated castor oil cortex fiber composites at 40% volume fraction

concentration at 70 °C, which means KMnO₄-22 chemical condition produced best interfacial shear value than KMnO₄-21,7,6.

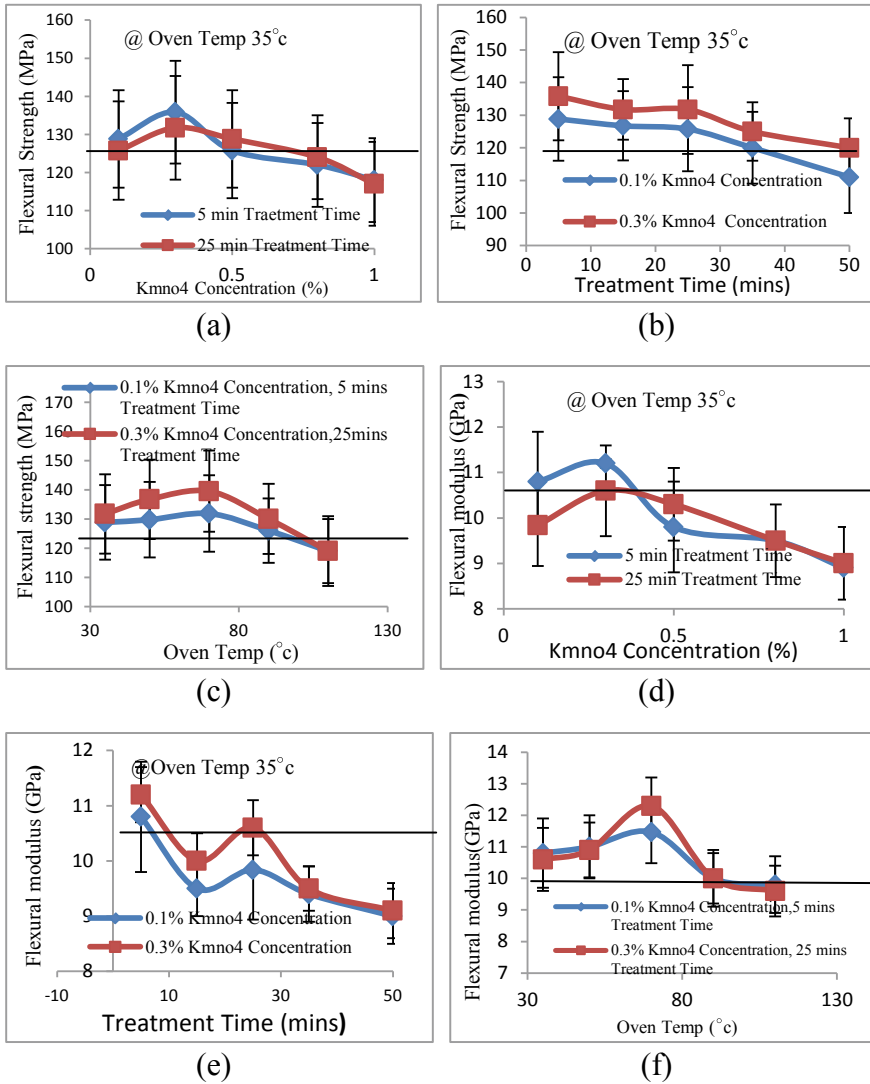


Fig. 3 Flexural strength and Flexural modulus of untreated and different conditions of KMnO₄ treated castor oil cortex fiber composites at 40% volume fraction

3.2 Fractography

The SEM image of composites was presented in Fig. 5. It was realized that from Fig. 5a, b. The represented voids, matrix cracking and deboning of fibers due to fiber pull-outs. This form of failure occurs only because of a lack of interfacial bonding between epoxy and fiber. But in the case of Fig. 5c represented the better interfacial

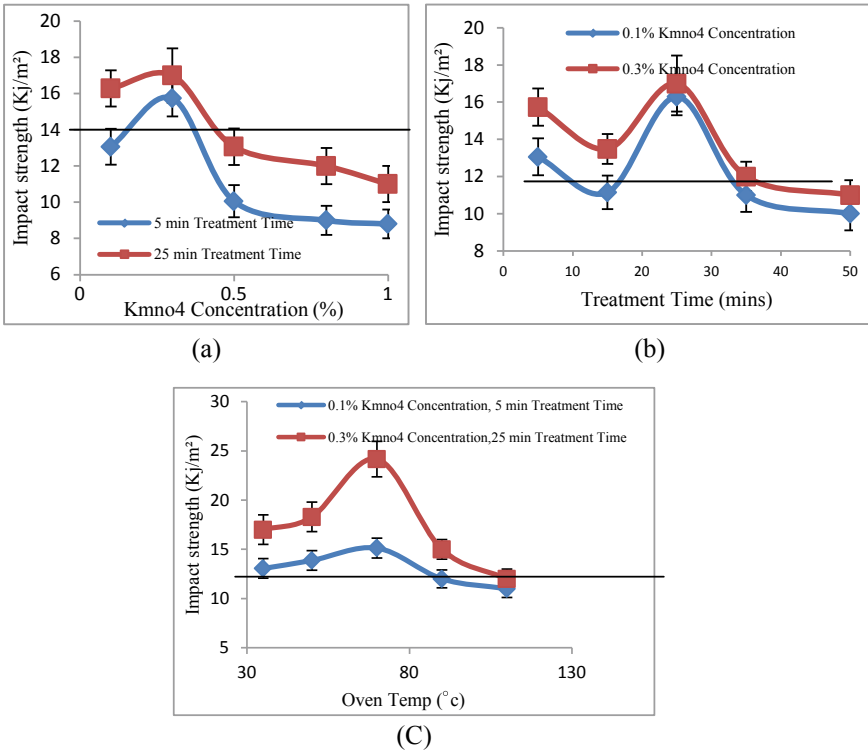


Fig. 4 Impact strength of untreated and different conditions of $KMnO_4$ treated castor oil cortex fiber composites at 40% volume fraction

bonding between fiber and matrix, more fibrillation and resin-rich due to proper treatment of fiber. In Fig. 5d showed fiber breakages, less bonding and more cracks between fiber and matrix (Table 2).

The best possible ranges are mentioned in Table 3 based on the experimental results.

4 Conclusions

- The mechanical values of the fiber composite are regulated by the fiber surface chemical treatments.
- Potassium permanganate treatment enhanced the interfacial strength of the castor oil fiber with the matrix addressing high mechanical properties compared to the untreated fibers.

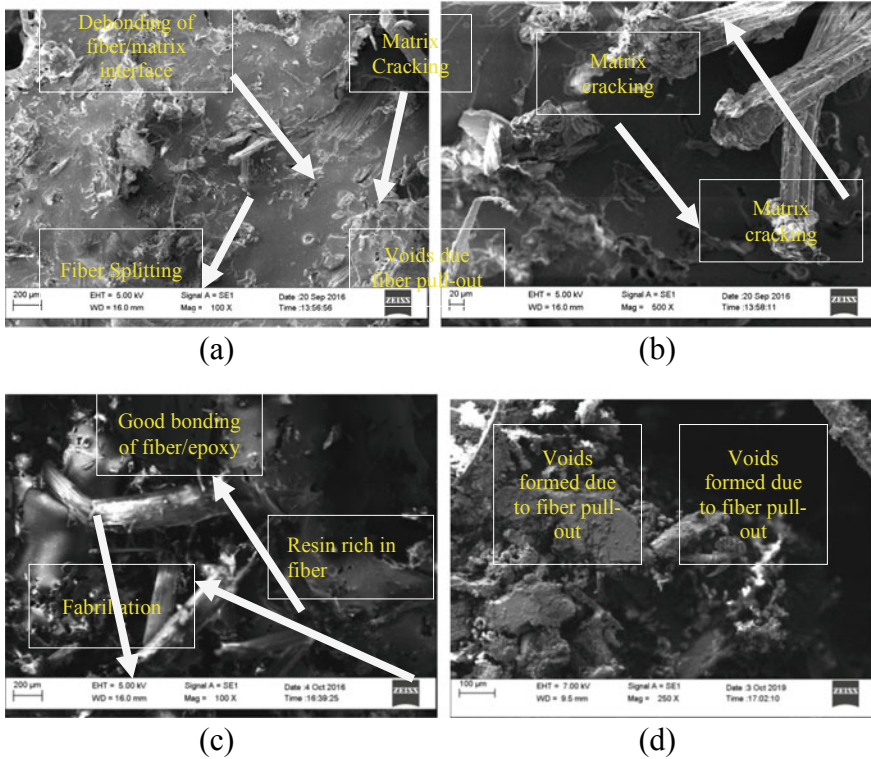


Fig. 5 SEM morphology of tensile fractured surfaces of: **a, b** untreated **c** KMnO_4 -22 treated, **d** KMnO_4 -13 treated Castor oil fiber composite

Table 2 Comparison with untreated fiber composites

Sl. No	Type of composite	Tensile strength (MPa)	Tensile modulus (GPa)	Flexural strength (MPa)	Flexural modulus (GPa)	Impact strength (KJ/m^2)
1	%100 epoxy	26.19 ± 0.84	0.64 ± 0.15	44.19 ± 8.11	1.8 ± 0.88	2.32 ± 0.11
2	Untreated	76.35 ± 4.3	6.35 ± 0.18	121 ± 13.66	10.66 ± 2.17	13.07 ± 0.86
4	KMnO_4 -21	80.63 ± 4.4	6.57 ± 0.09	136.73 ± 13.6	10.9 ± 0.87	18.28 ± 1.5
5	KMnO_4 -22	82.84 ± 4.5	6.994 ± 0.08	139.5 ± 13.9	12.3 ± 0.9	24.17 ± 1.8

Table 3 Best possible ranges

S. No.	Name of the parameter	Units	Range
1	Concentration	%	0.1–0.5
2	Soaking time	mins	5–25
3	Drying temperature	$^{\circ}\text{C}$	35–70

References

1. Faruk O, Bledzki AK, Fink H-P, Sain M (2012) Biocomposites reinforced with natural fibers: 2000–2010. *Prog Polym Sci* 37:1552–1596
2. Fotouh A, Wolodko JD, Lipsett MG (2014) Fatigue of natural fiber thermoplastic composites. *Composites: Part B* 62:175–182.
3. Chakar FSR, Ragauskas AJ (2004) Review of current and future softwood kraft lignin process chemistry. *Ind Crop Prod* 20(2):131–141
4. Zhou Y, Fan M, Chen L (2016) Interface and bonding mechanisms of plant fibre composites: an overview. *Compos B* 101:31–45
5. Azwa ZN, Yousif BF, Manalo AC, Karunasena W (2013) A review on the degradability of polymeric composites based on natural fibres. *Mater Design* 424–442
6. George G, Tomlal Jose E, Jayanarayanan K, Nagarajan ER, Skrifvars M, Joseph K (2012) Novel bio-commingled composites based on jute/polypropylene yarns: effect of chemical treatments on the mechanical properties. *Compos: Part A* 43:219–230
7. Cai M, Takagi H, Nakagaito AN, Li Y, Waterhous GIN (2016) Effect of alkali treatment on interfacial bonding in abaca fiber-reinforced composites. *Compos: Part A* 90:589–597
8. Nam TH, Ogihara S, Tung NH, Kobayashi S (2011) Effect of alkali treatment on interfacial and mechanical properties of coir fiber reinforced poly(butylene succinate) biodegradable composites. *Compos: Part B* 42:1648–1656
9. Kostic M, Pejic B, Skundric P (2008) Quality of chemically modified hemp fibers. *Biores Technol* 99:94–99
10. Goriparthi BK, Suman KNS, Mohan Rao (2012) Effect of fiber surface treatments on mechanical and abrasive wear performance of polylactide/jute composites. *Compos Part A* 43:1800–1808
11. Zhu J, Zhu H, Immonen K, Brighton J, Abhyankar H (2015) Improving mechanical properties of novel flax/tannin composites through different chemical treatments. *Ind Crops Prod* 67:346–354
12. Egala R, Setti SG (2017) Experimental investigation on tensile property of *Ricinus communis* L plant fiber to make polymer reinforced composites. *Mater Today Proc* 4:8633–8637
13. Srinivasan VS, Rajendra Boopathy S, Sangeetha D, Vijaya Ramnath B (2014) Evaluation of mechanical and thermal properties of banana–flax based natural fibre composite. *Mater Design* 60:620–627
14. Egala R, Setti SG (2018a) Effect of short and randomly oriented *Ricinus communis* L (Castor oil) plant on mechanical behavior of *Ricinus communis* L/Epoxy LY556 composites. *Mater Today Proc* 5:8065–8072
15. Egala R, Setti SG (2018b) Impact characterization of epoxy LY556/*Ricinus communis* L plant natural fiber composite materials. *Mater Today Proc* 5:26799–26803
16. ASTM D638–89 (1989) Standard test method for tensile properties of plastics. ASTM International, 29 Jan 1989
17. Hazizan Md, Akil IM, Rosa De, Santulli C, Sarasini F (2010) Flexural behavior of pultruded jute/glass and kenaf/glass hybrid composites monitored using acoustic emission. *Mater Sci Eng A* 527:2942–2950
18. ASTM D256–88 (1988) Standard test method for impact resistance of plastics and electrical insulating materials. ASTM International, 25 Mar 1988

Effect of Fiber Hybridization on the Mechanical Behaviors of Basalt/Borassus Fruit Fiber (BFF)-Reinforced Epoxy Composites



Nitish Kumar and Abhishek Singh

1 Introduction

Presently, in the unsustainable environmental condition, natural fiber-reinforced composites serve better regarding biodegradability, lightweight, readily available, corrosion resistance, high specific strength and low cost as compared with synthesis fiber-reinforced composites [1–3]. Natural fiber-based composite development rate increases day to day due to its various applications in automobile, plastic industry, construction, biomedical, etc. [4, 5]. Global conditions have made it possible to create new markets for natural fiber composites due to their biodegradation properties. Over the various fruitful advantages in natural fiber composites, some limitations are also present in it like low mechanical strength, hydrophilic in nature as well as low thermal resistance [6–9]. One of the important parameters to improve their mechanical properties to some extent is a hybridization of two or more fibers. Many researchers are working in this direction to improve mechanical properties by hybridization methods. Aji et al. [10] described the effect of hybridization of kenaf and pineapple leaf fiber-reinforced composites, and the results show that hybridization of fiber improved the tensile strength and flexural strength of the composites developed. It has also been shown that tensile strength and module increase with an improvement in the percentage of pineapple leaf fiber in a composite. Sathiskumar et al. [11] experimentally investigated that the impact of hybridization on the mechanical and damping properties of sisal fiber and cotton fiber woven mat reinforced polymer composites and found that increased fiber content improves the mechanical and damping properties of hybrid composites by up to 40 percent. Ramesh et al. [12] experimentally investigated that fabrication of hybrid composites reinforced hemp carbon fiber with polymer resin and found that hybrid composites withstand the

N. Kumar (✉) · A. Singh

Department of Mechanical Engineering, National Institute of Technology Patna, Patna, Bihar 800005, India

e-mail: nitish.nitp15@gmail.com

maximum mechanical behavior. Barvarz et al. [13] described the effect of hybridization of flax fiber with glass fiber and found effect on mechanical behavior and the percentage of water absorption of composites. After the experiment, they concluded that hybridization improves the mechanical properties as well as also indicated that mechanical behavior of hybrid composites depends upon the amount of glass fiber content. Amount of glass fiber increases in hybrid composites corresponding to improve the modulus and tensile strength and impact strength as well as hardness. Bulut et al. [14] found the effect of hybridization of Kevlar/glass/epoxy composites and investigated the damping, tensile and vibration characteristics of hybrid composites. It is concluded after investigation hybrid Kevlar/glass/epoxy composites improve the tensile, damping and vibration characteristics as compared to non-hybrid glass/epoxy and Kevlar/epoxy composites. Patel et al. [15] investigated the effect of fiber loading and filler materials on mechanical, physical and wear properties of wood fiber-reinforced composites and found that tensile strength increases up to 10% of WF composites and then after further increases the weight % of WF decreases the same. It was also indicated that hardens value increases up to 20% WF composites and rate of moisture content increases with an increase in both WF and gum rosin concentration. Gujjala et al. [16] investigated the effect of hybridization of jute/glass/epoxy composites with different fiber staking sequences of jute and glass fiber and found that stacking sequence of GJJG composites obtained maximum flexural strength after neat glass fiber.

Similarly, staking sequence of GJJG composites obtained maximum tensile strength after neat glass fiber composites. Patel et al. [17] investigated the effect of a different fiber content and fiber length on mechanical properties of sour weed/polyester composites and found that 6% fiber weight ratio and 15 mm fiber size composites obtained superior mechanical properties as compared with other developed composites. Shakeri et al. [18] studied the effect of hybridization of newspaper/glass fiber-reinforced composites and show that tensile strength increases with increase in glass fiber content and optimum value of tensile strength 55 MPa and tensile modulus obtained 4.1 GPa for hybrid composites containing 10 wt% of newspaper and 20 wt% of glass fiber.

From the literature reviews above, it is shown that hybridization of natural fiber composites significantly affects the mechanical properties of different composite groups. Therefore, a new class of hybrid composites is being developed in the present experimental work based on borassus fruit fiber and basalt fiber-reinforced epoxy composites and their effect on mechanical behaviors such as tensile strength and modulus, flexural strength and modulus, impact strength as well as microhardness of hybrid and non-hybrid composites. In addition to these, water absorption behaviors of hybrid and non-hybrid developed composites were also investigated.

2 Materials and Methodology

2.1 Materials

Borassus fruit fiber (BFF) was extracted from borassus fruits using water immersion methods. These fibers are mostly wastage in the local area without any usages. Borassus fruit is collected from the locality and then extract fiber from these. Extracted fibers were cut with the help of tobacco cutting machine of uniform size approximately 5–10 mm length. Bidirectional basalt fiber (400 GSM) was supplied by Composite Tomorrow Private Limited, Gujarat, India. These fibers were also cut with uniform length 5–10 mm for same tobacco cutting machine. Epoxy resin LY556 and hardener HY951 series were purchased from Go-Green Private Limited Chennai, India. Other required materials were taken from the local market.

2.2 Fabrication of Composite Sheets

Composite materials were fabricated by hand layup techniques. In this technique initially, wooden mold was prepared with a dimension of $200 \times 170 \times 6 \text{ mm}^3$ used for fabrication of composites. The Teflon sheets were placed on the bottom of the mold to obtained good dimensional accuracy and surface finishing. The releasing agent sprays on the surface of the mold to easily remove the composite sheets after curing and prevent to stick to the Teflon sheets. Epoxy and hardener were mixed in 10:01 ratio by weight percentage recommended by suppliers. Three types of composite sheets were laminated under the same condition: (i) 100% chopped BFF, (ii) 100% chopped basalt fiber and (iii) 50% chopped basalt fiber and 50% chopped BFF mixture was taken. The fiber and matrix were taken in the ratio of 70:30 by weight for all three types of fabrication and mixed uniformly in a glass jar. After that, mixture was poured into a wooden mold and roller was used to uniformly distribute the fiber and matrix mixture throughout the mold as well as removing the air bubble entrapped inside the mold. Finally, another Teflon sheets were placed on top of the mold and again roller was used to roll the wet fiber and matrix composition to conform air removed inside the mold. After rolling, a load approximately 50 kg was applied on the top of a mold for 24 h to conform curing, and composite sheets were cut for mechanical testing according to ASTM standard.

2.3 Specimen Preparation for Mechanical Characterization

For the various mechanical characterizations, specimens were prepared according to ASTM standards. Tensile and flexural test specimens were prepared based on ASTM D638 and ASTM D790, respectively, and the test was performed on the same

Zwick/Roell UTM machine. The Charpy and Izod test specimens were prepared based on ASTM A370 and ASTM D256, respectively, and the test was performed on pendulum types of digital impact testing machine. The Rockwell hardness testing specimens were prepared based on ASTM D785-98. Similar to the water absorption test, the specimens were prepared based on ASTM D570-98 standard. For all above types of mechanical testing and water absorption, at least three specimens were tested and the average value is taken for result analysis.

3 Result and Discussion

3.1 Effect of Hybridization on Tensile Strength and Modulus

Tensile strength and tensile modulus of developed hybrid BFF/basalt/epoxy composites and non-hybrid BFF/epoxy and basalt/epoxy composites were experimentally calculated. The result indicated that tensile strength and tensile modulus significantly improved with hybridization of fiber. Figures 1 and 2 indicate tensile strength and tensile modulus of hybrid BFF/basalt/epoxy composites and neat BFF/epoxy and neat

Fig. 1 Effect of hybridizations on tensile strength of BFF/basalt fiber-reinforced composites

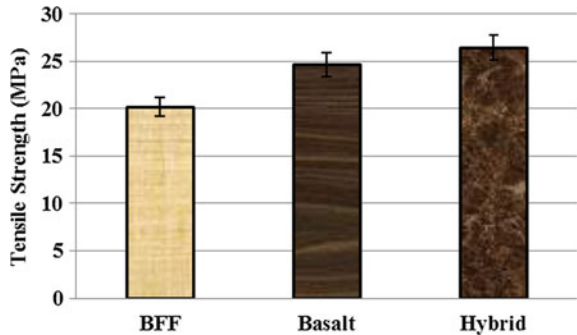
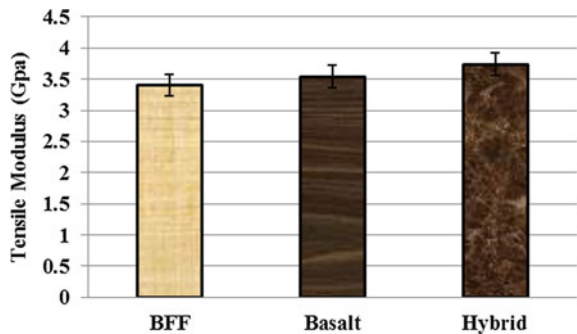


Fig. 2 Effect of hybridizations on tensile modulus of BFF/basalt fiber-reinforced composites



basalt/epoxy composites. It shows that maximum tensile strength of 26.44 MPa and tensile modulus of 3.74 GPa obtained for hybrid composites followed by basalt/epoxy composites 24.67 MPa and 3.54 GPa, respectively, and minimum tensile strength of 20.23 MPa and modulus of 3.40 GPa obtained for BFF/epoxy composites.

Hybridization improves tensile strength 30.70% and tensile modulus 9.60% as compared with neat BFF/epoxy composites, similarly 7.20% and 5.43% higher than basalt/epoxy composites, respectively.

Kakou et al. [19] investigated effect of hybrid composites of coir/oil palm-reinforced polystyrene composites on mechanical properties and found that addition of both fibers into HDPE improved the tensile strength and other mechanical properties. Haneefa et al. [20] showed that tensile strength and tensile modulus increase with hybridization of banana/glass/polystyrene composites.

3.2 Effect of Hybridization on Flexural Strength and Modulus

Flexural strength and modulus of fabricated hybrid BFF/basalt/epoxy composites and non-hybrid BFF/epoxy and basalt/epoxy composites are shown in Figs. 3 and 4. Flex-

Fig. 3 Effect of hybridizations on flexural strength of BFF/basalt fiber-reinforced epoxy composite

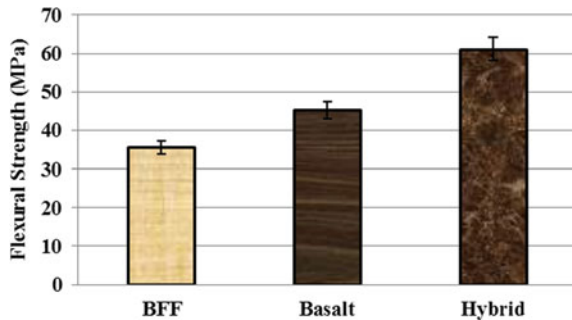
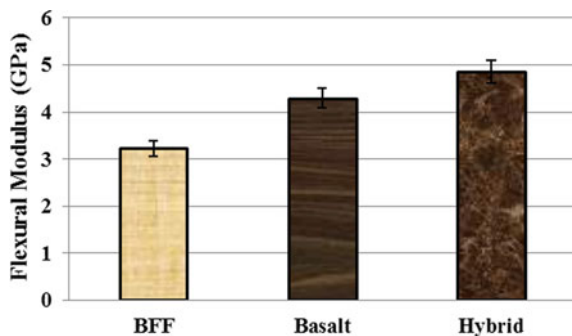


Fig. 4 Effect of hybridizations on flexural modulus of BFF/basalt fiber-reinforced epoxy composites



ural strength and flexural modulus both also significantly influenced by hybridization of fiber in composites and obtained similar trained as tensile strength and modulus. Both flexural strength 61.11 MPa and modulus 4.85 GPa obtained maximum in hybrid BFF/basalt/epoxy composites, and minimum flexural strength 35.57 MPa and modulus 3.22 GPa are obtained in non-hybrid BFF/epoxy composites. Hybridization increases the flexural strength 71.80% and flexural modulus 50.43% as compared to BFF/epoxy composites, similarly 34.91% and 13.04% higher flexural strength and modulus, respectively, as compared to basalt/epoxy composites. Dorigato et al. [21] obtained a similar result by using carbon/basalt fiber hybrid composites and reported that flexural strength and flexural modulus increase with hybridization. Sathish et al. [10] investigated the mechanical properties of snake grass fiber and hybridization with banana and coir randomly distributed fiber, and result shows that after experiment hybridization of snake grass/coir fiber and snake grass/banana fiber composites has obtained maximum flexural properties compared to neat snake grass fiber composites.

3.3 Effect of Hybridization on Impact Strength

The composite specimens, after fabrication with hybridization and non-hybridization, are subjected to impact testing. Impact testing under dynamic loading is necessary for studying material behaviors. Impact test examines the behavior of materials under high instant applied dynamic loading, generally bending, tension or torsion. This test is important for brittle materials because, in ductile materials, it undergoes bending. For brittle materials, both Izod and Charpy can be used to measure toughness. Impact energy is obtained after Charpy and Izod test, as shown in Figs. 5 and 6, respectively.

Highest impact energy obtained for both Charpy and Izod tests was 6.51 J and 3.43 J, respectively, for hybrid BFF/basalt/epoxy composites followed by basalt/epoxy composites and minimum impact energy obtained in BFF/epoxy composites, i.e., 3.51 J and 2.3 J, for Charpy and Izod tests, respectively. Radzi et al.

Fig. 5 Effect of hybridizations on Charpy impact energy at the break of BFF/basalt fiber-reinforced epoxy composites

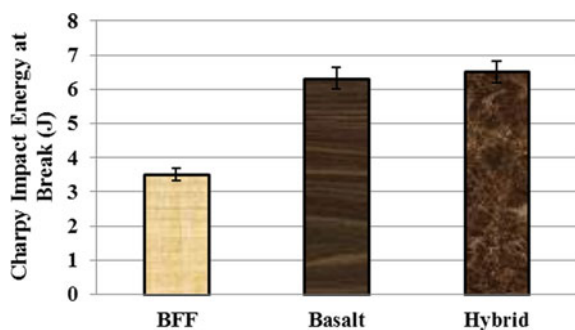
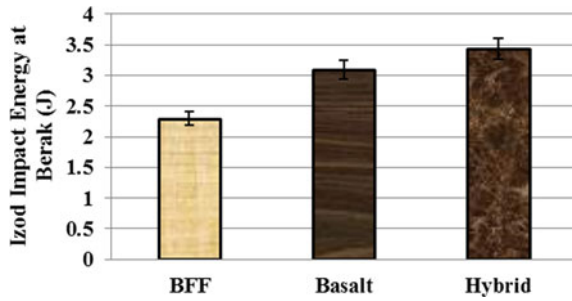


Fig. 6 Effect of hybridizations on Izod impact energy at the break of BFF/basalt fiber-reinforced epoxy composites



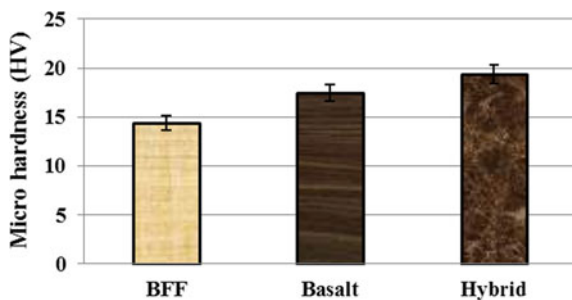
[22] investigated the mechanical properties of hybrid roselle/sugar palm fiber (treated and untreated)-reinforced thermoplastic polyurethane composites and found that untreated roselle/sugar palm hybrid composites obtained maximum impact strength.

3.4 Effect of Hybridization on Microhardness

Vickers hardness testing machine was used to carry out microhardness testing of developed hybrid BFF/basalt/epoxy composites and non-hybrid BFF/epoxy and basalt/epoxy composites. This test was performed on five different points on the same specimens, and average values were taken for consideration.

Figure 7 shows that the microhardness of hybrid and non-hybrid composites, in this graph, indicated that microhardness increases with hybridization of fiber. Microhardness of hybrid BFF/basalt/epoxy composites obtained maximum 19.4 HV followed by basalt/epoxy composites and minimum microhardness obtained in BFF/epoxy composites 14.4 HV. Hybridization improves hardness value 34.72% as compared to BFF/epoxy composites and 11.23% as compared to basalt/epoxy composites.

Fig. 7 Microhardness of hybrid BFF/basalt fiber-reinforced composites



3.5 Effect of Hybridization on Water Absorption Behaviors.

Water absorption test was performed in distilled water; the specimens of water absorption were prepared based on ASTM D570 standards. The test specimens of water absorption dropped into a glass jar for 24 h time intervals, and after that measure, the weight, before cleaning the specimens for dry cloth and the same process was repeated for regular time intervals at normal room temperature and atmospheric pressure up to saturation point. The water absorption percentage was determined according to the given Eq. (1)

$$\% \text{ of water absorption} = \frac{w_f - w_i}{w_i} \times 100 \quad (1)$$

where w_i and w_f are initial weight (before water absorption) and final weight (after water absorption), respectively.

Figure 8 shows that maximum percentage of water absorption is indicated in non-hybrid BFF/epoxy composites because BFF is parts of plant fiber which is hydrophilic in nature and absorbed moisture from the environment. The percentage of water absorption minimum was found in non-hybrid basalt/epoxy composites, because basalt fiber is a type of mineral fiber hydrophobic in nature. In hybrid BFF/basalt/epoxy composites, percentage of water absorption is obtained in between both non-hybrid composites because in hybrid composites there are 50% hydrophilic fiber and 50% hydrophobic fiber.

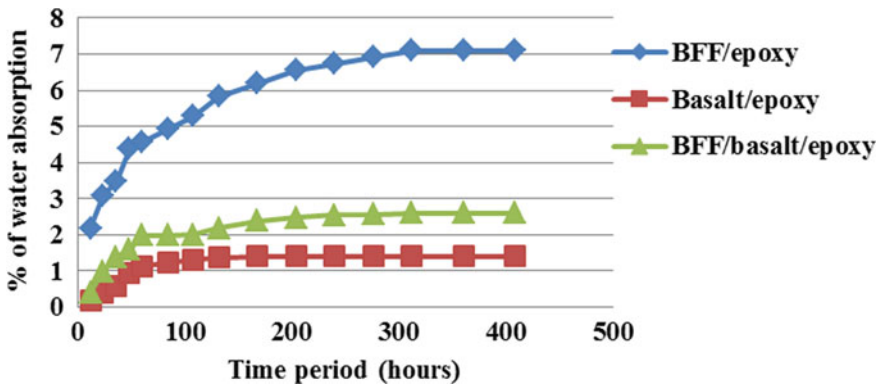


Fig. 8 Percentage of water absorption of hybrid BFF/basalt fiber-reinforced composites

4 Conclusions

Mechanical properties and water absorption behaviors of hybrid basalt/borassus fruit fiber/epoxy composites and non-hybrid borassus fruit fiber/epoxy and non-hybrid basalt/epoxy composite laminates were experimentally investigated. The important conclusions from this investigation can be summarized as follows.

- The mechanical properties and water absorption behavior of the composite specimens are significantly affected by the hybridization of BFF/epoxy, and basalt/epoxy composites laminate about BFF-reinforced composites and basalt fiber-reinforced epoxy composites.
- Hybrid composites obtained 30.70% and 7.20% higher tensile strength and 9.60% and 5.43% higher tensile modulus as compared to BFF/epoxy composite and basalt/epoxy composites, respectively.
- Similarly, hybrid composites obtained 71.8% and 34.91% higher flexural strength and 50.42% and 13.04% higher flexural modulus as compared to BFF/epoxy and basalt/epoxy composites, respectively.
- Water absorption behaviors of hybrid composites increased as compared to basalt/epoxy composites and decreased as compared to BFF/epoxy composites.

References

1. Faruk O, Bledzki AK, Fine HP, Sain M (2012) Biocomposites reinforced with natural fiber: 2000–2010. *Prog Polym Sci* 37:1552–1596
2. Ardanuy M, Claramunt J, Filho RDT (2015) Cellulosic fiber reinforced cement-based composites: a review of recent research. *Constr Build Mater* 79:115–128
3. Das G, Biswas S (2016) Effect of fiber parameters on physical, mechanical and water absorption behaviour of coir fiber-epoxy composites. *J Reinf Plast Comp* 35(8):1–10
4. Ramesh M (2016) Kenaf (*Hibiscus cannabinus* L.) fiber based bio-materials: a review on processing and properties. *Prog Mater Sci* 78:1–92
5. Liu Y, Xie J, Wu N, Ma Y, Menon C, Tong J (2019) Characterization of natural cellulose fiber from corn stalk waste subjected to different surface treatments. *Cellulose* 26:4707–4719
6. Huang J, Yu C (2019) Determination of cellulose, hemicellulose and lignin content using near-infrared spectroscopy in flax fiber. *Text Res J* 89(23–24):1–9. <https://doi.org/10.1177/0040517519843464>
7. Kumar N, Singh A, Ranjan R (2019) Fabrication and mechanical characterization of horse hair (HH) reinforced polypropylene (PP) composites. *Mater Today*. <https://doi.org/10.1016/j.matpr.2019.08.078>
8. Nayak SY, Heckadka SS, Thomas LG (2018) Evaluation of physic-mechanical characteristics of cashew nut shell liquid-epoxy composites with borassus and tamarind fruit fiber as reinforcements. *J Nat Fibers* 3:328–341
9. Kumar S, Gangil B, Prasad L, Patel VK (2017) A review on mechanical behaviour of bast-glass fiber based hybrid polymer composites. *Mater Today* 4:9576–9580
10. Aji IS, Zainudin ES, Abdan K, Sapuan SM, Khairul MD (2012) Mechanical properties and water absorption behavior of hybridized kenaf/pineapple leaf fiber-reinforced high-density polyethylene composite. *J Compos Mater* 47:979–990

11. Sathishkumar TP, Naveen J, Navaneethkrishan P, Satheeshkumar S, Rajini N (2016) Characterization of sisal/cotton fiber woven mat reinforced polymer hybrid composites. *J Ind Text* 47(4):429–452
12. Ramesh M, Deepa C, Arpitha GR, Gopinath V (2019) Effect of hybridization on properties of hemp-carbon fiber-reinforced hybrid polymer composites using experimental and finite element analysis. *World J Eng* 16(2):248–259. <https://doi.org/10.1108/WJE-04-2018-0125>
13. Barvarz MG, Duchesne C, Rodrigue D (2015) Mechanical, water absorption, and aging properties of polypropylene/flax/glass/fiber hybrid composites. *J Compos Mater* 49(30):3781–3798
14. Bulut M, Erklig A, Yeter E (2015) Experimental investigation on influence of Kevlar fiber hybridization on tensile and damping response of Kevlar/glass/epoxy resin composite laminates. *J Compos Mater* 50(14):1–12. <https://doi.org/10.1177/0021998315597552>
15. Patel VK, Rawat N (2017) Physico-mechanical properties of sustainable sagwan-teak wood flour/polyester composites with/without gum rosin. *SM&T*. <https://doi.org/10.1016/j.susmat.2017.05.002>
16. Gujjala R, Ojha S, Acharya SK, Pal SK (2013) Mechanical properties of woven jute-glass hybrid reinforced epoxy composite. *J Compos Mater* 48(28):3445–3455
17. Patel VK, Chauhan S, Katiyar JK (2018) Physico-mechanical and wear properties of novel sustainable Sour-weed fiber reinforced polyester composites. *Mater Res Express*. <https://doi.org/10.1088/2053-1591/aabdd4>
18. Shakeri A, Raghimi M (2010) Studies on mechanical performance and water absorption of recycled newspaper/glass fiber reinforced polypropylene hybrid composites. *J Reinf Plast Comp* 29:994–1005
19. Kakou CA, Essabir H, Bensalah MQ, Bouhfid R, Rodrigue D, Qaiss A (2015) Hybrid composites based on polyethylene and coir/oil palm fiber. *J Reinf Plast Comp* 34(20):1–14. <https://doi.org/10.1177/0731684415596235>
20. Haneefa A, Bindu P, Aravind I, Thomas S (2008) Studies on tensile and flexural properties of short banana/glass hybrid fiber reinforced polystyrene composites. *J Compos Mater* 15:1471–1489
21. Dorigato A, Pegoretti A (2014) Flexural and impact behavior of carbon/basalt fiber hybrid laminates. *J Compos Mater* 48:1121–1130
22. Radzi AM, Sapuan SM, Jawaid M, Mansor MR (2019) Effect of alkaline treatment on mechanical, physical and thermal properties of roselle/sugar palm fiber reinforced thermoplastic polyurethane hybrid composites. *Fiber Polym* 4:847–855

Influence of Cryorolling on Spray-Formed Al–Si Alloy



S. K. Chourasiya and G. Gautam

1 Introduction

Al–Si alloys exhibit excellent properties such as low density, outstanding wear and corrosion resistance, good castability, high thermal conductivity and small thermal expansion coefficient that's why they are preferred to make a large number of components for aerospace, sports, marine and automobile applications [1]. These alloys are classified based on Si quantity, namely hypoeutectic, eutectic and hypereutectic. In the eutectic alloy, the amount of Si is 11–13%. When the alloy consists of Si less than eutectic composition, then they are called hypoeutectic; however, alloy consists of Si greater than eutectic composition then, they are termed as hypereutectic [2]. These alloys consist of hard Si particles with different morphologies and less uniformity, which leads to producing inadequate tensile properties like strength parameters and ductility [3]. The tensile properties of these alloys are generally improved by the addition of secondary reinforcement particles [4, 5] or by the modification in microstructure (modifying the morphology of the silicon particles and microstructure) [6]. However, material researchers are given more attention to the modification in the morphology of silicon particles by many processes [1, 7]. The spray forming process produces less segregation and finer size of particles along with equiaxed morphology of matrix grains in the material, which leads to improving the properties and performance of the material. This process has a high rate of metal discharge and rapid solidification [7, 8]. But, this process generates porosity in the materials, which is the major drawback of it [9, 10]. The secondary process, namely the cryorolling,

S. K. Chourasiya

Department of Mechanical Engineering, THDC Institute of Hydropower Engineering and Technology Bhagirathipuram, Tehri, Uttarakhand 249124, India

G. Gautam (✉)

Department of Metallurgical and Materials Engineering, Indian Institute of Technology Roorkee, Roorkee, Uttarakhand 247667, India

e-mail: gauravgautamm1988@gmail.com

a single-step process, minimizes the porosity accumulated during the process and refines the microstructure which leads to more accumulating the dislocation density [11].

Therefore, in the present work, the cryorolling has been subjected to the spray-formed Al–Si alloy and investigated its effect with different thickness reductions on microstructure, porosity and hardness of the Al alloy through different characterization techniques.

2 Experimental Procedures

The Al alloy consists of 6 wt% of Si which was produced in the form of the disc by the spray forming process using the inert gas through a divergent and convergent type of nozzle. The nitrogen was used as an atomizer gas. The molten Al alloy was prepared at 850 °C in the muffle furnace, and it was passed through the delivery tube, which was attached with the atomizer. After the disintegration of melt, the semisolid droplet of the alloy was deposited on the copper disc, and Al alloy was presented in the shape of the disc.

Further, the prepared disc of the Al alloy was sectioned into the dimensions of $25 \times 20 \times 10 \text{ mm}^3$, which was followed by the polishing using different grades of emery papers. This was done to remove the scratches and the cutting marks from the surfaces of the samples. After removing all defects appeared on the surface, the samples were subjected for cryorolling process. The cryorolling was carried out on non-reversible rolling mills which had the rollers diameter of 110 mm and rotation speed of 8 rpm. The samples were rolled with a different thickness reduction (25% and 50). The samples were dipped frequently into the liquid nitrogen for a time of 10 min to keep the constant temperature under the rolling process.

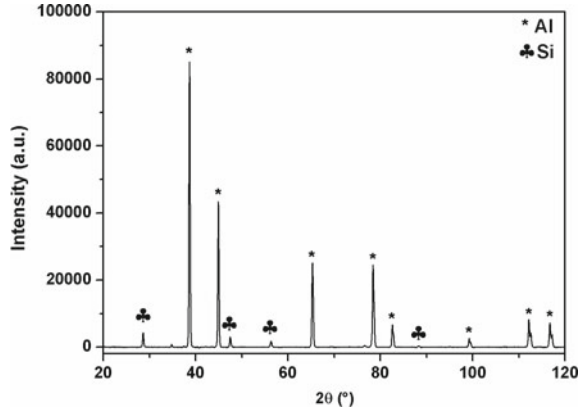
However, the mirror finishing of the surface was done using fine velvet cloth with a liquid slurry of MgO powder. The porosity of the samples in both the conditions was measured experimentally through the Archimedes principle (ASTM B962–08). To the hardness evaluation, the indentation test was done on polished Al alloy surfaces. Load of 10 N with a dwell time of 15 s was used in the test. The average of 10 readings was reported as the hardness of the samples. XRD analysis was also conducted to find the presented phases in the spray-formed Al alloy.

3 Results and Discussion

3.1 Phase Analysis

Figure 1 is the XRD spectrum of the Al–Si alloy produced by spray forming technique.

Fig. 1 XRD spectrum of Al-Si alloy produced by spray forming technique



The XRD spectrum indicates that alloy consists of Al and Si peaks. It indicates that the alloy is Al-Si alloy, and no other phases are present.

3.2 Microstructural Analysis

The microstructural analysis of α -aluminium and morphological studies of silicon particles of the spray-formed and cryorolled Al-Si alloy is also examined under different microscopes. Figure 2 shows the optical micrograph of Al-Si alloy produced by spray forming technique. It is observed from Fig. 2 that the alloy consists of equiaxed grains of α -aluminium along with porosity. It is the characteristic features of the process. Figure 3 shows the optical micrograph of the cryorolled alloy after a 25% reduction. It is seen that the alloy in this condition also exhibits the equiaxed

Fig. 2 Optical micrograph of spray-formed Al-Si alloy

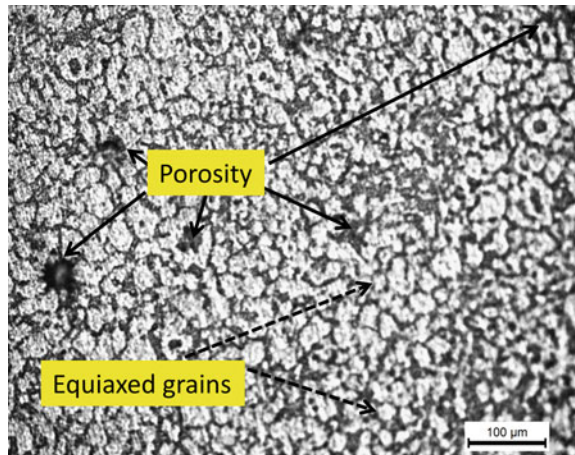
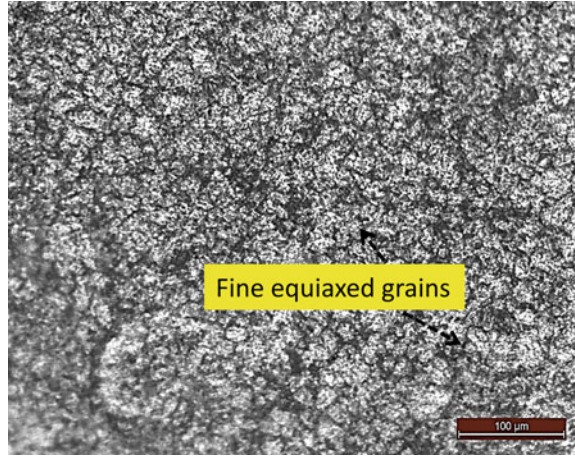


Fig. 3 Optical micrograph of 25% cryorolled spray-formed Al-Si alloy



grains of α -aluminium along with porosity. However, the size of α -aluminium grains is less than that of the previous one, which has been shown in Fig. 2. Additionally, the porosity also reduces in size and places in this case. These phenomena will get stronger as an increase in the thickness reduction under cryorolling. The high cooling rate and turbulent fluid flow do not permit the time for the dendritic growth; subsequently, supercooling helps to form a non-dendritic equiaxed grain structure [12]. The secondary process may generate shear stress and plastic deformation, which may refine the grains of α -Al in the alloy [13].

The SEM micrographs of the spray-formed and cryorolled Al alloy are shown in Figs. 4, 5 and 6. It is seen that the spray-formed Al-Si alloy consists of coarse Si particles, which are distributed along the grain boundary of α -Al. Additionally, some agglomeration is also observed of the Si particles at the few places along the

Fig. 4 SEM micrograph of spray-formed Al-Si alloy

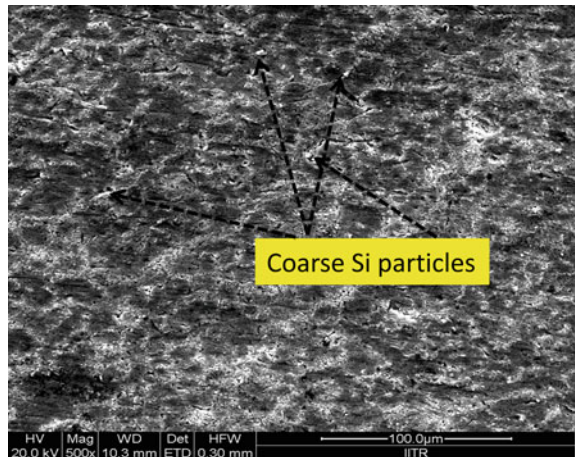


Fig. 5 SEM micrograph of 25% cryorolled spray-formed Al–Si alloy

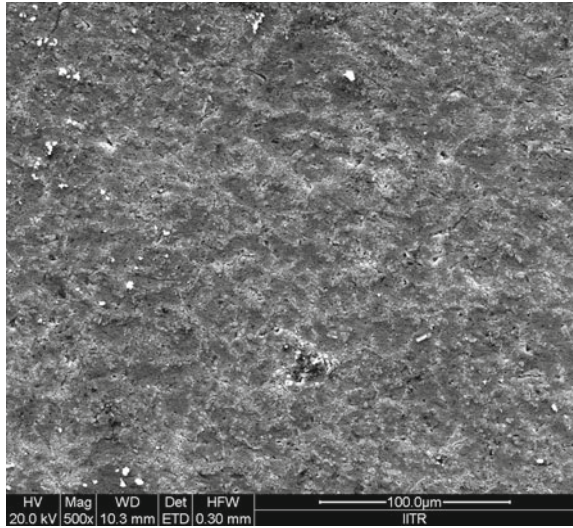
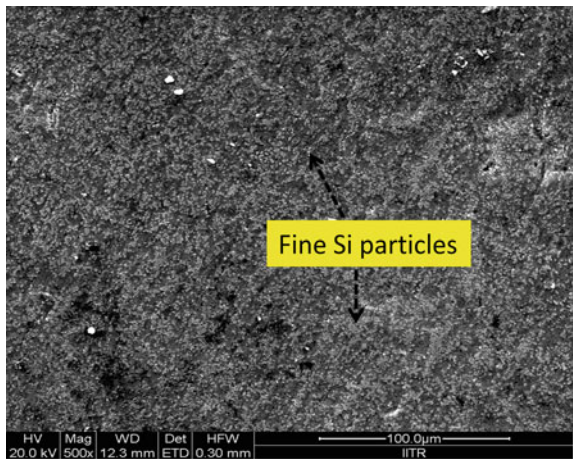


Fig. 6 SEM micrograph of 50% cryorolled spray-formed Al–Si alloy



grain boundary (Fig. 4). The porosity also appears in the spray-formed condition of the Al–Si alloy. The reason behind the agglomeration may be due to different flow characteristics of the materials which are adding under the fabrication process.

Figures 5 and 6 are the SEM micrographs of the cryorolled spray-formed Al–Si alloy with different thickness reductions. It is seen that with an increase in thickness reduction under cryorolling, the size of the Si particles decreases and the distribution of these particles improves. In addition to that, some area of the porosity is also observed in the Al–Si alloy after the cryorolling process, which indicates that the

porosity is not completely eliminated. It may be attributed to the severe plastic distortion. The cryogenic temperature under the rolling process suppresses the dynamic recovery and improves the formation of the higher density of dislocations [14].

3.3 Porosity and Hardness Behaviour

In the spray generated material, porosity is unavoidable, and it depends on many parameters like gas entrapment and solidification shrinkages. Additionally, it also affects by operating parameters of the process. The porosity is the characteristic feature of the spray deposited process, and it represents a significant drawback as reported by material researchers [9].

Figure 7 shows the porosity and hardness variation with the cryorolling thickness reduction. It is seen that the porosity (vol.%) value decreases by cryorolling, and it decreases continuously by increasing the cryorolling thickness reduction. The value of porosity (vol.%) is 11.6, 3.25 and 1.56 in 0% CR, 25% CR alloy and 50% CR alloy, respectively. The CR is representing the cryorolled condition of the alloy. However, the hardness value shows an opposite trend that means it increases continuously with increasing the cryorolling thickness reduction. The value of hardness is 42.50, 52.56 and 63.25 VHN in 0% CR, 25% CR alloy and 50% CR alloy, respectively. The hardness of the Al–Si alloy is improved by the resistance which feels by the dislocation under motion. The refinement of α -Al grains, finer size of Si particles, fewer agglomerations and porosity, all contribute to increasing the resistance in the motion of dislocation. With the increase in cryorolling thickness reduction, all these

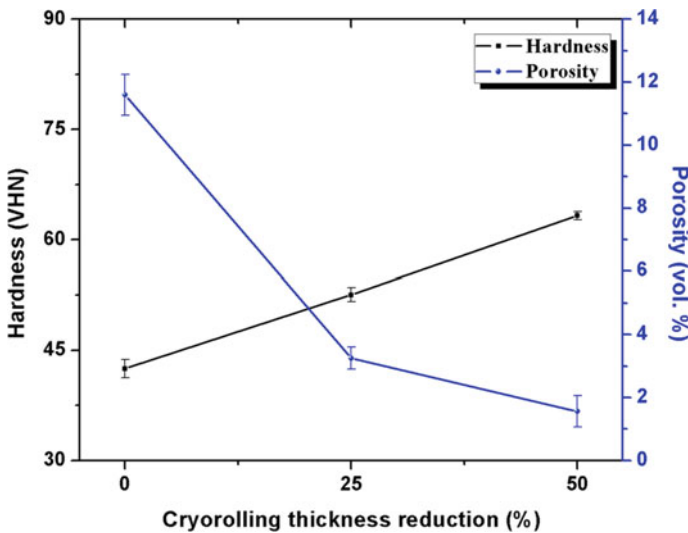


Fig. 7 Porosity and hardness variation with cryorolling thickness reduction

parameters strengthen and generate more resistance in the movement of dislocation, which leads to improving the hardness of the alloy.

4 Conclusions

The main conclusions have been drawn from the present investigation, which are the following:

- The equiaxed grain size of α -Al-rich phase in the Al–Si alloy decreases by cryorolling, and it decreases continuously with thickness reduction.
- The porosity (vol.%) of the Al–Si alloy shows a decreasing trend with an increasing percentage of thickness reduction under cryorolling.
- The agglomeration of coarse Si particles reduces under cryorolling, and it continuously reduces with an increase in thickness reduction.
- The hardness of the spray-formed Al–Si alloy improves by the cryorolling, and it continuously improves with thickness reduction. This is due to the refinement of α -Al grains, finer size of Si particles, fewer agglomerations and porosity.
- The maximum improvement in the properties of spray-formed Al–Si alloy is observed by the cryorolling with a 50% reduction.

Acknowledgements The authors are thankful to the Department of Metallurgical and Materials Engineering, Indian Institute of Technology Roorkee for providing the facility to conduct the work.

References

1. Tiwari K, Gautam G, Kumar N, Mohan A, Mohan S (2018) Effect of primary silicon refinement on mechanical and wear properties of hypereutectic Al–Si alloy. *Silicon*. 10:2227–2239. <https://doi.org/10.1007/s12633-017-9755-2>
2. Dwivedi DK (2010) Adhesive wear behaviour of cast aluminium-silicon alloys: Overview. *Mater Design* 31:2517–2531. <https://doi.org/10.1016/j.matdes.2009.11.038>
3. Guru PR, Mohan FK, Panigrahi SK, Ram GDJ (2015) Enhancing strength, ductility and machinability of a Al–Si cast alloy by friction stir processing. *J Manuf Process* 18:67–74. <https://doi.org/10.1016/j.jmapro.2015.01.005>
4. Han Y, Liu X, Bian X (2002) In situ TiB₂ particulate reinforced near eutectic Al–Si alloy composites. *Compos Part A-Appl S* 33:439–444. [https://doi.org/10.1016/S1359-835X\(01\)00124-5](https://doi.org/10.1016/S1359-835X(01)00124-5)
5. Yi H, Ma N, Li X, Zhang Y, Wang H (2006) High-temperature mechanics properties of in situ TiB_{2p} reinforced Al–Si alloy composites. *Mat Sci Eng A-Struct* 419:12–17. <https://doi.org/10.1016/j.msea.2005.10.020>
6. Chourasiya SK, Gautam G, Singh D (2019) Mechanical and tribological behavior of warm rolled Al-6Si-3 Graphite self-lubricating composite synthesized by spray forming process. *Silicon* 1–12. <https://doi.org/10.1007/s12633-019-00175-9>

7. Chourasiya SK, Gautam G, Singh D (2019) Performance-enhancing of spray formed Al/Graphite alloy composite by rolling. *Met Mater Int* 1–12. <https://doi.org/10.1007/s12540-019-00547-1>
8. Chourasiya SK, Gautam G, Singh D (2019) A novel technique for automatic quantification of porosities in spray formed warm rolled Al-Si-Graphite composite. *Mater Res Express* 1–9. <https://doi.org/10.1088/2053-1591/ab4a58>
9. Cai W, Lavernia EJ (1998) Modeling of porosity during spray forming: Part II. effects of atomization gas chemistry and alloy compositions. *Metall Mater Trans B* 29B:1097–1106. <https://doi.org/10.1007/s11663-998-0079-x>
10. Chourasiya SK, Gautam G, Singh D (2020) Influence of rolling on wear and friction behavior of spray formed Al alloy composites. *Mater Today*. <https://doi.org/10.1016/j.matpr.2019.12.304>
11. Kumar A, Godasu AK, Pal K, Mula S (2018) Effects of in-process cryocooling on metallurgical and mechanical properties of friction stir processed Al7075 alloy. *Mater Charact* 144:440–447. <https://doi.org/10.1016/j.matchar.2018.08.001>
12. Ojha KV, Tomar A, Singh D, Kaushal GC (2008) Shape, microstructure and wear of spray formed hypoeutectic Al-Si alloys. *Mat Sci Eng A-Struct.* 487:591–596. <https://doi.org/10.1016/j.msea.2007.10.032>
13. Rajeshkumar R, Udhayabanu V, Srinivasan A, Ravi KR (2017) Microstructure evolution in ultrafine grained Al-Graphite composite synthesized via combined use of ultrasonic treatment and friction stir processing. *J Alloy Compd* 726:358–366. <https://doi.org/10.1016/j.jallcom.2017.07.280>
14. Panigrahi SK, Jayaganthan R, Chawla V (2008) Effect of cryorolling on microstructure of Al-Mg-Si alloy. *Mater Lett* 62:2626–2629. <https://doi.org/10.1016/j.matlet.2008.01.003>

Optimization of Hybrid Aluminium Metal Matrix Composite Using Red Mud and Wheat Husk Ash



Rishi Dewangan, Pankaj Kumar Pandey, Nitesh Singh Rajput , and Rajeev Dohare

1 Introduction

Nowadays, aluminium metal matrix (AMC) composite is extensively paying attention in the area of aerospace, food industry, aviation, automobile industry and also in packaging industry due to its better strength-to-mass ratio, superior wear and corrosion resistance [1]. Ceramic materials such as Al_2O_3 , SiC and ZnO can improve the mechanical properties of aluminium alloys considerably. Wheat husk ash (WHA) and red mud (RM) have the potential to replace these ceramic materials due to its low cost and high hardness, better abrasion wear and corrosion resistance, low and optimum thermal conductivity, etc. [2]. At present red mud and wheat straw are utilized in numerous applications, for example, the advancement of clay brick material [3], pozzolanic material [4], used for silica extraction [5, 6], poly composite [7], concrete and composite material [3, 8], used as bio-sorbent material for deduction of heavy material from aqueous solution [9–11], expelling overwhelming and lethal and toxic metals from watery arrangement and metals [12–14], construction materials [15, 16], adsorbents, catalysts [17], and for the advancement of submerged welding flux [18, 19].

There is almost limited work done on the development of aluminium metal matrix composite using red mud with wheat husk ash. The present work, aimed to develop

R. Dewangan · N. S. Rajput (✉)

Department of Mechanical Engineering, Amity University, Jaipur, Rajasthan 303002, India
e-mail: niteshthakur72@yahoo.com

R. Dewangan

e-mail: rishi.coolguy06@gmail.com

P. K. Pandey

Department of Chemical Engineering, Amity University, Jaipur, Rajasthan 303002, India

R. Dohare

Department of Mechanical Engineering, Malaviya National Institute of Technology, Jaipur 302002, India

a hybrid metal matrix composite using wheat husk ash and red mud through the stir casting process. Mechanical properties were compared; also, these properties are optimized using ANOVA analysis, and its regression equation is tabulated.

2 Experimentation

2.1 Materials

Hybrid aluminium metal matrix composite was prepared using wheat husk ash with red mud in 5, 10 and 15 wt% individually in the stir casting process with varying stirrer from 50 to 100 rpm at 800 °C. Here, red mud was procured from Balco mines, Chhattisgarh. This red mud was dried and crushed to get uniform and moisture-free. Table 1 [20] and Table 2 [6] shows the chemical composition of red mud and wheat husk ash, respectively.

The wheat husk was procured from agriculture farm, Satna, Madhya Pradesh (MP). As MP is rich in wheat production, so tons of wheat husk are produced, and so, some of the unused wheat husks are utilized for reinforcement. Chopped wheat husk was dried and burned in a crucible to get moisture-free ash content; in a similar way, red mud is also exposed in sunlight for removing its moisture content; red mud and wheat husk ash pictures are shown in Fig. 1. Both the mixtures were crushed and sieved to obtain particle size up to 150 μm for getting better and uniform with a homogeneous distribution of reinforcement with Al material. Table 3 shows the elemental composition of the developed hybrid Al MMC.

Based on Table 3, nine cylindrical bars of size 18 mm diameters with 450 mm length are prepared in a cupola furnace. This cast piece is kept in normal atmospheric temperature for 1 h to cool down. Entire samples are further characterized and prepared for various testing. The developed composite is shown in Fig. 2.

Archimedes method was used to check its density. For this purpose, optimized defect-free 20-mm long workpiece mass was measured in a fluid medium where its actual density was calculated [20]. Tensile strength of the developed composite was determined in universal testing machine based on ASTM E08 specimen model.

Table 1 Composition of red mud

Constituent	Al ₂ O ₃	Fe ₂ O ₃	SiO ₂	TiO ₂	Na ₂ O	CaO	MnO ₂
wt%	18–21	35–37	6–6.5	17–19	5.2–5.5	1.7–2.2	0.5–2.0

Table 2 Composition of wheat husk ash

Constituent	SiO ₂	K ₂ O	MgO	Fe ₂ O ₃	Na ₂ O	MnO ₂	CaO
wt%	43.22	11.305	1	0.84	0.16	0.02	6.30



Fig. 1 Wheat husk ash and red mud

Table 3 Elemental composition of the developed composition

S. No.	1	2	3	4	5	6	7	8	9
Red mud (wt%)	5	5	5	10	10	10	15	15	15
WHA (wt%)	5	10	15	5	10	15	5	10	15

Fig. 2 Developed Al composite



2.2 Methodology

The main raw material for the development of metal matrix composite was 6000 series aluminium. For reinforcement, red mud and wheat, husk ash was used in varying percentage of 5–15 wt% of the overall composition. Its mechanical behaviour such as density, Rockwell hardness, yield strength and ultimate tensile strength is given in Table 4. All these mechanical behaviours were optimized through ANOVA and regression analysis in Minitab software by taking red mud (RM) and wheat shell ash (WHA) as a continuous predictor. Density, ultimate tensile strength (UTS) and yield strength regression equation are as follows:

$$\text{Density} = 2.302 + 0.0187 \text{ red mud}(\%) + 0.0340 \text{ Wheat husk Ash}(\%) - 0.00190 \text{ red mud}(\%) * \text{Wheat husk Ash}(\%)$$

$$\text{UTS} = 52.90 + 2.217 \text{ red mud}(\%) + 1.448 \text{ Wheat husk Ash}(\%)$$

Table 4 Mechanical behaviour of developed aluminium matrix composite (AMC)

S. No.	Rockwell hardness (HRB)	Density (kg/m ³)	Ultimate tensile stress, UTS (MPa)	Yield stress (MPa)
1	55	2.61	66.48	42.62
2	57	2.7	74.23	51.21
3	66	2.7	78.12	40.58
4	68	2.64	82.34	67.83
5	70	2.7	79.4	58.07
6	72	2.8	83.702	51.65
7	74	2.75	82.818	53.03
8	68	2.6	89.28	58.05
9	70	2.65	85.06	55.78

$$- 0.0940 \text{ red mud (\%)} * \text{Wheat husk Ash (\%)}$$

$$\text{yield stress} = 52.3 + 0.60 \text{ red mud (\%)} - 0.99 \text{ Wheat husk Ash (\%)} \\ + 0.048 \text{ red mud (\%)} * \text{Wheat husk Ash (\%)}$$

3 Results and Discussion

3.1 Density Outcome

The density of composites varied from 2.6 to 2.8 kg/m³, and density was improved with an increased amount of wheat husk ash. This is because wheat husk ash possesses a good amount of SiO₂ and K₂O which acts as good binder and also enhances flowability of cast materials.

3.2 Hardness Outcome

Mechanical behaviour is shown in Table 4 15% red mud with 5% wheat husk ash (sample 7) possessed better hardness than the others. This was followed by sample 6. Hardness value enhances with red mud content since red mud has a good amount of industrial compound (Fe₂O₃, Al₂O₃, TiO₂, etc.) which promotes hardness of composite material. Hardness value also optimized by ANOVA analysis which is shown in Table 5:

It has concluded that red mud, wheat husk ash and their contribution are optimum within the acceptable limit (*P*-value below 0.10). The impact of red mud is supreme,

Table 5 Analysis of variance for Rockwell hardness, using adjusted SS for tests

Source	DF	Seq SS	Adj SS	Adj MS	F	P	Contribution (%)
A	1	192.67	148.60	148.60	10.78	0.022	56.80
B	1	20.17	74.67	74.67	5.42	0.067	5.96
A * B	1	56.25	56.25	56.25	4.08	0.09	16.64
Error	5	68.92	68.92	13.78			
Total	8	338.00					

Red mud = A, wheat husk ash = B

followed by a combination of both (wheat husk ash and red mud). Wheat husk ash has least contributed on hardness result since red mud improves hardness and strength [4].

3.3 Tensile Strength Outcome

It has shown that from mechanical behaviour (Table 4) that (sample) 8, which has 15% red mud with 10% wheat husk ash having better ultimate tensile strength than others, also sample 4 having 10% red mud with 5% wheat husk best yield stress. Both yield stress and ultimate tensile strength value enrich with improving the amount of reinforcement since a good amount of Al₂O₃ and TiO₂ present in red mud promotes strength, toughness and hardness. Considerable amount of SiO₂ present in wheat husk ash good oxidizer which promotes overall strength of composite material. Ultimate tensile strength (UTS) value is given in Table 6 and optimized by ANOVA analysis:

ANOVA result, indicated that red mud significantly contributed to the mechanical properties of the sample which was followed by wheat husk and mixture of red mud and wheat husk ash. The red mud is best for developing hybrid metal matrix composite with little quantity of wheat husk.

Table 6 Analysis of variance for UTS, using adjusted SS for tests

Source	DF	Seq SS	Adj SS	Adj MS	F	P	Contribution (%)
A	1	244.04	105.36	105.36	9.95	0.025	68.04
B	1	38.73	44.93	44.93	54.24	0.094	10.80
A * B	1	22.08	22.08	22.08	2.09	0.208	6.16
Error	5	52.94	52.94	10.59			
Total	8	358.59					

Red mud = A, wheat husk ash = B

4 Conclusions

Nine samples of the low-cost hybrid aluminium metal matrix were effectively developed using red mud (industrial waste) with wheat husk ash (agricultural waste) by the stir casting process. Hence, “Waste is wealth” statement is verified. The hardness of metal matrix composite varies from 55 to 74 HRB, and also, hardness value is increased with the increment of red mud content. This hardness increased beyond 15 wt% red mud with 5 wt% wheat husk ash. Tensile and yield strength values are improved with an increased amount of reinforcement. Yield strength value varies from 42 to 68 MPa, and tensile strength value ranges from 66 to 89 MPa. ANOVA analysis has been done by adjusted SS test within 90% probability level and found that for all mechanical behaviour, red mud contribution is maximum followed by wheat husk ash and combination of wheat husk with red mud.

References

1. Li J, Li F, Wu S, Lü S, Guo W, Yang X (2019) Variation of microstructure and mechanical properties of hybrid particulates reinforced Al-alloy matrix composites with ultrasonic treatment. *J Alloy Compd* 789:630–638. <https://doi.org/10.1016/j.jallcom.2019.03.074>
2. Narasaraju G, Raju DL (2015) Characterization of hybrid rice husk and fly ash-reinforced aluminium alloy (AlSi10Mg) composites. *Mater Today* 2(4–5):3056–3064. <https://doi.org/10.1016/j.matpr.2015.07.245>
3. Ahmad S, Iqbal Y, Muhammad R (2017) Effects of coal and wheat husk additives on the physical, thermal and mechanical properties of clay bricks. *Boletín de la Sociedad Española de Cerámica y Vidrio* 56(3):131–138. <https://doi.org/10.1016/j.bsecv.2017.02.001>
4. Ahmad MR, Sharif MB, Ali HA, Hussain M, Chen B (2019) Experimental investigation of pozzolanic concrete containing wheat straw ash. *Can J Civil Eng* 1–5. <https://doi.org/10.1139/cjce-2017-0419>
5. Shaikh IR, Shaikh RA, Shaikh AA, War JA, Hangirgekar SP, Shaikh AL, Shaikh RR (2015) H-ZSM-5 zeolite synthesis by sourcing silica from the wheat husk ash: characterization and application as a versatile heterogeneous catalyst in organic transformations including some multicomponent reactions. *J Catal* 5:189–205. <https://doi.org/10.1155/2015/805714>
6. Ma Y, Chen H, Shi Y, Yuan S (2016) Low cost synthesis of mesoporous molecular sieve MCM-41 from wheat husk ash using CTAB as surfactant. *Mater Res Bull* 77:258–264. <https://doi.org/10.1016/j.materresbull.2016.01.052>
7. Mavani SI, Mehta NM, Parsania PH (2007) Synthesis, fabrication, mechanical, electrical, and moisture absorption study of epoxy polyurethane–jute and epoxy polyurethane–jute–rice/wheat husk composites. *J Appl Polym Sci* 106(2):1228–1233. <https://doi.org/10.1002/app.24647>
8. Silva JVF, Bianchi NA, Oliveira CAB, Caraschi JC, de Souza AJD, Molina JC, de Campos CI (2019) Characterization of composite formed by cement and wheat straw treated with sodium hydroxide. *BioResources* 14(2):2472–2479
9. Robinson T, Chandran B, Nigam P (2002) Effect of pretreatments of three waste residues, wheat straw, corncobs and barley husks on dye adsorption. *Biores Technol* 85(2):119–124. [https://doi.org/10.1016/S0960-8524\(02\)00099-8](https://doi.org/10.1016/S0960-8524(02)00099-8)
10. Patil YP, Gajre B, Dusane D, Chavan S, Mishra S (2002) Effect of maleic anhydride treatment on steam and water absorption of wood polymer composites prepared from wheat straw, cane bagasse, and teak wood sawdust using novolac as matrix. *J Appl Polym Sci* 77(13):2963–2967. [https://doi.org/10.1002/1097-4628\(20000923\)77](https://doi.org/10.1002/1097-4628(20000923)77)

11. Gupta VK, Jain R, Varshney S (2007) Removal of Reactofix golden yellow 3 RFN from aqueous solution using wheat husk—an agricultural waste. *J Hazard Mater* 142(1–2):443–448. <https://doi.org/10.1016/j.jhazmat.2006.08.048>
12. Zouboulis I, Kydros KA (1993) Use of Red Mud for Toxic Metal Removal: The case of nickel. *J Chem Technol Biotechnol* 53:95–101. <https://doi.org/10.1002/jctb.280580114>
13. Genç-Furman H, Tjell JC, Mcconchie D (2004) Adsorption of Arsenic from Water Using Activated Neutralized Red Mud. *J Environ Sci Technol* 38:2428–2434. <https://doi.org/10.1021/es035207h>
14. Gupta VK, Sharma S (2002) Removal of cadmium and zinc from aqueous solution using red mud. *J Environ Sci Technol* 36:3612–3617. <https://doi.org/10.1021/es020010v>
15. Tsakiridis PE, Agatzini-Leonardou S, Oustakadis P (2004) Red Mud Addition in the raw meal for the production of Portland Cement Clinker. *J Hazardous Mater B* 116:103–110. <https://doi.org/10.1016/j.jhazmat.2004.08.002>
16. Singh M, Upadhayay SN, Prasad PM (1996) Preparation of special cement from red mud. *J Waste Manage* 16(8):665–670. [https://doi.org/10.1016/S0956-053X\(97\)00004-4](https://doi.org/10.1016/S0956-053X(97)00004-4)
17. Wang S, Ang HM, Tade MO (2008) Novel application of red mud as coagulant, adsorbent and catalyst for environmentally benign processes. *Chemosphere* 72:1621–1635. <https://doi.org/10.1016/j.chemosphere.2008.05.013>
18. Dewnangan R, Khan MZ (2012) Development of submerged arc welding flux using red mud. In: International conference on agile manufacturing, IIT (BHU), Varanasi, pp 365–367
19. Spierings AB, Schneider M, Eggenberger R (2011) Comparison of density measurement techniques for additive manufactured metallic parts. *Rapid Prototyping J* 17(5):380–386. <https://doi.org/10.1108/13552541111156504>
20. Paramguru RK, Rath PC, Misra VN (2006) Trends in red mud utilization—a review. *Mineral Process Extractive Metall Rev* 26:1–29. <https://doi.org/10.1080/088275004904>

Investigation of Efficiency of Flat Plate Collector Using CuO–H₂O Nanofluid



Nitesh Singh Rajput, Sudhanshu Singh, and Shweta Kulshreshtha

1 Introduction

Nanofluid is a colloidal suspension of metallic and non-metallic nanoparticles in the base fluid (water, ethylene glycol and oil). Nanofluids contain nanosized particles (usually <100 nm) which are uniformly distributed and possess the capability of heat transfer. In recent years, nanofluids are gaining the most attention due to their improved thermophysical properties. This distinctive feature promotes its application as a heat transfer agent in solar stills or solar water heaters [1–4]. Solar energy is an abundant source of renewable energy throughout the world. Nowadays, the research is being carried out to utilize the untapped potential of solar energy in generating electricity, heating and purifying water. To achieve this, new equipment to harness solar energy has been developed, such as solar-powered cell for electricity generation, water heaters for heating water, solar stills for purifying water [5, 6]. Rapid growth has been observed in the development of equipment for harnessing solar energy. This equipment can be installed in the multi-storeyed buildings for hot water availability for domestic purposes. It can be used in swimming pools, to desalinate saline water, to operate engines and pumps, generate electricity, for domestic and industrial purposes [7].

The total renewable energy potential of India was estimated as 900 GW, and the contribution of solar energy in this was 750 GW [8]. The Ministry of Non-Renewable Energy resources (MNRE) had taken up initiatives in 2010 to popularize

N. S. Rajput (✉)

Department of Mechanical Engineering, Amity University Rajasthan, Jaipur 303002, India

e-mail: niteshthakur72@yahoo.com

S. Singh

Department of Electronics and Communication Engineering, Amity University Rajasthan, Jaipur 303002, India

S. Kulshreshtha

Department of Biotechnology, Amity University Rajasthan, Jaipur 303002, India

solar power systems and launched National Solar Mission in 2010 with the phase I target for solar collectors application, i.e. 7 million square metres. Currently, it is in phase III, with a target of 20 million square metres solar collector applications [9]. Financial support by the government encourages the installation and application of solar devices for various purposes. The application of solar energy in the heating water through solar heaters is an important step to move towards a renewable solar energy system. Household energy consumption can be reduced by 13% on using solar water heaters. The education/awareness and high income are the supporting factors in the installation of solar collectors [10]. The solar water heaters not only provide a continuous supply of hot water throughout the day in a safe manner irrespective of a power cut but also used to control skyrocketing prices of non-renewable fuel. The solar water heater has an absorber to collect solar radiation. These water heaters render the collection of incident solar radiation and convert into heat energy, which is used to heat the water to 75 °C [11]. A number of modifications in the design have been researched with the aim of increasing the efficiency of the collectors [12, 13]. Since last decade, application of nanoparticles is emerging as a new field in various medical and environmental applications. The nanoparticles have also been applied to the solar water heater to find out their effect on efficiency. A number of investigators have reported the usage of nanoparticles in solar water heaters of both types, i.e. flat plate collector and evacuated tube collectors [14–21].

Nanofluids with higher stability and properly dispersed nanoparticles have to be used in collector to upsurge efficiency. Any increase in viscosity of nanofluid decreases the pressure and pumping power. These are the guiding factors to decide the suitability of nanoparticles' application in flat plate collectors [22]. In another experiment, Qinbo et al. [23] reported boost in collector efficiency by 23.83% by using Cu–H₂O nanofluids. Similarly, Moghadam et al. [24] reported 21.8% rise in productivity using the CuO–H₂O nanofluid. Therefore, there has been a proven record of enhancement in the productivity of the solar collector by using nanoparticles and nanofluids.

In the present study, nanofluid was prepared using CuO/distilled water. It was used as a working fluid in collector having 1.95 m² absorber area. It was also fitted with a collector tube having 12 mm in diameter. It was tested to find its efficiency in the Jaipur, Rajasthan, for implementing the technology.

2 Materials and Methods

2.1 Test Set-Up

In this study, solar flat plate collector Model No. JSR 9 from Jain Irrigation is used as depicted in Fig. 1. The schematic diagram (Fig. 2) demonstrates the experimental set-up for collector. As the efficiency of the collector is directly related to absorbing maximum radiation, hence flat plate collector should be set at a particular angle to



Fig. 1 Experimental set-up

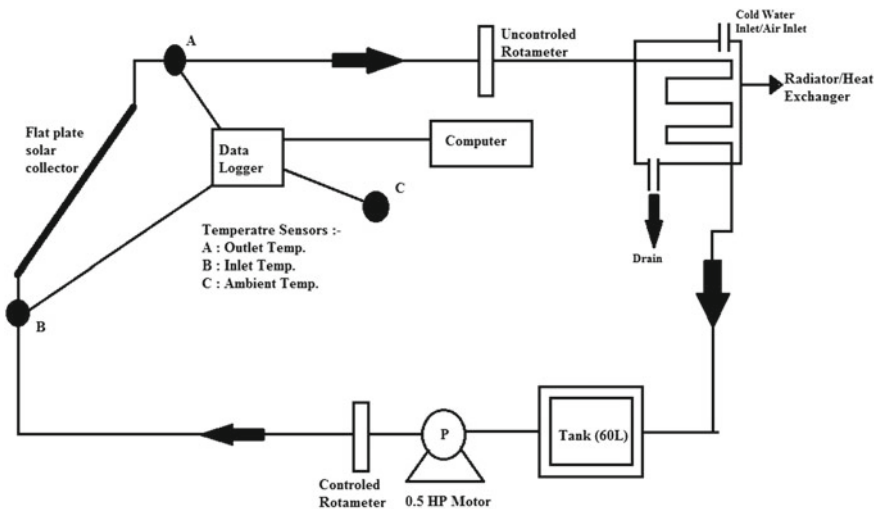


Fig. 2 Schematic diagram

absorb maximum radiation. Keeping this in mind, the flat plate collector was set at 27° for collecting radiation. Area of the collector was 2.23 m^2 , area of absorber plate was 2 m^2 , toughened glass cover 4 mm thick, nine copper tubes with 13.7 mm outer diameter and 12.5 mm inner diameter. Centrifugal pump was used to pump working fluid, i.e. water and nanofluid into the flat plate collector and flow of these fluids were

controlled by the use of rotameter with a range of 0.017–0.17 kg/s, accuracy $\pm 1\%$. This collector was also fitted with three K-type thermocouples with six-channel data logger, i.e. temperature logger from Embuilt Technologies was used to measure the temperature of inlet and outlet fluid and ambient air. Solar radiations were recorded using digital solar metre from Tenmars Technologies with a range of 1–2000 W/m² and accuracy $\pm 5\%$.

2.2 Nanofluid

Nanoparticles with 20–45 nm diameters and 99.9% purity from Nanoshel Industries, India, were employed to assess the efficiency of the solar water heater. Weighing balance from Sartorius Industries was used to measure the weight of copper oxide (CuO) nanoparticles.

The nanoparticles do not mix uniformly with water. Therefore, a surfactant is required to prepare a homogenous solution of nanoparticles. Two-step method was used to prepare nanofluid. In the first step, sodium dodecyl sulphate (SDS), a detergent (fisher scientific), was used to mix insoluble nanoparticles with water. The different content, i.e. 0.1, 0.2, 0.3 and 0.4% of CuO nanoparticles, was suspended in distilled water along with SDS. In the second step, this suspension was ultrasonicated for 8 hours using ultrasonicator of Labman, LMUC Series in order to obtain a homogenous solution. The whole procedure of preparing nanofluid was performed at room temperature.

3 Testing

ASHARE Standard 93-86 was employed to calculate instantaneous efficiency, which further, assessed the thermal performance of the collector. This was determined by measuring solar irradiance, the temperature of the water at the inlet of collector and ambient temperature under standard conditions. As per ASHARE Standard 93-86, solar irradiance, atmospheric temperature and temperature of the fluid at the inlet of collector and mass flow rate should be under the specified limit, i.e. ± 50 W/m², ± 1.5 K, ± 0.1 K and $\pm 1\%$, respectively, under steady-state conditions [25].

3.1 Efficiency Calculation

The whole experiment was conducted according to the ASHARE Standard 93-86. To calculate the efficiency of CuO nanofluid, collector was used according to the aforesaid mentioned conditions during the daytime from 10 AM to 4 PM at different

flow rates and various concentrations. The solar irradiation varied between 500 and 800 W/m².

The performance of flat plate collector depends on the heat gain and instantaneous efficiency. These were calculated using the following equations [26]:

The useful heat gain,

$$Q_g = \dot{m}C_P(T_o - T_i) \quad (1)$$

$$Q_g = A_C F_R [G_T(\tau\alpha) - U_L(T_i - T_a)] \quad (2)$$

Efficiency,

$$\eta_i = \frac{\dot{m}C_P(T_o - T_i)}{A_C G_T} \quad (3)$$

$$\eta_i = F_R(\tau\alpha) - F_R U_L \left[\frac{T_i - T_a}{G_T} \right] \quad (4)$$

where Q_g is absorbed heat (W), \dot{m} is the mass flow rate (kg/s), C_p is the heat capacity (J/kg K), T_a is the ambient temperature (K), T_o is the temperature of nanofluid at the outlet (K), T_i is the temperature of the fluid at the inlet (K), A_C is collector area (m²), F_R is a factor for heat loss, $(\tau\alpha)$ is a product of absorptivity and transmissivity, G_T is global solar radiation (W/m²), U_L is the total heat loss.

According to Eq. (5), $F_R(\tau\alpha)$ and $F_R U_L$ will be constant under normal incidence conditions. If the graph of efficiency versus $\left[\frac{T_i - T_a}{G_T} \right]$ is plotted, a straight line will be obtained from the averaged values. The vertical axis represents the efficiency of collector, the horizontal axis represents $\left[\frac{T_i - T_a}{G_T} \right]$, the point at which straight line meets the vertical axis will be absorbed heat $F_R(\tau\alpha)$, and slope represents heat loss ($F_R U_L$). The minimum value of collector can be determined by the stagnation point at which straight line meets the horizontal axis where the efficiency of collector will be zero.

The following equation was used to estimate the heat capacity of nanofluid:

$$C_{p(nf)} = C_{p(np)}(\varphi) + C_{p(bf)}(1 - \varphi) \quad (5)$$

where (φ) shows the nanoparticles content; $C_{p(nf)}$, $C_{p(np)}$ and $C_{p(bf)}$ are the heat capacity of nanofluid, nanoparticles and base fluid, respectively. Heat capacity of nanoparticles was 530 J/kg K, and base fluid was 4182 J/kg K.

3.2 Experimental Uncertainty Analysis

Uncertainty analysis was done by the following equation:

$$U_T^2 = \sum_{k=1}^n U_{P_i}^2 \quad (6)$$

where, U_{P_i} is the uncertainty of individually analysed parameter and U_T^2 is uncertainty of overall analysed parameter. The uncertainty of the volumetric flow of nanofluid was $\pm 1\%$; the solar intensity was $\pm 5\%$; the temperature difference was $\pm 1.4\%$.

4 Results and Discussion

The fundamental working of flat plate collector depends upon the acquisition of incident solar energy which is the most important factor to direct the efficiency and productivity of collector. The information on thermal response and productivity helps in deciding the suitability of flat plate collector to heat water. This efficiency of collectors may be influenced by the presence of nanoparticles in the working fluid. Therefore, in this study, the efficiency of the collector was measured by the incorporation of copper oxide nanoparticles in the working fluid.

At first, the nanoparticles were characterized by FTIR technique, and the resultant graph was shown in Fig. 3. The FTIR spectrum of a copper oxide (CuO) nanoparticle showed broad absorption bands between 2700 and 4000 cm^{-1} mainly ascribed to –OH and C–O groups on the surface of the CuO crystal nanostructure. The presence of bands between 500 and 1700 cm^{-1} indicated bending vibration of Cu–O bond in

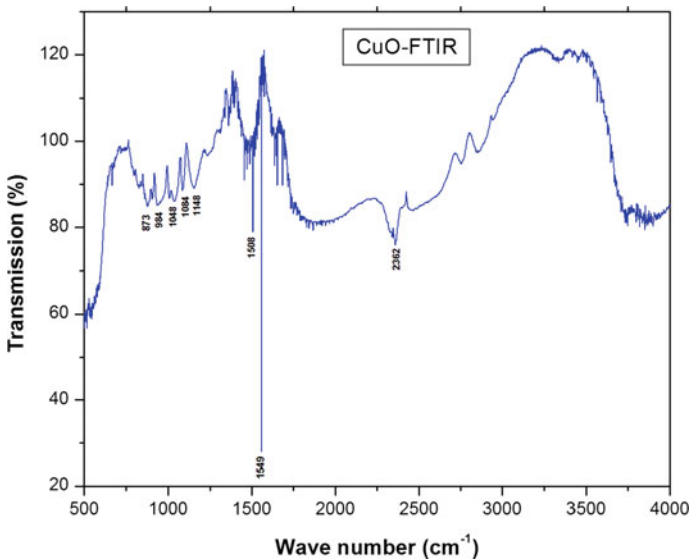


Fig. 3 FTIR image of CuO nanoparticles

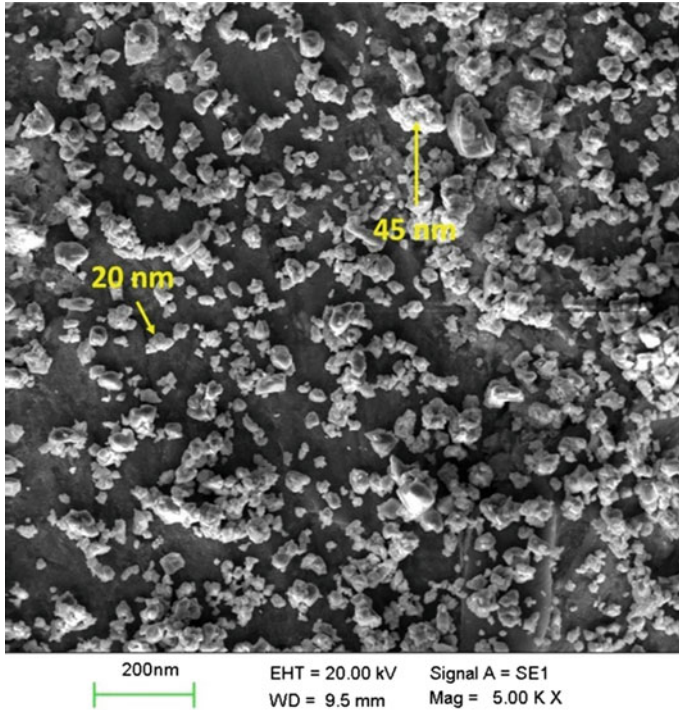


Fig. 4 SEM image of CuO at 5000X

various modes. Further, FTIR showed the peak at 1639 cm^{-1} indicated stretching vibration of the Cu–O bond of copper.

The copper oxide nanoparticles were further characterized by scanning electron microscopy (SEM). Figure 4 showed an SEM image of copper oxide nanoparticles in the base fluid. It showed that the phase formation of nanoparticles with a base solution was homogenous. Further, the particle size of nanoparticle was found to be in a range of 20–45 nm.

4.1 Effect of Mass Flow Rate

Flat plate collector was set for, i.e. 0.017, 0.033 and 0.050 kg/s flow rate to calculate its performance. The obtained experimental data were used to plot a graph of efficiency versus $\left[\frac{T_i - T_a}{G_T} \right]$ (reduced temperature parameter) (Fig. 5).

Data of efficiency with respect to $\left[\frac{T_i - T_a}{G_T} \right]$ at various flow rates, i.e. 0.017, 0.033 and 0.050 kg/s of copper oxide (CuO) nanofluid showed its best fit to Eqs. (1)–(6). The maximum efficiency of the collector was recorded at 0.033 kg/s mass flow rate.

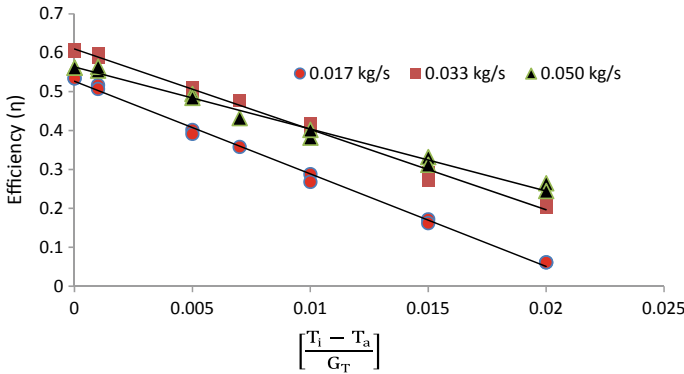


Fig. 5 Efficiency versus $\left[\frac{T_i - T_a}{G_T}\right]$ at various flow rates

There was an increase in the efficiency of the collector with the rise in the rate of flow. However, it decreased at 0.050 kg/s. The possible reason for this is the reduced retention time of nanofluid in the flat plate collector on increasing the flow rate, which further reduced the exposure time to absorb heat. It is pertinent to note that absorbed heat ($F_R(\tau\alpha)$) was a dominant factor at lower data of $\left[\frac{T_i - T_a}{G_T}\right]$ while heat loss parameter ($F_R U_L$) was dominant at higher data of $\left[\frac{T_i - T_a}{G_T}\right]$. Data of $F_R(\tau\alpha)$ were 0.534, 0.6042, 0.5618 at 0.017 kg/s, 0.033 kg/s and 0.050 kg/s, respectively (Fig. 4). The best flow rate was obtained at 0.033 kg/s due to the highest value of absorbed heat $F_R(\tau\alpha)$. Similarly, Moghadam et al. [24] obtained highest value of $F_R(\tau\alpha)$ at 0.033 kg/s.

4.2 Effect of Nanoparticle Concentration

The optimum rate of 0.033 kg/s was selected for further experimental investigation. In this study, the efficiency tends to increase with increasing the nanoparticles content (0.1–0.4% by volume). The graph was drawn for the efficiency with respect to nanoparticles concentration which revealed the increase in efficiency on increasing the nanoparticle concentration (Fig. 6). This shows that nanoparticles can boost the efficiency of the system.

The values of $F_R(\tau\alpha)$ for 0.1, 0.2, 0.3 and 0.4% concentration were 0.6489, 0.6976, 0.7338 and 0.6689, respectively (Fig. 6). Moreover, $F_R U_L$ was also found to be decreased with increasing flow rates. The value of $F_R U_L$ at 0.4% concentration of nanofluid was lower as compared to that obtained at 0.3% concentration. Nevertheless, $F_R(\tau\alpha)$ at 0.3% concentration was higher than that of 0.4% concentration.

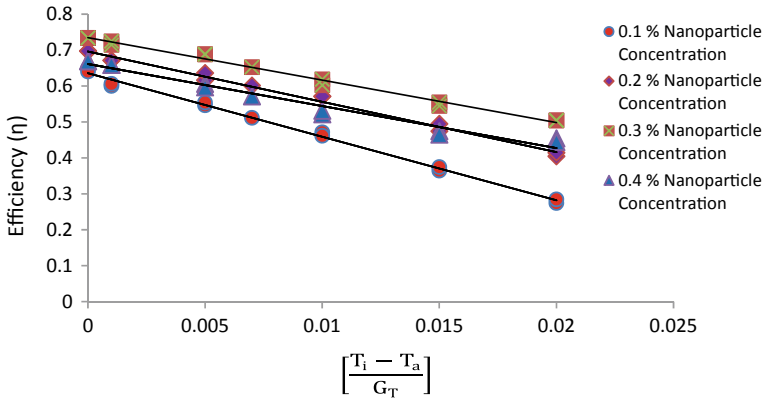


Fig. 6 Efficiency versus $\left[\frac{T_i - T_a}{G_T} \right]$ at 0.033 kg/s

Possibly, nanofluids with a high concentration of nanoparticles tend to make clumps due to which nanofluids lose its stability and homogeneity. This loss affected the efficiency of the collector. The optimum efficiency was obtained at a lower concentration of nanoparticles in a nanofluid. The optimum value of $FR(\tau\alpha)$ was 0.7338 for 0.033 kg/s (Fig. 4) and for 0.033 kg/s was 0.6042 (Fig. 3). These values were used to analyse the efficiency of the collector. Results of the study revealed the increase in efficiency up to 21.45% on using nanoparticles as compared to water. Therefore, nanoparticles can be used to increase the efficiency of the collector.

The findings from this study were correlated with Elcioglu's and colleague's findings [27]. Similar to our results, the positive outcome of nanoparticles on the thermal efficiency of collectors (< 0.04/0.25 vol%) was noted by Elcioglu and his colleagues [27]. According to Saffarian and colleagues [28], the thermal conductivity was increased by 4% on using copper oxide nanoparticles. So, our findings are in line with the previous studies on nanoparticles supplementation in flat plate collector and an increase in its efficiency.

5 Conclusions

Flat plate solar collector, an equipment, was used to provide sensible heat to water using solar radiations, and the effect of nanofluid on its efficiency was assessed in this study during the daytime, i.e. 10 h to 16 h at four concentrations of nanofluids (0.1–0.4%) and different flow rates (0.017–0.050 kg/s). Results obtained from this study are as follows:

- Upsurge efficiency was observed on increasing the nanoparticle concentration, and a maximum of 21.45% increment in efficiency was observed at a volumetric

concentration of 0.3% and 0.033 kg/s due to highest values of absorbed heat $FR(\tau\alpha)$.

- Efficiency increased till optimum mass flow rate achieved, however, decreased due to agglomeration of nanoparticles. Peak efficiency was achieved at 0.033 kg/s. Therefore, the conclusion drawn out from this study is in favour of using nanoparticles in the collector.

References

1. Kalogirou SA (2004) Solar thermal collectors and applications. *Prog Energy Combust* **30**(3):231–295. <https://doi.org/10.1016/j.peccs.2004.02.001>
2. Zamzamin A, KeyanpourRad M, KianiNeyestani M, Jamal-Abad MT (2014) An experimental study on the effect of Cu-synthesized/EG nanofluid on the efficiency of flat-plate solar collectors. *Renew Energy* **71**:658–664. <https://doi.org/10.1016/j.renene.2014.06.003>
3. Goudarzi K, Shojaeizadeh E, Nejati F (2014) An experimental investigation on the simultaneous effect of CuO–H₂O nanofluid and receiver helical pipe on the thermal efficiency of a cylindrical solar collector. *Appl Therm Eng* **73**(1):1236–1243. <https://doi.org/10.1016/j.applthermaleng.2014.07.067>
4. Michael JJ, Iniyani S (2015) Performance of copper oxide/water nanofluid in a flat plate solar water heater under natural and forced circulations. *Energy Convers Manag* **95**:160–169. <https://doi.org/10.1016/j.enconman.2015.02.017>
5. Linga D, Liua G, Moa G, Lia J, Wang X (2015) Research on annual thermal performance of solar water heating balcony system. *Energy Procedia* **70**:71–78. <https://doi.org/10.1016/j.egypro.2015.02.100>
6. Hashim WM, Shomran AT, Jurmut HA, Gaaz TS, Kadhum AAH, Al-Amiery AA (2018) Case study on solar water heating for flat plate collector. *Case Stud Thermal Eng* **12**:666–671. <https://doi.org/10.1016/j.csite.2018.09.002>
7. Bhowmik H Amin R (2017) Efficiency improvement of flat plate solar collector using reflector. *Energy Rep* **3**:119–123. <https://doi.org/10.1016/j.egy.2017.08.002>
8. Ministry of New and Renewable Energy (MNRE) 2015–2016 Annual Report, https://mnre.gov.in/file-manager/annual-report/2015-2016/EN/Chapter%201/chapter_1.htm
9. Ministry of New and Renewable Energy (MNRE) -Resolution, <https://mnre.gov.in/file-manager/annual-report/2018-2019/English/pdf/chapter-1.pdf>
10. Aydin E, Eichholtz P, Yönder E (2018) The economics of residential solar water heaters in emerging economies: the case of Turkey. *Energy Econ* **75**:285–299. <https://doi.org/10.1016/j.eneco.2018.08.001>
11. Khan MZH, Al-Mamun MR, Sikdar S, Halder PK, Hasan MR (2016) Design, fabrication, and efficiency study of a novel solar thermal water heating system: towards sustainable development. 1–8. <https://doi.org/10.1155/2016/9698328>
12. Ullah S, Kasi JK (2019) Fabrication of low cost solar flat plate collector. *Sci J Mehmet AkifErsoy Univ* **2**(2). <tr/en/pub/sjmakeu/issue/45542/571891>
13. Khan MZH, Al-Mamun MR, Sikdar S, Halder PK Hasan MR (2016) Design, fabrication, and efficiency study of a novel solar thermal water heating system: towards sustainable development. *Int J photoenergy* 1–8. <https://doi.org/10.1155/2016/9698328>
14. Chougule SS, Sahu SK, Pise AT (2013) Performance enhancement of two phase thermosyphon flat-plate solar collectors by using surfactant and nanofluid, *Front Heat Pipes* **4**(1):1–6. <https://doi.org/10.5098/fhp.v4.1.3002>
15. Fotukian SM, Nasr Esfahany M (2010) Experimental study of turbulent convective heat transfer and pressure drop of dilute CuO/water nanofluid inside a circular tube. *Int Commun Heat Mass Trans.* **37**(2):214–219. <https://doi.org/10.1016/j.icheatmasstransfer.2009.10.003>

16. Gao L, Zhou XF (2006) Differential effective medium theory for thermal conductivity in nanofluids. *Phys Lett A* 348(3):355–360. <https://doi.org/10.1016/j.physleta.2005.08.069>
17. Lu L, Liu ZH, Xiao HS (2011) Thermal performance of an open thermosyphon using nanofluids for high-temperature evacuated tubular solar collectors. Part 1: indoor experiment. *Sol Energy* 85(2):379–387. <https://doi.org/10.1016/j.solener.2010.11.008>
18. Mints HA, Roy G, Nguyen CT, Doucet D (2009) New temperature dependent thermal conductivity data for water-based nanofluids, *Int J Therm Sci* 48(2):363–371. <https://doi.org/10.1016/j.ijthermalsci.2008.03.009>
19. Karami M, Akhavan-Behabadi MA, Raisee-Dehkordi M, Delfani S (2016) Thermo-optical properties of copper oxide nanofluids for direct absorption of solar radiation. *Sol Energy Mater Sol Cells* 144:136–142. <https://doi.org/10.1016/j.solmat.2015.08.018>
20. Goudarzi K, Nejati F, Shojaeizadeh E, Asadi Yousef-abad SK (2015) Experimental study on the effect of pH variation of nanofluids on the thermal efficiency of a solar collector with helical tube. *Exp Therm Fluid Sci* 60:20–27. <https://doi.org/10.1016/j.expthermflusci.2014.07.015>
21. Chaji H, Ajabshirchi Y, Esmailzadeh E, Heris SZ, Hedayatzadeh M, Kahani M (2013) Experimental study on thermal efficiency of Flat plate solar collector using water and nanofluid. *Mod Appl Sci* 7(10):60–69. <https://doi.org/10.5539/mas.v7n10p60>
22. Said Z, Sajid MH, Alim MA, Saidur R, Rahim NA (2013) Experimental investigation of the thermophysical properties of Al_2O_3 -nanofluid and its effect on a flat plate solar collector. *Int Commun Heat Mass Trans* 48:99–107. <https://doi.org/10.1016/j.icheatmasstransfer.2013.09.005>
23. He Q, Zeng S, Wang S (2014) Experimental investigation on the efficiency of flat-plate solar collectors with nanofluids. *Appl Therm Eng* 88:165–171. <https://doi.org/10.1016/j.applthermaleng.2014.09.053>
24. Moghadam AJ, Farzane-Gord M, Sajadi M, Hoseyn-Zadeh M (2014) Effects of CuO/water nanofluid on the efficiency of a flat-plate solar collector. *Exp Therm Fluid Sci* 58:9–14. <https://doi.org/10.1016/j.expthermflusci.2014.06.014>
25. ASHRAE Standard 86–93 (1986) Methods of testing to determine the thermal performance of solar collectors. Atlanta, GA, USA
26. Gupta HK, Agrawal GD, Mathur J (2015) Investigations for the effect of Al_2O_3 - H_2O nanofluid flow rate on the efficiency of direct absorption solar collector *Case Stud Thermal Eng* 5:70–78. <https://doi.org/10.1016/j.csite.2015.01.002>
27. Elcioglu EB, Genç AM, Karadeniz ZH, Ezan MA, Turgut A (2019) Nanofluid figure-of-merits to assess thermal efficiency of a flat plate collector. *Energy Convers* 204:1–11. <https://doi.org/10.1016/j.enconman.2019.112292>
28. Saffarian MR, Moravej M, Doranehgard MH (2020) Heat transfer enhancement in a flat plate solar collector with different flow path shapes using nanofluid. *RenewEnergy* 146:2316–2329. <https://doi.org/10.1016/j.renene.2019.08.081>

Numerical Study of Copper Oxide/Therminol VP-1 Nanofluid in Solar Parabolic Trough Collector



Gopal Nandan and Nafees Alam Wani

1 Introduction

Enhancement in the heat transfer enhancement in heat exchanging devices like solar collectors, heat exchangers, etc., plays an important role in system design. There are several types of solar collectors which concentrate the solar radiation energy to give high fluid temperature. In PTC, incident solar radiation is converted to heat energy which is transported by the fluids which circulate through the collector. The linear tube is placed at the focal line of the parabolic reflector. The fluid which transports the heat is referred to as heat transfer fluids (HTF). The concentration of solar energy enables outlet fluid temperatures to achieve as high as 400 °C in PTC, which is suitable for power generation. In industrial processes, water, ethylene glycol, synthetic oil, molten salts, etc., are used as HTF. The thermal efficiency of PTC can be further improved by using HTF having more thermal conductivity as compared to conventional fluids. The thermal efficiency can be ameliorated considering nanofluid as HTF, due to their improved thermal characteristics of it. Use of additional coatings and fins to collector tube increases thermal collection. The application of evacuated tubes decreases heat loss and increases the thermal yield.

The metallic oxide-based nanofluid is used in many heat exchange applications. Nanofluids are an amalgamation of a nanoparticle (fine size and shape) and conventional fluids. Nanoparticles are oxides of metals having good thermal conductivity; the fine particles are uniformly spread in the conventional fluid. There are two methods for the preparation of nanofluids. The conventional fluids are referred to as base fluids. It is anticipated that the thermal conductivity of the nanofluids will have better concerning conventional fluid. The use of nanofluids may have sedimentation problems, and pressure drops may increase also. Due to certain advantages, nanofluids are used in the solar collector as compared to base fluids. This makes a

G. Nandan (✉) · N. A. Wani

Mechanical Engineering Department, Amity University, Noida, Uttar Pradesh 201313, India

e-mail: gopalnandan@gmail.com

more efficient heat collection system. The surface area is increased due to nano-size particles. This shows very high scattering and absorption of the incident radiation range as compared to the base fluids. The output temperature is increased; hence, the collector efficiency will also be increased. To get a similar collector efficiency, complex manufacturing processes are required for creating efficient heat transfer surfaces. This can be easily used in place of the based fluid in the existing system with different volumetric fractions as per requirement [1]. The thermal characteristics of nanofluid depend on properties of solid particles and base fluid [2–15]. The application of nanofluids will lead to internal fouling and erosion of the channel. The modeling of nanofluids flow in the PTC for heat transfer study has remained in the interest of the researcher. He et al. [16] considered a single-phase model (SPM) and used changed values of thermal and fluid flow properties of nanofluids. These properties are thermal conductivity, density, viscosity, etc., in the modeling. A comparative study of SPM and a two-phase model (TPM) were done numerically. TPM is more preferable in comparison with SPM, due to good agreement with experimental results. The heat transfer rate prediction using PTM was closer (about 8% error) with respect to the single-phase model (about 16% error) as compared to the experimental result for Cu-water nanofluid [16]. Davarnejad and Jamshidzadeh [4] used three models, namely (a) SPM (b) TPM and (c) volume of fluids. TPM's result was a very good larger volume fraction of nanoparticle in the fluids. The results based on single-phase are about 11% with respect to the experimental result. In this research, the work forced convection heat transfer, considering CuO/Thermal-VP1 the PTC by considering constant heat flux over horizontal receiver tube has been studied using finite volume based software, *ANSYS Fluent*. The volumetric fraction has been considered from 1 to 5%. Understanding the thermal behavior will help in the proper design of the collector.

2 Literature Survey

Several authors numerically studied PTC using constant heat flux on it. The heat transfer modeling has been done assuming 1-D. The mass and energy equations were solved simultaneously. The results were validated with Sandia National Laboratory's experiment data [14]. Kumar et al. studied CuO/water using single-phase modeling. The solar flux solar load cell and S2S radiation model were used [10]. Kaloudis et al. [17] simulated the SEGS LS2-module PTC with Al_2O_3 -Syltherm 800 nanofluid. For nanofluid modeling, TPM was used and validated with experimental data. The maximum relative error in the collector efficiency was 7.3%. For simulation, up to 4%, volumetric concentrations were used, and at this concentration, collector efficiency was amplified by 10%. Basbous et al. [18] coded for modeling of PT by considering all type losses from PTC. They used Al_2O_3 -Syltherm 800 as HCE. Considering losses, the heat transfer coefficient can be elevated up to 18%. The useful heat gain of a PTC depends on the heat loss from the operating temperature of

the heat absorber tube. An evacuated concentric glass was used, and it was numerically studied by Daniel et al. [19]. The effect of the evacuated tube with the selective coating with different wind velocity conditions was studied. Kasaeian et al. [20] modeled constant heat over PTC and used Al_2O_3 /synthetic oil nanofluid. For the velocity pressure compounding, SIMPLE algorithm is used. They considered three equations of the 3D Navier–Stokes equation. The heat transfer rate is related to nanoparticle concentration in the nanofluid and Reynolds number (Re). They considered the volume fraction of nanofluids up to 5%. The thermal and thermodynamic performances of a PTC with Al_2O_3 /synthetic oil nanofluid are presented based on the second law of thermodynamics and entropy generation [21]. With nanofluids, the heat transfer rate increased up to 76% when the volumetric fraction increased to 8% from 0%. Optimal value Re was calculated for minimum entropy generation in the receiver. Beyond the optimal value of Re, use of nanofluids is thermodynamically useless [22]. A code was developed in Fortran language based on finite difference method to study the thermal behavior of PTC. This shows the improvement in heat absorption using Cu-water nanofluid. Kasaeian et al. [23] considered constant solar heat flux for modeling of PTC using Al_2O_3 /synthetic oil nanofluid. The convection heat transfer coefficients increase with Reynolds number and particle concentration level in the nanofluid. Based on CFD simulation, overall efficiency by 0.125% Al_2O_3 water nanofluid is performed [24]. Experimental and simulation results were differed by 8% approximately. The thermal efficiency was found to improve by 12.5% with a nanoparticle concentration varying from 0 to 6%. Numerical simulation for heat transfer coefficient along with experimental results on titania nanofluid in a laminar flow condition (low Reynolds number) was performed at 0.6 vol% and 4000 W/m^2 heat flux. The coefficient of transfer of heat is much relying on the thermal conductive property and has a less effect from viscosity, Brownian force, and thermophoretic forces. Simulation of straight tubes showed marked improvements in the heat transfer coefficient using titania nanofluid at the entry portion of the tube. A simulation model with Syltherm 800 with dispersed alumina and cuprous oxide nanoparticles was performed, and 50% enhancement of heat transfer coefficient was obtained [2]. The efficiency of the model is decreased by 14% as the temperature of Syltherm oil 800 is increased from 25 to 325 °C. Numerical simulation of a PTC was carried out with CFD along with the MCRT technique. PTC with a concentration ratio of 113 was studied for its performance [25]. The results suggested receiver performance improvement by 12.5% at a nanoparticle concentration of 6%. Al_2O_3 and $\text{CuO}/\text{H}_2\text{O}$ nanofluids are considered as HTF, and results were obtained using the $k-\varepsilon$ model [26]. Wang et al. [27] simulated based on the finite element method to study PTC performances using Al_2O_3 /synthetic oil nanofluid. The temperature of the absorber tube using normal base fluid was high, which was reduced by Al_2O_3 /synthetic oil. It was also observed that the temperature gradients are low with respect to the base fluid. Numerical simulation of a PTC under conditions of varying solar flux was performed to investigate the absorber tube [28]. The circumferential temperature difference (CTD) decreases with the discharge rate and inlet temperature of fluids in the channel. However, it increases with the increase of DNI. At a velocity of 1 m/s and DNI (500 W/m^2), the circumferential temperature difference of 22 K was attained

in the model. The heat transfer study using CuO/water nanofluids in a rectangular shallow cavity was performed for 0–4 vol.%. As the volumetric fraction increased, the Nu values and the coefficient of transfer of heat are increased. Interesting studies like radial and axial temperature profiles have been attempted, and the mathematical model was developed to facilitate calculation of heat transfer of PTC [3]. Simulation for optical efficiency, cosine factor, and receiver efficiency was attempted, and under normal incidence conditions and a tracking error of 12 min radian angle, optical efficiency of 53% was attained [29]. The CuO/water nanofluid in a parabolic shaped trough collector was used, and this model was created and subjected to CFD simulation. Agreement of results of experimental and simulation studies was obtained with a marginal difference of 5.75% at a flow of 18 L per hour. The thermal efficiency in the model is improved by 6% when the HTF volumetric fraction was 0.01%. The fluid flow affects the heat transfer rate in the system [30–36].

3 Simulation of Parabolic Trough Collector

The numerical modeling was done by solving three equations, namely continuity equation (Eq. 1), momentum equation (Eq. 2), and energy conservation equation (Eq. 3) using ANSYS Fluent.

$$\frac{\partial \rho}{\partial t} + \frac{\partial(\rho u_j)}{\partial x_j} = 0 \quad (1)$$

$$\frac{\partial(\rho u_i)}{\partial t} + \frac{\partial(\rho u_i \rho u_j)}{\partial x_j} = \frac{\partial}{\partial x_j} \left[\rho \delta_{ij} + \mu \left(\frac{\partial u_i}{\partial x_j} + \frac{\partial u_j}{\partial x_i} \right) \right] + \rho g_i \quad (2)$$

$$\frac{\partial(\rho C_p T)}{\partial t} + \frac{\partial(\rho u_i C_p T)}{\partial x_i} - \frac{\partial \left[\lambda \frac{\partial T}{\partial x_j} \right]}{\partial x_j} = S_T \quad (3)$$

In this effort, the absorber tube is modeled as a copper tube with nanofluid flowing through it. Single-phase model is used in the ANSYS Fluent for simulation in the laminar flow range.

4 Modeling of the PTC

This section covers the modeling using *Design Modeler* and solution using boundary conditions.

4.1 Geometry of PTC

The dimensions that are going to be used are given in Table 1. The PTC receiver is modeled as per the dimensions in the ANSYS *Design Modeler*. The current analysis is done by assuming that the absorber tube is not covered with the glass envelope. The model meshed, and respective domains are named as solid and fluid. The specification of heat absorber is as per commercial parabolic receivers. The boundary conditions were defined for the cylindrical wall, inlet, and outlet of the geometry. The heat transfer fluid (HTF) is nanofluid.

In the simulation, in ANSYS *Fluent*, the energy equation kept in ON position. All the simulations are done in the laminar range. So, the viscous model is kept as the laminar. In modeling, the absorber tube material is copper, and HTF is the CuO/Therminol VP1. The properties of the nanofluid are calculated using correlations given in equation no. 4–7. The density of nanofluid is calculated using Eq. (4)

$$\rho_{nf} = (1 - \phi)\rho_{bf} + \phi\rho_{np} \tag{4}$$

The specific heat is calculated from

$$C_{p,nf} = \phi\rho_{np}C_{p,np} + (1 - \phi)\rho_{bf}C_{p,bf} \tag{5}$$

The thermal conductivity is given by the Maxwell model

$$k_{nf} = \frac{k_{np} + 2k_{bf} + 2\phi(k_{np} - k_{bf})}{k_{np} + k_{bf} - \phi(k_{np} - k_{bf})}k_{bf} \tag{6}$$

The viscosity of the nanofluid is given from the general Einstein’s formula

$$\mu_{nf} = (1 + 2.5\phi)\mu_{bf} \tag{7}$$

where subscripts *nf* are for nanofluids, *bf* is for base fluids, and *np* is for nanoparticles and ϕ is the volume fraction of nanofluids. The properties of the materials are given in Table 2.

Table 1 Geometric dimensions of PTC

I. D. of the absorber tube	0.0244 m
O. D. of Absorber tube	0.0254 m
Aperture width	1.22 m
Aperture length	6 m
Aperture area	7.32 m

Table 2 Thermal fluid flow properties of the materials

Material	Volume fraction percent (ϕ)	Density (ρ)	Thermal conductivity (k)	Specific heat (Cp)	Dynamic viscosity (μ)
Copper-Therminol VP1 nanofluid (30 °C)	0	1056	0.135	1575	0.00328000
	1	1110.44	0.13901	1488.1628	0.00336346
	2	1164.88	0.14310	1409.9428	0.00344992
	3	1219.32	0.14727	1339.1858	0.00353952
	4	1273.76	0.15152	1274.9349	0.00363242
	5	1328.2	0.15587	1216.3900	0.00372876
CuO	–	6500	20	535.6	–

4.2 Boundary Conditions

The receiver tube is modeled with the inner surface as stationary with the no-slip condition. The heat transfer has been considered only in the radial direction. It has been neglected in the other direction. The direct radiations from the sun are modeled as the constant heat flux on the receiver tube. The heat flux around the circumferential surface is assumed to be constant. In this case, the heat flux is taken as 10 kW/m². The initial condition of the velocity inlet and temperature of fluids were specified.

5 Results and Discussion

5.1 Effect of the Volume Fraction on Temperature

The volumetric fractions that were used in this work were 1–5%, and the length of the tube is considered 6 m. Normally, the volume fraction up to 6% is advised in the thermal application. Beyond this, the power required to maintain the flow is not justified.

The surface temperature of the heat receiver tube and the bulk fluid temperature are directly proportional to the volumetric concentration. The surface temperature of the receiver tube increases in the axial direction in the HTF flow direction (Fig. 1). As the fluids flow in the forward direction, the heat transfer rate is high owing to the lower temperature of the fluids; hence, lower surface temperature of the tube is observed. The effect of volumetric fractions is also crucial. At any of the locations along with the flow, the surface temperature of the tube is inversely proportional to the volumetric fraction. The mean outlet bulk temperature is maximum for a maximum volumetric fraction (5%) of nanofluids (Fig. 2). The heat transfer coefficient initially is very high in thermal entry length, and it decreases later on and finally becomes almost constant along the flow direction. The heat transfer coefficient also increases

Fig. 1 Surface temperature variation along the length of absorber tube at $Re = 1500$

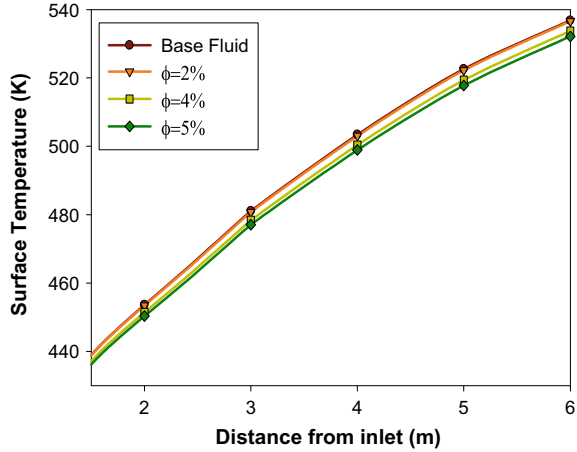
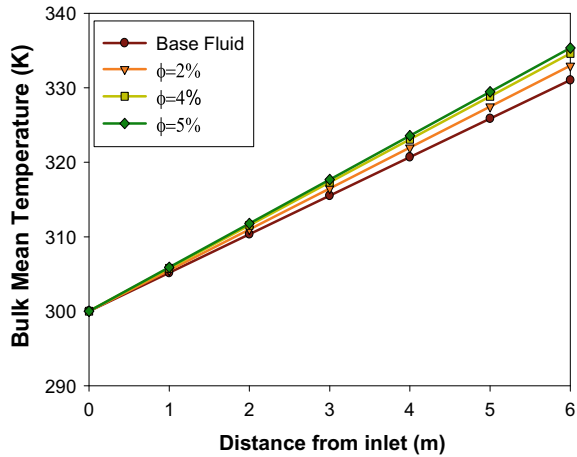


Fig. 2 Bulk mean temperature variation along the length of tube at $Re = 1500$



nanoparticle concentration in the nanofluid. It is the maximum for volumetric fraction 5 and lowest for base fluid. In the analysis, results have been presented for Reynolds number of 1500. The surface heat transfer coefficient is shown in Fig. 3.

5.2 Effect of Volume Fraction on Pressure Drop in the Tube

There is a need to simultaneously study the pressure drop due to the increase in the volumetric fraction. The density and viscosity result in the increase in fluid friction and thus pressure drop. Hence, there will be an additional pressure drop in the flow, which is disadvantageous, because it will have more pump power work.

Fig. 3 Surface heat transfer coefficient in the fully developed region at $Re = 1500$

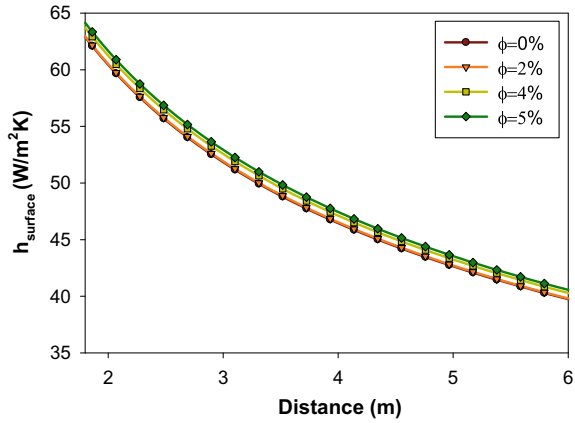
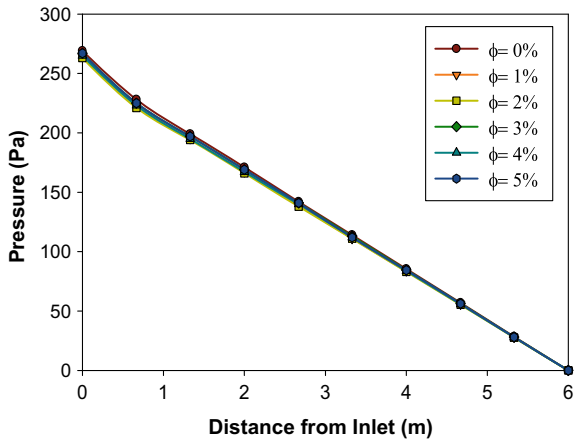


Fig. 4 Pressure drop along the length at $Re = 1500$



The optimization study is very important. Figure 4 shows the pressure drop along the length of the tube at different volumetric fractions of nanofluids. The pressure drop for base fluid and nanofluids shown in the graph in Fig. 4 is not very significant. The pressure drop in the tube is almost the same for all volumetric fraction. This is due to the very high Prandtl number of base fluids. Even the very little variation in the viscosity has been observed (Table 2).

5.3 Effect of Volume Fraction on Nu

The value of Nu along the length for the base fluid as well as the nanofluid at different volume fractions was obtained in the laminar flow range. The simulation data is compared with Shah correlations for Nu [37]. All the simulations were done

in the laminar range for the Re of 1500. The simulated data is per the correlations. For Therminol VP-1, simulation results are close to Hausen’s correlation, whereas it shows deviations with Shah’s correlation (Fig. 5). A similar trend is for nanofluids at a volume fraction of 1%.

The variation of Nu on the tube at volume fractions 2, 3, 4, and 5 is shown in Figs. 5, 6, 7, 8, 9, and 10, respectively. It is concluded that in the laminar flow region, CFD simulation provides very good results in the fully developed flow. In the present analysis, the hydrodynamic entry length is 1.83 m. In the developing flow region, the Nu number is very high, and it decreases very fast. This trend is visible from the graphs.

Fig. 5 Nu along the length of PTC

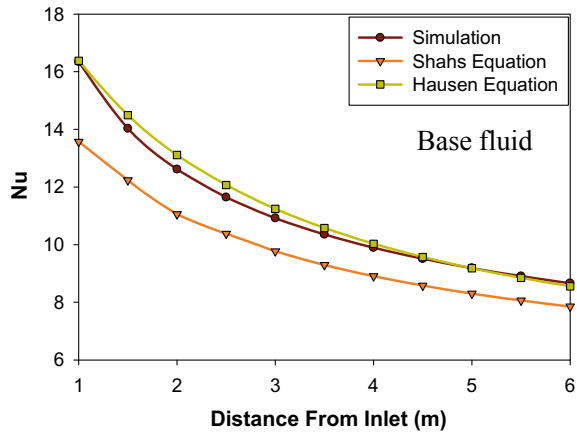


Fig. 6 Nu along the length CuO/Therminol

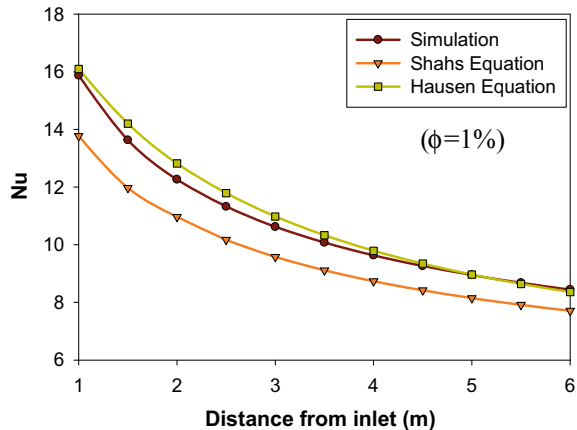


Fig. 7 Nu along the length CuO/Therminol VP-1

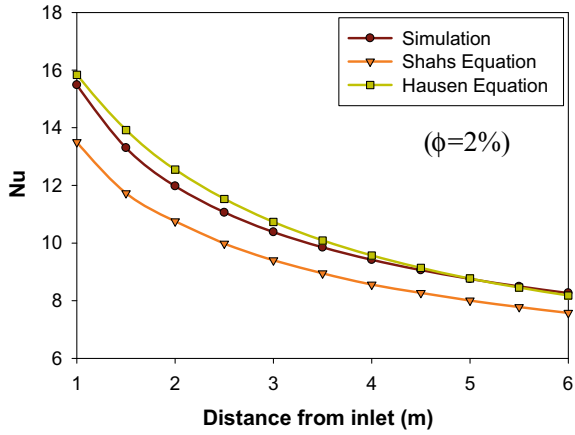


Fig. 8 Nualong the length CuO/Therminol VP-1

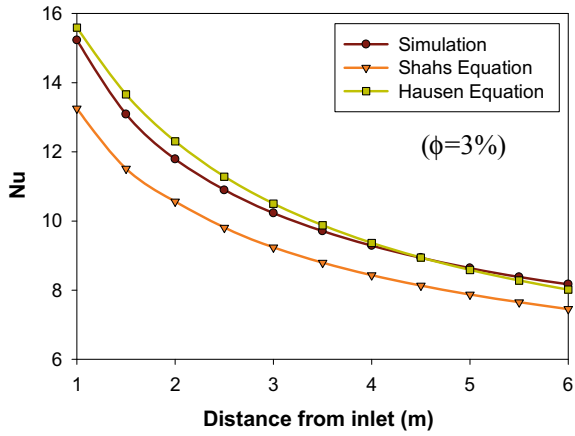


Fig. 9 Nu along the length CuO/Therminol ($\phi = 4\%$)

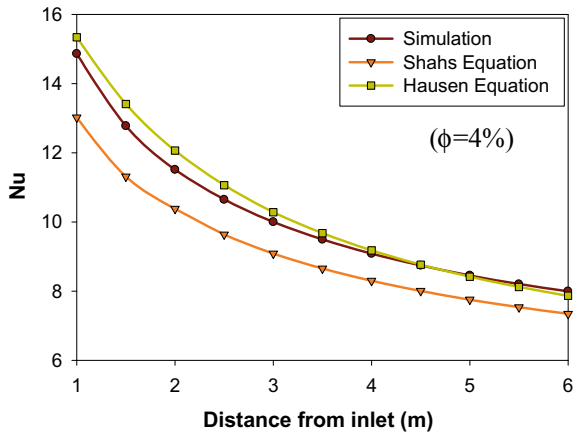
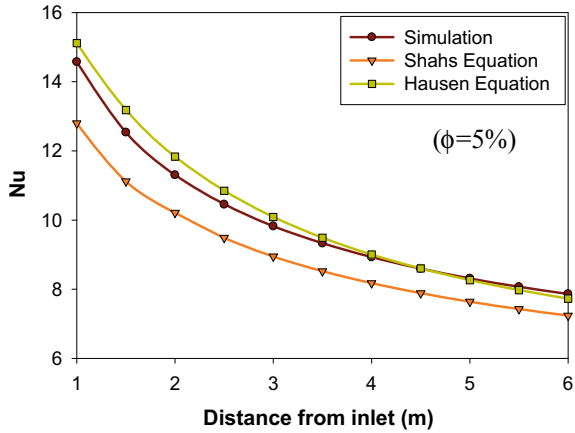


Fig. 10 Nu along the length
CuO/Therminol ($\phi = 5\%$)



6 Conclusion

The simulation of the heat receiver tube of a linear trough collector considering copper oxide/Therminol VP-1 nanofluid is investigated using *ANSYS Fluent* software. The effect of nanofluid volume fractions has been reported. The modeling work can be concluded as:

- (a) The volume fraction of the nanofluid plays a very crucial role in the thermal performance of the PTC. The thermal performance of the collector increases with an increase in the nanofluid volumetric concentration. The exit temperature of the nanofluid in the absorber is the increasing function of the volume fraction of the nanofluid for the same boundary conditions. As the volume fraction is increased, the absorber surface temperature decreases, and the bulk means that the temperature of the fluid increases. Also, the heat transfer coefficient increases.
- (b) The density and viscosity of the fluid increase with the volume fraction of the nanofluid; hence, pressure drop is also affected. This will increase fluid friction. An increase in the value of particle concentration leads to an increase in the pressure drop, and consequently, it increases the pumping power. It will increase the operating cost of the system. Therefore, the larger values of the viscosity and density are not desirable in our case. Volume fraction up to 5% is used. At higher values of volume fraction, it will increase the risk of sedimentation of the nanoparticles in the tube at lower discharge rates.
- (c) The mean bulk temperature of nanofluid depends on the discharge rate. It was seen that the mean bulk temperature of the nanofluid increases with the decrease in volume flow rate and vice versa.
- (d) The increase in the volume fraction causes a slight decrease in the variation of Nusselt number along the length for the same conditions of heat flux and Reynolds number.

References

1. Hussein AK (2016) Applications of nanotechnology to improve the performance of solar collectors recent advances and overview. *Renew Sustain Energy Rev* 62:767–792
2. Bellos E, Tzivanidis C (2017) Parametric investigation of nanofluids utilization in parabolic trough collectors. *Thermal Sci Eng Progress* 2:71–79
3. de Oliveira Siqueira AM, Gomes PEN, Torrezani L, Lucas EO, da Cruz Pereira GM (2014) Heat transfer analysis and modeling of a parabolic trough solar collector: an analysis. *Energy Procedia* 57:401–410
4. Davarnejad R, Jamshidzadeh M (2015) CFD modeling of heat transfer performance of MgO-water nanofluid under turbulent flow. *Eng Sci Technol Int J* 18(4):536–542
5. Sekhar TVR, Prakash R, Nandan G, Muthuraman M (2017) Preparation of $\text{Co}_3\text{O}_4\text{-H}_2\text{O}$ nanofluid and application to CR-60 concentrating solar collector. *Progress Ind Ecol Int J* 11(3):227–246
6. Suresh AK, Khurana S, Nandan G, Dwivedi G, Kumar S (2018) Role on nanofluids in cooling solar photovoltaic cell to enhance overall efficiency. *Mater Today Proc* 5(9):20614–20620
7. Sekhar TVR, Prakash R, Nandan G, Muthuraman M (2018) Performance enhancement of a renewable thermal energy collector using metallic oxide nanofluids. *Micro Nano Lett* 13(2):248–251
8. Sharma R, Gupta A, Nandan G, Dwivedi G, Kumar S (2018) Life span and overall performance enhancement of Solar Photovoltaic cell using water as coolant: a recent review. *Mater Today Proc* 5(9):18202–18210
9. Krishn S, Goyal M, Nandan G, Kumar S, Kumar P, Shukla AK (2019) Pool boiling using nanofluids: a review. In: *Lecture Notes in Mechanical Engineering*. Springer Singapore, pp 325–336
10. Kumar M, Patel D, Sehrawat V, Gupta T (2016) Experimental and CFD analysis of $\text{CuO-H}_2\text{O}$ (di) nano fluid based parabolic solar trough collector. *Int J Inn Res Sci Eng Technol* 5(8)
11. Nandan G (2019) Performance of solar photovoltaic panel using forced convection of water-based CuO nanofluid: an understanding. In: *IOP conference series: materials science and engineering* 691, 012088
12. Sekhar TVR, Prakash R, Nandan G, Muthuraman M (2018) Pressure drop characteristics & efficiency enhancement by using $\text{TiO}_2\text{-H}_2\text{O}$ nanofluid in a sustainable solar thermal energy collector. *Int J Environ Sustain Develop*
13. Wani NA, Nandan G (2019) Modelling of solar parabolic trough collector considering unsymmetrical heat flux. In: *3rd international conference on recent developments in control, automation & power engineering (RDCAPE)*. IEEE
14. Padilla RV, Demirkaya G, Goswami DY, Stefanakos E, Rahman MM (2011) Heat transfer analysis of parabolic trough solar receiver. *Appl Energy* 88(12):5097–5110
15. Sekhar TVR, Nandan G, Prakash R, Muthuraman M (2018) Investigations on viscosity and thermal conductivity of cobalt oxide-water nano fluid. *Mater Today Proc* 5(2):6176–6182
16. Fard MH, Esfahany MN, Talaie M (2010) Numerical study of convective heat transfer of nanofluids in a circular tube two-phase model versus single-phase model. *Int Commun Heat Mass Trans* 37(1):91–97
17. Kaloudis E, Papanicolaou E, Belessiotis V (2016) Numerical simulations of a parabolic trough solar collector with nanofluid using a two-phase model. *Renew Energy* 97:218–229
18. Basbous N, Taqi M, Belouaggadia N (2015) Numerical study of a parabolic trough collector using a nanofluid. *Asian J Curr Eng Maths* 4(3):40–44
19. Daniel P, Joshi Y, Das AK (2011) Numerical investigation of parabolic trough receiver performance with outer vacuum shell. *Solar Energy* 85(9):1910–1914
20. Sokhansefat T, Kasaiean A, Abbaspour MJ, Sokhansefat M (2012) Numerical study of heat transfer enhancement by using Al_2O_3 /synthetic oil nanofluid in a parabolic trough collector tube. *World Acad Sci Eng Technol* 69:1154–1159
21. Mwesigye A, Huan Z, Meyer JP (2015) Thermodynamic optimisation of the performance of a parabolic trough receiver using synthetic oil 2 o 3 nanofluid. *Appl Energy* 156:398–412

22. Ghasemi SE, Ahangar GRM (2014) Numerical analysis of performance of solar parabolic trough collector with cu-water nanofluid. *Int J Nano Dimens* 5(3):233–240
23. Chandrasekar M, Suresh S, Senthilkumar T (2012) Mechanisms proposed through experimental investigations on thermophysical properties and forced convective heat transfer characteristics of various nanofluids a review. *Renew Sustain Energy Rev* 16(6):3917–3938
24. Ajay K, Kundan L (2016) Experimental and CFD investigation on the efficiency of parabolic solar collector involving $\text{Al}_2\text{O}_3/\text{H}_2\text{O}$ (DI) nanofluid as a working fluid. *Int J Renew Energy Res* 6(2):392–401
25. Mwesigye A, Huan Z, Meyer JP (2016) Thermal performance and entropy generation analysis of a high concentration ratio parabolic trough solar collector with Cu-therminolVP-1 nanofluid. *Energy Conv Manag* 120:449–465
26. Ghasemi SE, Ranjbar AA (2016) Thermal performance analysis of solar parabolic trough collector using nanofluid as working fluid: a CFD modelling study. *J Mol Liquids* 222:159–166
27. Wang Y, Xu J, Liu Q, Chen Y, Liu H (2016) Performance analysis of a parabolic trough solar collector using Al_2O_3 /synthetic oil nanofluid. *Appl Thermal Eng* 107:469–478
28. Wang Y, Liu Q, Lei J, Jin H (2015) Performance analysis of a parabolic trough solar collector with non-uniform solar flux conditions. *Int J Heat Mass Trans* 82:236–249
29. Huang W, Hu P, Chen Z (2012) Performance simulation of a parabolic trough solar collector. *Solar Energy* 86(2):746–755
30. Agrawal T, Ajitkumar R, Prakash R, Nandan G (2018) Sodium silicide as a hydrogen source for portable energy devices: a review. *Mater Today Proc* 5(2):3563–3570
31. Rathour RS, Chauhan V, Agarwal K, Sharma S, Nandan G (2019) Cooling of solar photovoltaic cell: using novel technique. In: *Lecture notes in mechanical engineering*. Springer Singapore, pp 521–529
32. Rawat KS, Thakur HC, Nandan G (2016) CFD analysis of a pentagonal rib over absorber plate of a solar air heater. In: *3rd international conference on manufacturing excellence*, Amity University, Uttar Pradesh, Noida, India, pp 191–196
33. Kumar S, Nandan G, Singh GK (2016) Numerical study of natural convection and radiative heat transfer of heated inner cylinder placed inside a isothermally cooled circular enclosure. In: *Third international conference on manufacturing excellence*. Amity University, Uttar Pradesh, Noida, India, pp. 179–183
34. Singh GK, Kumar V, Vates UK, Nandan G (2016) Parametric analysis of electro-discharge diamond face grinding of HSS using regression analysis. In: *Third international conference on manufacturing excellence*. Amity University, Uttar Pradesh, Noida, India. pp 36–41
35. Sekha T, Nandan G, Prakash R, Tiwari AK (2016) An overview on parabolic trough solar collectors. In: *Third international conference on manufacturing excellence*. Amity University, Uttar Pradesh, Noida, India, pp 203–211
36. Shukla AK, Sharma A, Sharma M, Nandan G (2018) Thermodynamic investigation of solar energy-based triple combined power cycle. *Energy Sourc Part A Recov Utilizat Environ Eff* 41(10):1161–1179
37. Celata GP, D'Annibale F, Mariani A, Saraceno L, D'Amato R, Bubbico R (2013) Heat transfer in water-based SiC and TiO_2 nanofluids. *Heat Trans Eng* 34(13):1060–1072

Physical Modelling of Terrain Using Different File Formats: A Review



Jagdish Rana and Sanat Agrawal

1 Introduction

The term additive manufacturing was standardized by the ASTM F42 committee. A part or model is fabricated by addition of material layer by layer of the product by using CAD, 3D scan, GIS, MRI or satellite data. In the last few years, this technology has become a substitute for conventional manufacturing technology in certain fields. However, it cannot substitute the conventional process completely. This technology is mostly used for customized products like shoes, helmets, goggles, implants, tissue engineering, terrain modeling, etc. This technology is used to make complex products in less time and cost with no or a little human intervention. The input of this technology is CAD file or GIS data. This input file format is converted into a suitable file format as per the requirement of the 3D printing machine. Most of the 3D printing machines take an STL file; this file consists of a disordered list of triangular facets which represent the outside surface of an object. There are two data formats, one is DSAA, and another is DSBB. (DSAA represents data in surfer grid ASCII format), (DSBB represents data in surfer grid binary format). The ASCII STL file is human-readable; however, it is larger in size than that of the binary format [1]. The resolution of a model can be changed with the help of software packages like Ultimaker Cura, Simplify3D, Slic3r, KISSlicer, etc. The printing time of a product depends upon the resolution chosen. The resolution can be changed according to the application of the product. Ultimaker Cura is a software package which can be used to change the percentage deposition of material. This saves time as well as the

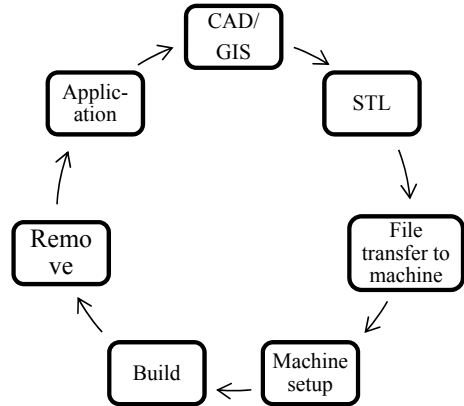
J. Rana · S. Agrawal (✉)

Department of Mechanical Engineering, National Institute of Technology, Uttarakhand, Srinagar (Garhwal), Uttarakhand 246174, India

e-mail: sanata@nituk.ac.in

J. Rana

e-mail: jagdishrana025@gmail.com

Fig. 1 Process chain

cost of the material. Additive manufacturing (AM) technology is also called the third industrial revolution. In the AM process, there is no need for jig and fixtures [2].

1.1 Process Chain

Figure 1 shows the complete process of additive manufacturing technology from the input to the final product. The input data can be either a CAD file or GIS data. Almost all the 3D printing machines accept the STL file format, which breaks the model into a number of polygons, e.g., triangles, and almost all the CAD system can output this file format. The STL file which describes the part is transferred to the 3D printing machine. The 3D printing machine is set up with suitable parameters before the part is built. The settings include the build parameters such as constraints of material, source of energy, the thickness of each layer [3]. The part building is an automated process, and the machine can mostly work without supervision. After printing the product or the terrain model, it is removed from the 3D printing machine. The next stage is post-processing depending upon the application. Product may require support during fabrication in the AM machine. The support material may be the same as the product material, or it can be different. The support is removed after complete printing.

1.2 Stereolithography (STL)

STL files have an output of either ASCII formats or binary format. The ASCII format of STL file is not popular in industries. However, it is easier to understand. Therefore, it is mostly utilized for representation and instruction purposes. The STL file is generally written with an STL extension which is case insensitive. However, some

additive manufacturing systems may accept a different or more specified file extension. An STL file is a triangulated model of the part. When the STL file is created, the points are converted into triangles using the nearest neighbor interpolation. The STL file created is the file that the software of the AM machine will use to generate the physical model [4, 5].

2 Classification

Figure 2 shows the broad classification of additive manufacturing (AM) processes. This is classified according to the availability of material either in solid, liquid or powder forms. SLA and poly-jet modeling are the most widely used liquid-based techniques. FDM is the most widely used solid-based technology. SLS and 3D printing are the most widely used techniques of powder-based AM technology [6–8].

2.1 Stereolithography Apparatus (SLA)

Stereolithography is a liquid-based manufacturing process. This is the first technique and still mostly used as it is less expensive compared to several other techniques. This

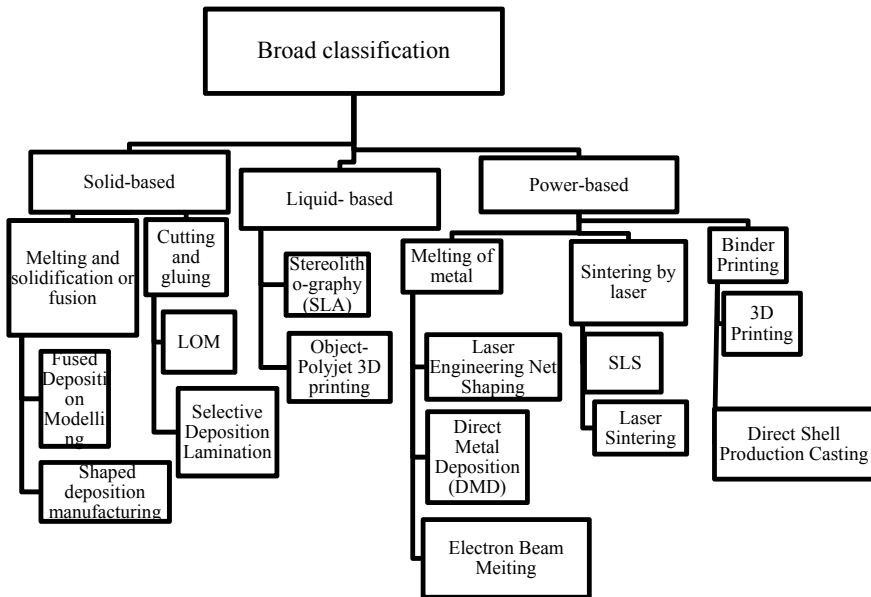


Fig. 2 Broad classification of AM process

technique provides high accuracy and good surface finish. The layer thickness in this process varies from 0.076 to 0.50 mm. The thinner layer provides better resolution and more intricate shapes, but processing time is larger. This is the first liquid-based technique that was commercialized. The SLA process is patented in 1986 by Charles W. Hull of ultraviolet products (UVP). It has been awarded more than 40 United States patents and 20 International patents, with additional patents filed or pending internationally. He–Cd laser is used to solidify the liquid layers. The laser scan speed is typically 500–2500 mm/s. There are a lot of advantages of the SLA process like round the clock operation, good user support, build volume, good accuracy, surface finish and wide range of materials.

2.2 Fused Deposition Modeling (FDM)

AM systems based on the fused deposition modeling (FDM) process are the most widely used. In this process, the raw material is in the form of wire or filament. The fused deposition modeling process was initially developed by Scott Crump in 1988 and got a patent in the USA in 1992. FDM is an extrusion-based technique in which the material is extruded from the nozzle of the printer. The parameter on which the printing time depends is the nozzle diameter, temperature, geometry, speed, deposition rate, etc. There are some advantages of the FDM process like fabrication of functional parts, minimum wastage, easy of support removal and easy of a material change, etc.

2.3 Laminated Object Manufacturing (LOM)

This technology was developed in 1985. It is a type of solid-based AM process used to create low-cost 3D model using a laser. The layer thickness in this process varies from 0.001 to 0.005 inch. The most common material used in LOM is thermoplastics such as PVC and composites. LOM layer of plastics or paper is fused or laminated together using heat and pressure and cut into the desired shape using a computer. The LOM systems are not being produced at present.

2.4 Selective Laser Sintering (SLS)

Selective laser sintering (SLS) is an additive manufacturing technique that uses a laser as the power source to sinter powder material, aiming the laser automatically at points in space defined by a 3D model, binding the material to create a solid structure. There are some advantages of this additive manufacturing process like good part ability, a wide range of processing materials, no part supports required,

little post-processing required no post-curing required and advance software support. This process creates a 3D object by using a CAD or GIS file. The material is available in the form of powder. The powder is sintered by using a CO₂ laser.

3 File Conversion

Different AM processes are particularly suitable for different applications. In the present time, most of the research is done to make a product by using polymers, metals, ceramics, etc. Some researchers have prepared a physical terrain model with AM technology by using GIS data and convert it into a printable file format as per the requirement of a 3D printing machine. Most of the 3D printing machine takes stereolithography (STL) file format. The terrain model gives better information flow and more effective transmission of the design intent. Agrawal et al. [9] converted GIS data of catchment area into a 3D STL file for additive fabrication. The STL file is loaded in Magics RP software package to produce a solid STL part, which is then downloaded to a 3D printing machine to print a physical terrain model. Raju et al. state that sustainable groundwater resource management is done by exploring crystalline rocky terrain using modern geospatial techniques [10]. Remote sensing and GIS play a pivotal role in the assessment of groundwater. Agrawal et al. converted GIS data directly into a 3D STL file by developing their own software. As data conversion stages increase, the errors will be more, and the model may become defective. This work also eliminates the data loss associated with the translation of data into an intermediate file format [11]. Modi and Agrawal obtained 3D PLY part from DEM ASCII XYZ skin data directly without any intermediate file conversion for terrain modeling by additive fabrication [12]. Rase printed a fully colored physical terrain model using Z406 model of the machine from Z Corp. using the rapid prototyping technique [13]. In 2001, Z Corporation introduced the 3D printer, Z406 with integrated coloring. The major limitation of 3D plotter, Z406 is that it cannot print a part of size greater than $20 \times 25 \times 20$ cm and the layer thickness varies from 0.076 to 0.254 cm. Ollayos made a 3D model from a few distinct kinds of geographic data frameworks (GIS) utilizing quick prototyping or AM systems [14]. Gibson and Ming discussed the future of color 3D printing and discussed the hardware and software issues [15]. The demand for additive manufacturing technology is increasing day by day. Some researchers prepare a physical terrain model for unmanned aerial vehicle (UAV) by using satellite data. The model is very much helpful in finding optimized flying routes for a drone. The terrain model can help in the planning of war during battle [16]. Pullar and Springer prepared a physical terrain model of the catchment area by using a geographical information system to control the pollution at any point, which is helpful for conservation management.

4 GIS Data

Geographical information system (GIS) can describe state, county, Natural World Heritage Sites or nation-wide information. GIS data can easily be found by government agencies, private organization or the Internet. The information comes in a different file format like DEM ASCII XYZ, PLY, ArcInfo ASCII, etc. Understanding of contents is difficult due to different file formats. One of the widely used software packages for GIS data is Global Mapper, which is available at affordable prices. The GIS data gives the x , y and z coordinate with regular spacing [18]. GIS data is used in multiple disciplines like agriculture, geography, business, engineering, military science, natural resource management, etc. [19].

5 Software

Software provides a major role to convert GIS data into STL file format. There are several design software packages available in the market, as shown in Table 1. Many of them are freely available, and some are at affordable prices. The following table shows the list of software packages and the file formats they can import or export [20].

Table 1 Significant formats supported by some GIS software

GIS software	Import file extension	Export file extension
Accu Trans 3D	3DMF, ASC, KMZ, RWX	STL, COA, COB, RWX
ArcGIS desktop	DWG, DGN, DXF, STL	STL, SDC, DXF, DGN
Global mapper	DEM, PLY, STL, USGS	STL, OBJ, 3DS, 3D PDF
GLview	DXF, VRL, VRML, WRL	STL, VRML, VRL
Hexagon media	OBJ, 3DS, DXF, A3D	CAR, OBJ, A3D
IMAGINE VirtualGIS	DEM	VRML
Land desktop	DEM	DXF
Maptitude mapping	DWG, DFX, ASC, ADF, SDE	DXF, CDF, DBG, WRK
STAIFO GIS	DEM	DXF, STL
3D Object converter	STL,3DS,DXF, SHP	WRL, TIN, SLC, STL

6 STL File Format

The STL term is the abbreviation of ‘stereolithography’. STL file can be obtained as either binary or ASCII file format. An STL file comprises arrangements of triangles. Each triangle is particularly recognized by a unit typical vector or three vertices or corners. In spite of the fact that the STL design is very basic, there can at present be errors in records transformation like unit changing, vertex to vertex rule, spilling STL document, declined features and so forth. The size of ASCII file is bigger than the binary STL file [21].

7 Future Scope

The physical model gives a superior perspective on landforms. The creators intend to create programming for interpretation and control of DEM and STL information and other pertinent record positions. Sometimes the size of the STL file becomes large. The user can reduce the number of triangles as per requirement depends upon the function of the model. Additional GIS information would be needed for this process to have a wider application. Further work would be needed to add these types of GIS data to the model. Nowadays, there are a variety of 3D printing machines utilizing different materials. Terrain model by using GIS or CAD data will be helpful for town planning, catchment management, natural conservation management and for teachers to communicate to students [22]. There is a scope to develop your own material for 3D printing machine. After developing a smart material, there is scope of 4D printing in future [24, 25].

8 Conclusions

Physical terrain model can be made using GIS data in rapid prototyping (RP) machine. The complex geometries of the landforms were created with ease and great accuracy. The digital elevation model (DEM) ASCII XYZ data was converted into an STL part using different methods. The terrain model is not easy to prepare by conventional manufacturing processes. It becomes a costly and time-consuming process [23]. The physical terrain model can provide maps for the blind and visually impaired persons. Rapid prototyping can make model in less time and cost. This technology is used to convert satellite images into a physical model easily. These terrain models are significant tools for cartographers, conservation management team, civil engineers, architects, city planners and teachers.

References

1. Chua CK, Leong KF (2017) 3D printing and additive manufacturing: principles and applications, 5th edn. World Scientific Publishing Co Pte Ltd
2. Huang SH, Liu P, Mokasdar A, Hou L (2013) Additive manufacturing and its societal impact: a literature review. *Int J Adv Manuf Technol* 67(5–8):1191–1203
3. Prototyping to direct digital manufacturing. Springer Science, New York
4. Giannatsis J, Dedoussis V, Karalekas D (2002) Architectural scale modelling using stereolithography. *Rapid Prototyp J* 8(3):200–207
5. Hao J, Fang L, Williams RE (2011) An efficient curvature-based partitioning of large-scale STL models. *Rapid Prototyp J* 17(2):116–127
6. Wong KV (2012) A Hernandez 2012 a review of additive manufacturing. *ISRN Mech Eng* 1–10
7. Ahmed N (2019) Direct metal fabrication in rapid prototyping: a review. *J Manuf Process* 42:167–191
8. Dimitrov D, Schreve K, De Beer N (2006) Advances in three dimensional printing state of the art and future perspectives. *Rapid Prototyp J* 12(3):136–147
9. Agrawal S, Antunes JP, Theron E, Truscott M, De Beer DJ (2006) Physical modeling of catchment area by rapid prototyping using GIS data. *Rapid Prototyp J* 12(2):78–85
10. Raju RS Raju GS Rajasekhar M (2019) Identification of groundwater potential zones in Mandavi River basin Andhra Pradesh, India Using Remote Sensing. *GIS MIF Tech HydroRes* 2:1–11
11. Agrawal S, De Beer DJ, Modi YK (2014) Conversion of a GIS surface data directly to a 3D STL part for terrain modeling. *Rapid Prototyp J* 20(5):422–430
12. Modi YK (2014) Obtaining 3D PLY part from DEM surface data for terrain modeling by additive fabrication. *Int J Eng Sci Technol* 6(4):177–187
13. Rase WD (2002) Physical model GIS object by Rapid Prototyping. In: *Proceeding of the ISPRS technical commission IV symposium on geospatial theory, processing and application*, Ottawa, 8–12 July
14. Ollayos MW (2006) Using rapid prototyping to link landform models to GIS information research. *Experience for Undergraduates*, Milwaukee School of Engineering, 1–7
15. Gibson I, Ming LW (2001) Color RP. *Rapid Prototyp J* 7(4):212–216
16. Yang C, Tsai M, Kang S, Hung C (2018) UAV path planning method for digital terrain model reconstruction a debris fan example. *Autom Constr* 93:214–230
17. Pullar D, Springer D (2000) Towards integrating GIS and catchment models. *Environ Model Softw* 15(5):451–459
18. Modi YK, De Beer DJ, Agrawal S (2012) Physical modelling of terrain directly from surfer grid and ARC/INFO ASCII data formats. *South African J Ind Eng* 23(2):230–241
19. Mogaji KA, Omobude OB (2017) Modeling of geoelectric parameters for assessing groundwater potentiality in a multifaceted geologic terrain, Ipinsa Southwest, Nigeria a GIS-based GODT approach. *NRIAG J Astron Geophys* 6(2):434–451
20. Ajibade FO, Olajire OO, Ajibade TF, Nwogwu NA, Lasisi KH, Alo AB, Owolabi TA, Adewum JR (2019) Combining multicriteria decision analysis with GIS for suitably siting landfills in a Nigerian state. *Environ Sustain Indic* 3–4:1–14
21. Bagyaraj M, Tenaw A, Gnanachandrasamy G, Gemechu B (2019) Data of remote sensing and GIS to demarcate the potential sector of groundwater in Debre Berhan. *Amhara Region Ethiopia Data Brief* 26:1–11
22. Grayson RB and Ladson AR (1991) Digital terrain modelling : a review of hydrological. *Geomorphol Biolog Appl* 5:3–30
23. Osborne PE, Alonso JC, Bryant RG (2001) Modelling landscape-scale habitat use using GIS and remote sensing: a case study with great bustards. *J Appl Ecol* 38:458–471
24. Jacobs LD (2003) *Terrain modeling using rapid prototyping*, Milwaukee School of Engineering, WI, USA.

25. Block AJ, Modeling sub-aqueous terrain using rapid prototyping, Milwaukee School of Engineering, WI, USA

Finite Element Modeling and Analysis of Natural Fiber-Reinforced Composite



Subham Prasad, Vaibhav Mishra, Vikas Khoj, and Vikas Kukshal

1 Introduction

The use of natural fibers for the fabrication of composite materials and its products has seen rapid growth and advancements. A broad classification of the natural fiber used in the fabrication of the composites is presented by Sharma et al. [1]. Hybrid composites with different volume fractions are analyzed in various mechanical domains. The past researches have obtained the simulation results of composites using ANSYS® software and validated with experimental results [2–4]. Testing of hybrid natural fiber composites for structural applications and equivalent simulation using certain assumptions were carried out with the results being acceptable for its usage in various applications [5]. Himalayan nettle (*Girardinia diversifolia* L.) fibers were found out to possess the ultimate stress value of about twice as much as European nettle (*Urticadioica* L.) fiber, and tensile strength was also significantly high [6].

Chemical treatment of natural fibers leads to sensible improvement in its properties. It would allow government enforcement to replace natural fiber usage over its plastic or synthetic counterpart, not just for economic transformations, but also form a foundation to foresee environmental challenges [7]. Fiber-processing techniques and study of the fiber–matrix interface and its effects have been studied and reviewed successfully [8]. The sandwich frame structure of the natural fiber-based composites was also analyzed for static loading conditions with satisfactory remarks [9]. Finite element analysis results of polylactic acid-jute composite were compared with the epoxy-based graphite composite, and the results show the higher strength of the natural fiber composite, clearly depicting the possibilities of replacing natural fibers over conventional ones [10]. Improvement in tensile strength of soil was observed by

S. Prasad · V. Mishra · V. Khoj · V. Kukshal (✉)

Department of Mechanical Engineering, National Institute of Technology, Uttarakhand, Srinagar, Garhwal, Uttarakhand 246174, India

e-mail: vikaskukshal@nituk.ac.in

the mere addition of natural fibers in small quantities [11]. A detailed comparison of experimental results with finite element analysis at different ply angles of jute, hemp and epoxy shows that the elongation was a maximum at 90°. Moreover, the tensile strength, flexural strength, impact strength and hardness show higher values at 90° ply angle [12]. However, a study on hybrid hemp and a sisal fiber-based composite with different stacking sequence concluded with contradictory results that the single fiber stacking sequence using hemp as reinforcement showed slightly higher tensile and compressive strengths as compared to a hybrid of hemp and sisal fibers [13]. The present chapter focuses on the modeling and analysis of multiple fiber (hemp and Himalayan nettle)-reinforced epoxy composites consisting of 2, 4 and 6 ply. The mechanical and fracture toughness properties of the modeled composite were determined using ANSYS® software. The obtained results were compared with the result available in the literature for validation.

2 Methodology

The different units of ply using 2(NH), 4(NHNH) and 6(NHNHNH) lamina layers (where N is an abbreviation used for Himalayan nettle, and H stands for hemp fiber) were modeled using ANSYS® 19 software. The composites consisting of 2, 4 and 6 ply are designated further in this chapter as NH, NHNH, NHNHNH. The composite was modeled in a manner such that the Himalayan nettle lamina being on the top of hemp lamina. The angle of orientation of ply was kept at zero degrees in each case. The thickness of each ply was considered to be 0.5 mm with the length and width being 200 mm and 20 mm, respectively. Each lamina was made with fibers aligned in a unidirectional manner and considered to be isotropic. The fibers were stacked in an anti-symmetric manner. Table 1 represents the properties of Himalayan nettle and hemp fiber used in the analysis [14, 15]. The diameters of the Himalayan nettle and hemp fiber were assumed to be 0.1 and 0.05 mm. Similarly, the properties of epoxy used in the analysis are presented in Table 2 [12].

Table 1 Properties of Himalayan Nettle and Hemp fiber

Properties	Himalayan nettle	hemp
Young's modulus (GPa)	62	60
Density (g/cm ³)	1.25	1.48
Tensile strength (MPa)	86	725

Table 2 Properties of epoxy used in the composite fabrication

Young's modulus (GPa)	5
Density (g/cm ³)	1.16
Tensile strength (MPa)	73
Poisson's ratio	0.3

Properties of lamina constituting Himalayan nettle with epoxy and the lamina of hemp fibers with epoxy were calculated analytically using the rule of mixture [16] as shown below:

$$E_{\text{nettle with epoxy}} = E_{\text{nettle}} V_{\text{nettle}} + E_{\text{epoxy}} V_{\text{epoxy}} \quad (1)$$

$$E_{\text{hemp with epoxy}} = E_{\text{hemp}} V_{\text{hemp}} + E_{\text{epoxy}} V_{\text{epoxy}} \quad (2)$$

where E denotes Young's modulus of the composite lamina, V is the volume fraction, and the suffix denotes the distinct material.

In order to calculate the properties in different directions, the rule of mixture for the composite [17] was applied, which is shown below:

$$E_C = E_{\text{hemp}} V_{\text{hemp}} + E_{\text{nettle}} V_{\text{nettle}} + E_{\text{epoxy}} V_{\text{epoxy}} \quad (3)$$

$$E_X = E_{\text{hemp}} V_{\text{hemp}} + E_{\text{epoxy}} V_{\text{epoxy}} \quad (4)$$

$$E_Y = E_Z = \frac{E_{\text{hemp}} E_{\text{epoxy}}}{V_{\text{hemp}} E_{\text{epoxy}} + V_{\text{epoxy}} E_{\text{hemp}}} \quad (5)$$

$$G_{XZ} = G_{YZ} = \frac{G_{\text{hemp}} G_{\text{epoxy}}}{V_{\text{hemp}} G_{\text{epoxy}} + V_{\text{epoxy}} G_{\text{hemp}}} \quad (6)$$

$$\mu_{XZ} = \mu_{\text{hemp}} V_{\text{hemp}} + \mu_{\text{epoxy}} V_{\text{epoxy}} \quad (7)$$

$$E_X = E_{\text{nettle}} V_{\text{hemp}} + E_{\text{epoxy}} V_{\text{epoxy}} \quad (8)$$

$$E_Y = E_Z = \frac{E_{\text{nettle}} E_{\text{epoxy}}}{V_{\text{nettle}} E_{\text{epoxy}} + V_{\text{epoxy}} E_{\text{nettle}}} \quad (9)$$

$$G_{XZ} = G_{YZ} = \frac{G_{\text{nettle}} G_{\text{epoxy}}}{V_{\text{nettle}} G_{\text{epoxy}} + V_{\text{epoxy}} G_{\text{nettle}}} \quad (10)$$

$$\mu_{XZ} = \mu_{\text{nettle}} V_{\text{nettle}} + \mu_{\text{epoxy}} V_{\text{epoxy}} \quad (11)$$

The properties for both the lamina layers, i.e., hemp fiber with epoxy and nettle fiber with epoxy, are presented in Table 3. The properties were used to determine the tensile and flexural strength of the composite using finite element analysis. However, for simplicity, the composite properties are considered for analysis instead of the properties of individual ply.

where E , G and μ denote Young's modulus, shear modulus and Poisson's ratio, respectively, and the suffix denotes the axis. Since the ply was modeled geometrically, there were no voids present in the composite, and there exists a perfect bonding

Table 3 Properties of hemp-epoxy and nettle-epoxy lamina

Properties	Lamina	
	hemp-epoxy	nettle epoxy
Density (g/cm ³)	1.204	1.274
E_x (MPa)	23,450	21,050
E_y (MPa)	4895	4881
E_z (MPa)	4895	4881
G_{xy} (MPa)	2334	2316
G_{yz} (MPa)	2334	2316
G_{xz} (MPa)	1758	1755
μ_{xy}	0.04	0.05
μ_{yz}	0.04	0.05
μ_{xz}	0.23	0.23

between the fibers and matrix. Thus, any kind of voids, breakage, slippage between fibers and matrix, knitting errors and other defects are excluded in the present study. The porosity of the fiber is also neglected while determining the tensile and flexural properties of the composite using finite element analysis.

3 Results and Discussion

3.1 Tensile Analysis

The nettle–hemp laminate with a different number of ply was analyzed by fixing one end and applying tensile load at another end. The magnitude of the applied load is determined using the yield strength of laminate with different ply's. The load is applied to each composite test model, and the equivalent von Mises stress is determined. It is observed that the finite element results for 2, 4 and 6 ply of nettle–hemp laminate shows higher tensile strength when compared with experimental results of hemp-epoxy and nettle-epoxy laminates [12, 18]. The tensile stress of nettle–hemp-epoxy composite for the 2 ply laminate is found to be 48.55 MPa as compared to 37.80 MPa for hemp-epoxy composite [12]. Similarly, tensile stress values of nettle–hemp-epoxy composite are higher as compared to the nettle-epoxy composites [18]. The tensile stress of the modeled 4 and 6 ply nettle–hemp-epoxy laminate is found to be 52.26 and 58.54 MPa, respectively. The simulation result for the tensile test of 2 ply nettle–hemp composite laminate is shown in Fig. 1.

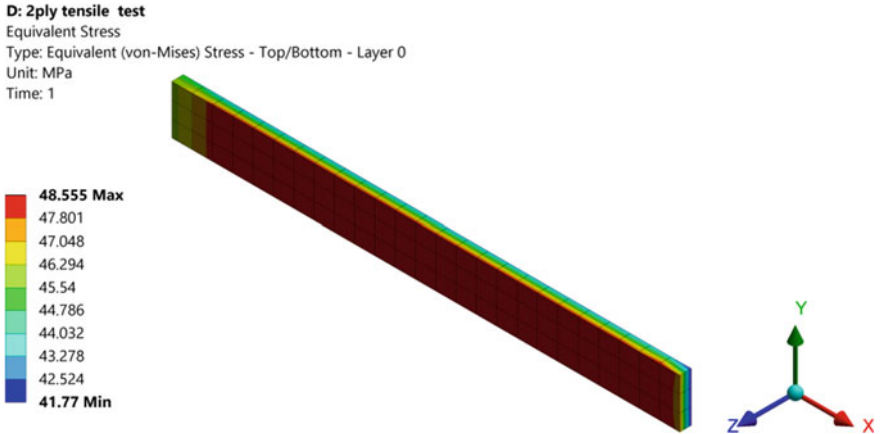


Fig. 1 Tensile stress of 2-Ply nettle–hemp-epoxy laminates

3.2 Flexural Analysis

The geometrical model was subjected to the load at the midpoint in the simply supported condition in order to determine the flexural strength of the composites.

The simulated results were compared with the results available in the literature [18]. The value of the flexural strength for the 2 ply nettle–hemp-epoxy laminate is found to be 21.48 MPa. Figure 2 shows the simulation results for the 2 ply nettle–hemp-epoxy laminate. The flexural strength for 4 and 6 ply nettle–hemp-epoxy laminate is 26.04 MPa and 45.69 MPa, respectively. The result shows that the nettle–hemp-epoxy laminate with varying ply stacking sequence shows a higher

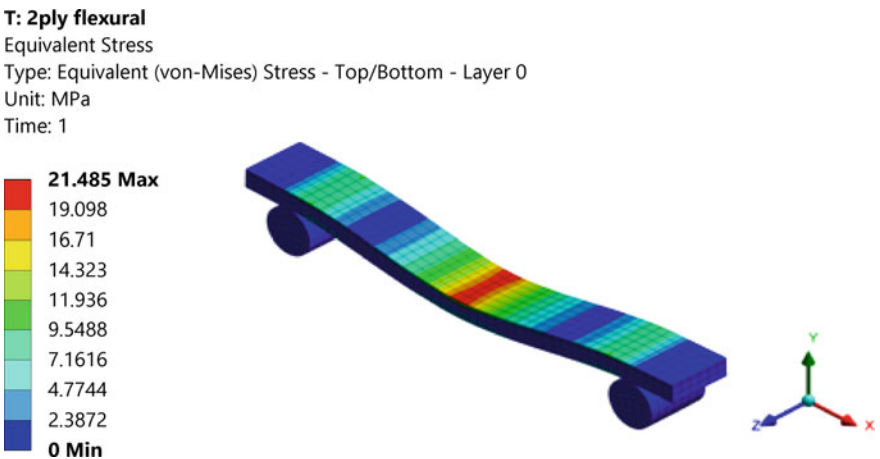


Fig. 2 Flexural strength of 2-Ply nettle–hemp-epoxy laminates

value of flexural strength as compared to the nettle-epoxy laminates of the same dimensions.

4 Conclusions

The present paper studies the modeling and simulation of natural fiber (Himalayan nettle and hemp fiber) reinforced composite using ANSYS software. The tensile and flexural behaviors of nettle–hemp laminates were analyzed. The results indicate that the 2, 4 and 6 ply nettle–hemp laminates show higher tensile and flexural strength as compared to single fiber-based composite. Additionally, it is found that the tensile and flexural strength increased with the increase in the number of ply in the nettle–hemp-epoxy laminate. Therefore, it can be concluded that the composite with more than one fiber can potentially replace the mono-fiber-synthetic composites in various applications.

References

1. Sharma A, Bhojak V, Kukshal V, Biswas SK, Patnaik A, Patnaik TK (2019) Mechanical and erosion characteristics of natural fiber reinforced polymer composite: effect of filler size In: *Automotive tribology*. Springer. 101–116. https://doi.org/10.1007/978-981-15-0434-1_6
2. Nayak S, Sadarang J, Panigrahi I, Nayak RK (2018) Development of carbon/glass fibre reinforcement polymer hybrid composite through modeling and simulation. *Mater Today: Proc* 5(9):17838–17844. <https://doi.org/10.1016/j.matpr.2018.06.109>
3. Kukshal V, Gangwar S, Patnaik A (2015a) Experimental and finite element analysis of mechanical and fracture behavior of SiC particulate filled A356 alloy composites: Part I. *Proc Instit Mech Eng Part L J Mater Design Appl* 229(2):91–105. <https://doi.org/10.1177/1464420713499513>
4. Kukshal V, Gangwar S, Patnaik A (2015b) Experimental and finite element analysis of mechanical and fracture behaviour of Al₂O₃ particulate-filled A356 alloy composites: Part II. *Proc Instit Mech Eng Part L J Mater Design Appl* 229(1):64–76. <https://doi.org/10.1177/1464420713499514>
5. Kumar YGSP, Anandh N (2017) Fabrication and analysis of Jute/Hemp reinforced fiber. *Int J Adv Res Ideas Innov Technol* 3(6):982–990
6. Seitl S, Miarka P, Sobek J, Klusak J (2017) A numerical investigation of the stress intensity factor for a bent chevron notched specimen: Comparison of 2D and 3D solutions. *Procedia Struct Integ* 5:737–744. <https://doi.org/10.1016/j.prostr.2017.07.164>
7. Mohanty AK, Misra MA, Hinrichsen GI (2000) Biofibres, biodegradable polymers and biocomposites: An overview. *Macromol Mater Eng* 276(1):1–24. [https://doi.org/10.1002/\(SICI\)1439-2054\(20000301\)276:1%3C1::AID-AME1%3E3.0.CO;2-W](https://doi.org/10.1002/(SICI)1439-2054(20000301)276:1%3C1::AID-AME1%3E3.0.CO;2-W)
8. Saheb DN, Jog JP (1999) Natural fiber polymer composites: a review. *Adv Poly Technol J Poly Process Inst* 18(4):351–363. [https://doi.org/10.1002/\(SICI\)1098-2329\(199924\)18:4%3C351::AID-ADV6%3E3.0.CO;2-X](https://doi.org/10.1002/(SICI)1098-2329(199924)18:4%3C351::AID-ADV6%3E3.0.CO;2-X)
9. Grover N, Maiti DK, Singh BN (2013) A new inverse hyperbolic shear deformation theory for static and buckling analysis of laminated composite and sandwich plates. *Compos Struct* 95:667–675. <https://doi.org/10.1016/j.compstruct.2012.08.012>

10. Kalita K, Chaudhari R, Ramachandran M (2015) Mechanical characterization and finite element investigation on properties of PLA-jute composite. *Int J Comput Appl.* 123(13):17–21. <https://doi.org/10.5120/ijca2015905537>
11. Sharma V, Vinayak HK, Marwaha BM (2015) Enhancing compressive strength of soil using natural fibers. *Constr Build Mater* 93:943–949. <https://doi.org/10.1016/j.conbuildmat.2015.05.065>
12. Sowmya C, Ramesh V, Karibasavaraja D (2018) An Experimental investigation of new hybrid composite material using hemp and jute fibres and its mechanical properties through finite element method. *Mater Today Proc* 5(5):13309–13320. <https://doi.org/10.1016/j.matpr.2018.02.323>
13. Thiagamani SMK, Krishnasamy S, Muthukumar C, Tengsuthiwat J, Nagarajan R, Siengchin S, Ismail SO (2019) Investigation into mechanical, absorption and swelling behaviour of hemp/sisal fibre reinforced bioepoxy hybrid composites: Effects of stacking sequences. *Int J Biol Macromol* 140:637–646. <https://doi.org/10.1016/j.ijbiomac.2019.08.166>
14. Mahendrakumar N, Thyla PR, Mohanram PV, Sabareeswaran A, Manas RB, Srivatsan S (2015) Mechanical and dynamic properties of nettle-polyester composite. *Mater Exp* 5(6):505–517. <https://doi.org/10.1166/mex.2015.1263>
15. Shah DU (2013) Developing plant fibre composites for structural applications by optimising composite parameters: a critical review. *J Mater Sci* 48(18):6083–6107. <https://doi.org/10.1007/s10853-013-7458-7>
16. Alger N (1996) *Polymer science dictionary*. Springer Publishing. ISBN 0412608707
17. Kaw AK (1997) *Mechanics of composite materials*. CRC Press Boca Raton, New York
18. Kumar S, Mer KKS, Gangil B, Patel VK (2019) Synergistic effect of hybrid Himalayan Nettle/Bauhinia-vahlilii fibers on physico-mechanical and sliding wear properties of epoxy composites. *Def Technol.* <https://doi.org/10.1016/j.dt.2019.08.006>

Numerical Simulation of Spinning Kinetic Energy Projectile Against Reinforced Concrete Target Using ANSYS AUTODYN



Ghanshyam Singh Kushwah, B. V. S. Nagendra Reddy, Mukesh Kumar, and Pravendra Kumar

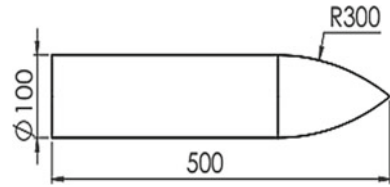
1 Introduction

Reinforced concrete has been used to construct various structures such as bridges, tunnels and nuclear-powered reactor control. In defence applications, reinforced concrete is also used for the construction of military fortification, nuclear containments, civil defence installations and protective constructions. It is a heterogeneous substance. Every component of reinforced concrete has dissimilar hardness and modulus of elasticity. When reinforced concrete blocks subjected to different load, these element materials distort at dissimilar rates. Concrete is familiar for its convenience, economical and high compressive strength as a mechanical property. Concrete material has some limited properties like brittleness, inelastic deformation before failure and low tensile strength. Structural engineers have avoided its weakness using reinforced concrete. This arrangement of steel rod and concrete increases its mechanical property.

Mu et al. [1] found that increasing the impact velocity of projectile, erosion, crushing and bending of the projectile increases significantly leading to a lesser penetration in a concrete target. The crater depth trials carried out by Forrestal et al. [2] on concrete target strength of target [62.5 and 51 MPa] by steel projectiles (7 length-to-diameter ratio) found that the crater depth increased in concrete block (200 mm to 1000 mm) targets by the rise of the striking velocity of projectile (350–1200 m/s) until the nose erosion became excessive. The reinforced experiment conducted by Hanchak et al. [3] concrete block of compressive strength 48 and 140 MPa reinforced

G. S. Kushwah (✉) · B. V. S. Nagendra Reddy
Mechanical Engineering Department, National Institute of Technology, Kurukshetra, Haryana
136119, India
e-mail: gkushwah014@gmail.com

M. Kumar · P. Kumar
Terminal Ballistics Research Laboratory, Defence Research & Development Organisation,
Chandigarh, ChandigarhChandigarh, India

Fig. 1 Projectile

concrete has three layers of the rods (diameter of rod 6 mm and length 76 mm) both ways and the steel projectile (length-to-diameter ratio 6). They found that ballistic resistance of reinforced blocks is almost the same as a concrete block if the projectile perforated the block with and without striking the embedded rod. Tham [4] demonstrated the numerical simulation using 3.0 CRH steel ogive-nose projectile, which is being fired against a cylindrical concrete target using AUTODYN-2D. Rajput [5] examined the ballistic performance on the plain as well as reinforced concrete targets when subjected to impact loading. The aim of this study was to measure the impact and residual velocity of the projectile and crack observed in the target.

In this paper, numerical simulation is conducted for two cases of velocity. In the first case, a linear velocity of 300 m/s is taken, whereas in second case linear as well as angular velocity is taken. In both cases, initial kinetic energy remains the same. The penetration depth in case 1 is compared with the penetration depth obtained by an empirical equation. Studies are also done to see the effect in penetration depth, energy, crater diameter and deceleration profile when at an angular velocity in case 2. The projectile velocity define in two cases, in case 1 projectile has a linear velocity of 300 m/s, and in case 2, projectile velocities of 298 m/s linear and 1000 rad/s angular velocity. In both cases, the same projectile is used.

2 Projectile

A projectile having a length of 500 mm, the diameter of 100 mm and a nose shape of 3 calibre-radius-head (CRH) are made of steel 4340 as shown in Fig. 1.

3 Reinforced Concrete Target

The target is a concrete block of shape $1000 \times 1000 \times 1000 \text{ mm}^3$, and it has meshed with eight-node hexahedron solid elements, reinforced with iron-C.E rods. The dimension of reinforced iron-C.E rods perpendicular to the axis of a projectile is of 16 mm diameter with 900 mm length and parallel to an axis of the projectile of 8 mm diameter with 850 mm length as shown in Fig. 2. The material model for concrete material and iron-C.E. is RHT concrete model and Johnson–Cook model,

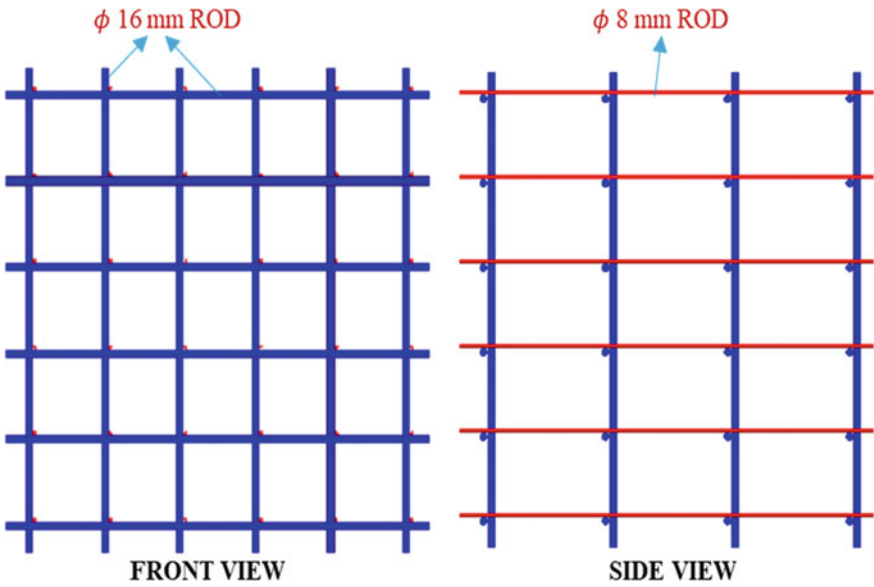


Fig. 2 Reinforced rod

respectively; and the compressive strength of the concrete block is 35 MPa. Concrete block with reinforced is shown in Fig. 3.

Fig. 3 Reinforced concrete block

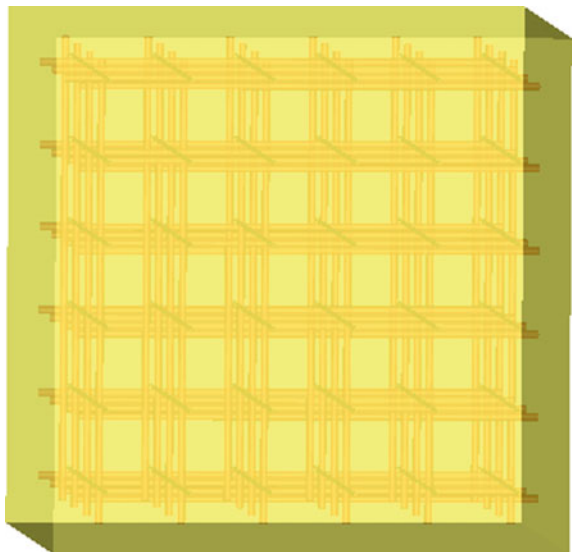


Table 1 Geometrical and the mass Properties

Target density (kg/m ³)	Projectile mass (kg)	Projectile radius R (mm)	Empirical constant (E) (MPa)	Calibre-radius C_r (mm)
2800	26.5	50	415	300

4 Analytical Method

Forrestal et al. give a formula for calculating penetration depth in the concrete target for nose-shaped projectiles [6]. The penetration depth in the target can be divided into two separate parts, that is crater generation, which initiates from the surface of the block to a depth of two projectile shaft diameter (i.e., 2D), and tunnelling, which stays from the depth of the crater to the ending penetration depth. The Forrestal formula having a constant, E, mentioned to the target resistance, it can obtain a set of penetration trails. Here, P is the depth of penetration, ρ is the density of the reinforced concrete block, whereas m and d were the projectile mass and projectile diameter. Table 1 shows the mass and geometrical properties of the projectile and the reinforced concrete block.

5 Empirical Equations

$$P = \frac{M}{2\pi R^2 \rho N} \ln\left(1 + \frac{N\rho V^2}{E}\right) + 2d \quad (1)$$

$$V^2 = \frac{MV_i^2 - 4\pi R^3 E}{M + 4\pi R^3 N\rho} \quad (2)$$

$$N = \frac{8C_h - 1}{24C_h^2} \quad (3)$$

$$C_h = \frac{C_r}{D} \quad (4)$$

where P = penetration depth, C_h = calibre-radius-head (CRH), M = mass of projectile, V_i = impact velocity, ρ = target density, R = projectile radius and C_r = calibre-radius.

6 Numerical Simulation

Nowadays, in this simulation time, the use of software power is growing faster and cheaper that allows hydrocodes to show an important role in forecasting the impact

of projectiles with the target. These hydrocodes are named as computer codes. The penetration process of projectile penetration with the reinforced concrete block was numerically simulated. The geometric modelling of the reinforced concrete target and the projectile was carried out in the ANSYS AUTODYN 3D. Numerical simulation is performed in AUTODYN 3D software with mesh element of concrete block $25 \times 25 \times 25 \text{ mm}^3$ (Fig. 4). Lagrange/Lagrange interaction between projectile and reinforced are done in forced concrete block. The numerical simulation is done in two cases, and in case 1, velocity of projectile is 300 m/s linear velocity. In case 2, the velocity of projectile is 298 m/s linear velocity and 1000 rad/s angular velocity. For both cases, the initial kinetic energy of projectile remains the same in the numerical simulation. It used tetrahedrons meshing for a projectile and hex-dominant meshing used for reinforced concrete target. A number of elements and nodes for projectile are 136,920 and 25,150, 64,000 and 270,641 for reinforced concrete target. The material model and mechanical properties of materials used in this simulation for different materials are given in Tables 2 and 3. Figure 5 shows the initial condition of hydrocode model.

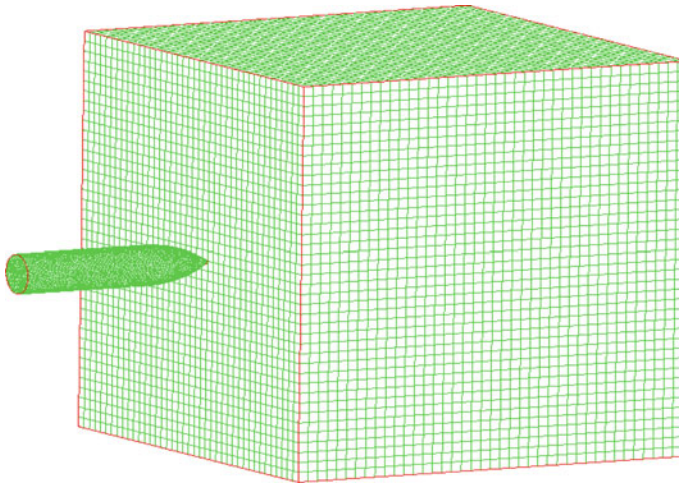


Fig. 4 Projectile and reinforced concrete target

Table 2 Material model

Material used	Strength model	Equation of state	Failure model
Steel 4340	Johnson-cook	Linear	None
Concrete 35 MPa	RHT concrete	P alpha	RHT concrete
Iron-C.E	Johnson-cook	Linear	None

Table 3 Mechanical properties of materials

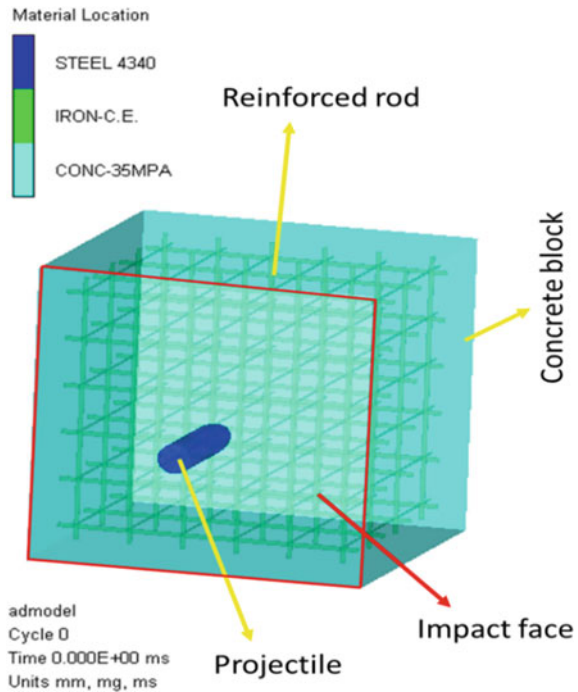
Steel 4340		Concrete 35 MPa				Iron-C.E	
Equation of state	Linear	Equation of state	P alpha	Strength	RHT concrete	Equation of state	Linear
Reference density	7.83 (g/cm ³)	Reference density	2.75 (g/cm ³)	Shear modulus	1.67E+07 (kPa)	Reference density	7.89 (g/cm ³)
Bulk modulus	1.59E + 08 (kPa)	Porous density	2.314 (g/cm ³)	Compressive strength (fc)	3.5E+04 (kPa)	Bulk modulus	1.64E+08 (kPa)
Reference temperature	3.0E+02 (K)	Porous soundspeed	2.92E+03 (m/s)	Tensiles (ft/fc)	1.0E-01 (none)	Reference temperature	3.0E+02 (K)
Specific heat	4.77E+2 (J/kgK)	Initial compaction pressure	2.33E+04 (kPa)	Shear strength (fs/fc)	1.8E-01 (none)	Specific heat	4.52E+02 (J/kgK)
Thermal conductivity	0.0E+0 (J/mKs)	Solid compaction pressure	6.0E+06 (kPa)	Intact failure surface constant A	1.6E+00 (none)	Thermal conductivity	0.0 (J/mKs)
Strength	Johnson-Cook	Compaction exponent	3.0 (none)	Intact failure surface exponent N	6.1E-01 (none)	Strength	Johnson-Cook
Shear modulus	8.18E+07 (kPa)	Solid EOS	Polynomial	Tens./Comp. meridian ratio (Q)	6.80E-01 (none)	Shear modulus	8.0E+07 (kPa)
Yield stress	7.92E+05 (kPa)	Bulk modulus A1	3.52E+07 (kPa)	Brittle to ductile transition	1.05E-02 (none)	Yield stress	2.9E+05 (kPa)
Hardening constant	5.1E+05 (kPa)	Parameter A2	3.95E+07 (kPa)	Elastic strength/ft	7.0E-01 (none)	Hardening constant	3.39E+05 (kPa)
Hardening exponent	2.6E-01 (none)	Parameter A3	9.04E+06 (kPa)	Elastic strength/fc	5.3E-01 (none)	Hardening exponent	4.0E-01 (none)

(continued)

Table 3 (continued)

Steel 4340		Concrete 35 MPa			Iron-C.E		
Equation of state	Linear	Equation of state	P alpha	Strength	RHT concrete	Equation of state	Linear
Strain rate constant	1.4E-02 (none)	Parameter B0	1.22 (none)	Failure	RHT concrete	Strain rate constant	5.5E-02 (none)
Thermal softening exponent	1.03E+00 (none)	Parameter B1	1.22 (none)	Damage constant, D1	4.0E-02 (none)	Thermal softening exponent	5.50E-01 (none)
Melting temperature	1.793E+03 (K)	Parameter T1	3.53E+07 (kPa)	Damage constant, D2	1.0E+00 (none)	Melting temperature	1.811E+03 (K)
Ref. strain rate (/s)	1.0E+00 (none)	Parameter T2	0.00E+00 (kPa)	Minimum strain to failure	1.0E-02 (none)	Ref. strain rate (/s)	1.0 (none)
Strain rate correction	1st Order	Reference temperature	3.0E+02 (K)	Residual shear modulus fraction	1.3E-01 (none)	Strain rate correction	1st Order
Failure	None	Specific heat	6.5E + 02 (J/kgK)	Tensile failure	Hydro (Pmin)	Failure	None

Fig. 5 Initial condition for the hydrocode model



7 Results and Discussions

Results of the depth of penetration obtained from ANSYS AUTODYN are compared with empirical calculation results. The deceleration profile of the projectile is compared for both the cases and also comparing the total energy of different material.

7.1 Depth of Penetration

Figure 6 compares the depth of penetration of all the cases. The penetration depth in a first case is compared with the analytical method, the error in penetration depth about 3.5%, because of some limitation of numerical simulation like mesh size and material model. The penetration depth in a second case is more than the first case at approx. 35 mm. In both cases, the initial kinetic energy of the projectile remains the same, and angular velocity increases the depth of penetration in the target. In case 1, the penetration depth is 437.5 mm, as shown in Fig. 7. In case 2, the penetration depth is 475 mm, as shown in Fig. 8.

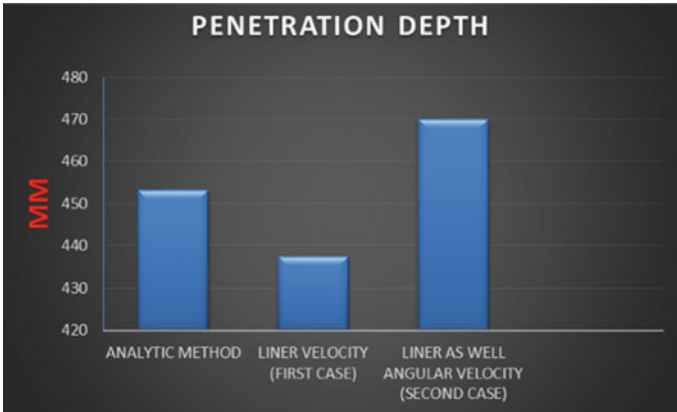
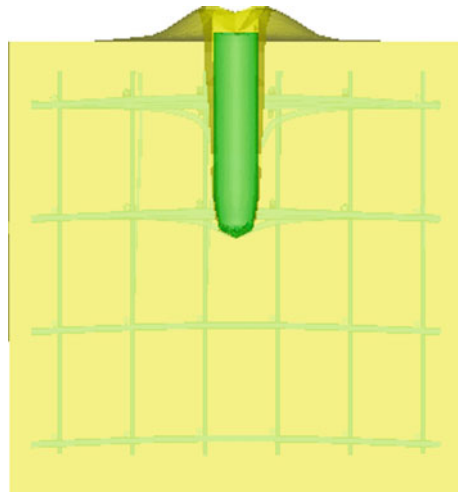


Fig. 6 Compare penetration depth

Fig. 7 Penetration depth (in case 1)



A. Crater Diameter

Crater diameter in case 1 and case 2 are 137.5 mm and 125 mm, respectively. Figure 9 and Fig. 10 show the crater diameter in the reinforced concrete block for case 1 and case 2, respectively. Table 4 shows the penetration depth and crater diameter of different cases.

B. Deceleration of Projectile

The deceleration of projectile is shown in Figs. 11 and 12 for case 1 and case 2, respectively. In case 1, extreme retardation is 32654 g, and average retardation is 7760 g. In case 2, maximum retardation is 23200 g, and average retardation is 6390 g. Case 2 has less retardation than case 1, thus giving more penetration depth.

Fig. 8 Penetration depth (in case 2)

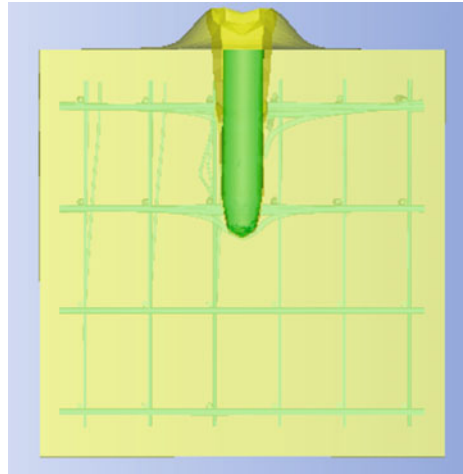
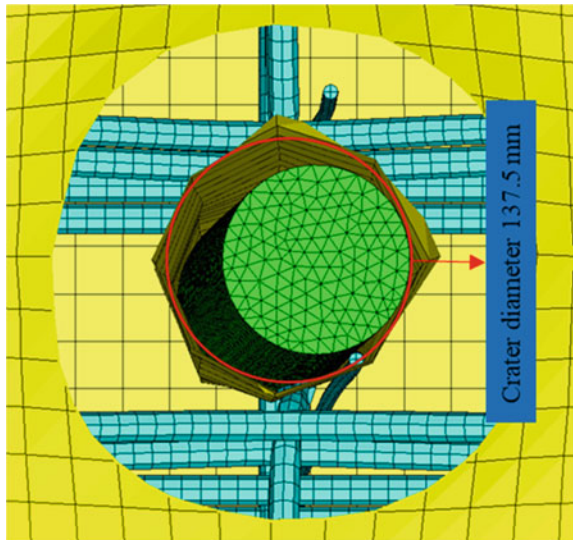


Fig. 9 Crater diameter in case 1



C. Total Energy

The projectile impacts into a reinforced concrete block with initial kinetic energy. When projectile strikes into the reinforced block, the energy of projectile decreases, then the energy of reinforced concrete blocks increases in the form of strain energy. In case 1, the total energy of all material is shown in Fig. 13 with respect to time. The maximum energy of the projectile is 1.72×10^6 J at time 0 ms, and the maximum total energy of the reinforced concrete block is 6.04×10^5 J at time 4 ms. In case 2,

Fig. 10 Crater diameter in case 2

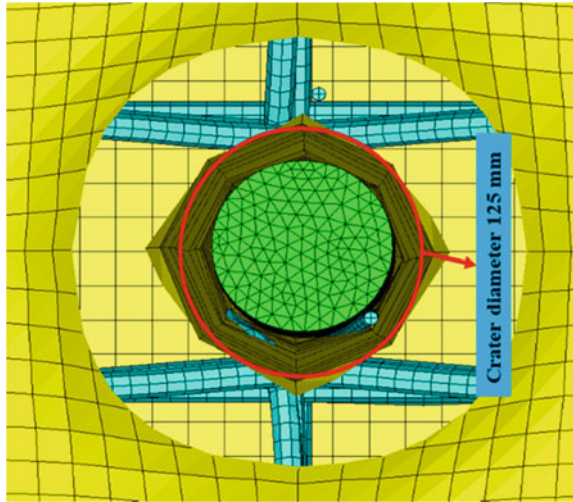
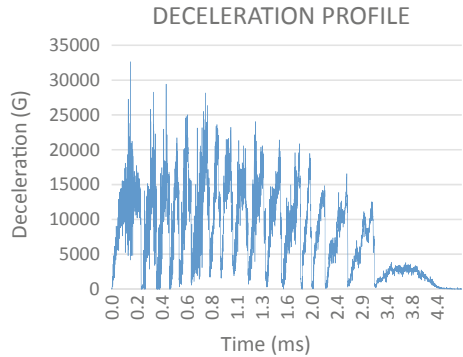


Table 4 Penetration depth and crater diameter

No	Analytical method	Numerical simulation	
	Penetration depth	Penetration depth	Crater diameter
Case 1	444 mm	437.5	137.5 mm
Case 2	Empirical eq. not available	470	125 mm

Fig. 11 Deceleration profile in case 1



the maximum energy of the reinforced concrete block is 6.28×10^6 J at time 4 ms. The total energy profile of case 2 is shown in Fig. 14. Case 1 energy transfer in the reinforced concrete block is more than case 2.

Fig. 12 Deceleration profile in case 2

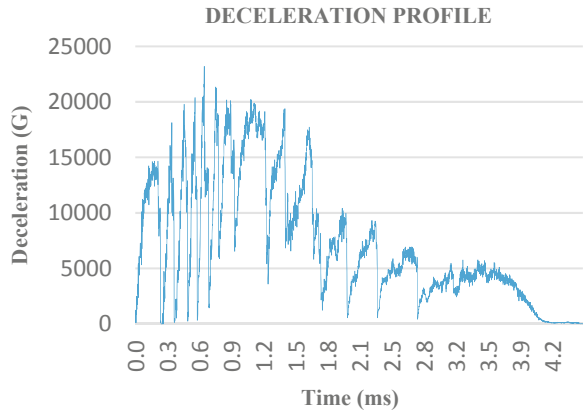
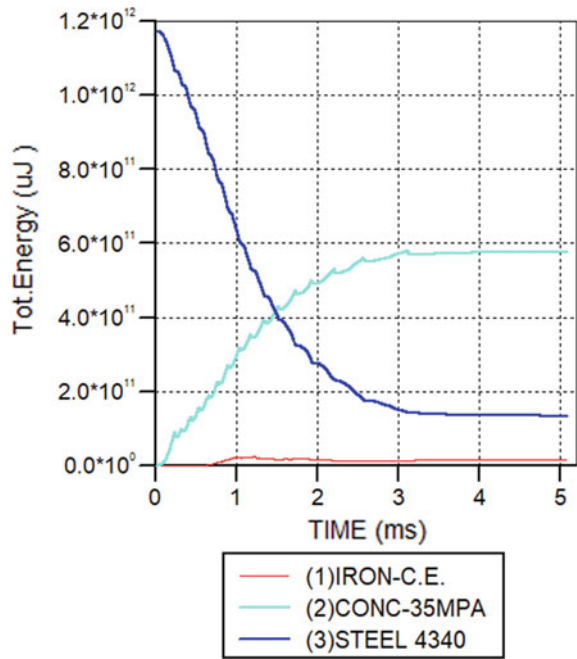


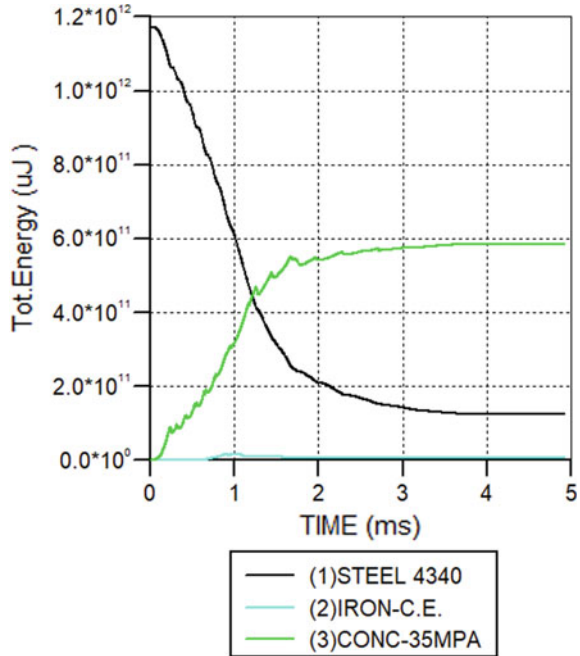
Fig. 13 Total energy of different material in case 1



8 Conclusions

Here, numerical simulation was done for both cases of velocity against a reinforced concrete block. The result of numerical simulation good agreement with an analytical method in the first case. The results of both the cases are compared in terms of penetration depth, total energy, crater diameter and deceleration profile. Comparison

Fig. 14 Total energy of different material in case 2



parameters are penetration depth, crater diameter and deceleration profile. Based on numerical simulation, it can be concluded that:

1. Angular velocity of the projectile increases the depth of penetration in the reinforced concrete block targets.
2. The projectile has angular velocity, and it can reduce the crater diameter in a target.
3. Retardation in the second case is lesser than the first case, so it achieves more penetration depth.
4. Projectile having linear as well as angular velocity has less transfer rate of energy in reinforced concrete block.

References

1. Mu Z, Zhang W (2011) An investigation on mass loss of ogive projectiles penetrating concrete targets. *Int J Impact Eng* 38(8-9):770-778
2. Forrestal MJ, Piekutowski AJ (2000) Penetration experiments with 6061-T6511 aluminum targets and spherical-nose steel projectiles at striking velocities between 0.5 and 3.0 km/s. *Int J Impact Eng* 24(1):57-67
3. Hanchak SJ, Forrestal MJ, Young ER, Ehrgott JQ (1992) Perforation of concrete slabs with 48 MPa (7 ksi) and 140 MPa (20 ksi) unconfined compressive strengths. *Int J Impact Eng* 12(1):1-7

4. Tham CY (2006) Numerical and empirical approach in predicting the penetration of a concrete target by an ogive-nosed projectile. *Finite Elem Anal Des* 42(14–15):1258–1268
5. Rajput A (2016) Experimental study of plain and reinforced concrete targets subjected to impact loading. *Procedia Eng* 144:124–131
6. Forrestal MJ, Frew DJ, Hickerson JP, Rohwer TA (2003) Penetration of concrete targets with deceleration–time measurements. *Int J Impact Eng* 28:479–497

Fracture Mechanism Characteristics Study of Explosive Bolt Through Explicit Analysis Tool



Prashant Kumar, P. C. Tewari, and Subhash Chander

1 Introduction

Explosive bolts are a device used for fastening-release functionality for the sleds according to time requirement. It is used as a temporary fastening device for sled and payload. The complete body of the explosive bolt (EB) can be of different stainless steel grades or aluminium alloys and the cavity inside the bolt can be filled with a combination of primary explosives, i.e. lead azide (LA), lead styphnate and secondary explosives, i.e. PETN (1.50, 1.26), RDX. The explosive bolts (EBs) find application in thrust termination, payload release mechanism, launcher operation and stage separation [1, 2]. EBs can be grouped as pressure-type EBs and high-type EBs [3]. The EBs using high explosives break by the effect of the shock wave created due to the explosion, whereas pressure-type EBs break by the pressure produced by detonation inside the cavity. The pyroshock generated due to explosion also defines the separation mechanism characteristics. Near-field, mid-field and far-field are different types of pyroshock depending upon the type of source of explosion (Table 1), i.e. point source and line source [4]. Line source produces more fragments and rough surfaces as compared to point source. Laser Doppler vibrometer is used to measure the pyroshocks of frequencies lying between 10 and 100,000 Hz [9]. EBs have been active in satellite take-off vehicle tasks for the separation of the mechanical subsystems, i.e. stage and satellite separation [7].

In the present study, ANSYS AUTODYN 19.2 is used to simulate the fracture mechanism characteristics of EBs. Simulation done in AUTODYN can be used to

P. Kumar (✉) · P. C. Tewari
Department of Mechanical Engineering, National Institute of Technology Kurukshetra,
Kurukshetra, Haryana 136119, India
e-mail: prashant95kumar@gmail.com

S. Chander
Terminal and Ballistics Research Laboratory, Defence Research and Development Organisation,
Chandigarh, India

Table 1 Pyroshock types

Pyroshock types	Source/hardware distance/mm		Influencing factor	Spectrum content/Hz
	Point source	Line source		
Near-field	<30	<150	Wave propagation	>10,000
Mid-field	30–150	150–160	A combination of propagation and structural resonances	3000–10,000
Far-field	>150	>600	Structural resonances	<3000

analyse fracture speed, fracture time and separation shock [8]. The important parameters involved in a simulation are pressure created by the explosion, amount of explosives and thickness of separation distance.

2 Separation Mechanism Characteristics

In the ongoing study, EB is designed on previous experience and the existing EBs on the online platform. Materials like SS304 and SS4340 are used for complete EB body, and explosives like PETN and RDX are used for explosion. Figure 1 shows different values of yield stress at different values of plastic strain for SS304 suggested by Steinberg Guinan. A nichrome wire filament is used to initiate the priming material, i.e. LA and LS, which further detonates high explosives, i.e. PETN and RDX. The separation plane can be seen in Fig. 2. The separation mechanism is analysed using AUTODYN, which is capable of handling and modelling complex materials, Lagrange models and Euler/Lagrange interactions. To reduce complexity, 2D axisymmetric is used for analysis.

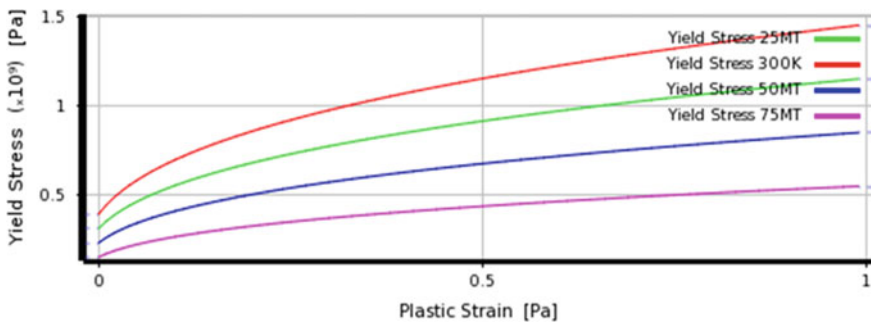


Fig. 1 Yield stress versus plastic strain for SS304

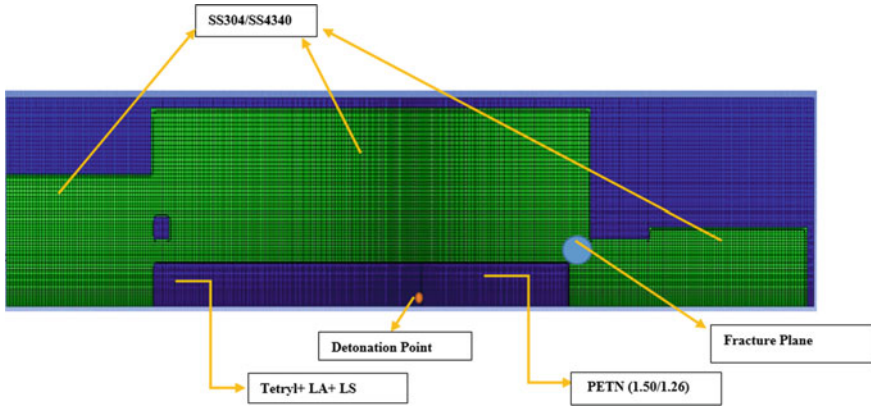


Fig. 2 Material location at 0 cycle

3 Procedure of Analysis

For analysis, ANSYS AUTODYN is used. From the navigation bar of AUTODYN, interface options like materials, initial conditions, boundaries, parts, etc. can be used. The 2D axisymmetric model is being used, while providing interaction Euler–Lagrange interaction is selected. For modelling high explosives, JWL EOS, Mie–Gruneisen form of equation of state (EoS) to model propagation of shock in metal and Johnson–Cook strength model and Steinberg–Guinan equation for metals have been utilized [5, 6]. Detonation point is given at the left bottom point of the explosive in the two-dimensional model (Fig. 2) with direct/indirect path.

3.1 Material Modelling

In the present study, material properties of SS304, PETN, SS4340, Tetryl, LS and LA are required. Among them, SS304 and SS4340 require EoS, failure, strength and erosion models, while PETN, LA, LS and Tetryl requires only EoS.

3.1.1 Stainless Steel 304 and SS 4340

Mi-Gruneisen form of Equation of State (EOS), shock EOS which uses the shock hughoniot as a reference is being used to model the behavior of shock propagation in metal. Also in order to model the metal properties, Johnson Cook model (for SS4340) and Steinberg Guinan model (for SS304) are used.

Table 2 Properties of SS304

S. No.	Property	SS304	SS4340	Unit
		Value	value	
1	Density	7900	7830	Kgm ⁻³
2	Specific heat	423	477	Jkg ⁻¹ C ⁻¹
3	Initial yield stress	3.4E+08	7.92E+08	Pa
4	Maximum yield stress	2.5E+09	–	Pa
5	Hardening constant	43	5.1E+08	–
6	Hardening exponent	0.35	0.25	–
7	dG/dp	1.74	–	–
8	dG/dT	– 3.504E+07	–	Pa C ⁻¹
9	dY/dp	0.007684	–	–
10	Melting temperature	2106.09	1519.9	C
11	Shear modulus	7.7E+09	8.18E+10	Pa
12	Bulk modulus	–	1.59E+11	Pa
13	Gruneisen constant	1.93	–	–
14	Parameter C ₁	4570	–	ms ⁻¹
15	Parameter S ₁	1.49	–	ms ⁻¹
16	Strain rate constant	–	0.014	–
17	Strain rate correction	–	1st Order	–
18	Thermal softening constant	–	1.03	–
19	Reference strain rate	–	1	–

3.1.2 Explosives and Base Charge

To estimate pressure generated by primary and secondary explosives, Jones–Wilkins–Lee equation of state is used. The standard properties of Tetryl and PETN (1.26 and 1.50) are columned in Table 3.

Table 3 Properties of Tetryl and PETN (1.50, 1.26)

Property	Value (Tetryl)	Value (PETN 1.50)	Value (PETN1.26)	Unit
Parameter A	5.868300E ⁰⁸	6.253000E ⁰⁸	5.731000E+008	KPa
Parameter B	1.067100E ⁰⁷	2.329000E ⁰⁷	2.016000E+007	KPa
Parameter R1	4.40	5.25	2.016000E+007	None
Parameter R2	1.20	1.6	1.800000	None
Parameter W	0.27500	0.28	0.280000	None
C-J detonation velocity	7.910000E ⁰³	7.450000E ⁰³	6.540001E+003	m/s
C-J energy/unit volume	8.200000E ⁰⁶	8.560001E ⁰⁶	7.190001E+006	KJ/m ³
C-J pressure	2.850000E ⁰⁷	2.200000E ⁰⁷	1.400000E+007	KPa

4 Separation Mechanism Characteristics Analysis

The analysis is done in 2D axisymmetric mode. The required material is loaded from a material library, and its properties are modified as per requirement, i.e. erosion, material EoS. The components of the EB are filled in the void which is created in part section by selecting fill geometric space. The purpose of creating a void is to observe the flow of shock wave and consequently fracture. The dimension of the void is taken as per the dimension of the EB. Zoning is done to define a number of nodes and elements. Further grade zoning in X- and Y-direction can be done to refine the mesh. To view, the proper flow of shock wave grid and vector option can be enabled from the navigation bar. The interaction or coupling is important for this type of nonlinear phenomenon. Euler/Lagrange and Lagrange/Lagrange are two interactions that are available in this section. The detonation can be given in the form of point, line, circle and sphere. The path is provided to the detonation process (direct or indirect). After that output and control options are used. The output window enables us to give the type of output from calculation like start cycle, end cycle increment, etc., and the control window enables us to define solution controls for our model like cycle limit, energy fraction, energy reference cycle, etc. Figure 2 shows the positions of a metal body, primary and secondary explosives, detonation point and fracture plane at 0 cycle. In Fig. 3, the behaviour of shock wave and movement of particles in all direction from detonation point after growth of pyroshocks at 100 cycles. Figure 4 shows the material status at 900 cycles with the red coloured region showing the bulk failure around the separation plane. In Fig. 5, grid/mesh in Euler space at higher cycles (1375 cycles) with velocity vector (pyroshocks) is shown. Figure 6 shows the

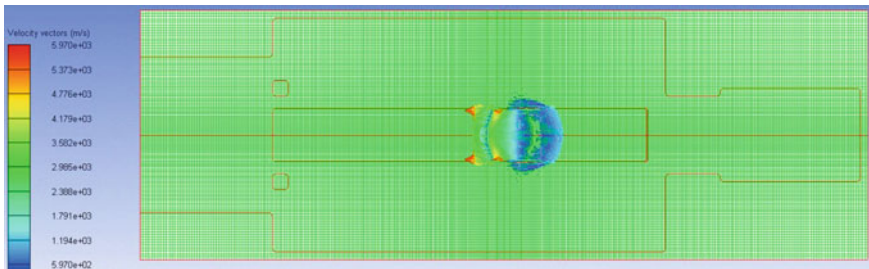


Fig. 3 Velocity vector at 100 cycles

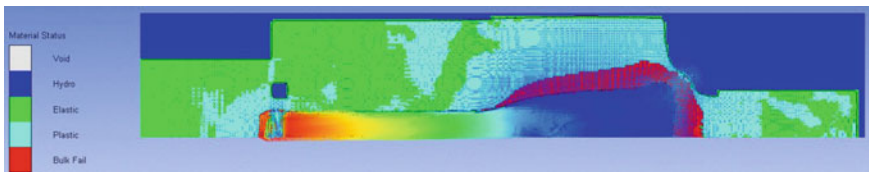


Fig. 4 Material status at 900 cycles (axisymmetric)

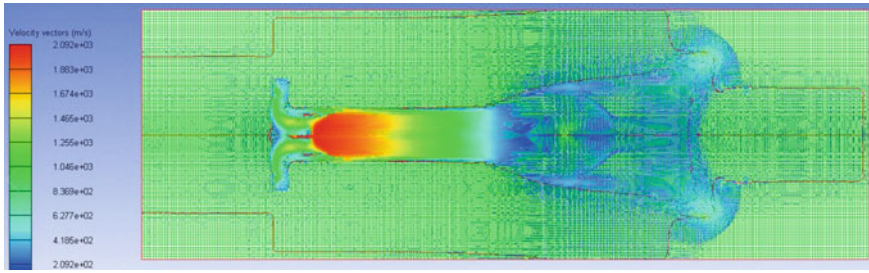


Fig. 5 Velocity vector with grid at 1375 cycles

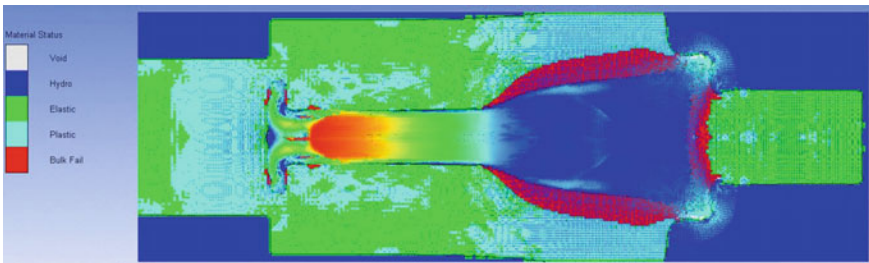


Fig. 6 Material status (vector) at 1375 cycles

material status in vector form at 1375 cycles showing the explosive particles flowing out of the metal body, while Fig. 7 (1375 cycles) and Fig. 8 (1500 cycles) show the same with mesh/grid. In Fig. 9, pressure contour after separation phenomenon and the distribution of pressure inside the metal body. Figure 10 shows the distribution of von Mises stress at 1500 cycles with the red-coloured region showing the maximum stress distribution. The rate at which material is being eroded (1375 cycles), and the pressure variation with distance (1375) is shown in Fig. 11 and Fig. 12, respectively. The following images will clear out the separation mechanism analysis.

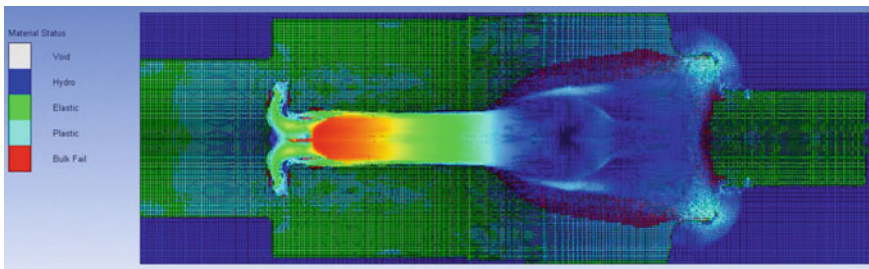


Fig. 7 Material status with grid at 1375 cycles

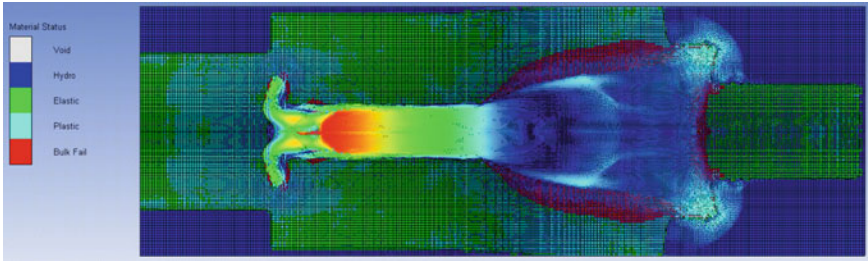


Fig. 8 Pressure contour at 1450 cycles

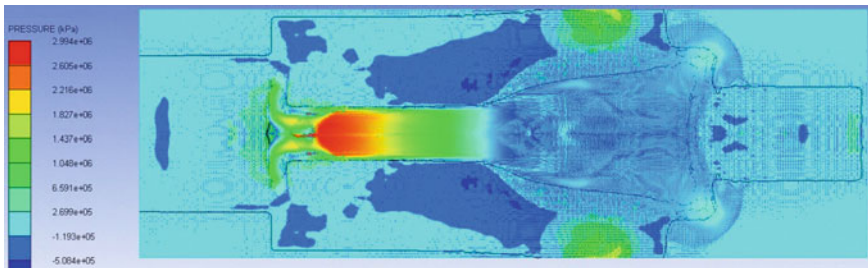


Fig. 9 Material status (with grid) at 1500 cycles

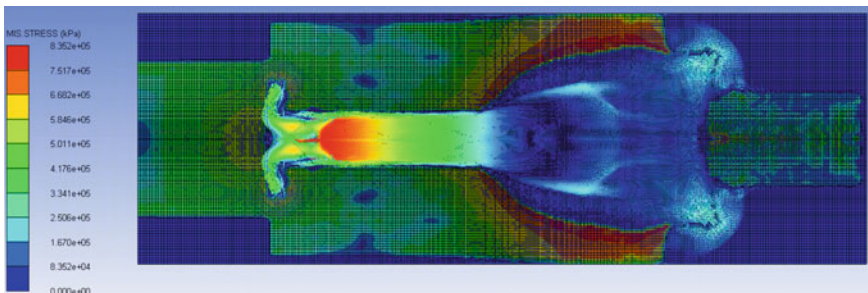


Fig. 10 Von Mises stress at 1500 cycles

5 Conclusions

From this paper, it can be concluded that the correct amount of explosives, material selection and setting up of input parameters in the navigation bar is quite important. The repetitive experiments also give the user some idea about the correct setting in AUTODYN and explosive amount. The type of EB and pyroshock also defines the separation mechanism characteristics. The time step safety factor ($f = 0.6$ or 0.7) should be taken to ensure the accuracy and stability of the simulation. This designed EB comes under point source where an explosion takes place in a controlled manner

Fig. 11 Effective plastic strain vs. distance at 1375 cycles

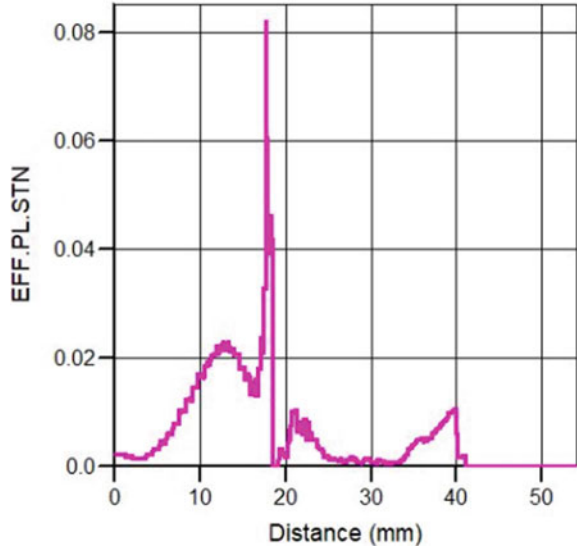
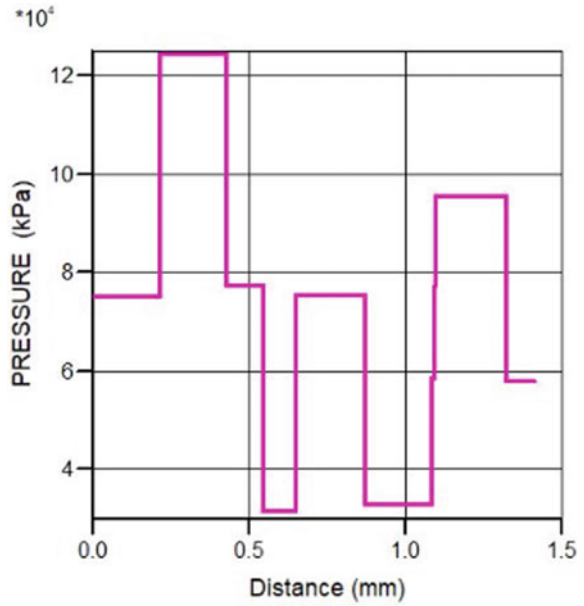


Fig. 12 Pressure vs distance at 1375 cycles



as compared to a line source. The thickness of the fracture distance from secondary explosive also decides the separation mechanism.

In the current study, the main focus is given on the fracture mechanism characteristics with a defined amount of primary and secondary explosives. The entire study

is conducted by taking into account the explosive bolt of strength between 1 and 2 tons.

References

1. Bement LJ, Schimmel ML (1995) A manual for pyrotechnic design, development and qualification. NASA, NASA Technical Memorandum 110172. <https://ntrs.nasa.gov/archive/nasa/casi.ntrs.nasa.gov/19950024937.pdf>
2. Brauer O (1974) Handbook of pyrotechnics. Chemical Publishing Co., New York
3. Lee J, Han J-H, Lee Y, Lee H (2014) Separation characteristics study of ridge-cut explosive bolts. *Aerosp Sci Technol* 39:153–168
4. Zhang M, Xiang S (2014) Review of recent advances in pyroshock for space system. *Vibroengineering Procedia* 4:86–90
5. Lee J et al (2015) A parametric study of ridge-cut explosive bolts using hydrocodes. *Int J Aeronaut Space Sci* 16(1):50–63
6. Li YH et al (2017) Identification of pyrotechnic shock sources for shear type explosive bolt. *Shock Vibr Article ID* 3846236. <https://doi.org/10.1155/2017/3846236>
7. Choi M, Lee J-R, Kong C-W (2014) Development of a numerical model for an expanding tube with linear explosive using AUTODYN. *Shock Vibr Article ID* 436156. <https://doi.org/10.1155/2014/436156>
8. Li YH et al (2019) Numerical simulation of separation shock characteristics of a piston type explosive bolt. *Vibroengineering Procedia* 21:214–219
9. Litz CJ Laser Doppler vibrometer, unique use of Doe/Taguchi methodologies in the arena of Pyroshock (10–100,000 Hz) Response spectrum. In: Proceedings of the first international conference of vibration measurements by laser techniques: advances and applications. Ancona, Italy, pp 432–449, 1994.

Numerical Simulation and Parametric Study of Penetration Effect for an Ogive-Nose-Shaped Projectiles Against Concrete Target



Patel Yash Bipinbhai, P. C. Tewari, Mukesh Kumar, and Pravendra Kumar

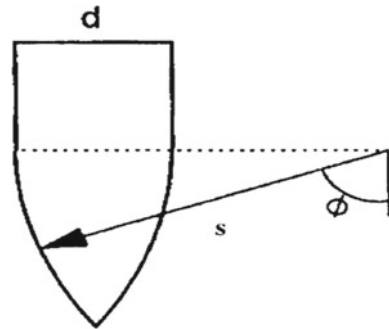
1 Introduction

Kinetic energy projectile is a weapon mostly used in defence and military applications which contains an explosive charge. It works on a principle to attain a high velocity, generally up to hypervelocity and strike the target material, converting kinetic energy into shock waves and heat. Hence, they are designed in such a way to defeat military bunkers, high aircraft shelters, deep buried targets, etc. Penetration of projectile into a concrete target is an interesting topic for many scholars. Many researchers were investigating various parameters of penetration by calculating projectile depth of penetration, the effect of concrete target diameter on the depth of penetration, etc. Forrestal [1] derived an empirical formula to examine the depth of penetration into the concrete target. From the last three decades, three major techniques were castoff to envisage the interaction of projectile with concrete material. Concrete is remembered because of its low cost and wide availability. It was well defined by its unconfined compressive strength and its ubiquity, but has certain demerits like brittleness, weak in tension, inelastic deformation before failure, etc. Due to the formation of cracks, spalling and scabbing on the target arise erratically. A continuous analysis on the physical and mechanical behaviour of concrete and its composition at the macroscopic level is obedient as concrete is a complex material widely used in structural applications such as bunkers, buildings, dams. The reinforced concrete, i.e. a mixture of steel and concrete, is used to enhance the bending stress of concrete and improve its tensile strength.

P. Y. Bipinbhai (✉) · P. C. Tewari
Department of Mechanical Engineering, National Institute of Technology, Kurukshetra, Haryana
136119, India
e-mail: yashbpatel1005@gmail.com

M. Kumar · P. Kumar
Terminal Ballistics Research Laboratory, Defence Research and Development Organisation,
Chandigarh, India

Fig. 1 Design of ogive-nose
[10]



Rajput et al. [5] studied the effect of plain and reinforced concrete by impacting hard ogive nose steel projectile at a tremendous velocity. Here, crater diameter was estimated and residual versus impact velocity was observed and related amongst these two targets. Wu et al. [6] prophesied the velocities which are remained as a residue of a projectile afterwards normally perforating the thin UHP-SFRC barriers. Wu et al. [7] analysed high-velocity penetration of the concrete target material with different shapes of a projectile using two constituents. Over here, penetration depth and trajectory stability of these projectiles were analysed. Outcomes disclosed that double-nose projectile had specific drag reduction, high penetration ability. In the interim, projectile with groove-tapered owned good trajectory stability as its curved part had tapering shank which helped in restoring moment for stabilization. Feng et al. [8] replicated sets of experiments to study the effect of thick PCT to high-velocity penetration of an alloy steel projectiles by varying its striking velocities. The crater diameter increased linearly with the striking velocity. Oucif and Mauludin [9] evaluated the geometric modelling of high-speed impact of ogive nose-shaped projectile against reinforced concrete panel using Johnson–Holmquist damage model.

In the facts mentioned above, the present work is conducted by impacting conventional ogive-nose-shaped projectiles, as shown in Fig. 1 with two shapes of the projectile of different CRH and penetrating into the concrete target. Moreover, the penetration depth and the crater damage on the impact face of the targets are analysed.

2 Numerical Simulation Tool

ANSYS AUTODYN user interface is an analytical tool required to model nonlinear dynamics of solids, fluids, gas, and its interaction. It is easy to use, fully integrated, and enable us to set up, run, and post-process given problems. AUTODYN has been functionalized in a vast range such as enhancing and designing of anti-armor systems, building protection in contradiction of blast marvels, risk identification in contrast to aircraft impact, material characterization lay open to impact and dynamic loading, drop test, etc.

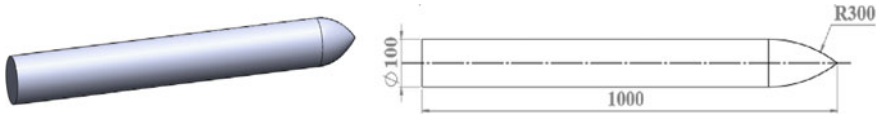


Fig. 2 Ogive-nose shape with 1.5 CRH

Table 1 Mixture ratio of M35 grade of concrete

Unconfined compressive strength (MPa)	Cement	Sand	Coarse aggregates
35	1	1.6	2.907

3 Design

3.1 Projectile

A 100-mm-diameter, 1-m-long ogive-nosed projectiles are designed for impacting the concrete target. They are machined from steel 4340 rods. Here, two projectiles of 1.5 and 3.0 CRH are tested against the concrete target. Ogive-nose CRH outlines the ratio of ogive radius to the projectile or shank diameter. Figure 2 simply shows the difference projectile nose shape. It is accelerated at an impact velocity of 350 m/s towards the target. Here, it is assumed that the projectile is kept rigid, i.e. deformation or damage free. Therefore, no failure criteria were applied to this material.

3.2 Concrete Target

In this study, plain concrete target (PCT) and reinforced concrete target (RCT) have taken as target materials. The material applied for the target is M35 grade of concrete, namely CONC-35 MPa; see Table 1.

Concrete is good in compression rather than tension. The reinforcement is suitable to provide strength against tension. Figures 3 and 4 display the front and isometric view of the reinforced concrete target. The thick PCT size of 500 × 500 × 1500 mm is modelled in ANSYS AUTODYN, and reinforcement is filled in case of RCT. The reinforcement material is preferred as cast iron.

3.3 FEM for Meshing

In the analysis, meshing is necessary to achieve accurate results. A fine mesh is required to compute complex problems. The finite element method (FEM) is the best numerical technique which generates fairly accurate solutions by discretizing a

Fig. 3 Front view of RCT

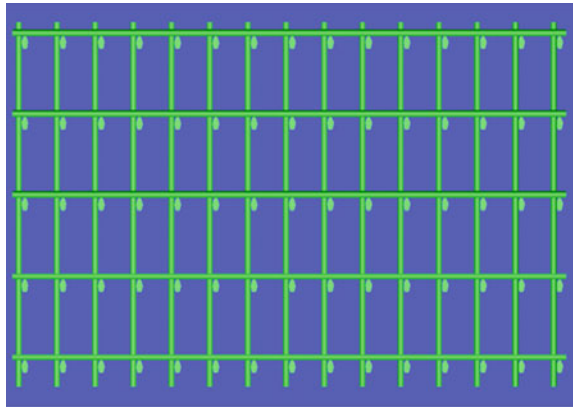
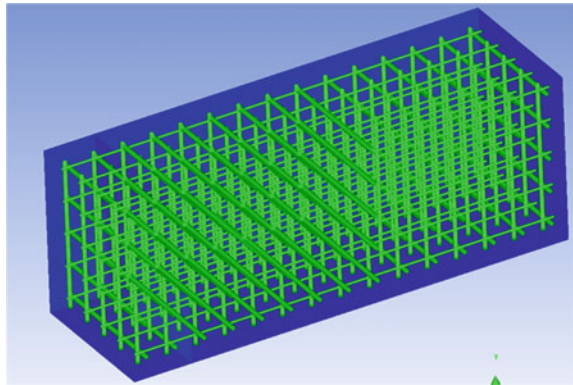
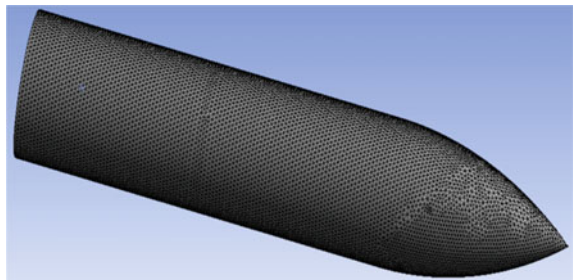


Fig. 4 Isometric view of RCT



complicated problem into a small number of elements. The point connecting between them is defined by nodes and the complex system of these points, which produce a grid named as mesh. The element size for projectile mesh is 7 mm, as shown in Fig. 5 while that of the concrete target is $25 \times 25 \times 25$ mm.

Fig. 5 Four-node tetrahedron projectile meshing



3.4 Material Model

Material model is distributed based on three major criteria:

- (a) Equation of state
- (b) Material strength model
- (c) Material failure model

(a) **Equation of State (EOS)**

For projectile and reinforcement material, linear EOS criteria are used which express $P = f(\rho, e)$. Here, $\rho =$ density and $e =$ internal energy.

For concrete target, porous-alpha polynomial EOS is designed in AUTODYN due to its compaction and compressibility.

(b) **Material Strength Model**

Initially, all solid materials react elastically in nature, but over an extreme dynamic loading condition, they can extend to stress where it exceeds yield stress and then deforms plastically.

Johnson–Cook equation

$$\sigma = [\sigma_0 + B\epsilon^n] \times [1 + c(\epsilon/\epsilon_0)] \times [1 - \{(T - T_r) / (T_m - T_r)\}^m] \quad (1)$$

where $\sigma =$ yield stress, $\sigma_0 =$ static yield stress, $B =$ hardening constant, $n =$ hardening exponent, $c =$ stress-rate constant, $\epsilon_0 =$ reference strain rate, $T_m =$ melting point, $T_r =$ reference temperature, $m =$ thermal softening constant.

(c) **Material Failure Model**

Material may fail under high hydrodynamic loading conditions, resulting in the occurrence of crack. Considering in mind that concrete fails under tensile load rather than in compressive load, the failure model of the M35 grade of concrete is simulated under the hydrodynamic tensile failure criteria. The material model for projectile penetration into concrete target material is presented in Table 2.

4 Empirical Formulae

Numerical simulation results are compared with the empirical equation. Forrestal et al. formulated an equation to determine the DOP equation for an ogive-nose-shaped projectile penetrating M35 grade of the concrete target. The below-mentioned

Table 2 Material model

Material composition	EOS	Strength criteria	Failure criteria
SS 4340	Linear	Johnson–Cook	–
M35 grade of concrete	Porous-alpha	RHT concrete	RHT concrete
IRON–C.E	Linear	Johnson–Cook	–

Table 3 Calculated depth of penetration (DOP) for both nose shapes of projectiles

CRH	Mass (kg)	<i>N</i> value	DOP (mm)
1.5	58.336	0.2037	1135
3.0	56.72	0.1065	1152

penetration equation is obtained from post-test scrutiny of soil and concrete target material [1]. The penetration in concrete is subdivided into two definite processes, viz. formation of crater and tunnelling phenomena. By using this penetration equation, depth of penetration comes out and is revealed in Table 3.

$$P = \frac{m}{2\pi a^2 \rho N} \ln\left(1 + \frac{N\rho V^2}{R}\right) + 4a \tag{2}$$

$$V^2 = \frac{m V_s^2 - 4\pi a^3 R}{m + 4\pi a^3 N\rho} \tag{3}$$

$$N = \frac{8\psi - 1}{24\psi^2} \tag{4}$$

$$\psi = \frac{r}{2a} \tag{5}$$

Here, *P* = depth of penetration, *m* = mass of projectile, ρ = target density, *a* = projectile radius, *V_s* = striking velocity, Ψ = calibre-radius-head (CRH), *r* = calibre-radius, *R* = empirical constant (410 MPa), *N* = nose shape factor.

5 Results and Discussions

The main objective of this study was to observe the behaviour between plain concrete and reinforced concrete and its effect on penetration depth and crater formation on the front as well as rear faces. Numerical simulation is conducting using below mentioned four cases of projectile, viz. shown in Table 4. Lagrange interaction is applied between projectile and concrete target. Figure 6 expresses the preliminary setup of complex problem interaction in AUTODYN-3D.

Table 4 Various cases of ogive-nose-shaped projectile

Case	Target	CRH value
I	PCT	1.5
II	RCT	1.5
III	PCT	3.0
IV	RCT	3.0

Fig. 6 Interaction using 1.5 CRH projectile

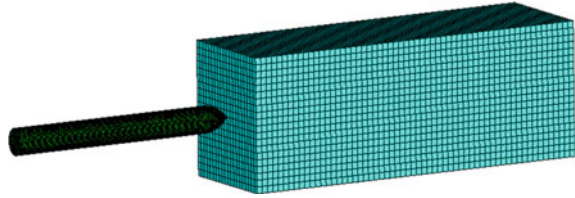
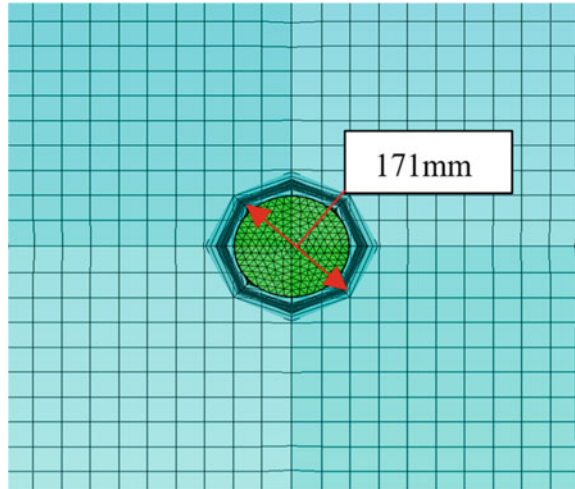


Fig. 7 Crater diameter at $t = 9.785$ ms (case-I)



Here, it is obtained results of crater diameter and penetration depth through numerical simulations along with their results is compared with empirical results.

5.1 Crater Diameter

Crater diameter is generated due to high-velocity impact of the projectile against the target material. Figures 7 and 8 describe these much value of crater diameter caused during penetration in target for all the cases. The figure illustrates the damage produced at the front face of plain as well as the reinforced concrete target.

5.2 Depth of Penetration (DOP)

The penetration depth or depth of penetration (DOP) for all these cases obtained from the AUTODYN is given in Figs. 9 and 10. The results are compared with the

Fig. 8 Crater diameter at $t = 8.002$ ms (case-II)

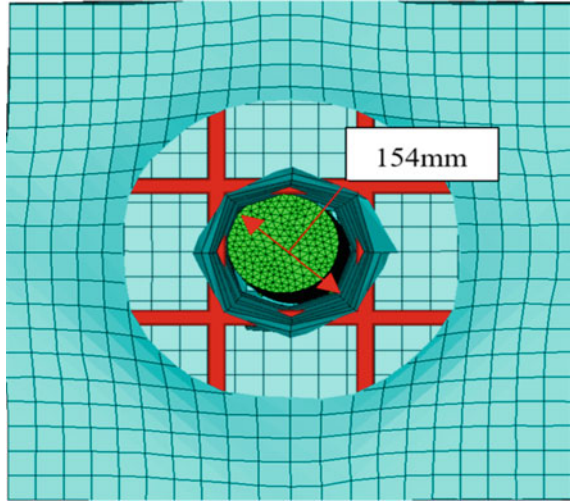


Fig. 9 Penetration depth at $t = 9.785$ ms (case-I)

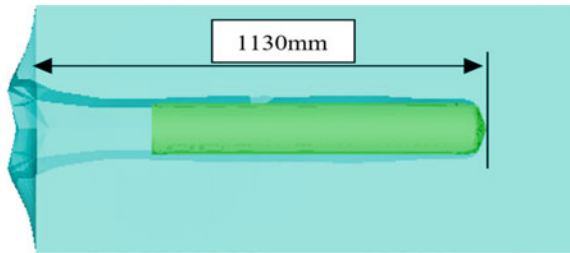
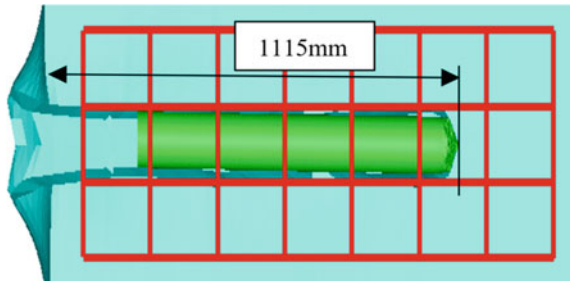


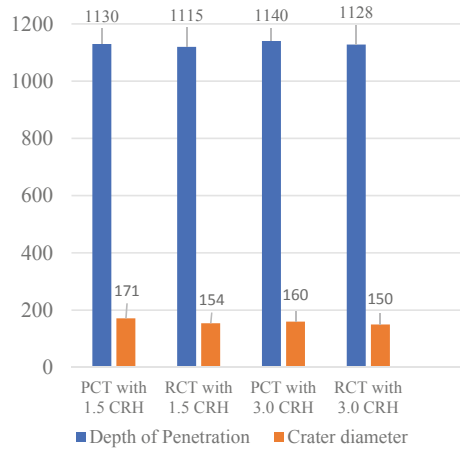
Fig. 10 Penetration depth at $t = 8.002$ ms (case-II)



empirical approach, viz. known as Forrestal penetration equation. One observation was clarified that there is less variation in penetration depth in both RCT and PCT.

Finally, all these results are gathered and displayed as a bar chart shown in Fig. 11 which is appeared from the numerical simulation. Here, maximum and minimum DOP is achieved in PCT with 3.0 CRH projectile and RCT with 1.5 CRH projectile, respectively. PCT with 1.5 CRH projectile has maximum crater damage, while RCT

Fig. 11 Outcomes from numerical simulation



with 3.0 CRH projectile has least crater damage. Due to technical constraints, up to 7% of error is considerable in the value of the results of penetration when compared with empirical equations because of some limiting factors such as mesh size, meshing method, interactions, irrelevant selection of the material model.

6 Conclusion

From this paper, the multifaceted interaction of a projectile with target material is an interesting topic of research for ballisticians. From the simulation results, it may be concluded that by adding steel fibres in the concrete, there is an appreciable decrease in spalling and scabbing on the concrete target. Forrestal et al. [1] empirical formulae are used as a benchmark for comparing results with numerical simulation. The results obtained from the penetration equation are validated upright promise with the results of numerical simulation.

References

1. Forrestal MJ, Altman BS, Cargile JD, Hanchak SJ (1994) An empirical equation for penetration depth of ogive-nose projectiles into concrete targets. *Int J Impact Eng* 15(4):395–405
2. Frew DJ, Forrestal MJ, Cargile JD (2006) The effect of concrete diameter on projectile deceleration and penetration depth. *Int J Impact Eng* 32(10):1584–1594
3. Tham CY (2006) Numerical and empirical approach in predicting the penetration of a concrete target by an ogive-nosed projectile. *Finite Elem Anal Des* 42(14–15):1258–1268
4. Ulrika N, Kent G (2011) Comparative numerical studies of projectile impacts on plain and steel-fibre reinforced concrete. *Int J Impact Eng* 38(2–3):95–105
5. Rajput Abhishek R, Jakka BMP, Iqbal MA (2016) Experimental study of plain and reinforced concrete targets subjected to impact loading. *Procedia Eng* 144:124–131

6. Wu H, Peng Y, Fang Q, Gong ZM, Liu JZ (2016) Residual velocities of projectiles after normally perforating the thin Ultra-High-Performance steel fibre reinforced concrete slabs. *Int J Impact Eng* 97:1–9
7. Wu H, Zhang S, Zhang X, Liu J, Huang F (2017) High-velocity penetration of concrete targets with three types of projectiles: experiments and analysis. *Lat Am J Solids Struct* 14(9):1614–1628
8. Feng J, Li W, Li W, Song M, Sun W, Weng L (2018) Thick plain concrete targets subjected to high speed penetration of 30CrMnSiNi2A steel projectiles: tests and analyses. *Int J Impact Eng* 122:305–317
9. Oucif C, Mauludin LM (2019) Numerical modelling of high-velocity impact applied to reinforced concrete panel. *Undergr Space* 4(1):1–9
10. Chen XW, Li QM (2002) Deep penetration of a non-deformable projectile with different geometrical characteristics. *Int J Impact Eng* 27(6):619–637

Process Parameters Optimization of Wire EDM on AISI 304 Using the Taguchi Method



Vidyanand Kumar, Manjeet Kharub, Rajesh Kumar,
and Pawan Kumar Rakesh

1 Introduction

Wire electrical discharge machining (WEDM) has widely used for machining of high strength and conductive materials for generating an intricate profile that would be very difficult to produce using any conventional machining. The machining process is used in the automobile, aerospace and tool manufacturing industries where close tolerance and dimensional accuracy are required. WEDM is a non-traditional machining process in which material is being removed from the workpiece by a series of sparks between workpiece and wire separated by a dielectric fluid without any contact. The dielectric fluid in machining not only washes detritus produced between them, but it restricts them to become an obstacle for the next spark. It also acts as a cooling agent for the cutting zone. When a potential difference has established between wire and workpiece, then the emission of electron starts. These electrons collide with the dielectric fluid that breaks it into ions and an electron that forms a plasma. A high amount of heat is generated that melts the material nearby sparking zone and evaporated [1]. The current intensity is a more dominant factor on surface roughness, and also an excellent surface finish has been obtained at a low value of current intensity as well as pulse-on time [2–4]. Varun et al. [5] used grey relational analysis (GRA) coupled with genetic algorithm (GA) to study the effect of input parameters on the out responses (MRR) on EN353 alloy steel. Mathew et al. [6] optimized the parameters of WEDM on AISI 304 steel against the MRR and SR, and it was found that MRR and SR increased with an increase in servo voltage up to a specific range.

V. Kumar (✉) · M. Kharub
Mechanical Engineering Department, CVR College of Engineering, Hyderabad 501510, India
e-mail: vidyanandk75@gmail.com

R. Kumar · P. K. Rakesh
Design Innovation Center, National Institute of Technology Utrakhand, Srinagar, Uttarakhand
246174, India

Durairaj et al. [7] study the analysis of WEDM on stainless steel to optimize the parameters against the performance characteristic such as kerf width and surface finish. Rebolo et al. [8] investigated the effect of EDM process parameters on the material removal rate and surface quality on high strength copper-beryllium alloys. They have developed the mathematical model using response surface methodology for MRR and SR to determine the relationship between process parameters and machining performance. An abrasive particle mixed with dielectric fluid shows better machining rates at the desired surface quality [9, 10]. However, the machining parameters have selected for experimental work on AISI 304 steel, and their effect on the output characteristics was studied.

2 Experimental Method

The experiments have executed on three-axis CNC controlled WEDM (ELECTRONICA ULTRA CUT 51), as shown in Fig. 1. A brass wire having a diameter of 0.25 mm is used as an electrode. De-ionized water has used as the dielectric medium for the experiment. The work material is AISI 304 steel of size $150 \times 50 \times 5$ mm plate, and their constituents are shown in Table 1.

The working range of WEDM parameters was selected based on a trial experiment, and their levels are shown in Tables 2, 3 and 4. The machine variables have validated



Fig. 1 Photograph of WEDM

Table 1 Chemical composition of AISI 304

Element	Cr	Ni	Mn	M	Si	P	C	Fe
%	19.04	7.93	1.74	1.24	0.368	0.018	0.019	Remaining

Table 2 WEDM parameters and their levels

Parameters	Level 1	Level 2	Level 3
T_{on} (μs)	100	105	110
T_{off} (μs)	55	59	63
Servo voltage (V)	20	30	40

Table 3 L9 orthogonal array

S. No.	Process parameters coded value		
	T_{on} (μs)	T_{off} (μs)	Servo voltage (V)
1	1	1	1
2	1	2	2
3	1	3	3
4	2	1	2
5	2	2	3
6	2	3	1
7	3	1	3
8	3	2	1
9	3	3	2

Table 4 Experimental results

S. No.	Process parameters			Responses	
	T_{on} (μs)	T_{off} (μs)	Servo voltage (V)	MRR (mm^3/min)	Ra (μm)
1	100	55	20	0.7471	1.619
2	100	59	30	0.6849	1.683
3	100	63	40	0.8343	1.443
4	105	55	30	3.4860	1.993
5	105	59	40	1.5396	1.809
6	105	63	20	0.6953	1.947
7	110	55	40	2.8640	2.639
8	110	59	20	2.6982	2.952
9	110	63	30	1.4375	2.869

by performing confirmation experiment.

In the present research work, Taguchi L9 orthogonal array has used for the design of experiment (DOE) and three levels of each process parameters have selected.

The output response has been recorded in the form of MRR and SR. Machining time has been kept constant for each experiment. Surface roughness is measured using an apparatus called as Talysurf.

3 Results and Discussion

After experimentation, MRR and SR were calculated and arranged in a tabular form corresponding to each parameter combination. According to Taguchi technique, S/N ratio is the relation of signal to noise where the signal is desirable value and noise is undesirable value. As MRR value should be high for machining, and surface roughness value should be less for sound application. Since MRR should be maximum, then higher the better characteristic is used for the calculation of S/N ratio. The surface roughness should be minimum for machined parts, thus, lower the better characteristic is used for the calculation of S/N ratio, as shown in Table 5. The experimental results were analysed by ANOVA to find the significance of each process parameter on the material removal rate and surface roughness.

3.1 Material Removal Rate

The results obtained by Taguchi analysis indicate that MRR increases with an increase in pulse-on time as the duration of sparks increases, the discharge energy increases with T_{on} . Similarly, it has observed that with an increase in pulse-off time, the MRR decreases. There is no current supply to the electrode as time duration between two sparks is increased. Figure 2 shows the plot for the effect of the S/N ratio on MRR. Table 6 shows the S/N ratio of each parameter and its relation with MRR. From the responses, S/N ratio for MRR is calculated for larger the better by Taguchi analysis;

Table 5 S/N ratio value for MRR and SR

Ex. No.	S/N ratio of MRR	S/N ratio of SR
1	-2.5324	-4.18494
2	-3.2875	-4.52168
3	-1.5736	-3.18533
4	10.8465	-5.99015
5	3.7482	-5.14877
6	-3.1566	-5.78732
7	9.1395	-8.42879
8	8.6215	-9.40233
9	3.1522	-9.15461

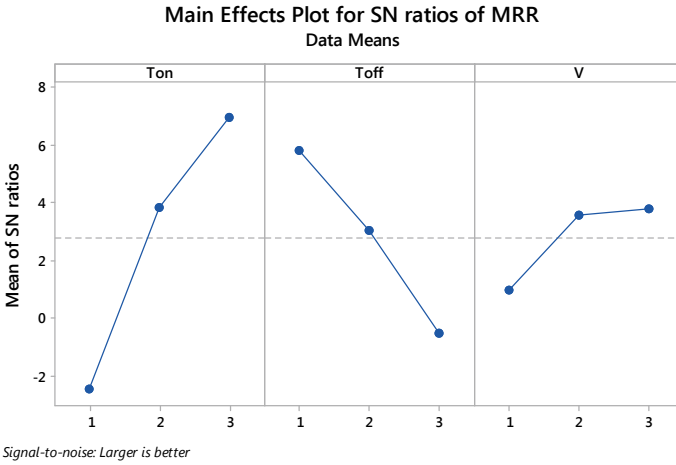


Fig. 2 Effect of parameters on MRR

Table 6 Response for S/N ratios for MRR

Level	T_{on}	T_{off}	V
1	-2.4645	5.8179	0.9775
2	3.8127	3.0274	3.5704
3	6.9710	0.5260	3.7714
Delta	9.4355	6.3438	2.7939
Rank	1	2	3

the ranks are (1) pulse-on time (T_{on}), (2) pulse-off time (T_{off}) and (3) servo voltage (V).

3.2 Analysis of Variance

Influence of process parameters on MRR and SR has calculated, and the contribution of each parameter on response has presented in Table 7. From Table 7, ANOVA shows the importance of selected input parameters on MRR. It has concluded that the MRR is influenced by T_{on} of 56.72%, T_{off} contributes of 19.60% and servo voltage (V) contributes of 6.89%.

Table 7 ANOVA results for MRR

Source	DF	Seq SS	Contribution (%)	Adj SS	Adj MS	F-value	p-value
T_{on}	2	0.34852	56.72	0.34852	0.17426	3.38	0.228
T_{off}	2	0.12044	19.60	0.12044	0.06022	1.17	0.461
V	2	0.04236	6.89	0.04236	0.02118	0.41	0.709
Error	2	0.10314	16.79	0.10314	0.05157		
Total	8	0.61446	100.00				

3.3 Surface Roughness (Ra)

The results obtained from Taguchi analysis for surface roughness (Ra) indicate that with an increase in pulse-on time, the surface roughness decreases. Similarly, an increase in pulse-off time, the Ra shows slight variation. Figure 3 shows the plot of S/N ratio effect on surface roughness. Table 8 shows the S/N ratio of each parameter and its relation with surface roughness. S/N ratio for Ra has calculated for smaller

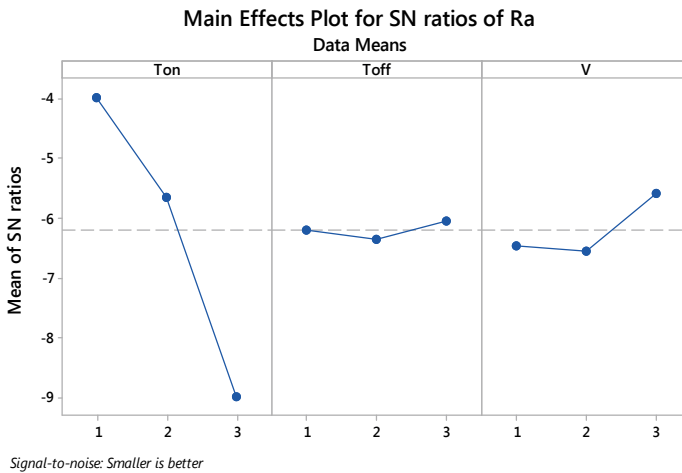


Fig. 3 Variation of S/N ratio with selected parameters for Ra

Table 8 Response for S/N ratios for Ra

Level	T_{on}	T_{off}	V
1	-3.964	-6.201	-6.458
2	-5.642	-6.358	-6.555
3	-8.995	-6.042	-5.588
Delta	5.031	0.315	0.968
Rank	1	3	2

Table 9 ANOVA result for surface roughness

Source	DF	Seq SS	Contribution (%)	Adj SS	Adj MS	F-value	p-value
T_{on}	2	0.050328	95.71	0.050328	0.025164	6688.24	0.000
T_{off}	2	0.000169	0.32	0.000169	0.000084	22.42	0.043
V	2	0.002081	3.96	0.002081	0.001040	276.52	0.004
Error	2	0.000008	0.01	0.000008	0.000004		
Total	8	0.052585	100.00				

the better by Taguchi analysis; the ranks are (1) T_{on} , (2) T_{off} and (3) servo voltage (V).

The ANOVA constructed from the experimental data for surface roughness (Ra) shows that the percentage contribution of each control factor on Ra. From Table 9, it can conclude that surface roughness (Ra) is profoundly affected by T_{on} which is contributed by 95.71%, servo voltage contributes of 3.96% and T_{off} contributes of 0.32% with an error of 0.01%.

3.4 Grey Relational Analysis

The most popular optimization techniques used for multiple responses in engineering problems is grey relational analysis. In GRA, multiple quality responses have been converted into a single grade. GRA used as the performance measurement characteristic where multiple parameters against the multiple responses have to be optimized.

Based on grey relational normalized and grey relation coefficient value, the grey relational grade has been calculated corresponding to each response value. From the grey relation grade (GRG), the value which nearer to one corresponding to that GRG process parameters is the optimum parameters for maximum MRR and minimum surface roughness value for the operation on AISI 304, which is depicted in Table 10.

It has concluded that the experiment number 4 has the highest grey relation grade value, i.e., nearer to one, thus, a perfect combination of process parameters for MRR and SR.

4 Conclusions

The experiments were conducted based on the L9 orthogonal array on AISI 304 steel using WEDM. The following conclusion has drawn from the present study:

- (a) The optimized input parameters for maximum MRR are pulse-on time of 110 μ s, pulse-off time of 55 μ s and servo voltage of 40 V.

Table 10 Optimized grey relational grade

Ex. No.	GR normalized value		GR coefficient value		Grey relational grade
	MRR	SR (Ra)	MRR	SR (Ra)	
1	0.022206	0.883366	0.338342	0.810854	0.574598
2	0	0.840954	0.333333	0.758673	0.546003
3	0.053336	1	0.345623	1	0.672811
4	1	0.63552	1	0.578383	0.789191
5	0.30513	0.757455	0.418456	0.67336	0.545908
6	0.003713	0.666004	0.33416	0.599523	0.466842
7	0.777944	0.207422	0.692467	0.386824	0.539646
8	0.718753	0	0.640003	0.333333	0.486668
9	0.26868	0.055003	0.406068	0.346022	0.376045

- (b) From the analysis of variance for MRR, pulse-on time and pulse-off time is the significant factor.
- (c) From grey relational grade, it has observed that the optimum process parameters combinations are the pulse-on time of 105 μ s, pulse-off time of 55 μ s and servo voltage of 30 V for better MRR and Ra.

References

- Müller F, Monaghan J (2000) Non-conventional machining of particle reinforced metal matrix composite. *Int J Mach Tools Manuf* 40(9):1351–1366
- Peuratos I (2004) Analysis of the influence of EDM parameters on the surface quality, MRR and EW of WC-Co. *J Mater Process Technol* 153:1026–1032
- Vijaya Babu T, Soni JS (2018) Investigation of process parameters optimization in die-sinking and wire-cut EDM to improve process performance using Taguchi technique. *Mater Today Proc* 5(13):27088–27093
- Varun A, Venkaiah N (2015) Simultaneous optimization of WEDM responses using grey relational analysis coupled with genetic algorithm while machining EN 35. *Int J Adv Manuf Technol* 76(1–4):675–690
- Mathew B, Benkim, Babu J (2014) Multiple process parameters optimization of WEDM on AISI 304 using Taguchi grey relational analysis. *Int Conf Adv Manuf Mater Eng* 5:1613–1622
- Nayak BB, Mahapatra SS (2016) Optimization of WEDM process parameters using deep cryo-treated Inconel 718 as work material. *Eng Sci Technol Int J* 19(1):161–170
- Durairaj M, Sudharsun D, Swamynathan N (2013) Analysis of Process parameters in wire EDM with stainless steel using single objective Taguchi method and multi-objective grey relational grade. *Procedia Eng* 1(64):868–877
- Rebolo JC, Morao Dias A, Mesquita R (2000) An experimental study on electro-discharge machining and polishing of high strength copper-beryllium alloys. *J Mat Process Technol* 103(3):389–397
- Rabindranath B, Madhu V, Gogia AK (2015) Multi response optimization of wire-EDM process parameters of ballistic grade aluminium alloy. *Eng Sci Technol Int J* 18(4):720–726

10. Kumar A, Maheswari S, Sharma C, Beri N (2010) A study of multiobjective parametric optimization of silicon abrasive mixed electrical discharge machining of tool steel. *Mater Manuf Process* 25(10):1041–1047

Modelling and Analysis of Pivoted Slipper and Its Component at 40 Ton Load



Amit Yadav, Ajai Jain, and Subhash Chander

1 Introduction

Slipper invention is concerned with high-speed rail travel, particularly, at the speed where wheels are considered unrealistic for design. They are component of rocket sled which is responsible for keeping the sled on track during its high-speed motion. Rocket sled is a structure which houses the payload/unit under test (UUT) and is propelled by rocket motors on specially designed tracks at high acceleration with appropriate instruments installed on it. Slippers are provided with intended clearance or gap to account for any imperfection in the track alignment. This gap also allows the sled to move freely in a vertical and lateral direction. They are also known as 'sliding shoes'. RTRS has penta-rail track system for a trial test of various kinds of payload. The track being used here is SAIL's UIC 60, which has a weight of 60 kg/m. The rail track is made up of 1080 steel and runs for approximately 4 km. The penta-rail track system provides various gauge options for a trial test. The rail track has a minimum gauge width of 0.7 m and a maximum gauge width of 4.8 m. The various gauge options present here allows testing of payloads/UUT of several sizes and capabilities.

Slippers can be classified into various groups based on materials, coatings, joints/connections, designs, load-carrying capacity, shapes, speeds, aerodynamics and interaction with the track. Classification of slippers is given in Table 1. In high speed, testing of missiles and other equipment at RTRS, slippers or sled shoes are important parts of sled system. They guide the UUT on rail track during its motion. Slippers get subjected to gouging phenomenon above 1.5 km/s of sled speed [1, 2].

A. Yadav (✉) · A. Jain

Mechanical Engineering Department, National Institute of Technology, Kurukshetra, Haryana 136119, India

e-mail: amit.insan77@gmail.com

S. Chander

Rail Track Rocket Sled, Terminal Ballistics Research Laboratory, Chandigarh 160003, India

Table 1 Classification of slippers

Material	Coating	Joints/connections	Design	Load capacity	Interaction	Speed	Aerodynamics	Use	Shape
DSS 2205, EN24, Mild Steel, VascoMax 300, T250, 4130 Steel, 0Cr18Ni9Ti, etc	Coated slippers and un-coated slippers	Bolted slippers, welded slippers, pivoted/pinned slippers and hybrid slippers	Basic slippers, insert slippers, hybrid slippers, adjustable slippers and air bearing slippers	Light load-carrying slippers and heavy load-carrying slippers	Physical contact slippers and Maglev slippers	Low-speed slippers and high-speed slippers	Normal slippers and aerodynamic slippers	Single-use slippers and reusable slippers	U-shaped slippers and C-shaped slippers

Note: Coated slippers are used to arrest the formation of a gouge. Hybrid slippers are a combination of more than one joint. Reusable slippers usually have one problem that is the clearance between the slipper and track increases with a number of trials which affects the stability of the sled system. U-shaped slippers are not wrapped at the bottom of rail track's head flange, and C-shaped slippers are wrapped all around the head flange portion of the rail track

This is a major problem which restricts attaining of higher Mach speed. At high Mach speed, sled bounces on the track due to various aerodynamic forces. Since the track is assumed to be rigid, frequent bouncing of the sled induces vibration in the track. If these track vibrations match with the slipper vibrations, resonance is created, and track fails [3, 4]. They also get subjected to various loads due to which sled moves vertically and laterally, along with its tangential (horizontal) motion. They experience severe sliding friction which results in thermal softening of slipper material due to frictional heat generation [5]. (Note: At high Mach speeds, aerodynamic drag is more critical than sliding friction.) Slippers are intentionally made with less strength material than tracks so that damage occurs on the slipper instead of the track as replacement of slippers are much easier and economical than track. This leads to wastage of millions of rupees and a large number of human workforce hours utilised to do that trial. Thus, robust slipper having lightweight, high strength, higher melting point temperature and toughness are needed, which has a lower cost.

Bolted, welded and hybrid type of slippers are usually used during a test at RTRS. They have numerous problem associated with them like the development of residual stresses, change in material properties during welding, induce deformation in sled if tightening force exceeds the critical limit in bolted slippers and uneven thermal expansion of sled and slipper material during welding. This leads to the introduction of pivoted slippers which has removed these bottlenecks with some added advantages of easy installation, adjustment and removal. Pivoted slippers also have room for adjustment of angular imperfection in track, but bolted, welded and hybrid type of slippers once installed, restrict the small angular adjustment of slippers on track. These angular imperfections may be due to joining of rail track sections to form one continuous rail. (Note: Lateral and vertical imperfection in the track are adjusted by providing intentional clearance between the slipper and track.) In this study, the focus has been given on finding out the critical deformation and stress zones in the pivoted slipper set during application of 40 ton tensile load.

2 Design of Slipper

Model is made and assembled on SolidWorks 2017. Slipper set consists of slipper, pin, bush and box. The slipper is having a minimum thickness of 37.7 mm, length of 250 mm and width of 152 mm. It has three holes for pin installation. Two side slipper holes have an external diameter of 25 mm, and the middle slipper hole has a diameter of 37 mm. The basic slipper, along with its components, is shown in Fig. 1. Figure 2 shows the cross-sectional view of the slipper set.

Three pins have a length of 152 mm. Two side pins are similar with a diameter of 24 mm, and the middle pin has a diameter of 36 mm. (Note: Pins are considered as nut and bolt with no pretension effect with a slipper. Bolt head and nut have the same thickness of 18 mm for all pins. They have a diameter of 56 mm for the middle pin and 40 mm for two side pins. Also, nut and bolt are assumed to have bonded contact.) Figure 3 shows the clearance between the slipper, pin and bush.

Fig. 1 Slipper set with its various components

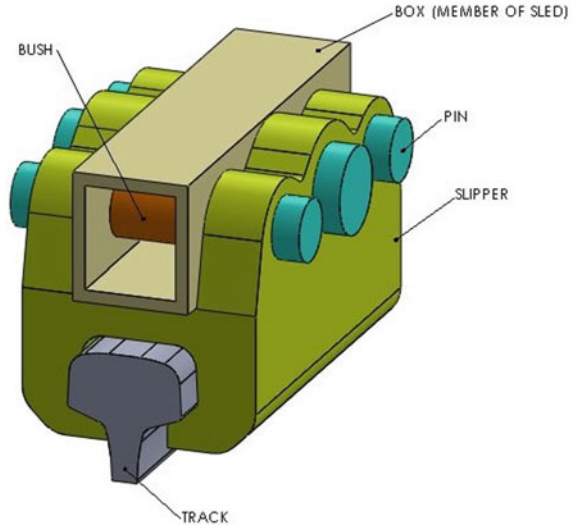


Fig. 2 Sectional view of slipper set

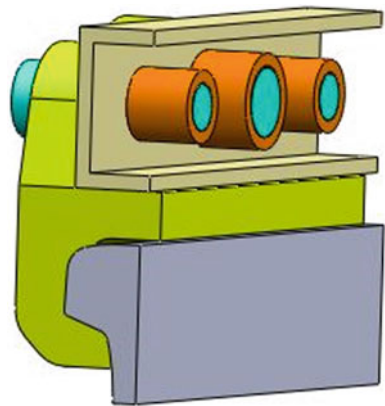
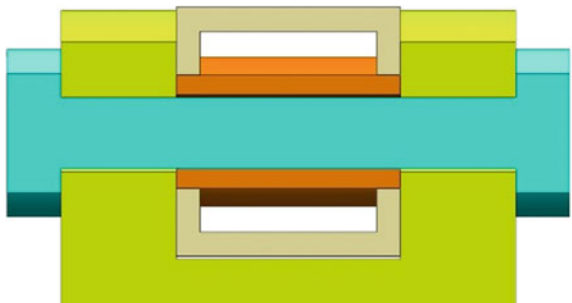


Fig. 3 Close up view of slipper, pin, bush and box connection



Two side bushes have an external diameter of 25 mm, and the middle bush has a diameter of 37 mm. All three bushes are of the same length that is 75 mm and same thickness of 6.5 mm. (Note: Bushes are welded to the box, i.e. a member of the sled). Box has a dimension of $75 \times 83 \times 8$ mm with the provision of holes for bushes.

3 Analysis for Designed Slipper

In the analysis, the track is fixed, and the sliding motion of slipper on the track is arrested by providing 'Displacement' constraints in the sliding direction. The motive of analysis is to explore the use of pivoted slipper at 40 ton load during trials. Thus, it is not concerned about the deformations and stresses generated in the box. The stresses and deformations in the box would be lesser than predicted here as it would be connected to other members of the sled.

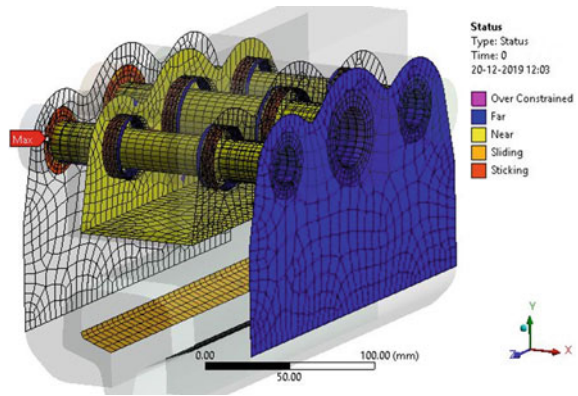
3.1 Contacts

In total, there are 24 contacts. Two contacts between slipper and track are taken as 'No Separation'. Six contacts between slipper and pin are taken as 'Frictional' with a friction coefficient of 0.2 and other three contacts between slipper's pinhole surface area, and pin's surface area is taken as 'Frictionless'. Three contacts between bush and box are taken as 'Bonded'. Three contacts between bush and pin are taken as 'Frictional' with a friction coefficient of 0.15 as they can slide. Six contacts between slipper and bush are taken with 'No Separation' as the connection type. One contact between slipper and box is taken as 'Frictional' with a friction coefficient of 0.3. Slipper and track are used with 'Pure Penalty' as formulation. Box and bush are used with 'MPC' as formulation. All other contacts have 'Augmented Lagrange' as formulation. Contact connections established in the analysis are given in Fig. 4.

3.2 Meshing

Mesh physics is taken as 'Mechanical'. In 'Size Function', the curvature is kept on, and Relevance Centre is taken as fine. Slow transition and medium smoothing are done. The settings mentioned above are done as Global Mesh Controls. Various local mesh controls are also used such as method, mapped face meshing. In a method, we have used hex dominant, multizone and sweep type of mesh. Hex dominant type of mesh is used for the slipper body. Multizone type of mesh is used for three pins. Sweep mesh method is used for three bushes. Mapped face meshing is used for all the internal holes surface area. Total nodes created are 2, 22 and 207 during meshing. Figure 5 shows the meshing done on the slipper and its components.

Fig. 4 Contact connections status for slipper set



3.3 Boundary Conditions

To restrict all the six degrees of freedom, fixed support is provided to the track. The tensile force of 40 ton is applied normal to the top face of the box. The box is the member of sled to which our pivoted slipper is attached. Displacement is provided to one face of the slipper, so that slipper set does not slide along z-axis during analysis. Various constraints applied can be seen in Fig. 6.

4 Numerical Results

From the analysis result, it is found that maximum deformation in slipper set is of 0.76783 mm, which is recorded at the box. Pins, bush and slipper have maximum deformation of 0.444 mm, 0.449 mm and 0.164 mm, respectively. Thus, the maximum deformation is recorded in the bush (0.449 mm) and pin (0.444 mm). These are present in smaller diameter bush and pin which are located at the side of the slipper.

Severe deformation for slipper occurs at the top inner side of holes in a slipper. Pins have a major deformation zone at the centre. Bushes which are welded to box have maximum deformation area near the edges due to compression and stretching of the box. Box severely deforms at the open end. Total deformation of the slipper and its components is shown in Fig. 7.

Severe stress zone for pins is found at the top and below central part due to its expansion and contraction as a result of load applied. This region recorded maximum stress of 399.44 MPa on smaller diameter pin. Slipper has dominant stress at the upper inner side of pinholes with a maximum stress of 462.89 MPa on smaller hole due to stress concentration at a sharp corner. This can be reduced by providing fillet at the edges. Other areas of the slipper have stress value well below 250 MPa. Bushes have major stress area along the top and bottom outer side with maximum stress recorded as 491.95 MPa. This is due to a welded connection between bushes and box. Since

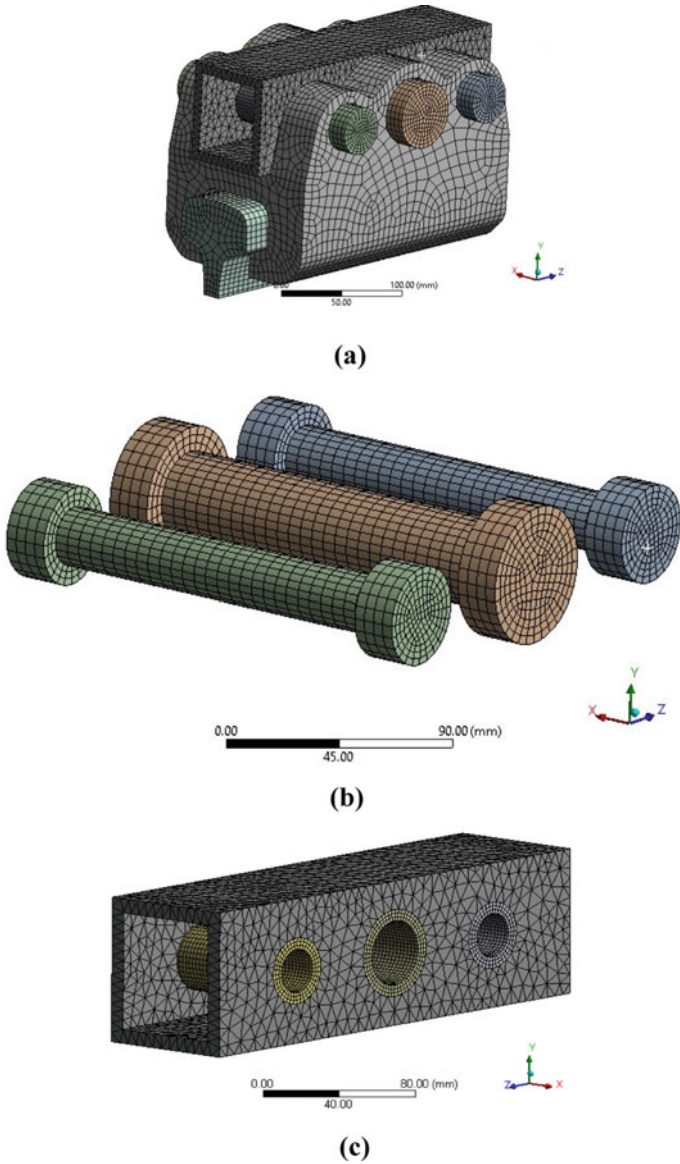
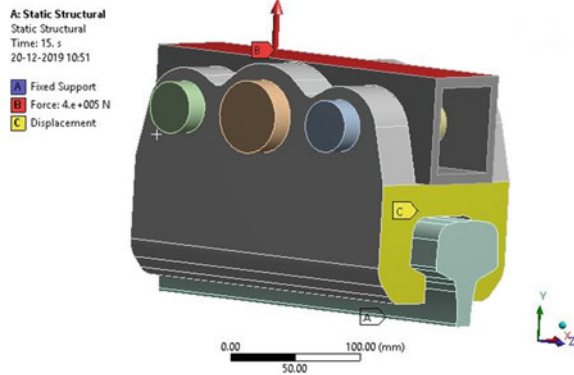


Fig. 5 Mesh of a full slipper set, b pin, c bush and box

box records maximum deflection and stresses, these are transferred to the bushes. Box has a maximum stress region at the top face and on the top side of bush, holes opening. It has a maximum stress value of 504.71 MPa on the top face. (The stresses in the box would be lesser in original due to its connection with the rest of the sled

Fig. 6 Boundary conditions applied on the slipper set



which will restrict/share the stresses and deformation on it.) Equivalent (Von-Mises) stress for slipper and its component are shown in Fig. 8.

5 Conclusions

The analysis result shows a good resemblance to the observed severe stress pattern in a slipper. The deformation and stress concentration regions obtained are actually predicted. The deformation in the box is effecting the deformation in the bush. As the deformation and stresses in the box would be lesser than the simulation value due to its connection with the sled, this would limit the stresses and deformation value in other parts such as bush, pin and slipper. The pin has maximum stress region near top and down central part. This is due to stretching of the bush bonded to box. The slipper has maximum stress at the upper inner side due to stress concentration at edges. This stress concentration region develops in slipper due to pin's stretching in the normal direction because of the applied load. Box has a maximum stress region at the top face and on the inner top side of the bush hole due to applied load of 40 ton as it is not connected to the sled. Therefore, pin and bush should be designed with higher yield strength material.

6 Future Scope

Aerodynamic test of the slipper is needed for the study of the high-speed motion of sled. Lateral and vertical movement effect of sled on the slipper and frictional wear of slipper at high Mach speed need to be studied. Gouge formation at a higher speed can be examined, keeping in mind the future requirement of RTRS. The effectiveness of coatings to arrest the formation of the gouge is an area of interest for researchers.

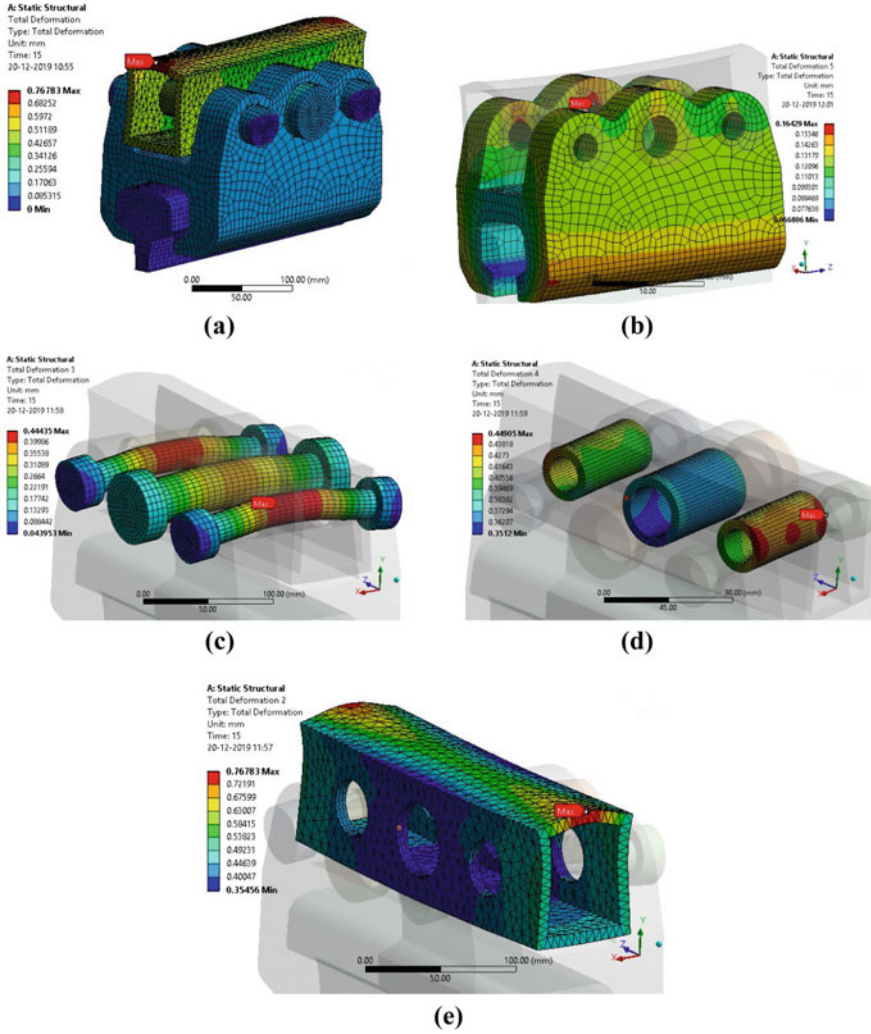


Fig. 7 Total deformation of a full slipper set, b slipper, c pin, d bush, e box

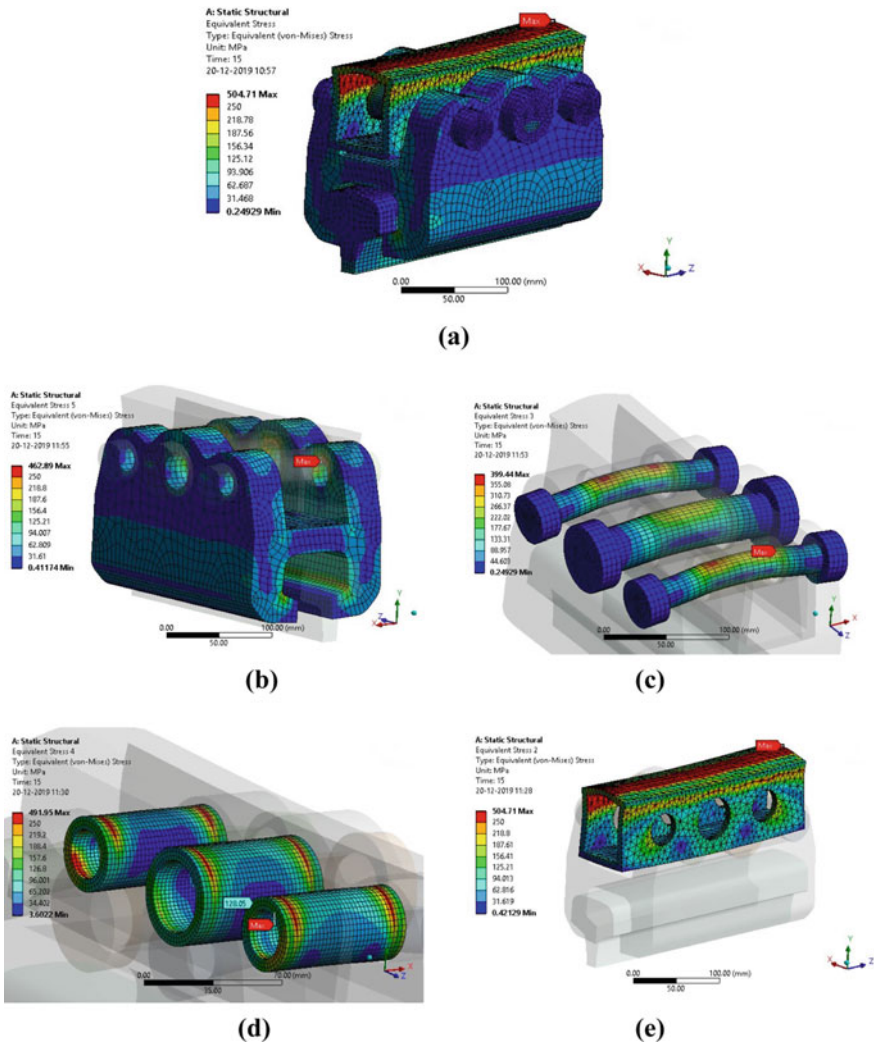


Fig. 8 Von-Mises equivalent stress of **a** full slipper set, **b** slipper, **c** pin, **d** bush, **e** box

References

1. Tachau RDM, Yew CH, Trucano TG (1995) Gouge initiation in high-velocity rocket sled testing. *Int J Impact Eng* 17(4–6):825–836
2. Lamb JL (2000) Critical velocities for rocket sled excitation of rail resonance. *Johns Hopkins APL Tech Dig* 21(3):448–458
3. Wuertemberger L, Palazotto AN (2016) Evaluation of flow and failure properties of treated 4130 steel. *J Dyn Behav Mater* 2(2):207–222
4. DeLeon LC, Baker WP, Palazotto AN (2019) Modeling a nonlinear melt region as a result of high-speed sliding. *J Thermophys Heat Transfer* 1–9

5. Yeo C-D, Palazotto A, Song J, Buentello R (2016) Evaluation of thermomechanical damage of a slipper and rail in a rocket sled system. *J Test Eval* 44(4):1443–1453

Moisture and Flammability Behaviour of flax Fibre and Natural Fillers-Based Hybrid Epoxy Composites



Sudhir Kumar Chaudhary , Hitesh Sharma , and Gaurav Kumar 

1 Introduction

Two or more different materials with different physical and chemical properties are combined to form a new material which possesses properties entirely different from main constituents are acknowledged as composite materials. There has been striking growth of composites as they provide the materials with stiffness and toughness. The biggest advantage associated with composites is that their properties can be customized and manipulated. Natural fibre-based composite has been used in the fabrication of aircraft parts, submarine structure, production of sports good and medical instruments [1, 2]. Natural fibre-based composites found its uses in many applications. However, they are still vulnerable to fire and moisture and limited studies have been reported. As they found their application in aircraft parts, construction works, hence, the risk of catching fire can be dangerous [3]. However, natural fillers-based composites have found their various applications against the synthetic fillers-based composites as they are abundant in nature and relatively low cost associated with them. Several properties of the natural fibre-based composite are superior to those of glass fibre-based composite [4]. Initially, these composites are used in indoor application as they are very vulnerable to moisture and fire, but as more research has been done on these natural fibres-based composites, they have also found their use in outdoor applications. Different types of parts are manufactured using natural fibres without compromising the mechanical strength of the material. Natural filler and fibre-based composites are also seen as alternatives for synthetic materials as they do less harm to nature and easily biodegradable as compared with those of synthetic composite.

S. K. Chaudhary (✉) · H. Sharma · G. Kumar
Department of Mechanical Engineering, National Institute of Technology Uttarakhand, Srinagar
Garhwal 246174, India
e-mail: sudhir.mechmt18@nituk.ac.in

Moreover, natural fibres-based composites are renewable and producing at less cost and involve lesser CO₂ absorption [5]. Several matrix materials have been used to produce quality material. Fillers are also added in the polymer to enhance the mechanical properties. Barczewski et al. [6] studied the effect of sunflower husk, hazelnut shell and walnut shell as fillers for epoxy-based hybrid composite. They concluded large amounts of voids were present in composite with the highest aspect ratio and particle size of fillers material used.

1.1 Flax Fibre

Flax is the oldest fibre that has been used in the textile industry. Its evidence can be found in the graves of Egypt around 5000 BC back [7]. Its property dependent of numerous factors like thickness of walls of fibre between the bottom to the top of the stem [8], harvesting weather, extraction method [9], area of extraction and still a lot of factors is unknown for mechanical characterization of flax fibre [10]. Like most of the plant fibre and flax fibre also contains a long cell with thick cell walls, and this kind of structure gives them stiffness and strength [11].

1.2 Structure

The structure of flax fibre is crystalline in nature which gives them more strength and stiffness compared to other natural fibres. It mainly contains cellulose, hemicellulose, wax, pectin and lignin [7, 9]. Each fibre of flax made of the concentric cell wall, which is different from each other with respect to thickness [7]. The outer cell wall is designated as the primary cell wall, which coats the secondary cell wall.

Each layer contains micro-fibrils and forms micro-fibrillar angle with fibre direction. S₂ is the thickest cell wall and contains large no. of crystalline cellulose micro-fibrils and amorphous hemicellulose at an angle of 10°. These micro-fibrils contribute to 70% weight of the flax fibre and act as reinforcement in composites [7, 9, 12].

In 2003, around 43,000 tonnes of bio-fibres were used in European union to make bio-composites, which increased to 315,000 tones, in 2010, and around 230,000 will be consumed by 2020. Flax is generally grown where weather is moderate like China, France and Belarus are the leading producers of flax [13]. With great usefulness of composites reinforced with suitable natural fibres and fillers comes a drawback, most of them are hydrophilic in nature and absorb more moisture from surrounding as compared with synthetic composites, this causes a reduction in the mechanical properties of the developed composite [14]. Poor adhesion between reinforcement and matrix gives the generation of voids, and this eventually increases the moisture intake [15]. Even the environment, such as temperature and moisture influences the moisture absorption capacity of the flax fibre-based composites [4]. These voids, in turn, create the area of failure and generally crack initiation starts at these locations.

Also, the properties of natural fibres and fillers strongly influenced by climatic condition, soil properties, harvesting methods and even the area of extraction of the plant [10]. The aim is to check how the different fillers changed the burning time of epoxy reinforced with flax fibres, and to study the effects of filler contents on the moisture absorption capacity of different natural fillers-based developed composites.

1.3 Effect of Fillers

Induction of fillers enhances the modulus of elasticity of the overall composite and help to strengthen the matrix material, as the surface of fillers is rough, hence, it helps to provide better bonding between matrix and reinforcement. By using the optimum amount of fillers content, the amount of matrix content can be reduced without reducing the strength of the composite. As most of the matrix materials are non-biodegradable and costly; hence, fillers can be seen as an alternate solution to reduce the matrix content and provide better strength.

2 Materials and Methods

2.1 Materials

Walnut shell powder and pistachio shell powder are purchased from local stores. These shells were washed thoroughly with distilled water to remove the impurities over the surface and then dried in direct sunlight for two days, followed by drying in an oven at 40 °C for 90 min and then at 120 °C for 2 h. These shells were ground in the grinder and sieved in mesh size of 250 µm.

Epoxy LY-556 with Hardener HY-951 and flax fibre woven fabric is obtained from the local market. This woven fabric is dried in over for four hours at 60 °C for removal of moisture and cut into the size of 150 × 150 mm for the fabrication purpose.

2.2 Fabrication of Composites

For preparing specimens, hand lay-up technique was used owing to the simplicity and cost-effectiveness of the process. For fabrication purposes, four layers of woven flax fibre were used for fabrication of different samples. Epoxy and hardener are appropriately mixed in the ratio of 10:1 and stirred manually up to 15 min. For easy removal of composites, the plastic sheet known as miller sheet is applied over the mould. The resin is poured on the mould and spread properly using the brush then

Table 1 Set of specimens with their composition

S. No.	Designation	Composition
1	S ₁	Control specimen
2	S ₂	Epoxy + flax fibre + 10% pistachio shell powder
3	S ₃	Epoxy + flax fibre + 10% walnut shell powder
4	S ₄	Epoxy + flax fibre + 5% walnut shell powder + 5% pistachio shell powder

a layer of woven flax fibre is placed over this resin, and a roller is rolled over fibre surface to any remove air bubbles and excess resin and wetting the surface properly. This process was repeated up to four layers of fibre. Remaining resin is poured over the last layer of flax fibre and mould is closed, for proper wetting of fibre surface, the weights are placed over the top surface of the mould and preserve this composite for 24 h. After 24 h, composite is taken out from the mould, and finally, samples were cut from this composite sheet for various testing. In this way, different composites were made with different fillers content. Their composition and designation are mentioned in Table 1.

3 Experimentation

3.1 Flammability Test

For this test, three specimens from each sample of size 125 × 13 mm were cut. The test is conducted according to ASTM D635-18 standards [16]. The average of the three tests for each composition has been reported. For test purpose, two points are marked one at 25 mm and other at 100 mm from the free end, and the tongue fixes another end. The flame is kept for 30 s at the free end as shown in Fig. 1. The flame is then burnt off, as the flame reaches to 25 mm mark. The reading is recorded using a stopwatch when it reached to 100 mm marks, and these readings were defined in Fig. 2.

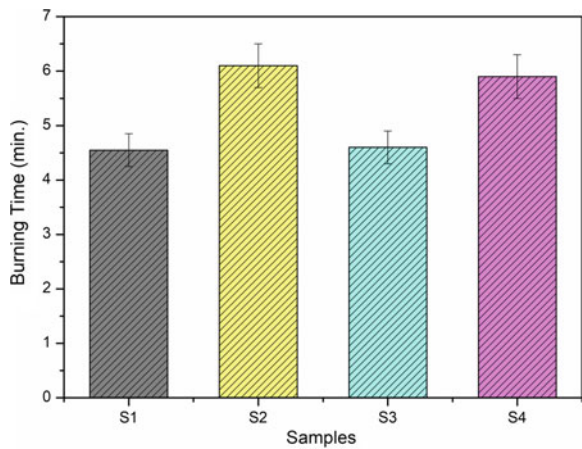
3.2 Moisture Absorption Test

This test is conducted as per ASTM D670 standards [16]. A specimen of size 76.4 × 25.4 mm is cut from each sample. Initially, the dry weight of each sample is recorded using the highly sensitive weighing machine. Then, these 4 samples are put into water and weight is recorded after 24 and 48 h. Before weighing each sample is wiped properly with cotton clothes and reading are taken immediately. The difference in weight gives the amount of moisture absorbed by different samples.

Fig. 1 Flammability test specimen



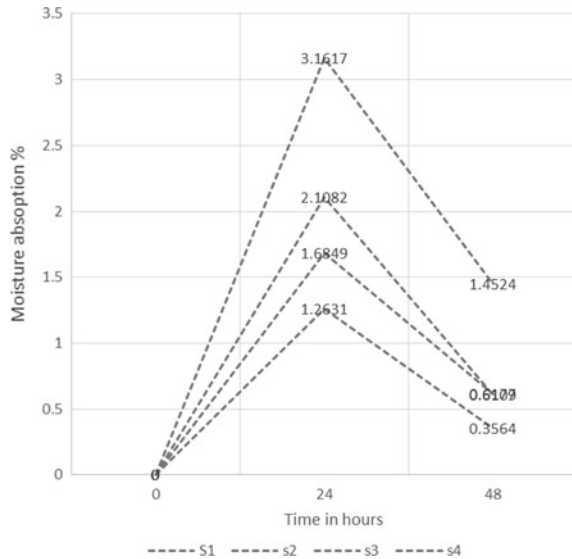
Fig. 2 Burning rate of different specimens



4 Results and Discussion

In the present study, flammability tests and moisture tests were carried out. The developed composites with 10% walnut shell powder showed the highest moisture absorption percentage in comparison with other specimens (Fig. 3). The developed composite with 10% pistachio shell showed less moisture absorption; hence, it can be concluded that walnut shell powder can be utilized as a filler material where the water resistance material needs to be developed.

Fig. 3 Moisture absorption behaviour of different samples



Flammability tests revealed that specimen with 5% pistachio and 5% walnut shell powder highest burning time and control specimen showed less burning time. This indicates that specimen S_4 is more fire retardant in comparison with other developed samples.

Composite materials have been gaining the popularity in construction and automobile sector as they provide a cheap alternative for metals and alloys, so efforts are made up to develop a composite which catches less fire or no fire and without swelling in a high damp environment.

In the present scenario, the composite developed using 10% walnut shell powder, which is more prone to fire and absorbs more amount of moisture compared to control specimen, whereas composites developed using 10% pistachio shell powder absorbed the least amount of moisture. By adding pistachio shell powder, the moisture absorption capacity of developed composite reduced when compared with control specimen. Hence, pistachio shell powder can be used as an alternate source to reduce the moisture absorption capacity of natural fibre-based composite.

Inclusion of walnut shell powder does not change the burning rate of the developed composite, but the addition of pistachio shell powder enhances some burning time of developed composite. Hence, pistachio can be seen as an excellent alternative to make fire retardant material rather than using flame retardant materials like boric acid, ammonium phosphates, zinc chlorides, borates, etc. [17].

5 Conclusions

Natural fillers recently are in trend to improve different properties of the composite, and low cost associated with them makes more fascinated towards the research. Following conclusions can be drawn from the present study:

1. The addition of walnut shell powder (250–300 μm) neither provides fire resistance to epoxy-based composite nor improves moisture absorption behaviour. This may happen as walnut contains more cellulose and hemicellulose content and hence more prone to absorb water from the environment.
2. Composite made of pistachio shell powder (S_2) improves the burning time by 34% and have a lower absorption rate. It absorbs only 1.26% extra moisture in 24 h compared to S_1 which absorbs 1.61% moisture in 24 h. Also, the moisture absorption rate decreases for 48 h in case of S_2 .
3. For the application of composites in the high-temperature environment, thermal stability needs to be improved, which can be done by hybridization of different fillers.
4. The addition of pistachio shell powder has improved the fire retardancy and reduced moisture absorption in the current study.

References

1. Chabba S, Netravali AN (2005) Green composites part 1: characterization of flax fabric and glutaraldehyde modified soy protein concentrate composites. *J Mater Sci* 40(23):6263–6273
2. Zhang Y, Sun G, Li G, Luo Z, Li Q (2012) Optimization of foam-filled bitubal structures for crashworthiness criteria. *Mater Des* 38:99–109
3. Rejeesh CR, Saju KK (2017) Methods and materials for reducing flammability behaviour of coir fibre based composite boards: a review. *Mater Today Proc* 4(9):9399–9407
4. Moudood A, Rahman A, Mohammad H, Hall W, Ochsner A, Francucci G (2018) Environmental effects on the durability and the mechanical performance of flax fiber/bio-epoxy composites. *Composite Part B Eng* 171:284–293
5. Lertloypanyachai P, Thongsang S (2018) Improving the mechanical properties of rubber floor tiles by rock powder particle as filler in natural rubber. *Mater Today Proc* 5(7):14907–14911
6. Barczewski M, Sałasińska K, Szulc J (2019) Application of sunflower husk, hazelnut shell and walnut shell as waste agricultural fillers for epoxy-based composites: a study into mechanical behavior related to structural and rheological properties. *Polym Test* 75:1–11
7. Yan L, Chow N, Jayaraman K (2014) Flax fibre and its composites—a review. *Composite Part B Eng* 56:296–317
8. Barbulée A, Gomina M (2017) Variability of the mechanical properties among flax fiber bundles and strands. *Procedia Eng* 200:487–493
9. Ramesh M (2019) Flax (*Linum usitatissimum* L.) fibre reinforced polymer composite materials: a review on preparation, properties and prospects. *Prog Mater Sci* 102:109–166
10. Mak K, Fam A (2019) Freeze-thaw cycling effect on tensile properties of unidirectional flax fiber reinforced polymers. *Compos Part B Eng* 174:107645
11. Fiore V, Scalici T, Nicoletti F, Vitale G, Prestipino M, Valenza A (2016) A new eco-friendly chemical treatment of natural fibres: effect of sodium bicarbonate on properties of sisal fibre and its epoxy composites. *Compos Part B Eng* 85:150–160

12. Flax Council (2016) Flax Council of Canada. pp. 0–5. <https://flaxcouncil.ca/>. Retrieved 30 Dec 2019
13. Lu MM, Van Vuure AW (2019) Improving moisture durability of flax fibre composites by using non-dry fibres. *Compos Part A Appl Sci Manuf* 123:301–309
14. Chilali A, Assarar M, Zouari W, Kebir H, Ayad R (2018) Analysis of the hydro-mechanical behaviour of flax fibre-reinforced composites: assessment of hygroscopic expansion and its impact on internal stress. *Composite Structures* 206:177–184
15. Baley C (2002) Analysis of the flax fibres tensile behaviour and analysis of the tensile stiffness increase. *Compos Part A Appl Sci Manuf* 33(7):939–948
16. Kejariwal RK, Gowda BSK (2017) Flammability and moisture absorption behavior of sisal-polyester composites. *Mater Today Proc* 4(8):8040–8044
17. Sain M, Park SH, Suhara F, Law S (2004) Flame retardant and mechanical properties of natural fibre—PP composites containing magnesium hydroxide. *Polym Degrad Stab* 83:363–367

TiO₂/PVDF-Based Polymer Nanocomposites and Their Various Characterizations



Sudhanshu Singh , Deepshikha Rathore , Nitesh Singh Rajput , and Umesh Kumar Dwivedi

1 Introduction

TiO₂ (semiconductor material), having a great scope of applications; such as single side, double side dye-sensitized solar cells, painting industries, coatings of various chemicals, and adhesive-based applications, it became a major part of the composite area. Also, it found many applications in paperboard (including paper), plastics/ceramics/printing ink/floor-based coverings/rubber/fabrics/textiles/catalyst bound systems and many more. It shows its existence in nature in rock and mineral sands. It is the ninth primarily component in the layer of the earth. TiO₂ (chemically inert) is a fair, hard inorganic material that is thermally stable, fire retardant, being classified as harmless as per the United Nation Globally Harmonized System of cataloguing and group of chemical (GHS) [1–8].

PVDF is a speciality plastic material in the fluoropolymer. Being polar polymer with excellent chemical, electrical, and mechanical properties, it finds much application in various domains, such as micro/ultrafiltration membranes, electrode-bound-binder in batteries of (lithium) Li-ion, microwave bound transducers, piezo/pyroelectric material and photocatalytic. Compared to other fluoropolymers, it has an easier melt process because of its relatively lesser melting point of around 177 °C, having a low density of 1.78 g/cm³. It is well known that nanoparticles are

S. Singh

Department of Electronics and Communication Engineering, Amity University Rajasthan, Jaipur 303002, India

D. Rathore · U. K. Dwivedi

Department of Physics, Amity University Rajasthan, Jaipur 303002, India

N. S. Rajput (✉)

Department of Mechanical Engineering, Amity University Rajasthan, Jaipur 303002, India
e-mail: niteshthakur72@yahoo.com

usually used to enhance the properties of the polymer by simple blending; the interfacial interaction between polymer and nanoparticles is crucial to the enhancement [9–13].

The innovation of the photolysis of water on the outside of the TiO_2 was launched forty years back of demanding study into the primary compound and substantial process implicated. Lone venerable disagreement is the vigorous configuration of group boundaries of the rutile and anatase polymorphs of TiO_2 .

The maximum wt% of TiO_2 was taken approx. 50% of the total sample weight. Also, the existing research work was done in sophisticated labs, which makes the cost high for making polymeric-based samples for various applications. Apart from this, the composition of PVDF and TiO_2 at room temperature (RT) was less reported with variable temperature and frequency. These gaps are established by the extensive literature review of the research done in the area of polymer with BaTiO_3 and TiO_2 [3–8, 14, 15]. Correlation between the various properties of polymeric films has been established in the current work.

In this work, a study on the composite films of TiO_2 and PVDF were made by melt press process, and crystallographic, thermal, and dielectric properties of these films have been studied.

2 Experimental Procedure

2.1 Films Preparation

Purified TiO_2 powder from Thermo Fisher Scientific (India) and PVDF material from Sigma Aldrich (USA), was used for current experimental work, related to the composite structured films. The purified substance of TiO_2 (variable wt%) is being well mixed in the PVDF powder in mortar and pestle till 1 hour. Followed by, the obtained mixture has been put within stainless steel die, available within hot isostatic press machine. Followed by mixing available samples, were then heated at 200 °C, with pressure 200 kg/cm², maintained for 10 min. Die's temperature cooled down to ambient temp (RT) and then freed up the pressure. The thickness of the composite film was measured 0.5 mm. The rounded indium electrodes (area of 2.0×10^{-3} cm²) were vacuum deposited on one surface of the film, and the other surface indium is vacuum deposited on a larger area.

2.2 XRD Characterization

This measurement was taken to locate the structure-based information in various types of pure and composite films using diffractometer. The XRD patterns of various samples; such as pure PVDF, 40 wt% TiO_2 + PVDF composite film, 0wt% TiO_2 +

PVDF composite film, 60 wt% TiO₂ + PVDF composite film, and pure TiO₂ were taken. The XRD scans were recorded using Anchor Scan Xpert-Pro. In the end, due to fragile behaviour of 60% samples, further work has been carried only on 50% of TiO₂: PVDF.

2.3 Magneto Dielectric Set-Up

The fabricated sample is kept at the origin of the electromagnet and LCR metre finds the electric properties of the fabricated samples. A current of the electromagnet is being varied, which allows the changes in a magnetic field and force on samples. Frequency from 20 Hz to 120 MHz can also experiment in this work.

2.4 Electrical Characterizations

Electrical analysis has been performed on prepared samples using an impedance analyser (MFIA-Zurich Instruments-Switzerland).

3 Results and Discussion

3.1 Variation of a Dielectric Property with Temperature

Figure 1 shows the dielectric performance of polymeric structured composite with respect to the varying temp. From Fig. 1, it is visible that as the temperature rises, and the dielectric constant getting its high values. This is a new kind of finding at varying temperature for different weight percentages of TiO₂: PVDF, unlike the other works, in earlier years. The electron–electron, ion–ion, and ion–electron orientation in the inside of TiO₂ are mainly responsible for such electrical and crystallographic behaviour. At 50%, PVDF and TiO₂ are best optimized. At lesser TiO₂, PVDF and TiO₂ make proper matrix formation, while on increasing TiO₂, space got decreases, to the main variation is due to only TiO₂. PVDF is a conductive polymer, which makes it much suitable for electrical and dielectric applications with TiO₂. Also, PVDF changes its phase from alpha to beta, on increasing the temperature in between the 100–300 °C.

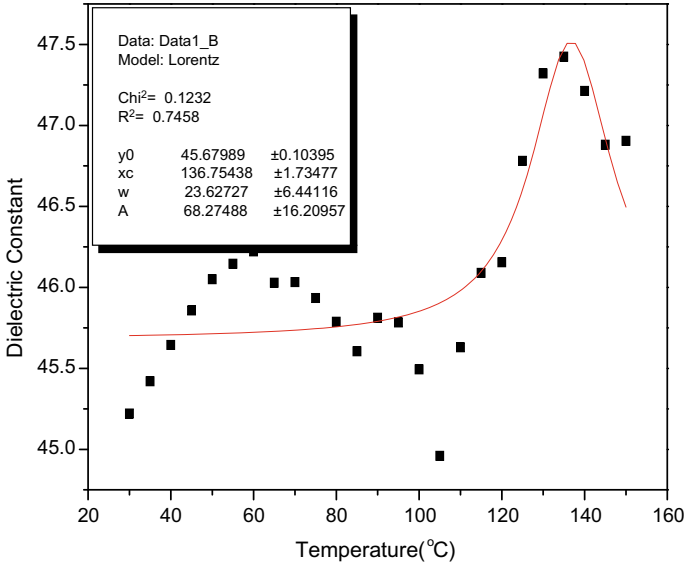


Fig. 1. 50 wt% (TiO₂ + PVDF) temperature versus dielectric constant at 10 kHz

3.2 Variation of Intensity with 2θ

The XRD pattern of pure PVDF, pure TiO₂, and different filler concentration of TiO₂:PVDF composite structured films at ambient temperature are shown in Fig. 2.

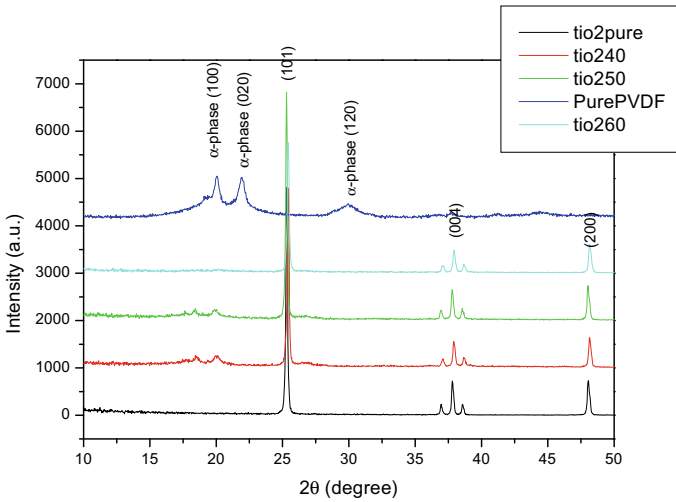


Fig. 2 XRD pattern of different filler concentration of TiO₂

While Fig. 2 shows the (β -phase) rutile phase formation of TiO₂ in all the composition of different filler concentration of TiO₂:PVDF composite without any additional phase at room temperature. X-ray diffraction peaks for planes (101), (004), (200), (100), and (200) at corresponding Bragg angle $2\theta = 25.23, 37.82, 48.06, 53.98$ and 55.08° correlate the formation of rutile structure of TiO₂ in the composite films at room temperature. From Fig. 2, it has been observed that the peak positions are identical for all the different filler concentration composites samples at room temperature, which indicates that there is no significant change in the lattice parameters as also demonstrated in work done by other researchers [2–6]. All of the diffraction peaks at corresponding Bragg angles (2θ) match with the typical facts for a rutile structure (JCPDS No.36-1451) of TiO₂, which establish the indication of PVDF does not affect in the improvement in the orientation of crystal geometry or change in better orientations of TiO₂. It is cleared that null diffraction peak has been observed at $2\theta = 13^\circ$ in the pure TiO₂ and different filler concentration of TiO₂ in PVDF composite films as shown in Fig. 2. The intensity of the peaks hikes along the amplify in filler concentration of titania in structured composite films. This indicates an increased crystallinity.

Figures 3, 4, 5, 6, 7 and 8 show the variation of various properties (capacitance, impedance, resistance, conductance, dissipation factor, and phase angle) of the prepared samples as the temperature increases. These have been done on the frequency at 1 kHz. Increased capacitance values of polymer nanocomposites make it suitable for high energy application. While decreasing phase angle behaviour of polymer nanocomposite makes it suitable for switching behaviour. The increase in

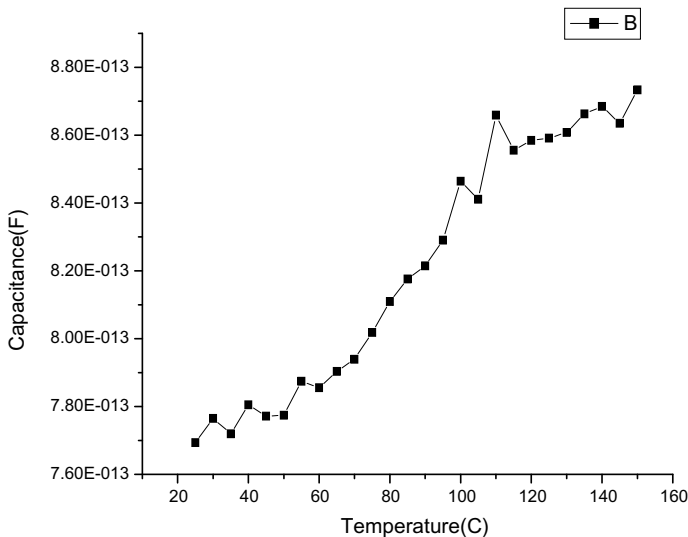


Fig. 3. 50 wt% (TiO₂ + PVDF) temperature versus capacitance at 10 kHz

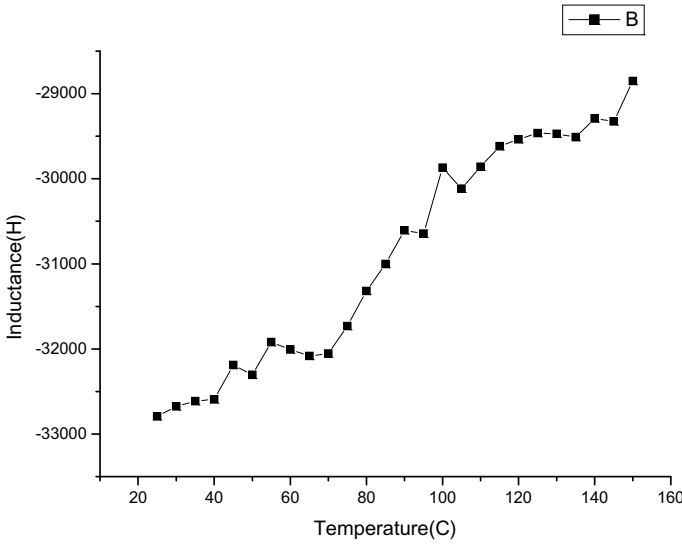


Fig. 4. 50 wt% (TiO₂ + PVDF) temperature versus inductance at 10 kHz

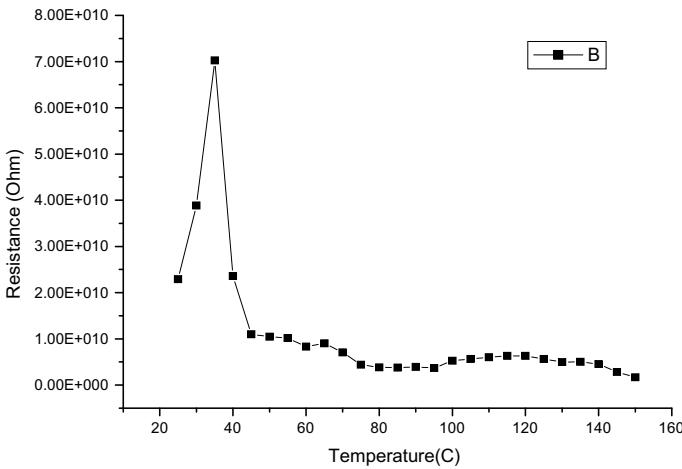


Fig. 5. 50 wt% (TiO₂ + PVDF) temperature versus resistance at 10 kHz

inductive values of polymer nanocomposite makes it suitable for magnetic applications. Decreasing resistance behaviour of polymer nanocomposite makes it suitable for electrical applications. Also, the increase in capacitance plot of polymer nanocomposite makes it suitable for high energy application. Varying dissipative behaviour of polymer nanocomposite makes it suitable for multi-layered capacitive conductors.

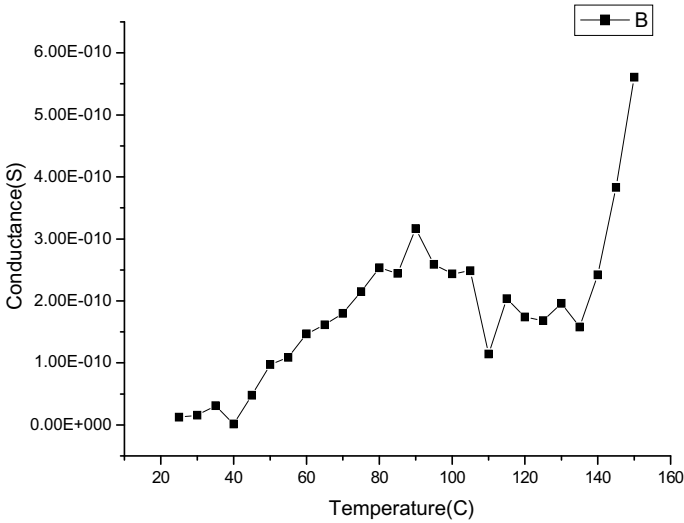


Fig. 6. 50 wt% (TiO₂ + PVDF) temperature versus conductance at 10 kHz

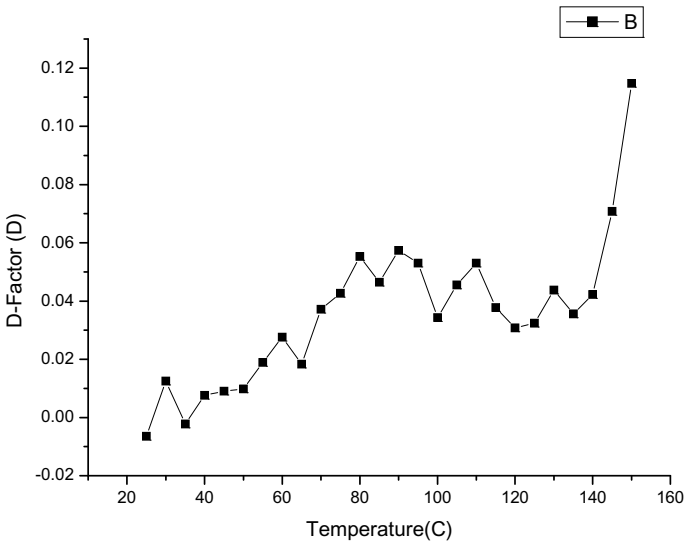


Fig. 7. 50 wt% (TiO₂ + PVDF) temperature versus dissipation factor at 1 kHz

4 Conclusions

In this experimental work, the morphology of TiO₂ nanostructures has been discussed. It is shown that TiO₂ nanostructures have a visible outcome on the electrical property of structured TiO₂: PVDF polymer nanocomposites. The main reason

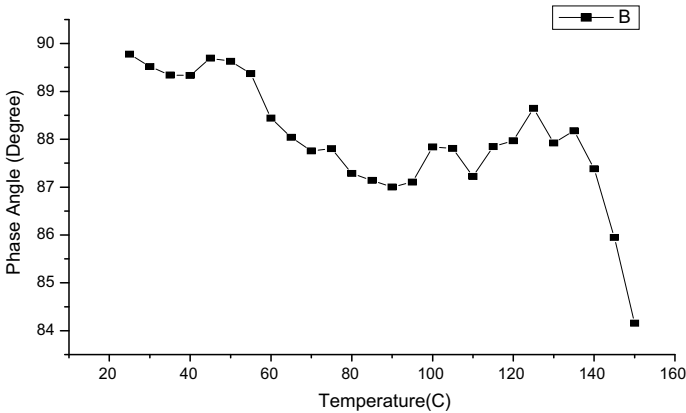


Fig. 8. 50 wt% (TiO₂ + PVDF) temperature versus phase angle at 10 kHz

for taking 50% is due to Dr Williamson effect, which establishes the maximum 50% is the optimized value of weight percentage of TiO₂ in PVDF polymer. After 50%, the fabricated samples became much fragile, and it behaves powder-like film on any surface. High capacitive and dielectric constant is having a quite high temperature and frequency in certain applications, for instance, high storage as well in telecommunication applications. The obtained 2θ values are in the range of 24–50 °C, while the pressure applied to the samples at around 200 kg/cm² and max temperature kept at around 300 °C. While the dielectric constant achieved around 48, the capacitance at approx. 2pF, phase angle near to 88 °C with dissipation factor approaching 0.045. To avoid the repeatability of wt% of TiO₂: PVDF, 50 wt% at room temperature was only considered in the present study. Also, the phase angle plot vs. temperature is describing its suitability for the switching behaviour applications.

Acknowledgements I would like to acknowledge the resource persons at MNIT Jaipur, University of Rajasthan as well as my colleagues at Amity University Rajasthan Jaipur for all characterizations and helping me.

References

1. Diebold U (2003) Structure and properties of TiO₂ surfaces: a brief review. *Appl Phys A* 76(5):681–687. <https://doi.org/10.1007/s00339-002-2004-5>
2. Gan WC, Abd Majid WH (2014) Effect of TiO₂ on the enhanced pyroelectric activity of PVDF composite. *Smart Mater Struct* 23(4):045026. <https://doi.org/10.1088/0964-1726/23/4/045026/meta>
3. Kumar N (2003) Ferroelectric polarization switching in KNO₃:PVDF films. *J Phys D: Appl Phys* 36:1308–1313. <https://doi.org/10.1088/0022-3727/36/11/311/meta>
4. Nath R (2004) Ferroelectric phase stability studies in potassium nitrate: polyvinylidene fluoride composite films. *J Appl Phys* 97(2):024105. <https://doi.org/10.1063/1.1821642>

5. Shi H (2013) Titanium dioxide nanoparticles: a review of current toxicological data. Part Fibre Toxicol 10(15). <https://doi.org/10.1186/1743-8977-10-15>
6. Li J, Cai C (2010) The preparation and tribological properties of PVDF/TiO₂ nanocomposites. Polym Plast Technol Eng 49(7):643–647. <https://doi.org/10.1080/03602551003664636>
7. Morán-Pineda M (2005) Physical properties of TiO₂ prepared by sol-gel under different pH conditions for photocatalysis. Superficies Vacío 18(1):46–49. [smcsyv/supyvac/18_1/SV1814605](https://doi.org/10.1016/S0950-4230(05)00018-1)
8. Wang JC (2012) Preparation and properties of poly(vinylidene fluoride) nanocomposites blended with graphene oxide coated silica Hybrids. Express Polym Lett 6(4):299–307. <https://doi.org/10.3144/expresspolymlett.2012.33>
9. Prasad K, Prasad A, Chandra KP, Kulkarni AR (2010) Electrical conduction in 0–3 BaTiO₃/PVDF composites. Integr Ferroelectr Int J 117(1):55–67. <https://doi.org/10.1080/10584587.2010.489425>
10. Li YC (2011) Dielectric properties of binary polyvinylidene fluoride/barium titanate nanocomposites and their nanographite doped hybrids. Express Polym Lett 5(6):526–534. <https://doi.org/10.3144/expresspolymlett.2011.51>
11. Bauk S (2011) Application of TiO₂ nanoparticles for obtaining self-decontaminating smart textiles. Sci Tech Rev 61(3–4):63–72
12. Iwagoshi J (2014) A study of vapor deposited PVDF/TiO₂ nanoparticle films by XPS. Surf Sci Spectra 21(10). <https://doi.org/10.1116/11.20130902>
13. Nayandeep Mishra KK, Nishad VR, Mehto DR, Pandey RK (2018) Unstrained PbSe/CdSe core shell nanostructures for broad band absorber and narrow band IR emitters. J Mater Sci: Mater Electron 29(12):10214–10221. <https://doi.org/10.1007/s10854-018-9072-6>
14. Kumar S, Hong H, Choi W, Akhtar I, Rehmanb MA, Seo Y (2019) Acrylate-assisted fractal nanostructured polymer dispersed liquid crystal droplet based vibrant colored smart-windows. RSC Adv 9(22):12645–12655. <https://doi.org/10.1039/C9RA00729F>
15. Singh S, Dey SS, Singh S, Kumar N (2017) Preparation and characterization of Barium Titanate composite film. Mater Today: Proc 4(2):3300–3307. <https://doi.org/10.1016/j.matpr.2017.02.216>

Fault Detection in Bevel Gear Using Condition Indicators



Mahendra Singh Raghav, Rahul Tiwari, and Ram Bihari Sharma

1 Introduction

Condition-based maintenance plays a vital role in minimizing unplanned downtime of machinery and preventing serious accidents in industrial companies. The most widely used technique, for fault detection in gearboxes, is vibration analysis. The vibration signals are measured using an accelerometer. The conventional techniques used for processing measured data are divided into three domains, viz., frequency domain, time domain and time–frequency domain. In this paper, condition indicators based on time-domain signals are used for diagnosing faults in bevel gear.

The bevel gear is the main components of the power transmission system in a rotorcraft. An enormous amount of research work has been carried out on condition monitoring of different types of gearboxes. However, a minimal amount of research work is available on condition monitoring of bevel gears. Statistical indicators are very promising tools for diagnosis of faults in gears [1–3]. Ozturk et al. [4] claimed that root-mean-square (RMS), peak to peak, kurtosis, crest factor and cepstrum analysis could expose extremely severe faults only. Zhao et al. [5] extracted 252 fault features for classification of fault in gear with a different level of severity of pitting. Dempsey et al. [6] used FM4 and NA4 for detecting natural gear pitting, while Lin et al. [7] proposed a parameter grounded on residual error signal called the fault growth parameter (FGP). Elasha et al. [8] in addition to RMS, Kurtosis and FM4 also applied to envelop and Spectral Kurtosis (SK) for detecting pitting phenomenon

M. S. Raghav (✉) · R. Tiwari · R. B. Sharma
Automobile Engineering Department, Rustamji Institute of Technology, BSF Academy Tekanpur,
Gwalior, Madhya Pradesh 475005, India
e-mail: msraghav@outlook.com

R. Tiwari
e-mail: rt74326@gmail.com

R. B. Sharma
e-mail: ram.rbsharma@gmail.com

in worm gear and found that pitting in worm gear can be easily detected using FM4 and SK. Combet et al. [9] also applied SK to detect pitting at an early stage. Kundu et al. [10] proposed a correlation coefficient-based fault detection, and the correlation coefficient of residual signal (CCR) of faulty gear was compared with CCR of healthy gear. Ahmed et al. [11] calculated RMS, crest factor and kurtosis over a multiple-pulse individually rescaled-time synchronous averaging (MIR-TSA) signal. They claimed the fault detection capability of RMS was enhanced. Wang et al. [12] presented the instantaneous time–frequency spectrum constructed by local mean decomposition. They also proposed the energy dispersion ratio as a new parameter which is sensitive to deterioration scenarios of low-speed helical gearboxes.

In the present work, statistical parameters are applied on vibration signals to identify faults in bevel gear. Five statistical indicators, i.e., RMS, crest factor, kurtosis, peak to peak and skewness, have been implemented on the signal acquired from the bevel gearbox.

2 Statistical Indicators

The statistical parameters used in this study are described as follows:

(i) **RMS:** It shows the energy and amplitude of the vibration signal in the time domain. The RMS value can be obtained by calculating the summation of the squares of the signal samples, and then the square root of the average of the sum [13], and it is expressed as

$$\text{RMS} = \sqrt{\frac{1}{N} \left[\sum_{i=1}^N (x_i)^2 \right]} \quad (1)$$

where x_i is the i th sample of the signal and N is the total number of samples.

(ii) **Crest Factor:** The ratio of the magnitude of the peak value of the signal to RMS value of the signal is called the crest factor [13] and is given by

$$\text{CF} = \frac{x_{0-pk}}{\text{rms}_x} \quad (2)$$

where pk is the sample for the peak value of the signal and x_{0-pk} is the magnitude of the peak value of x at pk . Crest factor has no unit.

(iii) **Kurtosis:** Kurtosis can be defined as the fourth-order normalized moment of a signal. It gives a measurement of significant peaks of a signal, i.e., the number and amplitude of peaks existent in the signal [13, 14]. It is given by

$$K = \frac{N \sum_i^N (x_i - \bar{x})^4}{\left(\sum_i^N (x_i - \bar{x})^2\right)^2} \tag{3}$$

The kurtosis value of a Gaussian-like signal is close to 3. A gearbox in healthy condition is associated with the Gaussian distribution of samples of the signal.

(iv) **Skewness:** Skewness is the third statistical moment, and it is a measure of the asymmetry of the probability density function of the samples of the signal [13]. The following equation can express it:

$$s = \frac{n}{(n - 1)(n - 2)} \sum \left(\frac{x_i - \bar{x}}{s}\right)^3 \tag{4}$$

(v) **Peak to peak:** This statistical parameter can be defined as the difference between maximum and minimum amplitudes [13]. It may be given as follows:

$$p2p = x_{\max} - x_{\min} \tag{5}$$

3 Experimental Setup and Data Acquisition

The experimental study was conducted on machine fault simulator, as shown in Fig. 1. The test setup includes 1HP AC motor, a single-stage straight bevel gearbox, rotor shaft and motor controller. AC motor with a maximum speed of 3600 rpm is

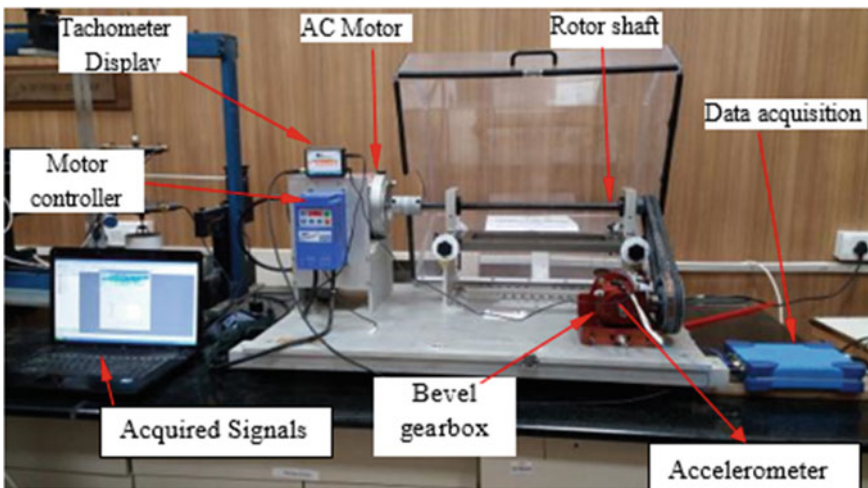


Fig. 1 Experimental setup and data acquisition system

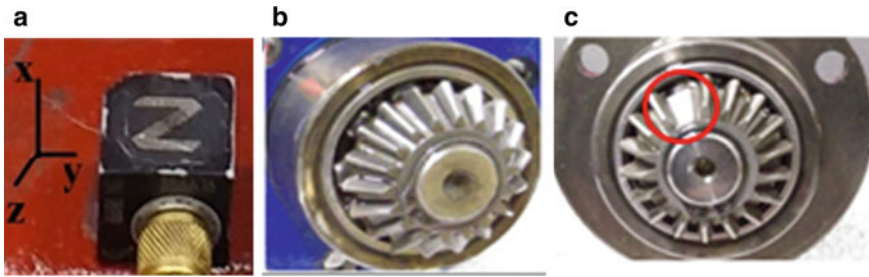


Fig. 2 a Zoomed view of the accelerometer, b healthy bevel gear and c missing tooth bevel gear

Table 1 Specifications of a gearbox

Gear ratio	1.5:1
Pitch angle (gear)	56°19'
Pitch angle (pinion)	33°41'
Pressure angle for gear and pinion	20°
Number of teeth in pinion	18
Number of teeth in a gear	27

connected to a rotor shaft. The input shaft of the bevel gearbox is connected to a rotor shaft via a belt drive to reduce the effect of vibration of an electric motor on the gearbox. An ICP-type triaxial accelerometer, with a range of 0.5 Hz to 5 kHz, is mounted on a housing of the gearbox as shown in Fig. 1. Figure 2a shows the enlarged view of accelerometer, and Fig. 2b, c shows the healthy and faulty bevel gear. An OROS OR34 data acquisition system with a maximum sampling rate of 52 k samples/s is used to acquire data from the sensor. The acquired data is recorded and processed using NVGate. The specifications of gears are mentioned in Table 1.

The tests were conducted at a constant input shaft speed of 420 rpm. The motor controller, as shown in Fig. 1, is used to run the motor at a constant speed of 420 rpm. The vibration signals were recorded for a healthy gear at 0 to 4 N load. The load is applied on gearbox using a magnetic controller attached to the output shaft of the gearbox. The vibration signals were recorded in all three directions, but signals from x-direction, i.e., horizontal radial direction, are used. Five samples of signals for a duration of 1.6 s, each with a sampling rate of 6400 samples, were recorded at all loading conditions. The tests were repeated with missing tooth gear also.

4 Results and Discussion

Figures 3 and 4 show the vibration signal of healthy bevel gear and gear with a missing tooth at 0–4 N load. The amplitude for the bevel gear with a missing tooth, as shown in Fig. 4, is higher than the amplitude for healthy gear at all load conditions.

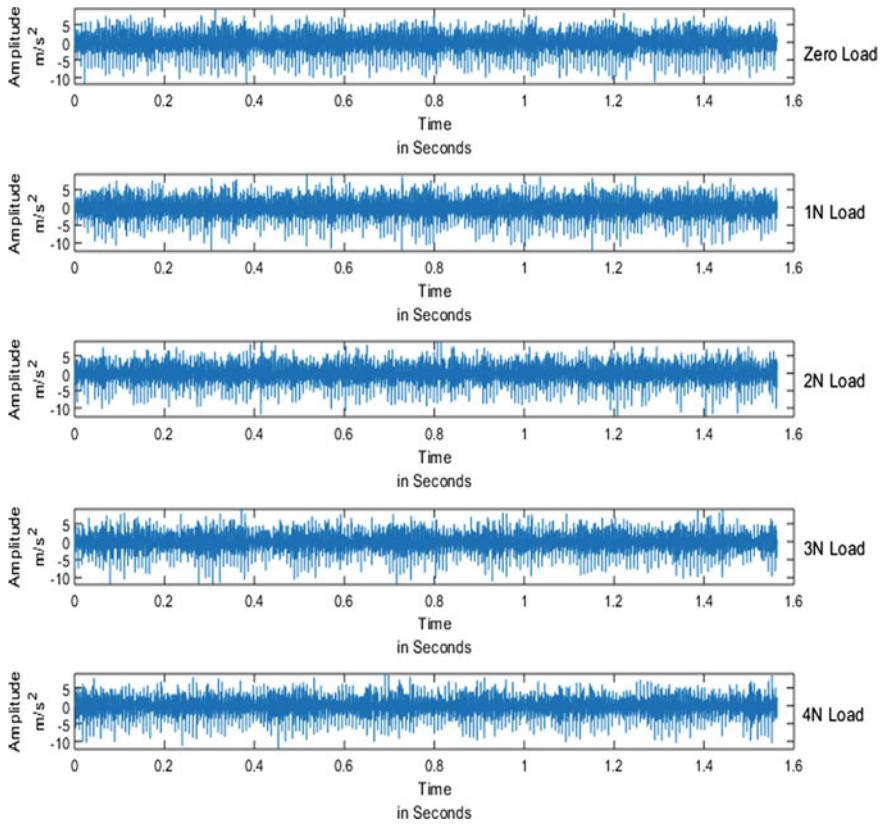


Fig. 3 Healthy bevel gear vibration signal at a constant speed of 420 rpm

It can be easily observed that the load has little effect on the amplitude of the vibration signal. The time-domain signals are converted in the frequency domain using fast Fourier transform (FFT). Figures 5 and 6 show the FFT of vibration signals of missing tooth bevel gear and healthy bevel gear, respectively. The gear mesh frequency (GMF) and its harmonics are visible in all cases. The amplitude of GMF and its harmonics do not show any increasing trend with the increase in load. However, in case of missing tooth gear, the amplitude of GMF and its harmonics are higher at all load conditions than that of healthy gear. It can be observed that the amplitude of sidebands is also higher in the case of missing tooth gear.

The statistical indicators, i.e., RMS, crest factor, peak to peak, kurtosis and skewness, were calculated over the acquired vibration signals, and the values obtained are shown in Fig. 7. The energy of the vibration signal of missing tooth gear is higher than healthy gear at all load condition, as indicated by RMS. The value of the crest factor for missing tooth gear is varying from 12 to 16. When the value of the crest factor exceeds 6, it indicates the possibility of fault in gear [15]. The kurtosis value

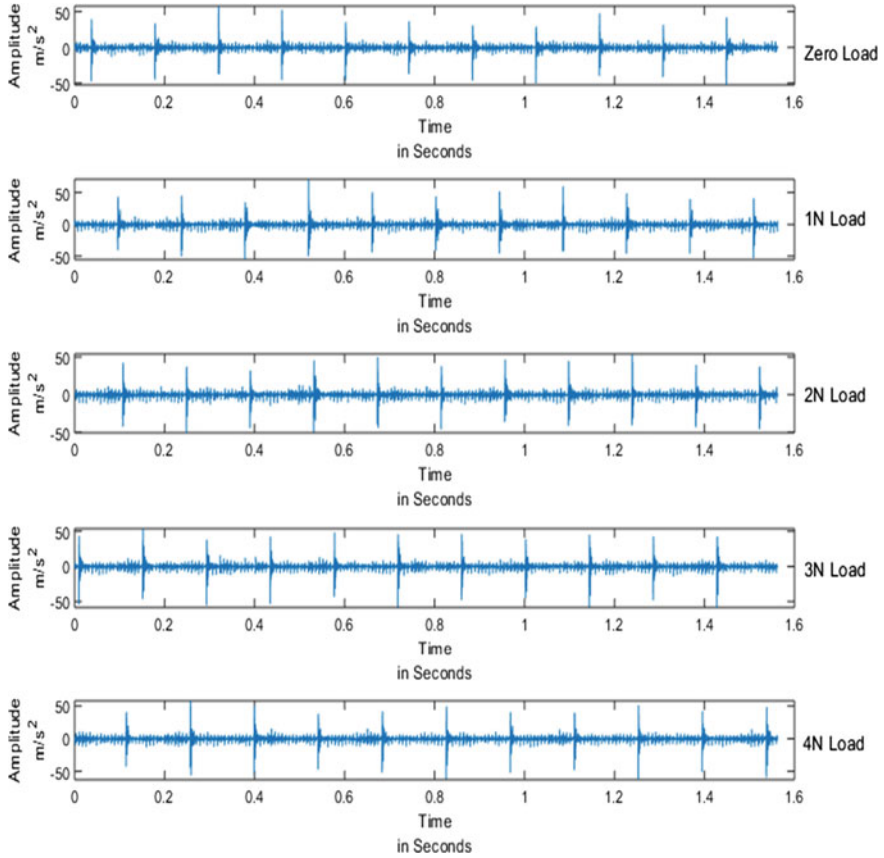


Fig. 4 Bevel gear vibration signal with a missing tooth at a constant speed of 420 rpm

of healthy gear vibration signal is around 3 for all load condition which is a confirmation of a healthy state [14]. However, in the case of missing tooth gear, kurtosis value lies in the range of 35–45. Kurtosis value of higher than 3 is a clear indication of faulty gear. Peak to peak also suggests that the value of peaks is higher at all load conditions due to the presence of missing tooth fault in the bevel gear. These parameters identify the missing tooth gear fault except skewness.

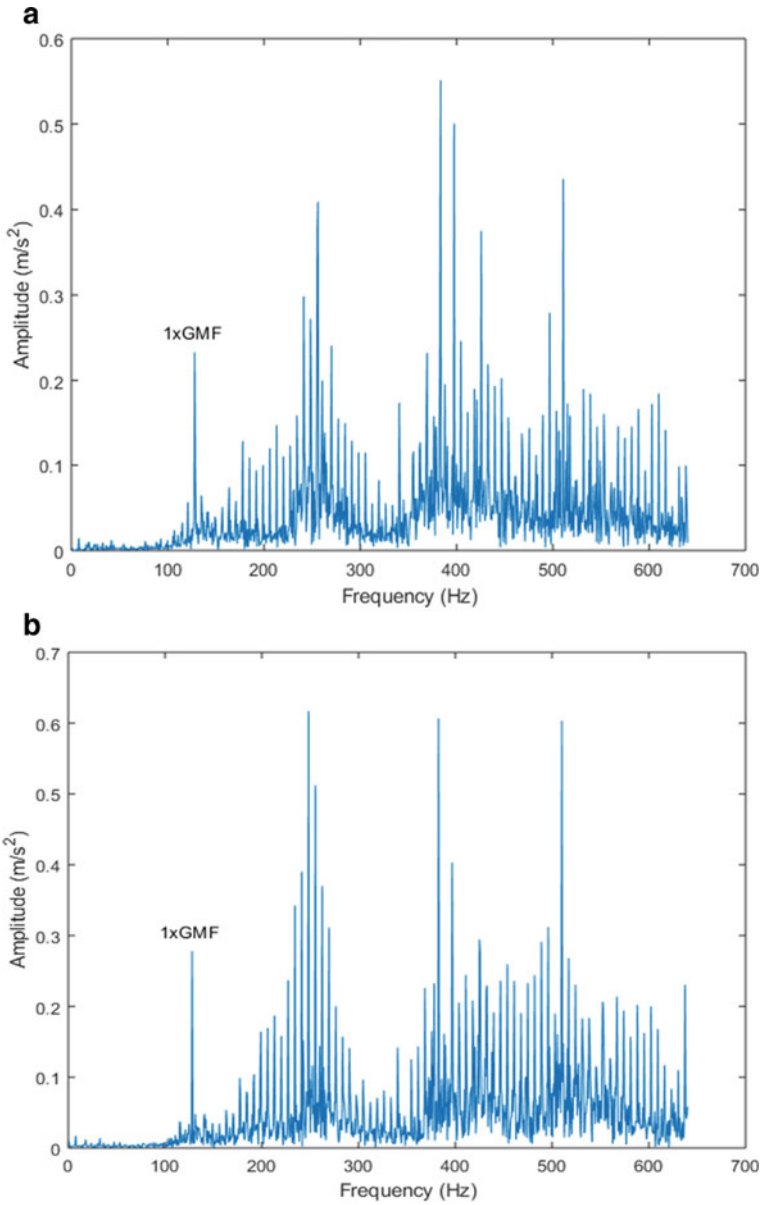


Fig. 5 FFT of missing tooth vibration signal at **a** zero load, **b** 1 N load, **c** 2 N load, **d** 3 N load and **e** 4 N load

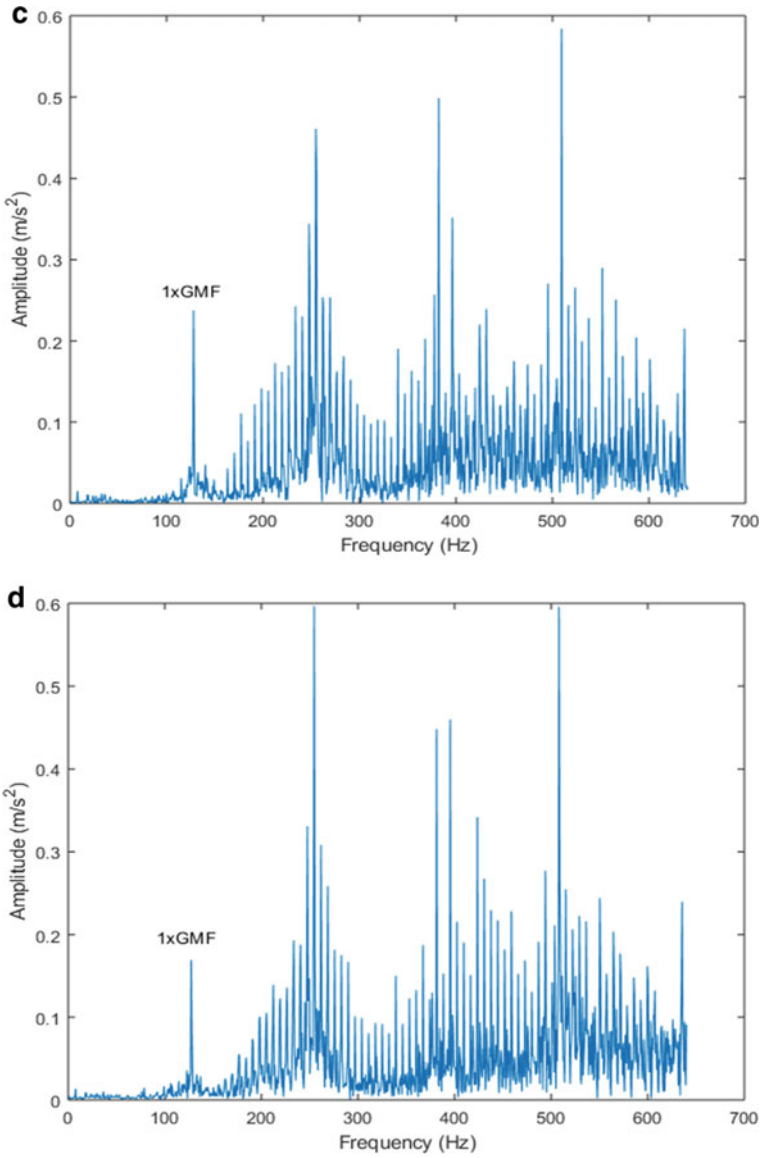


Fig. 5 (continued)

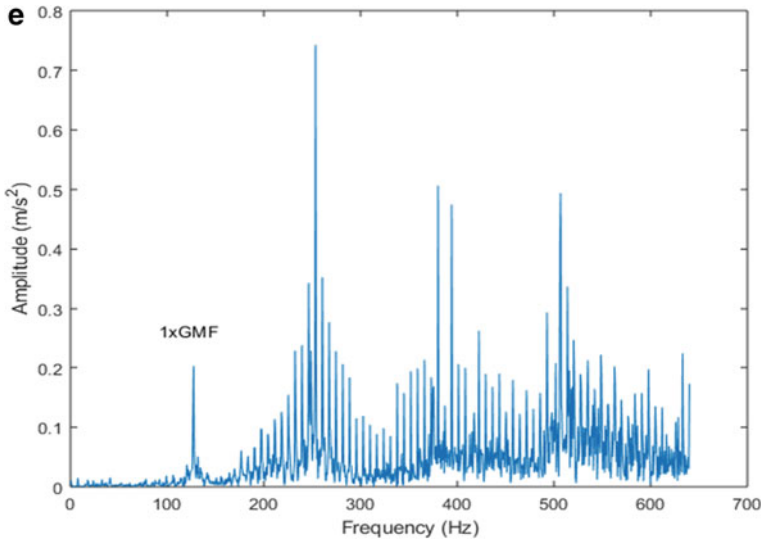


Fig. 5 (continued)

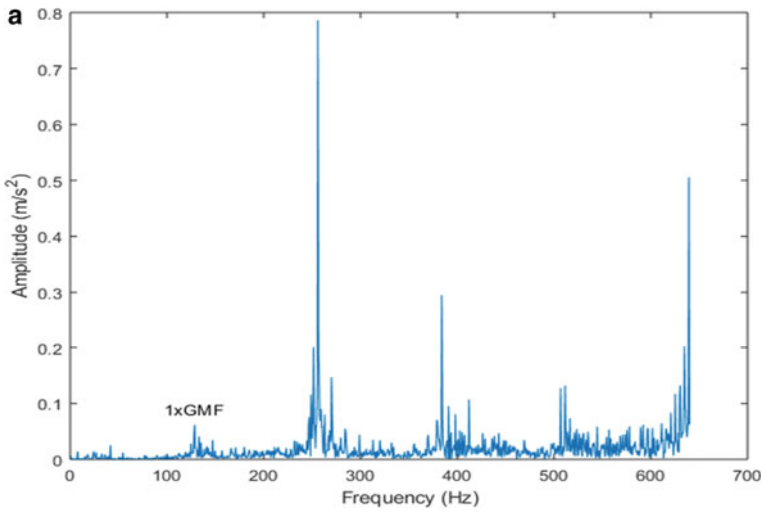


Fig. 6 FFT of healthy gear vibration signal at a zero load, b 1 N load, c 2 N load, d 3 N load and e 4 N load

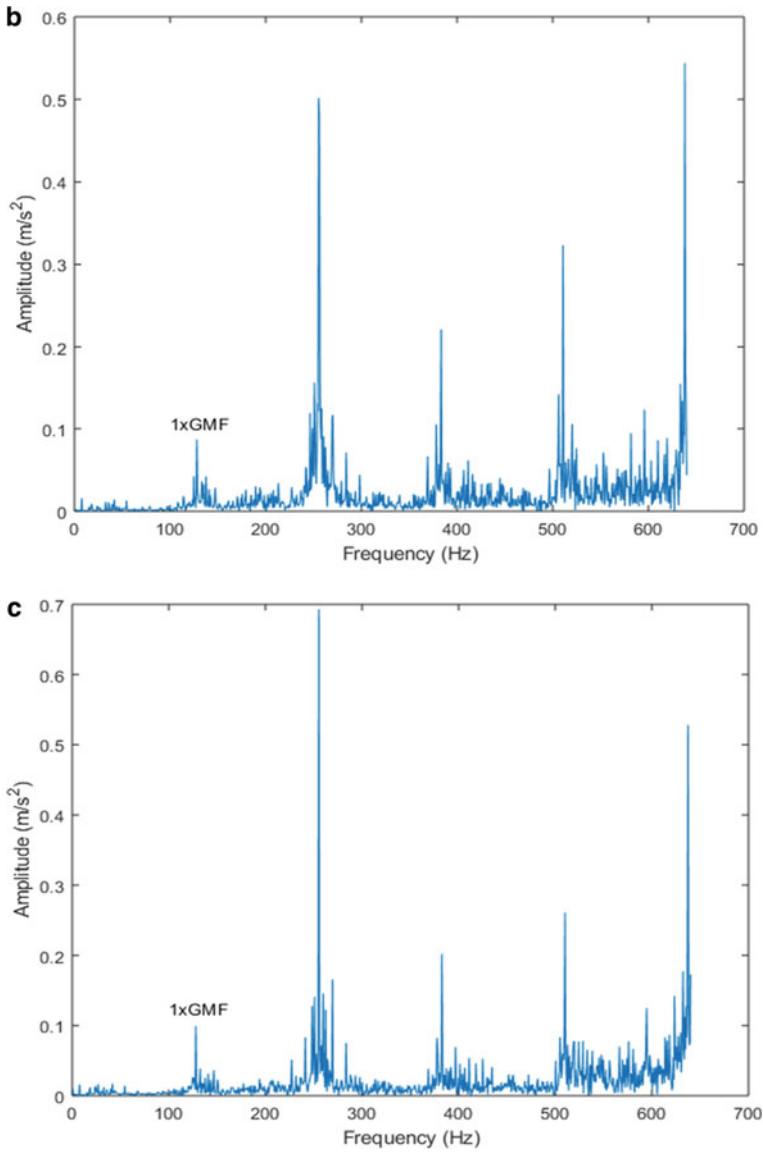


Fig. 6 (continued)

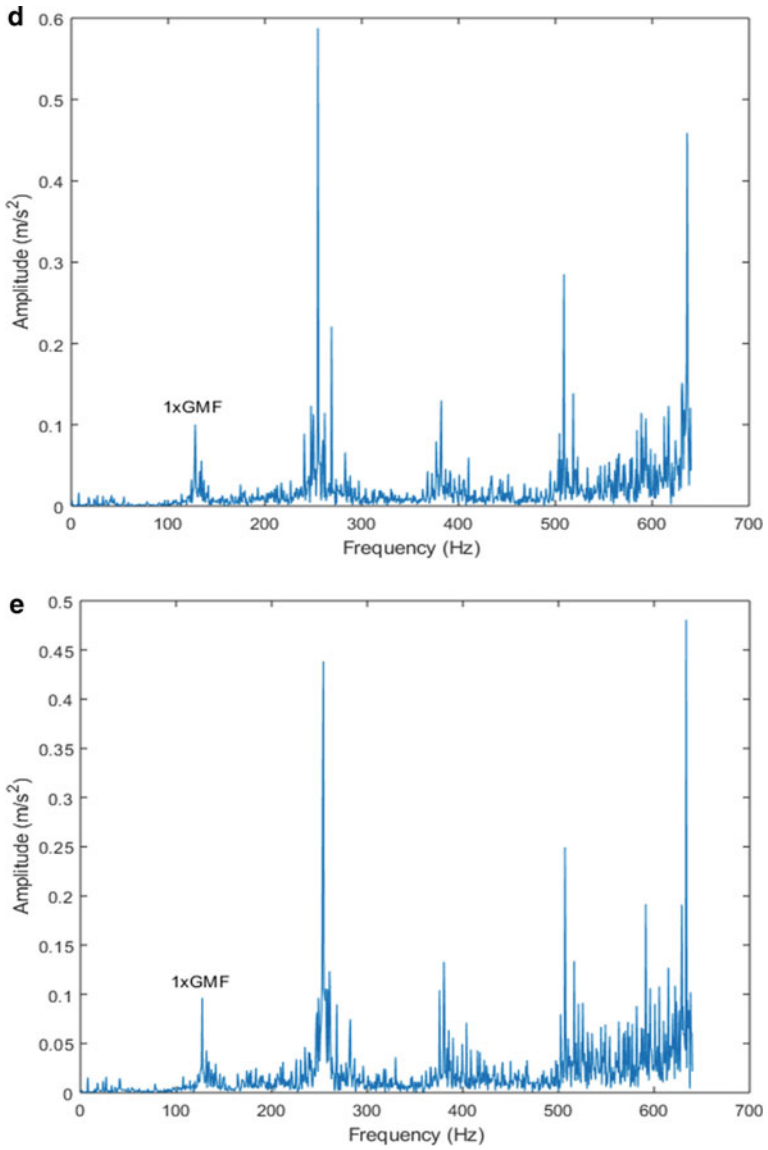


Fig. 6 (continued)

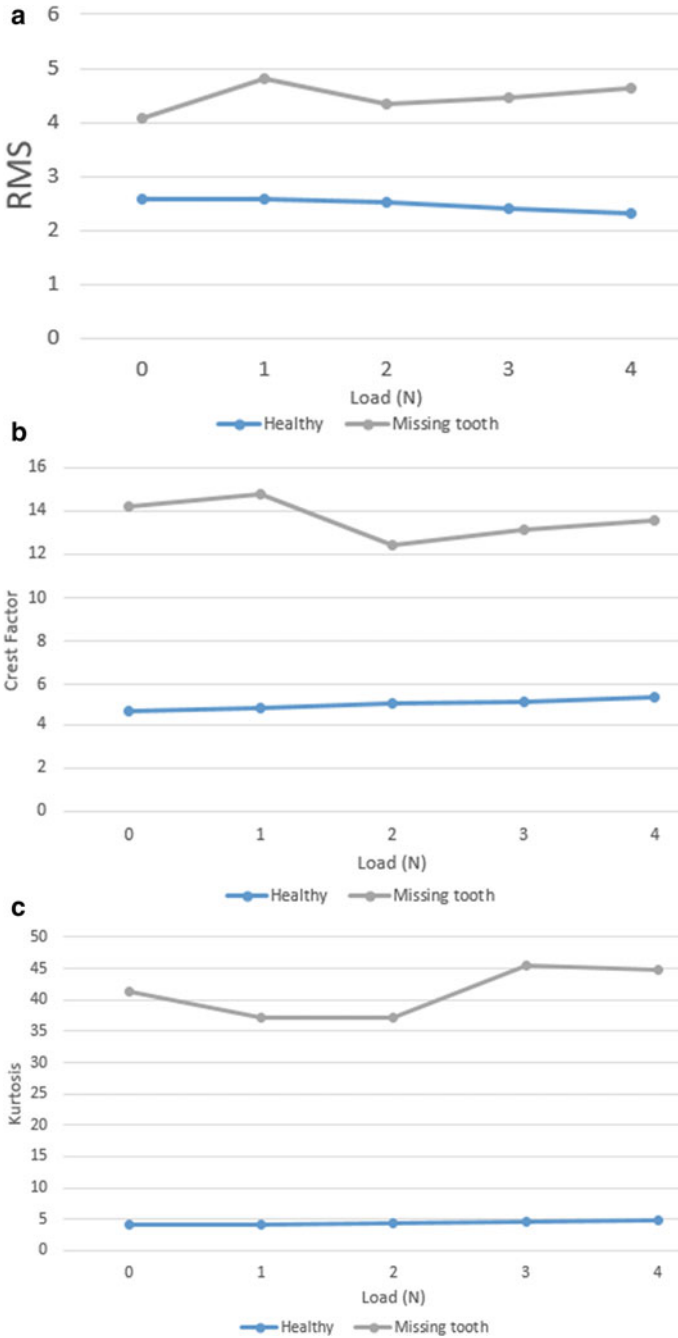


Fig. 7 Statistical parameters: a RMS, b crest factor, c kurtosis, d peak to peak and e skewness

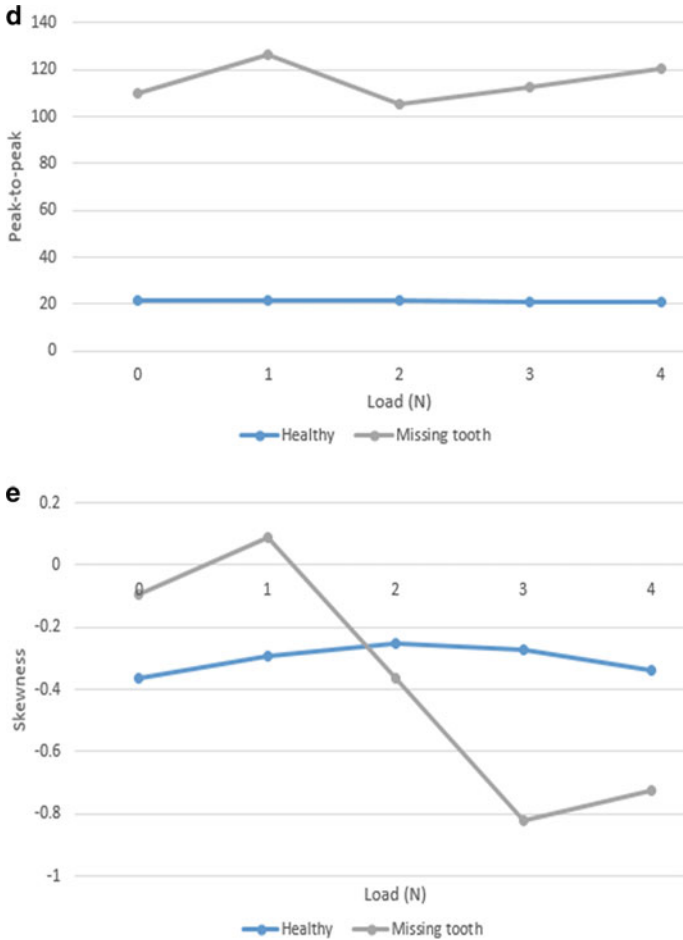


Fig. 7 (continued)

5 Conclusions

In the present work, an experimental study on fault diagnosis of bevel gear is presented. Statistical parameters are used over vibration signals acquired from missing tooth and healthy bevel gear. It is found that missing tooth fault can be easily identified using RMS, kurtosis, crest factor and peak to peak except for skewness.

Acknowledgements The sincere gratitude is expressed to Prof. Anand Parey, Indian Institute of Technology Indore, to allow for experimental investigation on MFS in Solid Mechanics Lab, IIT Indore.

References

1. Decker HJ, Lewicki DG (2003) Spiral bevel pinion crack detection in a helicopter gearbox (No. ARL-TR-2958). National aeronautics and space administration, U.S. Army Research Laboratory, Glenn Research Center, Cleveland, Ohio
2. Zakrajsek JJ, Handschuh RF, Lewicki DG, Decker HJ (1995) Detecting gear tooth fracture in a high contact ratio face gear mesh. <https://ntrs.nasa.gov/archive/nasa/casi.ntrs.nasa.gov/19950012710.pdf>
3. Saravanan N, Cholairajan S, Ramachandran KI (2009) Vibration-based fault diagnosis of spur bevel gear box using fuzzy technique. *Expert Syst Appl* 36(2):3119–3135
4. Ozturk H, Yesilyurt I, Sabuncu M (2010) Detection and advancement monitoring of distributed pitting failure in gears. *J Nondestruct Eval* 29(2):63–73
5. Zhao X, Zuo MJ, Liu Z, Hoseini MR (2013) Diagnosis of artificially created surface damage levels of planet gear teeth using ordinal ranking. *Measurement* 46(1):132–144
6. Dempsey PJ (2003) Integrating oil debris and vibration measurements for intelligent machine health monitoring. ISBN-13:978-1288916009
7. Lin D, Wiseman M, Banjevic D, Jardine AK (2004) An approach to signal processing and condition-based maintenance for gearboxes subject to tooth failure. *Mech Syst Sig Process* 18(5):993–1007
8. Elasha F, Ruiz-Cárcel C, Mba D, Kiat G, Nze I, Yebra G (2014) Pitting detection in worm gearboxes with vibration analysis. *Eng Fail Anal* 42:366–376
9. Combet F, Gelman L (2009) Optimal filtering of gear signals for early damage detection based on the spectral kurtosis. *Mech Syst Sig Process* 23(3):652–668
10. Kundu P, Darpe AK, Kulkarni MS (2019) A correlation coefficient based vibration indicator for detecting natural pitting progression in spur gears. *Mech Syst Sign Process* 129:741–763
11. Ahamed N, Pandya Y, Parey A (2014) Spur gear tooth root crack detection using time synchronous averaging under fluctuating speed. *Measurement* 52:1–11
12. Wang Y, He Z, Xiang J, Zi Y (2012) Application of local mean decomposition to the surveillance and diagnostics of low-speed helical gearbox. *Mech Mach Theory* 47(1):62–73
13. Zhu J, Nostrand T, Spiegel C, Morton B (September 2014) Survey of condition indicators for condition monitoring systems. In: Annual conference of the prognostics and health management society, vol 5, pp 1–13
14. Decker HJ (2002) Crack detection for aerospace quality spur gears (No. ARL-TR-2682). Army Research Lab Cleveland OH*
15. Lebold M, McClintic K, Campbell R, Byington C, Maynard K (2000) Review of vibration analysis methods for gearbox diagnostics and prognostics. In: Proceedings of the 54th meeting of the society for machinery failure prevention technology, May 1–4, 2000, pp 623–634

A Review on Forward and Inverse Kinematics of Classical Serial Manipulators



Randheer Singh, Vikas Kukshal, and Vinod Singh Yadav

1 Introduction

To develop mechanisms that are dexterous and intelligent is a dream of the human race since the dawn of human civilization. Since the beginning of civic establishments, many efforts are focused on creating machines that mimic the human body. This ambition is now turning out as our world's striking reality. The word robot is derived from "Robota" that implies forced worker in the Slav language. The collaboration of robots with humans was envisioned in 1940, by a writer Issac Asimov in his novel "Runaround." Three laws in his novel governed the interaction of robots with humans [1, 2]. Designers and researchers have divided the robot's development and denoted advancement as per robot generations. The generation of robots before the year 1980 is first, from 1980–1990 are second, from 1990 to 2000 are third and beyond 2000 are fourth-generation robots [3]. The broad classification of robots is shown in "Fig. 1" [3–6]. Among all the robots, the humanoid is the most researched and sought-after robot due to its similarity to a human body.

Thus, it can be deployed in human environments easily without involving any modification in the environment. However, robotics is an interdisciplinary field and comprised of mechanical, electrical, electronics, computer science, and IoT to name a few. Though each field has its importance, robot kinematics is the essential step in preparing a mathematical model for the robot. The mathematical model is further needed for the simulations of motion analysis. The study of dynamics is required for determining the torque requirements of the joints. After analyzing the kinematics and dynamics, modeling and design are performed. In the designed model, the actuators are fed with a control algorithm which helps the model to actuate according to the planned motion strategy. Any programming language can be used for developing the

R. Singh (✉) · V. Kukshal · V. S. Yadav

Department of Mechanical Engineering, National Institute of Technology, Uttarakhand, Srinagar (Garhwal), Uttarakhand 246174, India

e-mail: randheer.mechmt18@nituk.ac.in

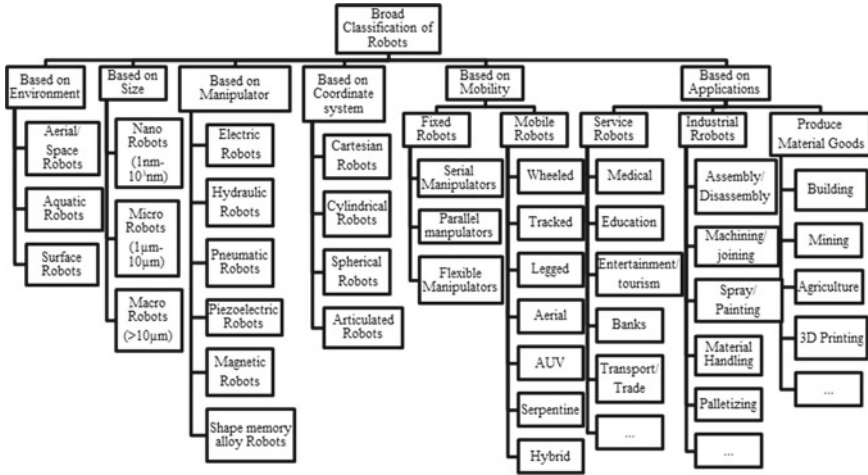


Fig. 1 Broad classification of robots

control algorithm compatible with the hardware system. The sensors and artificial intelligence are needed to make a feedback loop for the automation of the robot. Therefore, it is implied that robotics is a multi-disciplinary field. The basic elements of robots are shown in “Fig. 2.” The anatomy of humans is compared with a humanoid robot in several research papers [7–9].

However, robots are a product of human imagination designed to mimic human motions and hence bear a close resemblance with humans and animals. The industrial robots are a simplified replica of the human hand. Therefore, the studies of

Fig. 2 Elements of robotics

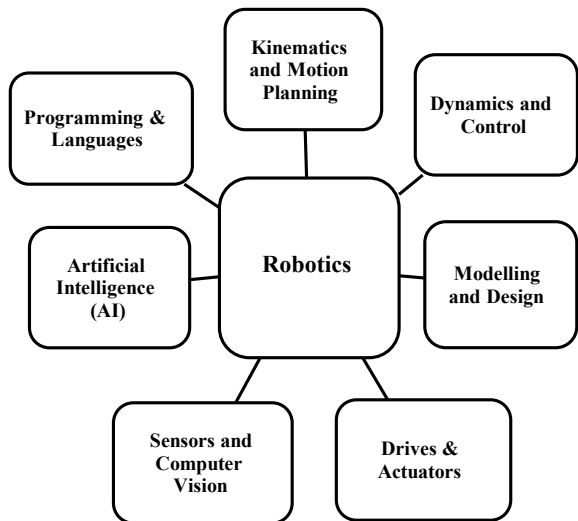


Table 1 Analogy between robots and humans

Robots components	Humans components
Link, joints, wrist, elbow, wrist	Bone/Skeleton, shoulder
End-effector or Gripper	Hand with finger
Sensors	Eye, ear, nose, skin
Drives and actuators	Heart and muscles
Control system and intelligence	Head/Brain

the humanoid robots are based on the kinematics of the human body. Similarly, quadrupeds are inspired by animals, and the ornithopters are derived from birds and insects. The basic analogy between robot links and corresponding human parts is presented in Table 1; the comparison of human and robot is based upon kinematic structure.

However, robots are a product of human imagination designed to mimic human motions and hence bear a close resemblance with humans and animals. The industrial robots are a simplified replica of the human hand. Therefore, the study of humanoid robots is based on the kinematics of the human body. Similarly, quadrupeds are inspired by animals, and the ornithopters are derived from birds and insects. The basic analogy between robot links and corresponding human parts is presented in Table 1; the comparison of human and robot is based upon kinematic structure.

2 Kinematics

Kinematics deals with the study of the motion of a particle or an object, without considering the cause of that motion. Mathematically, it deals with position and its higher derivatives. To study position and its derivatives, the position must first be defined with a suitable reference coordinate system. This is accomplished by defining the position and orientation of the link and joint. In robotics, this description is defined in three mutually perpendicular planes known as the sagittal, transverse and frontal plane. The sagittal plane divides a humanoid robot into two symmetrical parts. The frontal plane is in the $Y-Z$ plane, and similarly, transverse plane is in $X-Y$ plane [9]. A number of humanoid robots are designed for research and development purpose. Comparison based on weight, height and degrees of freedom of some most advanced humanoid robots across the globe is presented in Table 2 [10–14]. Kinematic structure of bipedal robots is most prone to instability due to the height of the center of gravity from the ground. During walking, the instability increases and the dynamics become even more complicated. The kinematic structure, including degrees of freedom, height and weight of the links, is the most important feature in the design process of the robot.

Table 2 Comparison of the world's most advanced humanoid robots

Name	Creators/Year	Weight (Kg)	Height (cm)	Degree of freedom
Asimo	Honda/2000	54	130	57
Atlas	Boston Dynamics/2013	86	170	19
Valkyrie	NASA/2013	125	190	44
NAO	Softbank Robotics/2008	4.5	57	25
Sony Qrio	Sony/2003	7.3	60	38
HUBO 2 (KHR-4)	KAIST/2008	45	125	41
HRP-4	Kawada Industries/2010	39	151	34
HOAP-2	Fujitsu Automation/2003	6.8	48	25
Wabian-2R	Waseda university/2006	64	1500	41

2.1 Kinematics Description

In the study of humanoid robots, the most important concern is the location of different parts in the space, more specifically the position and the orientation. In order to describe these two quantities, a frame or a coordinate system is assigned to each link. Further, a relation is defined among all these frames with respect to the base frame [15]. This relation between frames can be defined in a number of ways [16, 17], though the D-H notions have become almost a standard way in the books and research papers on robots [18]. Hayati pointed out that when two consecutive axes are parallel or near parallel, then the DH model becomes singular for that particular configuration [16, 17, 19]. However, for theoretical modeling, the D-H model is still preferred by most of the researchers for serial-chain manipulators. There are two versions of the D-H model, namely the classical DH model and the modified DH model. The later has a few variants, as discussed by Saha et al. [20]. The comparisons between classical and modified D-H models are shown in Table 3 [18, 21, 22].

The two variants are differentiated in terms of the assigned reference frames as discussed by Reddy et al. [21], and a decent comparison of both the variants is presented by Granja et al. [22]. In the classical convention, $Z(i - 1)$ axis is aligned with the i (th) joint axis, whereas in modified conventions, Z_i axis aligned with the i (th) joint axis. This difference in axes alignment creates a different homogeneous transformation for both the conventions, and transformation matrices are shown in Fig. 3a, b [21, 22].

The difference in homogeneous transformation matrix gives different D-H parameters for both the notations. Although both the notation provide the same forward kinematic model in spite of having different notations and D-H table values. However, choosing one between both notations solely depends on the convenience of the user.

Table 3 Comparison between modified and classical D-H models

D-H parameter	Classical convention	Modified convention
Joint axis	Z_{i-1} is for i axis	Z_i is for i axis
Link length (a_i)	The distance from O_i to the intersection of the Z_{i-1} and X_i axes along the X_i axis	The distance from Z_i to Z_{i+1} measured along X_i
Twist angle (α_i)	The angle from the Z_{i-1} axis to the Z_i axis about the X_i axis	The angle between Z_i to Z_{i+1} measured about X_i
Joint offset (d_i)	The distance from the origin of $(i - 1)$ frame to the intersection of Z_{i-1} with the X_i axis along Z_{i-1} axis	The distance from X_{i-1} to X_i measure along Z_i
Joint angle (θ_i)	The angle between X_{i-1} and X_i along Z_{i-1}	The angle between X_{i-1} to X_i along Z_i

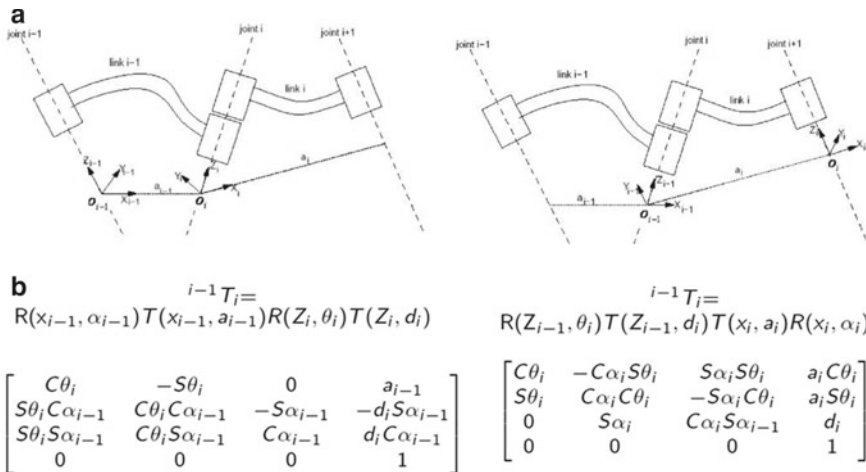


Fig. 3 Comparison of **a** modified D-H and **b** classical D-H and their corresponding homogeneous transformation matrices

2.2 Forward Kinematics

The forward kinematics for a serial-chain manipulator relates the position and orientation of two links when the link parameters and angular positions are already known. Forward kinematics is usually calculated to know the end-effector position and orientation with respect to the base link [6, 15, 23]. Forward kinematics is useful for the calculation of the center of the mass of the entire robot body, which is further used to define the current location of the robot to avoid a collision. Hence, forward kinematics is essential for developing the simulation algorithms of the manipulator [5]. Denavit–Hartenberg, a product of exponential methods, trigonometric method, cyclic coordinate descent method and dual-quaternion method are the most popular for the

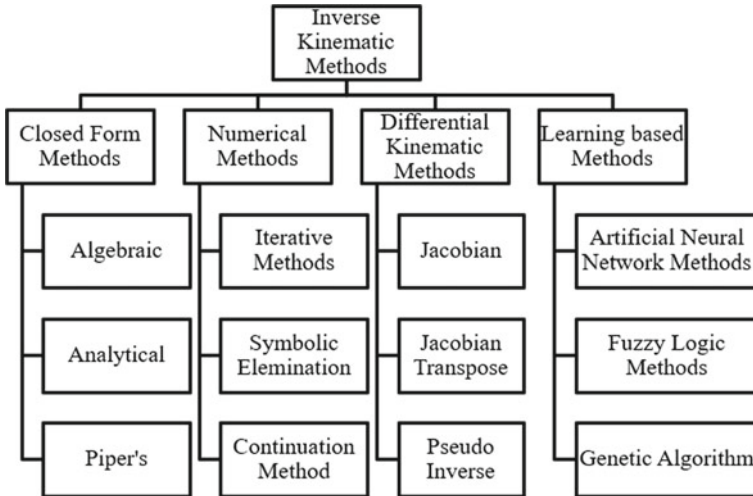


Fig. 4 Broad classification of inverse kinematic methods

formulation of forward kinematics of the serial-chain manipulators. Though D-H method is a consistent and most concise method of all, it has some limitations [24]. However, neural network estimation, quasi-closed solution, Taylor series approximation and support vector regression are used for the parallel manipulator robots. Neural network method is also the most suitable method to develop the forward kinematics in case of cable-driven robots [25–29].

2.3 Inverse Kinematics

Inverse kinematics is just the inverse process of the forward kinematics as it requires the position and orientation of the links as input and the angular parameters required to cause that particular position and orientation are to be determined. However, the geometric link parameter data similar to forward kinematics is to be provided [23]. This statement is specific to serial-chain manipulators which is the case for most of the humanoid robots. The inverse kinematic methods are divided into two categories, namely closed-form solutions and numerical solutions. All the inverse kinematic methods are expressed in “Fig. 4” [23].

2.4 Closed-Form Solutions

A closed-form solution method is based on an analytic expression or any polynomial having a degree less than four. This form of a solution takes advantage of

robot specific geometry to formulate the mathematical model. It is quite suitable and concise for simpler geometrical manipulators having simpler geometries. In the case of serial manipulators having higher degrees of freedom, closed-form kinematic solutions might not even exist. However, serial manipulators having six or more degree-of-freedom are not always solvable. In a particular case, the serial manipulators having six degrees of freedom are solved using a closed-form solution. The necessary conditions for this particular case are as follows [6, 15, 20, 23]:

1. Any three consecutive revolute joint axes intersect at a common point, as in a spherical wrist.
2. Any three consecutive revolute joint axes are parallel.

Closed-form solutions are further classified into two methods, i.e., algebraic methods and geometric methods.

Algebraic Methods Algebraic methods utilize any significant equation containing joint parameters and then reduce the transcendental equations into a single variable. Further, the joint variables are determined by mathematical calculations [30–33].

Geometric Methods In this method, the points on the manipulator are identified, and their position/orientation is expressed in terms of joint variables. This enables to decompose a spatial problem in different planner problem which are then solved by analytical manipulation of the obtained equations. This shows that the analytical and geometrical methods involve almost similar procedures. The only difference is in the approaches used to solve the problem [6, 15, 20, 23]. These methods are highly dependent upon the feasibility of finding the relations. Also, this method is robot specific and cannot be generalized. These methods are novel for almost every robot due to the dissimilarity of their geometry and kinematic configuration [34–41]. The humanoid robots used are mostly the serial-chain manipulators. They are designed such that their closed-form solutions exist. Basically, in the field of humanoids, closed-form solutions are preferred due to the speed of convergence of the solution. Nao by SoftBank Robotics and DARwIn-Op by Robotis are the two case studies among many humanoid robots, which used closed-form solution [42, 43].

2.5 Numerical Solution

When the polynomial obtained in the closed-form solution is having more than four degrees, then the robot cannot have close form solution, and numerical solution can be used to solve the inverse kinematic problem [23]. The basic concept of inverse kinematics involves calculating the error of the target position and position calculated by forward kinematics. The error is minimized through iterations or hit-and-trial methods. When the required accuracy is achieved, the solution stops or otherwise keeps repeating the above procedure of finding the error [5]. Further, these numerical methods are classified as:

Symbolic Elimination Method Symbolic elimination method involves algebraic manipulations to reduce the variables in a nonlinear equation and reduce it to a smaller set of equations. While the root provides one of the joint variables, the other joint variables are calculated from the other linear equations [5].

Continuation Methods In this method, the solution path is followed by a start system with a known solution to a target system whose solutions are to be determined [5].

Iterative Methods In an iterative, an initial guess is required; the speed of this solution highly depends upon the closeness of the initial guess to the actual solution. This process consists of a number of methods, such as Newton–Raphson, Taylor’s series expansion [5].

2.6 *Forward Instantaneous Kinematics*

The relationship between the joint rates and corresponding end-effector’s angular and linear velocities is presented with a matrix, which is called as Jacobian. This matrix is very useful to find singular configurations, analyze redundancies and to determine inverse kinematics algorithm for velocity analysis [20]. When the position of all the members of chain and all joints rates are given, and the end-effector velocity is calculated, then that problem in robotics is referred to as forward instantaneous kinematics. This task is accomplished with the help of a matrix containing joint rates, called Jacobian [5].

2.7 *Inverse Instantaneous Kinematics*

When the position of the all the links of the chain and the velocity of end-effector are given and the joint motion rates are to be determined, this problem in robotics is referred as instantaneous inverse kinematics. This is essential in point-to-point control, smooth trajectory and path generation [5]. This is achieved by computing the inverse of the Jacobian matrix. This also means that the process will require the inversion of the matrix resulting in singularities. A raw comparison between closed-form solutions and numerical solutions is presented in Table 4 [23, 26].

2.8 *Singularities in Kinematics*

The kinematic singularity of a robot can be explained in terms of the gunner shooting a flying target. The job of the gunner is to shoot the flying enemy plane while the pilot flies the plane. While shooting, the gun can have two motions, either azimuth or elevation. Using these two degrees of freedom, the gunner can direct the flow of

Table 4 Comparison of closed-form and numerical methods

Parameters	Closed-form methods	Numerical methods
Accuracy	High	Low
Speed	High	Low
Kinematics structure-specific	Yes	No
Preferred for real-time control	Yes	No
Computes all possible solutions	Yes	No

bullet in any desired direction within the upper hemisphere. When the enemy plane is at any azimuth, but a low elevation, the rate with which the gunner can change the azimuth is high. But when an enemy plane is spotted at one “O” clock and an elevation of 75 degrees, the enemy plane is moving so that it is achieving higher and higher elevations relative to the gunner. Suddenly the enemy plane is passing overhead, and the gunner is no longer able to change the azimuth at a very high rate. At this moment, changing the azimuth does not change the direction of the gun. This is due to the degeneracy of the mechanism, losing an effective degree of freedom. This kind of phenomenon is known as a kinematic singularity of the mechanism [15].

In closed-form and numerical solutions, there may exist multiple solutions. It can also be a case when there exist unbounded solutions, which lead to singularities in the solutions space [6, 15, 20]. Jacobian is a mapping between the vector of joint velocities and vector of end-effector velocities. It is also a function of joint variables. Those configurations for which rank of Jacobian decreases are of special significance in robot kinematics. Such joint configurations are called as singularities [37]. The significance of identifying singularities in design is as follows:

1. To determine the joint configuration for which the solutions may not be achievable from certain directions.
2. To determine the values of bounded end-effector velocities for which there exists an unbounded joint velocity value.
 1. To determine the values of bounded end-effector forces and torques for which there exist an unbounded force and torque values.
 4. To determine the values of point within the work-space of the manipulator.
 5. To determine the values of a point on the work-space of a manipulator.
 6. To determine the values near the singular point for which there exist multiple inverse kinematic solutions.

3 Conclusions

Both classical and modified D-H methods can be used for link description and forward kinematics. But if two consecutive axes are parallel or near parallel, then

D-H methods suffer singularities and alternatives, such as product of exponential method, and triangular methods are introduced for finding the forward kinematics. Further closed-form solutions are best for solving inverse kinematics of simple (DOF-6) serial-chain manipulators. However, closed-form solutions are robot or kinematics structure-specific, so these methods might not be able to find a solution for a higher degree of freedom. Although inverse kinematics for a maximum of six degree of freedom, manipulators can be solved with a closed-form solution using piper's method. Closed-form solutions may also suffer from singularities and do not always find a unique solution but can have multiple solutions. In this situation, the best solution is manually decided among the multiple solutions. There may also be some cases when closed-form methods cannot find a solution at all. Hence, the numerical techniques are used, which are not robot specific. These methods are slower than the closed-form methods because the speed depends upon the closeness of the initial guess to the actual solution. That is the reason, closed-form methods are preferred over other methods for real-time control. The numerical methods lack accuracy when compared to closed-form methods. There are some other methods for solving the inverse kinematics of robots, and these methods are the boon of machine learning and artificial intelligence. These methods use the initial data for training of the neural network. This training is based upon learning from the previous data. Any system can suffer from singularities, so identifying singularities is one of the most important steps in the kinematic analysis. Singularity identification allows determining the joint configurations for which solution might not be attainable from certain directions. It can also be used to determine unbounded joint velocities, unbounded force and torques values which may be infinitely high or undefined.

References

1. Siciliano B, Khatib O (2018). Humanoid robots: historical perspective, overview and scope. *Humanoid Robotics: A Reference*, 1–6. <https://doi.org/10.1007/978-94-007-7194-964-1>
2. Goswami A, Vadakkepat P (eds) (2019) *Humanoid robotics: a reference*. Springer, The Netherlands, pp 55–368
3. Dobra A (2015) General classification of robots. Size criteria. In: 23rd international conference on robotics in Alpe-Adria-Danube Region, IEEE RAAD 2014 - Conference Proceedings. <https://doi.org/10.1109/RAAD.2014.7002249>
4. Khan SS, Khan AS (2017) A brief survey on robotics. *Int J Comput Sci Mob Comput* 6(9):38–45. Retrieved from www.ijcsmc.com
5. Kajita S, Hirukawa H, Harada K, Yokoi K (2014) Springer tracts in advanced robotics 101 introduction to humanoid robotics. <https://doi.org/10.1007/978-3-642-54536-8>
6. Ben-Ari M, Mondada F (2017) Elements of robotics (robots and their applications). *Elements Robot*. <https://doi.org/10.1007/978-3-319-62533-1>
7. Asano Y, Okada K, Inaba M (2017) Design principles of a human mimetic humanoid: humanoid platform to study human intelligence and internal body system. *Sci Robot* 2(13):1–12. <https://doi.org/10.1126/scirobotics.aag0899>
8. Zhang Z, Niu Y, Yan Z, Lin S (2018) Real-time whole-body imitation by humanoid robots and task oriented teleoperation using an analytical mapping method and quantitative evaluation. *Appl Sci (Switzerland)* 8(10). <https://doi.org/10.3390/app8102005>

9. Yamane K, Murai A (2018) A comparative study between humans and humanoid robots. *Humanoid robotics: a reference*, 1–20. <https://doi.org/10.1007/978-94-007-7194-97-1>
10. Oh J, Hanson D, Kim W, Kim J, Park I, Womans E (2006) Design of android type humanoid robot albert HUBO, 1428–1433
11. Park I, Kim J, Lee J, Oh J (2012) Mechanical design of the humanoid robot platform, HUBO, 37–41. <https://doi.org/10.1163/156855307781503781>
12. O’Flaherty R, Vieira P, Grey MX, Oh P, Bobick A, Egerstedt M, Stilman M (2013) Kinematics and inverse kinematics for the humanoid robot HUBO2+. Georgia Institute of Technology, 2013-1. Retrieved from <https://www.golems.org/papers/OFlaherty13-hubo-kinematics-techreport.pdf>
13. Kofinas N, Orfanoudakis E, Lagoudakis MG (2015) Complete analytical forward and inverse kinematics for the NAO Humanoid Robot, 251–264. <https://doi.org/10.1007/s10846-013-0015-4>
14. Bellaccini M (2014) Manual guidance of humanoid robots without force sensors: preliminary experiments with NAO. In: 2014 IEEE international conference on robotics and automation (ICRA), pp 1184–1189. <https://doi.org/10.1109/ICRA.2014.6907003>
15. Baillieul J (2004) Introduction to ROBOTICS mechanics and control. *IEEE Trans Autom Control* 325:463–464. <https://doi.org/10.1109/tac.1987.1104613>
16. He R, Zhao Y, Yang S, Yang S (2010) Kinematic-parameter identification for serial-robot calibration based on POE formula. *IEEE Trans Rob* 26(3):411–423. <https://doi.org/10.1109/TRO.2010.2047529>
17. Yang X, Wu L, Li J, Chen K (2014) A minimal kinematic model for serial robot calibration using POE formula. *Robot Comput-Integrated Manuf* 30(3):326–334. <https://doi.org/10.1016/j.rcim.2013.11.002>
18. Hartenberg D (1955) A kinematic notation for lower-pair mechanisms based on matrices.pdf. (n.d.)
19. Hayati SA (1983) Robot arm geometric link parameter estimation. In: Proceedings of the IEEE conference on decision and control, vol 3, pp 1477–1483. <https://doi.org/10.1109/cdc.1983.269783>
20. Saha SK (2014) Introduction to robotics, 2nd ed. McGraw-Hill, Chennai
21. Reddy AC (2014) Difference between Denavit–Hartenberg (D-H) classical and modified conventions for forward kinematics of robots with case study. In: International conference on advanced materials and manufacturing technologies, pp 267–286
22. Granja M, Chang N, Granja V, Duque M, Llulluna F (2016) Comparison between standard and modified Denavit–Hartenberg methods in robotics modelling. In: Proceedings of the World Congress on mechanical, chemical, and material engineering, vol 1(1), pp 1–10. <https://doi.org/10.11159/icmie16.118>
23. Waldron K, Waldron K, Schmiedeler J, Schmiedeler J (2008) Handbook of robotics (Chapter 1) (Kinematics). *Robotics*, pp 9–33. <https://doi.org/10.1163/156855308X338456>
24. Bharath LV (March, 2018) Forward kinematics analysis of robot manipulator using different screw operators
25. Morell A, Tarokh M, Acosta L (2013) Engineering applications of artificial intelligence solving the forward kinematics problem in parallel robots using support vector regression. *Eng Appl Artif Intell* 26(7):1698–1706. <https://doi.org/10.1016/j.engappai.2013.03.011>
26. Sadjadian H, Taghirad HD (2006) Comparison of different methods for computing the forward kinematics of a redundant parallel manipulator. (2005), pp 225–246. <https://doi.org/10.1007/s10846-005-9006-4>
27. Ghasemi A, Eghtesad M, Farid M (2010) Neural network solution for forward kinematics problem of cable robots, pp 201–215. <https://doi.org/10.1007/s10846-010-9421-z>
28. Canutescu AA, Dunbrack RL Jr (2003) Cyclic coordinate descent : a robotics algorithm for protein loop closure 3:963–972. <https://doi.org/10.1110/ps.0242703.in>
29. Akash Bath Kumar M, Rana P (2018) Humanoid robot: forward kinematics of 12-DOF Legs. *Int J Adv Eng Res Dev* 5(3):434–439. 2348-4470

30. Asfour T, Dillmann R (2003) Human-like motion of a humanoid robot arm based on a closed-form solution of the inverse kinematics problem. In: Proceedings of the 2003 IEEE/RSJ international conference on intelligent robots and systems Las Vegas, Nevada
31. Zhao J, Wang W, Gao Y, Cai H (2008) Generation of closed-form inverse kinematics for reconfigurable robots 3(1):91–96. <https://doi.org/10.1007/s11465-008-0013-6>
32. Park HA, Ali MA, Lee CSG (2012) Closed-form inverse kinematic position solution for humanoid robots 9(3):1–28. <https://doi.org/10.1142/S0219843612500223>
33. Ho T, Kang C, Lee S (2012) Efficient closed-form solution of inverse kinematics for a specific six-DOF Arm 10:567–573. <https://doi.org/10.1007/s12555-012-0313-9>
34. Zaplana I, Basanez L (2018) A novel closed-form solution for the inverse kinematics of redundant manipulators through workspace analysis. Mech Mach Theory 121:829–843. <https://doi.org/10.1016/j.mechmachtheory.2017.12.005>
35. Bertrand S, Bruneau O, Ouezdou FB, Alfayad S (2012) Closed-form solutions of inverse kinematic models for the control of a biped robot with 8 active degrees of freedom per leg. MAMT 49:117–140. <https://doi.org/10.1016/j.mechmachtheory.2011.10.014>
36. Xiao W, Strauß H, Lohß T (2011) Closed-form inverse kinematics of 6R milling robot with singularity avoidance, pp 103–110. <https://doi.org/10.1007/s11740-010-0283-9>
37. Wang K, Lien TK (1989) Closed form solution for the inverse kinematics of a PUMA robot manipulator—II Demonstration. Robot Comput-Integrated Manuf 5(2–3):159–163. [https://doi.org/10.1016/0736-5845\(89\)90059-8](https://doi.org/10.1016/0736-5845(89)90059-8)
38. Wang K (1989) An efficient inverse kinematic solution with a closed form for five-degree-of-freedom robot manipulators with a non-spherical wrist 38(1):365–368
39. Williams RL (2012) DARwin-OP humanoid robot kinematics. In: Proceedings of the ASME design engineering technical conference, 4(PARTS A AND B), pp 1187–1196. <https://doi.org/10.1115/DETC2012-70265>
40. Kofinas N (2012) Forward and inverse kinematics for the NAO humanoid robot. Thesis Master, (July), 1–78.
41. Spong MW, Vidyasagar M (2008) Robot dynamics and control. Wiley
42. Vargas LV, Leite AC, Costa RR (2014) Overcoming kinematic singularities with the filtered inverse approach. In: IFAC proceedings volumes (IFAC-PapersOnline), vol 19. <https://doi.org/10.3182/20140824-6-ZA-1003.01841>
43. Dułęba I, Opalka M (2013) A comparison of Jacobian – based methods of inverse kinematics for serial manipulators 23(2):373–382. <https://doi.org/10.2478/amcs-2013-0028>

Whale Optimization Algorithm for Static and Dynamic Load Dispatch



Himanshu Raj and Manisha Sharma

1 Introduction

A mathematical subject optimization deals with the searching of maxima and minima of given objective functions under given practical constraints [1]. Soft computing techniques and artificial intelligence are gaining popularity nowadays, due to progressive development in the field of computer science. Because of fast response and superior complexity handling capability [2], meta-heuristic optimization-based optimization techniques are being used in all fields of optimization engineering. For difficult or complex problems, these algorithm can give a solution without confirming the highest quality of the solution. The metaheuristic algorithms are divided into three basic types, namely evolutionary algorithm, physics-based algorithm and swarm-based algorithm [3].

At the start, an evolutionary algorithm is population-based meta-heuristic established on concepts of evolution biologically: mutation, recombination along with final selection. In the second category, physics-based algorithm, rules of physics are in consonance with the interaction and moving of each search agent. In the last, the swarm-based algorithm is operated from group behaviour of social animals [4]. It is based on swarm interactions with one another. The advantage of the swarm-based algorithm in comparison with the evolutionary-based algorithm is that former is easy to implement due to a low number of operators. Table 1 shows swarm-based optimization algorithms developed till date.

These algorithms can be practiced in various problems due to their suppleness, firmness and effectiveness. Although various analyzers have developed methods for

H. Raj (✉) · M. Sharma
Electrical Engineering Department, National Institute of Technology, Hamirpur, Himachal Pradesh 177005, India
e-mail: rajhimanshu.raj88@gmail.com

M. Sharma
e-mail: manisha@nith.ac.in

Table 1 Developed swarm-based algorithms

S. No.	Algorithm	Inspiration	Proposed year	References
1	Squirrel Search Algorithm (SSA)	Squirrel	2018	[5]
2	Salp Swarm Algorithm (SSA)	Salp	2017	[6]
3	Butterfly Optimization Algorithm (BOA)	Butterfly	2017	[7]
4	Selfish Herd Optimizer (SHO)	Herd of animals	2017	[8]
5	Whale Optimization Algorithm (WOA)	Whale	2016	[9]
6	Virus Colony Search (VCS)	Virus	2016	[10]
7	Crow Search Algorithm (CSA)	Crow	2016	[11]
8	Ant Lion Optimizer (ALO)	Ant	2015	[12]
9	Grey Wolf Optimizer (GWO)	Wolf	2014	[13]
10	Krill-Herd (KH)	Krill Herd	2013	[14]
11	Bat Algorithm (BA)	Bat	2013	[15]
12	Dolphin Echolocation (DE)	Dolphin	2013	[16]
13	Cuckoo Optimization Algorithm (COA)	Cuckoo	2009	[17]
14	Glowworm Swarm Optimization (GSO)	Glowworm	2009	[18]
15	Firefly Algorithm (FA)	Firefly	2008	[19]
16	Wasp Swarm Algorithm (WSA)	Parasitic Wasp	2007	[20]
17	Cat Swarm Optimization (CSO)	Cat	2006	[21]
18	Honeybee Swarm Optimization (HSO)	Honeybee	2005	[22]
19	Termite Algorithm (TA)	Termite Colony	2005	[23]
20	Artificial Fish-Swarm Algorithm (AFSA)	Fish Swarm	2003	[24]
21	Bacterial Foraging Optimization(BFO)	Bacteria	2002	[25]
22	Marriage in Honey Bees Optimization Algorithm (MBO)	Honey Bees	2001	[26]
23	Particle Swarm Optimization (PSO)	Bird flock	1995	[27]
24	Ant Colony Optimization (ACO)	Ant	1991	[28]

optimization till date, however complications in problem are demanding to propose an efficient algorithm for finding the best dispatch solution. In this perspective, the motive of this paper is to demonstrate a population-based technique for the solution of practical static economic load dispatch (SELD) and dynamic economic load dispatch (DELD) problems, which can offer practical option over the existing techniques.

In this paper, a newly proposed meta-heuristic proposal motivated by whale special hunting strategy to catch prey called whale optimization algorithm (WOA) is carried out for thermal generation-based ELD problems solution related to a power system.

The efficacy of this algorithm has been implemented, tested and validated on two types of ELD problems.

2 Problem Model

The ELD problem is associated with the minimization of objectives as total cost over the specified time frame is subjected to associated operational constraints. The cost function of practical power generation units is represented as a quadratic cost function. The formulation of the objective function in the ELD problem is as follows:

$$\min(F) = \sum_{j=1}^N F_j(P_{gj}) \quad (1)$$

$$= \sum_{j=1}^N (a_j P_{gj}^2 + b_j P_{gj} + c_j) \quad (2)$$

where a full number of generators is N , the cost function of fuel is $F_j(P_{gj})$ for generation unit j in (Rs/h). The power generated is P_{gj} in MW and fuel cost coefficients are a_j, b_j, c_j of the j th generation unit.

A. Equality Restrictions (Balanced power restrictions)

The amount of power developed from generating entities must be equivalent to the required demand for power.

$$\sum_{j=1}^N P_{gj} - P_d = 0 \quad (3)$$

B. Inequality Restrictions (Restrictions on power limits)

The amount of power developed from every entity must lie in the range of maximum and minimum limits.

$$P_{gj}^{\max} \leq P_{gj} \leq P_{gj}^{\min} \quad \text{for } j = 1, 2, 3, \dots, N \quad (4)$$

where the upper limit is P_{gj}^{\max} , and the lower limit is P_{gj}^{\min} of particular power developed by the respective unit.

3 Whale Optimization Algorithm

WOA is a population-based meta-heuristic method that suggested to solve optimization problems. The main source for the vision of WOA has been the hunting behaviour by the humpback whales. There are two phases used for location search of prey, and attack by the search agent. In the initial phase, preys are encircled by the whales while in the second phase generate bubble nets. Considering optimization, the exploration phase is performed when humpback whales look for the search of prey, and the exploitation phase is performed during attacking behaviour.

3.1 Encircling of Prey

It was supposed by the whale-based algorithm that the objective prey they are looking for is the most favourable agent solution or is close to the most favourable. Once WOA defined its best agent, to upgrade their position, next to the hunting phase could be the option for another whale agent.

$$\vec{D} = \left| \vec{C} \cdot \vec{X}_{\text{best}(t)} - \vec{X}(t) \right| \quad (5)$$

$$\vec{X}(t+1) = \vec{X}(t) - \vec{A} \cdot \vec{D} \quad (6)$$

Calculation of vector \vec{A} and vector \vec{C} vectors is expressed as

$$\vec{A} = 2\vec{a} \cdot \vec{r} - \vec{a} \quad (7)$$

$$\vec{C} = 2 \cdot \vec{r} \quad (8)$$

In Eq. (7) value of \vec{a} decreased linearly in between [2,0] in updating steps of iterations (in exploitation and exploration phases) also, \vec{r} is an arbitrary vector and varies between 0 and 1.

3.2 Bubble-Net Attacking Strategy (Exploitation)

Two types of strategies have created for a mathematical picture of the bubble-net attitude of a group of whales.

3.2.1 Shortening Encircling Strategy

In this strategy, the value of \vec{a} in (7) is brought down to attain this behaviour. The new state of searching agent could be explained somewhere in between the reference state of the agent at coordinates (X, Y) and the state of the present best searching agent (X_{best}, Y_{best}) while explaining arbitrary values for the vector \vec{A} in between -1 and 1 .

3.2.2 Spiral Upgrading State

In this strategy, the first calculation is made of distance amid search agent positioned at coordinates (X, Y) and target food positioned at (X_{best}, Y_{best}) . Below is a helix-based nonlinear equation that is arranged between the state of search agent and its target food to emulate helix-shaped development related to search agents.

$$\vec{X}(t + 1) = \vec{D}' \cdot e^{bl} \cdot \cos(2\pi l) + X_{best}(t) \tag{9}$$

where $\vec{D}' = |\vec{X}_{best}(t) - \vec{X}(t)|$ and demonstrate the state of the j th search agent to the target food (most favourable result found till then), b denotes a fixed value for a meaning of logarithmic curl aspect, also l , an arbitrary no. varies in between -1 to 1 , and (\cdot) is the multiplication of element.

In order to procure a model of concurrent behaviour, half of the total probability to choose amid either the diminishing encompassing strategy or the curl shape to upgrade the state of whale agents in steps of optimization [9] is presumed initially.

$$\vec{X}(t + 1) = \vec{X}(t) - \vec{A} \cdot \vec{D}, \quad \text{if } p < \frac{1}{2} \tag{10}$$

$$\vec{X}(t + 1) = \vec{D}' \cdot e^{bl} \cdot \cos(2\pi l) + X_{best}(t), \quad \text{if } p \geq \frac{1}{2}$$

In Eq. (10), p denotes an arbitrary number ranging between 0 and 1 .

3.3 Hunt for Prey (Exploration)

This strategy is established on the alteration of vector \vec{A} that could be used in the hunting of target food (phase exploration). Whales hunt arbitrary in accordance with the state of one other. Hence, to mobilize whale agent, vector A has been practised with arbitrary values other than $[-1, 1]$. In exploration strategy, the position of the agent is upgraded on the foundation of arbitrarily selected search agent in place of most favourable agent till now. Below is the mathematical equation [9].

$$\vec{D} = \left| \vec{C} \cdot \vec{X}_{\text{rand}} - \vec{X} \right| \quad (11)$$

$$\vec{X}(t + 1) = \vec{X}_{\text{rand}} - \vec{A} \cdot \vec{D} \quad (12)$$

In Eq. (11), \vec{X}_{rand} represents an arbitrary state vector of whale chosen from the present community.

Its step-by-step process of implementation depicted below.

1stStep First initializes the community of humpback whale or the result vector.

2ndStep Then make sure initialized power from each unit does not violate the power limit, and if so, correct it.

3rdStep Calculate and rate of given compatibility function of every result (1), and also the output of the universal most favourable result.

4thStep Upgrade the numerical coefficient of vector A, the arbitrary numerical value of a, l and probability value p for every search agent.

5thStep if value of $p < \frac{1}{2}$ and if numerical value of absolute $|A| < 1$

6thStep Upgrade the state for the present humpback whale agent (Eq. 5).

7thStep else if value of absolute $|A| \geq 1$.

Choose an arbitrary agent or upgrade the state of the present whale (Eq. 12)

Then End.

8thStep else if probability value of $p \geq \frac{1}{2}$.

Upgrade the state of the present whale agent (Eq. 9).

Then End

9thStep keep control if any whale agent moves away from search space and if so, then rectify it.

10thStep Evaluate the compatibility of every whale.

11thStep Upgrade X_{best} if there exists a more favourable solution

12thStep In the following step, $t = t+1$ where number of iteration is denoted by t

13thStep if $t < \text{max. no. of iteration}$

Go back to the 4th step.

Else

Exit

Table 2 Application in optimization problems of WOA

S. No.	Problems/applications	References
1	Economic load dispatch	[29, 31, 37, 45, 46]
2	Voltage source inverters	[30, 41]
3	Optimal power flow	[32]
4	Solar photovoltaic	[33, 34]
5	Distribution systems	[35, 47]
6	Hydrothermal scheduling	[36]
7	Photovoltaic model identification	[38, 40]
8	Distribution networks	[39, 43]
9	Power system optimization	[41]
10	Radial distribution systems	[42, 44]
11	Load frequency control	[43]
12	Distribution systems	[47]

4 Applications in Optimization Problems of WOA

WOA has found applications in several areas in various industrial fields, for example, engineering optimization-related problems. Developing accurate problems and drafting appropriate arbitrary value and required objective functions are the main affairs that can assist in capable problem solving while proceeding with engineering applications. Table 2 shows a synopsis of applications of WOA in different power system problems.

5 Description of Problems and Results

To check the efficiency of the developed WOA [9] for the solution of real-world optimization, two dissimilar natures of optimal load dispatch problems are taken here. Type one includes the case of SELD of a problem with three generating unit system with diverse cost curve, where optimal scheduling is carried out for specific time period, where the second case is having a DELD problem with three generators where scheduling period of thermal plants is 1 day or 24 h with 24 intervals of 1 h each.

This algorithm has been carried out in MATLAB software and processed on Intel Corei3 PC with RAM 2 GB. Table 3 shows the WOA parameters with ranges.

WOA Technique Parameters: Population size is 10, Max no. of iterations = 50.

Case 1. Three Thermal Generation Unit Problem (SELD)

This system has three thermal generation units [48]. The power demands are considering as 585, 700 and 800 MW. Optimal scheduling of generating three-unit system

Table 3 Parameters tuning

S. No	Parameters	Ranges	Eq. No.
1	a	[2, 0]	(7)
2	A	[-1, 1]	(7)
3	C	[0, 2]	(8)
4	l	[-1, 1]	(9)

Table 4 Optimal scheduling of generating three-unit system by WOA technique (losses are neglected)

S. No.	Demand of power (MW)	$P(1)$ (MW)	$P(2)$ (MW)	$P(3)$ (MW)	Cost (Rs/h)	CPU time (s)
1	585	100.0000	344.6691	140.3310	5565.1	0.7940
2	700	390.6158	151.0594	158.3255	6490.3	0.8604
3	800	597.0539	100.0000	102.9462	7283.1	0.8623

Table 5 Comparative results

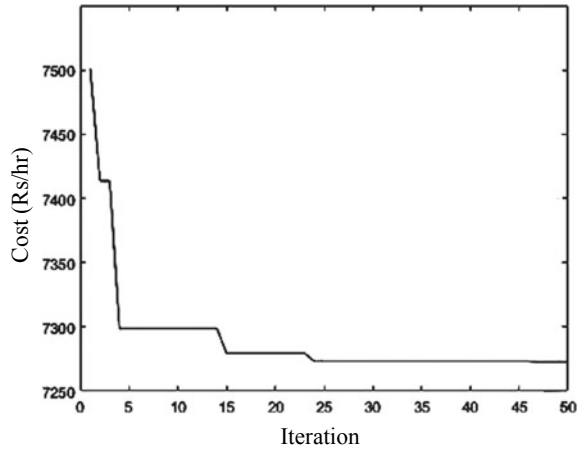
S. No.	Demand of power (MW)	Traditional technique (Rs/h) [48]	GA technique (Rs/h) [48]	PSO technique (Rs/h) [48]	WOA technique (Rs/h)
1	585	5821.4000	5827.5	5821.4	5565.1
2	700	6838.4056	6877.2	6838.4	6490.3
3	800	7738.5189	7756.8	7738.5	7283.1

by WOA technique is given in Table 4. While the comparison of obtained results with other methods is given in Table 5 for the same test available in recent literature, it is observed that WOA can be able to provide best power generation scheduling, in terms of minimum operational cost in comparison with GA [49], PSO [27] and traditional techniques. The cost convergence curve obtained by WOA is illustrated in Fig. 1, which is found to be fast and stable.

Case 2. Three Thermal Generation Unit Problem (DELD)

A three-unit system is considered here for the solution of DELD problem over the scheduled period of 24 h. The fuel cost is a second-order polynomial and adopted as the modification to previous reference [48]. The load profile over the 24 hours is adopted done to check the complexity addition of proposed method. The generation schedule corresponding to the best cost is compiled in Table 6.

Fig. 1 Cost convergence curve obtained by WOA for PD = 800 MW



6 Conclusion

After results, it can be profoundly said that the WOA technique can be strongly applied to solve the static and dynamic ELD problem with given constraints. The WOA technique has proved to have top features consisting of top quality results, balanced convergence features. It can be seen from the observation of results for the test cases 1 and 2, which clearly states that the developed technique is proficient of getting high-quality results effectively for static and dynamic ELD problems, respectively. The comparison of solutions with other techniques reported results states the efficiency of WOA over other technique. The convergence features of the developed technologies have tested for two different test cases. It is now crystal clear from the obtained results that the developed WOA technique can stay away from premature convergence, disadvantages of GA technique and can get high-grade results with better calculation efficacy and convergence feature.

Table 6 Generation scheduling of DELD problems (Case 2)

Hour	P1	P2	P3	PD (MW)
1	100.0000	344.6691	140.3310	585
2	284.5435	151.4996	158.9572	595
3	105.8885	354.1442	149.9679	610
4	130.5182	314.5200	134.9618	580
5	479.2410	125.7591	50.0000	655
6	332.6290	222.8760	134.4950	690
7	566.1445	100.0000	55.8556	722
8	452.4110	152.5523	75.0367	680
9	324.4695	294.0583	91.4724	710
10	487.7766	153.7037	113.5197	755
11	370.8331	317.9251	101.2428	790
12	318.5428	311.9775	169.4798	800
13	447.5718	232.8399	111.8399	792
14	336.7676	234.2212	178.0112	749
15	440.1982	144.0862	155.7159	740
16	416.1142	100.0000	172.8860	689
17	311.7535	188.7675	176.4790	677
18	399.8380	136.6234	96.5391	633
19	280.6123	197.4265	131.9616	610
20	122.7781	372.8516	106.3707	602
21	100.0000	364.8335	134.1668	599
22	156.7888	310.7135	124.4979	592
23	225.9822	171.7982	189.2197	587
24	203.5065	234.2662	152.2274	590
Total cost (Rs/Day)				149527.7

Acknowledgement The authors are grateful to the authorities of the National Institute of Technology, Hamirpur, for providing all facilities to complete this work.

References

1. Wood AJ, Wollenberg BF (1984) Power generation, operation and control. Wiley, New York
2. Tian D, Shi Z (2018) MPSO: Modified particle swarm optimization and its applications. *Swarm Evol Comput* 41:49–68
3. Dhiman G, Kumar V (2018) Emperor penguin optimizer: a bio-inspired algorithm for engineering problems. *Knowl-Based Syst* 159:20–50
4. Pacini E, Mateos C, Garino CG (2014) Distributed job scheduling based on swarm Intelligence: a survey. *Comput Electr Eng* 40(1):252–269

5. Jain M, Singh V, Rani A (2019) A novel nature-inspired algorithm for optimization: squirrel search algorithm. *Swarm Evol Comput* 44:148–175
6. Mirjalili S, Gandomi AH, Mirjalili SZ, Saremi S, Faris H, Mirjalili SM (2017) Salp swarm algorithm: a bio-inspired optimizer for engineering design problems 114:163–191
7. Qi X, Zhu Y, Zhang H (2017) A new meta-heuristic butterfly-inspired algorithm. *J Comput Sci* 23:226–239
8. Fausto F, Cuevas E, Valdivia A, Gonzalez A (2017) A global optimization algorithm inspired in the behaviour of selfish herds. *Biosystems* 160:39–55
9. Mirjalili S, Lewis A (2016) The whale optimization algorithm. *Adv Eng Software* 95:51–67
10. Li MD, Zhao H, Weng XW, Han T (2016) A novel nature-inspired algorithm for optimization: virus colony search. *Adv Eng Software* 92:65–88
11. Askarzadeh A (2016) A novel metaheuristic method for solving constrained engineering optimization problems: Crow search algorithm. *Comput Struct* 169:1–12
12. Mirjalili S (2015) The ant lion optimizer. *Adv Eng Software* 83:80–98
13. Mirjalili S, Mirjalili SM, Lewis A (2014) Grey wolf optimizer. *Adv Eng Software* 69:46–61
14. Gandomi AH, Alavi AH, Talatahari S (2013) Structural optimization using Krill Herd Algorithm. In: *Swarm intelligence and bio-inspired computation*, pp 335–349
15. Hasançebi O, Teke T, Pekcan O (2013) A bat-inspired algorithm for structural optimization. *Comput Struct* 128:77–90
16. Kaveh A, Farhoudi N (2013) A new optimization method: dolphin echolocation 59:53–70
17. Yang XS, Deb XS (December 2009) Cuckoo search via Lévy flights. In: *World Congress on nature & biologically inspired computing*. IEEE Publications, pp 210–214
18. Krishnanand KN, Ghose D (2009) Glowworm swarm optimisation: a new method for optimizing multimodal functions. *Int J Comput Intell Stud* 1:93–119
19. Yang XS (2008) *Nature-inspired meta-heuristic algorithms*. Luniver Press
20. Pinto PC, Runkler TA, Sousa JM (2007) Wasp swarm algorithm for dynamic MAX- SAT problems. In: *Adaptive and natural computing algorithms*. Springer, Berlin, pp 350–357
21. Chu SC, Tsai PW, Pan JS (2006) Cat swarm optimization. In: *Pacific Rim international conference on artificial intelligence PRICAI 2006: PRICAI 2006: Trends in artificial intelligence*, pp 854–858
22. Karaboga D (2005) An idea based on honeybee swarm for numerical optimization, Technical Report TR06, Erciyes University, Engineering Faculty, Computer Engineering Department
23. Roth M, Stephen W (2006) Termite: A swarm intelligent routing algorithm for mobile wireless Ad-Hoc networks. In: *Stigmergic optimization*. Springer, Berlin, Heidelberg, pp 155–184
24. Li X (2003) A new intelligent optimization-artificial fish swarm algorithm [Doctor thesis]. Zhejiang University of Zhejiang, China, pp 781–782
25. Passino KM (2002) Biomimicry of bacterial foraging for distributed optimization and control. *IEEE Control Syst Magazine* 22(3):52–67
26. Abbass HA (2001) MBO: marriage in honey bees optimization—a haplometrosis polygynous swarming approach. In: *Proceedings of the Congress on evolutionary computation*, pp 207–214
27. Kennedy J, Eberhart RC (1995) Particle swarm optimization. In: *Proceedings of the IEEE international conference on neural networks*, pp 1942–1948
28. Dorigo M, Maniezzo V, Coloni A (1991) The ant system: an autocatalytic optimizing process. Technical Report TR91-016, Politecnico di Milano
29. Kumar A, Bhalla V, Kumar P, Bhardwaj T, Jangir N (2018) Whale optimization algorithm for constrained economic load dispatch problems—a cost optimization. *Ambient Commun Comput Syst* 696:353–366
30. Nalcaci G, Ermis M (2018) Selective harmonic elimination for three-phase voltage source inverters using whale optimizer algorithm. In: *5th international conference on electrical and electronic engineering (ICEEE)*, pp 1–6
31. Mohamed FA, Abdel-Nasser M, Mahmoud K, Kamel S (2018) Economic dispatch using stochastic whale optimization algorithm. In: *International conference on innovative trends in computer engineering (ITCE)*, pp 19–24

32. Mahdad B (2018) Improvement optimal power flow solution under loading margin stability using new partitioning whale algorithm. *Int J Manage Sci Eng Manage*, pp 1–15
33. Xiong G, Zhang J, Shi D, He Y (2018) Parameter extraction of solar photovoltaic models using an improved whale optimization algorithm. *Energy Convers Manage* 174:388–405
34. Hasanien HM (2018) Performance improvement of photovoltaic power systems using an optimal control strategy based on whale optimization algorithm. *Electric Power Syst Res* 157:168–176
35. Reddy PDP, Reddy VCV, Manohar TG (2017) Whale optimization algorithm for optimal sizing of renewable resources for loss reduction in distribution systems. *Renewables: Wind, Water, and Solar*
36. Das S, Bhattacharya A, Chakraborty AK, Pandey V (2017) Fixed head short-term hydrothermal scheduling using whale optimization algorithm considering the uncertainty of solar power. In: *Ninth international conference on advanced computing (ICoAC)*. IEEE, New York, pp 179–185
37. Heris MN, Mehdinejad M, Mohammadi-Ivatloo B, Babamalek-Gharehpetian G (2017) Combined heat and power economic dispatch problem solution by implementation of whale optimization method. *Neural Comput Appl*, pp 1–16
38. Elazab OS, Hasanien HM, Elgendy MA, Abdeen AM (2017) Whale optimisation algorithm for photovoltaic model identification. In: *The 6th international conference on renewable power generation (RPG)*, Issue 13, pp 1906–1911
39. Reddy PDP, Reddy VCV, Manohar TG (2017) Optimal renewable resources placement in distribution networks by combined power loss index and whale optimization algorithms. *J Electr Syst Inf Technol* 5(2):175–191
40. Qazi SH, Mustafa MWB, Soomro S, Larik RM (2017) An optimal current controller for photovoltaic system based three phase grid using whales optimization algorithm. In: *IEEE conference on energy conversion (CENCON)*, pp 15–20
41. Medani KBO, Sayah S, Bekrar A (2017) Whale optimization algorithm based optimal reactive power dispatch: a case study of the Algerian power system. *Electr Power Syst Res* 163(Part B):696–705
42. Rosyadi A, Penangsang O, Soeprijanto A (2017) Optimal filter placement and sizing in radial distribution system using whale optimization algorithm. In: *International seminar on intelligent technology and its applications (ISITIA)*. IEEE, New York, pp 87–92
43. Saha A, Saikia LC (2017) Utilisation of ultra-capacitor in load frequency control under restructured STPP-thermal power systems using WOA optimised PIDNFOPD controller. *IET Generation, Transmission & Distribution*, pp 3318–3331
44. Neagu BC, Ivanov O, Gavrila M (2017) Voltage profile improvement in distribution networks using the whale optimization algorithm. In: *9th international conference on electronics, computers and artificial intelligence (ECAI)*. IEEE, New York, pp 1–6
45. Trivedi IN, Bhoje M, Bhesdadiya RH, Jangir P, Jangir N, Kumar A (2016) An emission constraint environment dispatch problem solution with microgrid using Whale Optimization Algorithm. In: *National power systems conference (NPSC)*. IEEE, New York, pp 1–6
46. Trivedi IN, Jangir N, Jangir P, Pandya MH, Bhesdadiya RH, Kumar A (2016) Price penalty factors based approach for emission constrained economic dispatch problem solution using whale optimization algorithm. In: *2016 IEEE 1st international conference on power electronics, intelligent control and energy systems (ICPEICES)*, pp 1–5
47. Prakash DB, Lakshminarayana C (2016) Optimal siting of capacitors in radial distribution network using Whale Optimization Algorithm. *Alexandria Eng J* 56(4):499–509
48. Sudhakaran M, Vimal Raj D, Ajay P, Palanivelu TG (2007) Application of particle swarm optimization for economic load dispatch problems. In: *The 14th international conference on intelligent system applications to power systems, ISAP*
49. Holland JH (1973) Genetic algorithms and the optimal allocation of trials. *SIAM J Comput* 2(2):88–105

A Comparison Between Passive Islanding Detection Methods in Grid Integrated Photovoltaic System



Isha Chandra and Mahiraj Singh Rawat

1 Introduction

The advancement in technologies, the concept of micro-grid has been evolving as a key component of smart grid, which uses modern power technology and integrates renewable-based DG sources such as gas turbines, solar power, wind energy, fuel cells, and energy storage devices together. The various renewable-based DGs are utilized based on their availability, but solar PV is one of the most popularized resources because of their low cost and easy maintenance. The PVs [1] are highly compatible with generating power from several KWs to MWs. For bulky power grids, the microgrid acts as a controllable power unit to fulfill the requirements of transmission and distribution grid. The microgrid can be operated in both grid and island mode. In grid mode, depending on generation and load demands, the microgrid can easily transfer power to load. However, in islanding mode, the generated power from DGs must satisfy the load demand even after discontinued from the main grid.

In the smart grid, the islanding operation can be classified as unintentional or intentional islanding. However, normally the intentional islanding operation is executed by utility persons to do maintenance and system reliability improvement [2]. It is quite difficult to control unintentional islanding as it occurs due to a fault or unwanted tripping of switches, etc. Islanding is the core issue for power engineers as the balance between generation and load demand can be the causes of abnormal voltages and frequencies in the islanded circuit. Hence, the DGs must have some provision to detect islanding situation and must be disconnected immediately from the main grid. This phenomenon is popularly known as anti-islanding.

I. Chandra · M. S. Rawat (✉)

Department of Electrical Engineering, National Institute of Technology Uttarakhand, Srinagar, Garhwal 246174, India

e-mail: msrawat@nituk.ac.in

I. Chandra

e-mail: ishachandra10@gmail.com

Unintentional islanding is one of the severe problems that can harm a lineman or electrical worker. The loss of grid synchronization during unintentional islanding has several impacts on power system stability and can cause damages to electrical devices and equipment. At the event of islanding, the DG supplies power to the grid through PCC (point of common coupling). The non-detection zone (NDZ), error detection ratio, detection-time, and power quality (in terms of THD) are the IDM's performance indices, which decides whether islanding is detected fast and accurately [3].

There are generally two methods employed for islanding [4–6] detection: (i) local method (ii) remote method. The local method is based on a measurement/variations of electrical parameters, e.g., voltage, current, phase angle and harmonic distortion, etc., and is further classified into active and passive methods. The injection of disturbance to PCC for monitoring the variation in voltage, frequency and harmonics is called active method [7]. However, the passive method [8] is based on directly monitoring the variation in voltage, frequency and current and comparing with a threshold value. Although the passive method shows large non-detection zone (NDZ) for small power mismatch and may fail to detect islanding during such an event. Remote method [6] based on remote monitoring of the status of the circuit breaker connected at the utility side. Due to certain advantages and disadvantages with active or passive methods, recently few authors have proposed hybrid methods which take advantage of both methods [9].

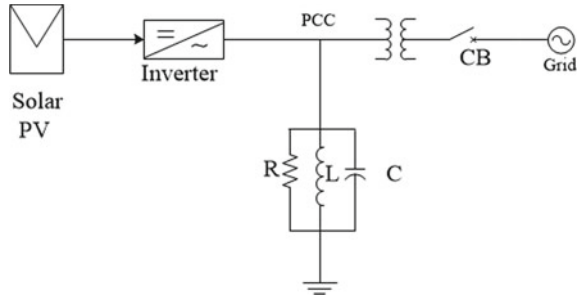
This paper analyzes the performance of various passive IDMs, i.e., over/under voltage, over/under frequency and ROCOF [10]. To check the accuracy of IDMs, a grid-connected 100 kW solar photovoltaic (PV) array has been used. Moreover, the authors have simulated passive IDMs under different test conditions. The change in voltage, frequency is measured at PCC during islanding condition [11–13].

2 Detailed Model of Grid Integrated PV System

The solar PV [14] is one of the cheapest and low maintenance required DG which converts light into electrical energy. It is highly in demand for its light locked capability. It provides reliability over a long period. The basic advantage of PV is that it is modular. Figure 1 represents the grid-connected solar PV system through PCC.

The systems contain a PV cell array, inverter, coupling transformers, RLC load and grid-connected through the utility circuit breaker. The generated power from the PV array is 100 kW at 1000w/m² irradiance and 25 °C temperature. A boost converter with switching frequency of 5 kHz is used to increase the voltage of PV from 272.4 to 500 V. To optimize the duty ratio for extracting the maximum power, the incremental conductance technique is utilized. Further, the DC voltage output into AC of boost converter, a three-phase inverter is used. This inverter converts the 500 V DC into 260 V AC at u.p.f. and the harmonic generated at the inverter output is filtered through RL filter and 10 kVAr capacitive filters. A transformer of 100 kVA, 260 V/20 kV and grid which consist of 110 kV transmission system a

Fig. 1 Grid-connected solar PV system



20 kV distributed feeder is connected. The sun power module (SPR-305E-WHT-D) of solar PV array is used, which includes 67 parallel strings of 5 series-connected modules. The incremental conductance method is utilized in this study to extract maximum power from the solar PV array [10]. This method depends on the ratio of incremental current and incremental voltage (dI/dV). The ratio dI/dV is compared with the instantaneous value of I/V . The mathematical expression of power (P) is represented using Eqs. (1) and (2).

$$P = V \times I \tag{1}$$

$$\frac{dP}{dV} = \frac{d(V \times I)}{dV} = I + V \frac{dI}{dV} \tag{2}$$

For maximum power extraction $dP/dV = 0$ and can be represented by Eq. (3),

$$\frac{dI}{dV} = -\frac{I}{V} \tag{3}$$

The MPPT algorithm controls the PWM signal of the boost converter until it satisfies Eq. (3). The flowchart diagram of the incremental conductance method is shown in Fig. 2.

To maintain the reactive and active power, during islanding condition, two controllers are used, one is the internal controller, and other is the external controller. An external controller is for controlling the DC link voltage across the capacitor (C_1 and C_2), whereas the internal controller is used for regulating the I_d and I_q current. I_d current control the active power output and I_q maintain the reactive power zero by maintaining unity power factor. V_q and V_d are the output voltage of I_q and I_d current, which get converted into three modulating signals. This modulating signal is fed into PWM. For synchronization purpose, PWM is generally preferred [15].

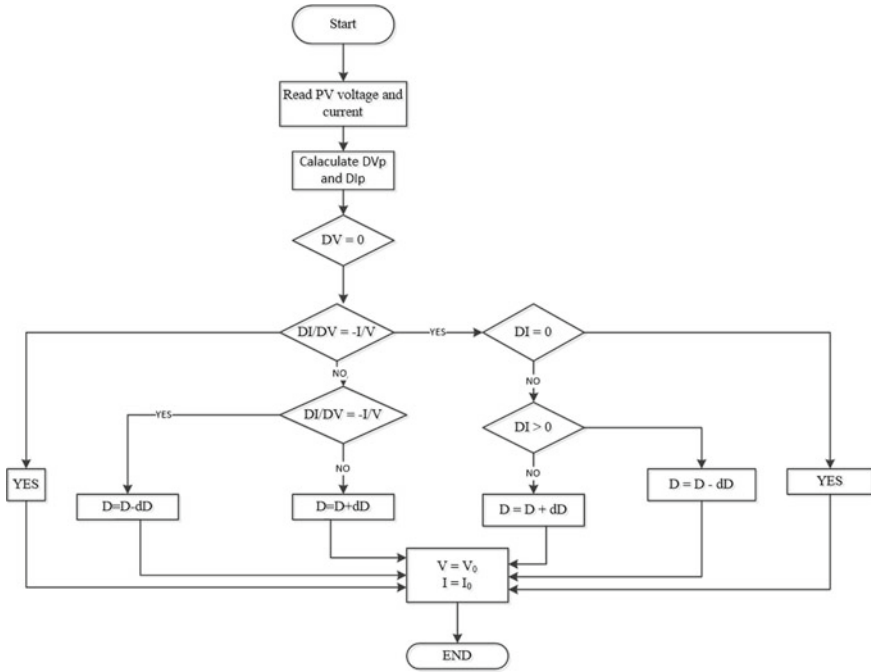


Fig. 2 Flowchart of MPPT using incremental conductance

3 Islanding Detection Methods

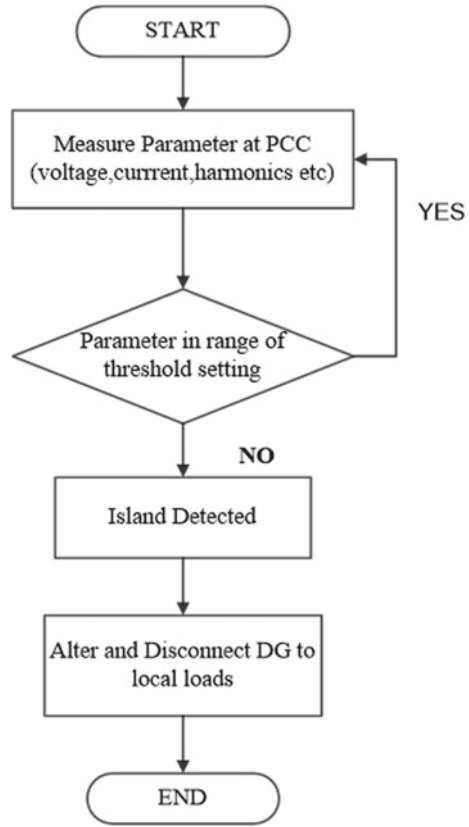
The IDMs are classified into local and remote methods. The local method includes the variation of voltage and frequency, whereas the remote method depends on communication purpose.

A. Passive Islanding Methods

The passive methods monitor the variations in voltage, current, frequency, phase angle, and total harmonic distortion (THD) at PCC. The basic advantage of these methods is that they do not deteriorate the system power quality; however, due to large NDZ, it fails to detect islanding. The grid and islanding mode can be distinguished based on the threshold value setting. If the measured parameter is larger than the threshold value, then the islanding detected. Figure 3 shows the flowchart diagram of typical passive IDM.

Over/Under Voltage This method monitors the voltage variation at PCC [8]. Due to the power mismatch during islanding condition, it causes a deviation in voltage. According to IEEE 1547 standard, the threshold value for islanding detection can be in the range from 88 to 110% of predefined voltage. If the voltage magnitude exceeds the set threshold value, the inverter will be disconnected from the main grid

Fig. 3 Flowchart diagram of passive IDM



and does not supply power to the connected load. For over/under voltage, NDZ [3] can be determined using Eq. (4).

$$\left(\frac{V}{V_{\max}}\right)^2 - 1 \leq \frac{\Delta P}{P} \leq \left(\frac{V}{V_{\min}}\right)^2 - 1 \tag{4}$$

where V_{\max} and V_{\min} are the minimum and maximum voltages; V and P represent the rated voltages and active power, respectively.

Over/Under frequency This method based on a variety of frequency [8] at PCC. If frequency exceeds the set threshold value, then the island event will be detected. The range of threshold is taken between $59.5 < f < 60.5$. For over/under frequency, NDZ [5] can be computed as follows:

$$Q_f \left(1 - \left(\frac{f}{f_{\min}}\right)\right)^2 \leq \frac{\Delta Q}{P} \leq Q_f \left(1 - \left(\frac{f}{f_{\max}}\right)\right)^2 \tag{5}$$

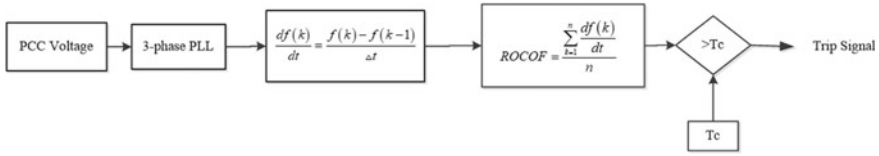


Fig. 4 ROCOF algorithm

where Q_f represents the quality factor, f_{\min} and f_{\max} are minimum and maximum frequencies, P represents the active power demand.

Rate of change of frequency (ROCOF) The methods monitor the df/dt [12] at PCC, which determines the microgrid is operating in island or grid-connected mode. If df/dt exceeds the threshold value, then an inverter gets shut down, and islanding detected. The conventional ROCOF algorithm is represented in Fig. 4.

where n = total no. of samples [13] and $k = 1, 2, \dots, nth$ sample, $f(k)$ measures the frequency at k th sample and $f(k - 1)$ measure frequency at $(k - 1)$ th sample. In this method, PLL is connected to the voltage of PCC to measure the frequency of voltage. This frequency has given to ROCOF block, and the value of ROCOF has been compared with the threshold setting. If it violates threshold value, generates a control signal and gives to trip the breaker.

4 Results and Discussions

The paper compares the various passive islanding methods and also compares the islanding and non-islanding effect. The detailed model of 100 kW grid-connected PV array is shown in Fig. 5 [14]. The parameters related to the PV array are shown in Table 1.

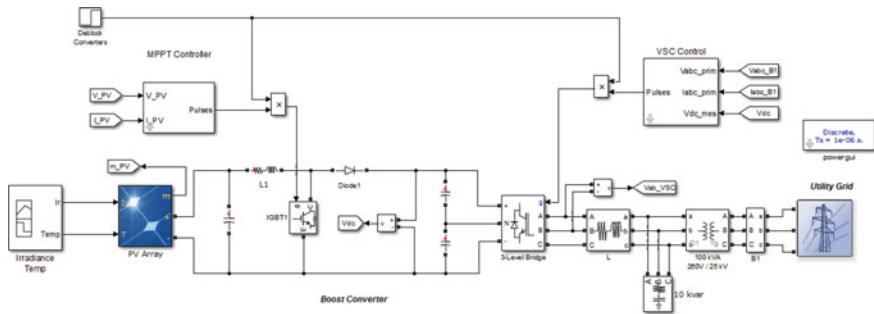


Fig. 5 MATLAB/Simulink diagram of grid-connected PV system

Table 1 Various parameters of PV array

S. No	Parameters	Values
1	Parallel strings	67
2	Series Module	5
3	No. of Cells	96
4	V_{oc}	64.2
5	I_{sc}	5.96
6	P_{max}	305
7	V_{mpp}	54.7
8	I_{mpp}	5.58

A. Normal Condition

During normal conditions, the DC output voltage of PV is 500 V, and the nominal frequency is 60 Hz. The grid voltage is maintained at 110 kV (RMS). It measures the voltage and current at PCC during the normal condition, and corresponding simulation results are shown in Figs. 6, 7, 8 and 9. At reasonable condition, there is no variation in voltage as well as current.

B. Islanding Condition

At the event of islanding, the grid side circuit breaker opens its contact from 0.4 to 0.7 s and referred as islanding period. The voltage varies on the PCC during this period shown in Figs. 10, 11 and 12 using different islanding method. Power quality does not get affected by applying all the three methods when islanding occurs.

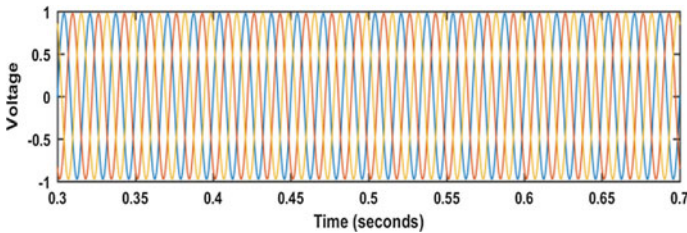


Fig. 6 Voltage profile at PCC

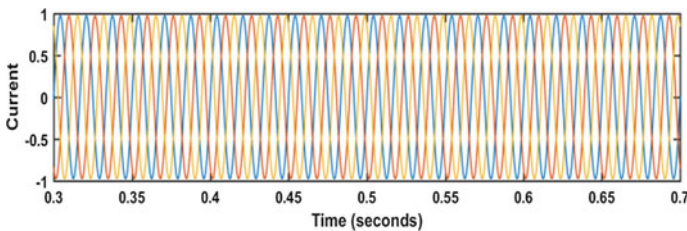


Fig. 7 Current at PCC

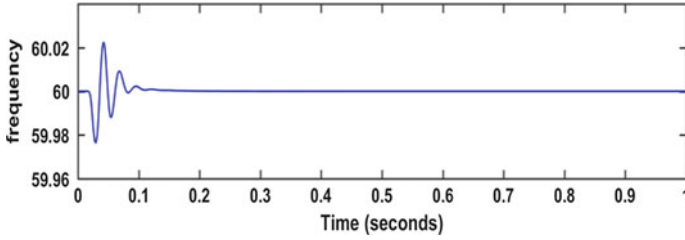


Fig. 8 Frequency at PCC

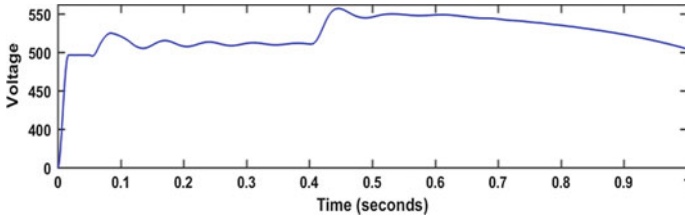


Fig. 9 DC voltage of PV array

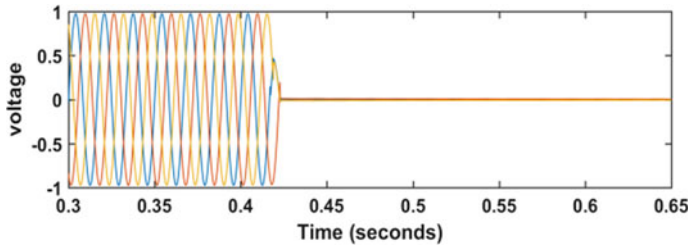


Fig. 10 Voltage profile at PCC for ROCOF-based method

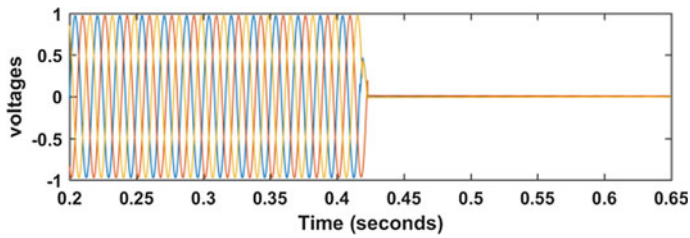


Fig. 11 Voltage profile of PCC for over/under frequency method

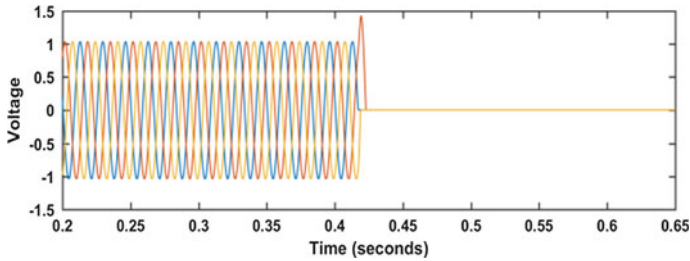


Fig. 12 Voltage profile of PCC for over/under voltage-based method

The ROCOF relay determined the variation in frequency and compared with the threshold value set for ROCOF relay and the voltage of PV's inverter. The ROCOF relay gets activated when both conditions satisfied. The results of the trip signal for studied passive methods are shown in Figs. 13, 14, 15 and 16.

This graph represents the comparative study of detection time of various islanding method. The opening time of breaker is coordinated to the islanded detection methods speed, and this phenomenon is known as the performance parameter of the method. The islanding does not be bared by the non-islanding system, and the system continuously delivers power to the load.

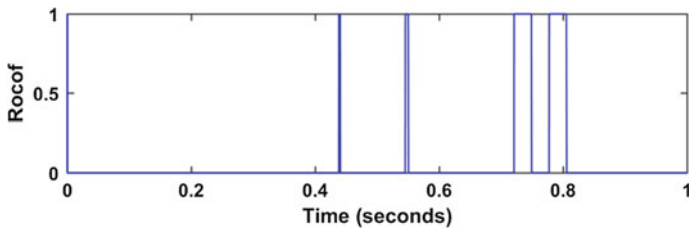


Fig. 13 Tripping signals of ROCOF method

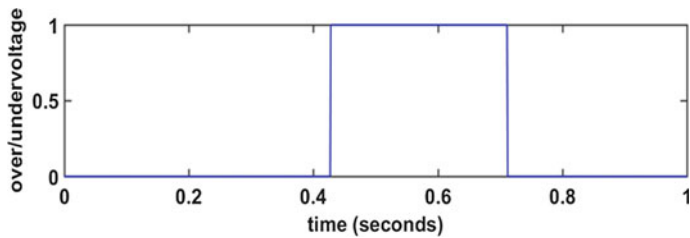


Fig. 14 Tripping signals of over/under voltage

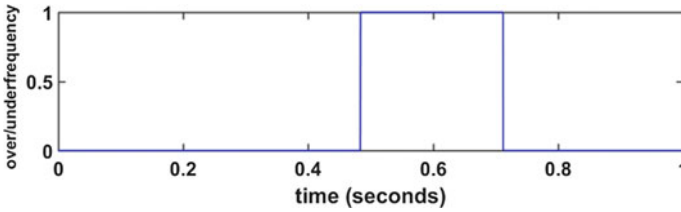
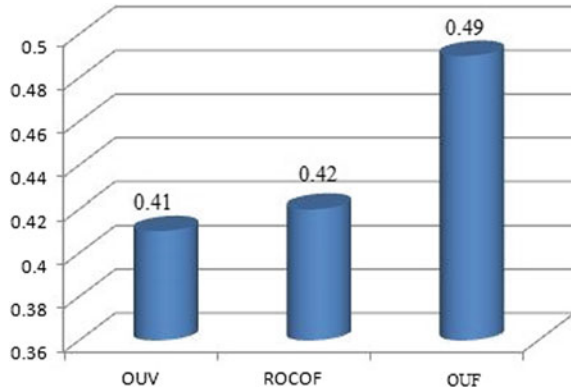


Fig. 15 Tripping signal of over/under frequency

Fig. 16 Comparison result of passive islanding method



5 Conclusion

The performance of passive IDMs such as over/under voltage, frequency and ROCOF is analyzed for grid integrated solar PV system. The passive islanding techniques depend on predefined set values, and grid failure can be identified by monitoring the variation in grid side parameters. The system power quality is not affected by these methods because the methods do not inject any disturbance, but the basic disadvantage of this method is that it has a large NDZ because of power mismatch. A grid-connected 100 kW PV array system is used to study the passive IDMs. The simulation has been performed in the MATLAB/Simulink environment. From the simulation results, it was concluded that among passive islanding detection methods, the over/under voltage method have less detection time compared to other methods. Although other islanding techniques such as ROCOF, over/under frequency has the ability to detect the islanding in the time specified by IEEE 1547 standards.

References

1. IEEE Std 1547-2003: Standard for Interconnecting Distributed Resources with Electric Power Systems. IEEE, (2003)

2. Panigrahi BK, Nandi R, Mahanta B, Pal K (2016) Islanding detection in distributed generation. In: International conference on circuit, power and computing technologies (ICCPCT). IEEE, Nagercoil, India, pp 1–5
3. Li C, Chi C, Cao Y, Kuang Y, Zeng L, Fang B (2014) A review of islanding detection methods for microgrid. *Renew Sustain Energy Rev* 35:211–220
4. Guha B, Haddad RJ, Kalaani Y (2015) Anti-Islanding techniques for distributed generation systems—a survey. In: SoutheastCon 2015, IEEE, Fort Lauderdale, FL, USA
5. Khamis A, Shareef H, Bizkevelci E, Khatib T (2013) A review of islanding detection techniques for renewable distributed generation systems. *Renew Sustain Energy Rev* 28:483–493
6. Banu V, Istrate M, Machidon D, Pantelimon R (2014) A study on anti-islanding detection algorithms for grid-tied photovoltaic systems. In: International conference on optimization of electrical and electronic equipment (OPTIM), pp 655–660, Bran, Romania
7. Ahmad KNEK, Selvaraj J, Rahim NA (2013) A review of the islanding detection methods in grid-connected PV inverter. *Renewab Sustain Energy Rev* 21:756–766
8. Sundarand DJ, Kumaran MS (2015) A comparative review of Islanding detection schemes in distributed generation systems. *Int J Renewab Energy Res* 5(4):1016–1023
9. Banu IV, Beniuga R, Istrate M (2013) Comparative analysis of the perturb-and-observe and incremental conductance MPPT methods. In: Proceedings of 8th international symposium on advanced topics in electrical engineering (ATEE). IEEE, Bucharest, Romania, pp 1–4
10. Yingram M, Premrudeepreechacharn S (2014) Investigation of relationship between voltage and non detection zone of OUV/OUF of local islanding detection techniques. *J Clean Energy Technol* 2(4):299–304
11. Freitas W, Xu W, Affonso CM, Huang Z (2005) Comparative analysis between ROCOF and vector surge relays for distributed generation applications. *IEEE Trans Power Delivery* 20(2):1315–1324
12. Jinjala SB, Vaidya BN (2018) Analysis of active and passive method for islanding detection of 3-phase grid-connected PV system. In: 2nd international conference on trends in electronics and informatics (ICOEI). IEEE, Tirunelveli, India, pp 592–597
13. Guha B, Haddad RJ, Kalaani Y (2015) A novel passive islanding detection technique for converter based distributed generation systems. In: IEEE power & energy society innovative smart grid technologies conference (ISGT), IEEE, Washington, DC, pp 1–5
14. IEEE Recommended Practice for Utility Interface of Photovoltaic (PV) Systems. In: IEEE Std 929–2000, (2000)
15. Kim MS, Haider R, Cho GJ, Kim CH, Won CY, Chai JS (2019) Comprehensive review of islanding detection method for distributed generation systems. *Energies* 12(837):1–21

Optimization of a Single-Channel Optical Communication System and an 8-Channel WDM System Using EDFA



Prem Babu, Maneesh Kumar Singh, and Sarika Pal

1 Introduction

An optical communication system based on total internal reflection uses a light signal for transmission through optical fiber cable for all types of data [1]. Literature tells us that optical fiber cable has three lowest attenuation regions also called as three optical windows for optical fiber communication [2]. Although the second window can be used for long-haul transmission, it prefers the third window. The reason behind this is the possible use of amplifiers operating at telecommunication wavelength, i.e., 1.5 μm in long-haul communication. Erbium-doped amplifier (EDFA) is a preferred amplifier among other amplifiers like praseodymium-doped fiber amplifier (PDFA) which increases the effect of nonlinearities in long-haul transmission [3, 4]. Optical amplifiers are the backbone of long-haul optical fiber communication as they amplify the light signal without any pre or post-conversion [5, 6]. All-optical amplifiers have a basic operation and characteristic of the creation of population inversion stimulated emission done by an incoming input signal. A certain power level of the signal, amplifier saturates, and this amplifier also adds noise to signal due to amplified spontaneous emission (ASE) [7]. The use of optical amplifiers solve the problem of power loss, its larger amplification bandwidth capability provides the advantage that gains of the amplifier can be insensitive to wavelength on incident signals and thus robust against a wide range of wavelength drifts [8–11]. There are primarily two types of optical amplifiers: semiconductor amplifiers and fiber amplifiers [12].

P. Babu · M. K. Singh · S. Pal (✉)

Department of Electronics Engineering, National Institute of Technology Uttarakhand, Srinagar, Garhwal 246174, India

e-mail: sarikapal@nituk.ac.in

P. Babu

e-mail: premtransiant@gmail.com

M. K. Singh

e-mail: maneesh.kr.singh@gmail.com

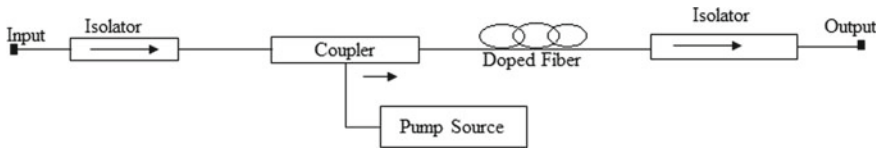


Fig. 1 General component of rare earth amplifier

Semiconductor amplifiers can be assumed as a laser diode which operates below the threshold so that it can amplify the input signal, but not able to produce coherent light by itself. In fiber amplifiers, a section is doped with ions to have a positive gain medium. Figure 1 shows the generic optical amplifier. The dopants play an important role, as they decide the gain bandwidth and the operating wavelength, whereas the silica plays the role of a host medium [13]. Erbium (Er), neodymium (Nd), praseodymium (Pr), thallium (Th), and ytterbium (Yb) are examples of few dopants.

The use of dopant decides the characteristic of the fiber amplifier. EDFA has got much attention because of its low-cost investment, wider operating bandwidth, lower noise figure and a high gain at 1550 nm wavelength [14, 15]. At this 1550 nm wavelength window, optical fiber cable has a minimum transmission loss. The EDFA is used exclusively with 1.55 μm lightwave systems [9]. The EDFA consists of a length of optical fiber cable, doped with ions of a rare earth element erbium. Within the fiber, the optical transmission signal wavelengths are mixed with a high powered signal from a pump laser [16]. This excites the ions in the erbium, and they give up this energy (of the same wavelength as signal 1500 nm) in the form of photons particle (in phase with input signal) which get added to the incoming photon particle (input data signal), thus amplifying it [17]. Nowadays due to the use of wavelength division multiplexing (WDM), the modern systems are capable of handling about 160 optical signals and thus expand a basic 100 Gbit/s systems over a single fiber pair over 16 Tbit/s [8]. When the spacing is less than 1 nm, it is dense WDM, and if the spacing is more than 5 μm it is Coarse WDM (CWDM) [9]. The CWDM operates with 8 channels in C-band, i.e., in the 1550 nm window. The DWDM systems can also operate in the C-band region in the 1550 nm window, but with only 40-channels and having the spacing of 100 GHz [11, 18]. In this paper, first, it performs the parametric analysis EDFA for a single-channel communication system, and after that, its optimized parameters for single and 8-channel WDM system.

2 Simulation Results and Performance Analysis

2.1 Parametric Analysis of Erbium-Doped Fiber Amplifiers

Erbium-doped fiber Amplifier is doped with Er^{+3} ions. Keeping the desire system criteria of fiber amplifiers design, the amplifier gain depends on various parameters such as the length of EDFA, the concentration of erbium atom in fiber, the wavelength of pump signal and input signal, the power of pump signal and input signal and pump configuration which varies the gain of EDFA [16]. In this paper, first of all, optimized these parameters are to obtain a reasonable flat gain for EDFA for schematic setup shown in Fig. 2.

2.1.1 Optimization of the length of EDFA

Increasing the length of fiber does not necessarily increase the gain as it starts decreasing on increasing the length of the fiber beyond a certain limit at a given pump power. Optimizing the length of EDFA includes analyzing the effect of its parameters such as gain effect, pump power effect, and signal power effect on length of EDFA [19]. The following analysis has been performed to optimize the length of EDFA.

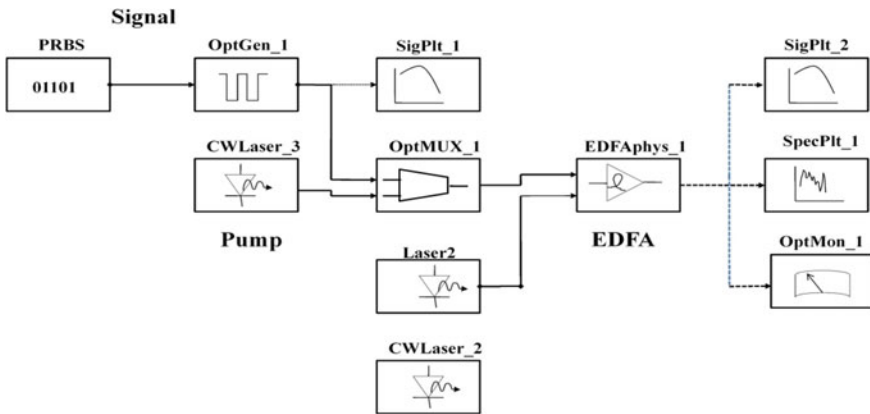


Fig. 2 Schematic setup for EDFA performance analysis

Optimization Based on Gain

The gain increases on increasing fiber length, i.e., up to 13 m, and it decreases after 16 m. It is observed that the gain is optimal (i.e., more than 35 dB) at length near 15 m. The pump signal of wavelength 980 nm is taken for the above simulation [7].

Optimization Based on Signal Power

The maximum gain is achieved at 15 m of EDFA length for any value of signal power. It is considered as -20 dB is the maximum input power, so the minimum EDFA length taken should be ~ 10 m.

2.1.2 Optimization of Wavelength

The following analysis will optimize the range of wavelength in the $1.55 \mu\text{m}$ window (approx. from 1500 to 1600 nm). This optimization considers the effect of poor signal and length of EDFA.

Optimization Based on Signal Power

The EDFA possesses different gain at different wavelengths; it has the nonzero gain for 1551–1640 nm and more than 25 dB for 1520–1565 nm wavelength range. A nearly flat gain region lies between 1530–1550 nm with a gain of more than approx. 25 dB for signal power of -12 dB and less. The maximum gain of 41.61 dB is achieved at a wavelength of 1530 nm at any signal power.

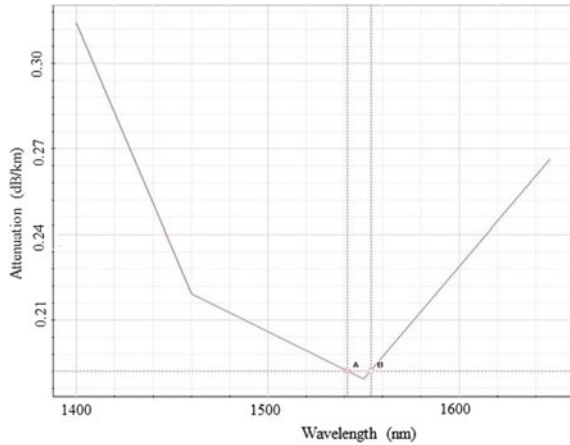
Optimization Based on EDFA Length

Flat gain is achieved for the 10–15 m length of EDFA in the wavelength range 1540–1560 nm. Precisely, it is least at 10 m length where the gain is almost flat.

2.1.3 Performance Analysis Based on Pump Configurations

There are three different configurations of which EDFA are pumped [4]. When the input signal and pump signal is in the same direction, it is named as co-pumping when they are in the opposite direction, it is termed as counter-propagating, and the third configuration is bidirectional pumping. It compares all these three configurations for a length of 14 m EDFA with input signal power of -20 dBm. It is observed that counter-propagating configuration provides better gain than co-propagating [3]. The

Fig. 3 Signal attenuation as a function of the signal wavelength



best approach is a bidirectional pumping scheme [1, 4, 20], which provides the best gain among all the three.

2.2 Communication System Without EDFA

A communication system without EDFA means a system without an amplifier. This system includes a transmitter, a fiber optic channel and a receiver; only the amplifier part is neglected. Such a system cannot be used for long-haul communication as the transmission distance using the optical fiber is not ideal due to the presence of various attenuation factors inside the fiber cable [18]. Here the aim to study how long it can transmit the signal without the use of amplifier directly by optic fiber cable. Optical fiber communication system without EDFA has three main parts of this communication system, i.e., transmitter, channel, and receiver.

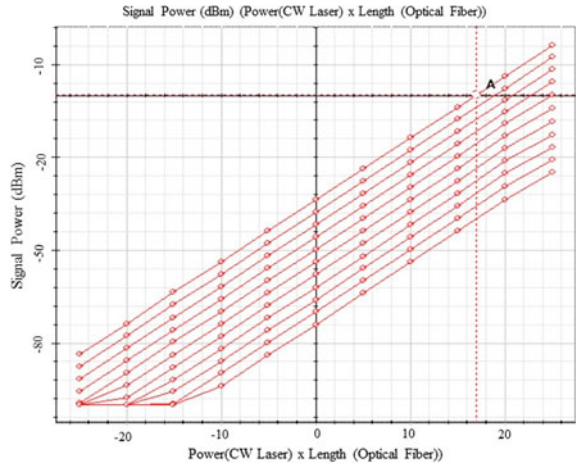
2.2.1 Results and Performance Analysis

The analysis of the system without EDFA is performed on the following parameters:

Range of Input Signal Wavelength

Here, its need to find out spectrum of signal with low attenuation. To obtain this, it calculated attenuation at different wavelengths. Figure 3 shows that the minimum attenuation of 0.189 dBm/km occurs for a signal having a wavelength of 1550 nm. The desired range of input signal wavelength is obtained from 1540–1555 nm.

Fig. 4 Signal output power vs input power for different fiber length



Length of Fiber and Input Signal Power

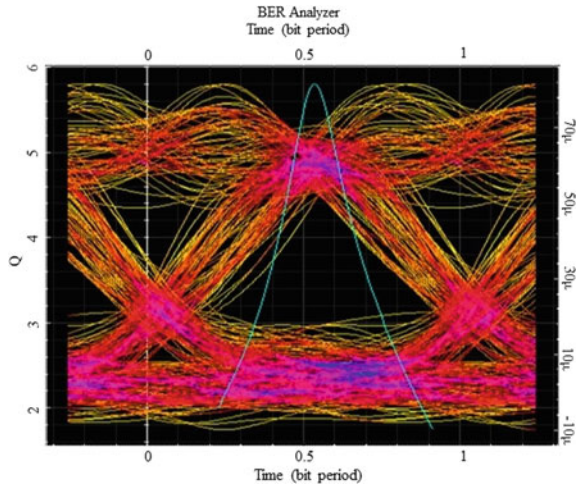
The length of fiber is function of input signal power. The higher the input power, longer the fiber length. Figure 4 shows output signal power (dBm) variation with input signal power for different fiber lengths.

It varies the input power from -25 to $+25$ dBm, the output signal power is observed for various fiber lengths from 0 to 100 km.

Length of Fiber, Input Signal Power and BER

The three parameters which decide the output power and maximum possible length are input signal wavelength, input signal power and BER of the obtained output signal. Figure 5 shows the BER analysis through an eye diagram. More the opening of the eye, better the output signal thus more accurate detection with lower BER [18]. The BER value is obtained as 3.2×10^{-9} . In this analysis, a single-channel communication system without EDFA, the wavelength of the signal is used as 1550 nm. On varying input signal power and length of fiber, the minimum input signal power required is 0 dBm for which the maximum length of fiber transmission without using amplifiers is 61 km with BER of 3.2×10^{-9} . The problem is that the output signal power is very low, i.e., -58.127 dBm. To have more than 0 dBm output power, the input power should be more than 30 dBm. Generating 30 dBm of input power is not economical at all. Thus, the next section presents an analysis of the same system on using EDFA.

Fig. 5 BER Analyzer



2.3 Communication System Without EDFA

In this section, analyses the performance of a single-channel optical communication system with EDFA.

2.3.1 Simulation Setup

Simulation setup used to perform the analysis is shown in Fig. 6. The block used in this simulation circuit consists of a transmitter, channel, receiver and amplifier. The channel used is the optical fiber channel which is connected to the input of EDFA at one end.

The attenuation caused by this fiber is considered during the analysis. EDFA is used as an optical amplifier to amplify the optical signal and thus increasing the output power. The length of EDFA taken here is 12.5 m. The operating wavelength is 1550 nm after that receiver is used to get back the original signal.

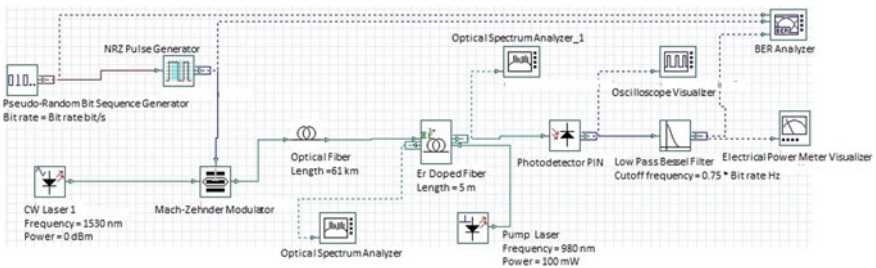


Fig. 6 A basic communication system using EDFA

2.3.2 Results and Performance Analysis

Firstly, analyzed the EDFA length and the pump power requirement, as shown in Fig. 7. Then it is observed that the change in BER while varying the length of optical cable fiber for different input signal power.

Fixing the EDFA Length and Pump Power for the System

Figure 7 shows variation in output signal power (dBm) with respect to the length of EDFA for different values of pump power. On increasing pump power, output power increases. Generating the pump signal with a higher power is not at all economical and sometimes not possible also. So here the maximum pump power that it considered is 20 dBm. Here the length is used as 12.5 m, and it gives maximum power. Bidirectional pumping with wavelength 980 nm and pump power 20 dBm is considered. The signal wavelength considered here is 1540–1555 nm based on the minimum attenuation effect, as explained in Sect. 1.

Further analysis involves finding the maximum length of the fiber. The analysis is done by varying the signal power from -25 to 0 dBm and optical fiber length from 0 to 100 km.

BER Improvement

Figure 8 is plotted using BER analyzer. EDFA not only reduces BER but the output power without increasing the input power is also improved. A large eye-opening shows minimum BER. It obtained BER of 5.13×10^{-20} , which is far lower than 10^{-9} . Thus, the use of EDFA significantly enhances the performance of far distance communication system. It is observed that without using the EDFA, the transmission

Fig. 7 Signal output power vs length for different input power

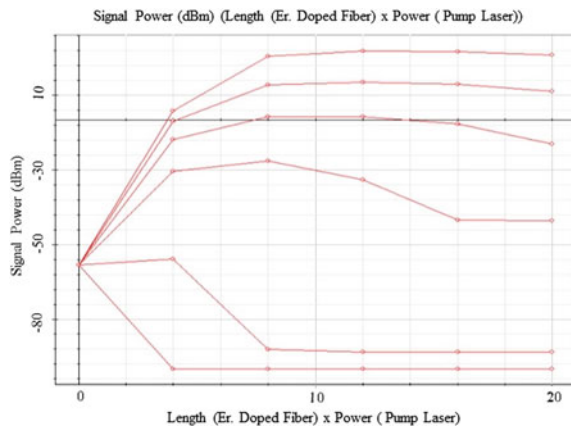
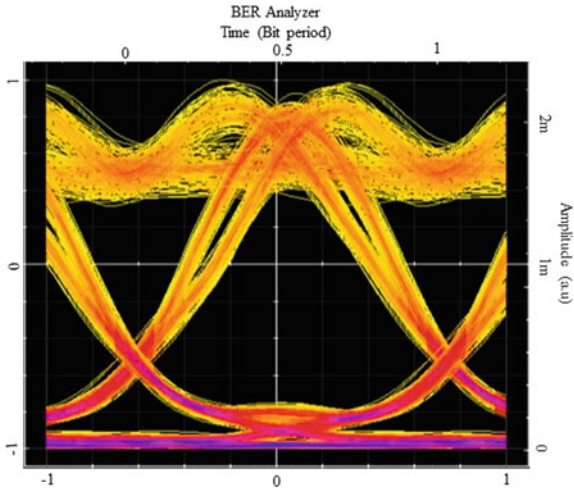


Fig. 8 BER Analyzer



distance that it can cover using simply optic fiber cable is 61 km with BER of 3.2×10^{-9} with an output power of -58.127 dBm for an input power of 0 dBm. On using EDFA in the same system, the maximum fiber length of 81 km is achievable at -20 dBm input power and 91 km for 0 dBm input power. Thus, the use of EDFA reduces BER to 5.13×10^{-20} and improves the output power without increasing the input power.

2.4 EDFA in WDM System

The EDFA gain optimization for WDM system optical network design consists of 8 input channels, an ideal multiplexer, two isolators, pump laser, optical amplifier, optical fiber, demultiplexer, PIN photodetector, low-pass Bessel filter, 3R regenerator and BER analyzer as shown in Fig. 9.

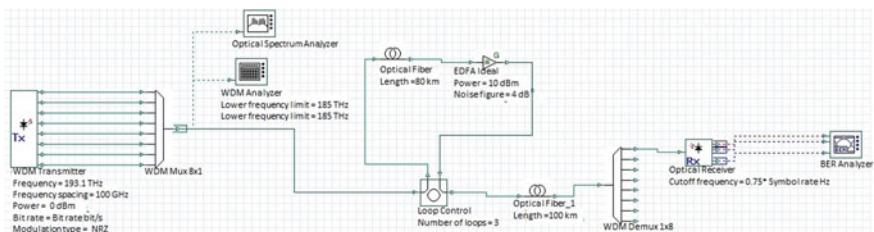
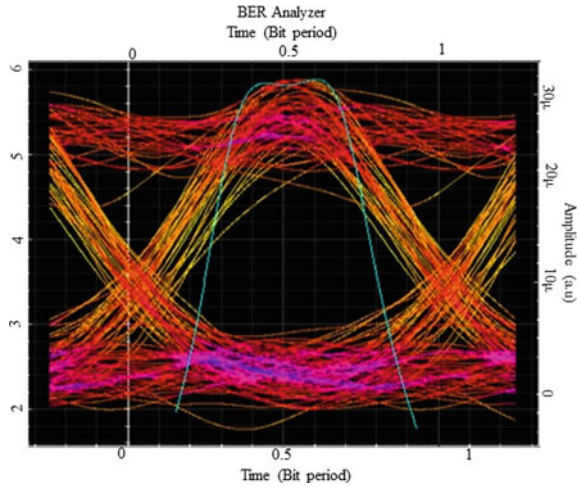


Fig. 9 Setup for a WDM system

Fig. 10 BER analyzer of the WDM system



2.4.1 Results and Performance Analysis

It used optical fiber cable along with inline EDFA having 10 dB gain and 4 dB as its noise figure. A fiber of length 80 km is attached with EDFA in loop control, thus giving a transmission distance of 240 km. Outside the loop, it has another fiber optic cable of length 100 km. So, it is capable of transmitting the optical signal through optical fiber over a distance of 340 km. The BER analyzer, as shown in Fig. 10, shows a good eye-opening, with BER of 1.9×10^{-9} .

3 Conclusions

First of all, the parametric analysis of the EDFA optical amplifier is done to optimize its performance. After that analysis of single-channel OFCS without and with use of EDFA is performed. The signal wavelength range considered is 1540–1555 nm for minimum attenuation. It is observed that without using the EDFA, the maximum transmission is 61 km with BER of 3.2×10^{-9} with an output power of 58.127 dBm for an input power of 0 dBm. To have more than 0 dBm of output power, the input power should be more than 30 dBm. But generating 30 dBm of input power is not economical at all. So the other option is to use amplifiers. With the use of EDFA in the same system, it is observed that the maximum fiber length of 81 km is achievable at -20 dBm input power and 91 km for 0 dBm input power. EDFA resulted not only in lower BER, 5.13×10^{-20} but also improved the output power without increasing the input power. It can undoubtedly use EDFA significantly to get the improved performance of the OFCS.

Lastly, 8-channel WDM system is demonstrated to get 10 Gbps data rate, on using MZ modulation schemes. The transmitter section consists of 8 channels, with -20

dBm input power. It used a single-mode fiber, of length 340 km and the channel spacing of 100 GHz. The BER achieved is 19×10^{-9} for all the channels. It is concluded that the proposed model can be used to design long-distance transmissions with EDFA and SMF to guarantee the communication signal quality.

References

1. Becker PC, Olsson NA, Simpson JR (1999) Erbium-Doped fiber amplifiers: fundamentals and technology. Academic Press, San Diego, pp 131–152. <https://doi.org/10.1016/B978-012084590-3/50007-7>
2. Liying L, Yu M, Jiuru Y (2013) Performance optimization-based spectrum analysis on OFRA and EDFA devices. TELKOMNIKA Indonesian J Electr Eng 11(7):3742–3749. <https://doi.org/10.11591/telkomnika.v11i7.2822>
3. Desurvire E (1992) Analysis of gain difference between forward- and backwards-pumped erbium-doped fiber amplifiers in the saturation regime. IEEE Photonics Technol Lett 4(7):711–714. <https://doi.org/10.1109/68.145247>
4. Mishra R, Shukla NK, Dwivedi CK (2017) Performance analysis and implementation of different pumping techniques on an EDFA amplifier. In: Third international conference on sensing, vol 40(2), pp 39–44 ICSSS, Chennai. <https://doi.org/10.1109/SSPS.2017.8071561>
5. Agrawal GP (2002) A fiber-optic communication systems, 4th ed. Wiley, pp 226–272. ISBN: 978-0-470-50511-3
6. Dignonnet MJF (2001) Rare-earth-doped fiber lasers and amplifiers, revised and expanded. CRC press, ISBN 0203904656, 9780203904657
7. Saktioto T, Ikhsan R (2019) Optical amplifiers for next-generation telecommunication. In: Telecommunication networks-trends and developments. Intech Open. <https://doi.org/10.5772/intechopen.79941>
8. Zyskind J, Srivastava A (2011) Optically amplified WDM networks. Academic press, ISBN: 9780080960982
9. Jordanova L, Topchiev V (2009) Amplification of the multi-wavelength signal by using edfa with constant gain. IJCSNS 9(12):38
10. Laming RI, Townsend JE, Paye DN, Meli F, Grasso G, Tarbox EJ (1991) IEEE Photon Technol Lett 3(3):253
11. Suyama M, Yokota I, Watanabe S, Kuwahara H (1991) Proceedings of the optical amplifiers applied optics society of America, pp 174. Washington, DC
12. Desurvire E (1994) Erbium doped fiber amplifiers a principles and applications. Republished in New York by Colombia University, ISBN: 978-0-471-26434-7
13. Ali S, Khalid AS, Al-Khateeb, Bouzid B (2009) A new erbium doped fiber amplifier. J Appl Sci 9:2498–2500. <https://doi.org/10.3923/jas.2009.2498.2500>
14. Becker PC, Olsson NA, Simpson JR (2002) Erbium-doped fiber amplifiers fundamental and technology, 2nd edn. Academic Press, New York
15. Desurvire JE (2002) Erbium-doped fiber amplifiers: device and system developments, 1st edn. Wiley, New York
16. Rottwitt K, Povlsen JH, Bjarklev AO, Lumholt O, Pedersen B, Rasmussen T (1992) Optimum signal wavelength for a distributed erbium-doped fiber amplifier. IEEE Photon Technol Lett 4(7):714–717
17. Dutta MK (2017) Design and performance analysis of EDFA and SOA for optical WDM networks: a comparative study. In: 2017 14th IEEE India council international conference (INDICON), pp 1–6
18. Ivaniga T, Ivaniga P (2017) Comparison of the optical amplifiers EDFA and SOA based on the BER and-factor in C-band. Adv Opt Technol

19. Jesmeen MZH, Hossen J, Bhuvaneswari T, Hasnayeem MA, Emerson Raja J, Tawsif K (2018) Performance evaluation of distributed gain offered by Raman amplifier in WDM and EDFA. In: Intelligent manufacturing mechatronics. Springer, Singapore, pp 537–545
20. Saraswathy L, Vaidyan VK (2015) Optimized flattened gain spectrum in C-Band WDM using automatic gain control in Bi-directionally pumped EDFA. IJERT 4(10)

Adaptive Unknown Input Observer for Actuator Fault Detection and Isolation of PEM Fuel Cell Systems



Vikash Sinha and Sharifuddin Mondal

1 Introduction

Fuel cell systems (FCSs) are based on the conversion of chemical energy into electrical energy. These systems utilize an electrochemical cycle. It also gets used to fuel cars, electronics, homes and electric grids. The fuel cell technology has gained increased attention in recent decades because of its clean processes and high efficiency. FCSs for mobile and stationary power applications are under intensive development phase. In particular, the proton exchange membrane fuel cell (PEMFC) systems are currently being used for applications in ground vehicles and stationary power [1–5]. Despite many works on PEMFC system modelling, relatively few were done for their control and observation [3–6]. Many types of UIOs for both nonlinear and linear systems have been proposed over the years [7–10]. A nonlinear adaptive observer estimated hydrogen partial pressure in the anode channel [3]. The problem of adaptive observer architecture, as discussed in [8, 9], has been applied to nonlinear multi-output single-input systems. AUIOs have been developed for Lipschitz systems [11–14] that operate under ideal operating conditions. The AUIO design is based on the selection of an appropriate parameterization technique. This design also uses adaptive laws for regulating system parameter [15, 16].

First, an AUIO design based on fault detection and isolation (FDI) algorithm is formulated. This is to detect and isolate the failure of PEMFC system actuators. The proposed AUIO is then used to produce residual signals. If the model and system match, zero residual results. On the other hand, this is certainly not zero due to model mismatch. This will be controlled by signals uniquely. The benefit of the AUIO strategy is that exogenous fluctuations at a steady state are decoupled from the

V. Sinha (✉) · S. Mondal

Department of Mechanical Engineering, National Institute of Technology, Patna, Bihar, India
e-mail: vikash.me15@nitp.ac.in

S. Mondal

e-mail: sharifuddin@nitp.ac.in

residuals. In MATLAB [17, 18], the linear matrix inequality (LMI) toolbox is used to derive adequate conditions for the observer to exist. An application to the PEMFC system is presented to demonstrate the efficacy of the observer-based FDI algorithm. This AUIO-based technique can be further used and extended to multiple actuator fault cases in the PEMFC system [5] and is easier to implement than other existing methods because it satisfies existence conditions of normal UIO. This is also very useful for the actuator fault diagnosis-based FTC design of the PEMFC systems.

2 Adaptive Unknown Input Observer Design

A PEMFC system is considered as

$$A\dot{x}_i(t) = Ax_i(t) + Bl_iu_i(t) + g(\bar{u}_i(t), x_i(t)) + D_id(t) \tag{1}$$

$$y_i(t) = Cx_i(t) \tag{2}$$

In (1) and (2), $x_i(t) \in R^n$, $u_i(t) \in R^m$, $y_i(t) \in R^p$, $d(t) \in R^q$, $\bar{u}_i \in R^r$ are state, input, output, unknown input and parameter vectors. Matrices of particular dimensions A, B, C and D_i are known. In (1) $l_i = \text{diag}[l_1, l_2, \dots, l_p]$, $l_i = 0 \sim 1, i = 0, 1, 2, \dots, p$. $l_i = 0$ is the stuck fault, and $l_i = 1$ denotes no fault. The following assumptions are stated before defining an AUIO for the system given by (1) and (2).

Assumption 1 The \bar{u}_i is constrained in the sense.

$$\|\bar{u}_i\|_2 \leq \sigma \tag{3}$$

such that σ is finite.

Assumption 2 The system meets this rank criterion.

$$\text{rank}(C) = n \quad \text{and} \quad \text{rank}(CD_i) = \text{rank}(D_i) \tag{4}$$

Assumption 3 The function $g(\bar{u}_i(t), x_i(t))$ is bounded and meets the global condition of Lipschitz.

$$\|g(\bar{u}_i(t), x_i(t)) - g(\hat{u}_i(t), x_i(t))\| = b_i\|\bar{u}_i(t) - \hat{u}_i(t)\| \leq \gamma\|\phi_i\| \tag{5}$$

where γ is the Lipschitz constant.

Assumptions 1–3 are the assumptions which are standard [7, 15]. The AUIO design problem can now be defined as follows that are given by Eqs. (1) and (2).

$$\dot{z}_i(t) = Nz_i(t) + Ly_i(t) + G_iu_i(t) + Pg(\hat{u}_i(t), x_i(t)) \tag{6}$$

$$\hat{x}_i(t) = z_i(t) - Hy_i(t) \quad (7)$$

$$\dot{\hat{u}}_i = \alpha_i r_i^T(t) P_e C P b_i = \alpha_i e_i^T(t) P_1 P b_i \quad (8)$$

In (6) - (8), $\hat{x}_i(t) \in R^n$, $\hat{y}_i(t) \in R^p$ and $\hat{u}_i \in R^r$ are estimated state, output and parameter vector; N , L , G_i , P and H are calculated for \hat{x}_i converging to x_i asymptotically. \hat{u}_i is adjusted using (8). b_i is the B 's i th column, and $\phi_i = \bar{u}_i - \hat{u}_i$ is the estimation error of \bar{u}_i ; $\alpha_i > 0$ is an adaptation rate and gives the adaptive estimation convergence rate. P_e and $P_1 = C^T P_e C$ are symmetric matrices, and r_i in (8) is $r_i = e_{y_i}(t) = y_i - \hat{y}_i = C e_i(t)$ where $e_i(t)$ is the state error defined below.

The error in the state is

$$e_i(t) = x_i(t) - \hat{x}_i(t) = x(t) - z_i(t) + Hy(t) = Px(t) - z_i(t) \quad (9)$$

with

$$P = I_n + HC \quad (10)$$

The observer's error dynamics is

$$\begin{aligned} \dot{e}_i(t) = & N e_i(t) + (PA - NP - LC)x_i(t) \\ & + (PBl_i - G_i)u_i(t) + PD_i d(t) + P(g(\bar{u}_i(t), x_i(t)) - g(\hat{u}_i(t), x_i(t))) \end{aligned} \quad (11)$$

If these conditions are met, then the dynamics of the error will become

$$PD_i = 0 \quad \text{gives} \quad (I_n + HC)D_i = 0 \quad (12)$$

$$PBl_i - G_i = 0 \quad \text{or} \quad G_i = PBl_i \quad (13)$$

$$PA - NP - LC = 0 \quad (14)$$

$$\dot{e}_i(t) = N e_i(t) + P(g(\bar{u}_i(t), x_i(t)) - g(\hat{u}_i(t), x_i(t))) \quad (15)$$

From (12), H is given as

$$H = -D_i(CD_i)^+ + Y(I_p - (CD_i)(CD_i)^+) = R + YS \quad (16)$$

in which

$$R = -D_i(CD_i)^+, \quad S = I_p - (CD_i)(CD_i)^+ \quad (17)$$

Then (10) gives

$$P = I_n + RC + YSC \tag{18}$$

G_i is found from (13) using (18). Then (15) is written in the Luenberger form [7] using a matrix K as

$$N = PA - KC. \tag{19}$$

By comparing (14) with (19), the following relation is obtained using (10)

$$K = L + NH \tag{20}$$

with the above matrices (15) is as

$$\dot{e}_i(t) = (PA - KC)e_i(t) + P(g(\bar{u}_i(t), x_i(t)) - g(\hat{u}_i(t), x_i(t))) \tag{21}$$

For PEMFC systems, this takes the form of the Luenberger-type observer error dynamics [7]. Now if the matrix K is determined, then $e_i(t) \rightarrow 0$ as $t \rightarrow \infty$, and (6) and (7) will be the PEMFC system’s AUIO given by (1) and (2). It can be proven that Lyapunov–Krasovskii theorem’s stability conditions are met [7]. The following theorem is proposed to calculate gain matrix K .

Theorem 1 For (1) and (2) with its AUIO (6) and (7) using Assumptions 1–3 and taking symmetric matrices P_1 and Q_1 with matrices \bar{Y} and \bar{K} , then.

$$\begin{bmatrix} X_{11} & 0 & X_{13} \\ 0 & -(1 - h_1)Q_1 & 0 \\ X_{31} & 0 & -I \end{bmatrix} < 0 \tag{22}$$

where $X_{11} = P_1(I + UC)A + ((I + UC)A)^T P_1 + \bar{Y}(VCA) + (VCA)^T \bar{Y} - \bar{K}C - C^T \bar{K}^T + Q_1 + \gamma I$, $X_{13} = \sqrt{\gamma} P_1(I + UC) + \sqrt{\gamma} \bar{Y}(VC)$, $X_{31} = X_{13}^T$ and $Y = P_1^{-1} \bar{Y}$ holds, $K = P_1^{-1} \bar{K}$ stabilize (21) for $g(\bar{u}_i(t), x_i(t))$ with γ as Lipschitz’s constant.

Proof

This theorem is proved like in [7] for similar cases. The proof is ignored here.

3 Stuck Fault Detection and Isolation Algorithm

Consider the following observer to isolate a stuck fault within the i th actuator

$$\dot{z}_i(t) = Nz_i(t) + Ly_i(t) + G_i u_i(t) + Pg(\hat{u}_i(t), x_i(t)) \tag{23}$$

$$\hat{x}_i(t) = z_i(t) - Hy_i(t) \tag{24}$$

where $G_i = PBl_i, l_i = \text{diag}[l_1, l_2, \dots, l_p], l_i = 0$ and $l_j = 1$ for $j \neq i$. Because \bar{u}_i is uncertain, the observer cannot be constructed with it. We will estimate that online. In (23), \bar{u}_i is replaced with its estimated value \hat{u}_i which guarantees the convergence on the estimated value. Using the following adaptive algorithm, \hat{u}_i is modified here.

$$\dot{\hat{u}}_i(t) = \alpha_i e_i^T(t) P_1 P b_i \tag{25}$$

where $\alpha_i > 0$ is the adaptation rate and this could be modified. It also affects the estimation convergence rate. P_1 is a definite symmetric matrix whose solution is given by (22). In the event of a no-fault situation, \hat{u}_i is within threshold values and \hat{u}_i crosses these values for the faulty scenario. And $\dot{e}_i(t)$ is

$$\dot{e}_i(t) = Ne_i(t) + P(g(\bar{u}_i(t), x_i(t)) - g(\hat{u}_i(t), x_i(t))) = Ne_i(t) + P b_i \phi_i \tag{26}$$

where $\phi_i = \bar{u}_i - \hat{u}_i$ is the stuck position estimation error of \bar{u}_i . The adaptation of the AUIO is a self-tuned process. It lets the calculated parameter converging to the actual value. It occurs such that the parameter residual is decreased gradually [15].

4 PEMFC System

The above algorithm is applied for the PEMFC [2] system stuck FDI. In this case, the system's state matrices and vectors are derived where $x(t) = [x_1 \ x_2 \ x_3]^T, u(t) = [u_1 \ u_2 \ u_3]^T$. The matrices and vectors for the system are as follows with this arrangement:

$$A = \begin{bmatrix} -22.9610 & -22.9610 & -22.9610 \\ -46.4930 & -46.4930 & -46.4930 \\ -0.3295 & -0.3295 & -0.3295 \end{bmatrix}$$

$$B = \begin{bmatrix} 367.5 & 7.739 & -289.668 \\ 367.5 & 29.104 & 0 \\ 367.5 & 0.118 & -942.225 \end{bmatrix}$$

$$C = \begin{bmatrix} 1 & 0 & 1 \\ 0 & 1 & 0 \\ 0 & 0 & 1 \end{bmatrix}$$

The parameter unknown is set to a constant value $\bar{u}_2 = 0.5$. The observer parameters are first selected based on the previous matrices and vectors as $\alpha = 1 \times 10^{-8}$ and $\sigma = 1$. The observer gain is calculated by using these parameters and assuming appropriate values for other parameters, and using the LMI toolbox in MATLAB [17]. The adaptive UIO is determined on the basis of the calculated observer gains. The observer initial values and the parameter unknown are set to zero. Three AUIOs are designed with $D_1 = [1 \ 0 \ 0]^T$, $D_2 = [0 \ 1 \ 0]^T$ and $D_3 = [0 \ 0 \ 1]^T$. $l_i = \text{diag} [1 \ 0 \ 1]$ and \bar{u}_2 is taken as constant. Initially, the system works without fault. One fault at the 50 s in actuator 3 is introduced after gaining steady state, respectively. Residuals of state and parameter are in Figs. 1 and 2 assuming fixed threshold values ϵ_i , respectively. When state residuals exceed their ϵ_i , the fault

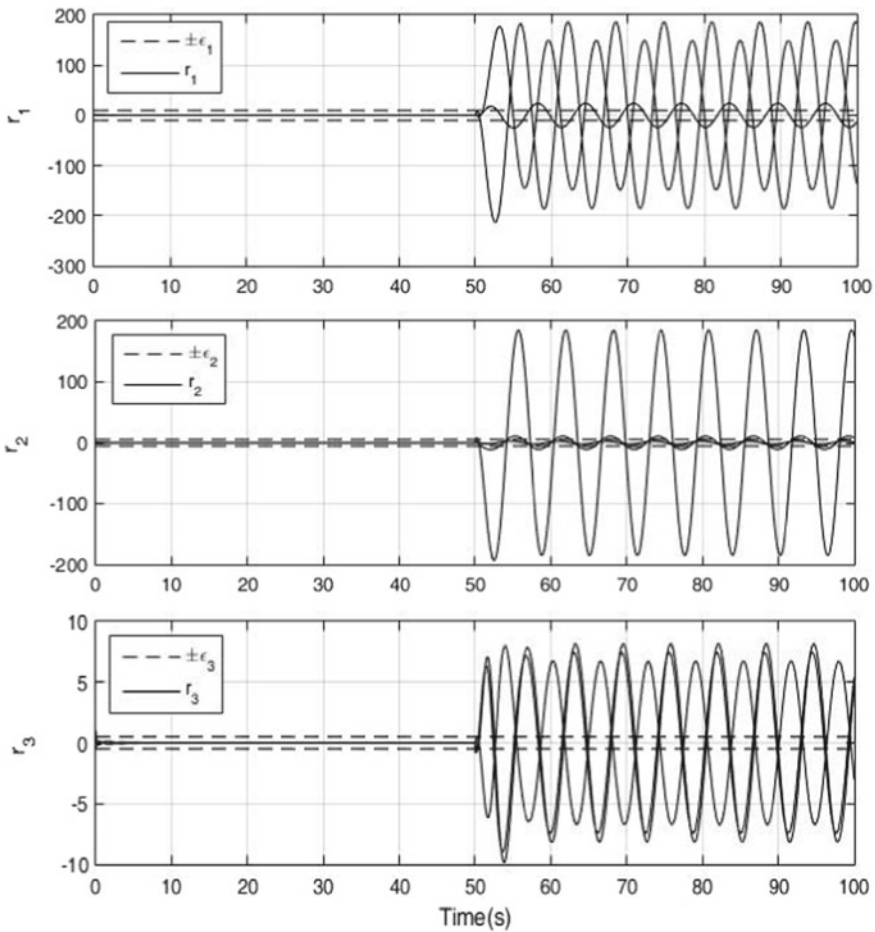


Fig. 1 State residuals

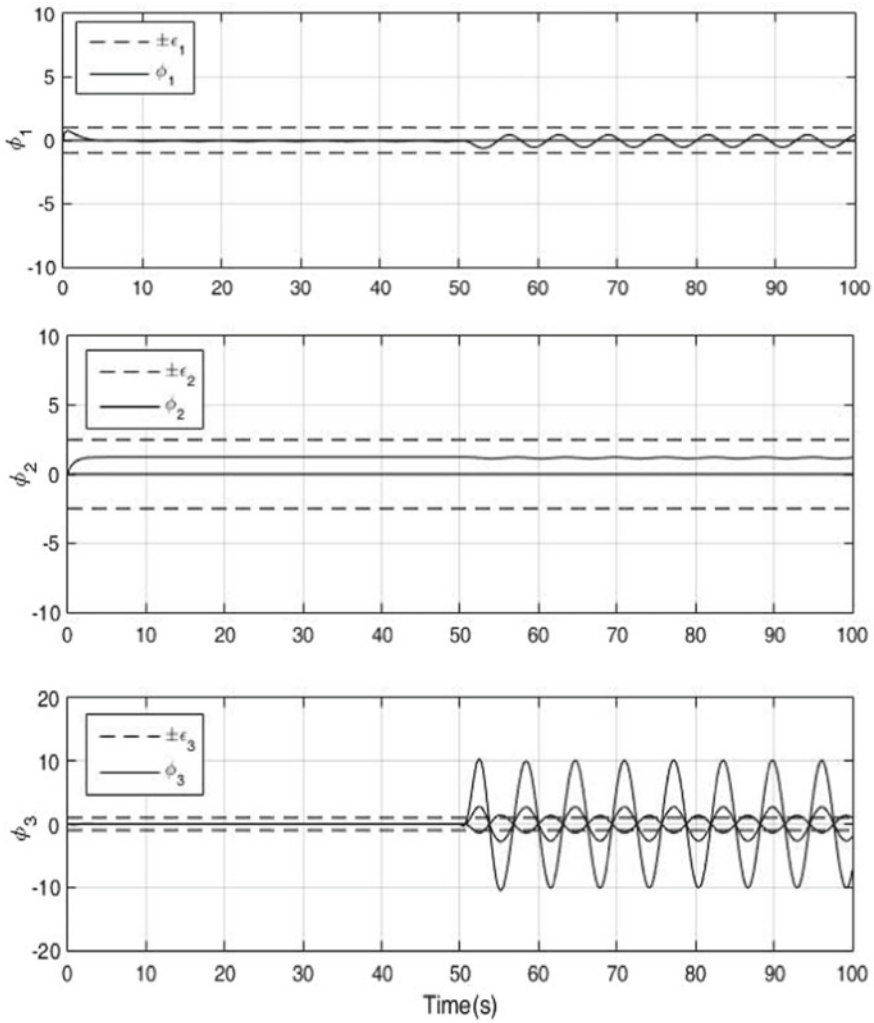


Fig. 2 Parameter residuals

persists in the system. Because the residual parameters ϕ_1 and ϕ_2 are within their respective threshold values, it is simple to isolate the fault. A table is formed to identify the faulty actuator depicted in Table 1. Thus, it is clear that fault is present in actuator 3 from the decision table.

Table 1 Decision table

State residuals	Is $r_i > \varepsilon_i$?	Decisions	Parameter residuals	Is $\phi_i > \varepsilon_i$?	Decisions
r_1	Yes	Fault is detected	ϕ_1	No	No fault in actuator 1
r_2	Yes		ϕ_2	No	No fault in actuator 2
r_3	Yes		ϕ_3	Yes	Fault in actuator 3

5 Conclusion

An AUIO is designed for PEMFC system. The AUIO is designed on the LMI method developed for PEMFC systems. This type of design has extensive applications, mainly in the fields of robust control and diagnosis of faults. Using simulation results, the efficacy of the proposed AUIO-based FDI algorithm is demonstrated. This adaptive UIO-based technique can be further used and extended to multiple actuator fault cases in the PEMFC system and is easier to implement than other existing methods. One of its advantages is that it satisfies the simple UIO existence conditions. This is very useful for the fault diagnosis and FTC of PEMFC systems.

References

1. Pukrushpan JT, Peng H, Stefanopoulou AG (2004) Control-oriented modelling and analysis for automotive fuel cell systems. *J Dyn Syst Meas Contr* 126:14–25
2. Kim E-S, Kim C-J, Eom K-S (2007) Nonlinear observer design for PEM fuel cell systems. In: Proceedings of the international conference on electrical machines and systems, Seoul, Korea, pp 1835–1839
3. Arack M, Gorgun H, Pedersen M, Varigonda S (2003) An adaptive observer design for fuel cell hydrogen estimation. In: Proceedings of the American control conference, Denver, Colorado, pp 2037–2042
4. Sinha V, Mondal S (2018) Recent development on performance modelling and fault diagnosis of fuel cell systems. *Int J Dyn Control* 6:511–528
5. Sinha V, Mondal S (2020) Adaptive unknown input observer approach for multi-fault diagnosis of PEM fuel cell system with time-delays. *J Control Decis*. <https://doi.org/10.1080/23307706.2020.1725917>
6. Dannenberg K, Ekdunge P, Lindbergh G (2000) Mathematical model of the PEMFC. *J Appl Electrochem* 30:1377–1387
7. Mondal S, Chung WK (2013) Adaptive observer for a class of nonlinear systems with time-varying delays. *Int J Adapt Control Signal Process* 27:610–619
8. Marino R (1990) Adaptive observers for single output nonlinear systems. *IEEE Trans Autom Control* 35:1054–1058
9. Marino R, Tomei P (1992) Adaptive observers for a class of multi-output non-linear systems. *Int J Adapt Control Signal Process* 6:353–365
10. Zhang Q, Delyon B (2001) A new approach to adaptive observer design for MIMO systems. In: Proceedings of the 20th American control conference, Arlington, VA, USA, pp 1545–1550

11. Cheng C-F (2001) Design of adaptive observation schemes for Lipschitz nonlinear systems. *JSME Int J: Ser, C* 44:863–866
12. Cho YM, Rajamani R (1997) A systematic approach to adaptive observer synthesis for nonlinear systems. *IEEE Trans Autom Control* 42:534–537
13. Dong Y-L, Mei S-W (2007) Adaptive observer for a class of nonlinear systems. *Acta Automatica Sinica* 33:1081–1084
14. Zemouche A, Boutayeb M (2009) A unified adaptive observer synthesis method for a class of systems with both Lipschitz and monotone nonlinearities. *Syst Control Lett* 58:282–288
15. Wang D, Lum K-Y (2007) Adaptive unknown input observer approach for aircraft actuator fault detection and isolation. *Int J Adapt Control Signal Process* 21:31–48
16. Zhang K, Jiang B, Cocquempot V (2008) Adaptive observer-based fast fault estimation. *Int J Control Autom Syst* 6:320–326
17. Gahinet P, Nemirovsky A, Laum A, Chilali M (1995) *LMI Control Toolbox: For Use with MATLAB*, The Mathworks Inc., Natick, MA, USA
18. Raghavan S, Hedrick JK (1994) Observer design for a class of nonlinear systems. *Int J Control* 59:515–528

Solving the Multi-server Queuing Model by Big-M Method



S. Vijay Prasad and Anil Kumar Birru

1 Introduction

Operations research (OR) is a giant subject, and linear programming is a subdivision of it. It is an application of matrix algebra, and the broad range of problems are solved, which is described by a system of linear equations. Queuing models interpret the concepts of having waiting lines. Some live examples are in waiting for lines in banks, supermarkets and public transport. The queuing models describe situations, where the consumer needs the service at the service centre, so that he/she has to wait for some time at the server in the waiting line, before availing the service and after that he leaves the centre.

By enhancing the efficiency skill of the service systems mechanism, one can reach the expectation of the consumer so that the consumer will be satisfied with it. If there are a small number of consumers in the queue, then using more capacity will imply expensive cost and inoperative time generates. So the decision-maker should opt the optimal level of service which should be neither at higher level nor a lower level, queuing theory which is a branch of OR facilitates the decision-maker to make decisions on workflow mechanism.

Song [1] in his article proposed a constant M_0 where big-M method converges if M is greater than M_0 . In 2016, Salvador et al. [2], in their article, depicted the use of the simplex method to compute the necessary treatment in radiotherapy of cancer. Huimin and Guozheng [3] in their research article applied the QT to evaluate the number of the service centre and the rate of optimal service.

S. V. Prasad (✉)

Department of Mathematics, Koneru Lakshmaiah Education Foundation, Guntur 522502, India
e-mail: indorevijay@gmail.com

A. K. Birru

Mechanical Engineering Department, National Institute of Technology Manipur, Imphal, India
e-mail: anilbirru@nitmanipur.ac.in

In this research article, the estimated number of customers in the system and the needed number of servers using LPP model, namely big-M method, without knowing the arrival rate, service rate and a number of servers of the multi-server queuing model.

2 Linear Programming (LP) Model for Multi-server Queuing Model

Operations research is an application of matrix algebra, and the broad range of problems are solved which is described by a system of linear equations. The linear equations are algebraic equations whose variable quantities are only in the first power, and the graph is a straight line. The LP problems are illustrated by an objective function which is to be maximized or minimized, subject to the constraints.

A standard form of the linear programming model is defined as follows:

$$\text{Maximize (or) Minimize } X = \sum_{i=1}^m A_i \alpha_i$$

$$\text{Subject to the constraints } \sum_{i=1}^m b_{ki} \alpha_i \leq \text{ or } = \text{ or } \geq c_k \text{ where } k = 1, \dots, n$$

$$\alpha_i \geq 0 \text{ Where } i = 1, \dots, m$$

The linear programming problem for M/M/S queuing model is followed:

Let S be the number of servers, L_s be expected a number of customers in the system, C_s be the service cost and C_w be the waiting cost of customer in the queue, then the total cost of the multi-server queuing system is defined as follows:

$$\text{Total cost} = C_s S + C_w L_s$$

The total cost is to be minimized, and the objective function of a linear programming problem is defined as follows:

$$\text{Min} Z = C_s S + C_w L_s$$

subject to the constraints

$$S + L_s \geq b_1, \quad S \geq b_2, \quad L_s \geq b_3, \quad S, L_s > 0$$

Here, b_1 is the sum of the least number of servers and the least number of customers in the system b_2 is the least number of the servers and b_3 is the least number of customers in the system. To obtain the number of servers (S) and the probable number

of consumers in the system (L_s), the minimum optimal cost using either a graphical method or big-M method. Vijay Prasad et al. [4] solved the problem using LPP graphical method.

From the values of S , L_s and for some independent value of $\mu > 0$, the probable arrival rate can be obtained by $0 < \frac{\lambda}{s\mu} < 1$ or $0 < \lambda < s\mu$ and also obtain the performance measures of the multi-server queuing model by Little’s law as follows:

$$W_s = \frac{L_s}{\lambda}$$

$$W_q = W_s - \frac{1}{\mu}$$

$$L_q = L_s - \frac{\lambda}{\mu}$$

3 Validation of the Model

For the formation of the linear programming problem, consider the required number of servers (S) and the number of customers in the system (L_s) are variables and considering the fixed service cost (C_s) for each server which is 150, the average waiting cost of each customer (C_w) which is 100. The objective function of the linear programming problem as follows:

$$\text{Min } Z = 150 S + 100 L_s$$

subject to the constraints

$$S + L_s \geq 12, \quad S \geq 2, \quad L_s \geq 8, \quad S, L_s > 0$$

The problem is solved by big-M method, and the result is the following:
Formulation of LP problem

$$\text{Min } Z = 150 S + 100 L_s + 0x_1 + 0x_2 + 0x_3 + MA_1 + MA_2 + MA_3$$

Subject to

$$S + L_s - x_1 + 0x_2 + 0x_3 + A_1 + 0A_2 + 0A_3 = 12$$

$$0S + L_s + 0x_1 - x_2 + 0x_3 + 0A_1 + A_2 + 0A_3 = 8$$

$$S + 0L_s + 0x_1 + 0x_2 - x_3 + 0A_1 + 0A_2 + A_3 = 2$$

For all $S, L_s, x_1, x_2, x_3, A_1, A_2, A_3 > 0$

Since all $C_j - Z_j > 0$, therefore, the optimal solution of the LPP is

$S = 2, L_s = 10$ and minimum $Z = 1300$ (Tables 1, 2, 3, 4).

For the values of $S=2$ and some independent value of $\mu = 2 > 0$, the expected arrival rate is $0 < \lambda < 4$ and performance measures of the multi-server queuing model computed by TORA software as follows:

Table 1 Initial iteration

C_j			150	100	0	0	0	M	M	M
Basic variables (B V)	Cost of B V	X_b	S	L_s	X_1	X_2	X_3	A_1	A_2	A_3
A_1	M	12	1	1	-1	0	0	1	0	0
A_2	M	8	0	1	0	-1	0	0	1	0
A_3	M	2	1	0	0	0	-1	0	0	1
$Z=22M$		Z_j	2M	2M	-M	-M	-M	M	M	MM
		$C_j - Z_j$	150-2M	100-2M	M	M	M	0	0	0

Table 2 Second iteration

C_j			150	100	0	0	0	M	M	M
Basic variables (B V)	Cost of B V	X_b	S	L_s	X_1	X_2	X_3	A_1	A_2	A_3
A_1	M	4	1	0	-1	1	0	1	-1	0
L_s	100	8	0	1	0	-1	0	0	1	0
A_3	M	2	1	0	0	0	-1	0	0	1
$Z=6M+800$		Z_j	2M	100	-M	M-100	-M	M	-M+100	M
		$C_j - Z_j$	150-2M	0	M	-M+100	M	0	2M-100	0

Table 3 Third iteration

C_j			150	100	0	0	0	M	M	M
Basic variables (B V)	Cost of B V	X_b	S	L_s	X_1	X_2	X_3	A_1	A_2	A_3
A_1	M	2	0	0	-1	1	1	1	-1	-1
L_s	100	8	0	1	0	-1	0	0	1	0
S_3	150	2	1	0	0	0	-1	0	0	1
$Z=2M+1100$		Z_j	150	100	-M	M-100	M-150	M	-M+100	-M+150
		$C_j - Z_j$	0	0	M	-M+100	-M+150	0	2M-100	2M-150

Table 4 Fourth iteration

C_j			150	100	0	0	0	M	M	M
Basic variables ($B V$)	Cost of $B V$	X_b	S	L_s	X_1	X_2	X_3	A_1	A_2	A_3
X_2	0	2	0	0	-1	1	1	1	-1	-1
L_s	100	10	0	1	-1	0	1	1	0	-1
S_3	150	2	1	0	0	0	-1	0	0	1
$Z = 1300$		Z_j	150	100	-100	0	-50	100	0	50
		$C_j - Z_j$	0	0	100	0	50	$M - 100$	M	$M - 50$

Table 5 For $S = 2$ and $\mu = 2$

Scenario	S	λ	μ	Ls_s	Lq	Ws	Wq
1	2	1	2	0.5333	0.0333	0.5333	0.0333
2	2	2	2	1.3333	0.3333	0.6666	0.1666
3	2	3	2	3.4285	1.9285	1.1428	0.6428
4	2	3.5	2	7.4666	5.7166	2.1333	1.6333
5	2	3.6	2	9.4736	7.6736	2.6315	2.1315
6	2	3.7	2	12.8138	10.9638	3.4632	2.9632
7	2	3.8	2	19.4871	17.5871	5.1282	4.6282
8	2	3.9	2	39.4936	37.5436	10.1265	9.6265

As $Ls = 10$ is known then from Table 5, $\lambda = 3.6$, and again for the values of $S = 2$ and some independent value of $\mu = 3 > 0$, the expected arrival rate is $0 < \lambda < 6$ and performance measures of multi-server queuing model computed by TORA software as follows:

As $Ls = 10$ is known then from Table 5, $\lambda = 5.4$. One can treat μ as an independent variable (>0) and can be obtained $\lambda (>0)$, and the independence of choosing μ gives the assurance of the existence of the λ .

4 Conclusion

The conclusions of this research paper are as follows:

- i. The big-M method can be used to find the performance measures and the optimal total cost of the multi-server queuing system when the arrival rate, service rate and the number of a required server are not known.
- ii. The arrival rate (λ) and service rate (μ) can be estimated by assuming anyone them is independent.
- iii. In Tables 5 and 6, the arrival rates are found by taking a fixed independent service

Table 6 For $S = 2$ and $\mu = 3$

Scenario	S	λ	μ	L_s	L_q	W_s	W_q
1	2	3	3	1.3333	0.3333	0.4444	0.1111
2	2	4	3	2.4000	1.0666	0.6000	0.2666
3	2	5	3	5.4545	3.7878	1.0909	0.7575
4	2	5.4	3	9.4736	7.6736	1.7543	1.4210
5	2	5.5	3	11.4782	9.6449	2.0869	1.7536
6	2	5.6	3	14.4827	12.6160	2.5862	2.2528
7	2	5.7	3	19.4827	17.5871	3.4188	3.0854
8	2	5.8	3	29.4915	27.5581	5.0847	4.7514

rate and compared with the performance measures of the multi-server queuing model, where it is matched with the number of customers in the system (L_S).

References

1. Song Z (2015) The Evaluation of parameter M in the big M method of linear programming. In: International conference on materials engineering and information technology applications. pp 37–40
2. Salvador TR, Carvalho SMS, Coelho MV (2016) Application of simplex method in the radiotherapy treatment. Appl Math 7:2229–2240
3. Huimin X, Guozheng Z (2010) The queuing theory application in bank service optimization. IEEE press, pp 1097–1100
4. Vijay Prasad S, Peter Praveen J, Tiwari A, Prasad K, Bindu P, Donthi R, Mahaboob B (2018) An application of LPP-graphical method for solving multi-server queuing model. Int J Mech Eng Technol 9(1066–1069):1066–1069

Ultra-Lightweight Cenospheres Cement for Lost Circulation Control with Improved Curing and Reduced Shrinkage



Gaurav Richhariya, T. K. Dora, Naveen Singhal, Mayur Rai, Yash Goyal, Preeti Rathi, Yash Gupta, Praman Singh, P. P. Kundu, Kishori Lal, and Pawan Kumar Rakesh

1 Introduction

Cementing of oil and gas well is an integral part of hydrocarbons drilling operations. The natural and induced fractures often lead to loss of cement slurry in the formation resulting in lost circulation. Since the inception of hydrocarbons drilling operations, the problems due to lost circulation and expenses to deal with those problems has gone a couple of folds [1]. The major causes of lost circulation are the formations with minimal fracture gradient and presence of permeable cracks and fissures. The lost circulation due to the presence of permeable cracks could be eliminated by the use of fibrous, flaky and granular materials [2]. However, a large number of lost circulation takes place due to fracture of weak formation.

Different approaches have been developed for control of lost circulation, such as water extended slurry, foam cement, cement with lightweight additives such as fly ash, cenosphere and hollow glass spheres [3]. The water extended cement slurries reduce the cement slurry density by increasing the water content leading to poor

G. Richhariya (✉) · T. K. Dora · N. Singhal · M. Rai · Y. Goyal · P. Rathi · Y. Gupta · P. Singh
Department of Petroleum and Energy Studies, DIT University, Dehradun 248009, Uttarakhand, India
e-mail: gaurav.richhariya@dituniversity.edu.in

P. P. Kundu
Department of Chemical Engineering, Indian Institute of Technology Roorkee, Roorkee 247667, Uttarakhand, India

K. Lal
Department of Cementing, Institute of Drilling Technology, ONGC, Dehradun, Uttarakhand, India

P. K. Rakesh
Mechanical Engineering Department, National Institute of Technology, Srinagar (Garhwal) 246174, Uttarakhand, India

compressive strength development [4]. The foam cement slurries rely on the reduction of cement slurry density through foam generation. Wide variety of foaming agents has been used as an effective barrier for lost circulation control [5–7]. The foam generation in cement slurry induces excessive porosity in the cement sheath leading to a reduction in compressive strength [6, 8, 9]. The hollow glass spheres are manufactured for crush resistance rating up to 18,000 psi [9]. Besides the advantage of hollow glass spheres, separation from cement slurry at the time of mixing and higher cost limits its application. Cenospheres are other lightweight additives obtained as a by-product of coal combustion during electricity generation [10–12]. Cenosphere produces lightweight cement with improved workability and reduced shrinkage [13, 14]. Cenospheres, when mixed with cement slurry, leads to improved mechanical properties [15, 16]. However, the perforation of cenosphere by Liu et al. (2017, 2019) increased the cement slurry density [17, 18]. Therefore, the present work aims at reduction of shrinkage without compromising the strength of cement slurry. The cement slurries were fabricated with cenospheres and expansive additives to make ultra-lightweight cement with reduced shrinkage and porosity.

2 Materials and Method

The Digvijay Cement Pvt. Ltd provided cement for present work. Cenospheres were bought from Cenosphere India Limited. Institute of Drilling Technology, ONGC Dehradun provided expansive additives such as dead burnt magnesia (DBM) and Microbond (MB). Cement slurries were prepared according to API standards for cement slurry design 10B.

Cement slurries were prepared from expansive additives via DBM and Microbond, each 4% by weight of cement for reduction of shrinkage [19]. Series of experiments were performed on the cement slurry such as expansion, consistency, rheology, morphology and compressive strength.

2.1 *Expansion of Cement Slurry Under Permeable/Impermeable Condition*

The ultra-lightweight cement slurries were fabricated using cenospheres, dead burnt magnesia (DBM) and Microbond. As the cement starts to set the free water gets reduced, leading to shrinkage of set cement. The shrinkage of set cement could be reduced by increasing the hydration of cement through the application of cenospheres as well as Microbond and dead burnt magnesia. The outer surface cement sheath remains in contact with the formation fluid while the inner surface of the cement sheath remains in contact with casing [20, 21]. Hence, the shrinkage properties of cement were studied under permeable and impermeable conditions. The cement

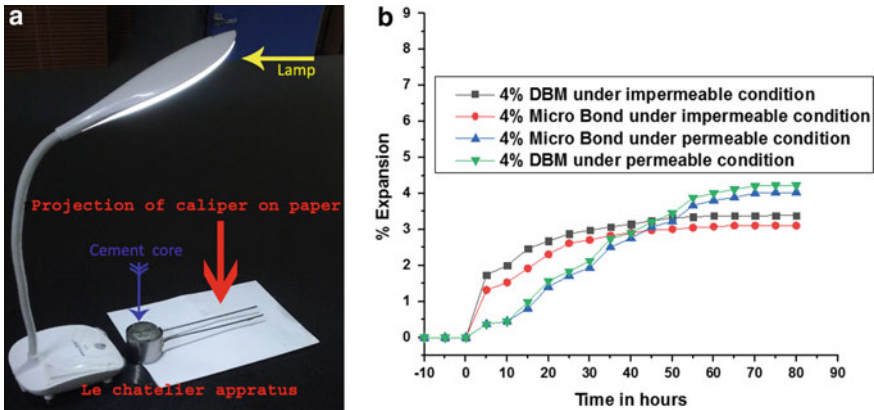


Fig. 1 **a** Expansion measurement with Le-Chatelier, **b** expansion of cement slurry under permeable and impermeable condition

core was prepared by placing the various composition of cenosphere cement along with DBM and Microbond. The expansion of cement slurry was assessed under permeable and impermeable conditions using Le-Chatelier apparatus. A change in distance between the callipers was measured by taking its projection on paper under the lamp, as shown in Fig. 1a.

Cement slurries containing 4% of DBM, and 4% of Microbond demonstrated expansion when cured under permeable and impermeable conditions [22]. The hydration of cement gets further enhanced due to the presence of cenospheres. However, the reduction in expansion of cement under impermeable conditions could be due to limited hydration of cement, as shown in Fig. 1b.

2.2 Consistency of Cement Slurry

Consistency of cement slurry is the period for which the cement slurry will remain pumpable under the effect of temperature and pressure [23]. Cement slurries with cenosphere dosage as 10, 20, 30 and 40% were tested for consistency. The quick thickening time of 10 and 20% cenosphere limits, it is an application to shallow depth as the cement gain plasticity. Cenosphere cement of 40% leads to extended thickening time and reduced compressive strength limiting its application, as shown in Fig. 2a. Figure 2b demonstrates the thickening time and temperature of 60 °C. The pressure of 2500 psi was applied during the determination of thickening time. Cenosphere cement of 30% slurry developed a consistency of 60BC after 2 h. Therefore, the cenosphere cement will remain pumpable for 2 h which is suitable for shallow water application.

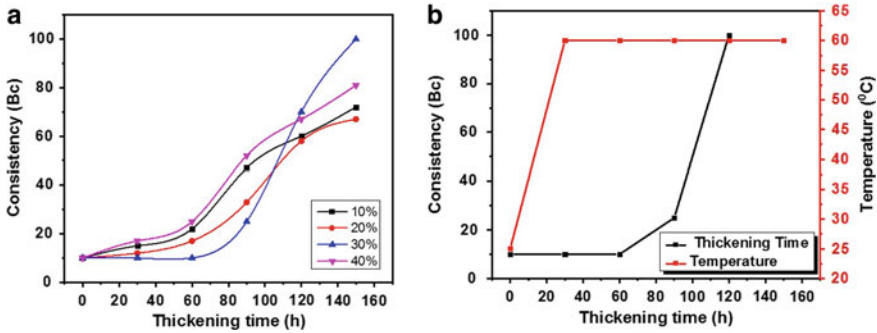


Fig. 2 a Thickening time of different percentage of cenospheres slurry b Thickening time of 30% cenospheres slurry

2.3 Rheology of Cement Slurry

The rheological properties of the cement slurries were studied to determine the fluid deformation under the influence of shear stress. Figure 3a demonstrates the comparison between the viscosity change as a function of shear rate of conventional 44% cement slurry over 30% cenosphere cement slurry. The cenosphere cement demonstrates low viscosity in comparison with neat cement. Hence, low pumping pressure is resulting in a reduction of formation fracture. The solid-phase interaction in the neat cement slurry leads to high initial viscosity; the viscosity further reduces with an increase in shear rate. In a later stage, the viscosity increases again due to hardening of the cement. The cement slurry with cenosphere demonstrates very little initial viscosity at later stages, as the viscosity rises due to hardening and reduced water.

In Fig. 3b, both the cement slurries demonstrate the increase in shear stress with time. However, the low shear stress developed by cenosphere in comparison with

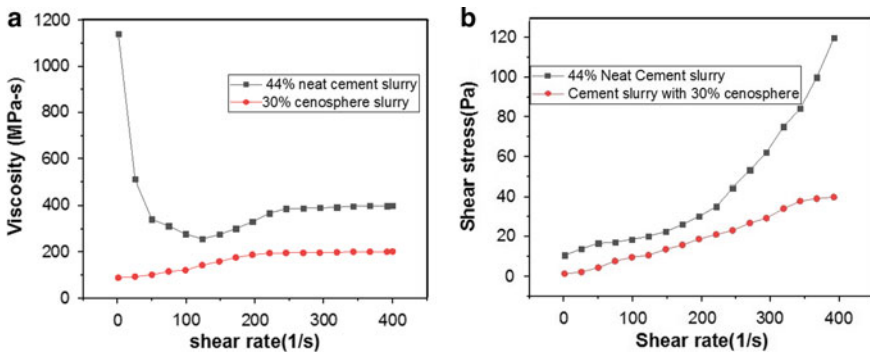


Fig. 3 a Effect of shear rate on viscosity, b effect of shear rate on shear stress

neat cement results in an efficient slurry displacement. The rise in shear stress could be due to the hardening of the cement.

2.4 Contact Angle of Cement Slurry

The SEM images of the synthesized cement core prepared from cenospheres and Microbond are shown in Fig. 4a–b. From the images, it can be observed that the pore space between the cenosphere got filled by cement slurry containing DBM homogeneously distributed in the cement core. Further, the contact angle measured, as shown in Fig. 5, on the surface of the cement sheath suggests the water phobic behaviour of the cement sheath.

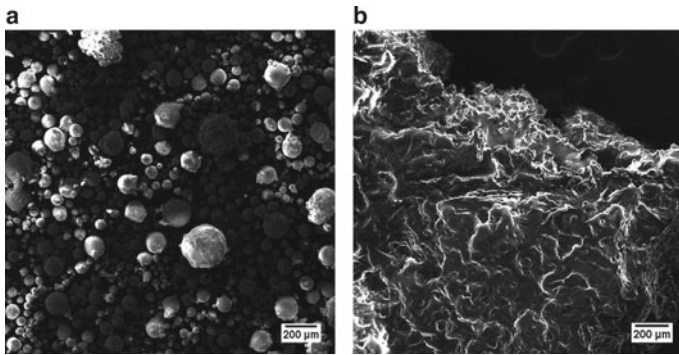


Fig. 4 SEM images of **a** cenospheres, **b** cenospheres in the cement sheath

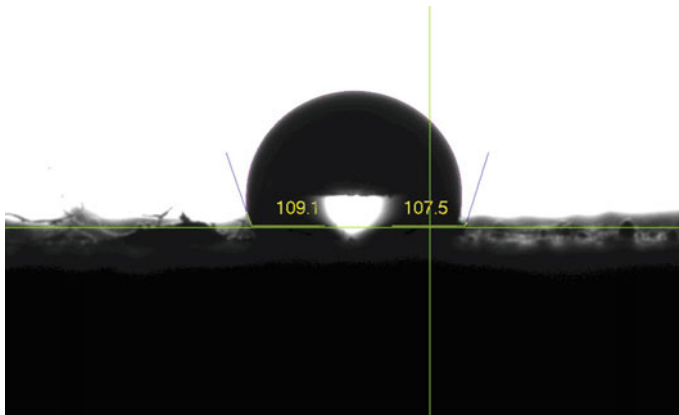
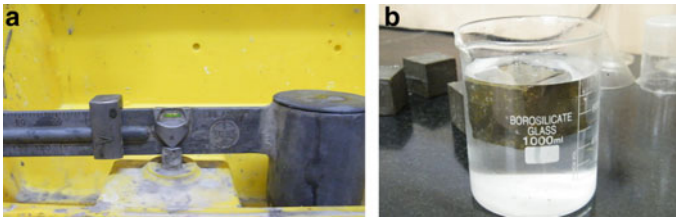


Fig. 5 Contact angle on the surface of the cement sheath

Table 1 Compressive strength of ultra-lightweight cenospheres cement slurry

Specific gravity	Composition	Curing conditions			Compressive strength (psi)
		Temperature (°C)	Pressure	Period	
0.98	Cement-100% + 50%water + 10% Microsilica + 30% Cenosphere + 4%DBM	80	1000Psi	24 h	2000
		80	1500Psi	48 h	2500
		80	2500Psi	24 h	3100
0.91	Cement-100% + 55% water + 10% Microsilica + 30% Cenosphere + 4% DBM	80	1000Psi	24 h	1700
		80	1500Psi	48 h	2100
		80	2500Psi	24 h	2900

**Fig. 6** **a** Density measurement with mud balance, **b** cement cube floating on the water surface

2.5 Compressive Strength

Since the geothermal gradient and pressure gradient in oil fields vary in the range of 80^o52C and 2000 psi at a depth of 4000 feet [24, 25]. Hence, the compressive strength of cement slurries was determined under a curing temperature of 80 °C and 1000–2500 psi pressure for 24 and 48 h. Table 1 demonstrates an increase in compressive strength as a function of curing pressure and temperature. Microsilica reduces the fluid loss of slurry along with the reduction of pore volume and development of early compressive strength of lightweight cement. The ultra-lightweight nature of cement cube is evident from Fig. 6a–b.

3 Conclusions

The 30% cenosphere cement slurry demonstrated excellent expansion with 4% DBM under permeable and impermeable conditions. The cenosphere cement slurry demonstrates the consistency of 30 BC after 2 h. Hence, the cenosphere cement slurry could be used at greater depth in low fracture gradient formations. The 30% cenosphere demonstrates an effective displacement of cement slurry by reducing pumping

pressure and cement slurry density. The high contact angle of cement core complements the compressive strength as the porosity got reduced without compromising the strength. The cenosphere cement slurry performs well in low fracture gradient formation. However, the low compressive strength and consistency of cenosphere limit its application to shallow depth formation with low fracture gradient.

References

1. Vidick B, Yearwood JA, Perthuis H (1988) How to solve lost circulation problems. Soc Pet Eng AIME SPE 927–932 17811
2. Bruton JR, Ivan CD, Heinz TJ (2001) Lost circulation control: evolving techniques and strategies to reduce downhole mud losses. Proc Drill Conf 1:334–342
3. Anya A (2018) Lightweight and ultra-lightweight cements for well cementing—a review. SPE West Reg Meet Proc 22–27. <https://doi.org/10.2118/190079-MS>
4. Tanner CH, Harms WM (1983) Unique ultra light-weight cement slurry compositions for use in unique well conditions, laboratory evaluation, and field performance. <https://doi.org/10.2118/11486-MS>
5. Benge OG, Spangle LB, Sauer CW (1982) Foamed cement—Solving old problems with a new technique. In: Proceedings spe annual technical conference and exhibition
6. Marriott T, Griffith J, Szutiak G (2005) Foamed conventional lightweight cement slurry for ultralow density and low ECDs solves lost-circulation problem across coal formations: a Case history. In: SPE Annual technical conference proceedings
7. Taiwo O, Ogbonna J (2011) Foam cementing design and application: a cure for low gradient-associated problems in deepwater operations in the Gulf of Guinea. Soc Pet Eng Niger Annu Int Conf Exhib 2011:343–349
8. Kearsley EP, Wainwright PJ (2001) Porosity and permeability of foamed concrete. Cem Concr Res 31(5):805–812
9. Bybee K (2006) Drilling and cementing technology: new ultralightweight-cementing technology combines benefits of current leading methods. J Pet Technol 58(2):65–66
10. Gupta DK, Rai UN, Tripathi RD, Inouhe M (2002) Impacts of fly-ash on soil and plant responses. J Plant Res 115(6):401–409
11. Van Hook RI (1979) Potential health and environmental effects of trace elements and radionuclides from increased coal utilization. Environ Health Persp 33:227–247
12. Adriano DC, Page AL, Elsewi AA, Chang AC, Straughan I (1980) Utilization and disposal of fly ash and other coal residues in terrestrial ecosystems: a review. J Environ Qual 9(3):333–344
13. McBride SP, Shukla A, Bose A (2002) Processing and characterization of lightweight concrete using cenospheres. J Mater Sci 37(19):4217–4225
14. Ngu LN, Wu H, Zhang DK (2007) Characterisation of cenospheres in fly ash from Australian power stations. In: 6th Asia-pacific conference combust ASPACC 2007. vol 31(9) pp 3437–3445
15. Anshits NN, Mikhailova OA, Salanov AN, Anshits AG (2010) Chemical composition and structure of the shell of fly ash non-perforated cenospheres produced from the combustion of the Kuznetsk coal (Russia). Fuel 89(8):1849–1862
16. Das A, Satapathy BK (2011) Structural thermal mechanical and dynamic mechanical properties of cenosphere filled polypropylene composites. Mater Des 32(3):1477–1484
17. Liu F, Wang J, Qian X, Hollingsworth J (2017) Internal curing of high-performance concrete using cenospheres. Cem Concr Res 95:39–46
18. Liu Z, Zhao K, Tang Y, Hu C (2019) Preparation of a cenosphere curing agent and its application to foam concrete. Adv Mater Sci Eng

19. Richhariya G, Dora TK, Kundu PP, Singal N, Gupta Y, Singh P (2019) Impregnation of novel additives in cement for preventing fluid migration through the cement sheath in oil well. In: AIP Conference proceedings, vol 2166
20. Backe SKLKR, Lile PSOB, Sveen J (1997) Shrinkage of oil well cement slurries. *J Can Pet Technol* 37(9):64–67
21. Sabins FL, Sutton DL (2007) Interrelationship between critical cement properties and volume changes during cement setting. *SPE Drill Eng* 6(02):88–94
22. Chatterji S (1995) Mechanism of expansion of concrete due to the presence of dead-burnt CaO and MgO. *Cem Concr Res* 25(1):51–56
23. Ramos RC (1992) Thickening time measure to simulate cementing operations on deepwater wells: Field laboratory validation. In: Proceedings annual offshore technology conference, May, vol 1992, pp 751–756
24. Roy S, Chapman DS (2012) Borehole temperatures and climate change : ground temperature change in south India over the past two centuries. vol 117, pp 1–12
25. Suppe J (2014) Fluid overpressures and strength of the sedimentary upper crust. *J Struct Geol* 69:481–492

Augmentation of Thermal Performances in a Tubular Heat Exchanger Using Internal Flow Baffle: Recent Study



Gopal Nandan, Nafees Alam Wani, and Satish Kumar

1 Introduction

Improvement in the thermal performance of the heat exchanger will lead to downsizing of the system and system costs. The heat transfer rate in the system can be improved by many techniques. The performance can be increased by either passive or active technique. The heat exchange between two fluids is separated by metallic walls. When the fluid flows, a boundary layer develops at the solid–liquid interface, which has a high thermal resistance. This heat exchange is very low due to this resistance. To increase the heat exchange rate, researchers used several techniques. These techniques can be summarized in three categories, namely (a) surface modification of the tube wall, (b) nanofluids flow, and (c) application of inserts in the flowing fluids [1–11]. These techniques are passive techniques. In the first category, the surface of the tube is modified, which creates the turbulence near the wall in the solid–liquid interface, and convection heat transfer improves. The internal surface of the tube is roughened. For surface modification, artificial roughness, microfin tubes, corrugated tubes, fins, threading, groove cut, dimpling tube, curving of the tube, thread cut, etc., have been attempted by several researchers. This shows improvements. In the second category, the application of nanofluids in the tube has shown tremendous improvement in the heat exchange rate. Nanofluids are enhanced fluids in which nanometer-sized metallic particles are uniformly distributed in the carrier fluids. Due to nanofluids, convection heat transfer properties improve [12–21]. The third category is the application of a turbulence promoter in the flowing fluids. The use of inserts in the form of twisted tapes in a heat exchanging device has resulted in a tremendous increase in thermal performance. This offers powerful turbulence

G. Nandan (✉) · N. A. Wani

Mechanical Engineering Department, Amity University, Noida 201313, Uttar Pradesh, India
e-mail: gopalnandan@gmail.com

S. Kumar

Mechanical Engineering Department, National Institute of Technology, Jamshedpur, India

intensity at the wall–liquid interface region, which results in heat transfer augmentation. It is due to the very simple, low cost, and simplicity of its installation inside the tube. Generally, the material of inserts should be such that it is unreactive to the fluid medium and should be light in weight. The most commonly used material for the inserts is aluminum and copper [11]. This provides continuous swirl flow and which results in near-wall turbulence and breaks sub-layer and increases fluids intermixing. Using inserts, Nusselt number (Nu) increases, and convective heat transfer coefficients increase. The application of inserts generates the swirl flow, which promotes turbulence and intermixes within the fluids [6, 9, 21]. Insertion of twisted tapes reduces a hydraulic diameter which increases fluid velocity. This leads to secondary motions of the fluids and intermixing of central core fluids and near-wall fluids [22]. An increase in heat transfer using inserts gives pressure drop penalty, which is not desirable. With the thermal advantage, it has a simultaneous disadvantage in terms of pumping power requirement increases in maintaining the flow into the pipe. Due to turbulence, pressure drop also increases. There are several factors on which heat transfer depends upon, such as friction penalty, pressure loss, etc. The heat transfer enhancement is dependent on fluid and fluid flow properties [23–26]. In this paper, the application of various types of inserts have been extensively summarized and explained. The inserts are modified by changing its dimension, twisting ratio, pitch, cut of twisted tapes at the periphery, perforation of tapes, other several modifications, etc., and experimentally observed that heat convection has been drastically elevated.

2 Type of Inserts in the Tube

In the early stage, researchers used twisted rectangular strip inserts. It is very easy to manufacture and use in the tube. The twisted tapes can be classified based on the number of twisted tapes, the cross-sectional area of tapes, tape placement in the flow direction, tape with rings at the periphery [2], cut on the periphery of the tape, perforation or piercing of tape, the combination of peripheral cut, and perforation as well as other combinations. Single, double, and triple twisted tubes have been experimentally studied. Researchers used conical strip, combined conical ring with twisted tape, multiple twisted tapes (double counter type, a varied axis of tapes, cross hollow, twisted tape with variation in terms of length, pitch, and twisting ratio etc. It was observed that certain modifications in the geometry of tape also provide further improvement in the thermal performance factor. Alteration of the placement of a pair of twisted shows good enhancement. The combination of perforation and V cut also has been experimentally studied.

3 Experimental Results

Most of the works are based on experimental studies. Experiments conducted with and without twisted tube tapes for laminar and turbulent flow regimes by imposing constant heat flux on the tube. The test section kept thermally insulated to minimize heat loss. Most of the authors used air as working fluids. The wall temperature of the tube is calculated based on the average temperature of temperature sensors installed at various points on the tube surface (outer) along its length as well as circumference. The bulk temperature of the fluid is an arithmetic average of inlet temperature and outlet temperature of the fluid. Using them, the heat transfer rate (wall to fluid or vice versa) is calculated. The friction factor (f) is calculated as:

$$f = \frac{\Delta P}{\frac{1}{2}\rho U^2(L/D_h)} \tag{1}$$

where U = Average fluid velocity

L = Length of tube

D_h = Hydraulic diameter

ΔP = Pressure drop

Performance enhancement was introduced by Webb [27], which is given in Eq. 2. For performance enhancement study, researchers used several terms like thermal enhancement index (η), heat transfer enhancement (ζ), thermal performance enhancement factor, enhancement efficiency (η), performance evaluation criteria (PEC), thermal-hydraulic performance factor (η) [28], etc. These terms have been used interchangeably. This ratio is calculated using Eq. 2 [27].

$$\eta = \frac{h}{h_o} \Big|_{PP} = \frac{Nu}{Nu_o} \Big|_{PP} = \frac{\frac{Nu}{Nu_o}}{\left(\frac{f}{f_o}\right)^{1/3}} \tag{2}$$

h_o = heat transfer coefficient without using inserts

h = heat transfer coefficient with inserts

Nu_o = Nusselt number without inserts

Nu = Nusselt number with inserts

f = Friction factor with inserts

f_o = Friction factor without inserts.

Experiments conducted using a single twisted tape in the tube in a turbulent flow regime range (Reynolds Number < 24989) by varying the ratio of pitch of twist and tube diameter (Fig. 1). For the lower value of Re, the heat transfer index increases

Fig. 1 Single twisted tape

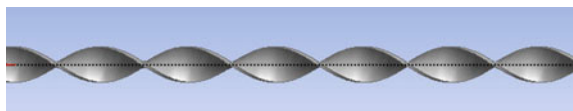
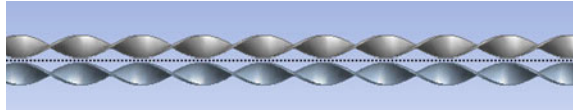


Fig. 2 Multiple twisted tapes



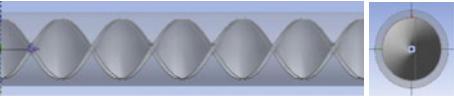
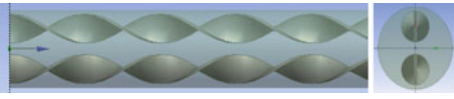
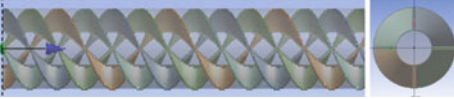
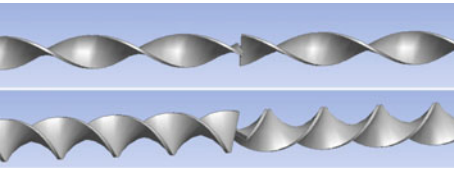
and decreases with increasing Re , and there is no change in heat transfer rate for Re more than 15,000 [2]. The highest heat transfer enhancement ratio was 1.756 when Re is 5183. Bhuiya et al. [4] used multiple twisted tapes, double counter type (Fig. 2). The heat transfer enhancement was more for the lower value of the twist ratio. With multiple tapes, they further conducted experiments to know thermal behavior by maintaining the clearance between the insert and tube wall. The heat transfer rate obtained up to 240% more than a plain tube with no insert. The performance of multiple twisted tapes further improved in comparison with single twisted tape. Suri et al. [16] used sets of four twisted tape with square perforations. All quadruple tapes were fixed in the fully developed flow region in the tube and used air for experimentation. All experiments conducted in the turbulent flow regime for Reynolds number ranging from 5000 to 27,000 and obtained maximum thermal-hydraulic performance equals to 3.8.

Eiamsa-ard and Promvong [11] placed of tapes alternatively in clockwise and counter-clockwise direction. They used aluminum strips of dimension 1000 mm by 18 mm by 1.0 mm thickness. After dividing the whole span length into three parts, it provided twisting to each segment alternatively in clockwise and counter-clockwise directions. The segment length and alternate axes of the inserts were varied for experimentation. Based on the experiment, they concluded the enhancement of up to 90% as compared to the plain tube without inserts. Experimental details of single and multiple inserts have been summarized in Table 1. Moreover, researchers cut the plane tape to improve the intermixing in the fluids near the wall. These cuts were on the periphery of the tapes by varying shape of cut, depth, width of cut, and frequency of cut. The performance of twisted tape with cut provided at periphery improves [29].

Using V-cut with different angles and different frequencies on twisted tape, the performance factors were increased in the range 1.07–1.27 if the twist ratio is inversely proportional to Nu and friction factor (Table 2).


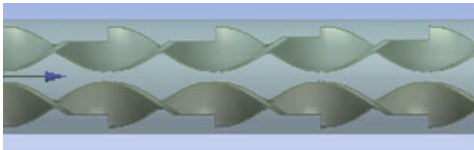
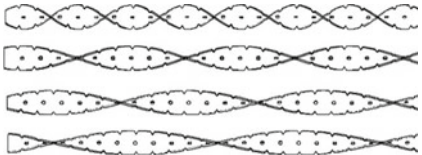
The experimental result of double twisted tape is with 30° V-shaped ribs. The value of Nu improves by 1.5–2.4 approximately further as compared to V-ribbed twisted tape [30]. The perforation on the tape is said when holes of different geometry are made on the tapes. The attempt made by Kumar et al. [31] by further making a perforated twisted tape with peripheral V-cuts with twist ratio 2–6. They conducted experiments for Re ranging from 2700–23400. The Nu improves by 1.48–2.9 and hydraulic performance range in the range of 1–1.5. The V-finned twisted tapes and quadruple counter-twisted tapes have also been attempted for $4000 < Re < 30,000$ and found that Nu increases with the rise of the winglet blockage ratio. Results of the performance of inserts have been summarized in Table 1. Hong et al. [32] used helical wire coils and experimentally observed that Nu is in the range of 1.46–2.49 concerning

Table 1 Performance of single and multiple inserts used in tubes

Sl. no.	Picture of the insert with the name of it	Working fluid and Re range	Overall heat transfer enhancement ratio	Ref. no
1	 <p>Rectangular strip inserts at variable clearance</p>	Air, >15,000	1.789	[2]
2	 <p>Double counter twisted tape</p>	Air, Re: 6950-50,050	1.6-3.4	[4]
3	 <p>Cross hollow twisted tape</p>	Air, > 600	1.281	[3]
4	 <p>Alternate and counter-clockwise tapes</p>	Water, Re: 3000-27,000	1.90	[11]

plain tube for turbulent flow, Re ranging from 6000 to 20,000. Keklikcioglu and Ozceyhan [1] used wire of triangular cross-sectional area and maintained the gap between the tube wall and the wire coils; the maximum thermal performance achieved 1.82 at lower $Re = 3429$. Nakhchi and Esfahani [33] analyzed thermal performance and hydraulic performance of a double V-cut twisted tape numerically. In their study, twisted tape, the twisted tape with cuts on the periphery (whether square cuts, V-cuts or U-cuts) was used. The tape with V-cuts generates an additional vortex flow near the cuts which increases the turbulent kinetic energy of the fluid and helps in the mixing of the fluid. In 25 mm diameter tube, a twisted having 20 mm width was used. The pitch was maintained 105 mm. The width (c) of V-cut was taken fixed as 5 mm while the depth (b) was varied as 3, 5, 7, and 9 mm giving cut ratio (b/c) as 0.6, 1, 1.4, and 1.8, respectively. In their analysis, water is the working fluid, and all experiments were conducted in turbulent flow ranges ($Re < 150,00$). The flow is considered turbulent, three-dimensional, steady, and incompressible. In the numerical model, the RNG K- ϵ turbulence model with enhanced wall treatment was selected, for boundary condition inlet velocity was employed. The gauge pressure at the outlet implemented zero. At the inlet, water with uniform velocity and temperature profile was considered at the

Table 2 Performance of inserts with the cut used in tubes

Sl. no.	Picture of the insert with the name of it	Working fluid and Re range	Overall heat transfer enhancement ratio	Ref. no
1	 <p>V-cut twisted tape</p>	Water, Re: 2,000–12,000	1.07–1.27	[29]
2	 <p>Double twisted tape with 30°V shape ribs</p>	Air, Re: 5300–24,000	1.09–1.4	[30]
3	 <p>V-cut in the perforated twisted tape</p>	Air, Re: 2,700–23,400		[31]

temperature of 300 K, and the tube wall was at a constant temperature at 350 K. The no-slip condition was selected on tube walls and twisted tape surface. The algorithm selected was simple with second-order upwind. It was observed that V-cuts increase the turbulent intensity of the fluid flow, which in general means higher heat transfer rate. High turbulent intensity is because of swirl flow created by twisted tape strikes with axial flow near the V-cuts. Twisted tape with V-cut having $b/c = 1.8$ has the highest heat transfer rate. The friction factor shows an increment up to 27.4% mainly due to the continuous contact of the fluid with twisted tape. According to their analysis, V-cut twisted tape with $b/c = 1.8$ has a thermal performance of 1.83, which is higher than most of the other dimensions of V shapes made on tape periphery in perforated helical twisted tapes (PHTT). The circular holes were made on the central longitudinal axis of the tape before it is twisted [34]. With aluminum sheet (1.5 m × 12. mm × 0.8 mm), PHTT is fabricated and experimentally studied. The diameter of the hole, width of the place, and pitch of the hole were varied for parametric analysis of this tape. Later on, correlations were predicted for Nu, f, and thermal performance which gave an error of up to 6%. Keklikcioglu and Ozceyhan [35] used wire inserts having an equilateral cross-sectional area to make the coil. By placing the sharp edge of wire in the flow facing direction, thermal performance observed maximum. Using coiled wire inserts in the near-wall region, boundary layer was destroyed, and heat transfer was enhanced. The clearance of 1 mm was kept near

the wall, and experiments were performed in the turbulent flow region ($2851 < Re < 27,732$). Eiamsa-ard et al. [22] numerically solved the Navier–Stokes equation and used $RNG k - \varepsilon$ methods considering turbulence intensity 10% at the inlet. Numerical results provided results up to $\pm 5\%$ with experimental results. A detailed modeling procedure has been elaborated by Fan et al. [36]. Numerous researches have been done to improve system thermal performance [37–42]. Mashoofi et al. [43] numerally studied the axial perforated twisted tapes. They used a different hole diameter, which was made on the simple twisted tapes. They created a hole in normal direction on the tapes to achieve a reduction in the pressure drop in the tube. The variation of heat capacity rate ratio affected the effectiveness of the heat exchanger.

4 Conclusions

The heat transfer enhancement in a heat exchanger using twisted tape inserts is the due increase in turbulence level in fluids flow. In the flow domain, inserts behave as turbulence promoters. It increases the tangential velocity, which breaks the fluids sub-layers near to the solid–liquid interfaces. The thickness of the sub-layer offers resistance in the heat flow. In the present study, efforts have been made to study the recent papers in the area of twisted tape inserts and the effect of geometrical dimensions of insets like width, thickness, twist ratio, perforation on the inserts, winglets, winglets with triangular, square, tetrahedron cut, etc. The modification in the inserts on its periphery and perforation on the tapes further improved the heat transfer. Most of the authors used air or water as working fluids in the range of Re ranging from 600 to 24,000. With the enhancement in the thermal performance, there is associated disadvantage in terms of pressure drop, which necessitates more power for the pump to maintain the flow, with the application of internal inserts.

References

1. Keklikcioglu O, Ozceyhan V (2016) Experimental investigation on heat transfer enhancement of a tube with coiled-wire inserts installed with a separation from the tube wall. *Int Commun Heat Mass Transfer* 78:88–94
2. Bas H, Ozceyhan V (2012) Heat transfer enhancement in a tube with twisted tape inserts placed separately from the tube wall. *Exp Thermal Fluid Sci* 41:51–58
3. Li P, Liu Z, Liu W, Chen G (2015) Numerical study on heat transfer enhancement characteristics of tube inserted with centrally hollow narrow twisted tapes. *Int J Heat Mass Transf* 88:481–491
4. Bhuiya M, Sayem A, Islam M, Chowdhury M, Shahabuddin M (2014) Performance assessment in a heat exchanger tube fitted with double counter twisted tape inserts. *Int Commun Heat Mass Transfer* 50:25–33
5. Sekhar TVR, Nandan G, Prakash R, Muthuraman M (2018) Modeling a renewable energy collector and prediction in different flow regimes using CFD. *Mater Today: Proc* 5(2):4563–4574

6. Sekhar TVR, Prakash R, Nandan G, Muthuraman M (2018) Performance enhancement of a renewable thermal energy collector using metallic oxide nanofluids. *Micro Nano Lett* 13(2):248–251
7. Sharma R, Gupta A, Nandan G, Dwivedi G, Kumar S (2018) Life span and overall performance enhancement of solar photovoltaic cell using water as coolant: a recent review. *Mater Today: Proc* 5(9):18202–18210
8. Sekhar TVR, Nandan G, Prakash R, Muthuraman M (2018) Investigations on viscosity and thermal conductivity of cobalt oxide- water nano fluid. *Mater Today: Proc* 5(2):6176–6182
9. Agrawal T, Ajitkumar R, Prakash R, Nandan G (2018) Sodium Silicide as a hydrogen source for portable energy devices: a review. *Mater Today: Proc* 5(2):3563–3570
10. Wani NA, Nandan G (2019) Modelling of solar parabolic trough collector considering unsymmetrical heat flux. In: 3rd International conference on recent developments in control, automation and power engineering (RDCAPE). IEEE (Oct 2019)
11. Eiamsa-ard S, Promvong P (2010) Performance assessment in a heat exchanger tube with alternate clockwise and counter-clockwise twisted-tape inserts. *Int J Heat Mass Transf* 53(7–8):1364–1372
12. Sekhar TVR, Prakash R, Nandan G, Muthuraman M (2017) Preparation of $\text{Co}_3\text{O}_4\text{-H}_2\text{O}$ nanofluid and application to CR-60 concentrating solar collector. *Prog Indus Ecol An Int J* 11(3):227–246
13. Vadhera J, Sura A, Nandan G, Dwivedi G (2018) Study of phase change materials and its domestic application. *Mater Today: Proc* 5(2):3411–3417
14. Sekhar TVR, Prakash R, Nandan G, Muthuraman M (2018) Pressure drop characteristics and efficiency enhancement by using $\text{TiO}_2\text{-H}_2\text{O}$ nanofluid in a sustainable solar thermal energy collector. *Int J Environ Sustain Develop*
15. Jain T, Singh G, Dwivedi G, Nandan G (2018) Study of emission parameter of biodiesel from non edible oil sources. *Mater Today: Proc* 5(2):3581–3586
16. Suri ARS, Kumar A, Maithani R (2017) Heat transfer enhancement of heat exchanger tube with multiple square perforated twisted tape inserts: experimental investigation and correlation development. *Chem Eng Process* 116:76–96
17. Singh A, Nandan G, Rohatgi P (2019) A prediction of the temperature of a recessed LED panel ceiling light. In: 3rd International conference on recent developments in control, automation and power engineering (RDCAPE). IEEE (Oct 2019)
18. Krishn S, Goyal M, Nandan G, Kumar S, Kumar P, Shukla AK (2019) Pool boiling using nanofluids: a review. In: *Lecture notes in mechanical engineering*, Springer, Singapore, pp 325–336
19. Rathour RS, Chauhan V, Agarwal K, Sharma S, Nandan G (2019) Cooling of solar photovoltaic cell: using novel technique. In: *lecture notes in mechanical engineering*, Springer, Singapore, pp 521–529
20. Nandan G (2019) Performance of solar photovoltaic panel using forced convection of water-based CuO nanofluid: an understanding. In: *IOP Conference series: materials science and engineering*, vol 691, pp 012088
21. Suresh AK, Khurana S, Nandan G, Dwivedi G, Kumar S (2018) Role on nanofluids in cooling solar photovoltaic cell to enhance overall efficiency. *Mater Today: Proc* 5(9):20614–20620
22. Eiamsa-ard S, Somkleang P, Nuntadusit C, Thianpong C (2013) Heat transfer enhancement in tube by inserting uniform/non-uniform twisted-tapes with alternate axes: effect of rotated-axis length. *Appl Therm Eng* 54(1):289–309
23. Kumar S, Nandan G, Singh GK (2016) Numerical study of natural convection and radiative heat transfer of heated inner cylinder placed inside a isothermally cooled circular enclosure. In: *Third international conference on manufacturing excellence*, Amity University Uttar Pradesh, Noida, India (Mar 2016), pp 179–183
24. Kumar R, Nandan G, Sahoo PK, Chatterjee B, Mukhopadhyay D, Lele HG (2010) Ballooning of pressure tube under LOCA in an Indian pressurised heavy water reactor. In: *14th International heat transfer conference, IHTC 14 7*, pp 317–323

25. Majumdar P, Chatterjee B, Nandan G, Mukhopadhyay D, Lele HG (2011) Assessment of the code "PTCREEP" for IPHWR pressure tube ballooning study. *J Pressure Vessel Techno Trans ASME* 133(1)
26. Nandan G, Majumdar P, Sahoo PK, Kumar R, Chatterjee B, Mukhopadhyay D, Lele HG (2012) Study of ballooning of a completely voided pressure tube of Indian PHWR under heat up condition. *Nucl Eng Des* 243:301–310
27. Webb R (1981) Performance evaluation criteria for use of enhanced heat transfer surfaces in heat exchanger design. *Int J Heat Mass Transf* 24(4):715–726
28. Pourahmad S, Pesteei S (2016) Effectiveness-NTU analyses in a double tube heat exchanger equipped with wavy strip considering various angles. *Energy Conver Manage* 123:462–469
29. Murugesan P, Mayilsamy K, Suresh S, Srinivasan P (2011) Heat transfer and pressure drop characteristics in a circular tube fitted with and without v-cut twisted tape insert. *Int Commun Heat Mass Transfer* 38(3):329–334
30. Tamna S, Kaewkohkiat Y, Skullong S, Promvong P (2016) Heat transfer enhancement in tubular heat exchanger with double v-ribbed twisted-tapes. *Case Stud Therm Eng* 7:14–24
31. Kumar B, Kumar M, Patil AK, Jain S (2018) Effect of v cut in perforated twisted tape insert on heat transfer and fluid flow behavior of tube flow: an experimental study. *Exp Heat Transf* 32(6):524–544
32. Hong Y, Du J, Wang S, Huang SM, Ye WB (2018) Heat transfer and fluid flow behaviors in a tube with modified wire coils. *Int J Heat Mass Transf* 124:1347–1360
33. Nakhchi M, Esfahani J (2019) Performance intensification of turbulent flow through heat exchanger tube using double v-cut twisted tape inserts. *Chem Eng Processing Process Intensification* 141:107533
34. Nanan K, Thianpong C, Promvong P, Eiamsa-ard S (2014) Investigation of heat transfer enhancement by perforated helical twisted-tapes. *Int Commun Heat Mass Transfer* 52:106–112
35. Keklikcioglu O, Ozceyhan V (2018) Experimental investigation on heat transfer enhancement in a circular tube with equilateral triangle cross sectioned coiled-wire inserts. *Appl Therm Eng* 131:686–695
36. Fan A, Deng J, Guo J, Liu W (2011) A numerical study on thermo-hydraulic characteristics of turbulent flow in a circular tube fitted with conical strip inserts. *Appl Therm Eng* 31(14–15):2819–2828
37. Sharma S, Nandan G, Rohatgi P, Prakash R (2019) Recent advances in self-healing materials. *Mater Today: Proc* 18:4729–4737
38. Verma S, Sharma B, Ahmad J, Dwivedi G, Nandan G (2018) Impact assessment of ethanol as fuel for engine operation. *Mater Today: Proc* 5(2):6115–6120
39. Shukla AK, Sharma A, Sharma M, Nandan G (2018) Thermodynamic investigation of solar energy-based triple combined power cycle. *Energy Sources Part A: Recov Utilization Environ Effects* 41(10):1161–1179
40. Nandan G, Sahoo PK, Kumar R, Chatterjee B, Mukhopadhyay D, Lele HG (2010) Experimental investigation of sagging and ballooning for a completely voided pressure tube of Indian PHWR under heatup condition. *World Acad Sci Eng Technol* 61:197–204
41. Nandan G, Lele HG, Sahoo PK, Chatterjee B, Kumar R, Mukhopadhyay D (2007) Experimental investigation of heat transfer during LOCA with failure of emergency cooling system. In: 5th International conference on heat transfer, fluid mechanics and thermodynamics
42. Rawat KS, Thakur HC, Nandan G (2016) CFD analysis of a pentagonal rib over absorber plate of a solar air heater. In: 3rd International conference on manufacturing excellence, Amity University Uttar Pradesh, Noida, India (Mar 2016), pp 191–196
43. Mashoofi N, Pourahmad S, Pesteei S (2017) Study the effect of axially perforated twisted tapes on the thermal performance enhancement factor of a double tube heat exchanger. *Case Stud Therm Eng* 10:161–168

Analysis of Mechanical Behavior of Sandwich Panels



Swati Devi, Yogesh K. Prajapati, and Vinod Singh Yadav

1 Introduction

The sandwich structure is a special class of composite, but it is not a composite. In this type of structure, composites are used as a face sheet (skin) and also as a core, so it is called a sandwich structure composite. Structural sandwich composite fabricated by fastening of two thin face sheets at the top and bottom of the low weight core, whereas the core is employed to unconnect the thin faceplates. Such material increases flexural stiffness as the skin's surfaces diverge. The purpose of employing structural sandwich is to decrease weight and raised strength.

Since many years, sandwich structures have been progressively applicable in aerospace industries and aviation, as well as in mechanical, civil, and marine engineering. Nowadays, it is getting more attention due to higher stiffness along with higher strength-to-weight ratio [1]. Fabrication of structural sandwich is very simple in the early use, fabric, thin metal sheets used as facing and wood as a core. The application of sandwich structure can be found from the second war of the nation, and at the same time, British De Havilland Mosquito bomber had used such type of structure in aerospace [2].

In order to construct sandwich structures, various materials have been used. However, structural sandwich has been more emphasized with the evolution of innovative core design and faceplates [3].

S. Devi (✉) · Y. K. Prajapati · V. S. Yadav
Department of Mechanical Engineering, National Institute of Technology Uttarakhand, Srinagar
(Garhwal), Uttarakhand 246174, India
e-mail: swati.mechmt18@nituk.ac.in

Y. K. Prajapati
e-mail: yogesh.k@nituk.ac.in

V. S. Yadav
e-mail: vsyadav@nituk.ac.in

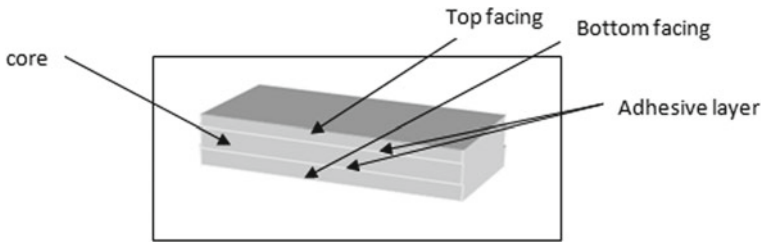


Fig. 1 General view of the sandwich panel

Paik et al. [4] analyzed the mechanical properties of both the facings and honeycomb core of the sandwich structure. Authors used theoretical as well as experimental techniques and conducted flexural test, axial compression together with lateral crushing loads to investigate the mechanical properties. Froud et al. [5] sum up in what manner or way to form a structural sandwich composite to achieve superior stiffness properties together with bending strength. Gibson et al. [6] describe the sandwich beams maximum stiffness wt./unit of core utilized foam as a core material. The outcomes are such core density; the thickness of core and faceplates has got most advantageous. Jan et al. [7] examined experimentally and analytically the structural flexural properties and fabricated such as core made up of aluminum honeycomb along with glass fiber used as facing material. Rao et al. [8] analyzed the bending effect of composites based panels of a sandwich theoretically. Honeycomb panels of aluminum and rods of aluminum's strength-to-weight ratio are compared to obtain the final outcome. Verma et al. [9] summarized sandwich structure's flexural way of behaving. Materials employed in the fabrication of core are polyurethane foam, glass fabric, and epoxy that is utilized as the materials of facing. Herranen et al. [10] studied the dissimilar core of beam of a sandwich so to promoting current materials for composite and also evaluate the design together with mechanical characteristics. Koissin et al. [11] conducted a study on a core of panels of sandwich made up of foam along with its strength characteristics. They also analyzed here the low-velocity impact together with an indentation which subjected to compression in a sandwich structure. Arbaoui et al. [12] interrogated the polypropylene honeycomb core mechanical properties of a multilayered structural sandwich. Effect of intermediate layers, along with a thickness of the core, is also investigated [13].

Here, neat flax fiber mat, dry orange peel, chopped wheat straw/fodder, epoxy, and hardener are used to fabricate the composite for the core. Aluminum is used as facing material. Both the arrangement of core in the presented work is shown in Fig. 2.

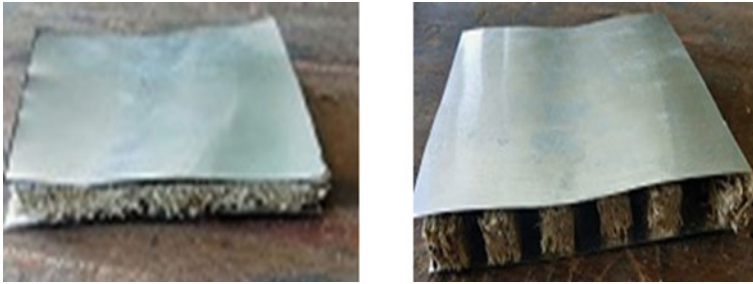


Fig. 2 Two different arrangements of core

2 Materials and Methodology

2.1 Materials

In experimental analysis, aluminum is used as the faceplate, and neat flax fiber mat, dry orange peel, and dry wheat straw/fodder are used as raw material for core which also utilized LY 556 epoxy resin along with HY 951 hardener as a material matrix in a proportion of 10:1 as shown in Figs. 3, 4, 5 and 6.

Sample ‘A’

See Fig. 3.

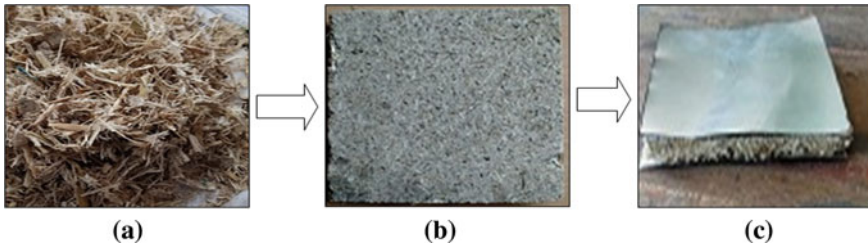


Fig. 3 a Dry straw/fodder, b Core of fodder, and c Final sandwich structure

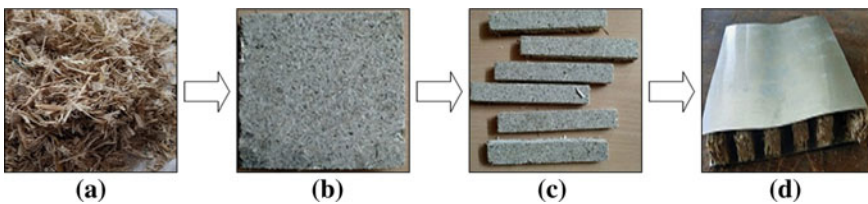


Fig. 4 a Dry fodder, b Core made by dry wheat fodder, c Strips for core, and d Finished sandwich structure

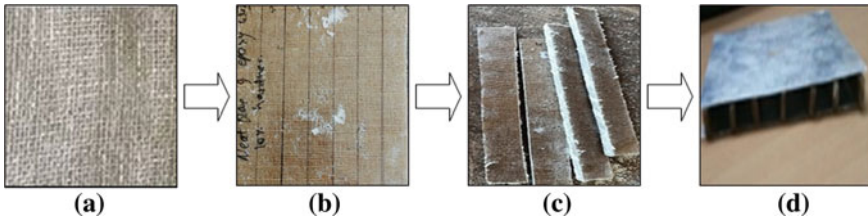


Fig. 5 a Neat flax fiber mat, b Core made by neat flax fiber mat, c Strips of composite for core, and d Finished sandwich structure

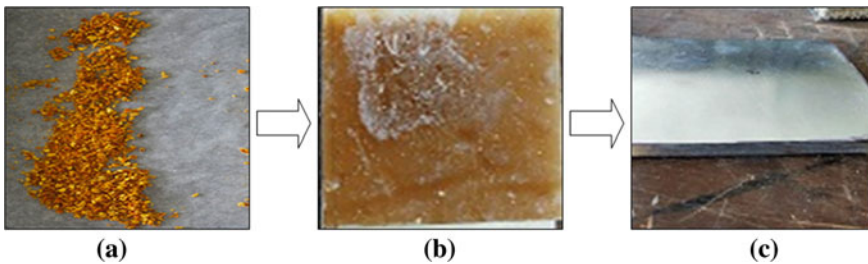


Fig. 6 a Dry orange peel, b Core made by dry orange peel, and c Final structural sandwich

Sample 'B'

See Fig. 4.

Sample 'C'

See Fig. 5.

Sample 'D'

See Fig. 6.

2.2 Methodology

Aluminum alloy. Aluminum alloy sheet is used as top and bottom faceplate to fabricate the sandwich structure. It is assembled to the core with the help of a very thin layer of epoxy and hardener. It is a very important part of a structural sandwich. Aluminum alloy sheet is shown in Fig. 7.

Epoxy. In current research work, epoxy LY 556 is preferred as a material matrix. Bisphenol-A-diglycidyl-ether is the common name of matrix epoxy. Hardener HY 951 is suitable for epoxy resin, and both are shown in Fig. 8.

Core Materials. Cores of a sandwich structure are fabricated by dry wheat fodder, dry orange peel, and neat flax fiber mat. The thin top and bottom faces are separated

Fig. 7 Aluminum alloy sheet



Fig. 8 Epoxy LY 556 and hardener HY 951



by composite core and bonded together with the help of epoxy + hardener thin layer. In the present work, four samples are investigated with three different core materials along with two different core arrangements. These four samples can be fabricated by employing a very simple procedure.

Manufacturing Process. The structural sandwich is a special class of composite fabricated by mold box specifications. Chopped dry wheat straw/fodder take in with normal glue to construct laminated structural core for sample 'A' and 'B.' Dry chopped orange peel and neat flax fiber mat were separately comprised in the epoxy matrix to the formed structural laminated core for sample 'C' and 'D.' After then, facings of aluminum alloy sheet are placed top and bottom of all four cores to make final finished sandwich structure for present research work.

3 Mechanical Tests

3.1 Tensile Test

As per ASTM C-297 standards, the samples were fabricated for the tensile test and evaluated on computerized UTM. $150 \times 12 \times 4$ mm is the tensile test sample dimension.

3.2 Compression Test

This test is employed to evaluate the maximal loading amount in compression earlier than the breakage of the material. The compression test sample is examined according to ASTM C-365 standards with dimensions of $50 \times 10 \times 4$ mm.

3.3 Flexural Test

In flexural test, evaluate flexural characteristics commonly using three-point bending test. This test is employed to determine the modulus along with flexural strength of all kinds of products along with materials. The properties are tested on computerized UTM, and the specimens for the flexural test were manufactured as per ASTM C-393 standards, and the standard dimension of a specimen used is $80 \times 10 \times 4$ mm.

3.4 Impact Test

The impact test is useful to determine the impact energy of specimen materials against sudden impact or force. The ASTM D-30 (ASTM D 7136–05) standards are following for the evaluation of a specimen. The dimensions of sample $50 \times 10 \times 4$ mm were used.

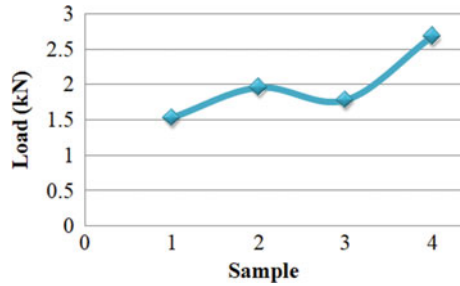
4 Results and Discussion

All the sandwich specimen are examined to determine the tensile, compression, flexural, and impact characteristics using the computerized UTM. Here, the strength of composite specimen is analyzed, which is fabricated in the present work with respect to different core materials to various structural to be reinforced.

Table 1 Tensile test loading values

S. No.	Samples	Values of load (kN)
1	Sample A	1.53
2	Sample B	1.96
3	Sample C	1.78
4	Sample D	2.68

Fig. 9 Load versus sample



4.1 Tensile Test

It is also called as testing of tension, which is a basic science of materials together with tests of engineering in which a specimen is treated till failure in tension.

Tensile test values for all specimens are given in Table 1. Fig. 9 represents the load-bearing capacities of all four fabricated samples.

4.2 Compression Test

It is used to decide the crushing conduct of material undergoing loading condition.

Values of load for all samples for compression test are given in Table 2. The variation of load-carrying capacities is shown in Fig. 10.

Table 2 Values of load for compression test

S. No.	Samples	Values of load (kN)
1	Sample A	4.49
2	Sample B	8.36
3	Sample C	6.5
4	Sample D	7.8

Fig. 10 Load versus sample

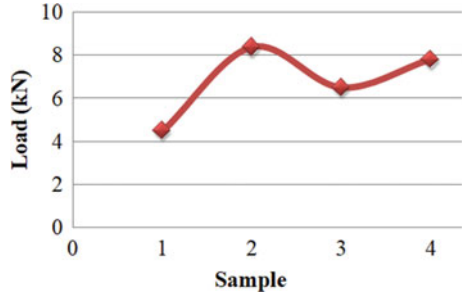
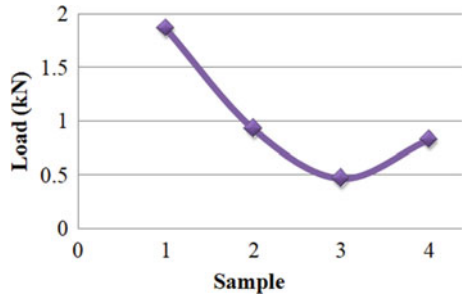


Table 3 Values of load for flexural test

S. No.	Samples	Values of load (kN)
1	Sample A	1.87
2	Sample B	0.93
3	Sample C	0.47
4	Sample D	0.83

Fig. 11 Load versus samples



4.3 Flexural Test

The main aim of performing this test is to calculate flexural strength. It is the maximum value of stress in compression or tension at the outmost fiber of specimen.

The values of load for three-point bending test of different specimen represented in Table 3. As a result, flexural strength also determines the indications for which a material can be used. The more strength a material offers, the more units a restoration can include. Figure 11 shows the load and sample graph for different samples.

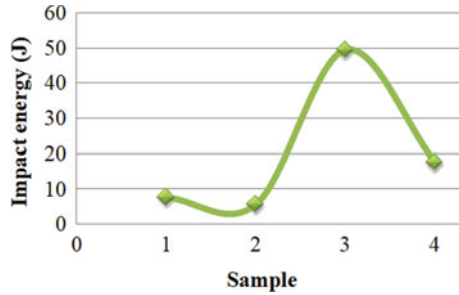
4.4 Impact Test

It is used to determine material behavior at higher deformation speed.

Table 4 Value of impact energy for Charpy test

S. No.	Samples	Values of impact energy (J)
1	Sample A	7.64
2	Sample B	55.68
3	Sample C	49.4
4	Sample D	17.6

Fig. 12 Values of impact energy versus sample graph



The ‘Charpy impact test’ values of impact energy for all the four fabricated samples are given in Table 4. For the selection of materials, these values are very helpful and also required in the process of rapid loading.

5 Conclusions

Tensile, compression, flexural, and impact tests are the different mechanical test which was performed on the fabricated specimen. For the testing of all composite structural sandwiches, different ASTM standards are followed here.

- In the tensile testing of all the samples, it was noticed that the sample 1 could effortlessly rip up when the loading is linear. The gain for tensile loading testing of sample 1 is 1.53 KN which is 1.75 times the smallest than that of sample 4 because it had strong bonding among the particles and the sample 4 having 2.68 KN tensile loading capacity which is also comparatively much higher than others specimens.
- In the compressive testing, the much higher value is obtained for sample 2 as compared to other samples. Sample 4 shows similar characteristic as sample 2 and chemical bonding of materials which stick them with each other during when the loading is applied linearly to the axis. For sample 1, the compressive loading value is 4.49 KN which is much lesser because it is tending to crush very effortlessly at the time of compression.
- For the flexural test, it was perceived that sample 1 has the maximum bending loading value of 1.87 kN and sample 3 has the lowest value of 0.47 kN. This

indicates that sample 1 has four times much highest flexural strength as compared to sample 3.

- To study the effect of impact test on sandwich panel, an investigation has been conducted, and significant differences in energy absorption were found under the Charpy impact test for the entire four designed structural sandwiches. The value of impact energy for sample 3 is 49.4 J, much higher as compared to sample 2 (5.68 J). The sample 3 absorbed almost three times more energy as compared to sample 2.

Acknowledgements We would like to thank the Design and Innovation Center, NIT Uttarakhand, and TEQIP III for assisting in the completion of this work.

References

1. Lok TS, Cheng HQ (2000) free vibration of clamped orthotropic sandwich panel. *J Sound Vib* 229(2):311–327
2. Albert SL (1967) *Structure design concepts*. Washington D. C.: NASA SP-5039, 6.
3. Yuan WX, Dawe DJ (2002) Free vibration of sandwich plates with laminated faces. *Int J Number Math Eng* 54:195–217
4. Paik JK, Thayamballi AK, Kim GS (1999) The strength characteristics of aluminum honeycomb sandwich panels. *Thin-Walled Struct* 35(3):205–231
5. Froud GR (1980) Your sandwich order, Sir?? *Composites* 11:133
6. Gibson LJ (1984) Optimization of stiffness in sandwich beams with rigid foam cores. *Mater Sci Eng* 67:125–135
7. Jan S, Khan RU, Ahmad S, Amjad M, Badshah S, Ahmad M (2015) Flexural strength of honey comb sandwich structures. *Int J Appl Sci Eng Res* 4(1). ISSN 2277–9442
8. Rao KK, Rao KJ, Sarwade AG, Varma BM (2012) Bending behaviour of aluminum honey comb sandwich panels. *Int J Eng Adv Technol (IJEAT)* 1(4). ISSN: 2249–8958
9. Varma ST, Suresh RME, Padmanabhan K (2014) The flexural properties of glass fabric/epoxy-rigid polyurethane foam core sandwich composites at different span to depth ratios and densities. *Int J Struct Anal Design– IJSAD*. ISSN 2372–4102:26–30
10. Herranen H, Pabut O, Eerme M, Majak J, Pohlak M, Ker J, Saarna M, Allikas G, Aruniit A (2012) Design and testing of sandwich structures with different core materials. *Mater Sci (Medziagotyra)* 18(1)
11. Koissin V, Shipsha A, Skvortsov V (2009) Compression strength of sandwich panels with sub-interface damage in the foam core. *Compos Sci Technol* 69:2231–2240
12. Arbaoui J, Schmitt Y, Pierrot JL, Royer FX (2014) Effect of core thickness and intermediate layers on mechanical properties of polypropylene honeycomb multi-layer sandwich structures. *J Metallurgy Mater* 59
13. Yalkin HE, Icten BM, Alpyildiz T (2015) Enhanced mechanical performance of foam core sandwich composites with through the thickness reinforced core. *J Compos Mater* 79:383–439

Development of Pellet Machine for Utilization of Biogas Slurry



Madhuri More, Chitranjan Agrawal, Deepak Sharma, Neelam Rathore, and Kapil Samar

List of symbols

MT	Million tons
T	Tons
N	Nitrogen, percent
P	Phosphorus, percent
K	Potash, percent
BS	Biogas slurry
S	Soil
NPW	Net present worth, \$
BCR	Benefit–cost ratio
PP	Payback period, years
IRR	Internal rate of return, percent
\$	Dollar
%	Percent

1 Introduction

Biogas plants are focused on the conversion of organic waste into energy and organic fertilizer for the increasing economy. These biogas plants provide an average annual

M. More (✉) · D. Sharma · N. Rathore · K. Samar
Department of Renewable Energy Engineering, Maharana Pratap University of Agriculture and Technology, Udaipur 313001, India
e-mail: moremadhuri1992@gmail.com

C. Agrawal
Department of Mechanical Engineering, Maharana Pratap University of Agriculture and Technology, Udaipur 313001, India

savings of about 7.09 million LPG equivalent cylinders and produce approximately 8.84 MT of organic bio-manure per year, equivalent to approximately 31,100 T of urea per year in India [1]. Biogas slurry is a product of biogas plants produced from anaerobic digestion for the animal waste and biodegradable material, which is a good source of plant nutrients and can improve soil properties and crop yield [2–5]. Biogas slurry having moisture content of 90–93 %, in which 7–10 % of dry matters. The dry matters including 4.5–7.5 % of organic matter 2.5–5.5 % of inorganic matters, which is very helpful to crop growth. Biogas slurry contains macro (N, P, and K) and micronutrients (Mn, Zn, and B) [6, 7]. Biogas slurry can be assisted in building the soil life of crop production. Biogas slurry has great potential to improve the physical and biological condition of the soil [8]. Biogas digestion provides essential nutrients to improve water absorption capacity, increase soil fertility, accelerate root growth, and prevent weed seed germination [6, 8]. Lack of sufficient nutrients and poor soil structure are major obstacles to the agricultural production system. Chemical fertilizers are not the right solution to overcome these problems. Additional use of chemical fertilizers is expensive and is unacceptable to human health and their environment [7–9]. Excessive use of chemical fertilizers adversely affects the soil and decreases organic carbon in the soil, and increased use of nitrogen fertilizers pollutes water bodies and also poses health risks to humans and animals [7]. The use of biogas slurry can reduce the use of chemicals by up to 50% and give farmers the benefit of their cost of cultivation and soil texture [9].

The biogas slurry contains 90–93% water, and therefore, difficult to use and transport. It becomes bulky, so that problems are created by the management of slurry. Generally, farmers distribute a biogas supplement to the adjacent biogas plant and dispose of it through an irrigation channel. Biogas slurry cannot be used directly as a fertilizer due to the continuous production of slurry and therefore needs to be maintained. Slurry storage is especially needed because it should be used at certain times of the growing season. Reducing travel costs and reducing the amount of biogas saturation by pressing on the pellet form. Biogas slurry recycling can improve durability, reduce travel costs, and make these materials easier to manage. The main objective of this research project is to reduce the storage space of biogas slurry for ease of transportation and to reduce travel costs, easy management of biogas slurry and to improve compost management to increase crop yields. It can fulfill these requirements in the quest for easy access to simple technologies using locally available biogas materials such as slurry and clay soils as a binder. It is proposed to design and manufacture a pellet machine to compress biogas slurry, performance testing of biogas slurry, and pellets.

2 Materials and Methods

The pellet machine for biogas slurry was developed in the Department of Renewable Energy Engineering, CTAE, MPUAT, Udaipur, Rajasthan (India). Biogas slurry was

Table 1 Design parameter of pellet machine

Sr. no.	Parameters	Values
1.	Machine capacity	50 kg hr ⁻¹
2.	Diameter of screw	150 mm
3.	Pitch of the screw	90 mm
4.	Thickness of screw flight	5 mm
5.	Diameter of shaft	40 mm
6.	Speed of rotation	40 rpm
7.	Power rating of electrical motor	1 hp

collected from the KVIC biogas plant. The properties of raw material were calculated in terms of moisture content, total solid content, bulk density, angle of repose, coefficient of friction, etc.

2.1 Design Consideration of Pellet Machine

Machine design is required to produce pellets from biogas slurry to convert its organic fertilizer. It is proposed to develop a simple and efficient screw conveyor type pellet machine of 50 kg h⁻¹ capacity for the mixture of biogas slurry and soil. The specification of the major components of the pellet machine is given in Table 1.

The detailed design calculations were calculated in terms of screw design, theoretical screw volume, number of pitches, shaft power, design of gear, and specific energy consumption using standard formulas [10–12]. The constructed pellet machine consists of the hopper, the barrel, a shaft on which is welded the screw, the thrust bearings, gearbox, portable wheels, and the frame as shown in Figs. 1 and 2. The machine was made by mild steel of 150 mm diameter of the screw and rotated in the clockwise direction. The raw material having different feeding ratio was placed to the hopper with different combinations like 90:10 (90% BS and 10% S), 80:20 (80% BS and 20% S), and 70:30 (70% BS and 30% S). These combinations were analyzed in terms of pelleting efficiency, pelleting capacity, and throughput capacity.

2.2 Performance Evaluation of Pellet Machine

Performance of pellet machine was evaluated, and three trail tests were performed on two levels, namely: raw material moisture content and a combined ratio of biogas slurry and soil. The test was performed at the same screw shaft speed of 40 rpm with the screw conveyor given a torque of 98.88 N-m, and all others operating conditions remain constant. The samples weighing 5 kg based on raw material combination

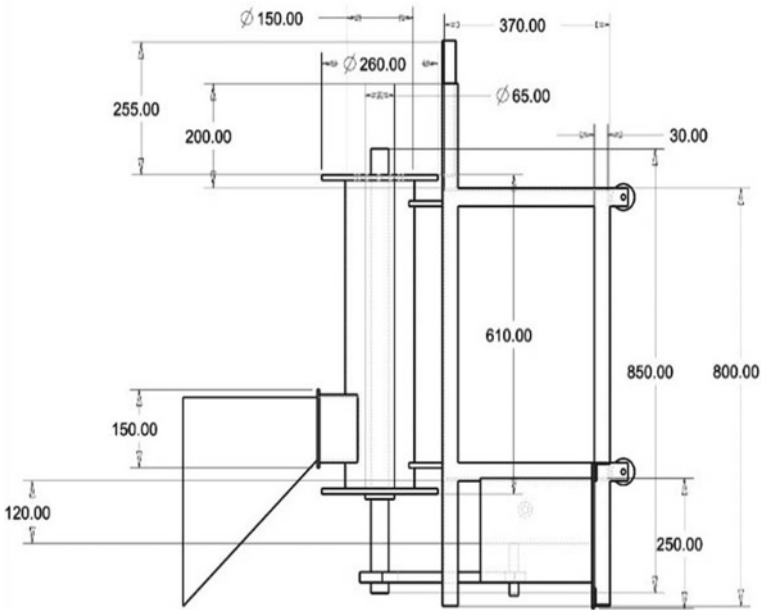


Fig. 1 Layout of the fabricated pellet machine

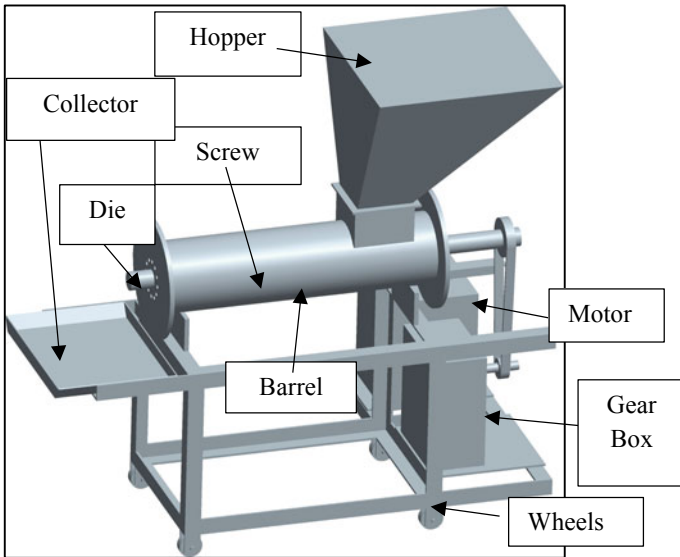


Fig. 2 Pellet machine

ratios (90:10, 80:20, and 70:30), respectively, were compressed each of the samples. The processing time of material was 10–15 min, respectively.

Pelleting efficiency [13–15] determined using;

$$\eta P = \frac{W_P}{W_T} \times 100 \quad (1)$$

where ηP is pelleting efficiency in percentage, W_P is the total mass of pellets produced by the machine (kg), and W_T is the total mass of input (kg).

The pelleting capacity of a machine is the following equation obtained from the ratio of total pellets produced by the machine (W_P) to the total time (T).

$$P_C = \frac{W_P}{t} \quad (2)$$

Throughput capacity [13] calculated by;

$$T_C = \frac{W_A}{t} \quad (3)$$

where T_C is throughput capacity in kg per hour, W_A is total mass output from the machine in kg, and t is the time taken for the machine to produce pellets in an hour.

3 Results and Discussion

3.1 Characteristics of Raw Material (Biogas Slurry (BS) and Clay Soil (CS)) for Pelletization

The pellet machine for biogas slurry was developed. The raw material was processed in terms of 90:10, 80:20, and 70:30 ratio. The physical properties of raw material evaluated in terms of moisture content (64–65%), total solid content (35–36%), bulk density (1224 kg m⁻³), angle of repose (38), and static coefficient of friction (0.57) (Table 2).

Table 2 Characteristics of raw material

Sr. no.	Properties of raw material	Values
1.	Moisture content (%)	64–65
3.	Bulk density (kg per cubic meter)	1224
4.	Angle of repose	38
5.	Static coefficient of friction	0.57



Fig. 3 Front view of fabricated pellet machine

3.2 Specification of Pellet Machine

The pellet machine of capacity of 50 kg/h was developed for the present study (Figs. 3 and 4) and technical specification of developed machine mentioned in Table 3. Pellet machine consists of a driving motor, screw, die, hopper, and power transmission system. Chain drive was used to transmit power from the motor to the screw. The raw material was fed to the hopper, which conveys it to the screw by gravity. The material was pushed, it was compressed, and bound material comes out of dying in the form of pellets.

The pellet machine consists of a drive motor, screw, die, hopper, and power steering system. Chain drive was used to transfer power from the car to the screw. The unripe material was carried by a hopper, which transmitted it to the skin by gravity. The cloth was driven, pressed, and bound with material coming out of death in the form of aprons.

3.3 Performance Evaluation of Pellet Machine

The evaluation of pellets machine parameters was considered in terms of a number of treatments and replications. The performance of pellet machine was found 76% of pelleting efficiency, 18 kg h⁻¹ of pelleting capacity, and 24 kg h⁻¹ of throughput capacity for 80% BS and 20% S (Figs. 5 and 6).

Fig. 4 Side view of pellet machine**Table 3** Design parameter of pellet machine

S. no.	Parameters	Values
1.	Machine capacity (Q)	50 kg hr^{-1}
2.	Die diameter (D_d) in mm	150 mm
3.	Bulk density raw material (p) in kg m^{-3}	1200 kg m^{-3}
4.	The diameter of the screw (D) in mm	150 mm
5.	Pitch of the screw (S) in mm	90 mm
6.	The thickness of screw flight	5 mm
7.	Theoretical screw volume (V_s)	0.0015 m^3
8.	Helix angle (θ)	10^0
9.	Screw conveyor length (l)	0.63 m
10.	Number of screws (N_s)	7
11.	Drive power	0.36 kW
12.	Torque on the screw	169.3 N-m
13.	Power on shaft	0.45 kW
14.	Motor power	0.83 hp
15.	Diameter of shaft	40 mm
16.	The volume of the hopper (V_H)	0.28 m^3
17.	Specific energy consumption (E)	0.75 kJ kg^{-1}

Fig. 5 Performance evaluation of pellet machine for combination 2 (80:20) in terms pelleting efficiency

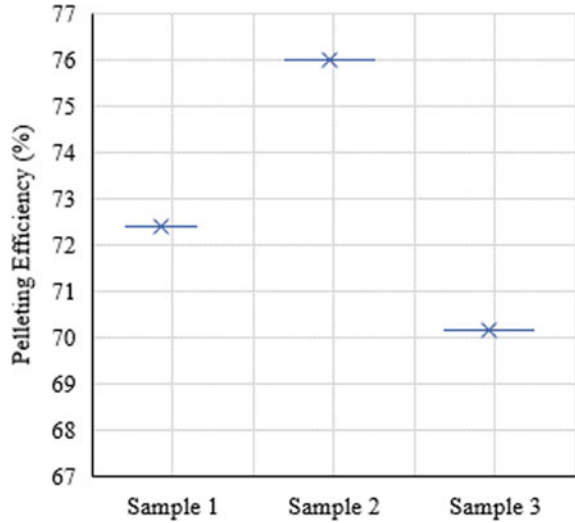
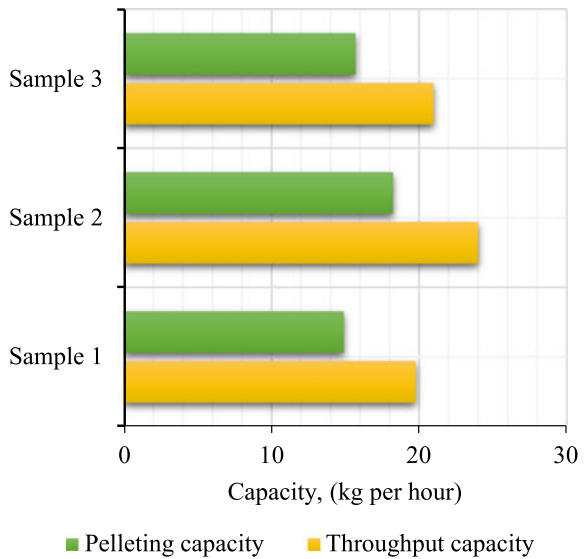


Fig. 6 Performance evaluation of pellet machine for combination 2 (80:20) in terms of pelleting capacity and throughput capacity



3.4 Physiochemical Properties of Pellets

The physical properties of pellets after three days were recorded. The test results of the produced pellets from the developed pellet machine were calculated based on length, diameter, weight, volume, size, particle size, thickness, and strength of the radial compresses as given in Table 4. Romallosa and Cabarles [17] reported that the average length of pellets was 1.2 cm, an average diameter of pellets was

Table 4 Physical properties of pellets

Sr. no.	Parameters	Values
1.	Average length (cm)	4.23
2.	Average diameter (cm)	1.163
3.	Average weight (g)	2.41
4.	Average volume (cm ³)	4.50
5.	Average density (g cm ⁻³)	0.36
6.	Average particle density (g cm ⁻³)	0.68
7.	Porosity of pellets (%)	0.40
8.	Durability of pellets (%)	78
9.	Radial comprehensive strength (kgf mm ⁻²)	0.71

0.4 cm, the average weight of pellets was 0.138 g, and average density of pellets was 0.318 g cm⁻³ made from a mixture of corn starch, and hot water for fish feed production by roller pellet machine.

Chemical properties of produced pellets in terms of nitrogen, phosphate, and potash were calculated. The higher percentage of chemical properties was found for 80% BS and 20% S in terms of NPK. It was found 1.6% N, 0.8% P, and 0.8% K, respectively. The combination 2, 80% biogas slurry with 20% clay soil (80:20), is better than the farmyard manure (FYM) having nutrient content of 0.5 to 1.0% N, 0.5 to 0.8% P, and 0.5 to 0.8% K, respectively [4].

3.5 Evaluation of Techno-economic Feasibility of Pelletization Process

Economic feasibility of pellet machine is dependent highly on the availability of raw material. The analysis was evaluated by considering the current investment [16, 17]. The results obtained were enlisted in Table 5 for an economic analysis of the system.

Table 5 Economic analysis for pellet machine

S. no.	Economic indicators	Values
1.	Net present worth	\$3066
2.	Benefit–cost ratio	1.40
3.	Payback period	11 month
4.	Internal rate of return	108%

4 Conclusions

A pellet machine was developed and tested for the utilization of biogas slurry. The screw conveyor of pellet machine was simple in design and which is easily developed and easy in operation. The cost of pellet machine was \$540. The best performance of pellet machine for the ratio 80:20 (80% BS and 20% CS), and efficiency of pellet machine was 76%. The machine is conceived as ideal, easy to maintain, and economical for commercial uses. The best physical and chemical properties of pellets were found in combination 2, with the ratio of 80:20 (80% BS and 20% CS). The higher percentage of chemical properties found in terms of nitrogen, phosphate, and potash was 1.6%, 0.8%, and 0.8%, respectively. The overall research study concluded that the combination 2 with the ratio of 80:20 was the best for pelletization and its use as organic manure to maintain soil fertility.

Acknowledgements Partial funding support was provided by the Indian Council of Agricultural Research (ICAR), All India Coordinated Research Project (AICRP) on EAAI, MPUAT, Udaipur-313001.

References

1. Ministry of New and Renewable Energy (2017) Potential of Renewable Energy in India. (<http://mnre.gov.in/file-manager/annual-report/2015-2016>). Cited on date: 06 July 2018
2. Ghosh SK (2016) Potential of economic utilization of biomass waste in India: implications towards SDGs. In: Seventh regional 3R forum in Asia and the Pacific, 2 to 4 November 2016, Adelaide, SA, Australia
3. Dahiya AK, Vasudevan P (1986) Biogas plant slurry as an alternative to chemical fertilizers. *Biomass* 9(1):67-74
4. Yu FB, Luo XP, Song CF, Zhang MX, Shan SD (2010) Concentrated biogas slurry enhanced soil fertility and tomato quality. *Acta Agriculturae Scandinavica Section B-Soil and Plant Science* 60(3):262-268
5. Mittal S, Ahlgren EO, Shukla PR (2018) Barriers to biogas dissemination in India: a review. *Energy Policy* 112:361-370
6. Islam R, Syed ME, Rahman MD, Rahman M, Deog Hwan OH, Chang RA (2010) The effects of biogas slurry on the production and quality of maize fodder. *Turk J Agricu* 34:91-99
7. Kumar S, Malav LC, Malav MK, Khan SA (2015) Biogas slurry: source of nutrients for eco-friendly agriculture. *Int J Extens Res* 2:42-46
8. Khan SA, Malav LC, Kumar S, Malav K, Gupta N (2014) Resource utilization of biogas slurry for better yield and nutritional quality of baby corn. *Adv Environ Agric Sci* 382-394
9. Islam MS (2006) Use of bio-slurry as organic fertilizer in Bangladesh agriculture. In: Prepared for the presentation at the international workshop on the use of bioslurry domestic biogas programme, Bangkok, Thailand
10. Chikwado UK (2013) Development and performance test of poultry feed mixing and pelleting machine. *Int J Sci Res* 4(6):1161-1166
11. Orisaleye J, Ojolo S, Fashina A (2009) Design and development of a livestock feed pelleting machine. *J Eng Res* 14(1)
12. Mandwe DS (2010) Design and development of briquetting machine for eco-friendly fuel, Ph.D. Thesis, Maharana Pratap University of Agriculture and Technology, Udaipur, Rajasthan

13. Ojomo AO, Agbetoye LAS, Ologunagba FO (2010) Performance evaluation of a fish feed pelletizing machine. *Asian Res Publishing Netw (ARPN)* 5:88–97
14. Burmamu BR, Aliyu B, Tya TSK (2015) Development of a manually operated fish feed pelleting machine. *Int J Res Eng Adv Technol* 2(6)
15. Morad MM, Afify MK, Kaddour OA, Daood VM (2007) Study on some engineering parameters affecting the production of the fish pelleting machine. Published Doctoral dissertation, Zagazig University, Egypt. vol 24(2), pp 259–282
16. Narale PD, Rathore NS, Kothari S (2013) Study of solar PV water pumping system for irrigation of horticulture crops. *Int J Eng Sci Invention* 2(12):54–60
17. Romallosa ARD, Cabarles JC Jr (2015) Design and evaluation of a pellet mill for animal feed production. Central Philippine University, Iloilo, Philippine

Analysis of the Effect of Shock Waves on Fretting Behavior of Graphene Hydroxyl Reinforced Aluminum 6061 Composites



M. R. Srinivasa, Y. S. Rammohan, and M. Sadashiva

1 Introduction

Aluminum is the material abundantly available in nature next to nitrogen. By the advantageous properties like strength-to-weight ratio, lightweight, easy to compose, and cheap its application is getting wider in the area of aviation, navy, automobile, railways, sports, and many other. The aluminum composite makes many of the components in Linke Hofmann Busch (LHB) railway coaches and signifies the application of the material considering strength-to-weight ratio. The Indian railways are replacing the coaches manufactured with steel with aluminum as a major structural material in the view of reduction of weight. According to reports, the European countries and Japan have been using aluminum coaches for at least 15 years. Reduction in weight results in savings in transportation costs and enhanced acceleration/deceleration. Better corrosion resistance would result in lesser maintenance requirements in the workshops. All these factors signify the use of aluminum in the field of manufacturing of structural components. The chemical and mechanical properties of aluminum are as given in Tables 1 and 2.

Aluminum as a monolithic material is having less wear strength compared to other materials and limits its utilization where the application involves wear. Reinforcing of other material into aluminum enhances the wear strength of the base material, so that it can be used for application which requires better wear strength [1]. The

M. R. Srinivasa (✉) · M. Sadashiva
Department of Mechanical Engineering, P. E. S. College of Engineering, Mandya 571401,
Karnataka, India
e-mail: srinivasamr77@gmail.com

M. Sadashiva
e-mail: sadashiva015@gmail.com

Y. S. Rammohan
Department of Mechanical Engineering, B.M.S. College of Engineering, Bengaluru 560019,
Karnataka, India

Table 1 Chemical properties of aluminum 6061

Element	Mg	Si	Fe	Cu	Mn	Ti	Zn	Cr	Al
% wt.	1.03	0.52	0.27	0.28	0.03	0.01	0.06	0.09	Bal

Table 2 Mechanical properties of aluminum 6061

S. No.	Property	Value
1	Density	2700 kg/m ³
2	Young's modulus of elasticity	69 MPa
3	Poisson's ratio	0.33

advantage of reinforcement of graphene in aluminum is not limited to tribological properties, but it results in enhancement of other mechanical properties like hardness, tensile strength and compressive strength [2].

Graphene hydroxyl (GoH) is the material which is known for its low density (0.4 gms/cc) and high tensile strength (0.5TPa to 1TPa) and having a noble wear resistance because of its self-lubricating properties. Rao et al. [3] revealed about graphene that it has become an existing factor and involved with many other parameters which are yet to be investigated as many properties of graphene are yet to be explored. Since it is an allotropic form of carbon material, it shows a pro factor concerning the tribological properties and can be used as a reinforcing material with other matrix materials like metals, plastics and polymers [4]. It is an allotropic form of carbon material derived from graphite. It has a hexagonal lattice structure and noble fracture strength. These properties of the material are requisites for the structural components in aviation, naval and automobile field. To make use of its advantageous properties of aluminum, the graphene in the form of graphene hydroxyl is used as reinforcing material.

Shock waves are the waves generated when the speed of the object in movement is more than that of the speed of the sound in the medium. These waves carry the energy and across the shock, there will be a rapid increase in pressure, temperature, as well as flow density. The energy dissipation of shock waves depends on the distance of travel with an increase in entropy. The present study focuses on the use of energy stored in shock waves for analysis of molecular changes at the surface of the material. The shock waves can be used for altering the surface texture of the material. S. Venkatesan et al. [6] revealed that wear of the surface material could be reduced by strain hardening of the material.

Fretting wear is the phenomenon of removal of material when two surfaces are in contact and the motion of the components is relatively small. Vibrations cause fretting or due to the application of bulk fatigue stress to one or both of the contacting parts, and usually occurs at the interface between two parts with relative motion. It occurs when there is small amplitude oscillatory relative movement such as dovetail roots of compressor blades in the aviation industry, cables in overhead conductors and hoists, riveted joints and prostheses. Many studies have shown that the combined actions of fretting and fatigue had a significant effect on the fatigue limit of materials

like aluminum alloys. Fretting results in removal of material from the surface of the material which causes a reduction in strength of the material. This also leads to surface crack initiation, which may propagate during working conditions. The crack propagation may lead to failure of mechanical members causing loss. The fretting fatigue damage is known as cyclic axial loading, contact pressure, relative slip motion, surface conditions, etc.

Shivalingappa et al. [5] and Jagadish et al. [7] conducted the wear and strain hardening due to shock wave treatment. The surface of the wear of the material could be reduced by hardening the surface, and this can be achieved by strain hardening [8, 9]. However, investigations were conducted for materials other than aluminum composites. It is intended to conduct the fretting wear analysis for aluminum composites reinforced with various percentage of graphene as reinforcing material.

2 Experimentation

Graphene hydroxyl in nanopowder form with grain size and more than 98 percent purity is reinforced with aluminum as a matrix to enhance the wear strength and tensile strength. The reinforcing material is composed in varied weight percentage of matrix material viz as-cast (0%), 0.5%, and 1.0% of the weight of aluminum 6061. The stir casting method is used for fabrication of the material. Graphene billets are made to avoid the agglomeration and to have a uniform distribution. Aluminum is melted for a temperature of 690 °C, and then, the graphene billets are added to the molten metal. The mixture is stirred for six minutes with a stirring speed of 600 rpm in clockwise and anticlockwise eventually. The molten mixture is then poured into molds and allowed for natural solidification and air cooling, as shown in Fig. 1.

The samples of specimens are then subjected to the microstructural analysis to analyze the uniform distribution of the graphene hydroxyl particles in the matrix. Scanning electron microscope with make TESCAN VEGA3 LMU with an SEM voltage 5–30 kV is having a resolution of 3 nm. EDAX and XRD graphical representations show an even distribution of reinforcing material. The images of the test are as shown in Fig. 2.



Fig. 1 Material casting process

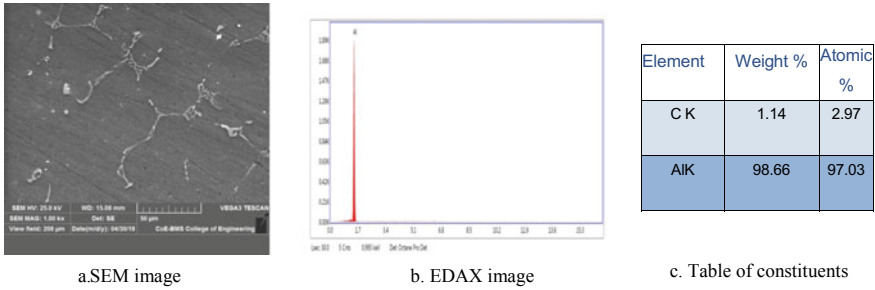


Fig. 2 SEM/EDAX images for 1% graphene hydroxyl with Al 6061

The specimens prepared are machined as per the specifications of ASTM E-8 for testing of basic mechanical properties. The properties of composite specimens were tested, and a significant enhancement is found in tensile, compressive, and wear strength as compared to aluminum 6061 alone. Plates of dimension 100 × 100 × 6 mm thickness are prepared for shock wave treatment. Shock waves are generated using Reddy’s shock tube, as shown in Fig. 3.

The shock tube is made up of three sections viz drive section, driven section and the test section. Wavefronts are generated by blasting the diaphragm fitted between drive and driven section. Wax paper of thickness 0.3 mm is used as a diaphragm and fixed by clamping. The air pressure is increased by pushing a hand-operated piston. An increase in pressure of 2.5 to 3 bars is enough to generate the shock waves. The pressure is increased up to a peak pressure up to 3.8 bars. The specimen is fixed to a fixture and kept in the test section, as shown in Fig. 4a–4c. These waves are made to hit the surface of the work specimen. Multiple numbers of shock waves viz 20, 40, and 60 number of shocks are made to hit the surface to analyze the effect on surface hardness and fatigue fretting behavior.

The fretting wear test is conducted on the graphene hydroxyl reinforced aluminum 6061 composites subjected to shock treatment and compared with the specimens of the same composition without shock treatment. Weight loss of the specimen is taken as a test parameter. The normal forces of 20 , 30 , and 40 N are applied on specimen via



Fig. 3 Specimens and holding fixtures

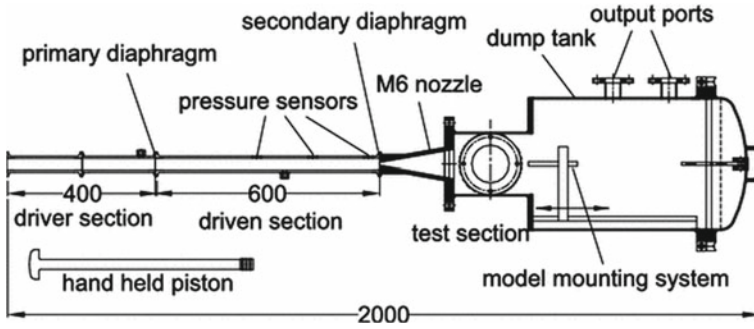


Fig. 4 Reddy shock tube

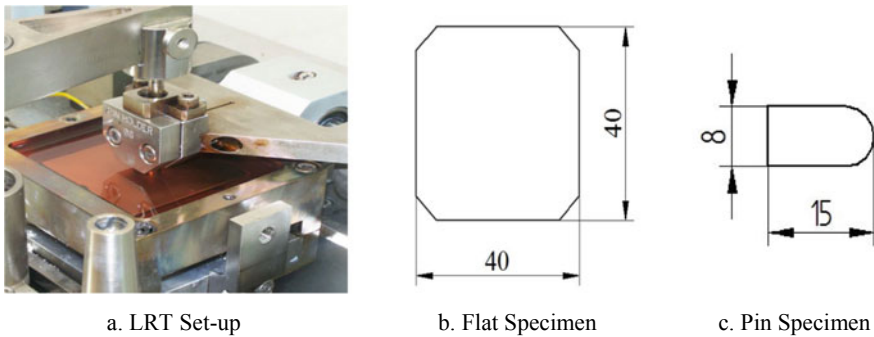


Fig. 5 Liner tribometer setup and specimen dimensions

pins with spherical geometry of the same material. The flat specimens are machined to $40 \times 40 \times 6$ mm thickness, and the pin is made to 8 mm diameter and 15 mm length, as shown in Fig. 5a–5c. The pin is fixed to the holder, and the normal load is applied on the specimen through it. The length of the stroke is 2 mm with a frequency of 50 Hz. The friction test is done for dry friction with room temperature.

3 Results and Discussions

3.1 Hardness

The hardness of the specimens with graphene reinforcement of as-cast, 0.25%, and 1.0% are tested using VHN hardness testing machine with the following specifications (Table 3);

The specimens are tested for Vickers hardness number for as-cast, 0.5% graphene and 1.0% graphene. The results obtained are given in Table 4.

Table 3 Specifications of VHN machine

Instrument used	HV hardness testing machine
Make	FIE
Capacity	25–1000 Gms
Load	500 Gms
Dwell time	10 s
Test method	IS 1501–2011

Table 4 Vickers hardness number of Al 6061 reinforced with various percentages of GoH

No. of shocks	0% GoH	0.5% GoH	1.0% GoH
0	70	86	74
20	80	91	109
40	89	97	105
60	93	107	112

The hardness of the specimen is tested for no shocks (0 shocks), 20, 40, and 60 number of shocks, as shown in Fig. 6. The hardness of the specimen is increased from 70 to 93 with an increase in graphene hydroxyl percentage as reinforcement material from 0 (as-cast) to 1 weight percent. It is also noticed that, as the number of shocks increases from no shocks to 60 numbers of shocks (multiple shocks), the hardness of the specimen found an increase from 70 to 93 for as-cast condition, 86 to 107 for 0.5%, and 94 to 112 for 1.0%.

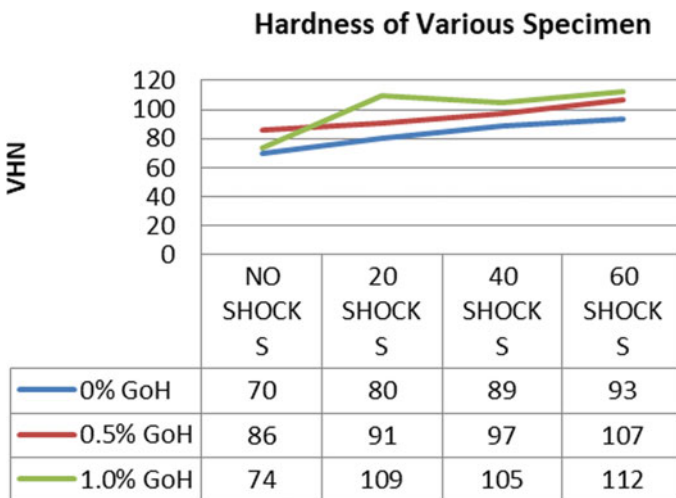


Fig. 6 Graphical representation of VHN hardness number

Table 5 Specifications of linear reciprocating tribometer (LRT)

Make	DUCOM India Pvt Ltd
Cylindrical pin indenter	Ø 8 × 15 mmL
Spherical ball indenter	8 mm dia
Flat specimen	40 × 40 × 5 mm
Normal load	20–200 N
Frequency	5–50 Hz
Stroke length	1–20 mm
Frictional force	Max 200 N
Temperature	Up to 300 °C
Equipment size	600 × 520 × 920 mm

Table 6 Weight loss of material due to fretting

No. of shocks	Weight loss due to fretting wear (Gms)		
	As-cast (0%)	0.5% GoH	1.0% GoH
No shocks	0.018	0.016	0.011
20	0.016	0.016	0.009
40	0.017	0.017	0.013
60	0.012	0.011	0.009

3.2 Fretting

The fretting analysis is conducted on the specimens using linear reciprocating tribometer (LRT) with the following instrument specifications (Table 5). The weight loss of material is measured and given in Table 6.

A significant reduction in weight loss has resulted as the percentage of graphene increases and as the number of shock waves increased, as shown in Fig. 7.

4 Conclusion

By analyzing the results, it can be concluded as follows:

1. Material is synthesized with aluminum 6061 as matrix and graphene hydroxyl as reinforcing material with various percentage.
2. The material so synthesized is treated with shock wavefronts produced at a maximum pressure of 3.8 bars using Reddy shock tube. Multiple shock wavefronts are passed on the specimen as no shocks, 20 shocks, 40 shocks, and 60 shocks.
3. The hardness of the specimen measured and found increased as the percentage of graphene hydroxyl increases from 70 to 93 (24%) for as-cast, whereas it can

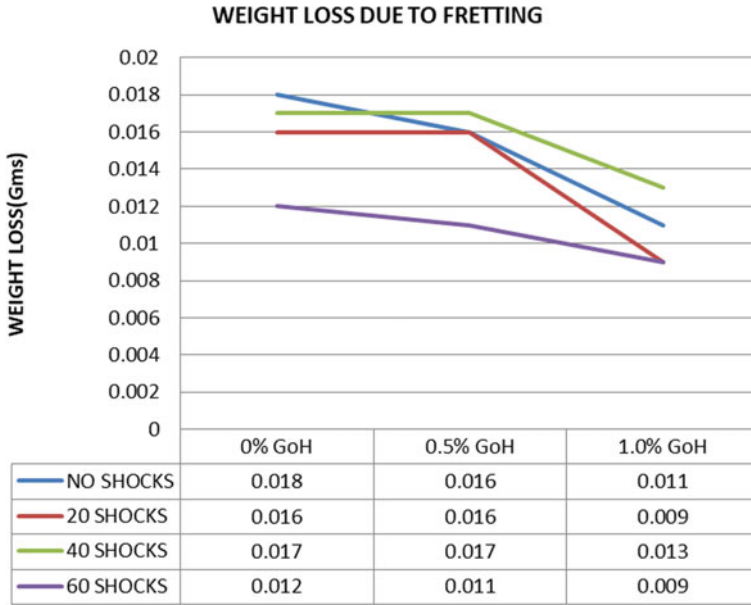


Fig. 7 Graphical representation of weight loss of material

also be concluded that hardness enhances as the number of shocks increases for the same specimen.

4. Reinforcement of graphene hydroxyl leads to minimizing the wear as graphene acts as self-lubricating material.
5. Wear loss found declined due to the surface hardening of the material since it is treated with shocks which compact the molecules at the surface level.
6. It is concluded that the method of shock treatment can be used as an additional treatment to minimize the wear of aluminum composites.

References

1. Prashantha Kumar HG, Anthony Xavier M (2014) Graphene Reinforced metal matrix composite (GRMMC): a review. *Procedia Eng* 97:1033–1040; 12th Global conference on manufacturing and management, GCM 2014, pp 1877–7058 <https://doi.org/10.1016/j.proeng.2014.12.381>
2. Garg P, Gupta P, Kumar D, Parkash O (2016) Structural and mechanical properties of graphene reinforced aluminum matrix composites. *J Mater Environ Sci* 7(5):1461–1473. ISSN: 2028–2508 CODEN: JMESC
3. Rao CNR, Kanishka Biswas, Subrahmanyama KS, Govindarajab A (2009) Graphene, the new nanocarbon. *J Mater Chem Royal Soc Chem* 19:457 2469–2467. <https://doi.org/10.1039/b815239j>
4. Prashantha Kumar HG, Xavier MA (2017) Effect of graphene addition and tribological performance of Al 6061/graphene flake composite. *Tribol Mater Surf Interfaces* 11(2):88–97

5. Kubsad SS (2012) Effect of shock waves on wear behavior of few metallic materials. *Int J Eng Sci Technol (IJEST)* 4(05). ISSN: 0975–5462
6. VenkatesanS, Anthony Xavior M (2017) Analysis of mechanical and tribological behaviour of Aluminum metal matrix composite reinforced with graphene-a review. *J Chem Pharm Sci* 10(1):1–4. ISSN: 0974–2115
7. Ray N, Jagadeesh G, Suwas S (2015) Response of shock wave deformation in AA5086aluminum alloy. *Mater Sci Eng A* 622:219-227.<https://doi.org/10.1016/j.msea.2014.10.010>
8. Bhatti NA, Pereira K, Wahab MA (2018) Effect of stress gradient and quadrant averaging on fretting fatigue crack initiation angle and life. *Tribol Int* 131:212–221
9. Jagadeesh G (2007) Application of shockwaves in pencil manufacturing industry. In; Proceedings of the 26th international symposium on shock waves, Gottingen Germany

A Review on Friction Stir Spot Welding of Similar and Dissimilar Materials



Neeru, Sarbjit Singh, and P. S. Satsangi

1 Introduction

The recent decrease of naturally available resources and increasing cost of the fuel lead to an increase in demand for lightweight materials in various aerospace and automobile industries. The lightweight materials reduce the consumption of fuel and enhance the performance of the automobiles. In this perspective, the utilization of lightweight material, such as aluminium and magnesium, has considered a great alternative of steel. The joining of lightweight materials is always a challenge to the research fraternity. Conventionally, riveting and resistance spot welding (RSW) is used for joining of aluminium and other lightweight materials of lesser thickness. However, these processes have many disadvantages such as high energy consumption and less production efficiency [1]. The friction stir welding (FSW) method was developed to overcome these limitations of the process, at The Welding Institute (TWI) in 1991. The FSW process has been successfully attempted for joining various non-ferrous, ferrous metals and polymers. The FSW set-up comprises of a tool, which rotates as well as moves along the seam. The relative motion amongst the tool and the workpiece material produces frictional heat, which tends to join the workpieces. A new process is derived from producing a weld on the spot named as friction stir spot welding (FSSW) by restricting the movement of the tool of the FSW process to rotation only. The cycle time of the FSSW process is less than the FSW process as it takes less time to produce spot weld than a seam weld [2].

The FSSW process joins the material in their solid state, i.e. the joining is done at a temperature, which is lesser than the melting point of the workpiece material to be weld and that too without any use of filler metal [3]. The process comprises of the three stages, namely plunging, stirring and retracting, as shown in Fig. 1. Initially, the

Neeru · S. Singh (✉) · P. S. Satsangi
Mechanical Engineering Department, Punjab Engineering College (Deemed to be University),
Chandigarh, India
e-mail: sarb1234.iitrookee@gmail.com

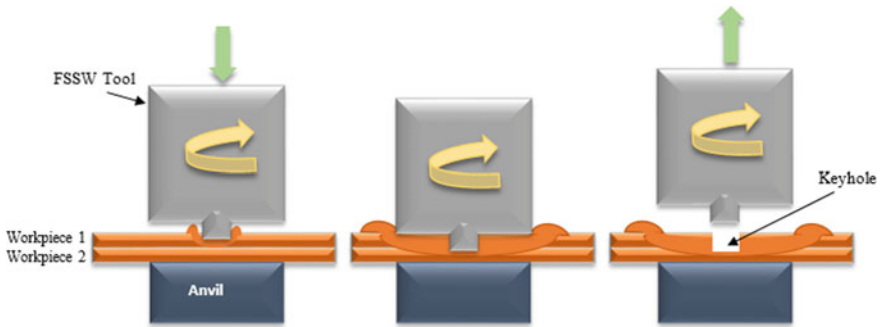


Fig. 1 Schematic diagram of FSSW process: **a** plunging, **b** stirring and **c** retracting

tool rotates and contact is made between the tool shoulder and the workpiece placed on top in lap position. After that, the tool penetrates the workpiece by applying a force to form spot weld. This stage is called plunging, and the material is expelled by the tool during this stage. When a predetermined depth is achieved, the stirring phase initiates. In the stirring step, the tool keeps on rotating in both workpieces. The material next to the tool is heated until it softens because of frictional heat, generated in both stirring and plunging phases and then mixed by stirring. At last, the tool is withdrawn or retracted from the workpieces, after a proper bonding is achieved [4]. The FSSW process is an intricate process which comprises of many process parameters such as rotation speed of the tool, plunge depth, dwell time and plunge rate and are defined as follows:

- Tool rotational speed: The term explains the rotational tool speed, and the direction of rotation is either counterclockwise or clockwise, as seen from the top.
- Plunge depth: The word used to explain the pin of the tool penetrates the workpiece.
- Plunge rate: Defined as the velocity at which the FSSW tool penetrates into the workpiece material.
- Dwell time: The term used for the time the FSSW tool remains in the workpiece.

The variation in the process parameters affects the various properties of the weld such as strength, hardness, microstructure and weld macrostructure. The macrostructure of the weld produced after FSSW process is categorized into four regions, i.e. stir zone (SZ), thermomechanically affected zone (TMAZ), heat-affected zone (HAZ) and parent material (PM).

Stir zone (SZ) was the region which is created underneath the shoulder and the tool pin when tool penetrated the workpiece, or it is a material which is in contact with the tool directly. HAZ is the region which is affected by the heat; however, there is not any deformation in the HAZ region. While the TMAZ region is affected by both deformation and heat [5]. Parent material (PM) is the base material which is away from the SZ and has experienced some heat; however, there is not any change in the microstructure of the material [6].

With the advancement in the process, researchers came out with various theories on different aspects of the process, and one of the main issues is the joining of dissimilar material. The objective of the paper is to present a literature review on FSSW of similar and dissimilar material and to provide some useful information that will be beneficial for future research.

2 Friction Stir Spot Welding of Similar Materials

2.1 Aluminium–Aluminium Joints

Due to the increasing environmental and global resource problems, reducing the weight of automotive bodies, high-speed cars, aerospace structures, etc., is gaining more attention and usage of lightweight material is found effective for the same. Aluminium alloys have many fine characteristics like lightweight, specific strength, corrosion resistance, high recycle and impact resistance [1]. Several researchers have considered the process of joining different aluminium alloys by FSSW over the years and some of them revealed that microstructural and mechanical properties of joints vary considerably with process parameters. Shen et al. [7] calculated the mechanical properties, failure mechanisms and microstructures of the weld produced by welding Al-6061 T4 sheets by FSSW process and reported that to obtain the desired appearance of the joint, the process should be done for a longer duration of time and at higher tool rotational speed. Tier et al. [8] stated that the foremost feature, which upsets the mechanical properties of welds that are made of aluminium alloys, is the Alclad distribution in the weld.

During the FSSW of aluminium alloys, the reasonable strain rate is generally complemented by a small rise in temperature, and it is the reason for the variations in the weld microstructure [9]. The experimental study of joining of Al-6082 and Al-7108 aluminium alloys by FSSW by Frigaard et al. [10] determined the strain rate during the process. The author reported the estimated values of the strain rate between 1.6 and 17 s^{-1} ; it is seen that these values have a lower magnitude than those calculated during the FSW process. The researchers also suggested that there is slippage between contiguous material in the SZ and the tool periphery.

Tensile strength of aluminium alloys depends on the parameters of the welding and existence of imperfections in the welds [11]. Li et al. [11] observed joints with hook defect and without hook defect and recorded that a higher value of the tensile shear load, i.e. 12 kN , was obtained in joint without hook defect, while for joints with hook defect, the value obtained was 6.9 kN . It is observed that tensile strength obtained by refill FSSW process is higher than the welds having a keyhole. Uematsu et al. [12] examined Al 6061-T4 aluminium alloy sheets, welded by both conventional FSSW and refill FSSW process. The values of tensile strengths of the joints obtained by refill FSSW process was 3.458 kN , while for joints having a probe hole, it is

2.645 kN. It means the refill process improved the value of tensile strength of the joint by 30%.

2.2 Magnesium–Magnesium Joints

Magnesium takes sixth place amongst the most abundant elements on the earth's surface, and because of their lightweight properties, they have an excellent specific strength, hot formability, sound damping capabilities, recyclability and good castability [13]. Magnesium alloys have an essential application in industries where weight reduction is required because of its relation between strength and weight and also where it is essential to decrease inertial forces. On account of this, many denser materials like cast iron, steels, copper alloys and even aluminium alloys are also substituted by magnesium alloys in different structural and automotive applications [14]. The crystal structure of magnesium is hexagonal cubic packing, i.e. HCP with a restricted amount of operative slip systems at the room temperature. Shen et al. [15] increased the temperature to improve the plastic deformation of alloys of magnesium, which, therefore, improved the fluidity of magnesium alloy in the course of heating FSSW process. Thus, the voids count in the welded joint decreases, also there was an improvement in the tensile shear load of the joint due to an increase in the temperature. The researchers also witnessed that the width of the bonded region got enlarged with the rise in the temperature during the welding process.

Various factors influence the joint strength, such as stir tool, the thickness of the sheet and hybrid welding. Xu et al. [16] noted that the strength of the FSSW magnesium alloy joint could be enhanced by adding Zn interlayer. This improvement was seen because the addition of Zn interlayer lowered the reaction temperature of the interface, which advances the diffusion reaction among Mg substrate and Zn interlayer, creating a bonded region. Consequently, there was a decrease in the hook defect and an increase in the bonded region area, and thus, the tensile shear load of the weld joint was improved.

2.3 Copper–Copper Joints

Welding of copper to copper by FSSW welding process has got less attention and has limited literature. Sansui et al. [17] joined commercially pure copper of 3 mm thickness by FSSW. The researchers scrutinized the microstructure of the joint and then conducted a corrosion test. The study was conducted at three different tool rotation speed, and a completely metallurgical bonded region was witnessed in stir zone with equiaxed and fine grains having their size bigger than those of base metal. Hook defect was observed, which showed that there was an inadequate flow of material during the stirring process. Some residuals were detected in the energy dispersive spectrometer (EDS) analysis which was supposed to come from the tool which could

negatively affect the corrosion property of the workpiece. It was witnessed that the joint made at 1200 rpm had the least potential to corrode, and also it performed worse than joints produced at 1600 rpm and 2000 rpm. Finally, the corrosion property of the joint was enhanced by processing the workpiece in 3.5% NaCl.

2.4 Steel–Steel Joints

Initially, only aluminium alloy was welded by FSSW process because of the trouble in choosing the suitable tool materials, which can survive the elevated temperature, produced while welding of steels by FSSW. Moreover, this procedure can be applied now to the steels after advancements in the tool materials [18]. Steel is essential for the structure of the body of all mass-produced, high-volume cars. The customers emphasize on safety and protection from corrosion, and this has increased the usage of galvanized steel [19]. Baek et al. [19] produced galvanized steel joints and considered the impact of tool penetration depth; also, the microstructure of the nugget was analysed. The researchers concluded that there was not any mechanically blended layer between the bottom and top workpiece plates at the nugget, and this was because of less tool penetration and small height of the tool as compared to the thickness of the steel plate. Sun et al. [20] scrutinized the mechanical properties and microstructure of joints made of mild steel with flat FSSW technique. The researchers performed a lap shear test, and interfacial mode of failure of the weld was observed. After failure, the load fell to zero in very less time.

On the other hand, when the fracture happened through plug mode, the load applied started to fell after the crack initiated. Researchers in their another study [21] carried out on FSSW of low carbon steel (LCS) plates and used a supplementary heat source in the form of high-frequency induction and stated that strong welds could be achieved with a small load and low tool rotation speed after preheating. Also, a maximum of 12.4 kN of the tensile shear load was achieved.

2.5 Polymer–Polymer Joints

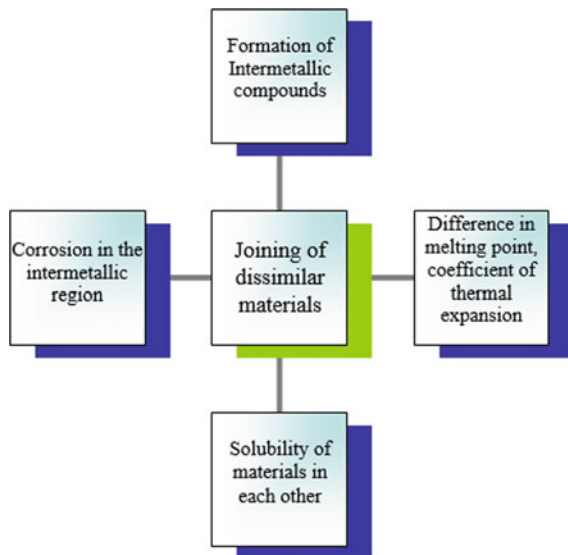
With the advancement in the technology, the polymers are now taking the place of various metals due to their low cost and lightweight such as polycarbonate (PC), acrylonitrile butadiene styrene (ABS) and high-density polyethylene (HDPE). Lambiase et al. [22] joined polycarbonate sheets and analysed the effect on rotational speed of the tool, dwell time, waiting time, preheating and plunge rate on mechanical properties of the workpiece, while Arici et al. [23] joined polypropylene sheets and optimized the tool penetration depth for maximizing the tensile strength of the weld. Bilici [24] also welded polypropylene sheets by FSSW process and observed the effect of the tool geometry on the weld formed. The author stated that the variation in the tool geometry affected the development of the SZ and the strength of the weld.

3 Friction Stir Spot Welding of Dissimilar Materials

Dissimilar material welding is the need of many industries to produce a structure with properties of different materials by joining them with different methods (Fig. 2). Joining dissimilar materials is the difficult task because of the variance in the melting temperature of the materials, development of intermetallic compounds (IMCs), poor solubility of the materials in each other, variance in coefficient of thermal expansion of the materials and corrosion in the intermetallic zone [25]. The main issue in welding of dissimilar materials is the development of brittle intermetallic compounds (IMCs). IMCs help in the propagation of cracks and thus lead to failure, also corrosion can occur in that region. The formation of IMCs occurs when two different materials melted and joined, which is common in various fusion welding processes. Joining of dissimilar material is made easy with the introduction of solid-state joining processes, which is lesser than the temperature of melting point of the material. FSSW is proved to be an efficient process for joining dissimilar materials. The following section provides a detailed study on different materials joined with FSSW and general trends in the joining of dissimilar materials.

Suhuddin et al. [26] joined AZ31 magnesium alloy and AA5754 aluminium alloy and analysed the microstructure of the joint. The author reported that the factors that affect the development of the grain arrangements in the SZ are grain boundary diffusion, dynamic recrystallization and interfacial diffusion, which results in the fine equiaxed grains in the weld centre. The author also analysed similar Al-Al and Mg-Mg welds and concluded that both similar welds had higher mechanical and microstructural properties as compared to dissimilar Al-Mg weld. Chowdhury et al. [27] studied the joint produced by welding AA5754-O aluminium alloy and

Fig. 2 Factors affecting joining of dissimilar materials



commercial AZ31B-H24 magnesium alloy by FSSW process. The author studied both Al–Mg and Mg–Al adhesive joint and observed that there was a unique interfacial layer containing intermetallic compounds in both joints. It was observed that either Al–Mg or Mg–Al adhesive welds had greater failure energy and lap shear strength than the Al–Mg weld without adhesive. While Sun et al. [28] welded a commercial 1 mm thick aluminium alloy 6061 and mild steel of the same thickness and had witnessed no evident IMCs layer present along the interface. Bozzi et al. [20] studied the formation of IMCs layer after welding AA 6016 aluminium alloy with a galvanized IF-steel sheet. The author witnessed that with the rise in the penetration depth and tool rotational speed, the thickness of the intermetallic compound (IMCs) layer increases. In addition, it is perceived that the presence of intermetallic compounds (IMCs) appeared to be essential to improve the strength of the weld, but in case the thickness of the intermetallic compound layer is large then the crack could propagate simply through that IMCs layer. Lee et al. [29] joined low carbon steels to Al–Mg alloy to scrutinize the influence of penetration depth of the tool on the development of IMCs. The author observed that the area in which IMCs are formed grew with the increase in the penetration depth of the tool. Table 1 shows the fssw process of dissimilar materials.

4 Conclusion and Future Scope

The FSSW process is suitable for producing joints of both similar and dissimilar metals as well as polymers. This paper is leading the way to the work done until now on FSSW of similar and dissimilar joints. FSSW belonging to a class of solid-state joining processes is a feasible mode of joining similar and dissimilar material. The process is attracting more researchers because of its many advantages like mass production, low energy utilization, cost reduction, etc. Earlier the FSSW method was used for welding aluminium alloys, but with time many more materials have also taken the interest of researchers like copper, steel, magnesium, polymers, etc. After an extensive literature survey, it is perceived that there are many studies related to FSSW of similar materials, but the field of dissimilar material joining still needs more attention. Polymers are gaining the interest of researchers, and its application can be seen in various fields like automobile, aerospace, etc. Also, polymer–metal dissimilar welding has been reported by various researchers by different technologies and their joining by FSSW still needs consideration. Copper is also least reported in the research. The difficulty in welding of the copper is that the metal gets corrode soon and when it is welded with dissimilar material, the formation of IMCs is more. Researchers can consider the material for future research and eliminate the shortcomings of the weld. The FSSW process is an efficient process for industrial use; innovation in the process can help to improve the production rate by FSSW process to increase its utility in industries.

Table 1 Research contribution in FSSW of dissimilar materials

Authors	Material/thickness	Findings
Piccini and Svoboda [30]	AA6063-T6/2 mm and an LCG-S/0.7 mm	Stirring and forging of the top sheet into the bottom sheet was improved by welding with the tools having shorter pins
Reilly et al. [31]	AA6111-T4/ 0.93 mm, DC04 (ungalvanized)/1 mm and DX54Z (galvanized) low carbon steel sheet/1 mm	Used fluted tools and observed that metal flow is circumferential, and it was seen that the tool and the central region of the workpiece stick to each other
Fereiduni et al. [32]	Al-5083/3 mm and St-12/1 mm	The joint strength or tensile shear strength of the weld first enhanced and then a depreciation was seemed with a rise in the dwell time and with this intermetallic layer was formed, and also there was growth in aluminium grains adjoining the exit-hole of the weld. So, the improvement in the optimum tensile shear strength was seen by increasing the rotational tool speed and decreasing the dwell time
Shen et al. [33]	ZEK 100 magnesium Alloy/1.5 mm and galvanized DP600 automotive steel sheets/0.9 mm	Mg-steel welds have higher effective bonded areas than Mg-Mg welds because of zinc brazing and presence of incomplete bonding about the periphery of the Mg-steel weld
Aliasghari et al. [34]	AA 5052 and propylene/2 mm	Polypropylene failed due to ductile failure having fibrous behaviour. Joints made using pretreated alloy have approx. 40% decrease in the crystallinity of the polypropylene whereas it is approx. 10% when the untreated alloy is used
Siddharth and Senthilkumar [35]	Al5083 and C10100/1.5 mm	Considered the influence of variations in plunge depth on the flow of materials within the weld zone

(continued)

Table 1 (continued)

Authors	Material/thickness	Findings
Ravi et al. [36]	Al6082-T6/15 mm and HDPE/0.8 mm	Used different tool profiles and determined that the tool with square pin was good for both tri-metallic and sandwich sheets, and also it was seen that joints of tri-metallic sheets performed better with every type of tool profile
Siddharth and Senthilkumar [37]	Al 5086 and C10100/1.5 mm	Found out the optimized values of the process parameters as 2.05 mm plunge depth, 1100 rpm tool rotational speed, 11.5 s dwell time, 2.234 kN of a maximum tensile shear failure load and 90.9 HV of minimum interface hardness
Rana et al. [38]	AA5052-H32/2 mm and HDPE/1 mm	It was observed that sandwich sheets than bimetallic sheets because of smaller peak temperature exhibited finer grain structure, and the size of grain increased after the rotational tool speed was increased because of the larger generation of heat

References

- Zhang Z, Yang X, Zhang J, Zhou G, Xu X, Zou B (2011) Effect of welding parameters on microstructure and mechanical properties of friction stir spot welded 5052 aluminum alloy. *Mater Des* 32(8–9):4461–4470. <https://doi.org/10.1016/j.matdes.2011.03.058>
- Badarinathan H, Shi Y, Li X, Okamoto K (2009) Effect of tool geometry on hook formation and static strength of friction stir spot welded aluminum 5754-O sheets. *Int J Mach Tools Manuf* 49:814–823. <https://doi.org/10.1016/j.ijmachtools.2009.06.001>
- Mathers G (2002) *The welding of aluminium and its alloys*. Woodhead Publishing
- Yang XW, Fu T, Li WY (2014) Friction stir spot welding: a review on joint macro- and microstructure, property, and process modelling. *Adv Mater Sci Eng* 2014. <https://doi.org/10.1155/2014/697170>
- Threadgill PL (2007) Terminology in friction stir welding. *Sci Technol Weld Joining* 12(4):357–360. <https://doi.org/10.1179/174329307X197629>
- Mubiayi MP, Akinlabi ET (2014) Friction stir spot welding of dissimilar materials: an overview. *Lecture Notes in Engineering & Computer Science*, 2214
- Shen Z, Yang X, Zhang Z, Cui L, Yin Y (2013) Mechanical properties and failure mechanisms of friction stir spot welds of AA 6061–T4 sheets. *Mater Des* 49:181–191. <https://doi.org/10.1016/j.matdes.2013.01.066>
- Tier MD, dos Santos JF, Olea CW, Rosendo T, Mazzaferro CP, Mazzaferro JAE, Strohaecker TR, da Silva AAM, Isakovic JT (2008) The influence of weld microstructure on mechanical

- properties of alclad AA2024-T3 friction spot welded (No. 2008-01-2287). SAE Technical Paper. <https://doi.org/10.4271/2008-01-2287>
9. Rosendo T, Parra B, Tier MAD, Da Silva AAM, Dos Santos JF, Strohaecker TR, Alcântara NG (2011) Mechanical and microstructural investigation of friction spot welded AA6181-T4 aluminium alloy. *Mater Des* 32(3):1094–1100. <https://doi.org/10.1016/j.matdes.2010.11.017>
 10. Frigaard Ø, Grong Ø, Hjelen J, Gulbrandsen-Dahl S, Midling OT (1999) Proceedings of 1st international symposium on friction stir welding, Thousand Oaks, CA, TWI, Great Abington, Cambridge, UK
 11. Li W, Li J, Zhang Z, Gao D, Wang W, Dong C (2014) Improving mechanical properties of pinless friction stir spot welded joints by eliminating hook defect. *Mater Des* 1980–2015(62):247–254. <https://doi.org/10.1016/j.matdes.2014.05.028>
 12. Uematsu Y, Tokaji K, Tozaki Y, Kurita T, Murata S (2008) Effect of re-filling probe hole on tensile failure and fatigue behaviour of friction stir spot welded joints in Al–Mg–Si alloy. *Int J Fatigue* 30(10–11):1956–1966. <https://doi.org/10.1016/j.ijfatigue.2008.01.006>
 13. Singh K, Singh G, Singh H (2018) Review on friction stir welding of magnesium alloys. *J Magnesium Alloys* 6(4):399–416. Luo AA (2013) Magnesium casting technology for structural applications. *J Magnesium Alloys* 1(1):2–22. <https://doi.org/10.1016/j.jma.2018.06.001>
 14. Trojanová Z, Král R, Chatey A (2007) Deformation behaviour of an AJ50 magnesium alloy at elevated temperatures. *Mater Sci Eng A* 462(1–2):202–205. <https://doi.org/10.1016/j.msea.2005.12.108>
 15. Shen J, Min D, Wang D (2011) Effects of heating process on the microstructures and tensile properties of friction stir spot welded AZ31 magnesium alloy plates. *Mater Des* 32(10):5033–5037. <https://doi.org/10.1016/j.matdes.2011.05.046>
 16. Xu RZ, Ni DR, Yang Q, Liu CZ, Ma ZY (2015) Influencing mechanism of Zn interlayer addition on hook defects of friction stir spot welded Mg–Al–Zn alloy joints. *Mater Des* 69:163–169. <https://doi.org/10.1016/j.matdes.2014.12.045>
 17. Sanusi KO, Akinlabi ET, Muzenda E, Akinlabi SA (2015) Enhancement of corrosion resistance behaviour of frictional stir spot welding of copper. *Mater Today: Proc* 2(4–5):1157–1165. <https://doi.org/10.1016/j.matpr.2015.07.027>
 18. Lakshminarayanan AK, Annamalai VE, Elangovan K (2015) Identification of optimum friction stir spot welding process parameters controlling the properties of low carbon automotive steel joints. *J Mater Res Technol* 4(3):262–272. <https://doi.org/10.1016/j.jmrt.2015.01.001>
 19. Baek SW, Choi DH, Lee CY, Ahn BW, Yeon YM, Song K, Jung SB (2010) Microstructure and mechanical properties of friction stir spot welded galvanized steel. *Mater Trans* 51(5):1044–1050. <https://doi.org/10.2320/matertrans.M2009337>
 20. Sun YF, Fujii H, Takaki N, Okitsu Y (2013) Microstructure and mechanical properties of dissimilar Al alloy/steel joints prepared by a flat spot friction stir welding technique. *Mater Des* 47:350–357. <https://doi.org/10.1016/j.matdes.2012.12.007>
 21. Sun YF, Shen JM, Morisada Y, Fujii H (2014) Spot friction stir welding of low carbon steel plates preheated by high frequency induction. *Mater Des* 1980–2015(54):450–457. <https://doi.org/10.1016/j.matdes.2013.08.071>
 22. Lambiase F, Paoletti A, Di Ilio A (2015) Mechanical behaviour of friction stir spot welds of polycarbonate sheets. *Int J Adv Manuf Technol* 80(1–4):301–314. <https://doi.org/10.1007/s00170-015-7007-4>
 23. Arici A, Mert Ş (2008) Friction stir spot welding of polypropylene. *J Reinf Plast Compos* 27(18):2001–2004. <https://doi.org/10.1177/0731684408089134>
 24. Bilici MK (2012) Effect of tool geometry on friction stir spot welding of polypropylene sheets. *Express Polymer Lett* 6(10). <https://doi.org/10.3144/expresspolymlett.2012.86>
 25. <https://www.totalmateria.com/page.aspx?ID=CheckArticle&site=ktn&NM=152>
 26. Suhuddin UFH, Fischer V, Dos Santos JF (2013) The thermal cycle during the dissimilar friction spot welding of aluminum and magnesium alloy. *Scripta Mater* 68(1):87–90. <https://doi.org/10.1016/j.scriptamat.2012.09.008>
 27. Chowdhury SH, Chen DL, Bhole SD, Cao X, Wanjara P (2012) Lap shear strength and fatigue life of friction stir spot welded AZ31 magnesium and 5754 aluminum alloys. *Mater Sci Eng A* 556:500–509. <https://doi.org/10.1016/j.msea.2012.07.019>

28. Lee CY, Choi DH, Yeon YM, Jung SB (2009) Dissimilar friction stir spot welding of low carbon steel and Al–Mg alloy by formation of IMCs. *Sci Technol Weld Joining* 14(3):216–220. <https://doi.org/10.1179/136217109X400439>
29. Bozzi S, Helbert-Etter AL, Baudin T, Criqui B, Kerbiguet JG (2010) Intermetallic compounds in Al 6016/IF-steel friction stir spot welds. *Mater Sci Eng A* 527(16–17):4505–4509. <https://doi.org/10.1016/j.msea.2010.03.097>
30. Piccini JM, Svoboda HG (2015) Effect of pin length on friction stir spot welding (FSSW) of dissimilar aluminum-steel joints. *Procedia Mater Sci* 9:504–513. <https://doi.org/10.1016/j.mspro.2015.05.023>
31. Reilly A, Shercliff H, Chen Y, Prangnell P (2015) Modelling and visualisation of material flow in friction stir spot welding. *J Mater Process Technol* 225:473–484. <https://doi.org/10.1016/j.jmatprotec.2015.06.021>
32. Fereiduni E, Movahedi M, Kokabi AH (2015) Aluminum/steel joints made by an alternative friction stir spot welding process. *J Mater Process Technol* 224:1–10. <https://doi.org/10.1016/j.jmatprotec.2015.04.028>
33. Garg A, Bhattacharya A (2017) Strength and failure analysis of similar and dissimilar friction stir spot welds: influence of different tools and pin geometries. *Mater Des* 127:272–286. <https://doi.org/10.1016/j.matdes.2017.04.084>
34. Piccini JM, Svoboda HG (2017) Tool geometry optimization in friction stir spot welding of Al-steel joints. *J Manuf Processes* 26:142–154. <https://doi.org/10.1016/j.jmapro.2017.02.004>
35. Zhou L, Zhang RX, Li GH, Zhou WL, Huang YX, Song XG (2018) Effect of pin profile on microstructure and mechanical properties of friction stir spot welded Al-Cu dissimilar metals. *J Manuf Processes* 36:1–9. <https://doi.org/10.1016/j.jmapro.2018.09.017>
36. Ravi KK, Narayanan RG, Rana PK (2019) Friction stir spot welding of Al6082-T6/HDPE/Al6082-T6/HDPE/Al6082-T6 sandwich sheets: hook formation and lap shear test performance. *J Mater Res Technol* 8(1):615–622. <https://doi.org/10.1016/j.jmrt.2018.05.011>
37. Siddharth S, Senthilkumar T (2018) Development of friction stir spot welding windows for dissimilar Al5086/C10100 spot joints. *Mater Today: Proc* 5(2):6550–6559. <https://doi.org/10.1016/j.matpr.2017.11.310>
38. Rana PK, Narayanan RG, Kailas SV (2018) Effect of rotational speed on friction stir spot welding of AA5052-H32/HDPE/AA5052-H32 sandwich sheets. *J Mater Process Technol* 252:511–523. <https://doi.org/10.1016/j.jmatprotec.2017.10.016>

Mechanism-Driven Piezoelectric Energy Harvester



Rajat Nayal and Anshul Sharma

1 Introduction

The current world has begun to understand the importance of energy sources as the requirement of energy is increasing day by day. The non-renewable sources of energy like coal, petroleum, etc., are also depleting at a faster rate. Therefore, a need for alternate sources of energy has occurred which brings us to alternate sources of energy like solar, wind, tidal, nuclear, geothermal, etc. But these alternate solutions were also found over 20 years from now. As the technology is booming at a faster rate, a clean and renewable source of energy is requirement of the day with little or no waste of energy. But we all know that some sources of energy like vibration, sound, heat, electromagnetic waves, and low speed winds are wasted into environment as there is very few technologies to harvest energy from these types of sources and a very few type of smart materials like piezoelectric, pyroelectric, thermo-electrics, etc., can scavenge energy from these sources. However, the energy harvested from these sources is generally in micro- or nano-watts. The new technology is developing at the micro- and nano-level, so these sources are perfect for powering these type of low-power electronic devices, such as micro-electromechanical systems (MEMS), wireless sensor nodes (WSNs), and structural health monitoring (SHM) sensors [1]. If these devices or they can be used in some of the remote locations which do not sustain human existence. There are mainly three types of mechanisms of energy conversion system to convert mechanical to electrical energy: electromagnetic, electrostatic, and piezoelectric [1]. This paper presented the use of piezoelectric material as its energy conversion efficiency is higher and it is easy to use. Hroncova et al. [2] developed a functional model of centric crank-slider mechanism in ADAMS/View software. And the effect of different parameters like effect of geometry, speed of crank rotation, and

R. Nayal · A. Sharma (✉)

Department of Mechanical Engineering, National Institute of Technology, Uttarakhand, Srinagar (Garhwal) 246174, India

e-mail: anshul@nituk.ac.in

eccentricity of crank is evaluated in the simulations. The velocity and acceleration graphs at different parameters are compared [2]. Chandrakar and Soni (2015) crank-slider mechanism simulation model is developed using the design software MSC ADAMS/View. Joint reactions and power consumptions at different crank speeds and crank lengths are simulated. Lower speeds and shorter crank lengths give less contact forces and lesser power consumption [3].

Many mechanisms have been developed to harvest different sources of energy with the assistance of piezoelectric materials. Viet et al. developed a floating energy harvester which harvests energy from intermediate and deep sea water waves. It works at d_{33} mode and generates a power of 103 W at an amplitude of 2 m wave [4]. Xie and Wang [5] developed a dual-mass piezoelectric bar harvester for harvesting energy from ambient vibrations of a vehicle suspension system. It works on d_{33} mode and generates 738 W of power with dimensions of piezoelectric bar being 0.015 m and 0.1 m (W \times H) [5]. Acciari et al. (2018) experimentally compared different rain-fall harvesting devices, namely: the cantilever, the bridge, and the floating circle; and also compared different rectifying circuits. The best harvesting structure is the cantilever, one and best performance is for full-bridge rectifying circuit system [6]. Wu et al. developed a piezoelectric energy harvester for rotational mechanisms working on non-contact magnetic force excitation of cantilever piezoelectric beam. The maximum power produced was found to be 1.28 mW at resonance [7].

Liu et al. [8] developed a micro-cantilever system which consists of one piezoelectric patch for air flow sensing and others for powering the system. Output voltage and power at the load resistance of 100 k Ω were measured to be 18.1 mV and 3.3 nW at flow velocity of 15.6 m/s [8]. Xie et al. [9] developed a model which generates electricity with the help of pyroelectric material. The assembly consists of a fan, a gear mechanism, and a crank-slider mechanism. A comparison between the charging times of 100 nF capacitor is done for different wind speeds. The slowest speed gave the best result [9]. Tao et al. [10] developed a mechanism consisting of a fan, driven by wind energy, and a Scotch-yoke mechanism. The fan drives the Scotch-yoke mechanism which in turn strikes the cantilever beams. A power up to 150 W can be harvested at the wind speed of 7.2 m/s, at an angular velocity of 50 rad/s [10]. Zhang et al. [11] compared two models of piezoelectric energy harvesters, one has a single cantilever and other has three cantilevers attached to the circular periphery of a casing. A maximum rms voltage of 160.2 V and a maximum power of 2566.4 μ W were found at the wind speed of 14 m/s in second model [11]. Heinonen et al. [12] proposed a model which consists of a small fan with permanent magnets embedded and a piezoelectric beam with a magnetic proof mass which interacts with the permanent magnets of fan to convert wind power into vibrational motion. It also works at a low cut in speeds of 0.9 m/s. From experiments, a power density of 2 mW/cm³ at 3.8 V was achieved [12].

This paper presents a simulation study of a piezoelectric energy harvesting mechanism which operates at low wind speeds. The mechanism is developed in CATIA V6.0, and the velocity and acceleration simulations are carried out in SolidWorks software. The accelerations are validated by the analytical formulas. The mechanism consists of an aerodynamic fan that converts the wind energy into rotational motion

of shaft and the shaft operates a crank-slider mechanism. The slider of this mechanism reciprocates in a predefined straight path. At the terminating point of path of slider, a cantilever beam is fixed with the frame. The beam consists of a piezoelectric patch toward the fixed end, and the slider hits the beam at free end. When the slider hits the beam, the beam vibrates which in turn activates d_{31} mode of piezoelectric material, and hence, a voltage is generated. For the angular speed range of $2\pi-6\pi$ rad/s, the maximum open circuit voltage obtained is 0.733 V.

2 Modeling and Design

The model was created and assembled in CATIA V6.0, and simulations of velocity and accelerations were performed on SolidWorks software. The numerical model of harvester mechanism is illustrated in Fig. 1.

2.1 Kinematic Analysis of Mechanism

The kinematic analysis (velocity and acceleration analysis) of crank-slider mechanism is carried out on SolidWorks platform. The velocity and acceleration response for an angular velocity of 2π rad/s are shown in Fig. 2.

2.2 Analytical Analysis of Slider of Mechanism

The acceleration of slider of mechanism was validated with the help of analytical formulas [2, 13] with respect to the simulation results obtained from SolidWorks.

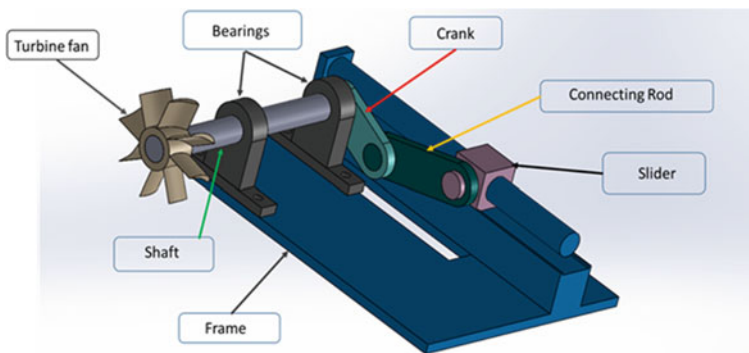


Fig. 1 Schematics of SolidWorks model of energy harvester mechanism model

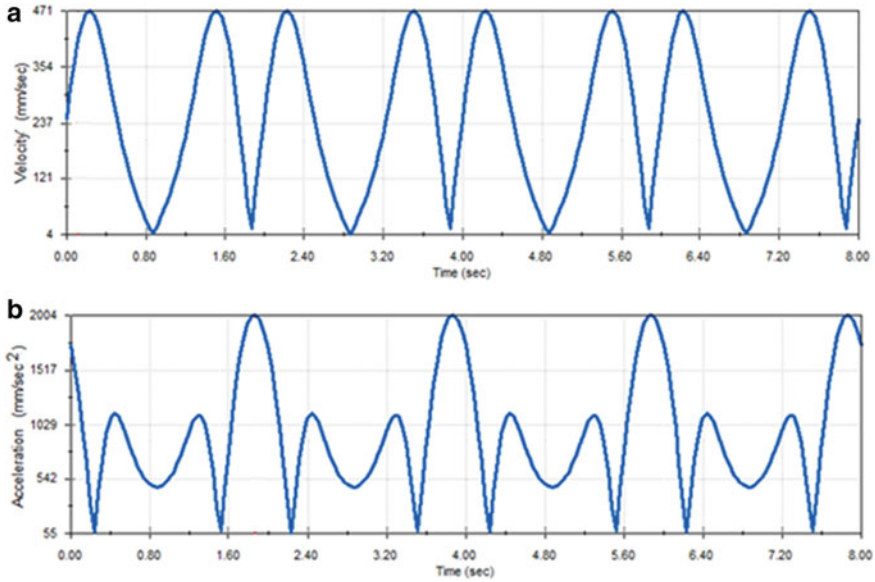


Fig. 2 Kinematic analysis of mechanism **a** velocity versus time graph of slider and **b** acceleration versus time graph of slider

The distance between crankshaft and slider may be represented as

$$x = r \left[1 - \cos \theta + (n - \sqrt{n^2 - \sin^2 \theta}) \right] \tag{1}$$

where n is the ratio of crank length to connecting rod. All the parameters are shown in Fig. 3.

The acceleration of the slider under the application of crank rotation can be calculated as

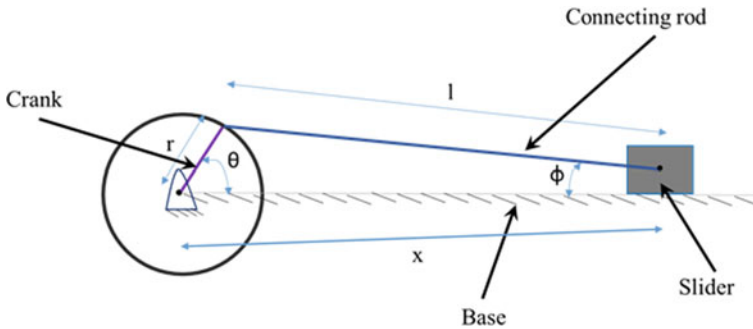


Fig. 3 Schematics of basic crank-slider mechanism

$$\ddot{x} = -r\omega^2 \left[\cos \theta + \frac{n^2 \cos 2\theta + \sin^4 \theta}{(n^2 - \sin^2 \theta)^{\frac{3}{2}}} \right] \tag{2}$$

For $\theta = 0^\circ$, slider will be at the farthest position from crank and will hit the piezoelectric beam. The slider will also have the maximum acceleration at that time and has maximum force which is required for the mechanism.

The force exerted by the slider corresponding to the different rpms of crank is shown in Fig. 4 and given in Table 1. It is to note that the parameters used to calculate the mass of the slider are volume of the slider (15.625 cm³), density of the slider material (2.68 g/cm³), and elastic modulus of the slider (70 GPa).

Fig. 4 Force of slider versus angular velocity of crank shaft of the mechanism

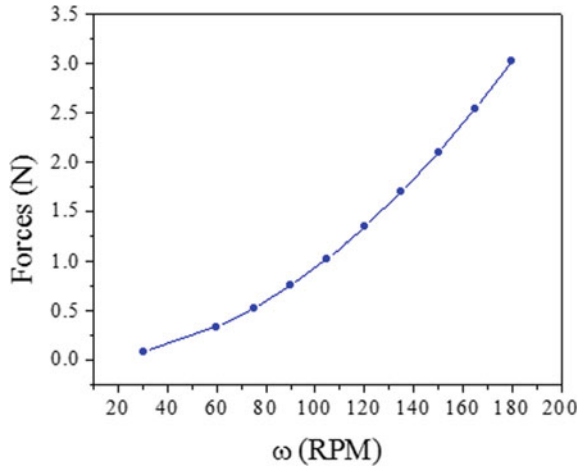


Table 1 Comparison of analytical and simulation values of slider acceleration

ω (rad/s)	ω (rpm)	Acceleration (simulation) (mm/s ²)	Acceleration (analytical) (mm/s ²)	Error (%)
2π	60	8010.22	8016	0.0721
2.5π	75	12,517.79	12,525	0.0575
3π	90	18,024.99	18,036	0.061
3.5π	105	24,537.68	24,549	0.0461
4π	120	32,050.34	32,064	0.0426
4.5π	135	40,559.16	40,581	0.0538
5π	150	50,081.01	50,100	0.0379
5.5π	165	60,598.81	60,621	0.0366
6π	180	72,111.390	72,144	0.0452

3 Finite Element Modeling of Energy Harvester

The piezoelectric energy harvester is modeled in ANSYS Workbench 19.0 using piezo and MEMS extension. The beam was first simulated in modal analysis for the investigation of mode shapes of beam, and then, the harmonic analysis was done on it. After that, the beam is simulated for open circuit voltage generation using piezo and MEMS extension.

The constitutive equation used in the modeling is

$$\begin{Bmatrix} T \\ D \end{Bmatrix} = \begin{bmatrix} c & -e \\ e & \varepsilon \end{bmatrix} \begin{Bmatrix} S_p \\ E \end{Bmatrix} \tag{3}$$

If some force is acted on piezoelectric material, then there will be some charge generation on the surface, and also for some stiffness and damping of material, there can be an equation of motion for the piezoelectric material subjected to external force. The equation of motion is as follows,

$$[M_{uu}]\ddot{r} + [C_{uu}]\dot{r} + [K_{uu}]r + [K_{u\varphi}]\varphi = \{F_{Extn.}\} \tag{4}$$

$$[K_{\varphi u}]r + [K_{\varphi\varphi}]\varphi = \{Q\} \tag{5}$$

where $[M_{uu}]$ is mass matrix, $[K_{uu}]$ is elastic stiffness matrix, $[K_{u\varphi}]$ is elastic-electric coupling matrix for piezoelectric layer, and $[K_{\varphi\varphi}]$ is electrical stiffness matrix.

The open circuit sensor voltage may be predicted using Eq. (5) assuming that there is no external charge applied.

$$\varphi = [K_{\varphi\varphi}]^{-1}[K_{\varphi u}]r \tag{6}$$

3.1 Geometric and Material Properties of Beam

The beam was modeled in the ANSYS Workbench 19.0 with the material of beam being aluminum and the piezoelectric material being PZT-5H. The geometric properties of beam and piezoelectric material are given in Table 2.

Table 2 Geometric properties of beam and piezoelectric patch

Properties	Beam	Piezoelectric layer
Length (mm)	285	25
Width (mm)	25	25
Thickness (mm)	3	2

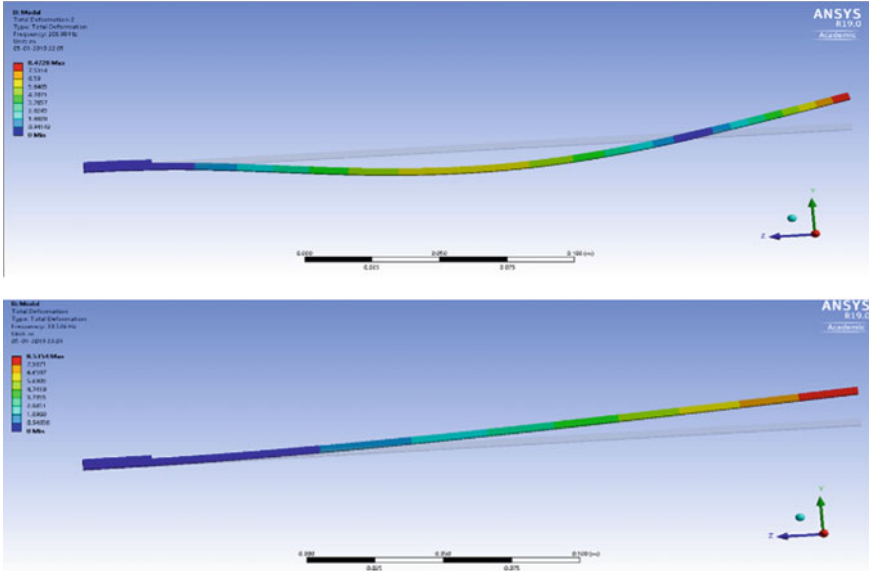


Fig. 5 Mode shapes of beam corresponding to a first and b second natural frequency

4 Results and Discussion

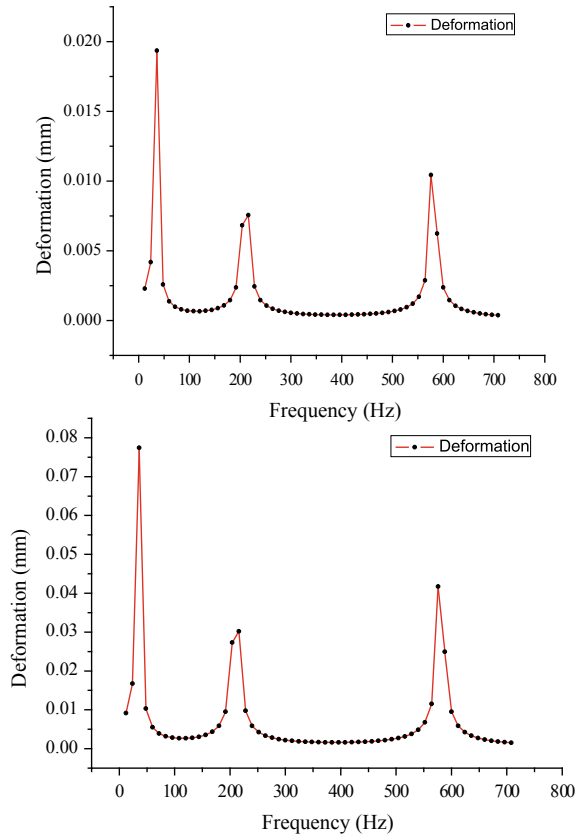
4.1 Modal Analysis

In the modal analysis, the material assignment was done for the geometries. The initial boundary condition of fixing one end was also provided. A fine mesh refinement with mesh size of 1 mm was given to the model with high smoothing. The mesh element was taken by default as quadrilateral element. The modal analysis is done to obtain the different resonance frequencies of the structure. The mode shapes also define the structure patterns during the activation of different harmonics/modes of frequency. The first two mode shapes obtained for the piezoelectric beam is shown in Fig. 5.

4.2 Harmonic Response Analysis

In the harmonic analysis, frequency range of 0–700 Hz is taken with solution interval of 50. The beam is fixed from the end toward which piezoelectric patch is applied, and a force of range from 0.336 to 3.030 N is applied at the free end for a speed range of 2π – 6π rad/s. The harmonic analysis gives the results in the form of maximum deformation of the free end of piezoelectric material corresponding to different frequencies. The deformation will be highest corresponding to the modal or resonating

Fig. 6 Frequency response of piezoelectric material at **a** 3π rad/s and **b** 6π rad/s

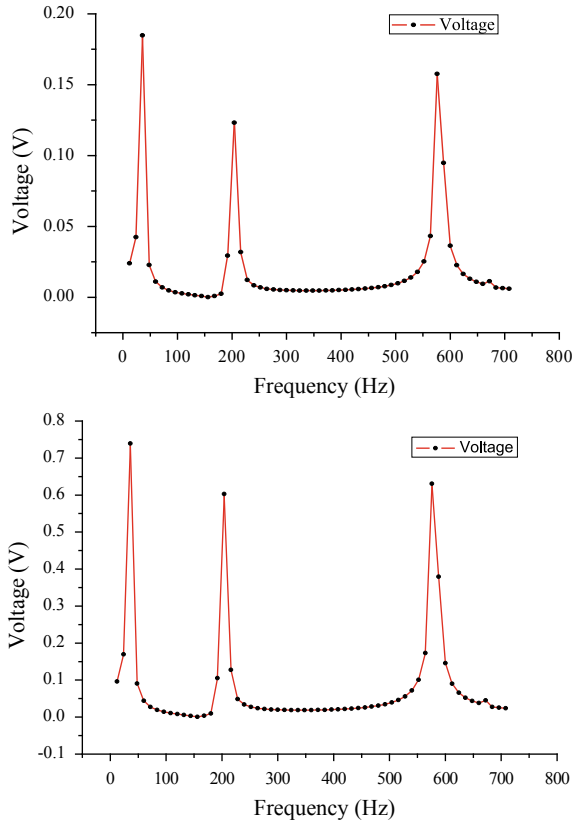


frequencies. As the load at free end activates bending mode only, therefore, maximum deformation is obtained corresponding to first, second, and fourth mode frequencies. With the help of piezo and MEMS extension, the voltage is produced corresponding to harmonic analysis. The bottom face of piezo layer is taken as ground or at zero potential to get the maximum voltage from the piezoelectric. Figure 6 presents the deformation at different frequencies corresponding to 3π and 6π rad/s angular speeds.

4.3 Open Circuit Voltage

The forces used for voltage and power investigation are converged to few values because of bulkiness and vast data range. The voltage and power are studied only for 3π and 6π rad/s angular speeds of crank shaft. The range of force is from 0.7575 to 3.030 N for the system. Figure 7 shows the variation of open circuit voltages for this force range.

Fig. 7 Open circuit voltage versus frequency at **a** 0.7575 N and **b** 3.030 N



The maximum open circuit voltages obtained are 0.1848, 0.328, 0.513, and 0.739 V for 3π , 4π , 5π , and 6π rad/s, respectively, for 36 Hz frequency.

5 Conclusion

An energy-harvesting mechanism model scavenging wind energy is simulated and analyzed using ANSYS 19.0. The mechanism has a crank-slider mechanism to convert wind energy into vibrational energy, and this mechanism produces a maximum force of 3.030 N at the maximum angular velocity of 6π rad/s of shaft rotating crank. The mechanism was modeled in SolidWorks, and the accelerations were compared with the analytical accelerations. Then, the cantilever beam and piezoelectric patch was modeled in ANSYS 19.0 in which the modal and harmonic analysis are done on the beam. The maximum open circuit voltage obtained is 0.739 V at the frequency of 36 Hz at a force of 3.030 N. If the increase in mechanical force, the output voltage also increases.

References

1. Batra AK, Alomari A (2017) Power harvesting via smart materials. SPIE Press, pp 1–15
2. Hroncova D, Binda M, Sarga P, Kicak F (2012) Kinematical analysis of crank slider mechanism using MSC Adams/View. *Procedia Eng* 48:213–222
3. Chandrakar B, Soni MM (2015) Design and optimization of slider and crank mechanism with multibody systems. *Int J Scie Researc* 2319–7064
4. Viet NV, Xie XD, Liew KM, Banthia N, Wang Q (2016) Energy harvesting from ocean waves by a floating energy harvester. *Energy* 112:1219–1226
5. Xie XD, Wang Q (2015) Energy harvesting from a vehicle suspension system. *Energy* 86:385–392
6. Acciari G, Caruso M, Fricano M, Imburgia A, Miceli R, Romano P, Viola F (2018) Experimental investigation on different rainfall energy harvesting structures. Thirteenth International Conference on Ecological Vehicles and Renewable Energies (EVER), pp 1–5
7. Wu WH, Kuo KC, Lin YH, Tsai YC (2018) Non-contact magnetic cantilever-type piezoelectric energy harvester for rotational mechanism. *Microelectron Eng* 191:16–19
8. Liu H, Zhang S, Kathiresan R, Kobayashi T, Lee C (2012) Development of piezoelectric microcantilever flow sensor with wind-driven energy harvesting capability. *Appl Phys Lett* 100:223905
9. Xie M, Zabek D, Bowen C, Abdelmageed M, Arafa M (2016) Wind-driven pyroelectric energy harvesting device. *Smart Mater Struct* 25:125023
10. Tao JX, Viet NV, Carpinteri A, Wang Q (2017) Energy harvesting from wind by a piezoelectric harvester. *Eng Struct* 133:74–80
11. Zhang J, Fang Z, Shu C, Zhang J, Zhang Q, Li C (2017) A rotational piezoelectric energy harvester for efficient wind energy harvesting. *Sens Actuators A* 262:123–129
12. Heinonen E, Juuti J, Leppavuori S (2005) Characterization and modelling of 3D piezoelectric ceramic structures with ATILA software. *J Eur Ceram* 25:2467–2470
13. Erturk A, Inman DJ (2009) An experimentally validated bimorph cantilever model for piezoelectric energy harvesting from base excitations. *Smart Mater Struct* 18:025009

Stabilizing x - y Inverted Pendulum via Variable Structure Control



Satyendra Kumar and Moina Ajmeri

1 Introduction

Inverted pendulum systems are nonlinear and unstable systems which are used in engineering laboratories to validate various new research ideas. The inverted pendulum is a system having nonlinear dynamics, unstable characteristics and under-actuated mechanics [1]. Hence, the inverted pendulum is known as an important problem which is widely used in control engineering [2–5]. The system of the inverted pendulum is used as a basic tool to overcome the various challenges in the control system. The inverted pendulum control may be studied in three cases. The first case deals with the swinging of shaft of the pendulum, which swings until the position achieves region of stabilization [6, 7]. The second case is inverted pendulum stabilization in the upward direction [8, 9]. The third case corresponds to maintain the position of pendulum such that it may follow a certain path [10, 11]. Generally, control literature refers to an inverted pendulum having a single degree of freedom [7, 12].

On the other hand, some of the researches deal with several degrees of freedom [10, 11]. Various PID controllers have been proposed previously to balance and to track the pendulum [1, 13–15]. Bugeja [1] stabilize swing-up control for an inverted pendulum system. Very few works have used variable structure control design for the stabilization of inverted pendulums [16].

In this paper, it has designed a VSC to ensure the robustness of the system and better responses if there are external disturbances or parameter variation of the system. Since it needs to set optimal values of the parameters of controllers during the controller design, there are various methods such as analytical method and nature-inspired optimization techniques. Most commonly known optimization techniques are particle swarm optimization technique, ant colony optimization technique, whale

S. Kumar (✉) · M. Ajmeri
Electrical Engineering Department, National Institute of Technology Patna, Patna 800005, India
e-mail: satyendra.ee17@nitp.ac.in

optimization algorithm, etc. The nature-inspired optimization techniques have some advantages over the conventional techniques which are as follows: (i) they can bypass local optima;

(ii) they may be implemented for a wide range of problems in engineering and other disciplines as well [17].

In this paper, a recently reported optimization technique, known as ‘whale optimization algorithm (WOA)’, is used to obtain the optimal values of the controller parameters. Further, it needs objective function and performance index in the MATLAB code of the optimization. Here, it used integral time absolute error (ITAE) as a performance index.

2 Mathematical Model of an x - y Inverted Pendulum

The x - y inverted pendulum system with control forces (F_x and F_y) is shown in Fig. 1. The pendulum is fitted on a pivot, and the controlling mechanism of the pendulum is based on the two horizontal control forces acting on the pivot.

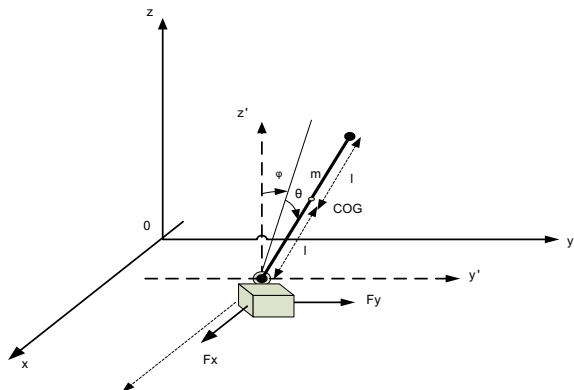
Total energy (i.e. kinetic energy and potential energy as a whole) of the pendulum is given by

$$K = \frac{1}{2}M(\dot{x}^2 + \dot{y}^2) + \frac{1}{2}m(\dot{x}_p^2 + \dot{y}_p^2 + \dot{z}_p^2), \quad P = mgz_p \tag{1}$$

where $x_p = x + l \sin \theta$, $y_p = y + l \cos \theta \sin \varphi$ and $z_p = z + l \cos \theta \cos \varphi$.

The x - y inverted pendulum dynamic model as given by Lagrange’s approach is as follows [13]:

Fig. 1 x - y inverted pendulum



$$\begin{cases} (M + m)\ddot{x} - ml\dot{\theta}^2 \sin \theta + ml\ddot{\theta} \cos \theta = F_x, \\ (M + m)\ddot{y} + ml\ddot{\theta} \cos \theta \cos \varphi - 2ml\dot{\varphi}\dot{\theta} \sin \theta \cos \varphi \\ - ml\ddot{\theta} \sin \theta \sin \varphi - ml \cos \theta \sin \varphi (\dot{\varphi}^2 + \dot{\theta}) = F_y, \\ \dot{\theta}l^2 + \ddot{x} \cos \theta + \ddot{y} \sin \theta \sin \varphi - l\dot{\varphi}^2 \cos \theta \sin \theta - g \sin \theta \cos \varphi = 0, \\ \ddot{y} \cos \varphi + l\ddot{\varphi} \cos \theta - g \sin \varphi = 0 \end{cases} \quad (2)$$

The state-space form of the above equations may be expressed as

$$\begin{cases} \dot{x}_1 = x_2 \\ \dot{x}_2 = \frac{F_1}{M^2 + Mm \sin^2 x_5 \cos^2 x_7 + Mm \sin x_7} + d_1 \\ \dot{x}_3 = x_4 \\ \dot{x}_4 = \frac{F_2}{M^2 + Mm \sin^2 x_5 \cos^2 x_7 + Mm \sin x_7} + d_2 \\ \dot{x}_5 = x_6 \\ \dot{x}_6 = \frac{F_3}{(M^2 + Mm \sin^2 x_5 \cos^2 x_7 + Mm \sin x_7)l} + d_3 \\ \dot{x}_7 = x_8 \\ \dot{x}_8 = \frac{F_4}{(M^2 + Mm \sin^2 x_5 \cos^2 x_7 + Mm \sin x_7)l \cos x_5} + d_4 \end{cases} \quad (3)$$

where

$$\begin{aligned} x_1 = x, x_2 = \dot{x}, x_3 = y, x_4 = \dot{y}, x_5 = \theta, x_6 = \dot{\theta}, x_7 = \varphi, x_8 = \dot{\varphi}, \\ F_1 = Mml \sin x_5 x_6^2 + Mml \cos^2 x_5 \sin x_5 x_8^2 - Mmg \cos^2 x_5 \sin x_5 \cos^2 x_7 \\ + m \cos^2 x_5 \sin^2 x_7 F_x + MF_x - m \cos^2 x_5 \sin x_5 \sin x_7 F_y, \\ F_2 = (M + m)F_y - m \cos^2 x_5 F_y + m \sin x_5 \cos x_5 \sin x_7 F_x \\ - Mmg \cos^2 x_5 \sin x_7 \cos x_7 \\ + Mml \cos^3 x_5 \sin x_7 x_8^2 - Mml \cos x_5 \sin x_7 x_6^2, \\ F_3 = m \cos x_5 \cos^2 x_7 F_x - (M + m) \cos x_5 F_x \\ + (M + m) \sin x_5 \sin x_7 F_y + M(m + M)g \sin x_5 \cos x_7 \\ - Mml \sin x_5 \cos x_5 \cos^2 x_7 x_6^2 - M(m + M)l \cos x_5 \sin x_7 x_8^2, \\ F_4 = -m \sin^2 x_5 \cos x_7 F_y - M \cos x_7 F_y + m \sin x_5 \cos x_5 \sin x_7 \cos x_7 F_x \\ + 2Mml \sin x_5 x_6 x_8 + M(m + M)g \sin x_7 + 2M^2 l \sin x_5 x_6 x_8 \\ - 2Mml \sin x_5 \cos^2 x_5 \cos^2 x_7 x_6 x_8 \\ - Mml \cos^3 x_5 \sin x_7 \cos x_7 x_8^2 - Mml \cos x_5 \sin x_7 \cos x_7 x_6^2 \end{aligned}$$

and d_1, d_2, d_3, d_4 are outer disturbances.

In the above equations, F_x and F_y are the control forces in x -direction and y -direction. These forces act on the pendulum to balance it in an upright direction. The l is pendulum length from the centre of gravity (COG), θ is the pendulum angle measured in the x -axis, φ is pendulum angle measured in the y -axis, m is pendulum

Table 1 Various pendulum constants

M (kg)	m (kg)	l (m)	g (m/s ²)
1	0.1	0.3	9.81

mass (assumed at COG) and M is cart mass which can move in both x -direction and y -direction. Values of pendulum constants are given in Table 1.

3 Whale Optimization Algorithm

There are various optimization techniques available to solve the complex engineering problem or to find optimal solutions. The ‘whale optimization algorithm’ is used here, which is a nature-inspired optimization technique. The optimization technique has been applied for various benchmark functions, which is found better compared to other similar method.

The algorithm is based on the prey search behaviour of the humpback whale [17]. The humpback whales hunt for their prey near the surface. They create a bubble net with the 9-shaped path. It has two phases:

- (1) *Exploitation phase* includes encircling a prey
- (2) *Exploration phase*, a random search of prey.

3.1 Exploitation Phase

To update a solution, the following equations are used which are the mathematical model of the movement of the whale for searching prey.

$$\vec{D} = \left| \vec{C} \cdot \vec{X}^*(t) - \vec{X}(t) \right| \tag{4}$$

$$\vec{X}(t + 1) = \vec{X}^*(t) - \vec{A} \cdot \vec{D} \tag{5}$$

where ‘ t ’ represents the current iteration, X^* and X represent the best solution and current solution, A and C represent coefficient vectors which may be obtained as follows:

$$\vec{A} = 2\vec{a} \cdot \vec{r} - \vec{a} \tag{6}$$

$$\vec{C} = 2 \cdot \vec{r} \tag{7}$$

where $a \in [0, 2]$, which linearly reduced to 0 starting from 2, and ‘ r ’ represents a random vector ($r \in [0, 1]$).

The values of ‘a’ may be decreased according to Eq. (8).

$$a = 2 - t \frac{2}{\text{MaxIter}} \tag{8}$$

where ‘MaxIter’ represents the maximum number of iterations. In this work, ‘MaxIter’ taken to be 30 and the population size is 12. Now an equation in the form of the spiral is created in between the best solution and current solution (to create a spiral path by the whale) which is as follows:

$$\vec{X}(t + 1) = \vec{D}' \cdot e^{bl} \cdot \cos(2\pi l) = \vec{X}^*(t) \tag{9}$$

where \vec{D}' represents the distance between a whale X and prey ($\vec{D} = |\vec{X}^*(t) - \vec{X}(t)|$), b is the spiral and ‘l’ ($l \in [-1, 1]$) is a random number. For modelling the shrinking mechanism and spiral path, 50% probability is assumed to choose between them as the following equation.

$$\vec{X}(t + 1) = \begin{cases} \text{ShrinkingEncircling(Eq. 5)} & \text{if}(p < 0.5) \\ \text{spiral_shapedpath(Eq. 9)} & \text{if}(p \geq 0.5) \end{cases} \tag{10}$$

where p ($p \in [0, 1]$) is the random number.

3.2 Exploration Phase

In this case, for updating the position, a randomly chosen solution is used. Here, a vector ‘A’ ($A \in [-1, 1]$) is taken such that the solution may remain away from best value of search agent. This mechanism may be modelled as follows:

$$\vec{D} = |\vec{C} \cdot \vec{X}_{\text{rand}} - \vec{X}| \tag{11}$$

$$\vec{X}(t + 1) = \vec{X}_{\text{rand}} - \vec{A} \cdot \vec{D} \tag{12}$$

where \vec{X}_{rand} represents a whale chosen randomly from the current population.

The optimal values of the parameters ($k_i, k_p, \lambda_1, \lambda_2$ and k_e) of the VSC system are obtained using a performance index known as ITAE which is given as follows:

$$\text{ITAE} = \int_0^{\infty} t|e(t)|dt \tag{13}$$

4 Variable Structure Controller Design for the Inverted Pendulum

The inverted pendulum is an unstable and nonlinear system. A modified variable structure control-based controller is designed, as shown in Fig. 2. The proposed VSC system is the modified VSC that is given in Ablay [9]. In the VSC system, it is generally defined as a sliding surface which is responsible for the desired behaviour of the system.

Further, a control equation is formed which derives the error trajectories of the system on this surface and keeps these trajectories on the surface.

The switching (sliding) surface defined here is as follows

$$\sigma = \lambda_1 e + \lambda_2 \dot{e} \tag{14}$$

where $e = r - y$ is tracking error with $y(t)$ and $r(t)$ are system output and set point, respectively, and $\lambda_1 (> 0)$, λ_2 are tuning parameter. In this paper, a new VSC is designed as follows:

$$\begin{cases} u = -y + k_p |\sigma|^{1/2} \text{sat}(\sigma) + u_1 + k_e e \\ \text{where } \dot{u}_1 = k_i |\sigma|^{1/2} \text{sat}(\sigma) \end{cases} \tag{15}$$

where k_p, k_e are proportional gains, k_i is the integral gain, $|u_1| \leq c_3$ for some $c_3 > 0$ and σ is the switching surface and $\text{sat}(\cdot)$ is the saturation function defined by

$$\text{sat}(\sigma) = \begin{cases} \sigma/|\sigma| \text{ or } \text{sgn}(\sigma), & \text{if } |\sigma| \geq 1 \\ \sigma & \text{if } |\sigma| < 1 \end{cases} \tag{16}$$

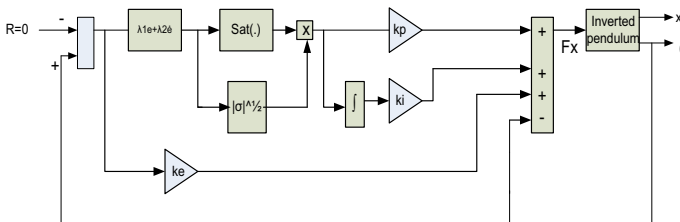


Fig. 2 VSC controller design for x inverted pendulum for angle control

5 Control of x - y Inverted Pendulum Using VSC with a PID Controller and Simulation Results

The VSC with PID control structure for x - y inverted pendulum is shown in Fig. 3. To control the position of the pivot, the parameters of the PID controller are $k_p = 25$, $k_i = 15$ and $k_d = 3$ [13]. Furthermore, the parameters of the VSC controllers are given below.

For VSC1, $k_p = -3.2$, $k_i = -0.03$, $k_e = -0.01$, $\lambda_1 = 2.0$, $\lambda_2 = 1.0$

and for VSC2, $k_p = -3.5$, $k_i = -0.01$, $k_e = -0.01$, $\lambda_1 = 2.0$, $\lambda_2 = 1.0$

5.1 x - y Inverted Pendulum Without Disturbance

MATLAB simulation is carried out for the pendulum model (as given in Eq. (3)) to control the pendulum angle and position without considering the disturbances ($d_1 = d_2 = d_3 = d_4 = 0$). Angle (i.e. θ and φ) responses of the system (pendulum) in the presence of the proposed VSC system given by Wang [13] are shown in Fig. 4. Figure 5 illustrates the pendulum cart position using the proposed method and the PID controller. From Figs. 4 and 5, it is observed that the proposed VSC controller has acceptable responses to maintain the pendulum cart position, and it has a faster response compared to Wang [13].

Figure 6 shows the control force F_x and F_y for both VSC and PID (proposed by Wang) controllers. These forces are used to balance the inverted pendulum at the centre of the x - and y -axis.

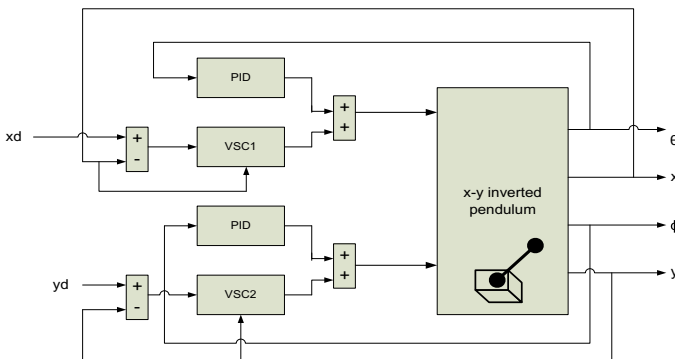


Fig. 3 Two VSC with PID controller design

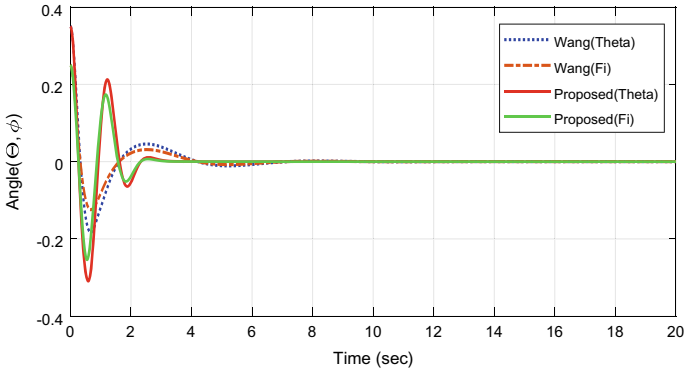


Fig. 4 Angles of the x - y inverted pendulum

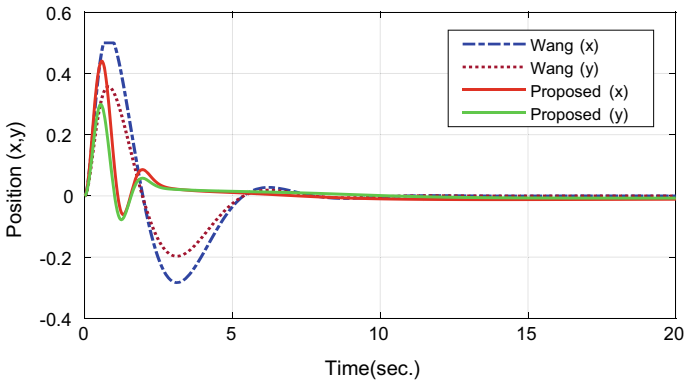


Fig. 5 Position of x - y inverted pendulum

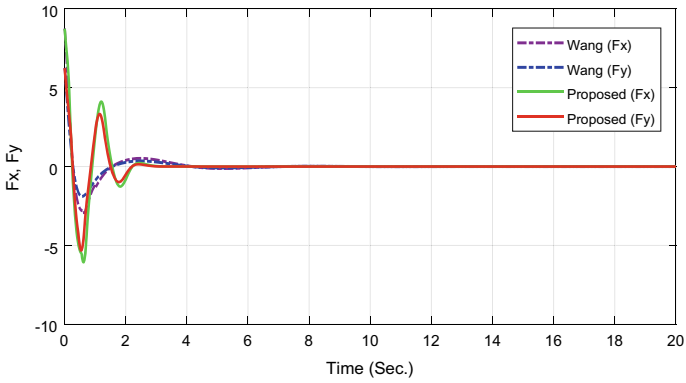


Fig. 6 Control signal of an x - y inverted pendulum

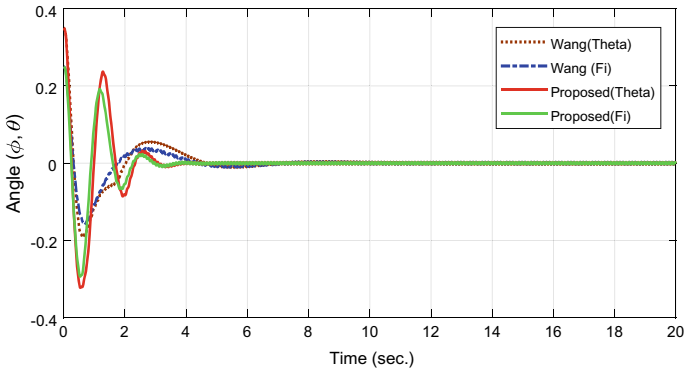


Fig. 7 Angle of an x - y inverted pendulum

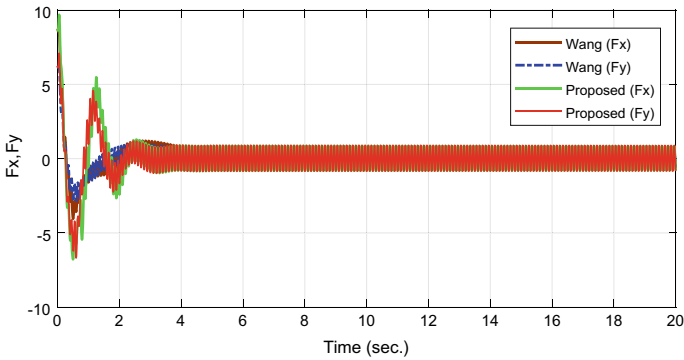


Fig. 8 Control signal of an x - y inverted pendulum

5.2 x - y Inverted Pendulum with Disturbance

Now the outer disturbance (Eq. 3) of magnitude $d_1 = d_2 = d_3 = d_4 = 20 \sin(20\pi t)$ is taken. Angle (i.e. θ and φ) responses of the system (pendulum) in the presence of the proposed VSC system are shown in Fig. 7. From the figure, it is noticed that the proposed controller gives faster and acceptable response compared to that proposed by Wang. Figure 8 shows the control signal of x - y IP by both the controllers, and it is observed that the VSC controller response is acceptable.

6 Conclusions

In this work, a variable structure control (VSC) is proposed, and MATLAB simulation is carried out using a mathematical model of the pendulum to stabilize it.

The parameters of the proposed VSC system are obtained using the whale optimization algorithm. From the simulation response, it is observed that the proposed VSC system gives improved performance to stabilize the x - y inverted pendulum in terms of settling time. The proposed controller is robust to outer disturbances also.

References

1. Bugeja M (2003) Non-Linear Swing-up and stabilizing control of an inverted pendulum system. In: The IEEE Region 8 European Conference, Computer as a Tool, Ljubljana, Slovenia, pp 437–441
2. Astrom KJ, Furuta K (2000) Swinging up a pendulum by energy control. *Automatica* 36:287–295
3. Hemalatha B, Kanchana A (2017) Stability control of inverted pendulum based on fractional order PID controller. *Int J Adv Res Educ Technol (IJARET)* 4(2):170–175
4. Chalupa P, Bobal V (2014) Modelling and predictive control of inverted pendulum. In: Proceedings 22nd European conference on modelling and simulation (ECMS), ISBN: 978-0-9553018-5-8
5. Wang Y, Ruan X (2010) The modelling and control of flywheel inverted pendulum system. In: 3rd international conference on computer science and information technology, IEEE, pp 423–427
6. Tao CW, Taur JS, Hsieh TW, Tsai CL (2008) Design of a fuzzy controller with fuzzy swing-up and parallel distributed pole assignment schemes for an inverted pendulum and cart system. *IEEE Trans Control Syst Technol* 16(6):1277–1288
7. Glück T, Eder A, Kugi A (2013) Swing-up control of a triple pendulum on a cart with experimental validation. *Automatica*. 49:801–808
8. Yi J, Yubazaki N (2000) Stabilization fuzzy control of inverted pendulum systems. *Artif Intell Eng* 14:153–163
9. Ablay G (2015) Variable structure controllers for unstable processes. *J Process Control* 32:10–15
10. Wai R, Chang L (2006) Adaptive stabilizing and tracking control for a nonlinear inverted-pendulum system via sliding mode control technique. *IEEE Trans Ind Electron* 53:674–692
11. Chang L, Lee A (2007) Design of nonlinear controller for bi-axial inverted pendulum system. *Inst Eng Technol (IET) Control Theory Appl* 1(4):979–986
12. Taylor P, Liu G, Neši D, Mareels I, Liu G, Nes D (2008) Non-linear stable inversion-based output tracking control for a spherical inverted pendulum. *Int J Control* 81(1):116–133
13. Wang JJ (2011) Simulation studies of the inverted pendulum based on PID controllers. *Simul Modell Practice Theory*. 19:440–449
14. Mason P, Broucke M, Piccoli B (2008) Time-optimal swing-up of the planar pendulum. *IEEE Trans Autom Control* 53(8):1876–1886
15. Bai Y, Chen Z, Ruan X (2017) Complex trajectory tracking of inverted pendulum using PID and LQR. In: International conference on manufacturing science and information engineering (ICMSIE), pp 516–524
16. Huang J, Guan Z, Matsuno T (2010) Sliding-mode velocity control of mobile-wheeled inverted-pendulum systems. *IEEE Trans Robot* 26(4):750–758
17. Mirjalili S, Lewis A (2016) The whale optimization algorithm. *Adv Eng Software* 9551–9567

Selection of Process Parameters and Their Machine Levels for Electro-discharge Face Grinding of D2 Steel



Akshat Srivastava Kulshrestha, Ashok Kumar Dargar,
and Deepak Rajendra Unune

1 Introduction

In today's modern industries, advanced engineering materials are considered as the backbone for their continuous and remarkable development. These advanced engineering materials, such as superalloys, hard steels, iron-nickel, cobalt-based alloys and carbides, shows a good resistance to elevated temperature, chemical degradation and wear [1]. Moreover, machining of these advanced materials is a great challenge with conventional machining processes due to involving of higher machining cost and less precision due to strength limitation of tool materials. Hence, to resolve the machining of these advanced materials, unconventional machining methods have been developed with its own potential and barrier. For giving complex geometrical shapes to these materials with high precision, electrical discharge machining (EDM) is widely in demand [2]. EDM machining of material takes place due to continuous sparking that occur between tools electrode and workpiece and that makes the unwanted material to melts and vaporize [3]. Grinding-EDM which is also called electro-discharge grinding (EDG) the principle of material removal is same like in EDM. In EDG, an conductive disk rotary tool electrode is involved not like the stationary tool electrode used in EDM [4]. Therefore, with the help of rotary motion by tool electrode, the molten material and debris formed during the machining are efficiently flushed from machining, zone avoiding debris buildup.

EDG can be operated in three different configurations.

- (i) Electro-discharge face grinding (EDFG),

A. S. Kulshrestha · A. K. Dargar (✉) · D. R. Unune
Department of Mechanical-Mechatronics Engineering, The LNM Institute of Information
Technology, Jaipur 302031, India
e-mail: ashok.dargar@lnmiit.ac.in

D. R. Unune
Department of Materials Science and Engineering, INSIGNEO Institute for in Silico Medicine,
University of Sheffield, Sheffield S1 3JD, UK

- (ii) Electro-discharge cut-off grinding (EDCG),
- (iii) Electro-discharge surface grinding (EDSG).

In EDFG, for performing the machining operation face side of the tool is taken. The tool (grinding wheel) was allowed along the vertical spindle axis and feed direction is upright to the workpiece maintained by servo-mechanism, which also prevents physical contact among the electrodes avoiding the arcing. The rotating motion of the grinding wheel enables better circulation of the dielectric fluid and thus expelling debris effectively from spark gap.

2 Literature Review

During past few years, a number of considerable researches have been made by the researchers over EDFG. Singh et al. [5, 6] proposed the optimization of parameters of electro-discharge diamond face grinding (EDDFG). Chow et al. [7] have placed a rotating electrode below the workpiece and claimed that removal rate of debris is due to the gravitational force and it significantly improved the MRR surface finish. Sato et al. [8] had discussed that the tool rotation serve in an effective flushing technique resulting in better material removal. Kozak et al. [9] observed that relative MRR for EDG was more than that of EDM. Shu et al. [10] and Yan et al. [11] investigated the EDFG and reported that the EDFG efficiency in terms of MRR is 3–7 times better than normal EDM operation. Shu and Tu [12] observed that due to the improvement in flushing techniques, higher material removal and better surface finish are obtained in EDM process. Unune and Mali proposed the use of powder mixed dielectric to improve the process performance of EDSG process in their work [13, 14].

It is cleared from the study of above-mentioned published papers that most of the work has been done to study the effect on response parameters by improving flushing action, tool electrode rotation and sparking efficiency during EDFG and no work have been reported on the selection of input process parameters and their machine levels for EDFG. So, in this work, an experimental study has been carried out to decide the machine levels of input process parameters electrode rotational speed, discharge current and pulse-on time during EDFG for D2 steel. The response parameters were MRR and ASR.

3 Experimentation

3.1 Selection of Workpiece, Tool and Dielectric

AISI D2 steel is high carbon chromium-based steel which is considered semi-stainless cold work steel. D2 steel has high wear and abrasion-resistant properties. The present of chemicals consists in D2 steel as work material is shown in Table 1.

Table 1 D2 steel chemical composition

Elements	Weight in %
C	1.551
Cr	12.01
Mo	0.802
V	0.904
Fe	Balance
Si	0.251
Mn	0.353

Circular rods of machined copper were used as electrode and generate cylindrical profile on workpiece while the mixture of de-ionized water and hydrocarbon oil is used as dielectric. AISI D2 steel has application in the areas that includes forming dies, shear blades, surgical tools and many more.

3.2 Parametric Study

The EDFG process parameters can be broadly classified into four groups: (a) electrical parameters; (b) non-electrical parameters; (c) electrode-related parameter and (d) workpiece-related parameters. Parameters, namely pulse-on time, discharge current and electrode rotational speed (in rpm), are employed as input process parameters in this probationary work, keeping others parameters constant. MRR, TWR and ASR are used as measures of performances parameters. The MRR were calculated using Eq. (1), respectively.

$$MRR = \frac{W_a - W_b * 1000}{\rho \times t} \text{ mm}^3/\text{min} \tag{1}$$

The ASR of the machined surface is measured by using surface roughness tester (Make: MITUTOYO). Three numbers of tests have been carried out and their average value was taken as experimental outcome. The TWR was found to be negligible so it is not considered further in this study.

In this work, one-factor-at-a-time (OFTA) approach is practiced and twenty-one experimental runs were planned subsequently. In OFTA, the value of one process parameters is incremented while the values of other parameters are kept at their central level within the available ranges. Due to the practiced of OFTA, a study of the effect of individual parameters onto the response parameters can be done. It was decided to complete three repetitions in each set of experiments. Table 2 presents the available range and the selected levels of input process parameters.

Table 2 Process parameters and levels

Input process parameters								
Process parameter	Range	Levels						
		L1	L2	L3	L4	L5	L6	L7
Ton (μ s)	0.5–3000	20	100	500	750	1000	1500	2000
IP (A)	0.5–40	5	10	15	20	25	30	35
E_R (rpm)	0–800	100	200	300	400	500	600	700
Fixed process parameters								
Process Parameter	Value	Selection criteria						
Servo voltage	50 V	Machining constraints						
Dielectric pressure	0.3							
Sensitivity	06							
Tool retardation	1.0							

4 Result and Discussions

After completing, the EDFG experimentation works successfully. The input process parameters effect for their level selection was studied for workpiece materials. In this study, MRR and ASR were taken as decision-making criteria and all the experiments were carried out in seven different levels (from Table 2).

4.1 Effect of Discharge Current

It is symbolized by the abbreviation as “IP” and it can be defined as the amount of energy passing through the electrodes in the form of current for the stated pulse. In the present work, it is evident from Fig. 1a that IP for 35 A provides the highest value of MRR, but also at that same value of current surface finish was worst. The best average surface finish was obtained at 5 A as shown in Fig. 1b. So, from the below-mentioned Fig. 1, it can be seen that improve MRR and required ASR can be obtained between range from 5 to 15 A because after 15 A the surface roughness is significantly increasing. Therefore, optimum levels for IP can be taken between 5 and 15 A for further study.

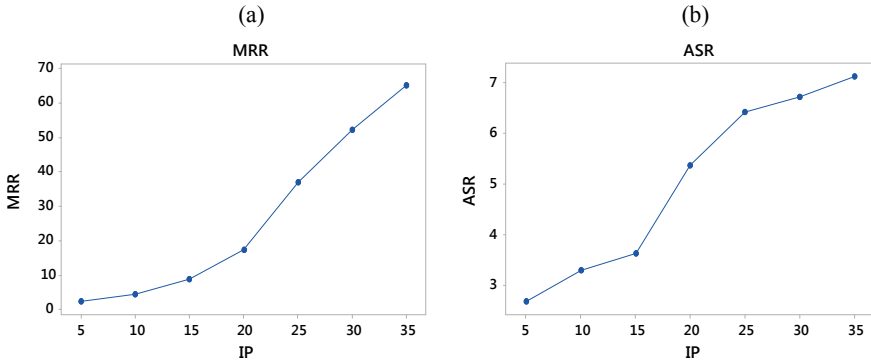


Fig. 1 Effect of discharge current

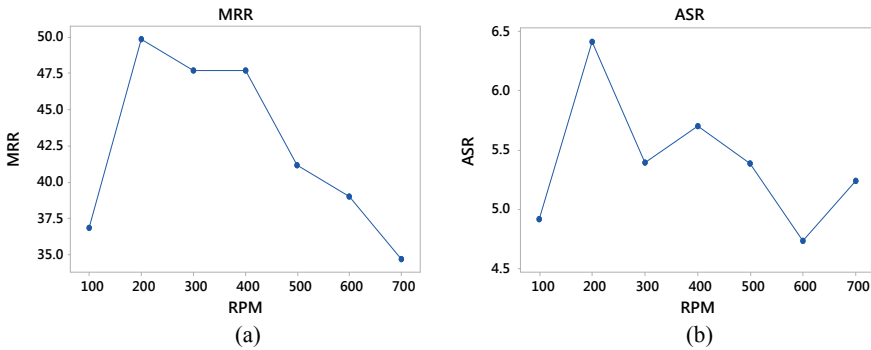


Fig. 2 Effect of electrode rotation (E_R)

4.2 Effect of Electrode Rotational Speed (ER)

The rotational movement of electrode (rpm) supports in improving the MRR and ASR because of effective flushing in working gap. It also helps in removing debris that are created during machining.

In the present work, the effect of ER is shown in Fig. 2. From Fig. 2a, it is marked that ER at 200 rpm provides the highest value of MRR, while the value of ER at 600 rpm provides the best ASR. So, it was decided that better MRR and required ASR can be obtained between 200 and 600 rpm for further study.

4.3 Effect of Pulse-On Time (Ton)

Term “Ton” is abbreviated for pulse-on time and it exemplifies the period of current in microseconds (μs). In the present work, it is evident from Fig. 3a that Ton of 100 μs

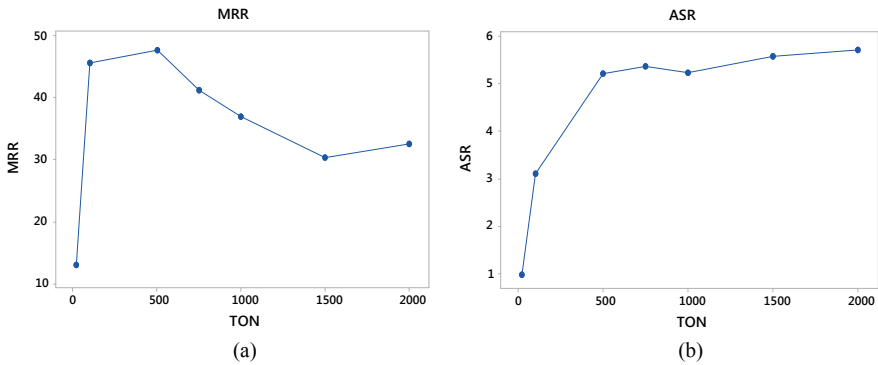


Fig. 3 Effect of pulse-on time (Ton)

Table 3 Optimal levels of process parameters

Parameters	Ton (μs)	IP (A)	ER (rpm)
For MRR	100	35	200
For ASR	20	5	100

provides the highest value of MRR, and simultaneously the Ton at 20 μs gives the best ASR as shown in Fig. 3b. In this study, MRR and ASR are taken as decision-making criteria. Therefore, the optimal level for Ton was decided between 20 and 100 μs for decision-making.

5 Confirmation Test

The confirmation experiment was done by choosing the best levels of the process parameters for MMR (mm^3/min) and ASR (μm) obtained from the resulted graphs as discussed above. The below-mentioned Table 3 represented the best levels for the parameters. The better value of MMR is found to be 55.65 mm^3/min at 100:35:200 and corresponding to that the value for ASR was 9.072 μm . Similarly, the best value of ASR is found to be 2.311 μm at 20:5:100 and corresponding to that MMR was 1.08 mm^3/min . Hence, a significant enhancement in MRR and ASR has been observed.

6 Conclusions

In the current work, the effect of process parameters and selection of their machine levels in EDFG were investigated. The effect of electrode rotational speed, Ton and IP has been investigated on MRR and ASR while machining AISI D2 steel using

EDFG process. Confirmation test has been carried out to verify the maximum MRR and best ASR. The future research could include the study of effect of other process parameters on process capability and their optimum level and surface integrity aspects of EDFG machined D2 steel parts.

References

1. Jain VK (2005) Advanced machining processes. Allied Publisher, New Delhi
2. Beri N, Sachin M, Chitra S, Anil K (2010) Technological advancement in electrical discharge machining with powder metallurgy processed electrodes: a review. *Mater Manuf Processes* 25:1186–1197. <https://doi.org/10.1080/10426914.2010.512647>
3. Pushpendra A, Bharti S, Maheshwari S, Sharma C (2012) Multi-objective optimization of electric-discharge machining process using controlled elitist NSGA-II. *J Mech Sci Technol* 26(6):1875–1883. <https://doi.org/10.1007/s12206-012-0411-x>
4. Hofy HE (2005) Advanced machining processes: nontraditional and hybrid machining processes. McGraw-Hill Companies, New Delhi
5. Singh GK, Yadava V, Kumar R (2012) Robust parameter design and multi-objective optimization of electro-discharge diamond face grinding of HSS. *Int J Mach Machinable Mater* <https://doi.org/10.1504/IJMMM.2012.044919>
6. Singh GK, Yadava V, Kumar R (2012) Modelling and optimization of electro-discharge diamond face grinding of cemented carbide–cobalt composite. *Int J Ind Syst Eng.* 12(2):141–164. <https://doi.org/10.1504/IJISE.2012.048858>
7. Chow HM, Yan BH, Huang FY (1999) Micro slitmachining using electro-discharge machining with modified rotary disk electrode (RDE). *J Mater Process Technol* 91:161–166. [https://doi.org/10.1016/S0924-0136\(98\)00435-X](https://doi.org/10.1016/S0924-0136(98)00435-X)
8. Sato T, Mizutani T, Yonemouchi K, Kawata K (1986) The development of an electro discharge machine for micro hole boring. *Precision Eng* 8:163–168. <https://doi.org/10.1007/s00170-007-1149-y>
9. Kozak J, Oczos KE (2001) Selected problems of abrasive hybrid machining. *J Mater Process Technol* 109:360–366. [https://doi.org/10.1016/S0924-0136\(00\)00824-4](https://doi.org/10.1016/S0924-0136(00)00824-4)
10. Shu KM, Tu GC (2003a) Study of electrical discharge grinding using metal matrix composite electrode. *Int J Mach Tools Manuf* 43:845–854. [https://doi.org/10.1016/S0890-6955\(03\)00048-8](https://doi.org/10.1016/S0890-6955(03)00048-8)
11. Yan BH, Wang CC, Liu WD, Huang FY (2000) Machining characteristics of Al₂O₃/6061Al₁ composite using rotary EDM with a disk like electrode. *Int J Adv Manuf Technol* 16:322–333. <https://doi.org/10.1007/s001700050164>
12. Shu KM, Tu GC (2003b) Study of electrical discharge grinding using metal matrix composite electrodes. *Int J Mach Tools Manuf* 43:845–854. [https://doi.org/10.1016/S0890-6955\(03\)00048-8](https://doi.org/10.1016/S0890-6955(03)00048-8)
13. Unune DR, Mali HS (2017) Parametric modeling and optimization for abrasive mixed surface electro discharge diamond grinding of Inconel 718 using response surface methodology. *Int J Adv Manuf Technol* 93:3859–3872. <https://doi.org/10.1007/s00170-017-0806-z>
14. Unune DR, Marani Barzani M, Mohite SS et al (2018). Fuzzy logic-based model for predicting material removal rate and average surface roughness of machined Nimonic 80A using abrasive-mixed electro-discharge diamond surface grinding. *Neural Comput Appl* 29:647–662. <https://doi.org/10.1007/s00521-016-2581-4>